
GAZİ ÜNİVERSİTESİ
Gazi
1926

DESIGN AND IMPLEMENTATION OF DOUBLE STAGE STARTER/GENERATOR FOR HYBRID PROPULSION SYSTEMS

A THESIS SUBMITTED TO
THE GRADUATE SCHOOL OF NATURAL AND APPLIED SCIENCES
OF
GAZİ UNIVERSITY

BY

Sami ARSLAN

IN PARTIAL FULFILLMENT OF THE REQUIREMENTS
FOR
THE DEGREE OF DOCTOR OF PHILOSOPHY
IN
ELECTRICAL – ELECTRONIC ENGINEERING

JUNE 2023

ETHICAL STATEMENT

I hereby declare that in this thesis study I prepared in accordance with thesis writing rules of Gazi University Graduate School of Natural and Applied Sciences;

- All data, information and documents presented in this thesis have been obtained within the scope of academic rules and ethical conduct,
- All information, documents, assessments and results have been presented in accordance with scientific ethical conduct and moral rules,
- All material used in this thesis that are not original to this work have been fully cited and referenced,
- No change has been made in the data used,
- The work presented in this thesis is original,

or else, I admit all loss of rights to be incurred against me.

Sami ARSLAN

22/06/2023

DESIGN AND IMPLEMENTATION OF DOUBLE STAGE STARTER/GENERATOR FOR HYBRID PROPULSION SYSTEMS

(Ph. D. Thesis)

Sami ARSLAN

GAZİ UNIVERSITY

GRADUATE SCHOOL OF NATURAL AND APPLIED SCIENCES

June 2023

ABSTRACT

The increasing demand for leadership in the socio-military sector has led to a growing focus on the integration of new, compact concepts into UAVs. Advancements in power electronics, motor drives, and material science have enabled the development of more efficient systems, which aligns with a otable trend in UAVs. The conversion of conventional mechanisms to compact electromagnetic systems, making Starter/Generator structures play a crucial role. The Starter/Generator serves two functions: acting as both the primary drive mechanism for initiating the piston engine and supporting the propulsion system in motor mode, while in generator mode, it charges the electronic system battery once the engine is running. Innovative progress in high energy density rare-earth magnets has also facilitated the development of magnetic couplers, enabling magnetically insulated, contactless power transmission between the shafts of the piston engine and the Starter/Generator. This thesis focuses on the development and application of a novel, highly efficient, high-speed, double-stage direct-drive magnetically coupled Starter/Generator, referred to as double stage DCSG. The aim is to provide a hybrid propulsion system for mini/small scale piston-engined surveillance UAVs, ultimately enhancing safety, reliability, usability, endurance, and flight time. The Starter/Generator is an inner-runner permanent magnet brushless synchronous machine, with specifications of 1 kW at 4500 rpm for motor mode and 1.25 kW at 5500 rpm for generator mode. The analytical design model efficiency of the Starter/Generator is 84%. However, through tuning with RMxprt sensitivity analysis, the efficiency is increased to 87%. Further evolutions are achieved through Maxwell 2D/3D FEA and optimizations, resulting in an efficiency of 90%. The magnetic couplers employed in the system adopt a radial synchronous magnetic coupler topology, while meeting stringent torque requirements of 6 N.m and 12 N.m. The coupler efficiency reaches 93.8% at the maximum operating speed and critical angle, and 96.9% at the minimum torque angle and minimum operating speed. By implementing the DCSG in designated mission zones, the UAV propulsion efficiency has been improved from 20% to 45% in cruising. As a result, the flight time has increased by 24%. The absolute error rates are determined to be 13% for the 2D and 6% for the 3D.

Science Code : 90514
Key Words : Hybrid UAV, magnetic coupler, piston engine, Starter/Generator
Page Number : 343
Supervisor : Assoc. Prof. Dr. Tuğba Selcen NAVRUZ
Co-Supervisor : Prof. Dr. İres İSKENDER

HİBRİT İTKİ SİSTEMLERİ İÇİN ÇİFT KADEME STARTER/GENERATOR TASARIMI VE UYGULAMASI

(Doktora Tezi)

Sami ARSLAN

GAZİ ÜNİVERSİTESİ

FEN BİLİMLERİ ENSTİTÜSÜ

Haziran 2023

ÖZET

Sosyo-askeri sektördeki liderlik talebinin artması, yeni ve kompakt kavramların İHA'lara entegrasyonuna olan ilginin büyümesine öncülük etmektedir. Güç elektroniği, motor sürücüleri ve malzeme bilimindeki ilerlemeler, daha verimli sistemlerin geliştirilmesini sağlamaktadır. Bu da İHA'larda dikkate değer bir trend olan geleneksel mekanizmaların kompakt elektromanyetik sistemlere dönüştürülmesiyle uyumlu bir şekilde Starter/Generatör yapılarının önemli bir rol oynamasının önünü açmaktadır. Starter/ Generatör iki işlevi yerine getirir: motor modunda, pistonlu motorun çalıştırılması için ilk tahrik mekanizmasını sağlar ve itki sistemini destekler, generator modunda ise, pistonlu motor çalıştıktan sonra elektronik sistem bataryasını şarj eder. Yüksek enerji yoğunluğuna sahip nadir toprak mıknatıslarında kaydedilen yenilikçi ilerlemeler ise, manyetik kuplörlerin geliştirilmesini kolaylaştırmış ve pistonlu motor ile Starter/Generatör şaftları arasında manyetik olarak izole edilmiş, temassız güç iletimini mümkün kılmıştır. Bu tez, çift kademe DCSG adı verilen yeni, yüksek verimli, yüksek hızlı, çift kademeli doğrudan tahrikli manyetik kuplörlü Starter/Generatörün geliştirilmesi ve uygulanması üzerine odaklanmaktadır. Amaç, mini/küçük sınıfında piston motorlu gözetleme İHA'lar için bir hibrit itki sistemi sağlamak ve böylece güvenliği, güvenirliliği, kullanılabilirliği, dayanıklılığı, ve uçuş süresini geliştirmektir. Starter/Generatör, iç rotorlu, kalıcı mıknatıslı fırçasız senkron bir makine olmakla birlikte, motor modunda 1 kW 4500 d/d, generatör modunda ise 1.25 kW 5500 d/d olacak şekilde tasarlanmıştır. Starter/Generatör'ün analitik tasarım modeline göre verimliliği %84'tür. Ancak RMxprt duyarlılık analizi parametrik çözümlemeleri ile verimlilik %87'ye yükseltilmiştir. Maxwell 2D/3D sonlu elemanlar analizleri ve optimizasyonları ile de verimlilik %90'a çıkarılmıştır. Sisteme entegre edilen manyetik kuplörler, sistem tork gereksinimlerini karşılayan bir radyal senkron manyetik kuplör topolojisini benimsemektedir. Kuplör verimliliği, maksimum çalışma hızı ve kritik açıda %93,8'e, minimum tork açısı ve minimum çalışma hızında ise %96,9'a ulaşmaktadır. DCSG modelinin belirlenen görev bölgelerinde uygulanmasıyla, İHA itki verimliliği seyir halindeyken %20'den %45'e geliştirilmiştir. Sonuç olarak, uçuş süresi %24 oranında arttırılmıştır. Mutlak hata oranları, 2D için %13, 3D için ise %6 olarak hesaplanmıştır.

Bilim Kodu : 90514
Anahtar Kelimeler : Hibrit İHA, manyetik kuplör, piston motor, Starter/Generator
Sayfa Adedi : 343
Danışman : Doç. Dr. Tuğba Selcen NAVRUZ
İkinci Danışman : Prof. Dr. İres İSKENDER

TEŞEKKÜR

Tez çalışmam boyunca her aşamada bana yardımcı olan, doktora tez çalışma süreci boyunca da akademik tecrübelerini benimle paylaşan ve bana rehberlik eden, karşılaştığım her zorlu durumda bana destek olan değerli danışmanlarım Prof. Dr. İres İSKENDER'e ve Doç. Dr. Tuğba Selcen NAVRUZ'a, çalışmama verdiği desteğin yanı sıra tez izleme sürecinde de sabrı ve hoşgörüsü ile her konuda yardımcı olan Prof. Dr. Timur AYDEMİR'e ve Prof. Dr. Ahmet KARAARSLAN'a, çalışmama verdiği kıymetli öneriler ve bitirmem konusunda desteklerini benden esirgemeyen Prof. Dr. Ahmet FENERCİOĞLU'na, Tez çalışma sürecinde tecrübelerini benimle her zaman paylaşan Dr. Tacettin KÖPRÜLÜ'ye ve tez yazım sürecindeki desteklerini esirgemeyen Serhat KARAÇAM'a, Başta Mustafa ÇAKMAK, Atıf Tolga DORUK ve Sait ERDEM olmak üzere birbirinden değerli mesai arkadaşlarıma ve kıymetli dostum Mustafa ÖZSOY'a, Tüm zorlu anlarımda maddi ve manevi desteklerini esirgemeyen Mustafa ERDEM ve Erdem Bobinaj ailesine, Tüm eğitim hayatım boyunca olduğu gibi doktora eğitimim ve tez yazma sürecinde de desteklerini her zaman hissettiğim annem Meral ARSLAN, kayınvalidem Fatma ÇELİK, babam Mustafa Sait ARSLAN, kayınbabam İsmail ÇELİK ve kıymetli kardeşlerim Özlem ARSLAN, Ahmet ARSLAN ve İbrahim ARSLAN'a, Akademik ve sosyal hayatımın tüm önemli noktalarında sabrını ve sevgisini benden esirgemeyen sevgili eşim Büşra ÇELİK ARSLAN'a ve her durumda içime ferahlık veren bal kızım İpek ARSLAN'a

Saygı, sevgi ve teşekkürlerimle…

Sami ARSLAN

TABLE OF CONTENTS

Page

ABSTRACT iv

ÖZET v

TEŞEKKÜR vi

TABLE OF CONTENTS vii

LIST OF TABLES xv

LIST OF FIGURES xvii

SYMBOLS AND ABBREVIATIONS xxvii

1. INTRODUCTION 1

2. LITERATURE OVERVIEW AND SCIENTIFIC CONTRIBUTION .. 5

2.1. Development of UAVs 5

2.1.1. Types of UAVs 7

2.1.2. Classification of the UAVs 8

2.1.3. Regulations 8

2.2. Evolution of More-Electric-Aircraft (MEA) 9

2.3. Progression of Hybrid UAVs 11

2.3.1. NO_x and CO_2 emissions 11

2.3.2. Energy source types for MEA systems 16

2.3.3. Voltage levels of the MEA UAVs 17

2.3.4. Hybridization degree identification of the hybrid UAV 19

2.3.5. Starting procedure and methods of the conventional UAVs 20

2.4. Advances in Starter/Generator (S/G) 22

2.4.1. Standard 27

2.4.2. Patent review 28

2.5. Problem Statement 29

Page

2.6. Proceedings of Magnetic Couplers 33

2.7. Objectives and Scientific Contribution of the Thesis 35

2.7.1. Objectives 35

2.7.2. Scientific contributions 37

3. ELECTRIC MACHINE TOPOLOGIES AND MATERIALS FOR STARTER/GENERATOR AND MAGNETIC COUPLER APPLICATIONS 39

3.1. Machine Topologies for Starter/Generators 39

3.1.1. Surface mounted permanent magnets 48

3.1.2. Interior mounted permanent magnets 49

3.1.3. Squirrel cage rotor bar-equipped permanent magnet machines 52

3.2. Rotor Topologies for Magnetic Couplers 53

3.2.1. Magnetic gear concept 57

3.2.2. Magnetic coupler or magnetic gear assisted electric machines 59

3.3. Materials for Starter/Generator and Magnetic Coupler Structures 63

3.3.1. Magnetism 63

3.3.2. Soft magnetic materials 65

3.3.1. Electrical steel 66

3.3.3. Hard magnetic materials 68

3.3.4. Permanent magnetism and permanent magnets 68

3.3.5. Materials utilized in magnetic couplers 79

4. ANALYTICAL DESIGN AND MODELLING OF SYNCHRONOUS MAGNETIC COUPLERS AND PERMANENT MAGNET STARTER/GENERATORS WITH CONTROL STRATEGIES 81

4.1. Analytical Design Methodologies of Magnetic Couplers 81

4.1.1. Stored energy in permanent magnets 81

4.1.2. Force between permanent magnets 85

Page

4.1.3. Analytical calculation of synchronous active radial magnetic couplers... 87

4.2. Mathematical Modelling of BLDC 97

4.3. Mathematical Modelling of Starter/Generator 101

4.3.1. Mathematical model of SPMSM 104

4.3.2. Mathematical model of IPMSM 106

4.4. Reference Frame Transformation of PM Starter/Generators 109

4.4.1. Matrix form reference frame transformation 110

4.4.2. ABC into dqn variables transformation in the stationary reference frame 111

4.4.3. Transformation between reference frames 112

4.4.4. Complex vector reference frame transformation 113

4.4.5. Torque equation of the Starter/Generator in the d-q axes 116

4.5. Performance Comparison of BLDC and PMSM 117

4.6. Control Strategies for Permanent Magnet Starter/Generators 121

4.6.1. 6-Step commutation in starter and motor mode 124

4.6.2. Field oriented control (FOC) of starter/generator 129

4.6.3. Pulse width modulation strategies 135

4.6.4. Space vector PWM 137

4.6.5. Control Approaches for Starter, Motor and Generator Modes of S/Gs 139

4.7. Analytical Design Equations of Inrunner Radial BLDC Starter/Generator 142

4.7.1. Calculation of direct dependent variables 144

4.7.2. Calculation of the back-EMF 145

4.7.3. Calculation of the magnetic and electric loadings 147

4.7.4. Calculation of the developed power and output equation 148

4.7.5. Calculation of main dimensions 149

4.7.6. Calculation of total flux, pole flux and stator tooth flux 149

4.7.1. Calculation of stator dimensions 150

Page

4.7.7. Calculation of back-EMF 151

4.7.8. Calculation of the stator slot area 152

4.7.9. Rough calculation of permanent magnet dimensions 153

4.7.10. Magnetic equivalent circuit calculation of permanent magnet dimensions 154

4.7.11. Updating process of the design parameters 156

4.7.12. Coil and phase resistance 157

4.8. Analytical Design Equations of Inrunner Radial PMSM Starter/Generator 158

4.8.1. Calculation of direct dependent variables 158

4.8.2. Calculation of the back-EMF 159

4.8.3. Winding factor 160

4.8.4. Calculation of the magnetic and electric loadings 162

4.8.5. Calculation of the developed power and output equation 164

4.8.6. Calculation of main dimensions 164

4.8.7. Calculation of total flux, pole flux and stator tooth flux 165

4.8.8. Calculation of stator dimensions 165

4.8.9. Calculation of the number of turns 166

4.8.10. Calculation of the stator slot area 166

4.8.11. Rough and magnetic equivalent circuit methods to calculate PM dimensions 167

4.8.12. Carter factor 167

4.8.13. Calculation of air gap flux based on the open-slotted type stator 171

4.8.14. Updating process of the design parameters 171

4.8.15. Coil and phase resistance with mean turn length 172

5. DESIGN AND OPTIMIZATION OF THE PROPOSED MAGNETICALLY COUPLED STARTER/GENERATOR (DCSG) 173

5.1. Overview of Proposed DCSG Model 173

Page

5.2. Design Parameters and Hybridization Rate 176

5.2.1. Determination of the inner rotor mounting dimensions of the magnetic couplers 177

5.2.2. Determination of the maximum outer diameter of the DCSG with housing 177

5.2.3. Torque and speed requirements of DCSG stages based on hybridization rate 179

5.3. Design Methodology 182

5.4. Design of Active Radial Magnetic Couplers for DLE-30 and 3W-70R2 Engine 185

5.4.1. Analytical design based on the Virtual Work method 186

5.4.2. Optimetric design approach based on Maxwell 2D magnetostatic FEA .. 189

5.4.3. Pullout torque investigation based on outer diameter and length 190

5.4.4. Determination of the PM thickness based on the static pullout torque 191

5.4.5. Locked-rotor torque investigation based on torque angle 192

5.4.6. Rotor yoke thickness determination 192

5.4.7. Investigation of the magnetic coupler model length 194

5.4.8. Determination of the pole numbers based on pullout torque 195

5.4.9. Optimetric design approach based on Maxwell 2D transient FEA 195

5.4.10. Repulsive torque examination at loss of synchronization 197

5.4.11. Parameter tuning based on Maxwell 3D optimization techniques 199

5.4.12. Magnetic coupler efficiency and losses based on Maxwell 3D FEA 200

5.4.13. Design of the retaining sleeve or bandage 203

5.5. Design of Active Radial Magnetic Couplers for a 3W-55XI Engine 209

5.5.1. Determination of the minimum outer diameter of the inner rotor 210

5.5.2. Correlation of effective air gap diameter based on 2D FEA 212

5.5.3. Investigation of optimum pole number based on 2D FEA 213

5.5.4. Investigation of the PM embrace and offset effect based on 2D FEA 214

Page

5.5.5. Effect of PM type, grade, and temperature on pullout torque based on 2D FEA 215

5.5.6. Investigation of negative torque at loss of synchronization based on 2D FEA 217

5.5.7. Static locked-rotor torque and transient torque ripple analyses..... 218

5.5.8. Investigation of different rotor materials..... 219

5.5.9. Study of pullout torque depending on misalignment length..... 219

5.6. Design of Starter/Generator 220

5.6.1. Operating points of Starter/Generator based on working modes..... 223

5.6.2. Determination of duty-cycle for S/G stages in the DCSG model..... 225

5.6.3. RMxprt sensitivity analyses for stator Slot/Pole number combinations... 227

5.6.4. Stator bore diameter and stack length separation based on RMxprt 228

5.6.5. Stator and rotor yoke thickness determination based on RMxprt..... 228

5.6.6. Air gap clearance investigation based on RMxprt..... 230

5.6.7. Determination of the thickness of permanent magnets based on RMxprt 230

5.6.8. Permanent magnet temperature effect on dynamic torque based on RMxprt 231

5.6.9. Determination of the Carter and Leakage factor based on 2D FEA..... 232

5.6.10. d-axis alignment of the stator and rotor..... 233

5.6.11. Demagnetization study based on 2D FEA..... 234

5.6.12. Matching specific magnetic loading based on 2D FEA 237

5.6.13. Static torque investigation in motor mode based on 3D FEA 238

5.6.14. Induced Back-EMF voltages in generator mode based on 3D FEA..... 239

5.6.15. Stator slot fill factor..... 240

5.6.16. Winding Scheme..... 242

5.6.17. Dynamic torque and torque ripple exploration based on 2D and 3D FEA 243

5.6.18. Investigation of cogging torque and skew techniques..... 245

Page

5.6.19. Investigation of the losses and efficiency of S/Gs based on 3D FEA 248

5.6.20. Retaining sleeve design for Starter/Generator stages 250

5.6.21. Optimization of the Starter/Generator 251

5.7. Field Weakening Control of Starter/Generator 253

6. PROTOTYPING AND TESTING OF DCSG SYSTEM 257

6.1. Prototyping Approach of Double Stage Magnetically Coupled Starter/Generator 257

6.1.1. Test bench setup based on torque measurement for MCs and S/Gs 258

6.1.2. Propeller bench setup based on thrust measurement 261

6.2. Prototyping and Testing of Magnetic Couplers 263

6.2.1. for 3W-55XI 263

6.2.2. for DLE-30 or 3W-70R2 267

6.3. Prototyping and Testing of Starter/Generator Stages as a Servo Motor 271

6.3.1. Hall sensor placement 273

6.3.2. Back-EMF Voltage and Rectification 275

6.3.3. Calculation of the d and q inductances 277

6.3.4. Dynamic load-tests 279

6.3.5. Locked-Rotor or static tests in overload conditions 281

6.3.6. Cogging torque tests 282

6.3.7. Efficiency calculation 283

6.4. Fuel Tests of DLE-30 285

6.5. Prototyping and Testing of Double Stage Magnetically Coupled S/G (DCSG) . 286

6.5.1. Prototyping of the single-stage model 286

6.5.2. Prototyping of the double-stage model 287

6.5.3. Total weight of the models with configurations 289

6.6. Thermal Analyses of DCSG with Magnetic Couplers and Starter/Generators ... 290

Page

6.6.1. Thermal analyses of magnetic coupler stages 290

6.6.2. Thermal analyses of Starter/Generator stages 292

6.7. Fuel Consumption and Flight Time Comparison of Hybrid UAV with DCSG model..... 292

6.7.1. Thermal operation of novel DCSG model..... 299

6.8. Operating both Starter/Generator Stages in Motor Mode 301

7. CONCLUSIONS – FUTURE RESEARCH..... 303

REFERENCES 309

APPENDIX..... 339

CURRICULUM VITAE..... 342

LIST OF TABLES

Table **Page**

Table 2.1. Global UAV classifications for various systems 8

Table 2.2. Advantages of conventional S/G systems 23

Table 2.3. Disadvantages of conventional S/G systems 23

Table 2.4. Comparison of Piston and Turbine Engines 29

Table 2.5. Catastrophic failure types of piston engines 30

Table 3.1. Comparison of IM, SRM and PM 41

Table 3.2. A comprehensive examination of electric machines for aerospace applications 42

Table 3.3. Comparison of 3-phase and multiphase electric machines 43

Table 3.4. Comparison of SMPMs and IMPMs 51

Table 3.5. Conditions for achieving qualified silicon-iron materials 66

Table 3.6. Curie temperature comparison of permanent magnets 74

Table 3.7. Comparison of rare-earth permanent magnets, NdFeB and SmCo 76

Table 3.8. Compound list as possible permanent magnets 78

Table 3.9. List of the materials used in magnetic couplers 80

Table 4.1. Ideal characteristic comparison of BLDC and PMSM 97

Table 4.2. Performance comparison of BLDC and PMSM 118

Table 4.3. Performance comparison of PWM techniques 136

Table 4.4. Switching vectors and sectors 138

Table 4.5. Comparison of voltage produced by different PWM techniques 139

Table 4.6. Selection of specific magnetic loading for BLDC 147

Table 4.7. Selection of specific electric loading for BLDC 148

Table 4.8. Specific magnetic loading for SPMSM 162

Table 4.9. Specific electric loading for SPMSM 163

Table **Page**

Table 5.1. Maximum performance data of DLE-30 with a 19x8 propeller and 3W-55XI with a 24x8 propeller 180

Table 5.2. Torque and speed requirement of DCSG stages for DLE-30 and 3W-55XI. 180

Table 5.3. Analytical calculations for preliminary dimensions 187

Table 5.4. Design parameters obtained by using Maxwell 3D optimization techniques 199

Table 5.5. Properties of Steel316L used in the analytical design of the retaining sleeve 204

Table 5.6. Summary of the analytical design of the retaining sleeve 208

Table 5.7. Analytical design calculations by virtual work approach for preliminary sizing 211

Table 5.8. Design data and constraint summary of the Starter/Generator stages 222

Table 5.9. Independent variables of analytical design 226

Table 5.10. Comparison of Starter/Generator design methods 226

Table 5.11. Coil angles of phase A in the S/G stages 243

Table 5.12. Retaining sleeve design for Starter/Generator 251

Table 6.1. Dimension and performance list of various MCs in summary 263

Table 6.2. Manufacturing methods for servo Starter/Generator model 273

Table 6.3. Back-EMF constant calculation for motor and generator modes 275

Table 6.4. Comparison of the weight and output power of different piston engines 289

Table 6.5. Total weight of the DCSG model with configurations 289

Table 6.6. Hybrid UAV working zone and thrust ratio determination 295

LIST OF FIGURES

Figure **Page**

Figure 2.1. UAV types 7

Figure 2.2. Comparison of aircraft deliveries 11

Figure 2.3. Overview of UAV propulsion systems 13

Figure 2.4. Progress of the global vehicle propulsion system 14

Figure 2.5. Conventional hybrid UAV 15

Figure 2.6. Energy density comparison of energy sources for MEA 17

Figure 2.7. Starting procedure of a conventional aircraft 20

Figure 2.8. Classical torque-speed characteristics of UAV engines across temperatures 22

Figure 2.9. Popular small-scale hybrid UAVs 25

Figure 2.10. Commercial large scale hybrid UAVs 27

Figure 2.11. Australian: (a) Aircraft engine occurrences (2012-2016) (b) The risk level of aircraft engine failure or malfunction (2009-2014) 31

Figure 2.12. Fundamental block diagram of the magnetically coupled double-stage S/G 36

Figure 3.1. Electric machines used in aerospace applications 40

Figure 3.2. Stator types: (a) Slotted-type (b) Slotless-type (c) Coreless-type 41

Figure 3.3. Brushless PM vs IM comparison: (a) Weight (b) Size 44

Figure 3.4. Classifications of permanent magnet synchronous Starter/Generators 45

Figure 3.5. (a) Sinusoidal Back-EMF-Disributed winding (b) Trapezoidal Back-EMF-Concentrated winding 46

Figure 3.6. Rotor and stator configuration: (a) In-Runner structure (b) Out-Runner structure 46

Figure 3.7. S/G topology comparison based on PM orientation (a) Radial flux (b) Axial flux 47

Figure 3.8. Surface mounted permanent magnets (a) d-axis path L_d (b) q-axis path L_q. 48

Figure 3.9. Interior mounted permanent magnets (a) d-axis path (b) q-axis apth (c) PM bridge 49

Figure **Page**

Figure 3.10. Types of IMPMs (a) Internal inset (b) Spoked (c) Specific-V shape..... 50

Figure 3.11. Specifically configured IMPMS (a) W-shape (b) U-shape (c) L-shape..... 51

Figure 3.12. (a) Rotor bars in PMSMs (b) Line-started PMSM 52

Figure 3.13. Comprehensive classifications of magnetic couplers..... 54

Figure 3.14. MCs based on direction of PM magnetization (a) Linear (b) Radial (c) Axial..... 55

Figure 3.15. MCs interaction types (a) Radial Active (b) Radial Reactive (c) Radial Eddy-current (d) Axial Hysteresis 55

Figure 3.16. Different MC rotor topologies..... 56

Figure 3.17. Types of magnetic gears..... 58

Figure 3.18. Coaxial flux modulated MG assisted PMM (a) Outrunner (b) Inrunner.... 61

Figure 3.19. Classification of split magnetically geared machines (a) Decoupled (b) Partially coupled (c) Coupled 62

Figure 3.20. Ring-stator magnetically geared machines..... 62

Figure 3.21. Wound modulator magnetically geared machines 63

Figure 3.22. Summary of magnetic materials..... 64

Figure 3.23. Hysteresis curve of soft and hard magnetic materials 65

Figure 3.24. Development of permanent magnets..... 70

Figure 3.25. Characteristics of ferromagnetic materials (a) Minor loops (b) Hysteresis curve 71

Figure 3.26. Permeance coefficient definition..... 75

Figure 3.27. Commercial coating types of permanent magnets..... 77

Figure 3.28. Orientations (a) Through thickness (b) Through length (c) Radially (d) Multipole (e) Axially (f) Outside diameter (g) Radially in segments (h) Axially in segments (i) Single face (j) Through diameter (k) Diametrically..... 77

Figure 3.29. Commercial rare-earth permanent magnets..... 79

Figure 3.30. Magnetic coupler yoke materials..... 79

Figure 4.1. Stored energy density in PMs..... 82

Figure **Page**

Figure 4.2. (a) Model with a PM and ideal iron (b) Ideal PM demagnetization curve ... 83

Figure 4.3. (a) Permanent magnet field (b) Force between two PMs 86

Figure 4.4. Simple synchronous MCs (a) Active type (b) Reactive type 88

Figure 4.5. Parameters of synchronous active radiallly oriented magnetic couplers..... 90

Figure 4.6. Synchronous active radial MC model for analytical calculations 92

Figure 4.7. Air gap area and volume at (a) Torque angle of zero (b) Torque angle of Θ (c) Axial displacement of zero (d) Axial displacement of dx 93

Figure 4.8. Definition of PM embrace 95

Figure 4.9. Definition of MC dimensions 96

Figure 4.10. (a) PMSM with distributed winding (b) BLDC with concentrated winding..... 98

Figure 4.11. Three-phase BLDC motor (a) Star connected (b) Delta connected 99

Figure 4.12. Armature current I_a in d-q reference system and PMSM operation modes 102

Figure 4.13. PMSM equivalent circuit (a) Motor notation (b) Generator notation 103

Figure 4.14. SPMSM model 104

Figure 4.15. Phasor diagram of SPMSM 106

Figure 4.16. IPMSM model 106

Figure 4.17. Phasor diagram of IPMSM 108

Figure 4.18. Reference frame notation (a) abc coordinates (b) d-q axes 109

Figure 4.19. Stationary reference frame transformation 111

Figure 4.20. Transformations (a) Stationary into rotating (b) Rotating into stationary.. 113

Figure 4.21. Complex space vector..... 114

Figure 4.22. Complex space vector with three-phase quantities 114

Figure 4.23. Rotating vector in an arbitrary reference frame 115

Figure 4.24. General ideal torque speed characteristics 119

Figure 4.25. Ideal model torque ripple comparison (a) BLDC (b) PMSM..... 120

Figure 4.26. Control strategies for Starter/Generators..... 121

Figure **Page**

Figure 4.27. Rotor position sensors (a) Hall sensor (b) Incremental encoder (c) Absolute encoder (d) Resolver 124

Figure 4.28. Driver system of BLDC motor 124

Figure 4.29. Types of Hall sensors 125

Figure 4.30. Hall sensor types (a) Unipolar (b) Latch/Bipolar (c) Omnipolar 126

Figure 4.31. Commutation sequence logic of three-phase BLDC 127

Figure 4.32. Block scheme of the sensorless back-EMF based BLDC driver..... 129

Figure 4.33. General principle of Field Oriented Control (FOC) 130

Figure 4.34. Block diagram of sensored FOC 131

Figure 4.35. Types of sensorless FOC 133

Figure 4.36. Position and speed estimation methods for sensorless FOC 133

Figure 4.37. Comparison of vector control algorithms 135

Figure 4.38. Classification of PWM techniques 136

Figure 4.39. Switching states of SVPWM (a) $V_0(0,0,0)$ (b) $V_1(1,0,0)$ (c) $V_2(1,1,0)$ (d) $V_3(0,1,0)$ (e) $V_4(0,1,1)$ (f) $V_5(0,0,1)$ (g) $V_6(1,0,1)$ (h) $V_7(1,1,1)$ 137

Figure 4.40. Exploration of the space vector diagram 138

Figure 4.41. Operational zone of modes for aerospace Starter/Generator..... 140

Figure 4.42. Simple configuration of the inverter/converter stage of Starter/Generator 140

Figure 4.43. Block scheme of the S/G using bidirectional converter topology 141

Figure 4.44. 2D magnetic circuit model illustration of surface mount PMMs 142

Figure 4.45. One-pole magnetic circuit model of surface mount PMMs 143

Figure 4.46. (a) Flux linkage (b) Back-EMF as a function of rotor..... 146

Figure 4.47. Phase flux linkage in real operation 146

Figure 4.48. Stator slot dimensions..... 150

Figure 4.49. Slot area explanation 152

Figure 4.50. Calculation approach for the rough method for magnet design 153

Figure 4.51. 4-pole machine exploration (a) Model (b) Magnetic equivalent circuit..... 155

Figure **Page**

Figure 4.52. Selection of permeance coefficient 156

Figure 4.53. Winding factor (a) Distribution factor (b) Pitch factor (c) Skew factor..... 160

Figure 4.54. (a) Flux diagram under a stator slot along one slot pitch (b) The behavior of the air-gap flux density along a slot pitch..... 168

Figure 4.55. Distribution of air-gap flux density at a distance of one slot pitch 169

Figure 4.56. Carter factor for closed-slotted stator type 169

Figure 4.57. Carter factor for open-slotted stator type..... 170

Figure 4.58. Air gap flux density over open-slotted stator 171

Figure 5.1. Advanced block scheme of the proposed multiple modular DCSG system. 174

Figure 5.2 Proposed DCSG model workout in the thesis (a) Full 3D model of DCSG structure for DLE-30 (b) Split 3D model of DCSG structure for DLE-30.. 175

Figure 5.3. The shaft dimensions of the (a) DLE-30 engine (b) 3W-55XI engine..... 177

Figure 5.4. Propeller for (a) DLE-30 (b) 3W-55XI 178

Figure 5.5. Stages of the DCSG model..... 179

Figure 5.6. Design flowchart of the DCSG system 182

Figure 5.7. Design scheme of DCSG system (a) Design methodology (b) Design flowchart 185

Figure 5.8. Magnetic coupler stage for DLE-30 and 3W-70R2 (a) Model (b) Dimensions..... 186

Figure 5.9. Definition of parameters for Virtual Work method..... 188

Figure 5.10. (a) Mesh distribution of model (b) Pole embrace and pole arc offset definition 189

Figure 5.11. (a) Pullout torque in outer diameter and length (b) Torque density depending on the outer diameter of the outer rotor..... 190

Figure 5.12. Static pullout torque with respect to changes in PM thickness 191

Figure 5.13. Locked-rotor torque depending on torque angle 192

Figure 5.14. Pullout torque with respect to changes in rotor yoke thickness 193

Figure 5.15. (a) Flux density of rotor yokes (b) flux distribution for the 10-pole configuration 193

Figure **Page**

Figure 5.16. Air gap flux density distribution at no-load and full-load 194

Figure 5.17. Pullout torque depending on coupler length 194

Figure 5.18. Pullout torque depending on the number of poles 195

Figure 5.19. (a) Dynamic torque without sleeve at critical angle (b) Dynamic torque with sleeve at critical angle (c) Torque ignoring dynamic model at critical angle 197

Figure 5.20. (a) Attraction torque at out of synchronization if piston shaft is not locked (b) Attraction torque at out of synchronization if piston shaft is locked ... 198

Figure 5.21. (a) Rotor core loss depending on torque angle (b) Hysteresis loss of PMs depending on torque angle (c) Induced eddy-current loss of PMs depending on torque angle (d) Induced eddy-current and hysteresis loss of retaining sleeve (e) Coupler efficiency at critical angle depending on operating speed (f) Coupler efficiency at maximum speed depending on torque angle 202

Figure 5.22. (a) Inner rotor parameters (b) Sleeve total deformation (c) Sleeve equivalent stress (d) Sleeve elastic strain (e) Sleeve X-axis directional deformation 205

Figure 5.23. 3D drawing of the single-stage DCSG model 209

Figure 5.24. Mounting illustration of the (a) Inner rotor; (b) Inner flange 210

Figure 5.25. Magnetic coupler model definitions of (a) Parameters (b) Materials 211

Figure 5.26. Pullout torque versus effective air gap length in model length 212

Figure 5.27. (a) Torque vs same pole number (b) Torque density vs different pole number 213

Figure 5.28. Pullout torque versus: (a) PM embrace (b) PM offset 214

Figure 5.29. Effect of PMs based on (a) Grade (b) Type (c) Orientation (d) Temperature 216

Figure 5.30. Negative torque at loss of synchronization depending on operating speed 217

Figure 5.31. (a) Locked-rotor torque versus torque angle (b) Torque ripple in revolutionM 218

Figure 5.32. Investigation of the effect of different rotor materials on torque 219

Figure 5.33. (a) Misalignment exhibition (b) Pullout torque versus misalignment length 220

Figure **Page**

Figure 5.34. (a) Single-stage DCSG integration (b) Integration dimensions 222

Figure 5.35. Output power and specific fuel consumption curves of (a) DLE-30 with 19x8 wooden propeller (b) 3W-55XI with 24x8 wooden propeller 224

Figure 5.36. Determination of duty-cycle of S/G stages 225

Figure 5.37. Stator slot and pole number selection (a) Parameters (b) Space harmonics 227

Figure 5.38. Stator bore diameter and model length separation 228

Figure 5.39. Thickness of stator and rotor yokes determination..... 229

Figure 5.40. Magnetic flux density distribution of the stator and rotor..... 229

Figure 5.41. Air gap determination based on specific electric loading 230

Figure 5.42. Air gap determination based on specific electric loading 231

Figure 5.43. Dynamic output torque versus magnet temperature changes 232

Figure 5.44. Carter factor determination of the single-stage Starter/Generator of the DCSG 232

Figure 5.45. Leakage factor of the single-stage S/G..... 233

Figure 5.46. Rotor alignment mechanical angle illustration..... 234

Figure 5.47. Demagnetization study approach 235

Figure 5.48. Demagnetization study (a) Worst-case (b) Overcase 236

Figure 5.49. Demagnetization over the surface of the PMs in the overcase situation.... 237

Figure 5.50. Determination of the specific magnetic loading based on 2D FEA 238

Figure 5.51. (a) Static torque examination versus absolute torque angle (b) i_d=0 control 238

Figure 5.52. Induced back EMF at (a) Minimum speed (b) Maximum speed..... 239

Figure 5.53. Output of the full-wave rectifier depending on different input voltages.... 240

Figure 5.54. Stator slot fill factor 241

Figure 5.55. Control schematics of the S/G staqes in (a) Motor mode (b) Starter mode..... 244

Figure 5.56. Output torque examination (a) Motor mode (FOC) (b) Starter mode (6-step)..... 245

Figure **Page**

Figure 5.57. Cogging torque investigation of the S/Gs stages 246

Figure 5.58. Skew techniques for minimization of cogging torque and torque ripple ... 247

Figure 5.59. Effect of the skew for the S/G stages 247

Figure 5.60. Loss table of Starter/Generator 248

Figure 5.61. (a) Efficiency map in motor and generator mode (b) 2D model (c) 3D model 250

Figure 5.62. Applicable optimization techniques using Ansys Maxwell 252

Figure 5.63. Optimization of the Starter/Generator stages 253

Figure 5.64 General ideal torque speed curve of surface mount Starter/Generator 254

Figure 5.65. S/G Phasor diagram in ideal operating conditions (a) At low speed (b) At rated speed (c) Beyond rated speed without I_d (not-feasible) (d) Beyond rated speed with I_d [389] 255

Figure 6.1. Organization scheme of system manufacturing for performance tests 258

Figure 6.2. Direct dynamic bench: (a) Magnetic couplers with servo (b) Magnetic couplers for hysteresis (c) Starter/Generator with hysteresis (d) Measurement panel 259

Figure 6.3. Propeller test bench for (a) Single DCSG (b) Sensor panel (c) Double DCSG 262

Figure 6.4. Various MC productions of: (a) 8-pole/0.8-embrace/3 mm-PM thickness/10 mm length; (b) 8-pole/0.98-embrace/4 mm-PM thickness/10 mm length; (c) 10-pole/0.8-embrace/4 mm-PM thickness/10 mm length; (d) 10-pole/0.98-embrace/4 mm-PM thickness/10 mm length; (e) 10-pole/0.98-embrace/4 mm-PM thickness/20 mm length 264

Figure 6.5. Assembly of (a) MC for dynamic tests (b) MC with piston engine and propeller 264

Figure 6.6. Locked-rotor test results of (a) Higher torque density (b) Lower torque density 265

Figure 6.7. Test results of the 10-pole, 0.98-embrace, and 10 mm length model (a) Pullout torque in transients (b) Static torque versus torque angle in magnetostatics 266

Figure 6.8. Transient pullout torque test results for MC with 20 mm length 268

Figure 6.9. Static torque results of the optimum model depending on the torque angle 269

Figure **Page**

Figure 6.10. Manufacturing of (a) Housing, flanges, stators (b) Windings (c) Shaft, rotors, sleeve (d) 3D model (e) Servo Starter/Generator (f) 0-3 kW Load bank for tests 271

Figure 6.11. Driving methods (a) FOC with encoder (b) 6-step with Hall sensor or sensorless..... 273

Figure 6.12. Summary of the test methods for direct-dynamic and propeller test systems 274

Figure 6.13. (a) Test bench back-EMF (b) FEA vs turn number (c) Motor mode back-EMF (d) Generator mode back-EMF (e) Rectified DC voltage for generator mode..... 276

Figure 6.14. (a) Shaft locking method (b) Inductance measurement..... 278

Figure 6.15. Output torque comparison of motor motor, generator mode and FEA 279

Figure 6.16. S/G thermal issues in generator mode (a) FloEFD CFD (b) Real time thermal..... 280

Figure 6.17. Static torque test comparison..... 282

Figure 6.18. Cogging torque determination (a) Maxwell FEA (b) Test bench..... 283

Figure 6.19. (a) Efficiency comparison of FEA and test results (b) Torque-Speed-Efficiency curve of S/G in motor and generator modes..... 284

Figure 6.20. DLE-30 fuel consumption and thrust test..... 285

Figure 6.21. Single stage S/G model 286

Figure 6.22. Double stage S/G model (a) Direct-mounted cross-section (b) Direct-mounted 3D (c) Magnetically coupled cross-section (d) Magnetically coupled 3D 288

Figure 6.23. Thermal analyses of MCs for DLE-30 and 3W-55XI engines with lengths of (a) DLE-30, 10 mm (b) DLE-30, 30 mm (c) 3W-55, 10 mm (d) 3W-55, 30 mm..... 291

Figure 6.24. Thermal analyses of S/G in generator mode: Worst-case in ambiant flow 292

Figure 6.25. 3W-55XI piston engine SFC and time spent curve 294

Figure 6.26. Efficiency comparison, piston engine, S/G and overall system 295

Figure 6.27 Optimizing the fuel consumption and flight time of hybrid UAVs..... 296

Figure 6.28. Hybrid system power capability vs conventional system..... 296

Figure **Page**

Figure 6.29. Weight reduction with (a) 100 kW piston prop aircraft versus hybridization rate (b) DCSG at 100% hybridization (c) DCSG at 50% hybridization 297

Figure 6.30. Performance comparison of DCSG structures versus conventional systems 299

Figure 6.31. Propulsion comparison of DCSG structures versus conventional systems 299

Figure 6.32. Thermal analyses of DCSG model (a) with cooling slots on front and back flanges (b) with fins on housing (c) air flow temperature 300

Figure 6.33. Temperature monitoring (a) at cruise speed (b) at rest after 1 hour operation..... 301

Figure 6.34. Output torque with torque ripple in motor modes of both S/G stages..... 302

SYMBOLS AND ABBREVIATIONS

The symbols and abbreviations used in this study are presented below with their explanations.

Symbols	Explanations
A	Area
ac	Specific electric loading
ar	Aspect ratio
B	Magnetic flux density
$\mathbf{B_{av}}$	Specific magnetic loading
$\mathbf{B_g}$	Air gap flux density
$\mathbf{B_m}$	Permanent magnet flux density
$\mathbf{B_r}$	Residual flux density
$\mathbf{BH_{max}}$	Maximum energy product
Ce	Cerium
Co	Cobalt
$\mathbf{CO_2}$	Carbon dioxide
d	Diameter
db	Desibel
dx	Axial displacement
dW	Change in energy
dϴ	Radial displacement
E	Back-emf voltage
f	Frequency
F	Force exerted
Fe	Iron
G	Output coefficient
h	Height
H	Magnetic field intensity
$\mathbf{H_{c,i}}$	Intrinsic coercivity

Symbols	Explanations
$\mathbf{HF_E}$	Hybridization factor for energy
$\mathbf{HF_P}$	Hybridization factor for power
$\mathbf{H_m}$	Permanent magnet field intensity
Hz	Hertz
i	Current
$\mathbf{K_f}$**, FF**	Fill factor
$\mathbf{k_s}$	Slope factor
$\mathbf{k_w}$	Winding factor
l	length
J	Current density
L	Inductance
$\mathbf{l_m}$	Permanent magnet length
m	Phase number
M	Mutual inductance
$\mathbf{M_r}$	Remanent magnetization
$\mathbf{M_s}$	Saturation magnetization
Nd	Neodymium
NdFeB	Neodymium-iron-boron
$\mathbf{NO_x}$	Nitrogen oxides
$\mathbf{N_m}$	Pole number
$\mathbf{N_p}$	Winding parallel path
$\mathbf{N_s}$	Stator slot number
p	Loss
P	Real power
$\mathbf{P_c}$	Permeance coefficient
$\mathbf{P_{EM,max}}$	Maximum power of the electric motor
$\mathbf{P_{ICE,max}}$	Maximum power of the ICE
$\mathbf{P_{max}}$	Overall power demand
Pr	Paraseodium
Q	Reactive power

Symbols	Explanations
r	Radius
R	Resistance
S	Apperant power
Sm	Samarium
SmCo	Samarium-cobalt
T	Torque
T_c	Critical temperature
t_g	Air gap width
T_{max}	Maximum temperature
u	Voltage component
v	Volume
V	Voltage
w	Angular velocity
W	Stored energy
W_g	Stored energy in the air gap
x	Displacement
μ_o	Free-space permeability
μ_r	Relative permeability
β	Pole embrace
ρ	Resistivity
η	Efficiency
ø	Flux
ψ	Flux linkage
τ_p	Pole pitch
α, Θ	Angle
°C	Degree celcius
∂A	Vector potential
ΔE_i	Power requirement of the electric motor
ΔE	Power demand
2p	Pole number

Abbreviations	Explanations
AI	Artificial intelligence
AMC	Active magnetic coupler
APU	Auxilary power unit
AWG	American wire gauge
BLDC	Brushless DC motor
cAca	Coil arm copper area
CAD	Computer aided design
cAsc	Single conductor copper area
CATO	Catapult assisted take-off
CFD	Computational fluid dynamics
CPSR	Constant power speed range
CSFC	Constant stator flux control
DCSG	Directly coupled Starter/Generator
DFO	Direct field oriented control
DoH	Degree of hybridization
DSPM	Doubly salient permanent magnet
DTC	Direct torque control
DUT	Device under test
EAG	Effective air gap
EASA	European union aviation safety agency
EGS	Electrical-generator set
EM	Electric machine
EMF	Electromotive force
EPGS	Electrical power-generation systems
EU	European union
FAA	Federal aviation administration
FEA	Finite element analysis
FEM	Finite element method
FF	Fill factor
FOC	Field oriented control

Abbreviations	Explanations
GA	Genetic algorithm
gAca	Coil arm gross area
gAss	Stator slot gross area
GCD	Greatest common divisor
GO	Grain oriented
HEV	Hybrid electric vehicle
HP	Horse power
HPS	Hybrid power source
ICE	Internal combustion engine
IFO	Indirect field oriented control
IEC	International electrotechnical commission
IM	Induction machine
IPM	Interior permanent magnet
IPMSM	Interior mounted permanent magnet synchronous machine
IMPM	Interior mounted permanent magnet
ISA	Integrated starter alternator
ISG	Integrated starter generator
IP	Integrated powder
IVD	Ion vapor deposition
JATO	Jet assisted take-off
LIDAR	Light detection and ranging
LoS	Loss of synchronization
LSPMSM	Line-started permanent magnet synchronous motor
MC	Magnetic coupler
MCEM	Magnetic coupler assisted electric machine
MEA	More electric aircraft
MG	Magnetic gear
MGEM	Magnetic gear assisted electric machine
MOGA	Multi objective genetic algorithm
MTPA	Maximum torque per ampere

Abbreviations	Explanations
NGO	Non-grain oriented
PDU	Power drive unit
PE	Piston engine
PLL	Phase-Locked Loop
PI	Proportional-Integral
PM	Permanent magnet
PMAC	Permanent magnet alternating current
PMFS	Permanent magnet flux switching
PMM	Permanent magnet machine
PMSG	Permanent magnet synchronous generator
PMSM	Permanent magnet synchronous machine
PTC	Positive temperature coefficient
PWM	Pulse width modulation
RMC	Reactive magnetic coupler
RPAS	Remotely piloted aircraft system
rpm	Revolution per minute
rps	Revolution per second
RPV	Remotely piloted vehicle
S/G	Starter/Generator
SFC	Specific fuel consumption
SI	Spark ignition
SMPM	Surface mounted permanent magnet
SNLP	Sequential nonlinear programming
SPM	Surface mount permanent magnet
SPMSM	Surface mounted permanent magnet synchronous machine
SRM	Switched reluctance machine
SPWM	Sinusoidal pulse width modulation
SVPWM	Space vector pulse width modulation
SWG	Standard wire gauge
TE	Turbine engine

Abbreviations	Explanations
UAS	Unmanned aerial systems
UAV	Unmanned aerial vehicle
UNFCCC	United nations framework convention on climate change
VFD	Variable frequency drive
VSI	Voltage source inverter
VVC	Voltage vector control
WFDSM	Wound-field doubly salient machine
ZCD	Zero crossing detection

1. INTRODUCTION

Unmanned aerial vehicles (UAVs) have emerged as a disruptive technology in the aviation industry, with their rapid development and proliferation across various domains. In recent years, UAVs have made significant strides in terms of technological advancements, and their use has gained momentum worldwide [1, 2]. UAVs have been employed for various applications, including aerial photography, surveying, mapping, scientific research, law enforcement, search and rescue operations, and military operations [3, 4]. Conventionally, UAVs are powered by internal combustion engines (ICEs) for propulsion. However, piston engines (PEs) have become increasingly popular in small and medium-sized UAVs due to their high cycle efficiency, shorter start-up time, lower maintenance requirements, and higher unit volume power density [5]. PEs are internal combustion engines that convert heat energy into motion energy and require the first actuation movement.

As environmental concerns continue to grow, along with the desire to improve the safety and reliability of all aircraft, the more-electric-aircraft (MEA) initiative has been launched [6-10]. This initiative has led to the need for piston-engined UAVs to adopt more efficient electrical systems that can increase endurance while avoiding heavy mechanical mechanisms [11]. Conventional UAV systems lack internal starters and require an external drive mechanism for the piston engine to start up [12]. They also require a large battery pack to meet all electrical system needs. These issues require the development of more efficient and innovative hybrid systems [13-18]. The significance of hybrid UAVs in military operations underscores their strategic value, while their rapidly growing socioeconomic relevance demands increased focus on research in this field and drives the urgent need to optimize the utilization of alternative platforms [19-22].

The integration of a Starter/Generator (S/G) with a piston engine has enabled the development of more efficient hybrid systems [23-26]. The development of power electronics, semiconductor materials, permanent magnets (PMs), and control engineering has ensured that S/G structures are a key function in increasing power density in hybrid UAV systems [27-31]. An S/G is a unique and efficient rotary electric machine that can operate as both a motor and a generator [32-34]. In this way, the PE can be driven first in motor mode, and the battery group can be charged in generator mode while cruising [35].

Motivation

Conventional hybrid UAV systems offer several benefits. However, they are also susceptible to catastrophic failures due to the direct coupling between the propeller and the rotor of the piston engine and Starter/Generator. In the event of shaft failure, this direct coupling can cause the entire aircraft to crash, leading to potential damage and loss of life [36-39]. Moreover, the use of out-runner S/G structures to accommodate the PE shaft and facilitate ease of installation leads to inefficient system insulation and cooling, thereby impeding the overall performance and reliability of the system [40]. Intensive efforts to alleviate these harmful conditions and limitations led to the idea of adopting magnetic couplers (MCs) and S/Gs as a combined solution [41]. Hence, the crucial task of effectively and covertly separating the shafts of the aircraft engine and the electrically powered system, usually the S/G, places a significant responsibility on the MCs [42-46]. MCs provide contactless torque transmission and hermetic separation using static seals or containment shrouds, which are essential for hybrid UAVs [47]. This ensures that the S/G can operate in motor mode in case of any malfunction, allowing for a safe landing of the aircraft on the ground [48].

This thesis proposes the design, manufacturing, and testing of a highly efficient, high-speed, direct-drive, double stage magnetically coupled Starter/Generator, introducing a novel concept to the 2iteratüre designated DCSG. Specifically, tailored for customised surveillance UAVs equipped with 3W-55X, 3W-70R2 and DLE-30 piston engines, this advanced technology provides a significant improvement in performance and capability, representing a pioneering breakthrough in the field of UAV technology. Through the modular manipulation of the DCSG stages, precise control over the hybridization rate of the system can be achieved, enabling seamless integration with a wide range of UAVs varying in size and power. This versatile approach offers enhanced flexibility and efficiency in coupling advanced hybrid propulsion systems, underscoring the potential of DCSG technology to revolutionize the field of UAVs. This innovation has practical applications and adds value to aeronautics research. The proposed hybrid propulsion system improves protection, usability, endurance, simplicity, maintenance and flight time, based on finite element analyses to overcome the challenges of conventional hybrid topologies. The unique design capability of the dual-stage DCSG allows it to be used primarily in aerospace applications, but also in many other industrial fields such as automotive, process engineering, hydraulics, waste-heat recovery systems, and compressors [49-51].

Thesis layout

Chapter 2 presents a detailed and comprehensive literature review that traces the evolution of various technologies that form the foundation of this thesis, including UAVs, more-electric aircrafts (MEAs), hybrid UAVs, Starter/Generators (S/Gs), Magnetic Couplers (MCs), and the double stage Magnetically-Coupled Starter/Generator (DCSG) concept. The chapter contextualizes the research and highlights the significance of the DCSG concept.

Chapter 3 of this document offers an in-depth examination of electric machine topologies that can be effectively employed in S/G structures and magnetic couplers for various applications. The chapter provides a detailed analysis of the different types of materials and electric machines that are most suitable for these structures, along with their specific features, advantages, and limitations.

Chapter 4 presents readers with an extensive analysis of the analytical equations for the MCs and S/Gs, along with their control structures, exploring their interdependence and impact on the overall system performance in a comprehensive manner.

Chapter 5 provides a comprehensive and in-depth analysis of the intricate electrical, magnetic, and thermal design of the magnetically coupled double-stage synchronous Starter/Generator (DCSG) system, expertly adapted to suit the requirements of 3W-55X, 3W-70R2, and DLE-30 piston engines. The chapter offers a comprehensive understanding of the electrical, magnetic, and thermal interplay of the DCSG system through a detailed design and implementation examination.

Chapter 6 occupies a pivotal position in the thesis, providing a detailed and inclusive account of the prototype production, rigorous testing procedures, and empirical results of the proposed DCSG systems. In addition, the chapter outlines the various testing protocols that were employed to ensure the robustness and reliability of the prototype, including dynamic response testing, static tests, and short-circuit testing.

Chapter 7 holds immense significance in the thesis as it presents a detailed and wide-ranging summary of the conclusions and recommendations drawn from the entire thesis, encapsulating the key findings and insights gained throughout the research process.

2. LITERATURE OVERVIEW AND SCIENTIFIC CONTRIBUTION

This section offers an in-depth analysis of UAV development, including various types of UAVs, engine types, market research, and regulations. Additionally, it delves into the emergence of More-Electric-Aircraft (MEA) and hybrid UAV systems, providing a thorough explanation of their numerous benefits over conventional UAVs, backed up by compelling real-world examples. The chapter meticulously explores the development of Starter/Generator (S/G) technology and its associated advantages, as well as the different S/Gs used in UAVs. Moreover, it thoroughly examines the hybridization rate in UAVs, identifies the limitations of conventional hybrid UAV systems, and proposes a novel model that offers an innovative solution. The proposed model's scientific contribution to the field is explained broadly, highlighting its potential to advance hybrid UAV systems and making it a valuable addition to the literature.

2.1. Development of UAVs

UAVs have a rich history dating back to the mid-19th century when balloons and kites were used for reconnaissance purposes during wars. The modern development of UAVs started in the 20th century, and they have been referred to by various names, including drone, RPV (Remotely Piloted Vehicle), and RPAS (Remotely Piloted Aircraft System). While there are some technical differences between these terms, they generally refer to the same system. However, due to the negative connotations associated with military drone strikes against civilians, the term Unmanned Aircraft System (UAS) is becoming more popular in civilian contexts. It is also common to use the term drone to refer specifically to small UAVs [52].

During World War II, both the Allies and Axis powers developed UAVs for reconnaissance and bombing missions. In the 1950s and 1960s, the United States Air Force began developing UAVs for reconnaissance purposes. The first successful UAV was Ryan Model 147, which was used in the Vietnam War [53]. In the 1970s, the United States military began using UAVs for reconnaissance and surveillance purposes. In the 1980s and 1990s, UAVs were further developed and used in conflicts such as the Gulf War and the Balkan conflicts [54]. The Predator drone, first introduced in the 1990s, was a significant breakthrough in UAV technology.

The United States developed the MQ-1 Predator in the 1990s, which was used extensively in the wars in Iraq and Afghanistan. In the early 2000s, Israel developed the Heron UAV, which has been used for both civilian and military purposes [55]. The European Union developed the EuroMALE UAV in the 2010s, which is a long-endurance surveillance drone. One of the most significant developments was the introduction of the MQ-9B SkyGuardian by General Atomics. The MQ-9B was an upgraded version of the Reaper, with improved sensors and communications systems [56].

In recent years, UAV technology has continued to advance rapidly. One of the most significant developments is the use of artificial intelligence (AI) to enable UAVs to fly autonomously and make decisions on their own [57]. This technology is expected to have a significant impact on military, and civilian applications such as agriculture, transportation, and public safety. One of the most notable examples of this is the Skyborg program by the US Air Force, which is developing autonomous UAVs to support manned aircraft in combat. In 2018, the US Air Force deployed the MQ-9 Reaper drone to Poland, marking the first time that the drone had been deployed to a NATO country in Europe. In 2019, Australian drone manufacturer Emesent launched Hovermap, a drone-mounted LIDAR (Light Detection and Ranging) mapping system that can be used to map underground spaces, such as mines and caves [58]. In 2020, drones were used extensively in the fight against the COVID-19 pandemic, with drones being used to deliver medical supplies and to disinfect public spaces [59].

In 2021, drone delivery services began to take off, with companies such as Amazon and Wingcopter conducting successful test deliveries in the US and Europe [60]. Additionally, in 2021, the US Air Force conducted the first flight test of the Skyborg unmanned aircraft system, which is designed to operate alongside manned aircraft and conduct a range of missions [61]. In 2022, drone technology continued to advance, with new drones being released for a range of applications, from aerial photography to industrial inspections [62].

UAVs have a broad range of applications, with defense being their most common use. They are utilized for surveillance, tracking, airborne data collection, and armed attacks . In contrast to manned flights, UAVs offer a low-risk and cost-effective solution in civilian areas [63].

With hyperspectral imagers, air composition sensors, and other equipment, UAVs have also found new applications in civilian areas, including agriculture, forestry, marine pollution and waste tracking, disaster monitoring, land mapping, wildlife and ecological monitoring, traffic monitoring, geoscience and mining studies, gas leakage monitoring, plant and forest species identification, climate change research, and environmental damage monitoring [64].

2.1.1. Types of UAVs

Various types of UAVs are available, which can be classified based on their intended applications and airframe designs, as depicted in Figure 2.1 [65, 66].

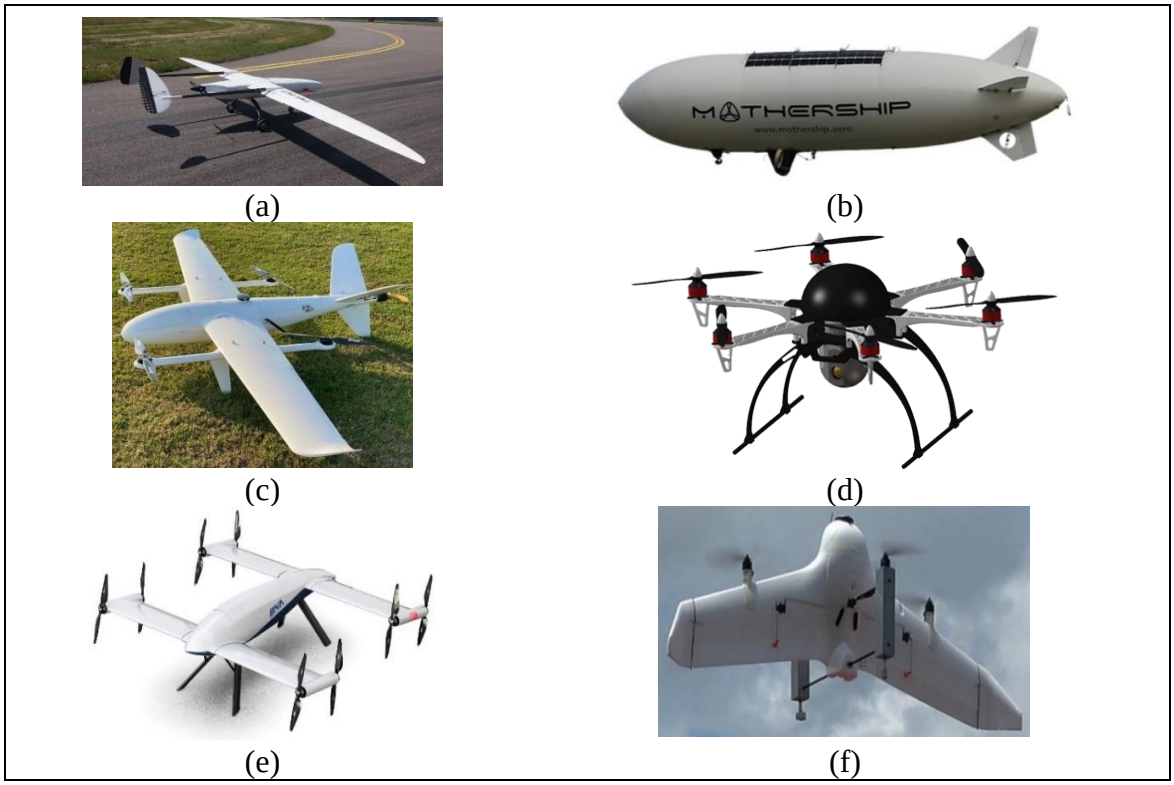


Figure 2.1. UAV types: (a) UAVOS fixed-wing (b) Mothership lighter-than-air (c) SkyLane VTOL (d) Rotovigil rotary-wing (e) BNA-Nurol tilt rotor (f) Skywalker tail sitter

The UAV market has witnessed the fastest growth rate among all segments of the global aviation industry since 2008, with nearly 50 countries engaged in UAV production. The leading UAV manufacturers in the world include Zipline, Measure, Cyberhawk, Hemav, Flirtey, Sky-Futures, Aerodyne, Terra Drone, Northrop Grumman, BAE Systems, General Atomics Aeronautical, Honeywell Aerospace, Qinetiq, and Israel Aerospace Industries [64].

Several classification schemes categorize UAV systems by their operational characteristics and capabilities. [62, 67-69]. These schemes aid in operational and regulatory purposes by assessing the risk of accidents such as ground impact or midair collisions.

2.1.2. Classification of the UAVs

Table 2.1 provides a comprehensive classification of UAVs, highlighting their diverse systems, capabilities, and differentiation [70].

Table 2.1. Global UAV classifications for various systems

	Mass (kg)	Range (km)	Altitude (m)	Endurance (h)
Micro	<5	<10	250	1
Mini/Small	<20/25/30	<10	150-300	<2
Close range	25-150	10–30	3000	2–4
Short range	50-250	30–70	3000	3–6
Medium range	150-500	70–200	5000	6–10
Medium range endurance	500-1500	>500	8000	10–18
Low altitude long endurance	15-25	>500	3000	>24
Medium altitude long endurance	1000-1500	>500	3000	24–48
High altitude long endurance	2500-5000	>2000	20000	24–48
Stratospheric	>2500	>2000	>20000	>48
Unmanned combat AV	>1000	1500	12000	2
Decoys	150-250	0–500	50-5000	<4

2.1.3. Regulations

UAV regulations in the European Union (EU) are defined by the European Union Aviation Safety Agency (EASA), which strives to ensure the highest level of safety and environmental protection in civil aviation. EASA develops and implements common rules and standards for aviation safety and environmental protection [71].

In the United States, the Federal Aviation Administration (FAA) is responsible for regulating all aspects of civil aviation, including UAS or drones. Collaborating with stakeholders, the FAA sets and enforces regulations for safe, efficient, and innovative use of UAS in the national airspace, while complying with relevant laws and regulations [72].

2.2. Evolution of More-Electric-Aircraft (MEA)

The pursuit of developing aircraft that rely primarily on electrical power dates back to World War II, as exemplified by the Vickers Valiant VBombers. As early as 1954, Vickers VC-10 represented the initial attempt to create a "more electric" solution [73]. While the Airbus A-380 is commonly regarded as the modern starting point for "more electric" aircraft, it, in fact, employs the same scheme as the VC10 50 years earlier. In the Vickers VC-10, the electric power was generated by four generators, each capable of producing 40 kVA, yielding a total onboard electrical power of 160 kVA. However, the concept failed to gain traction at the time due to technological limitations related to power generation and conversion [74].

In the 1990s, the early challenges and the increasing socio-economic significance of UAVs accelerated research and development efforts in this field, with their military applications making their use even more strategic. The rapid advancement of UAV systems and the desire to enhance their efficiency and safety have prompted the development of the more-electric-aircraft (MEA) initiative [75]. As technology has advanced, the MEA idea has become more feasible. MEA aimed to replace conventional hydraulic and pneumatic systems with more compact and lightweight electrical systems, such as electrical actuators, power electronics, and electric motors. The increasing utilization of MEA has highlighted the pivotal role played by S/G technologies in ensuring the optimal performance and operation of UAVs, emphasizing their criticality and indispensability in the field. The MEA concept gained traction in the aerospace industry as a means to enhance the performance and sustainability of aircraft systems [76].

In the 2000s, the MEA concept evolved to include the use of advanced electrical power systems and energy storage technologies, such as batteries, fuel cells, and ultra-capacitors. This evolution was driven by the growing demand for energy-efficient and environmentally friendly aircraft systems, as well as the increasing popularity of UAVs [77].

In the 2010s, the MEA concept gained further momentum as advances in electrical power systems and energy storage technologies enabled the development of more advanced and capable aircraft systems. The adoption of MEA systems in commercial and military aircraft systems expanded, as it offered advantages such as improved reliability, reduced maintenance requirements, and enhanced mission capabilities [78].

In 2020 and beyond, the MEA concept is expected to continue to drive innovation in the aerospace industry. The growing focus on sustainable aviation and electrification of aircraft systems is expected to further accelerate the development and deployment of MEA technologies [79]. Additionally, the increasing demand for advanced aircraft systems that can operate in challenging environments, such as high-altitude and remote locations, is expected to drive the adoption of MEA systems in a wide range of applications [80, 81].

The transition towards MEA is underpinned by a set of pivotal driving factors, which can be succinctly summarized as follows [82]:

- Reduced Weight: Electrical power systems are typically much lighter than hydraulic and pneumatic systems due to the absence of hydraulic fluids, resulting in reduced weight and improved fuel efficiency.
- Easy Maintenance: Electrical systems are faster and easier to replace than most pneumatic, hydraulic, and mechanical systems, and their modular nature allows for simple and efficient repair and maintenance, reducing downtime and maintenance costs.
- Increased Efficiency: The use of electrical anti-icing systems can significantly increase engine efficiency, resulting in improved fuel efficiency and reduced emissions.
- Manageability: Electrical systems provide a faster response to changes in power demand than pneumatic, hydraulic, and mechanical systems, resulting in improved performance and control.
- Configurability: Electrical systems are designed with automatic reconfiguration features that maintain functionality during fault conditions, improving reliability, safety, and system availability.
- Enhanced Diagnosis: Electrical systems constantly monitor their operation, providing intelligent management to prevent or mitigate future faults. This feature is critical during critical flight phases, ensuring safe and reliable operation.

2.3. Progression of Hybrid UAVs

As an initial stride towards the adoption of more electric powertrains within the framework of MEA, there has been a disclosure of all-electric, hybrid-electric and turbo-electric propulsion architectures for UAVs [83]. These powertrain architectures hold the potential to facilitate the shift from conventional to fully electric aircraft [84].

Intensive research and development efforts in hybrid and all-electric propulsion systems have presented a remarkable opportunity to revolutionize aviation. As illustrated in Figure 2.2, these systems have the potential to offer significant advantages over conventional systems, ushering in a new era of enhanced sustainability and efficiency [85].

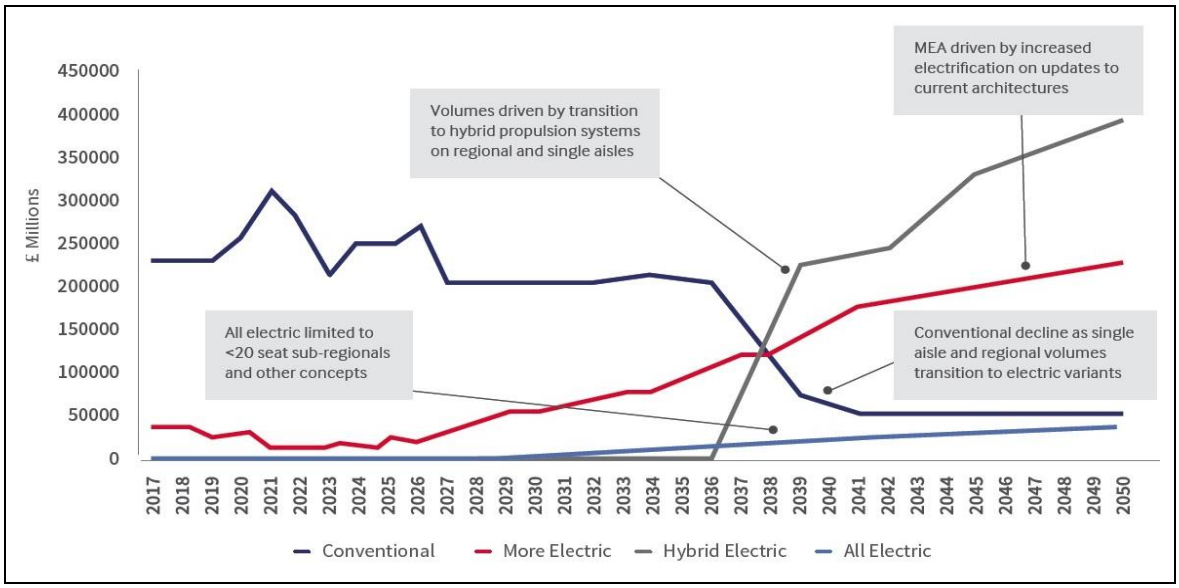


Figure 2.2. Comparison of aircraft deliveries [85]

2.3.1. NO_x and CO_2 emissions

MEA concept objectives over a 25-year period can be analysed under five categories: safety, noise reduction, capacity, mobility, and emissions [86].

In terms of safety, the main goal is to achieve a marked reduction in the number of fatal accidents.

Noise reduction remains a key focus area, targeting a decrease of 10 dB within a decade and 20 dB within 25 years. For capacity, the target is to triple the level of the 1990s [87].

The mobility goal is to halve the intercity flight time within a decade, reduce it by two-thirds within 25 years, and reduce the intercontinental flight time by half within 25 years. However, the aviation industry's use of fuel engines continues to result in growing emissions of carbon dioxide (CO_2) and nitrogen oxides (NO_x) [88]. Alarming statistics reveal that the CO_2 emissions of all flights departing from EU28 and EFTA have increased by 95%, from 88 to 171 million tons, between the 1990s and 2020s, according to the data reported by member states to the United Nations Framework Convention on Climate Change (UNFCCC) [89].

The aviation industry aims to decrease NO_x and CO_2 emissions significantly to tackle the urgent challenge of reducing emissions. By 2050, the industry aims to achieve a twofold reduction in emissions: a 70% reduction in NO_x emissions within the next decade, followed by an 80% reduction within the next 25 years, alongside a reduction of 25% in CO_2 emissions within the next decade and 50% within the next 25 years [90].

Hybrid-electric aircraft represent a promising solution for reducing fuel consumption and contrail generation, two critical issues currently facing the aviation industry. By utilizing electric motors as a supplementary thrust source during the take-off and cruise phases, hybrid systems allow for the use of smaller, more efficient fuel engines during flight [91]. This not only contributes to lower fuel consumption and greenhouse gas emissions, but also helps to reduce engine wear and noise pollution. In addition, the use of electric motors during the cruise phase can enable aircraft to fly longer distances without using their engines, thereby further reducing fuel consumption and environmental impact [92].

Moreover, hybrid systems present a multitude of additional benefits, serving as a catalyst for improved efficiency, especially at partial load, utilizing excess power generation to supply auxiliary loads such as pumps and pressurization systems [93]. They provide greater flexibility in the placement of electrical loads, resulting in reduced machinery volume, as well as minimized vibration and noise levels, revolutionizing the aviation industry towards a more sustainable and efficient future [94].

Propulsion systems are widely considered the most crucial subsystem in hybrid structures, and their development has been instrumental in the progress of aviation as a whole. As propulsion systems evolve, other subsystems are shaped accordingly.

Technological advancements have led to the diversification and enrichment of propulsion systems over the years. The development of propulsion systems, in terms of their performance and efficiency, is of paramount importance for aircraft at certain junctures. As the history of aviation unfolds, the ability to cover longer distances with greater payloads has progressed in direct proportion to the development of propulsion systems.

In the 1950s, speed was the primary driver of aviation development; in the 1960s, it was speed and capacity; in the 1970s and 1980s, the focus shifted to economy, fuel utilization, and efficiency; in the 1990s, the emphasis was on cost, noise, and capacity; and in the 2000s, priority was given to the environment, revenue, and cost. A close analysis of this trend reveals that most of the relevant parameters are linked to propulsion systems. UAV propulsion systems can be broadly categorized into three types based on their energy sources: fuel, hybrid fuel-electric, and all electric as shown in Figure 2.3 [95, 96].

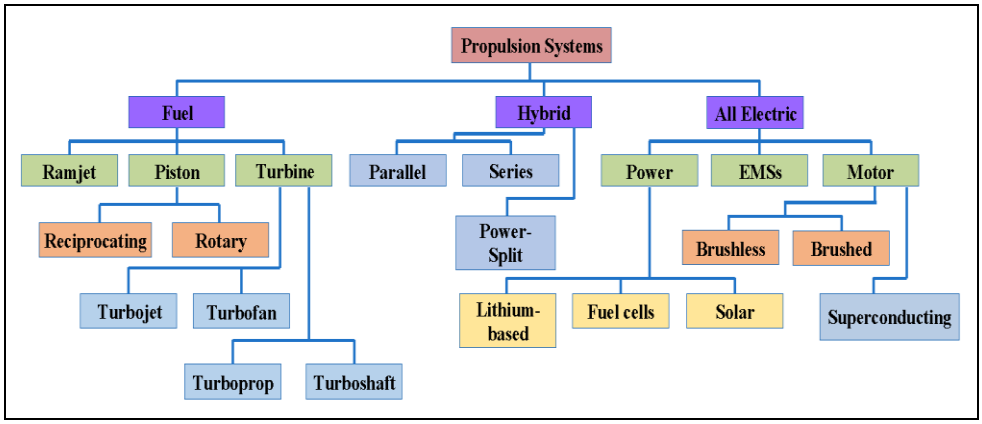


Figure 2.3. Overview of UAV propulsion systems

Fuel-based propulsion systems are essential to civil and general aviation, typically employing either aircraft kerosene-powered gas turbines or gasoline-powered internal combustion engines (ICEs), typically piston engines (PEs), which operate on the same principle as spark ignition (SI) engines. PE, a type of fuel-based propulsion, is categorized based on the number of cylinders (single/two-cylinder, etc.), cylinder arrangement (in-line, radial, opposed, V-type, etc.), and operating cycle (two-stroke and four-stroke) [97].

PE, a widely used type of fuel engine, is known for its high power-to-weight ratio, compactness, low cost, high efficiency, and reliability compared to ramjet and turbine engines. These features make PEs particularly effective and commonly used in small-sized UAVs [98].

Based on current projections, it is expected that ICE will continue to serve as the dominant means of propulsion for most vehicles, as indicated by the findings in Figure 2.4 [99].

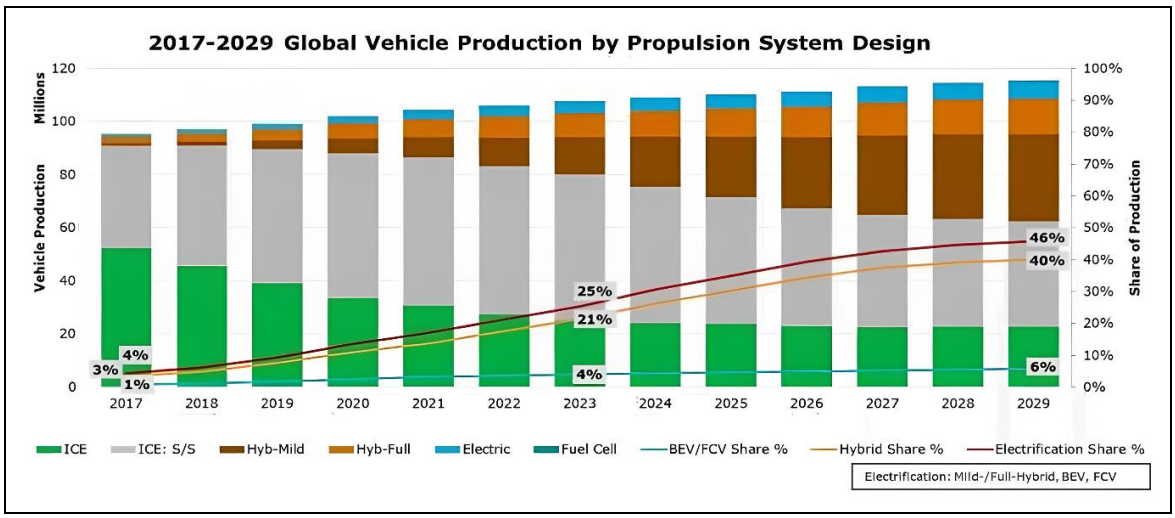


Figure 2.4. Progress of the global vehicle propulsion system [99]

The implementation of a pure electric propulsion system utilizes electric motors as the sole power source, offering numerous advantages [100]. These benefits include reduced carbon emissions, low levels of pollution, minimal costs, and high energy efficiency. Furthermore, pure electric UAVs possess a wider array of energy source options, including innovative alternatives such as lithium batteries, fuel cells, supercapacitors, and solar energy [101]. By harnessing these sustainable energy sources, pure electric UAVs effectively meet the environmental demands of energy conservation and emission reduction, making them a crucial avenue for the development of UAV technology.

However, as the aviation industry moves towards a future of fully electric structures, the development of hybrid propulsion systems has emerged as a crucial area of focus. These systems offer a means of providing an intermediate step towards the adoption of all-electric systems, while also addressing current deficiencies in electric powertrain technology [102-104].

The term "hybrid electric" refers to a propulsion system that utilizes multiple energy sources such as fuel/chemical and battery/electrochemical systems.

The hybrid electric configuration further branches off into series, parallel, and power split types based on the nature of the node connecting the two constituent energy sources. Figure 2.5 provides a comprehensive overview of conventional hybrid propulsion systems along with their respective summarised advantages [105].

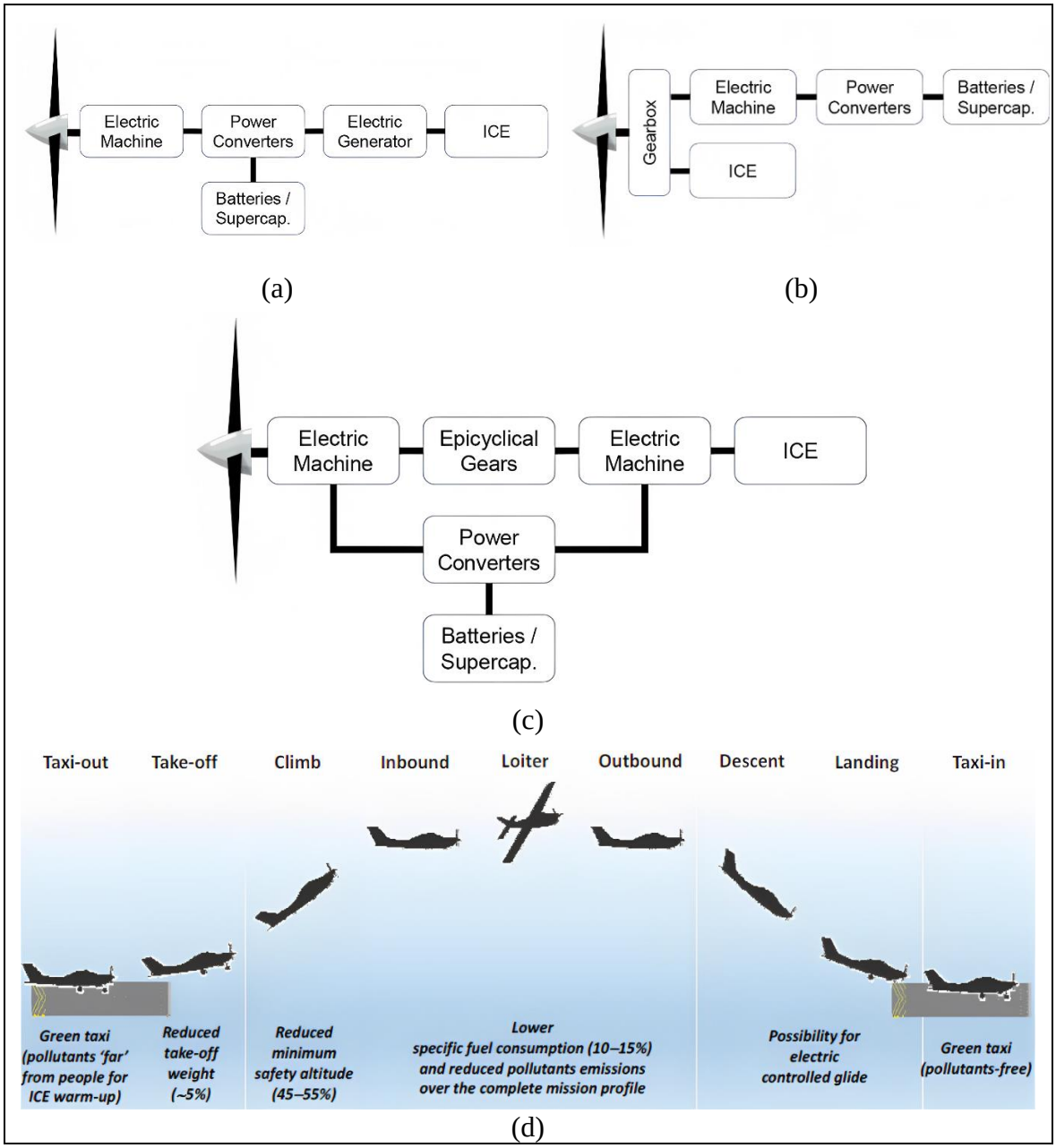


Figure 2.5. Conventional hybrid UAV (a) Series-hybrid propulsion (b) Parallel-hybrid propulsion (c) Power split-hybrid propulsion (d) Advantages of hybrid structures [105]

Parallel and series hybrid architectures offer significant advantages in contemporary UAV design [106].

Both architectures allow for downsizing of the ICE to provide the power required for cruising, with additional power during takeoff and other power-demanding manoeuvres provided by batteries or ultracapacitors through the electric motor [107].

The parallel architecture can be considered a highly modified state-of-the-art propulsion system, with the electric components managing a small percentage of the total propulsive power. The number of new components is limited to minimize economic effort [108].

On the other hand, the series architecture represents a new propulsion system in which the electric components manage the total propulsive power [109]. Although the series hybrid is closer to an all-electric propulsion system than the parallel hybrid, it has drawbacks, such as a greater economic effort required to develop it, greater mass and quantity of additional components leading to increased total mass, and reduced system efficiency due to the need for double power conversion.

In conclusion, the series hybrid architecture is generally more suitable for civil transport UAVs, adding to the gain of distributed propulsion. Conversely, the parallel hybrid architecture is more appropriate for smaller, lightweight UAVs, as it requires fewer additional components, allowing for optimal economic feasibility.

2.3.2. Energy source types for MEA systems

As the aviation industry continues to shift towards more-electric propulsion systems, the development of appropriate energy storage technologies has become an essential area of focus. In the past, various energy sources, including fuel cells, batteries, solar cells, and ultra capacitors, have been considered for this purpose, each offering distinct advantages and limitations. Figure 2.6 provides an overview of the power supplies found in MEA [110].

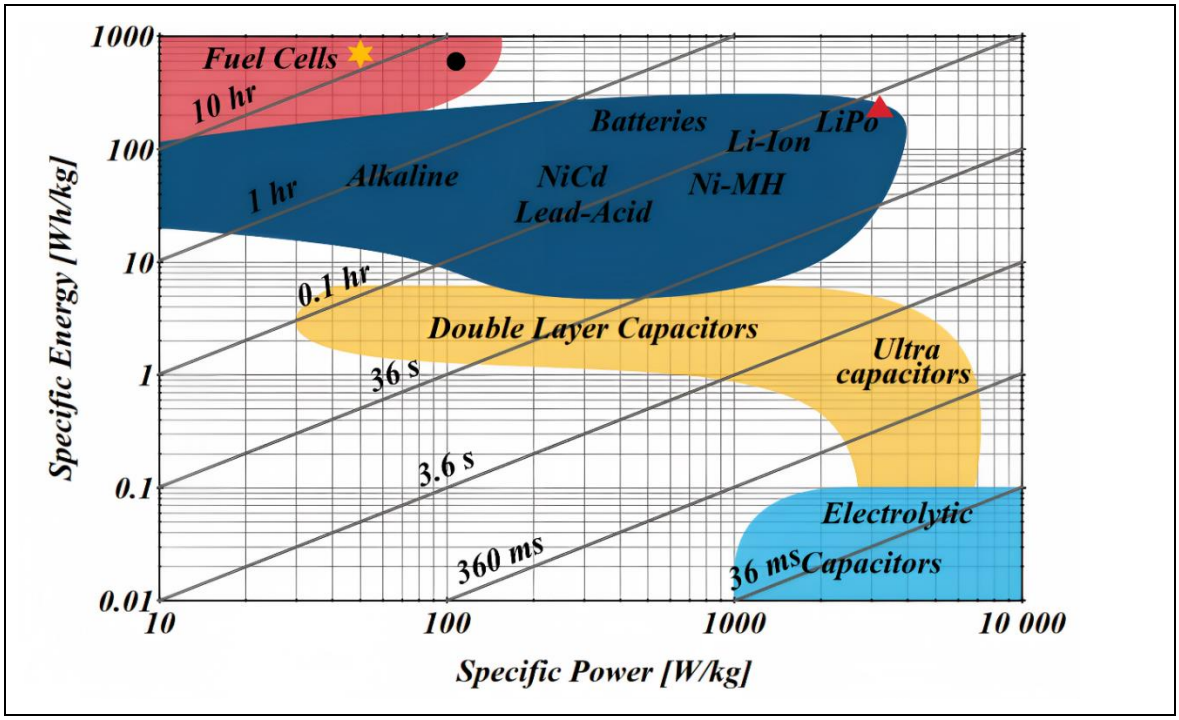


Figure 2.6. Energy density comparison of energy sources for MEA [110]

Fuel cells have attracted considerable attention as an energy storage technology for MEA systems due to their high efficiency and low emissions, which make them an attractive option [111]. However, their high cost and complex design have limited their widespread adoption. To address the limited lifespan and safety concerns of fuel cells, researchers are exploring alternative options such as ultracapacitors. Additionally, solar cells offer a promising source, providing long-term, sustainable energy solutions. Batteries have also emerged as a popular choice, due to their high energy density and low weight. Research on suitable energy storage are ongoing to identify the most effective and efficient solutions.

2.3.3. Voltage levels of the MEA UAVs

Aircraft electrical distribution systems follow several standards, including MIL-STD-704, with the following potential voltage and frequency levels [112]:

14 VDC: This voltage level is commonly used in general aviation aircraft, particularly those with piston engines. It is also used in some small UAVs and drones.

28 VDC: This is a newer standard that specifies a higher voltage level for 28 VDC electrical systems, with a maximum voltage of 32 VDC.

48 VDC: This voltage level is now employed for electric propulsion in mini and small-scale hybrid UAVs, predominantly used for surveillance.

270 VDC (bipolar ±135 V): Used in military aircraft and subsystems on larger aircraft.

270 VDC (unipolar): This voltage level is used in some commercial aircraft, particularly those with larger electrical loads. It is also used in some military aircraft.

115 V AC at 400 Hz: This voltage and frequency level is often used for larger loads on large commercial aircraft.

115 V AC Variable Frequency from 360 Hz to 800 Hz: This voltage level is used for certain subsystems on some aircraft.

400 Hz AC: There are other AC voltage levels that are used in aircraft electrical systems, including 26 VAC and 200 VAC at 400 Hz. These voltage levels are used for various types of electrical loads, including avionics, lighting, and galley equipment.

540 V DC (bipolar ±270 V): This voltage level is used for some high-power subsystems on larger commercial aircraft.

230 V AC at 400 Hz: This voltage and frequency level is commonly used for certain subsystems on large commercial aircraft.

It is essential to select the appropriate voltage level for an aircraft electrical system based on the application's power requirements. It is worth noting that there is a trend towards higher voltage levels in aircraft electrical systems, particularly in electric and hybrid-electric aircraft designs. This is driven by the need for higher power levels and the desire to minimize losses in the electrical distribution system [113]. However, higher voltage levels also bring additional safety considerations and design challenges. As such, careful consideration of the electrical load and the system's voltage is necessary to ensure safe and efficient operation.

2.3.4. Hybridization degree identification of the hybrid UAV

The level of hybridization of energy and power can have a significant impact on the performance and range of the aircraft. A higher level of hybridization of power indicates that more power is provided by the electric motor, which can improve the fuel efficiency and reduce emissions. On the other hand, it indicates that more energy is supplied by the battery, which can increase the range of the aircraft and reduce its reliance on fossil fuels.

The Degree of Hybridization (DoH) expresses the percentage of the total power required by an aircraft that comes from the electric system. However, the more commonly used parameters in the literature for expressing the level of hybridization are the Hybridization Factor for Energy (HF_E) and Power (HF_P). These factors provide insight into the allocation of power and energy sources on board the aircraft. HF_P is the ratio of the installed propulsion power of all electric machines (EMs) to the total installed propulsion power at the propeller shaft, while HF_E is defined as the ratio of the required transport energy delivered by nonconsumable batteries to the total required transport energy. The hybridization level of power for parallel-hybrid and series-hybrid aircraft is determined in Eq. 2.1 and Eq. 2.2 [114]:

$$HF_{P,ph} = \frac{P_{EM,max}}{P_{max}} \quad (2.1) \qquad HF_{P,sh} = \frac{P_{EM,max}}{P_{max}} \quad (2.2)$$

where $P_{EM,max}$ is the maximum power of the electric motors, P_{max} is the overall power demand, and $P_{ICE,max}$ is the maximum power of the ICE. This definition ensures that parallel-hybrid powertrains are identified by a hybridization level smaller than one, while serial-hybrid powertrains are identified by a hybridization level larger than one.

Another important parameter is the level of hybridization of energy, which is defined for each flight phase of a mission and determines the power demand from EMs and ICE in each phase, as determined in Eq. 2.3 [107].

$$HF_{E,i} = \frac{\Delta E_i}{\Delta E} \quad (2.3)$$

For initial sizing, the HF_E values for each flight phase are determined by the ratio between the power requirement of the EM and the power demand. These parameters must be used together to fully understand how the power sources are being utilized. For example, a configuration with a high hybridization factor of power due to an extremely powerful EM that is only used for a short period of the mission will result in a low battery energy on board, and hence, a low hybridization factor of energy. HF_E indicates the proportion of the electric part of the propulsion system that is being utilized.

2.3.5. Starting procedure and methods of the conventional UAVs

The startup process of an aircraft engine is a critical and complex procedure that requires careful attention and adherence to specific guidelines. An examination of the startup process can provide valuable insight into the specific requirements that a Starter/Generator (S/G) must satisfy. Figure 2.7 depicts the 30-second startup sequence and temperature variation for a conventional aircraft engine, which involves several key stages [115].

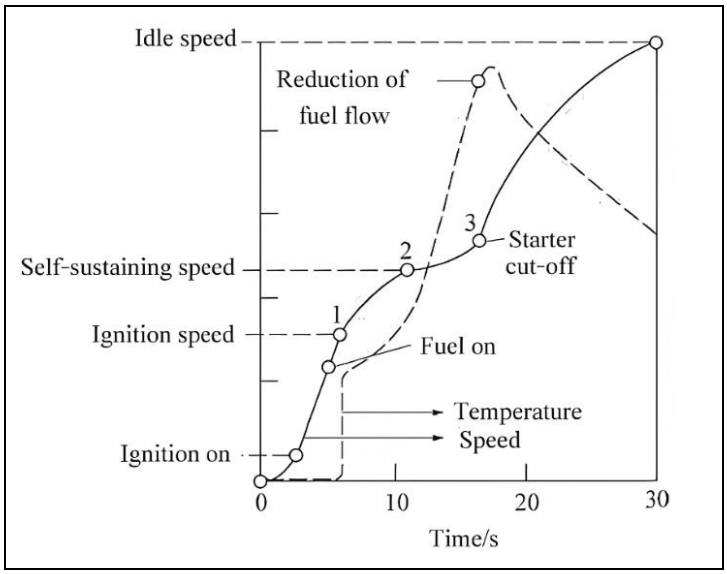


Figure 2.7. Starting procedure of a conventional aircraft [115]

First, the starter mechanism imparts torque to initiate acceleration of the engine until ignition is enabled. This torque is required to overcome the initial resistance of the engine and to set it in motion [116]. Subsequently, the engine experiences a proportional increase in airflow, resulting in a corresponding rise in engine speed.

This increase in airflow is essential for the combustion process, which requires a certain minimum airflow rate to ignite the fuel-air mixture.

Once the minimum airflow rate suitable for ignition is achieved, fuel injection commences, and the combustion process begins. Although the engine can now generate its own torque, it still benefits from auxiliary support from the starter mechanism. This is because the combustion process takes some time to stabilize, and the engine's own torque may not be sufficient to maintain a stable rotation during this period.

The self-sustaining speed represents the point where the engine's torque is adequate to accelerate it to idle speed, after which the starter is disengaged, and fuel flow is adjusted to attain idle speed. At this stage, the engine is fully operational and can generate enough power to maintain a stable rotation without the support of the starter mechanism.

Nonetheless, it is typical for the starter to continue assisting the engine rotation for speeds beyond the self-sustaining speed to minimize the startup duration. This is because the initial stages of the combustion process can be unstable, and the starter can help to maintain a stable rotation until the combustion process stabilizes.

On the other hand, the starter must be carefully designed to match the specific torque-speed characteristics of the engine, which can vary depending on environmental factors such as temperature. Figure 2.8 provides a typical profile of these characteristics, which shows that colder temperatures require higher torque to initiate engine rotation [117].

To provide adequate acceleration during the startup process, the starter must be capable of overcoming the torque requirements for the full range of temperatures that the engine may encounter. This requires careful consideration of the starter's design and specifications, including the type of motor, the number of poles, and the gear ratio [118]. In addition to meeting the torque requirements for engine startup, the starter must also be designed to operate reliably and efficiently over a wide range of conditions.

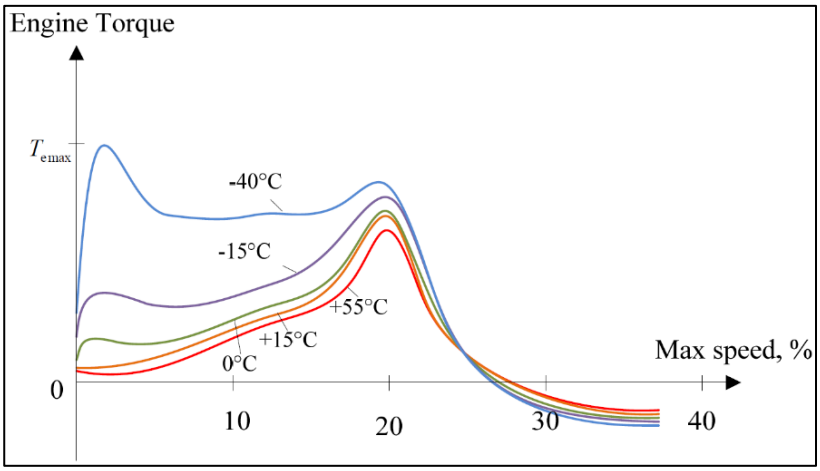


Figure 2.8. Classical torque-speed characteristics of UAV engines across temperatures [117]

The starter mechanism plays a crucial role in initiating the engine rotation and supporting it during the early stages of the combustion process. Proper startup procedures are critical for ensuring the safe and reliable operation of aircraft engines. Multiple approaches are available for driving an aircraft starter, including the use of air, hydraulics, gas, or electrical power [117]. Regardless of the method employed, all of these approaches must satisfy the starting requirements illustrated in Figure 2.7.

2.4. Advances in Starter/Generator (S/G)

The Starter/Generator (S/G) plays a critical role in the operation of hybrid UAVs, providing both the initial propulsion required for the UAV piston engine to take off (motor mode) and the charging of the battery pack that meets the power requirements of the electronic system while cruising (generator mode) [119].

This dual functionality of the S/G in UAV systems underscores its paramount importance as a technology that enables reliable and efficient power generation and management. During motor mode, the S/G provides the necessary torque and rotational speed to enable the UAV to achieve lift-off and overcome the high power demands associated with takeoff [120]. Subsequently, during generator mode, the S/G converts the engine rotational energy into electrical energy to charge the battery pack that powers the electronic system. As such, the successful integration and operation of the S/G are essential to ensure the overall performance, reliability, and safety of these vehicles. S/G systems offer both advantages and disadvantages, as outlined in Table 2.2 and Table 2.3, respectively [121-125].

Table 2.2. Advantages of conventional S/G systems

Advantages	Explanation
Low operating/maintenance costs	S/G offer energy-efficient solutions that reduce lifetime operating and maintenance costs.
Piston motor auto start feature	S/G has an automatic piston motor start for seamless engine start-up.
Power system battery charging	S/G charges the power system battery pack, ensuring uninterrupted power for UAV.
Elimination of the drivetrain	S/G eliminates the drivetrain, improving efficiency and streamlining the design.
Regenerative brake feature	S/G use regenerative braking to capture energy from UAV braking and recharge the battery pack.
Shorter start time	S/G has a shorter start time, allowing for faster and more reliable engine starts than traditional systems.
Lower start temperature	S/G can start the engine at lower temperatures than traditional systems, improving reliability.
Improved power quality	S/G offer more stable and consistent power to UAV than separate starter and generator units.
Improved control	S/G integrate with UAV control systems to enhance control over engine and electrical systems.
Improved system integration	S/G combines starter and generator functions, simplifying integration and reducing complexity.
Reduced space requirements	S/G can be more compact than separate starter and generator units, freeing up space for other systems.

Table 2.3. Disadvantages of conventional S/G systems

Disadvantages	Explanation
Cost of maintenance	Conventional brushed S/G may require more maintenance than separate units, increasing costs and reducing UAV availability.
Limited power during start-up	Separate units used for larger engines if S/G lacks sufficient power during start-up.
Electromagnetic interference	S/G can generate EMI that can affect other electrical systems in the aircraft, and may require special measures to mitigate, such as shielding or filtering.
Higher upfront cost	S/G can be more expensive to design and manufacture than separate starter and generator units, especially for high-power applications.
Complexity	S/G can be more complex than separate units, making troubleshooting and maintenance more challenging.
Cooling Mechanism	S/G may need extra cooling, adding weight and complexity to UAV, and are prone to complete power loss if the unit fails.
In the event of a failure	Replacing a failed conventional S/G requires the entire system to be replaced, whereas with separate units, only the failed unit needs to be replaced.

In the late 1990s, the exploration of S/G systems gained impetus and their utilization extended to multiple domains, such as aerospace [126], piston [127] and turbine engine systems [128], automotive [129], supercharger applications, hybrid [130] and electric vehicles [131], and others [132]. Among the notable developments in this domain is the Integrated Drive Generator [133] engineered by Hamilton Sundstrand Corporation. The system used in commercial aircraft provides both starting and power generation capabilities.

In the early 2000s, there was a noticeable shift towards more effective and lighter S/G systems. One such system is the 270 VDC S/G, which was developed by Safran Electrical & Power. It employed a brushless DC motor (BLDC) for starting and a brushless AC generator (PMSG) for power generation [134]. In 2001, Cheng et al introduced the doubly salient permanent magnet (DSPM) machine, which merged the structure of the switched reluctance machine (SRM) [135]. In 2002, Chau et al proposed the wound-field doubly salient machine (WFDSM), which utilized DC field windings for excitation flux instead of PMs [136]. In 2003, Mellor et al presented recent research on the use of an embedded generation system as a substitute for the emergency ram air turbine on aircraft [137]. In 2004, Mudannayake et al presented an analysis of the transient behavior of a prototype 42 V Integrated Starter Alternator (ISA) during sudden DC load changes [138]. Multiple electric machine types were surveyed and suggested for Integrated Starter/Generator (ISG) applications [139-141]. In 2005, El-Refaie proposed a fractional slot PMSG with Slot/Pole/Phase = 2/7 for an ISA application [142]. In 2006, Mudannayake et al presented the complete control design of an induction machine-based ISA for future automotive 42 V Power Net [143]. In 2007, Hasan et al implemented a higher power S/G system for a hybrid electric vehicle (HEV) using a 20-kW BLDC machine [144]. In 2008, a general-purpose three-phase permanent magnet flux switching (PMFS) machine was proposed to highlight its potential in ISG applications [145]. In 2009, Leuchter et al adopted a PM machine in an electrical-generator set (EGS) that used variable-speed constant-speed technology [146].

Extensive research and development efforts have yielded a multitude of sophisticated conceptual designs showcasing hybrid configurations that have been fabricated and operationalized with utmost precision. Hybrid UAVs are comprehensively classified into four primary configurations, namely, tail-sitter, dual-systems, tilt-wing, and tilt-rotor, as elaborated in [147]. As exemplified in Figure 2.9, these configurations are testament to the remarkable advancements achieved in the field.

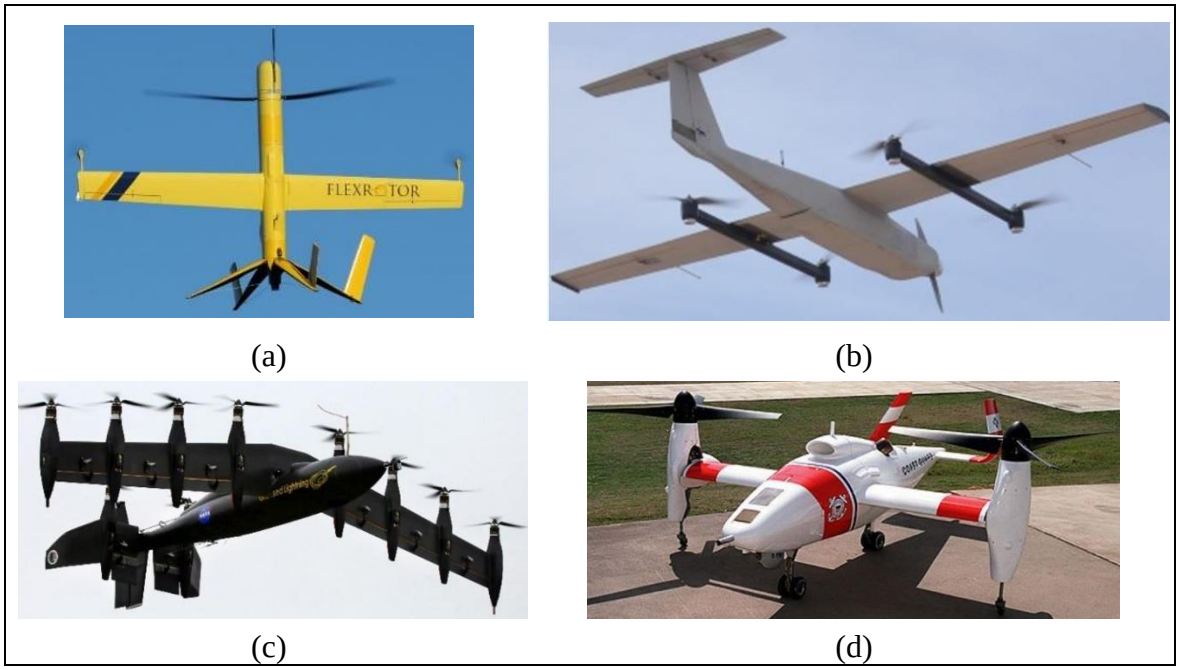


Figure 2.9. Popular small-scale hybrid UAVs: a) Aerovel Flexrotor, tail-sitter b) Arcturus Jump-20, dual-system c) Nasa GL-10, tilt-wing d) Bell Eagle Eye, tilt-rotor

In the second decade of the twenty-first century, research in the field of S/G systems continued to expand, with a particular focus on the design of highly efficient and constrained electric machines. In 2010, Legranger et al proposed the application of optimal multiphysics models to the design of interior permanent-magnet (IPM) machines intended for automotive ISGs [148]. In 2011, Jurkovic et al presented a comparative study of outer rotor permanent magnet AC (PMAC) machine candidates, including interior and surface mount permanent magnets (SPM) [149]. In 2012, Niu et al analysed three-phase and nine-phase pulse-width modulation (PWM) inverter modules with different three- and nine-phase brushless permanent magnet synchronous machine (PMSM) configurations [150]. In 2013, Friedrich et al. proposed a description of this phenomenon, which involved modelling it on the basis of nonlinear thermal resistances primarily associated with the rotation speed and air gap temperature [151, 152]. In 2014, Rocca et al proposed a practical and reliable cooling solution for a high power density, high-speed PMSM for an aero engine S/G system [153].

In 2015, Alnajjar et al presented a six-phase electrically excited starter generator for an aircraft DC power system [154]. In 2016, Salihu et al presented a new permanent magnet double-stator ISG for HEVs [155]. In 2017, Hosad et al. reviewed the mounting details, advantages, and benefits of ISG [156].

In 2018, Kong et al designed and optimized an outer-rotor PMSM with an amorphous stator core for plant protection UAVs [157]. Noland et al. [158] reviewed electric machines and power electronics for ISGs in MEA power systems in 2019, while Wei et al. [159] proposed a method for sensorless controlled starting of BSM in variable frequency AC power systems in civil aircraft. In the 2020s, significant advancements were made in the development of S/G systems for aerospace. Honeywell Aerospace recently announced the development of a new S/G that is specifically designed for use in small to medium-sized aircraft. In 2021, Ismagilov et al created an integrated S/G system based on BLDC technology with its own control unit for the APD-500 aircraft piston engine [160]. In the same year, engineers at the University of Warwick announced the development of a new S/G for small UAVs called REGEN.

This system uses a novel electromagnetic design that is expected to provide higher power output and greater efficiency compared to traditional systems. Similarly, researchers at the University of Nottingham have also developed a new S/G for use in hybrid-electric aircraft. As of 2022, integrated S/G systems have already been implemented in Boeing 787 and F-35 aircraft [161]. In addition, AeroTEC successfully tested its Hybrid Power Source (HPS) system in 2022, which includes an S/G system for use in hybrid-electric aircraft. Furthermore, Jarrah et al proposed a novel hybrid multirotor drone design in 2022, which uses two gasoline engines to provide the majority of the lift force and four electric motors to stabilize the drone. Rolls-Royce recently announced the development of a new S/G called the Power Drive Unit (PDU) for use in its hybrid-electric aircraft.

The development of Starter/Generator technology in aerospace applications has been driven by a combination of advances in materials science, power electronics, control systems, and magnetics [162-166]. These advancements have led to more efficient, reliable, and lightweight systems that are well-suited for use in a wide range of aerospace applications.

The S/G industry is dominated by established manufacturers who have gained a reputation for excellence through their commitment to innovation, quality standards, and exceptional performance. These companies include Honeywell Aerospace, Safran Electrical, UTC Aerospace, Hartzell Engine, GE Aviation, Rolls-Royce Electrical, Parker Hannifin, Sullivan Acutronic Power, Hirth Engines, UAV Propulsion Tech, Aero Engines, PBS, Power4Flight, Rotron UAV, UAV Engines, and Pegasus Aeronautics.

Figure 2.10 illustrates the significant advancements made in this field using turbine engines (TEs) [167].

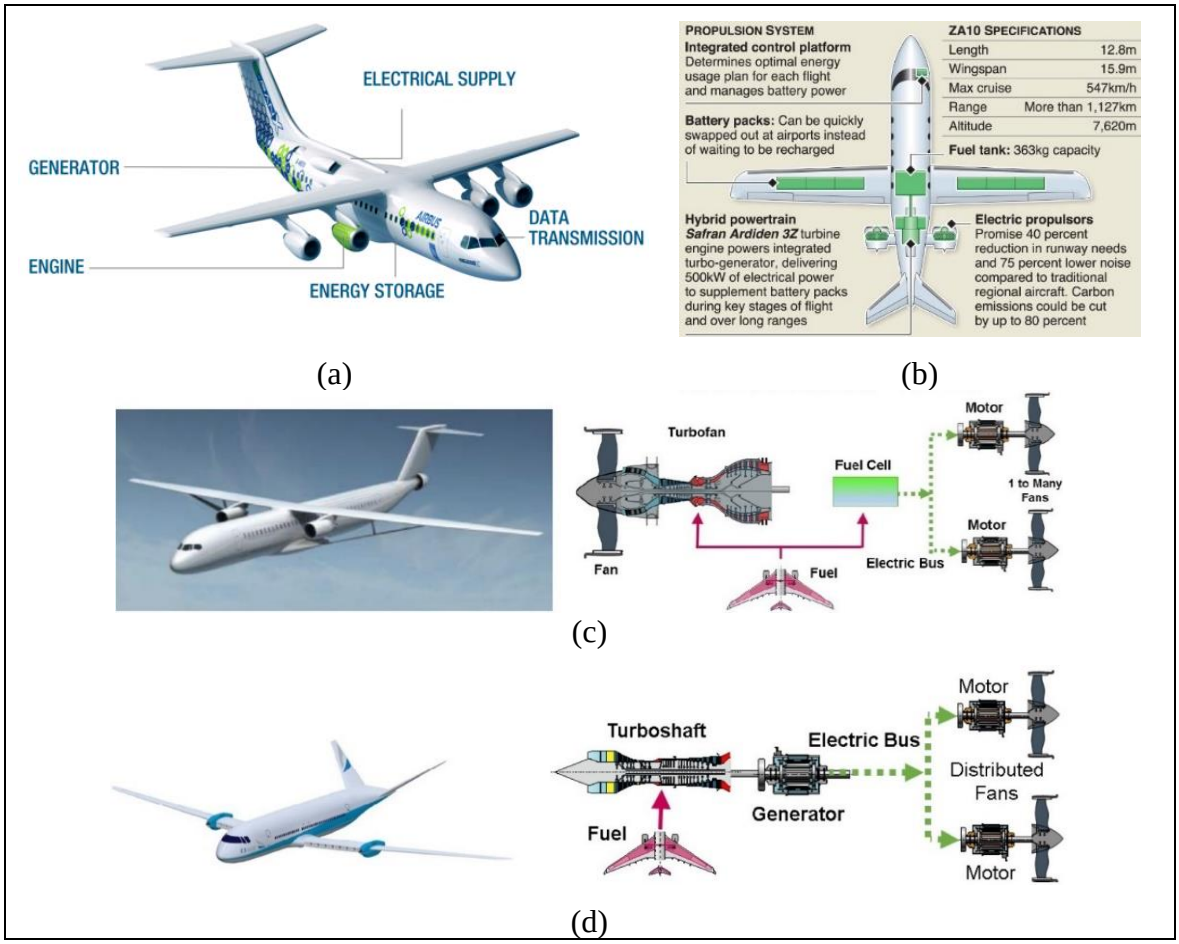


Figure 2.10. Commercial large scale hybrid UAVs: (a) Airbus, Rolls-Royce, Siemens E-Fan X (b) Zunum ZA10 (c) Boeing Sugar Freeze (d) ESAero ECO-150R

2.4.1. Standard

EASA and FAA enforce strict safety regulations through rigorous inspections and certifications in the aviation industry. The conventional S/G units adhere to the TSO-C56b:2006 and ETSO-C56bA1:2013 standards, and the power unit complies with the TSO-C71:1961, TSO-C73:1963, ETSO-C71:2003, and ETSO-C73:2003 standards [168].

2.4.2. Patent review

Document EP2962885A1 [169] presents a hybrid power system consisting of an ICE and an S/G. In document TR201708206A2 [170], an S/G structure is proposed as a means of stabilizing combustion engine drones, as well as starting the combustion engine. Document US201717175856A1 [171] describes a system utilizing two S/Gs as a regulator and stabilizer, capable of energizing or de-energizing the system. Document US2015180309A1 [172] proposes a system incorporating two S/Gs connected to a motor by a gearbox.

Document US2014203739A1 [173] discloses a system comprising a series of flywheels arranged on a line. Document US2017247114A1 [174] introduces a system consisting of two electric machines that function as a generator and starter. Document US2014013751A1 [175] describes a system comprising a rotor and gearbox connected to a turbine and an S/G that can perform generator/starter functions. Document FR2986566A1 [176] introduces a system consisting of an S/G connected to the compressor of a turbine engine, which provides or draws power from the compressor, and another S/G connected to the engine output shaft, which provides supplementary output power or receives power from the output.

Document US7915869B2 [177] proposes a generator system comprising an exciter for initial movement of the rotor, with an example of a PMSG connected to an aircraft turbine with a main generator/exciter. Document US7687928B2 [178] describes a system comprising two assemblies, each consisting of a main S/G and an exciter, connected to a shaft housing a PMSG. Document US6177734B1 [179] discusses an S/G system for ICE vehicles, including their connection methods. Document US2012/0211981A1 [180] proposes an S/G structure for turbine engines, including their control methods.

In document US2006/0087123A1 [181], an S/G structure with a two-stage rotor single-stage input and output structure is connected to the gas turbine shaft with a gear group. Document US2012/0212094A1 [182] introduces a multistage variable reluctance type S/G structure. In document US006098584A [183], an S/G structure is connected to the flywheel system to which the ICE is connected with the drivetrain. Document US005929537A [184] describes a permanent magnet S/G structure connected to small aircraft engines by a gear train, including their control units. Document US20120209456A1 [185] proposes a parallel hybrid-electric propulsion system for UAVs, which includes an S/G structure.

2.5. Problem Statement

Conventional hybrid UAV propulsion systems also employ traditional ICEs, including ramjet, piston, and turbine engines, in conjunction with highly efficient and specialized S/Gs. This combination of technologies is depicted in Figure 2.3 of Section 2.3. In Table 2.4, a comparative analysis of the piston engine and the turbine engine - two widely used propulsion technologies - is presented [186].

Table 2.4. Comparison of Piston and Turbine Engines

Feature	Piston Engine	Turbine Engine
Safety		✓
Simplicity	✓	
Reliability		✓
Availability	✓	
Engine Performance		✓
Fuel Efficiency	✓	
Power Output		✓
Ease of Start-Stop	✓	
Cruise Speed	Low	High
Weight	Light	Heavy
Size	Small	Big
Operating Cost and Expense	Cheap	Expensive
Overhaul	Short	Long
Working Altitude	Low Altitude	High Altitude
Fuel Consumption	Low at Small Powers (<200HP)	Low at High Powers (>200HP)
Efficiency	Efficient at Small Powers (<200HP)	Efficient at Higher Powers (>200HP)

Turbine engines (TEs) are preferred for high-power requirements (>200 HP) in hybrid UAVs due to their ability to operate at high altitudes and provide better power output and power-to-weight ratios compared to piston engines. [187].

On the other hand, piston engines (PEs) are generally preferred for hybrid UAVs with lower power requirements (<200 HP), due to their lower cost, greater fuel efficiency, and lower maintenance requirements [188]. The advantages of PEs have made them a preferred choice for a variety of UAVs, ranging from mini-scale to medium-scale, as outlined in Table 2.1.

Hybrid UAVs offer a promising solution for a wide range of applications due to their ability to combine the benefits of both electric and conventional propulsion systems. However, conventional hybrid UAVs have been found to exhibit several shortcomings that can significantly hinder their performance and capabilities, thereby limiting their utility in a variety of applications [41, 80, 189-193].

In the same vein, while conventional piston engines are widely recognized for their reliability and durability, they are also susceptible to various malfunctions and failures that can have severe consequences. Such failures can be attributed to a range of factors, including design defects, manufacturing errors, inadequate maintenance, and operational errors. Table 2.5 summarizes the types of catastrophic failures that can occur in PEs [127, 194].

Table 2.5. Catastrophic failure types of piston engines

Failure	Reason
Overheating	Excessive heat can result from blocked air intake or exhaust, low coolant levels, or a malfunctioning thermostat.
Detonation or preignition	An early or rapidly ignited fuel mixture can create excessive pressures in the cylinder, resulting in PE damage.
Foreign object damage	Foreign objects inside the engine can cause piston damage and result in engine failure.
Improper maintenance	Improper installation or maintenance can cause premature wear of the piston and eventual failure.
Material defects or fatigue	Piston failure can result from manufacturing defects, material fatigue, or other quality-related issues.
Oil leaks	Oil leaks, caused by worn or damaged gaskets, seals, or O-rings, can lead to loss of oil pressure, reduced lubrication, and increased wear on engine components.
Ignition system failure	A malfunction in any part of the ignition system, such as the spark plugs, ignition coils, or wiring, can lead to poor engine performance or complete engine failure.
Fuel system issues	Fuel system issues, such as contamination, clogged filters, or pump failures, can lead to poor engine performance, reduced power, and potentially engine failure.
Crankshaft / Piston Failure	Failure of the crankshaft and pistons can lead to catastrophic engine damage, including connecting rod or piston rod breakage, ultimately resulting in total engine failure. These components are subjected to high levels of stress and wear, making their failure a critical concern.

Studies have shown that a substantial number of turbine-engined UAV malfunctions can be attributed to the fuel engine [194]. In the case of piston-engined UAVs, the failure of a critical component such as the engine or crankshaft can result in dire consequences [37].

Crankshaft Failures: The crankshaft is a crucial engine component responsible for converting the reciprocating motion of the pistons into rotational motion, which drives the propeller. The following are common types of crankshaft failures:

- Fatigue failure caused by cyclic loading,
- Bending or twisting due to excessive loads or misalignment,
- Bearing journal wear due to inadequate lubrication or contamination,
- Crankshaft fracture due to excessive stress or material defects.

Piston Failures: The piston is another critical component responsible for transferring energy from combustion to the crankshaft. Common failures of pistons include the following:

- Piston seizure resulting from overheating or inadequate lubrication
- Piston ring failure causing loss of compression and increased oil consumption
- Piston skirt wear or scuffing due to excessive heat or insufficient lubrication
- Piston cracking or fracture due to material defects or detonation.

The graphical representation of data regarding the Australian turbine-engined UAV's occurrences can be observed in Figure 2.11(a), while Figure 2.11(b) provides an overview of the risk levels associated with piston failure for the piston-engined UAVs [37, 194].

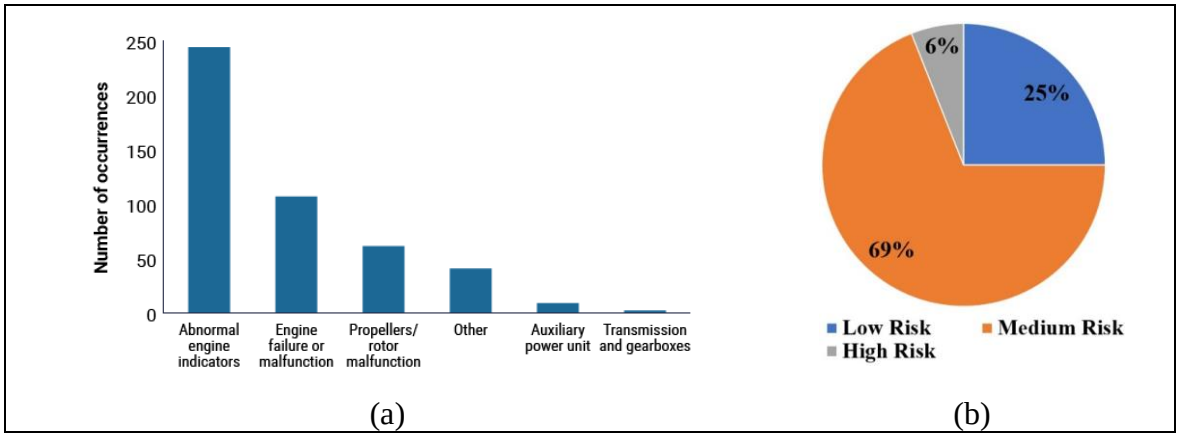


Figure 2.11. Australian: (a) Aircraft engine occurrences (2012-2016) (b) The risk level of aircraft engine failure or malfunction (2009-2014) [37, 194]

Engine failures or malfunctions are a significant issue that has been identified in the field of UAV technology, and they pose a serious risk to the safety and effectiveness of UAV operations. These can include the loss of human life, destruction of property, and significant financial costs associated with repairs and legal liabilities.

Although conventional S/Gs have potential advantages, there are also several challenges and limitations that must be addressed to fully realize their capabilities. These challenges encompass safety, endurance, cost-effectiveness, environmental impact, and other factors. Addressing these issues is crucial to enable more effective integration of systems and achieve optimal performance and efficiency [195-197].

- Hybrid UAVs crash due to piston motor shaft failure, degradation, or other electric propulsion system failures.
- Absence of Master/Slave operation.
- Lack of independent S/G operation for piston motor.
- Uncontrolled fuel consumption.
- Topology is not conducive for implementing algorithms like maximum flight time.
- Dependence on launch systems such as Jato/Cato.

Foremost among these limitations is their restricted flight time and range, which are predominantly attributed to their reliance on a conventional engine and limited energy storage capacity [198, 199]. Consequently, such hybrid UAVs can only remain airborne for a limited duration before necessitating a recharge or refuel. In addition, these UAVs may suffer from decreased reliability due to the complexity of their powertrain systems. The numerous components and systems that constitute their powertrain system could serve as potential failure points, which can ultimately result in costly repairs or total system failures.

Given the increasing importance and widespread use of hybrid UAVs in various industries, it is imperative to address the shortcomings of conventional powertrain systems and proactively mitigate the risk of catastrophic failures. A comprehensive understanding of the failure mechanisms of PEs is thus essential to implement effective preventive measures and make necessary improvements to ensure optimal performance and reliability.

In this context, the development of innovative, efficient, and up-to-date systems is crucial not only to reduce the risks of catastrophic failures but also to address the limitations of conventional hybrid UAVs in terms of flight time, range, and environmental impact [200].

2.6. Proceedings of Magnetic Couplers

In traditional aviation systems, the direct coupling of the propeller to the piston engine (PE) makes the aircraft prone to catastrophic failures in the event of any engine or crankshaft malfunction. To mitigate such damaging scenarios, considerable endeavors have been undertaken to incorporate Magnetic Coupler or Magnetic Coupling (MC) and Starter/Generator (S/G) mechanisms. These innovations enable noncontact torque, hermetic separation using static seals or containment shroud transfer and magnetic isolation of the PE and the S/G, thus ensuring safe operations in the event of malfunctions [201]. Specifically, the S/G can be used in motor mode to facilitate a controlled landing in the event of an unforeseen incident, thereby averting catastrophic outcomes.

Yonnet et al. [202] presented an analytical method for calculating torque in synchronous couplings, based on forces between permanent magnets. Ravaud et al. [203] developed three-dimensional analytical expressions for optimizing permanent magnet couplings, using the Coulombian model. Choi et al. [204] analysed the torque and conducted measurements for cylindrical air-gap synchronous permanent magnet couplings, using analytical magnetic field calculations. Carpentier et al. [205] proposed using the analytical virtual work approach within the volume integral method framework to calculate magnetic forces. Li et al. [206] derived 3D analytical torque equations with a closed form for an ideal radial MC.

Numerical methods using finite elements have been found to provide more realistic solutions for magnetic coupler design, albeit at the cost of increased solution time [207-209]. These methods are thus more effective in achieving optimal design and applying optimization techniques [210-212]. Baiba-Ose et al. [213] conducted research on the impact of permanent magnet width and the number of pole pairs on the mechanical torque of MCs. Sun et al. [214] presented a computational model for cylindrical permanent magnet MCs based on the magnetic field division method, taking into account the skin effect and the working point of the permanent magnet. Meng et al. [215] simulated the transient magnetic field for a permanent magnet MC in different states using Ansys Maxwell 3D software.

Ziolkowski et al. [216] compared transient, quasi-static, and fast-quasi-static modelling techniques to calculate force profiles using FEMs. Ose-Zala et al. [217] investigated the influence of basic design parameters on the mechanical torque for cylindrical magnetic couplers with rounded permanent magnets using QuickField software based on 2D FEMs.

Furthermore, it is worth noting that the study conducted a comprehensive comparison of various magnetic coupler types, including different topologies [218]. Moreover, a recent study focused on the development of axially magnetised coupling [219]. Another recent advancement in MCs is the development of magnetic gears, which have been proposed as a replacement for traditional mechanical gears [220, 221]. Building on the concept of magnetic gears, a magnetic gear-integrated permanent magnet machine [222] has also been proposed, which represents a significant advancement in the field. Additionally, the idea of a hybrid coupling study on torque calculation has emerged, which involves combining magnetic couplers of different topologies within a single structure [223]. These developments have greatly expanded the scope and potential of MC technology in various applications.

MCs have found widespread use in various industries, including automotive, marine, pump, and compressor applications, among others [224, 225]. A significant practical advantage of MCs is their ability to prevent mechanical faults by slipping when excessive torque is applied, particularly in critical applications [226]. MCs are also suitable for use in hazardous or corrosive environments, due to their ability to transmit torque through a containment shroud, offering increased safety and reliability [47].

Researchers have conducted optimization studies [227, 228] to achieve the most efficient design of MCs. In addition, studies have explored the potential of using magnetic bearings [229] in place of mechanical bearings to lower maintenance and operating costs. Although there are only a few studies available, the use of MCs in aerospace applications has been investigated [230-232]. For example, Charpentier et al. [233] examined ironless permanent magnet devices as a coupling and an axial bearing based on magnetic charge theory for naval propulsion. Bojoi et al. [6] compared radial and axial flux PM machines to evaluate the benefits, constraints, and drawbacks of the more electric engine.

Despite the availability of some market products, there is still a need for improvement in application-based designs.

A promising avenue for the development of new systems is the combination of MCs with S/Gs. This integration can allow for the utilization of the capabilities of these technologies to create more advanced and efficient systems that are better suited to meet the needs of diverse applications and address the limitations of conventional hybrid UAVs and conventional S/Gs. Such an approach can lead to notable enhancements in performance, reliability, and cost-effectiveness, among other factors.

2.7. Objectives and Scientific Contribution of the Thesis

As a contribution to the problem definition in Section 2.5, PEs generate excess power beyond typical flight requirements to satisfy high power demands during take-off, climbing, and manoeuvres. However, this requires flywheel systems for torque continuity and assisted take-off launch ramp systems such as JATO/CATO, resulting in increased system size and weight. The inefficient duty cycles of PEs during flight result in increased fuel consumption, reduced efficiency, and shorter flight duration [234]. Low-power systems require external starting, while larger power systems become unwieldy due to the need for separate electric machines for starting and generating functions. PE start-up delays, high temperatures, bearing/fuel tank failures, and shaft failure jeopardize system safety and reliability. Out-runner S/G structures are traditionally favored for ease of installation, compromise system insulation and cooling, reducing reliability and performance.

2.7.1. Objectives

The thesis was initiated to enhance the safety, reliability, durability, and capability of UAVs by comprehensively addressing the limitations of conventional UAVs, while also integrating and harnessing the all-in-one advantages. The study aimed to conduct a thorough analysis of the current technology shortcomings and propose innovative solutions to overcome these challenges, resulting in a substantial enhancement in performance and efficiency. To tackle the difficulties faced by UAVs, a pioneering solution has been put forth in the form of a magnetically coupled dual-stage Starter/Generator (DCSG). The system is patented under file number TR2020/22757, providing legal protection to intellectual property [235].

The DCSG optimizes the propulsion efficiency by assigning one or two DCSG stages as a motor during high thrust requirements such as climbing, where the PE consumes more fuel.

Meanwhile, during low thrust requirements such as cruising and diving, where the UAV consumes less fuel, the system battery group is charged by assigning one or two stages of the high efficiency DCSG as generators. As a result, the total fuel consumption of the PE is reduced, while the batteries are charged in the most efficient manner, thereby increasing the flight time. The fundamental block diagram of DCSG is demonstrated in Figure 2.12. The DCSG can be easily integrated into existing UAVs to hybridize or adjust the hybridization rate of hybrid UAVs.

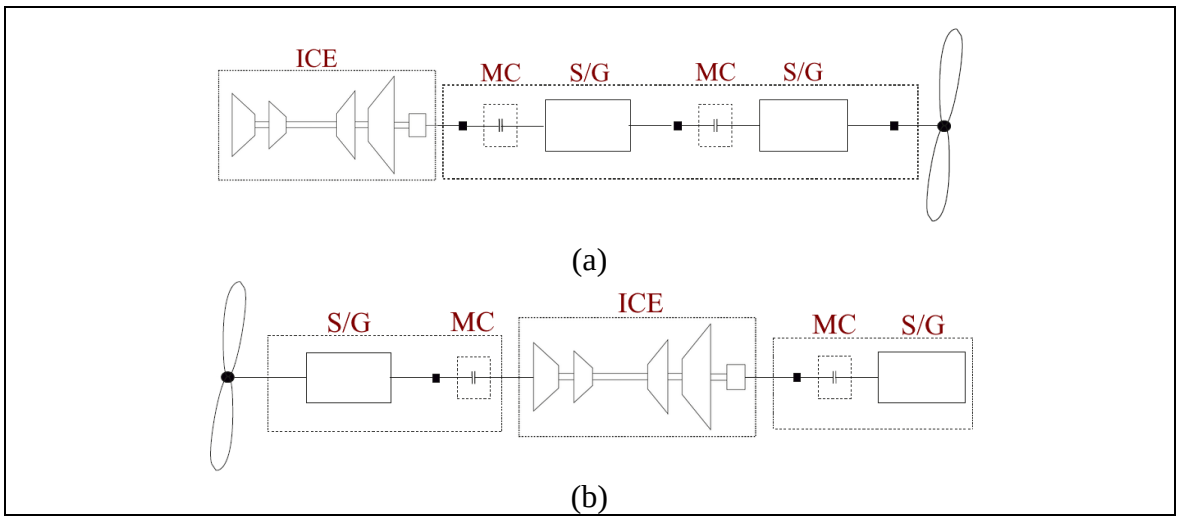


Figure 2.12. Fundamental block diagram of the magnetically coupled double-stage S/G (a) Puller aircraft connection (b) Pusher aircraft connection

For maximum propulsion system efficiency, DCSG stages can be motor/motor, motor/generator, or generator/generator depending on UAV power and flight route. Moreover, the DCSG system is designed with all shafts magnetically isolated using specially designed MCs between the PE and the first stage S/G, as well as between the first and second S/G stages. This ensures that, in the event of a shaft failure, one or more S/G stages will continue to operate as a motor, allowing the UAV to continue its mission.

Furthermore, the DCSG system provides a significant weight advantage compared to conventional systems, contingent upon the total propulsion system power and hybridization ratio of the UAV system in which it is integrated. This advantage is achieved through the reduction of required piston engine power, as the DCSG stages are able to participate in the propulsion system by acting as engines. However, it is important to note that the weight reduction benefit may not be appropriate for UAVs with less than 40 HP.

2.7.2. Scientific contributions

This thesis presents a revolutionary approach in the form of a smart modular hybrid propulsion system and its management method, which provides numerous significant benefits. These include a remarkable increase in system efficiency, a substantial reduction in total system weight, a significant decrease in fuel consumption, and a remarkable extension in flight time through coupling with conventional and/or hybrid systems.

The present thesis outlines the development of a propulsion system that comprises an ICE and multiple modular S/G stages. These stages can be operated as generators and/or motors, and all propulsion elements can be managed individually, enabling the identification of optimal combinations for efficient operation in various power requirements. The utilization of various MC conversion ratios enables the system to attain higher velocities on the propeller side, leading to a reduction in the size of the propeller.

Additionally, the UAV can function at high altitudes as the DCSG propulsion system takes over completely when the piston engine becomes inoperative. Designing MC and S/G modularly enables gradual combination of structures to fulfil rising power transmission requirements, avoiding redesign and production, and creating a versatile modular structure.

DCSG offers significant advancements beyond its primary function, including the following:

- Increased efficiency results in longer flight times and reduced fuel consumption. Alternatively, improving propulsion efficiency enables the use of a smaller PE to achieve the same flight duration and reduce system weight.
- A double-stage stator and rotor structure that is independently controlled, providing greater flexibility and efficiency.
- An embedded maximum flight time algorithm, optimizing the system's operation for maximum efficiency and flight time.
- Independent S/Gs enable master/slave operation, granting superior system control.
- Drivetrain lifting was made possible through magnetic couplers, improving the overall performance and reliability of the system.
- The ability to achieve the Start/Stop feature allows for increased levels of control over the system and reduces wear and tear on the components.

Moreover, the DCSG system offers a multitude of advantages, including:

- Intelligent and predictable warning system implementation for improved safety.
- Quieter start-ups and lower piston temperatures increase engine lifespan.
- Integrating regenerative braking enables energy recovery and reduces fuel usage.
- Smooth operation is ensured with low torque ripples, minimal noise, and vibration.
- Applicable to all systems using PE and TE, providing implementation flexibility.
- Ability to operate above nominal speed values through the use of flux weakening.
- DCSG's high power delivery enables instant manoeuvring and G-turning ability.

3. ELECTRIC MACHINE TOPOLOGIES AND MATERIALS FOR STARTER/GENERATOR AND MAGNETIC COUPLER APPLICATIONS

This chapter offers a detailed examination of the machine structures and materials employed in S/G and MC applications. Specifically, it emphasizes the benefits of permanent magnet brushless machines, which are notable for their high power density per unit volume. The chapter further categorizes rotor topologies and discusses the materials utilized in the design and manufacture of proposed double-stage magnetically coupled Starter/Generator (DCSG), outlining their respective properties. Through an enhanced understanding of critical design factors, the insights offer valuable guidance for component selection and optimization.

3.1. Machine Topologies for Starter/Generators

Electric machines are essential components of high-performance electrical power-generation systems (EPGSs) used in modern aerospace and military industries [236]. Their importance is particularly evident in the MEA of aircraft and spacecraft. Commercial planes shift to noble air, variable-frequency power distribution, and electrical actuation, while some military aircraft rely on MEA for primary and secondary flight control.

Recent developments in aerospace have created a surge in demand for EPGS power, resulting in increased operating voltages and reduced system losses, weight, and volume. However, these advancements have also created new power-quality and electromagnetic interference requirements to address quality and performance concerns. As a result, the number of installed EMs has significantly increased, posing challenges for their use. Therefore, it is necessary to improve the overall system performance and power-density for new-generation EMs while addressing cost constraints to make more affordable platforms.

EMs have been in use for over a century, with many of today's machines being invented during the early days of electrification when the theory was established. Recent aerospace advancements have created new challenges that require innovative solutions to maintain high levels of performance, reliability, and affordability. Figure 3.1 provides a review of small family EMs, featuring the most commonly used representatives in EPGSs for aerospace applications [236, 237].

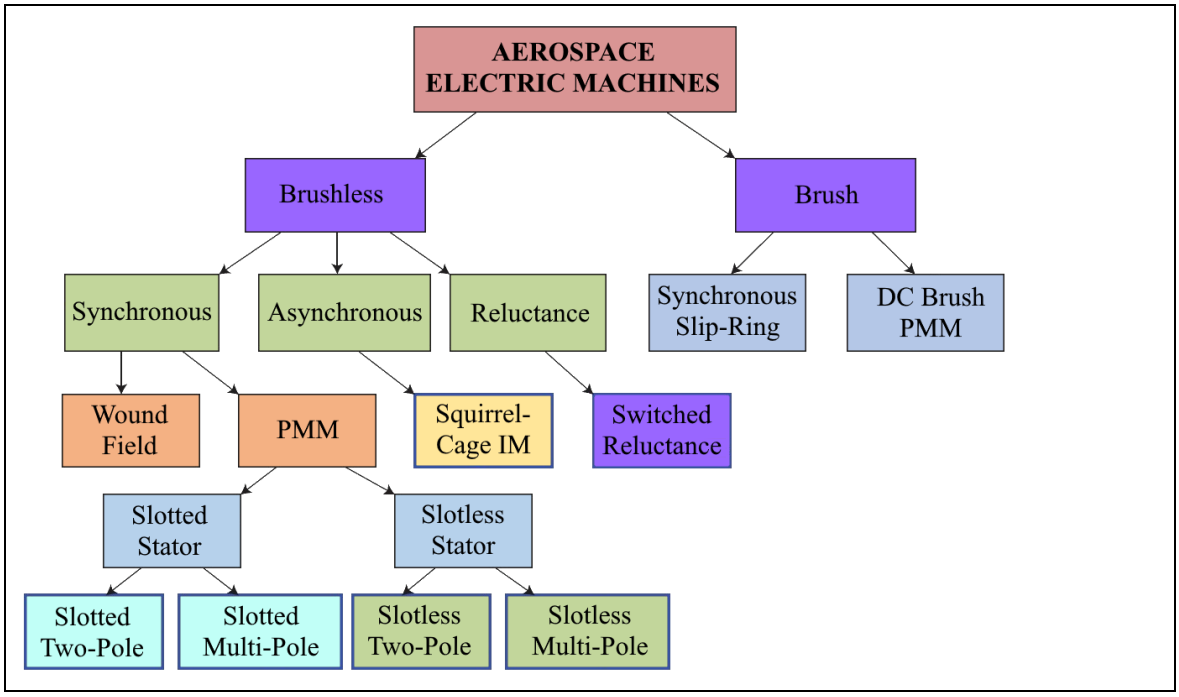


Figure 3.1. Electric machines used in aerospace applications

The use of mechanical contact for power transfer from the rotor in a DC brush permanent magnet machine (PMM) significantly reduces its reliability. In addition, frequent maintenance and wear resulting from mechanical friction present further challenges. Although brushed PMMs are commonly used for low-speed applications due to their simple structure and cost-effectiveness, a noticeable shift is taking place towards brushless designs. Higher cost and complex control aside, the long-term benefits of improved efficiency, and reliability can justify the investment in brushless PMMs. They produce less heat and noise and require less maintenance, as they do not have any brushes that can wear out. With technology advancing at an unprecedented pace, brushless electric machines will likely become even more prevalent in various applications in the future.

Brushless machines are comprised of three primary branches: synchronous, asynchronous, and reluctance. The switched reluctance machine (SRM) is the most commonly used due to its simple construction and high-speed capability. However, controlling SRMs can be challenging due to highly distorted nonsinusoidal fluxes, resulting in excessive losses in both the stator and rotor [236]. The noncylindrical rotor cross-section creates significant windage losses, while substantial rotor steel losses can lead to cooling difficulties. Moreover, SRM performance is highly sensitive to the air gap magnitude, and the rotor's laminated material results in insufficient stiffness, leading to certain mechanical integration issues.

The squirrel-cage induction machine (IM) is the most popular asynchronous type and is capable of operating directly from the bus, making it a cost-effective constant-speed drive. Recently, successful integrations of IMs for EPGSs have been achieved. However, IMs contain short-circuited copper or aluminum bars, which create an additional speed limitation. In Table 3.1, a comparison among the IM, SRM, and PMs can be observed [237].

Table 3.1. Comparison of IM, SRM and PM

Machine Type	Power Density	Torque Overload	Safety Aspects	Complexity
IM	Medium	Medium	Good	Low
PMM	High	Good	Moderate	Medium
SRM	Medium	Medium	Good	Low
WRM	Low	Good	Good	High

Synchronous machines can be divided into wound-field machines and PMMs. While wound-field machines are commonly used in power generation for main-engine and APU applications, their complex construction makes them unsuitable for high-performance EPGSs. On the other hand, brushless PMMs have three main stator constructions: slotted, slotless, and coreless types, as shown in Figure 3.2, and two rotor constructions: two-pole and multipole [238]. Slotless and coreless stators offer numerous advantages. First, a stator without teeth and slots eliminates cogging torque, resulting in easier motor starting. Second, in slotted stators, the space available for winding is limited due to coils being wound inside slots. In contrast, a slotless structure provides more free space and greater freedom of coil arrangement. Furthermore, slotless and coreless stators reduce iron loss, particularly during high-speed operation [239]. A two-pole PMM rotor has a single-piece magnet, while a multipole rotor has a more complex design with more magnets.

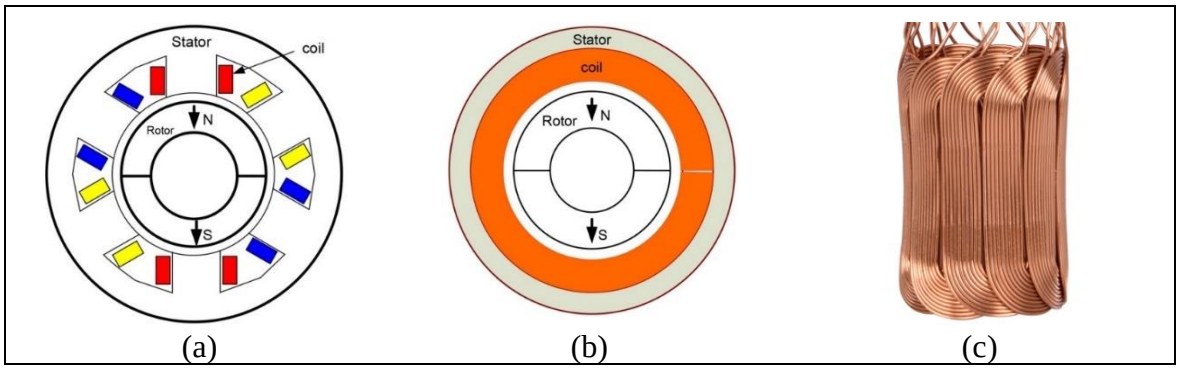


Figure 3.2. Stator types: (a) Slotted-type (b) Slotless-type (c) Coreless-type

The improvements in EMs as a component of an EPGS must be considered in conjunction with their integration into driver and electromechanical systems. The availability of low-cost power electronics, along with advancements in nonconventional bearing systems and more efficient cooling methods, has propelled EMs towards achieving better performance. Electric drives will be vital for future space vehicles, leading to an increased demand for high-quality electric power. Table 3.2 provides a detailed comparison of aerospace EMs [236].

Table 3.2. A comprehensive examination of electric machines for aerospace applications

Machine Type KCs*		Rating			
		IM	SRM	PMM Tooth	PMM Toothless
KC 1	Rotor Losses	6	6	10	10
KC 2	Stator Losses	8	8	10	9
KC 3	Windage Losses	5	1	9	10
KC 4	Rotor Thermal Limitation	8	10	4	4
KC 5	Cooling Options	5	5	9	10
KC 6	Rotor Mechanical Limitation	5	7	9	10
KC 7	Torque-to-Inertia Ratio	5	7	9	10
KC 8	Torque Pulsation	9	3	6	10
KC 10	High-Speed Capability	5	7	9	10
KC 11	Short-Circuit Behavior	10	10	4	3
KC 12	Machine Complexity	7	10	9	8
KC 13	Current Density	7	7	10	8
KC 14	Power Density	7	8	10	8

*1=worst, 10=best. [236]

Multiphase and three-phase electric machines have been the subject of extensive research and analysis [240, 241]. Although multiphase machines offer advantages such as decreased vibration and increased degrees of freedom, they also have certain limitations that must be considered. Nevertheless, they remain a popular choice due to their ability to increase power density through harmonic injection and alter the number of pole pairs without winding switch-over. On the other hand, three-phase machines are widely used and offer a variety of benefits over multiphase machines. Their simpler design and availability of components make them more cost-effective, and their simpler control algorithms require fewer components. They have a higher power factor, offer high efficiency at low loads, and have a long history of reliable performance. These qualities make them a versatile and dependable solution for aerospace applications. Table 3.3 provides an exhaustive overview of the most significant benefits and differences between these two systems [242].

Table 3.3. Comparison of 3-phase and multiphase electric machines [242]

	Three-Phase	Multi-Phase
Torque ripple frequency	$6f_1$	$2mf_1$
Lowest space harmonics	5 and 7	2m +- 1
Winding distribution factor	Lower	Higher
Power per phase	P/3	P/m
Winding connections	Star / Delta	>2 (depends on phase number)
Harmonic injection	Only with nonrotating component	Possible with higher time harmonics
Open-phase fault continue	No	Yes
Vibration level	Lower	Higher
Core loss	Lower	Higher

The utilization of brushless permanent magnet machines (PMMs) in Starter/Generators has gained significant attention in recent years due to their exceptional efficiency and power density. The gradual replacement of asynchronous and reluctance machines with these high-performance machines is largely attributed to advancements in speed control systems and frequency converters. The outstanding performance and efficiency of PMMs have significantly improved the reliability and cost-effectiveness of these applications.

PMMs are known for their additional advantages over other types of electric machines. The use of permanent magnets instead of windings in the rotor eliminates the need for rotor excitation current, reducing excitation losses and increasing efficiency. PMMs do not require a brush and collector system like DC machines, resulting in reduced maintenance costs and increased efficiency due to the absence of losses in the brushes. The absence of windings in the rotor leads to a reduction in weight, resulting in a shorter rotor length and low moment of inertia. The increased air gap induction allows for a reduction in the size of stator windings and outer diameter of the machine, resulting in a smaller volume and weight compared to DC and asynchronous machines of the same nominal power and speed. Since there are no windings on the rotor, cooling PMMs are easier. Figure 3.3 provides a comparison between the structures of PMMs and IMs, specifically in terms of their size and weight [243].

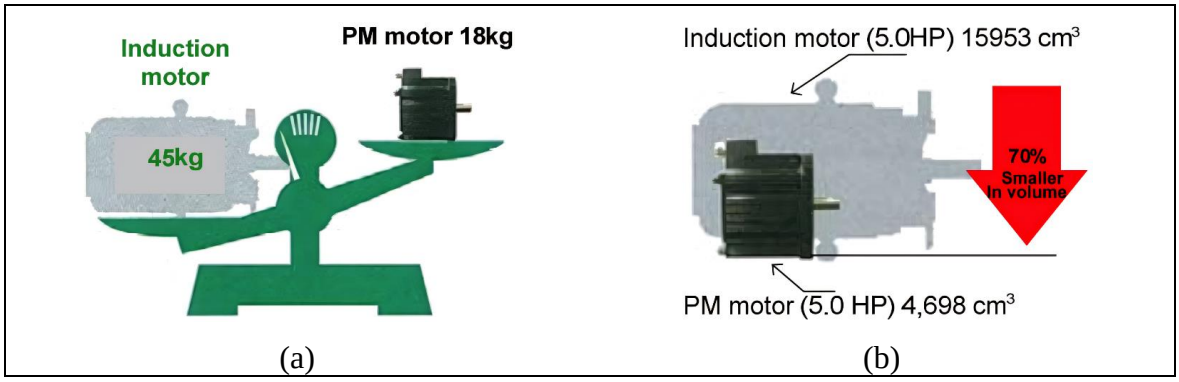


Figure 3.3. Brushless PM vs IM comparison: (a) Weight (b) Size [243]

Aerospace electric machines can be characterized based on their requirements, which refer to a select few characteristics of an end-unit product that have a significant impact on its performance. Selecting weight, volume, reliability, efficiency, and cost as performance metrics can lead to an optimized design. Below are the critical aerospace requirements :

- Weight is a critical factor in determining the performance of aircraft.
- Volume has become critical due to increased electrical component installations.
- Reliability affects mission success, maintenance, repair, and dispatchability.
- Efficiency drives fuel savings and is gaining momentum.
- Cost determines affordability and must be considered in the design phase.

The rapid development of permanent magnet S/Gs is attributed to three key factors [244]:

1) Advancements in magnet technology and increased competition: The 1980s discovery of NdFeB magnets revolutionized PMM technology, enabling a surge in development due to declining magnet prices from China in the 1990s, overcoming SmCo magnets' previous slow progress.
2) The rise of efficiency-focused applications: EMs are being increasingly used in aircraft subsystems and can replace traditional machinery due to their compactness and efficiency, and can be integrated with mechanical systems such as fuel engines.
3) Development of silicon sheet technology and coupling technology: The advancement of silicon sheet technology and coupling technology has enabled the construction of more efficient and compact machines, and has also facilitated improvements in the electromagnetic and mechanical properties of brushless PMMs.

On the other hand, given the technical characteristics and operational parameters, it is relevant to classify S/Gs as part of high-speed electric machines. The term "high-speed" in the EM industry typically denotes machines that operate above 3600 rpm, leveraging advanced materials and technologies to achieve higher power density and efficiency.

Increasing the shaft speed in EMs eliminates power transmission elements such as gearboxes, belts, and pulleys, which results in a reduction in size and weight, making them portable and more efficient. High-speed S/Gs, designed for specific systems, provide direct drive benefits, including cost savings and other advantages that include [245]:

- Congestion reduction,
- Enhanced portability,
- Simplified mechanical design,
- Efficient cooling,
- Minimal torque ripple.

The statement highlights that there is a diverse range of PMMs that differ in various aspects such as magnet orientation, slot/pole combinations, winding layout, driving method, magnet placement, and rotor position. The different types of PMMs utilized for synchronous S/G applications have been systematically categorized in Figure 3.4 [246-248].

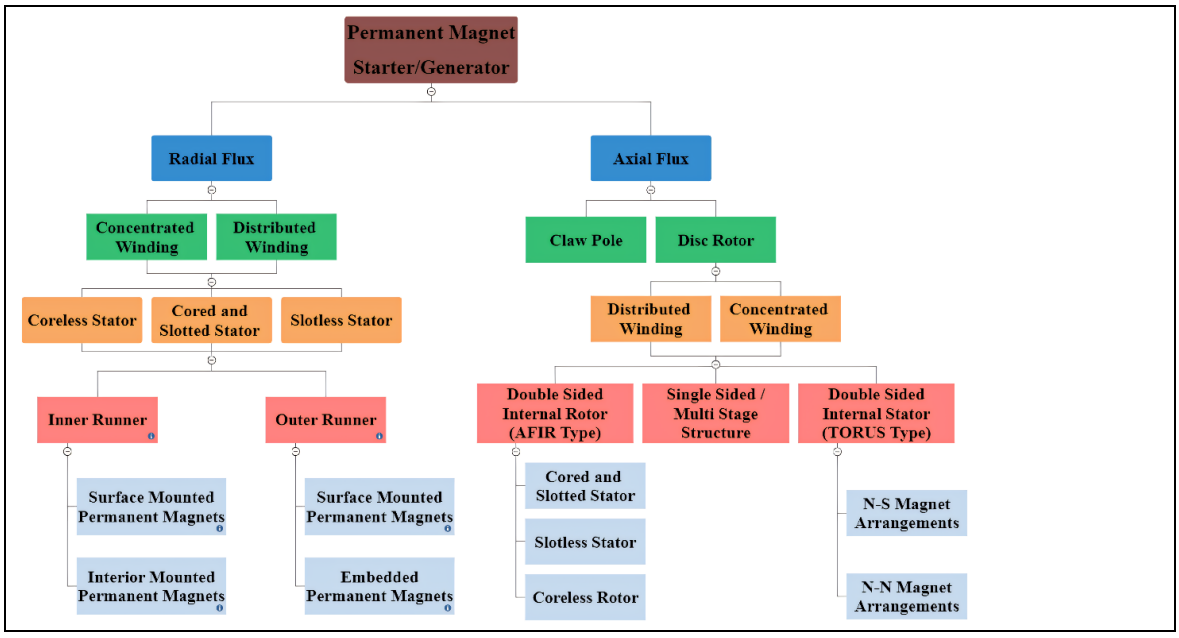


Figure 3.4. Classifications of permanent magnet synchronous Starter/Generators

Brushless PM motors can be categorized as AC or DC based on their back-EMF voltage [249]. AC machines require sinusoidal back-EMF, typically with distributed windings, whereas DC machines require a more trapezoidal waveform with concentrated windings, as illustrated in Figure 3.5. Some machines have intermediate waveforms that can work with either AC or DC control [250]. DC motors are suitable for power drives that can tolerate torque ripple and do not require substantial field weakening at high speeds. AC motors are more suitable for smooth operation and extended field weakening.

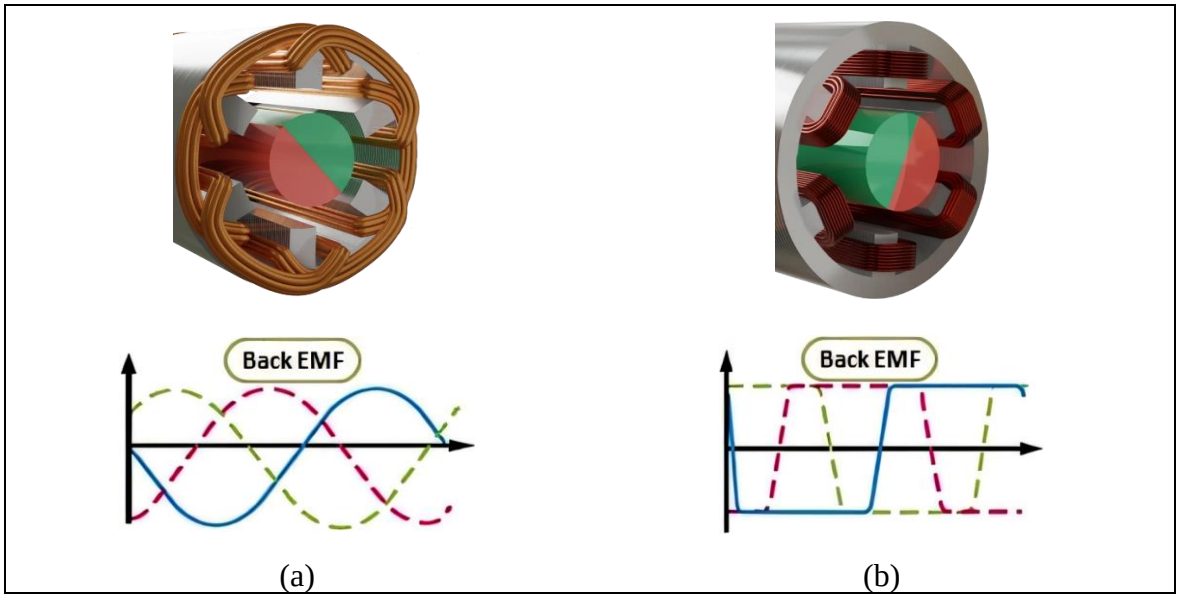


Figure 3.5. (a) Sinusoidal Back-EMF-Disributed winding (b) Trapezoidal Back-EMF-Concentrated winding [249]

In general, in-runner (inner runner) and out-runner (outer runner) topologies differ in their rotor and stator configurations, with in-runner machines having the rotor located inside the stator and out-runner machines having the rotor located outside the stator, as shown in Figure 3.6. Their design difference leads to significant distinctions in performance and applications.

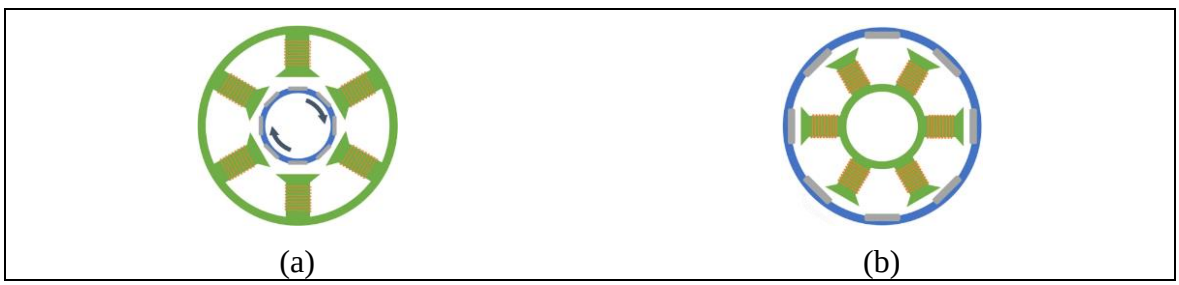


Figure 3.6. Rotor and stator configuration: (a) In-Runner structure (b) Out-Runner structure

The out-runner rotor configuration typically experiences high armature thermal load, copper loss, and current density, leading to reduced efficiency due to increased losses. Nevertheless, this configuration is favored for its smaller volume, lower cost, and short circuit current. In contrast, the in-runner rotor type, which shares the same PM geometry and characteristics, offers benefits such as higher output power and lower load resistance, armature current density, thermal load, and total losses [251]. The external rotor configuration is widely considered superior due to its lower total weight. Moreover, it offers additional advantages such as ease of installation and cooling, making it a popular choice for various applications. The choice between stator and rotor topologies depends on application requirements, considering power density, efficiency, cooling, and torque density trade-offs [252].

The benefits of axial and radial PMMs have been extensively researched and discussed. Axial flux machines have a shorter and more direct flux path, leading to higher efficiency and power density, while radial flux machines have a longer flux path, as shown in Figure 3.7, resulting in higher iron losses and lower efficiency [253]. Axial flux machines have superior winding designs and can use grain-oriented steel, improving efficiency, but require more PMs and are more complex to manufacture [254]. Radial flux machines have a simpler construction and are more environmentally friendly due to their reduced volume of PMs.

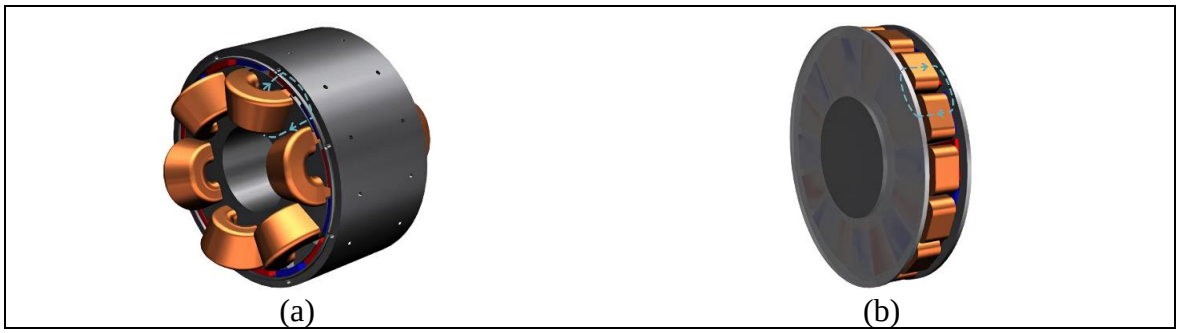


Figure 3.7. S/G topology comparison based on PM orientation (a) Radial flux (b) Axial flux

Axial flux structures with a larger rotor diameter and shorter length lead to increased rotor surface speed and higher stresses, resulting in higher maintenance costs and reduced machine continuity [255]. In contrast, radial flux structures with a smaller diameter and longer rotor generate smaller rotor stresses and enable higher speeds.

Radial flux structures can also incorporate effective protection methods to prevent damage to fragile PMs at high speeds, unlike axial flux structures. Therefore, radial flux PMMs are preferred in high-speed direct-drive S/G applications.

Rotor design for radial flux PMMs is a critical aspect and can have a significant impact on their performance. There are numerous rotor topologies available, each with its unique advantages and disadvantages. In general, rotor topologies can be classified into two primary types, namely surface magnet rotors and interior magnet rotors. Choosing an appropriate rotor topology depends on various factors, including specific application requirements such as torque, speed, and efficiency. Other factors such as manufacturing complexity, cost, and maintenance requirements also play a crucial role in selecting the right rotor topology.

3.1.1. Surface mounted permanent magnets

Surface-mounted permanent magnets (SMPMs) are attached to the rotor's outer surface in the form of thin strips or springs using robust adhesives. This cost-effective mounting method takes into account the air gap, which leads to equal magnetic fluxes of the d and q axes, as shown in Figure 3.8. However, the rotor's constant inductance with respect to the rotor position and the low stator inductance make field weakening difficult [245]. Moreover, due to the rotor's magnetic symmetry, machines with this rotor structure lack a reluctance moment. Despite its simplicity, this rotor structure results in a large air gap and poor induction response to pole flux, limiting the machine's effectiveness.

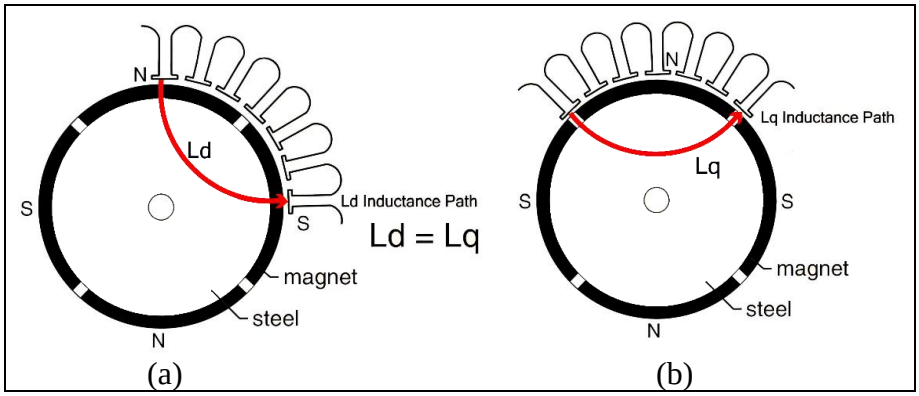


Figure 3.8. Surface mounted permanent magnets (a) d-axis path L_d (b) q-axis path L_q

The assembly of SMPMs offers significant advantages in terms of design, production, and cost-effectiveness, making it a popular choice. However, a major drawback of this simple rotor structure is the magnets' low resistance against centrifugal forces, which can cause damage to the rotor. However, attaching nonmagnetic materials to the rotor surface can enhance the robustness of surface magnet rotors. However, this method often leads to increased air gaps, which can decrease machine efficiency.

3.1.2. Interior mounted permanent magnets

Interior-mounted permanent magnets (IMPMs) have their magnets glued into cavities drilled directly into the rotor. This rotor shape offers the advantage of magnetic material covering the magnets, leading to the formation of the reluctance moment, an inevitable outcome. IMPMs exhibit a mechanical robustness advantage over SMPMs, which makes them highly resistant to centrifugal forces. Thus, they are preferred for high-speed applications where the production cost is insignificant. Additionally, they offer higher efficiency than SMPMs, primarily because air gaps are smaller. However, the biggest disadvantage of this design is its cost. Placing magnets inside the rotor requires advanced technology. The synchronous reactance in the q-axis is greater than in the d-axis, and the width of the bridge between neighboring PMs must be carefully selected, as illustrated in Figure 3.9 [243].

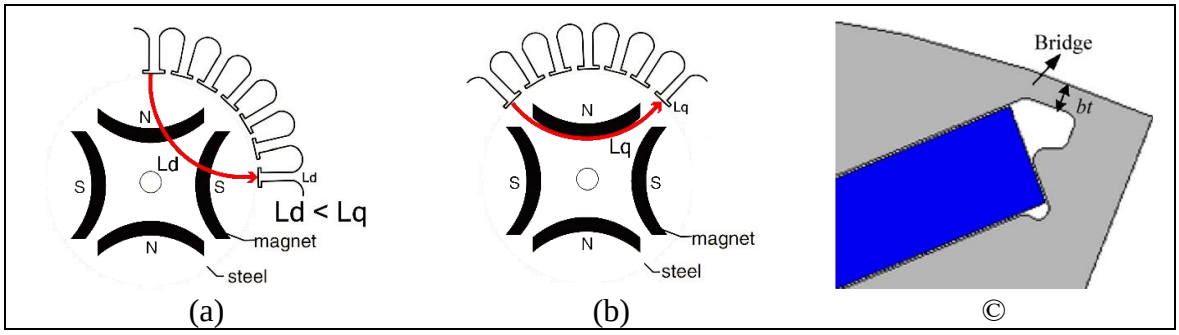


Figure 3.9. Interior mounted permanent magnets (a) d-axis path (b) q-axis apth (c) PM bridge

IMPMs can be realized in three types: internal inset, spoked and specific, as illustrated in Figure 3.10 [256]. Both of these structures create more roughness in high-speed applications and create a geometric dislocation that is useful for sensorless control. IMPMs also allow for effective flux weakening, which is difficult to achieve with SMPMs.

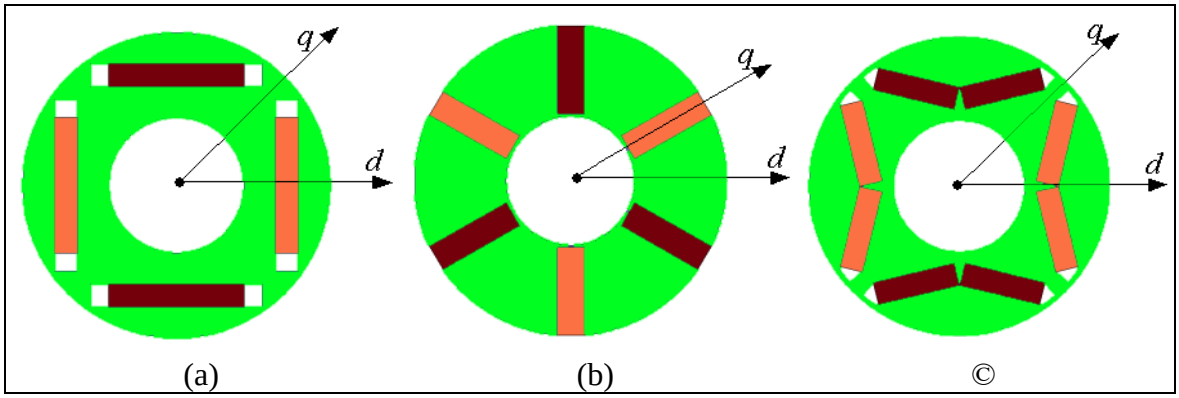


Figure 3.10. Types of IMPMs (a) Internal inset (b) Spoked (c) Specific-V shape

Radially fluxed buried PMs (Internal inset type)

Internal inset type rotors have embedded magnets that generate radial flux. In this type of structure, the q-axis inductance is higher than the d-axis inductance. As a result, flux concentration becomes possible, leading to higher flux density within the air gap than inside the magnet. The air gap is minimized, and the armature reaction is low [257]. By utilizing the flux weakening technique, the control of the machine in the constant power region can be as good as in the constant torque region. Torque generation is affected by both the excitation field and the reluctance moment [258]. In comparison to SMPMs, the peak value of rotor torque for the same magnet size is higher in this design because the magnets also generate the reluctance moment.

Tangentially fluxed buried PMs (Spoked type)

The primary characteristic of the spoked type is the generation of induction at the poles independent of the magnet working point, achieved by adjusting the magnet lengths [259]. This feature allows for very high air gap induction. The operating points of the magnets can also be created around the optimum operating point, leading to the rotor being referred to as a flux-compressed or flux-focused rotor. PMs are radially embedded in the rotor, providing high resistance to centrifugal forces, making this rotor design particularly attractive for high-speed systems. However, the high cost of the materials is a significant drawback [260]. The air gap in this design is larger than in others, which results in a small reluctance on the d axis and a large reluctance on the q axis due to the magnetic permeability of the PMs near the air.

Specific configurations

The use of SMPMs is more convenient at speeds below 10000 rpm due to low magnet losses, as silicon steel and bearing technology have advanced. In high-speed applications, special magnet conditions must be considered to reduce PM losses, protect from demagnetization risks, minimize cogging torque, and increase air gap flux density. Although such structures have advantages, they also have disadvantages such as increased flux leakages due to magnets being surrounded by magnetic material. While these disadvantages can be overcome by placing flux barriers between the magnets, this increases the complexity of the structure. Figure 3.11 illustrates various specific configurations of rotor types.

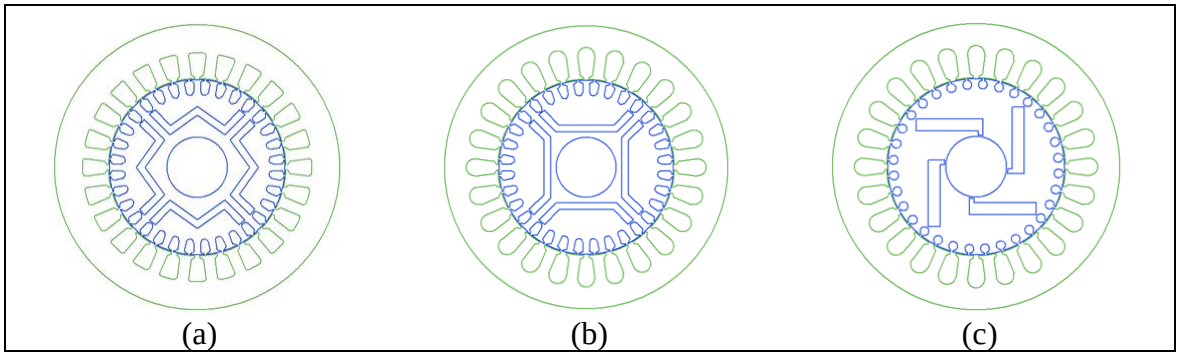


Figure 3.11. Specifically configured IMPMS (a) W-shape (b) U-shape (c) L-shape

Selecting the most suitable rotor structure for Starter/Generators requires a thorough comparison and evaluation of the strengths and weaknesses of both SMPMs and IMPMs. A comprehensive analysis of multiple factors, such as efficiency, output, cost, complexity, and other relevant aspects, is essential to make an informed decision about the optimal rotor structure, resulting in improved performance and cost-effectiveness in the long run.

Table 3.4. Comparison of SMPMs and IMPMs

Surface Mounted PM Machines	Interior Mounted PM Machines
Lower air gap flux density	Higher air gap flux density
Simple machine structures, lower cost	Complex machine structures, higher cost
Weak armature reaction, simple driver	Large armature reaction, complex driver
Sensitive PMs to armature fields	Insensitive PMs to armature fields
Challenging flux weakening	Easy flux weakening
Lack of reluctance torque	Existence of reluctance torque
Ease of design and manufacture	Difficulty of reluctance torque
Higher air gap length, lower efficiency	Lower air gap length, higher efficiency
Low mechanical strength at high speeds	High mechanical strength at high speeds
Less leakage flux in the magnet tips	More leakage flux in the magnet tips
Low iron losses	High iron losses
Less torque density (torque per volume)	More torque density (torque per volume)

3.1.3. Squirrel cage rotor bar-equipped permanent magnet machines

PMSMs can be classified into two types based on their power supply: line-fed and inverter-fed. In contrast to inverter-fed PMSMs, line-fed PMSMs (line-started PMSMs) cannot be started directly from the industrial power supply. However, this limitation can be overcome by adding short circuit bars to the rotor, as illustrated in Figure 3.12 [261]. During startup, these short circuit bars act as an asynchronous torque component in the motor, producing the necessary starting torque until the motor reaches synchronous speed. With the aid of these bars, the motor operates like an asynchronous motor until it reaches synchronous speed. Additionally, the rotor bars play a crucial role in preventing the motor from deviating from its synchronous speed when sudden changes in torque occur.

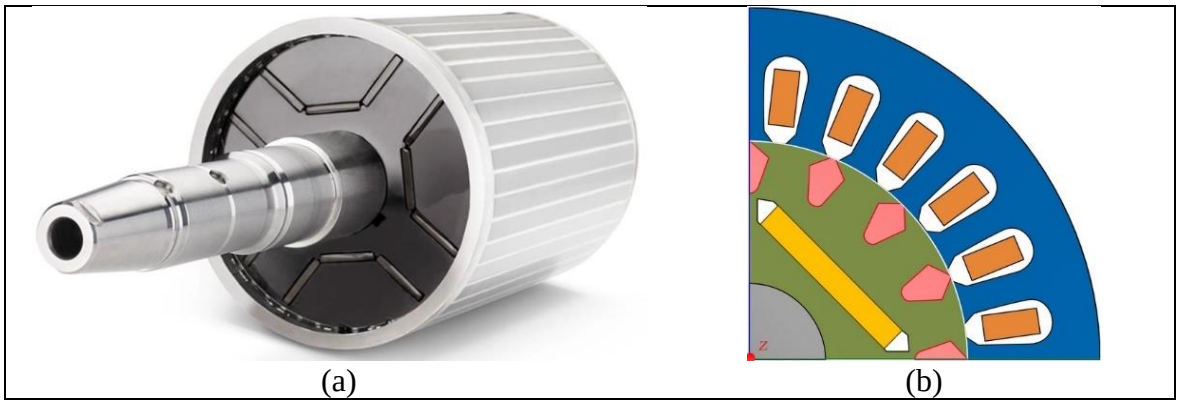


Figure 3.12. (a) Rotor bars in PMSMs (b) Line-started PMSM [261]

Line-started permanent magnet motors (LSPMSMs) offer numerous advantages over traditional induction motors, making them highly significant. These motors exhibit superior energy efficiency due to the inclusion of permanent magnets, which allows them to achieve higher power densities and operate at elevated efficiencies compared to induction motors. Moreover, LSPMSMs can be easily controlled and can operate at variable speeds with the use of a variable frequency drive (VFD) [262].

Another significant benefit is that LSPMSMs can reduce starting current, unlike traditional induction motors, which require a large amount of starting current. This helps minimize power quality concerns such as voltage sags. LSPMSMs are well-suited for frequent start-stop applications such as in aerospace, cranes, hoists, and elevators, as they have a lower starting current and can endure more frequent cycles without the risk of motor damage [263].

3.2. Rotor Topologies for Magnetic Couplers

In recent times, design of magnetic couplers (MCs) has gained considerable attention, and two primary approaches have been adopted for this purpose: analytical and numerical. These approaches have been utilized in several studies aimed at enhancing the performance and reliability of MCs. MCs have emerged as a superior magnetic coupler mechanism due to their numerous advantages such as overload protection, reduced maintenance requirements, a simple design, and the ability to tolerate shaft misalignment, vibration, and noise.

An MC is a type of machine that enables torque transmission between two or more parts without requiring direct contact. This is accomplished through the use of PMs, which interact with one another to transfer torque from one part to another. Unlike traditional couplers such as electromagnetic, electromechanical, and friction clutches, which rely on physical contact, MCs offer additional advantages, including reduced wear and tear, improved efficiency, and the ability to operate in hazardous or corrosive environments [264]. In addition, MCs can be designed to operate at high speeds, making them well-suited for a wide range of applications.

The operation of an MC involves the interaction of PMs and rotating parts. When an engine rotates the inner half of the coupling via its shaft, the PMs generate attraction and repulsion forces that cause the outer half of the coupling to rotate as well.

The interaction forces between the PMs and the MCs rotors work in both directions, meaning that when the inner rotor is driven, the outer rotor follows, and vice versa [265]. This feature makes MCs well-suited for applications where bidirectional torque transmission is needed.

The typical MC comprises several components, including permanent magnets (PMs), inner/internal and outer/external rotors, a protective cover, a containment shroud, and shafts. The PMs generate a magnetic field that interacts with the rotor yokes, enabling the transfer of torque between the coupled parts [201]. The protective cover is an essential component that shields the PMs from high speeds and external elements to prevent damage, which could lead to coupling inefficiency or failure. Similarly, the containment shroud plays a critical role in maintaining a sealed environment that prevents contamination or leakage, which could pose a risk to usage. The MC design can vary depending on the application requirements.

However, all types share the common characteristic of enabling magnetic torque transfer, which offers several advantages over conventional couplers.

Magnetic couplers fall under the category of noncontact electric machines, as demonstrated in the comprehensive grouping illustrated in Figure 3.13 [266].

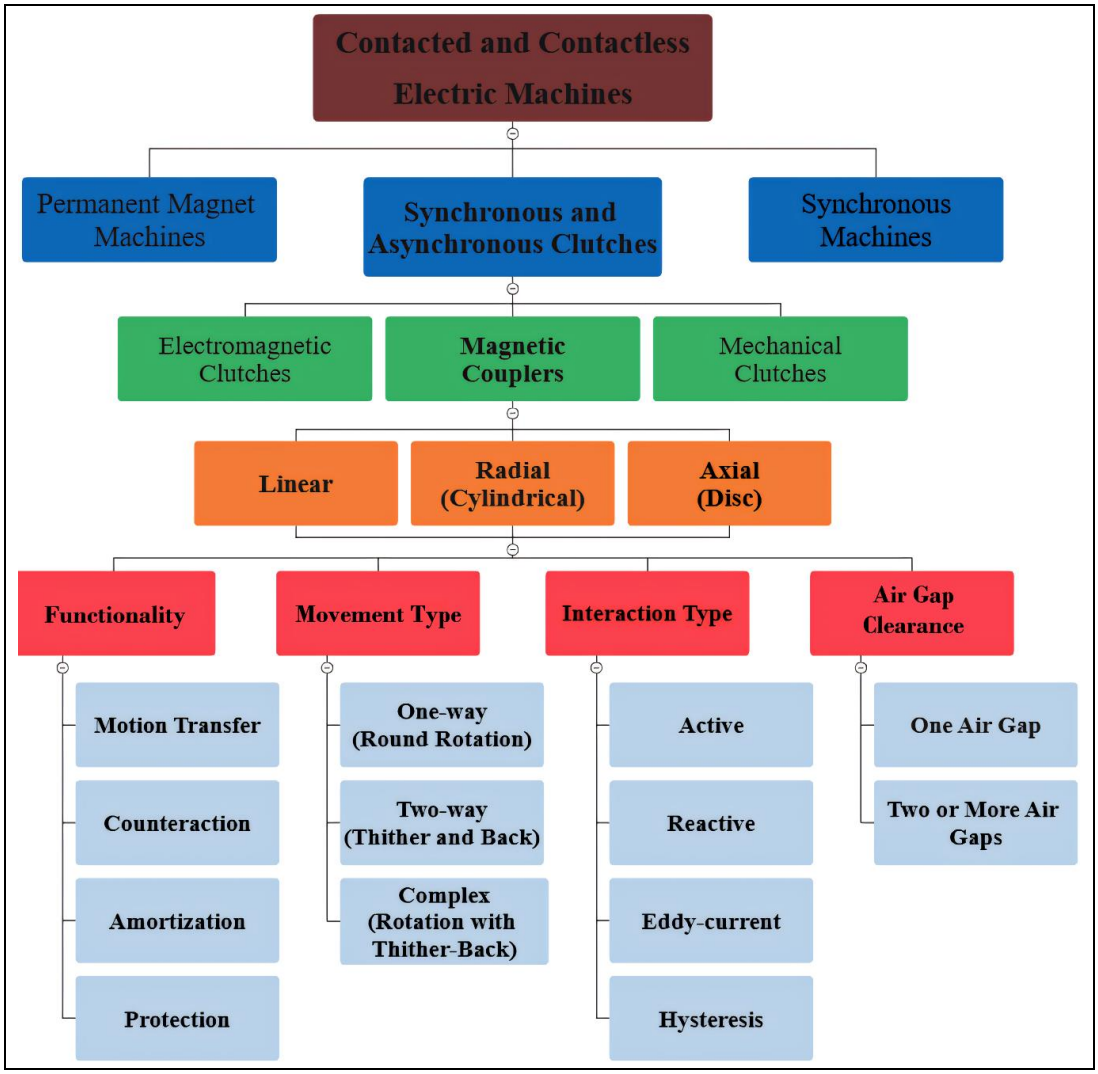


Figure 3.13. Comprehensive classifications of magnetic couplers

These couplings are further classified into two groups, namely synchronous and asynchronous, based on the rotor speeds and magnetic field depending on the load. Synchronous MCs have no rotor slippage, while asynchronous MCs have slippage due to the interaction between magnetic fields and conductive materials, resulting in power loss and reduced efficiency. Therefore, synchronous Mcs are more advantageous, providing better performance and efficiency as the inner and outer rotors rotate at the same speed [264].

Furthermore, depending on the direction of PM magnetization, MCs can be classified as linear, radial, or axial, as illustrated in Figure 3.14. Radial MCs are also referred to as cylindrical couplers, while axial MCs are known as disc-type couplers [44, 266].

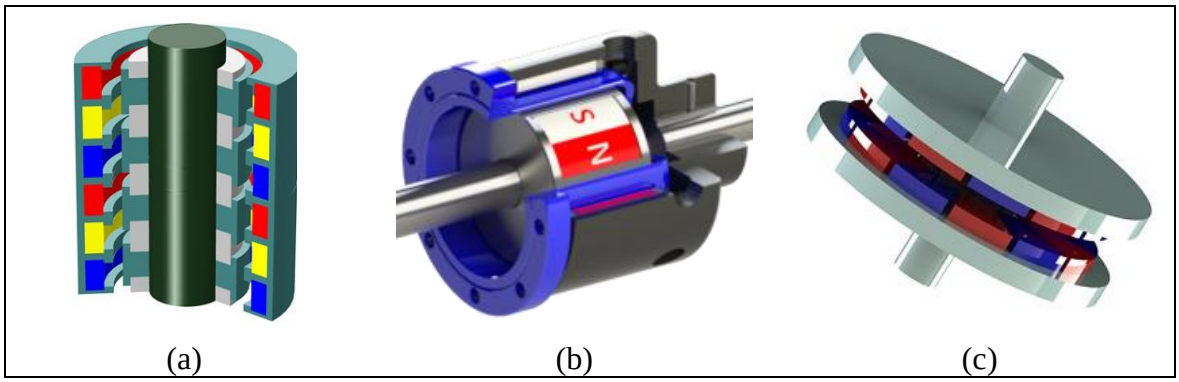


Figure 3.14. MCs based on direction of PM magnetization (a) Linear (b) Radial (c) Axial

MCs are further divided into four groups based on functionality, performance type, interaction type and air gap type. In turn, these groups are expanded as active, reactive, eddy current, and hysteresis couplings based on their interaction type, as shown in Figure 3.15. Additionally, according to the magnet type of the rotors, MCs can be classified as star-type PM, cylindrical-PM, ring-PM, separate-salient PM, and toothed-surface PM [267-269].

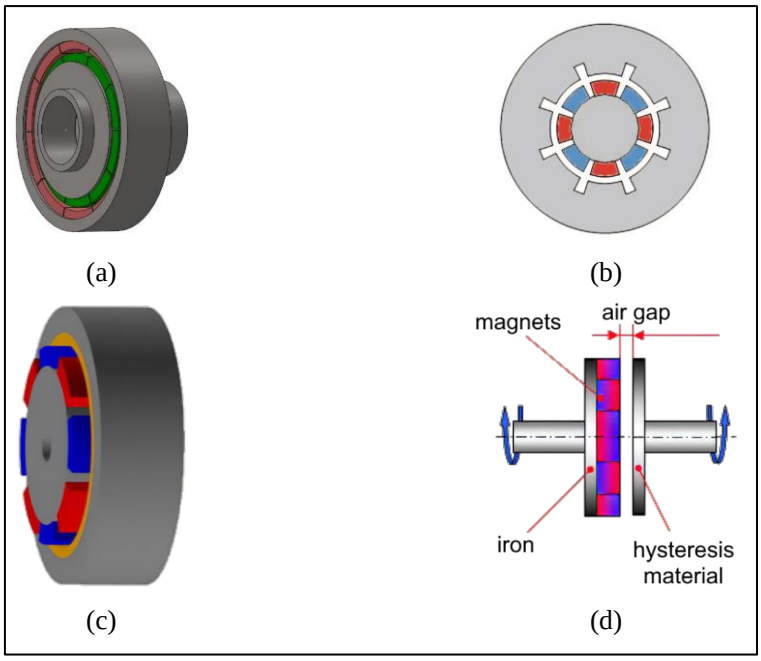


Figure 3.15. MCs interaction types (a) Radial Active (b) Radial Reactive (c) Radial Eddy-current (d) Axial Hysteresis

Synchronous radial magnetic couplers have gained significant importance in high-speed direct-drive aerospace applications due to the need for synchronous speed for both the inner and outer rotors.

In such applications, any deviation in speed between the rotors can lead to significant performance and efficiency issues. The use of radial synchronous MCs, which eliminate any slippage between the rotors, provides a reliable and efficient solution to this problem. Additionally, radial couplers have the advantages of compact design, low noise and vibration, and high torque density, making them suitable for aerospace applications where space and weight constraints are critical. Therefore, the use of radial synchronous magnetic couplers has become increasingly prevalent in the aerospace industry. The diverse rotor and magnet topologies utilized in MCs are depicted in Figure 3.16 [46, 201, 270].

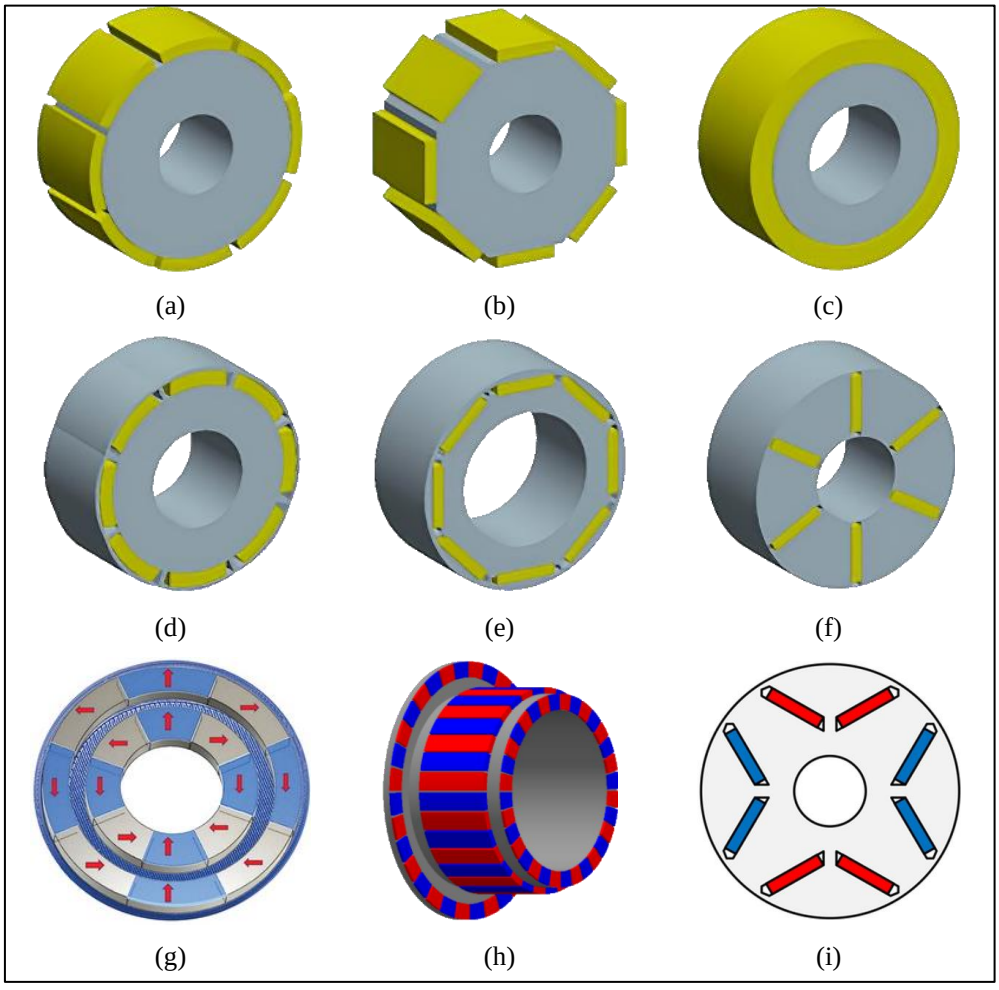


Figure 3.16. Different MC rotor topologies: (a) Arc surface-mounted; (b) Rectangular surface-mounted; (c) Ring-type; (d) Buried arc type; (e) Buried type; (f) Inset type; (g) Halbach arrays; (h) Enhanced hybrid (i) V-shape

3.2.1. Magnetic gear concept

A magnetic gear (MG) is a type of magnetic coupler that uses magnetic fields to transmit torque between an inner and outer rotor, which operate at different speeds. Traditionally, gearboxes have been used to transfer the high-speed, low-torque input to a low-speed, high-torque output via mechanical contact between gear sets. However, this mechanical interaction of gearbox components often leads to issues such as the requirement for frequent lubrication and maintenance, generation of acoustic noise, transmission of vibrations, and damage in overload conditions, resulting in low system utilization and labor-intensive maintenance and replacement of gearbox components [266].

In contrast, MG offers an attractive alternative to the mechanical gearbox. In case of over-load conditions, the "pole-slips," which may cause additional acoustic noise and vibrations, but no lasting damage should occur within the drivetrain [271]. The compliance of the MG significantly reduces the transmission of torsional vibrations, which is particularly beneficial in certain applications. Thus, the resulting drivetrain offers competitive advantages:

- Frictionless torque transfer: Torque is transmitted through magnetic forces, which eliminates wear and losses related to tooth meshing.
- Low maintenance: The bearings are the only components in a magnetic gear requiring lubrication, with minimal maintenance requirements.
- Overload protection: Magnetic gear slipping when the pull-out torque is exceeded protects other drivetrain components more effectively than mechanical gears.
- Reduced noise: Due to the smooth transfer of torque and the absence of tooth contact, magnetic gears are expected to operate quietly.
- High efficiency: Magnetic gears experience different power loss mechanisms than mechanical gears, allowing for high levels of efficiency.

MGs have also become increasingly important in aerospace applications, espacially in UAVs, due to their high torque density, high efficiency, reliability, durability and compact size. Their ability to operate without contact between the rotors allows them to function in harsh environments. A comprehensive overview of the various types of MGs, including conventional and unconventional designs, is available in Figure 3.17 [266, 272, 273].

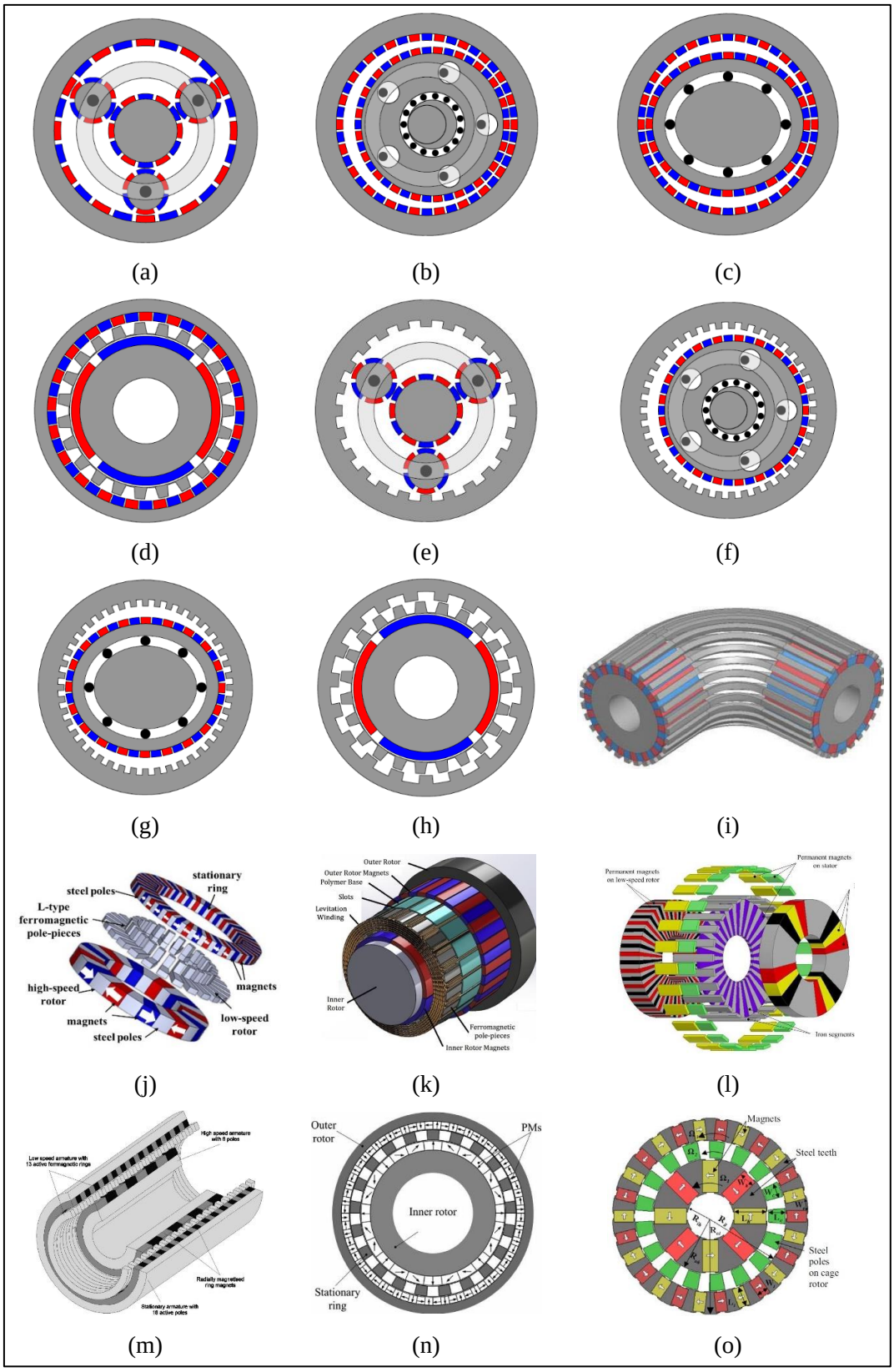


Figure 3.17. Types of magnetic gears (a) Planeraty (b) Cycloidal (c) Harmonic (d) Flux-modulated (e) Planeraty reluctance (f) Cycloidal reluctance (g) Harmonic reluctance (h) Flux-modulated reluctance (i) Intersecting-axes (j) L-shape axial (k) Bearingless (l) Hybrid (m) Linear (n) Hall-bach array (o) Interior

Invention of proposed magnetically coupled double stage Starter/Generator (DCSG)

The proposed DCSG structures offer significant advantages by using magnetic gears in the Starter/Generator stages:

- Different magnetic coupler conversion ratios allow the system to operate at higher speeds, and in some cases, at lower speeds.
- Higher coupler conversion ratios enable higher speeds to be achieved in the modular S/G rotors, as well as lower weight and more efficient designs for the same power. This also facilitates achieving higher propeller speeds, reducing the total system noise, and increasing G-turn manoeuvrability by reducing the propeller diameter.
- Lower coupler conversion ratios allow for lower speeds to be achieved in the modular S/G rotors and for the use of larger diameter propellers in special cases.
- The rotors to which magnetic couplings are attached have independent shaft operation capability, providing smoother torque transmission by reducing power transmission fluctuations (torque ripple).

Modular design of coupler structures allows higher power transmission needs to be met by combining multiple magnetic couplers without the need for redesign or manufacturing. As a result, a flexible modular structure was achieved.

3.2.2. Magnetic coupler or magnetic gear assisted electric machines

Magnetic coupler or magnetic gear assisted machines (MCEM or MGEM) are a promising alternative to mechanical gearboxes. These machines integrate a magnetic coupler, typically a magnetic gear, within a synchronous AC electrical machine, creating a physical and magnetic connection that allows for more efficient power transmission. A recent advancement in EMs involves the integration of PMMs with a magnetic gear, resulting in an MGEM [274]. This technology has the potential to deliver significant cost savings and environmental benefits, making it attractive for performance-critical applications [267].

High Efficiency: MGEMs offer high efficiency due to the absence of mechanical contact between the gears. MGEMs offer minimal energy loss and improved efficiency, resulting in reduced operating costs and lower carbon emissions.

High Power Density: The incorporation of magnetic gears within an electric machine enables a compact design, which allows MGEMs to deliver high power output in a smaller and lighter package than traditional mechanical gearboxes. This high power density makes MGEMs ideal for applications where space is limited and weight is a concern.

Reduced Maintenance: The lack of mechanical components in a magnetic gear results in less wear and tear, leading to fewer maintenance requirements compared to traditional gearboxes. This advantage leads to lower maintenance costs and reduced downtime, making MGEMs especially suitable for critical applications.

Improved Reliability: The use of magnetic gears eliminates the possibility of mechanical wear and tear, which can lead to gearbox failures. Consequently, MGEMs offer improved reliability, reduced downtime, and increased productivity. Furthermore, the absence of mechanical components also reduces the risk of oil leaks and environmental contamination.

Quiet Operation: MGEMs operate with very low noise levels compared to traditional mechanical gearboxes due to the absence of mechanical contact between gears. This feature makes MGEMs ideal for applications where noise levels need to be kept to a minimum, such as in residential or office environments.

MGEM have demonstrated the capability to achieve larger torque densities compared to their equivalent conventional PMMs. As a result, they may provide a competitive alternative to conventional machine-gearbox arrangements and have significant potential for use in the aerospace, automotive and wind turbine industries [273]. While MGs and MG-integrated PM machines are advancing from technology demonstrators and prototypes, research is shifting focus towards cost reduction and improved manufacturability. As the technology continues to find applications in various fields, such as downwell oil and gas, automotive traction motors, aerospace actuators, and marine propulsion, ease of manufacture and mechanical robustness have become important considerations in addition to electromagnetic performance. While many aspects of the technology have been investigated, some opportunities remain unexplored, and there is potential to further exploit the advantages of MG technology in a more robust and simple-to-manufacture manner.

The integration of an electric machine with a magnetic gear can be achieved through various types and configurations. Among these configurations, coaxial flux modulated MG integration is a popular choice for Starter/Generator applications. Figure 3.18 illustrates the inner and outer rotor structures of this configuration [275].

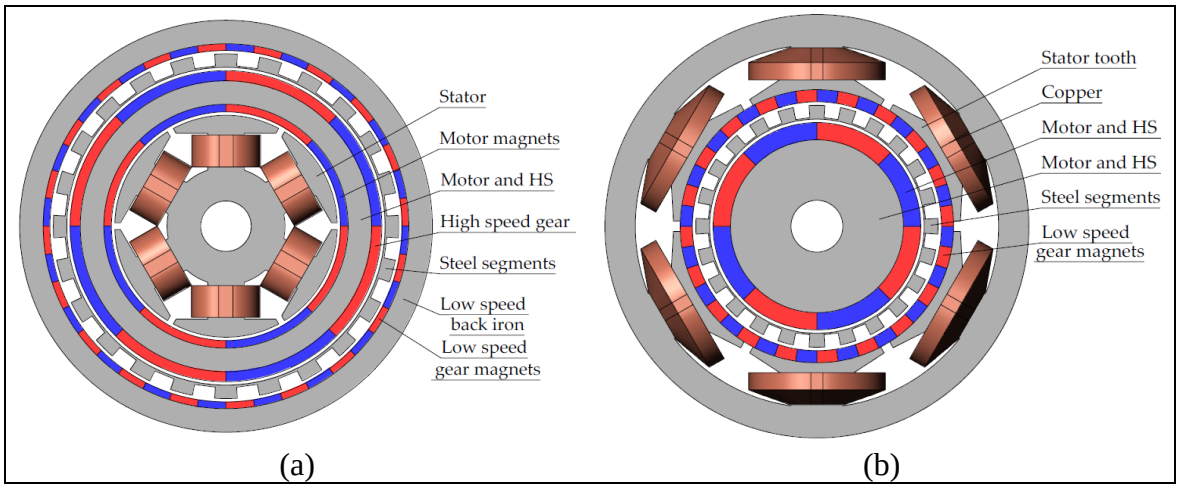


Figure 3.18. Coaxial flux modulated MG assisted PMM (a) Outrunner (b) Inrunner [275]

The outer stator configuration offers a simpler mechanical construction compared to the inner stator configuration, as it requires only two air gaps and allows for easier physical wire connections. Additionally, this design offers efficient cooling of the windings, as they are directly accessible. However, due to its larger size, the outer stator may require an oversized design, and can only accommodate low current before the MG reaches the slip torque.

MGEMs can be further classified into three main categories: split magnetically geared machines, ring-stator magnetically geared machines, and wound modulator magnetically geared machines. Split types are composed of a separate flux-modulated MG and a PMM, with a shared high-speed rotor situated between the modulator and the stator. They typically feature three air gaps, and can be configured as either magnetically decoupled, partially coupled, or coupled as demonstrated in Figure 3.19 [273].

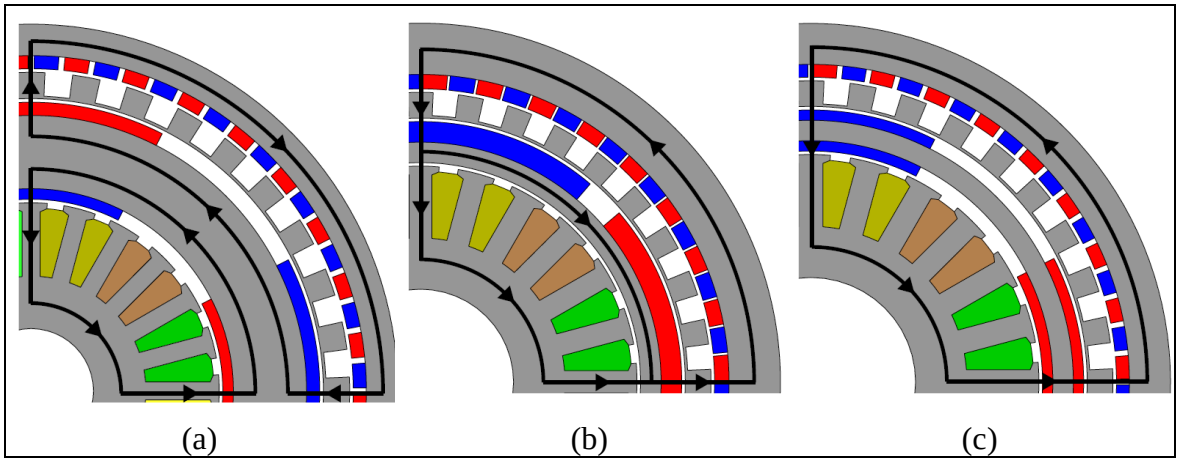


Figure 3.19. Classification of split magnetically geared machines (a) Decoupled (b) Partially coupled (c) Coupled [273]

An alternative integration method involves replacing the ring gear yoke with a stator, as demonstrated in Figure 3.20. This configuration eliminates one of the air gaps required for split-types, resulting in Ring-Stator Magnetically Geared Machines with only two air gaps. This simplicity in construction is a significant advantage of this method [267]. They are also classified as magnetically coupled EM, as the flux generated by the MG penetrates the stator.

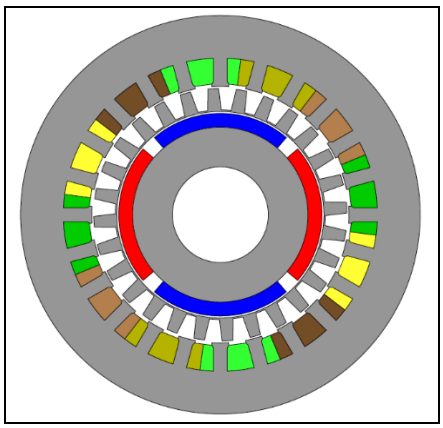


Figure 3.20. Ring-stator magnetically geared machines [267]

Another integration method involves the insertion of a stator winding in the gaps between the modulator segments of an MG, as demonstrated in Figure 3.21 [273]. This configuration offers the advantage of better utilization of the space occupied by the modulator, and requires only three concentric components with two air gaps, as opposed to the four components and three air gaps required by split-types. However, the pole-pair combinations that can be utilized with this configuration are limited.

However, the mechanical construction of this topology is rather challenging. It is important to note that the wound-type exhibits the strongest coupling between the flux generated by the magnetic gear and the stator.

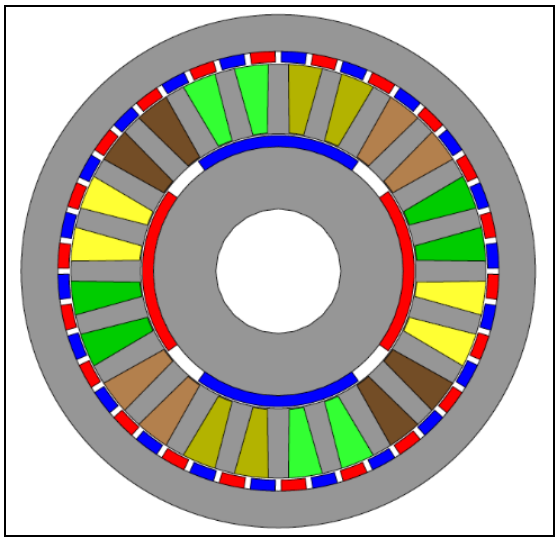


Figure 3.21. Wound modulator magnetically geared machines [273]

3.3. Materials for Starter/Generator and Magnetic Coupler Structures

The development of Starter/Generator and Magnetic Coupler designs involves the integration of diverse materials, each serving a unique purpose within the system. These materials can be broadly categorized into three groups: magnetic, conductive, and insulating materials. Of particular importance are advancements in permanent magnet and silicon silica sheet technologies, which are continuously evolving and influencing the capabilities of these systems. Gaining a more in-depth understanding of each of these material groups is essential for comprehending their significance in the design and function of S/G and MC systems.

3.3.1. Magnetism

Magnetic materials can be classified into five distinct categories based on their inherent magnetic properties: diamagnetic, paramagnetic, ferromagnetic, ferrimagnetic, and antiferromagnetic, as shown in Figure 3.22 [276, 277].

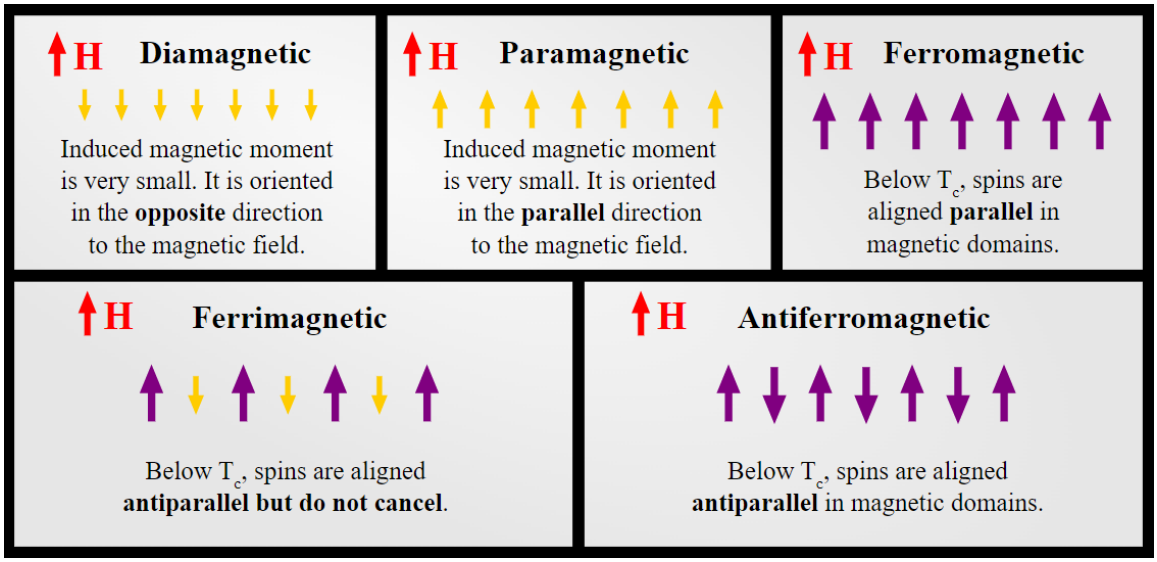


Figure 3.22. Summary of magnetic materials [276]

Diamagnetic materials do not have a net atomic or molecular magnetic moment, and they generate an opposing current when exposed to an external magnetic field. Paramagnetic materials possess a net magnetic moment at the atomic level, but the coupling between neighboring moments is weak. These materials align with an applied magnetic field, but alignment decreases at higher temperatures due to thermal excitation.

Ferromagnetic materials have a clear magnetic moment at the atomic level, and unlike paramagnetic materials, there is a strong coupling between neighboring moments [278]. This coupling enhances the spontaneous alignment of the moments in microscopic regions known as domains. When subjected to a magnetic field, the domains tend to align more strongly with the field. Antiferromagnetic and ferrimagnetic materials possess atomic moments oriented inversely parallel to each other, with one neighboring moment oriented inversely parallel to the other. The neighboring moments are equal, resulting in no net moment.

After extensive research aimed at increasing the mechanical strength of ferromagnetic materials and improving their magnetic properties, two distinct types of materials have been identified in terms of the durability of their magnetic properties: soft and hard magnetic materials [279]. Materials that exhibit a propensity for easily degraded magnetic properties or easily lost magnetization are classified as soft magnetic materials. Steel magnets, among the earliest types of artificial magnets, are generally soft magnets and are also mechanically applicable.

Soft magnets undergo a series of heat treatments to enhance the longevity of their magnetic properties. One of the goals of heat treatments applied to magnets is to reinforce their mechanical strength. On the other hand, materials that exhibit magnetic properties with resilience to deterioration or magnetization loss are referred to as hard magnetic materials.

3.3.2. Soft magnetic materials

Soft magnetic materials are characterized by high permeability and low coercivity, which make them easily magnetized and demagnetized. In contrast, hard materials have relatively low permeability and high coercivity, making them more difficult to magnetize and demagnetize [280]. The difference between these two types of materials is best illustrated by comparing their hysteresis curves, as shown in Figure 3.23. Soft magnetic materials are used to limit flux paths and increase the flux density in a given region. Soft materials used for this purpose include soft iron, iron-silicon alloys, nickel-iron, and soft ferrites. These materials find applications in many devices, such as transformers, relays, motors, inductors, and electromagnets. When selecting a soft material, its permeability, saturation magnetization, resistivity, and coercivity are important considerations. High permeability and magnetization are desirable for flux amplification and focusing, while resistance and coercivity are crucial in high-frequency applications. A high resistivity reduces eddy currents, while a low coercivity reduces hysteresis losses.

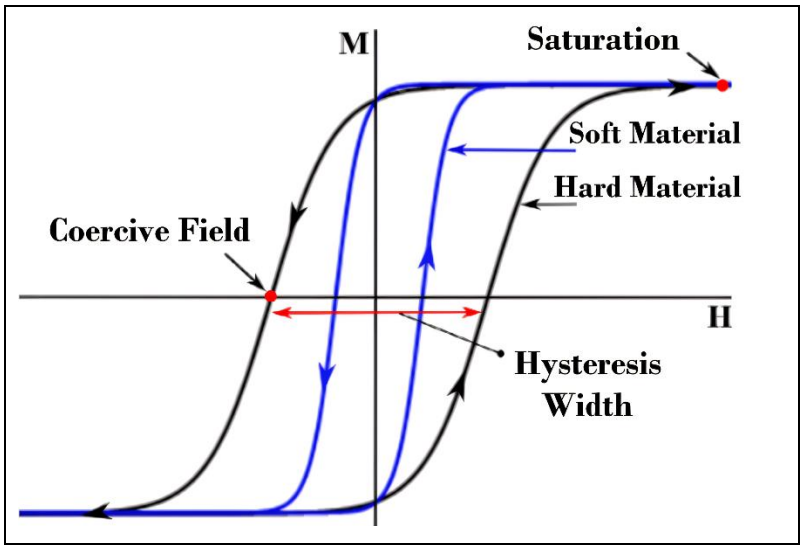


Figure 3.23. Hysteresis curve of soft and hard magnetic materials

Soft iron is extensively utilized in electromagnetic applications and as the core material of DC machines. However, in AC machines, they are being replaced by high resistivity materials owing to their low eddy current losses. Commercially available soft iron typically contains low doping. The addition of a low percentage of silicon to soft iron increases its resistivity, reduces its coercive force, and enhances its magnetic stability. An iron alloy with 3% silicon increases its resistivity by a factor of four compared to pure iron [281]. However, the presence of silicon causes a sharp decline in the saturation flux density. Moreover, the addition of more than 5% silicon makes the iron more brittle and difficult to work with. Despite silicon being an inexpensive material, siliconized iron is relatively expensive. The conditions necessary to achieve low losses and high permeability in silicon-iron materials can be outlined in Table 3.5 [282]. In practice, meeting all these conditions with a single material is not always possible.

Table 3.5. Conditions for achieving qualified silicon-iron materials

Lower eddy currents	Lower hysteresis losses	Higher permeability
Increase the alloy content	Use thinner material	Decrease the alloy content
Use a smaller particle size	Decrease the alloy content	Use a smaller surface size
Use thinner material	Use larger particle size	Minimize defects and surface roughness
Reduce defects and surface roughness	Low surface distortion	Use high purity materials to reduce impurities

3.3.1. Electrical steel

Electrical steels, also referred to as laminating materials for machine designers, can be classified into two types: nongrain-oriented (NGO) and grain-oriented (GO) stainless electrical steels based on their grain structure. The steel sheet is typically coated with a thin layer of insulating material to ensure proper insulation between laminations. For small motors, vapour bluing of one surface is commonly used for laminations, while organic or inorganic coating is applied to one or both surfaces of larger laminations.

NGO steel is a type of steel that is designed for use in EMs. It is composed of iron, nickel, and chromium, with small amounts of other elements such as molybdenum and copper. NGO steel is produced by casting and then rolling the steel to achieve the desired thickness. GO steel, on the other hand, is a type of steel that is designed for use in transformers and other electrical devices where high magnetic flux densities are needed. It is composed of iron and silicon, with small amounts of other elements such as aluminum and boron. GO steel is produced by a process called directional solidification, which aligns the crystal structure of the steel in a single direction, resulting in improved magnetic properties [245]:

Magnetic properties: GO steel has a higher magnetic flux density than NGO steel due to its directional alignment of the crystal structure.

Anisotropy: GO steel is anisotropic, meaning its magnetic properties are directionally dependent, while NGO steel is isotropic, meaning its magnetic properties are independent of direction.

Applications: NGO steel is typically used in electrical applications that require moderate magnetic properties, such as motors and generators. GO steel is used in applications where high magnetic flux densities are needed, such as in transformers.

Production: NGO steel is produced by casting and rolling, while GO steel is produced by directional solidification.

Cost: GO steel is generally more expensive than NGO steel due to its more complex production process.

The choice between NGO and GO stainless electrical steel depends on the specific application and the required magnetic properties. NGO steel is a more versatile material and can be used in a wider range of applications, while GO steel is ideal for high-performance applications that require high magnetic flux densities.

3.3.3. Hard magnetic materials

Hard magnetic materials are characterized by high coercivity and low permeability, which make them difficult to magnetize and demagnetize. Due to their long-lasting magnetic properties, they are referred to as permanent magnets (PMs) [283]. PMs are commonly used as field sources in electronic household appliances, computers, data storage devices, electromechanical devices, telecommunications equipment, and biomedical instruments.

The most critical properties include coercivity, saturation, and magnetization, all of which are related to the second quadrant of the hysteresis curve known as the demagnetization curve. To use a PM as a field source, it is polarized at an operating point on the demagnetization curve. This operating point can be obtained from the load line of the circuit, enabling designers to reduce magnet size and cost. PMs are typically composed of alloys of iron, nickel, and cobalt and exhibit large B-H curves, high permanent magnetization, and high demagnetizing force. There are three primary types of PMs, categorized according to their chemical structure: Alnico, Ferrite (Ceramic), and Rare-Earth PMs.

Alnico magnets have relatively high remanence and low coercive force, while ferrites have low remanence and relatively high coercivity. Ferrites are unique among the various types of PMs in that they are electrically and thermally insulating. They are often the most affordable option, thanks to the use of inexpensive and widely available raw materials. In contrast, Rare-Earth magnets have high values for both remanence and coercivity.

3.3.4. Permanent magnetism and permanent magnets

The history of permanent magnets (PMs) can be traced back thousands of years to ancient China, where lodestone, a naturally occurring magnetic mineral, was used to create the first compasses. However, the development of synthetic PMs began in the early 19th century. In 1820, Hans Christian Oersted discovered that an electric current produces a magnetic field, which led to the development of the electromagnet. This technology enabled the creation of temporary magnetic fields for various applications, including the telegraph and electric motors. The first synthetic PM was developed in 1824 by William Sturgeon. However, early PMs made of steel and aluminum were weak and lost their magnetization quickly. The use of PMs in various applications dates back to the discovery of Alnico magnets in the 1930s.

In the 1930s, Alnico magnets, made of aluminum, nickel, and cobalt, were discovered and widely used in various electrical applications, including electric motors and generators. In the 1960s, the development of ceramic magnets, also known as ferrite magnets, revolutionized the PM industry. These magnets are made of iron oxide and barium or strontium and are less expensive and more widely available than Alnico magnets. Ferrite magnets are still used today in applications such as loudspeakers and electric motors. In the 1980s, rare earth element magnets, such as samarium-cobalt (SmCo) and neodymium-iron-boron (NdFeB) magnets, were discovered and developed, and the widespread use of PMs in electric machines became possible [284]. These magnets are much stronger than Alnico or ferrite magnets and have enabled the development of high-performance electric motors and generators for various applications, including electric vehicles and wind turbines.

The development of PMs has been a continuous process of discovery and improvement, driven by the need for better, more efficient and cost-effective electrical machines. PMMs have several advantages over traditional wound coil machines. They have higher efficiency, higher power density, and lower energy consumption, making them suitable for applications where energy efficiency is crucial. Additionally, they have a simpler design and require less maintenance than traditional wound coil machines.

Today, PMs are used in various applications, and researchers are continuously looking for new materials and manufacturing techniques to further enhance their performance and reduce their cost. The continuous development of PM materials, including new alloys and composite materials, has resulted in further improvements in the performance and cost-effectiveness of PMMs. For example, the use of NdFeB magnets has facilitated the development of high-performance electric machines with a wide range of applications, such as aircraft machines, electric vehicles, wind turbines, and industrial machinery. In addition to their superior performance, permanent magnet motors have been found to have a lower carbon footprint than traditional wound coil machines. This is due to their higher efficiency, which results in lower energy consumption and reduced greenhouse gas emissions.

Although challenges remain in the use of rare earth element magnets, the continuous development of alternative materials is expected to further enhance the performance and cost-effectiveness of permanent magnet machines. Figure 3.24 illustrates the evolution of permanent magnets over the years [285].

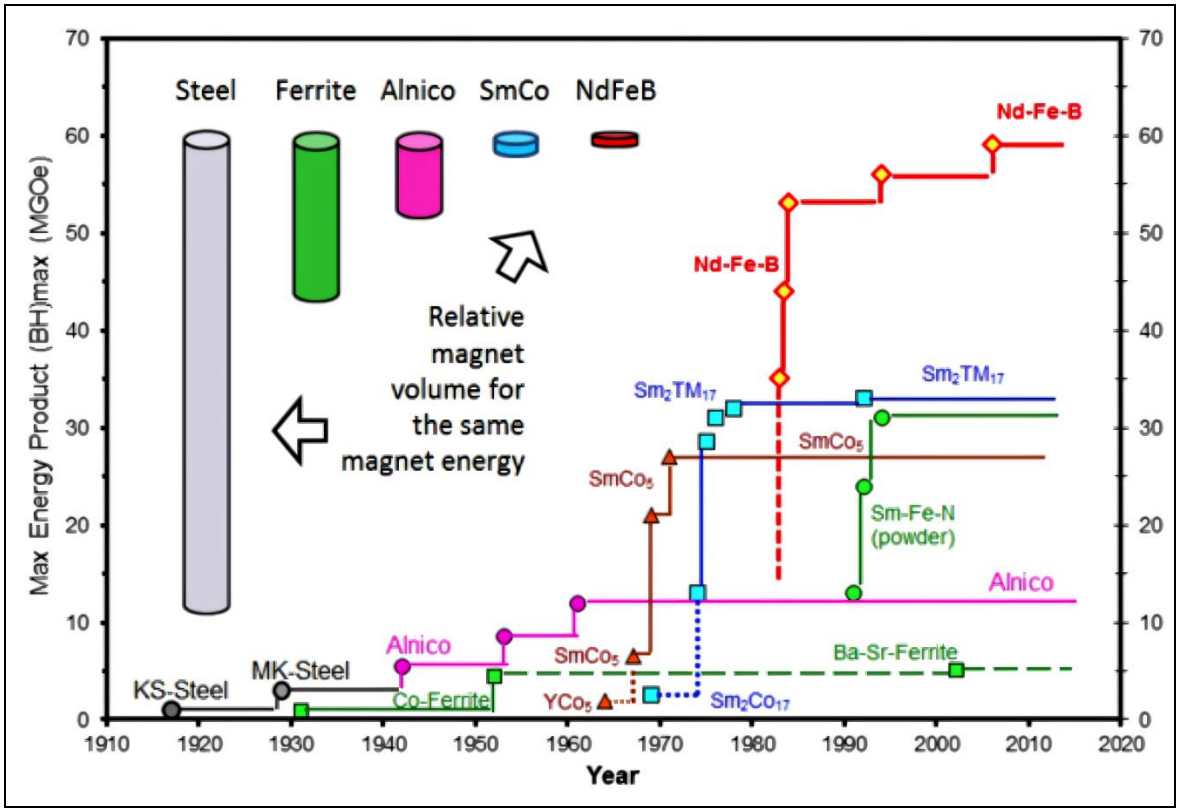


Figure 3.24. Development of permanent magnets [285]

Rare earth magnets are composed of alloys of the Lanthanide group of elements. The two Lanthanide elements most prevalent in the production of PMs are Neodymium and Samarium. There are numerous alloy formulations of rare earth magnets covered under many different patents but the most common commercial varieties are NdFeB and SmCo [286]. There are two types of PMs commonly produced commercially: sintered and bonded.

Sintered magnets are produced by compressing dry granules of elemental materials into a metal die and heating them at high temperatures to fuse the granules together. During the manufacturing process, sintered magnets are exposed to a magnetic field, which orients the magnetic domains in the material. The magnetic orientation of sintered magnets is fixed during processing and cannot be changed later, resulting in anisotropic magnetic material. The physical properties of sintered magnets are similar to ceramic materials; they are hard and brittle, making them unsuitable for applications where they will be subjected to shock. However, sintered neodymium magnets have the highest energy product of any permanent magnetic material. Their small size and high magnetic field strength have led to the miniaturization of many electronic components, such as motors and speakers, enabling the creation of highly portable electronic devices such as cell phones and tablet computers.

Bonded magnets are created by mixing magnetic metal powder with a polymer, which is then cast or extruded into the final shape. Depending on the polymer used in production, bonded magnets can be flexible. They do not have a fixed magnetic orientation and can be magnetized in complex patterns with many poles, resulting in isotropic magnetic material. Unfortunately, bonded magnets are weaker than sintered magnets, limiting their application.

Hysteresis

Hysteresis is a phenomenon that occurs in all magnetic materials, from soft to hard, with the degree of hysteresis increasing as the material becomes harder. PMs exhibit the most significant hysteresis among all magnetic materials. The hysteresis effect refers to the resistance of a magnetic material to change the direction of its magnetization, and it is a crucial property of PMs. The strength of the magnetic field produced by the magnet and its stability over time depend on the hysteresis properties of the material.

Despite having spontaneous magnetization, a block of ferromagnetic material can exist in a demagnetized state due to the presence of magnetic domains. Each domain is a volume of the material that is spontaneously magnetized, but is aligned in different directions, causing the net magnetization to be effectively minimized. In practice, if a positive field is applied to such a material and then gradually reduced, the magnetization will not return to its original value. This phenomenon is known as hysteresis, and a series of "minor" loops can be generated by applying larger fields and then reversing them. The hysteresis curve of the ferromagnetic materials, shown in Figure 3.25, is the envelope of all the minor loops [287].

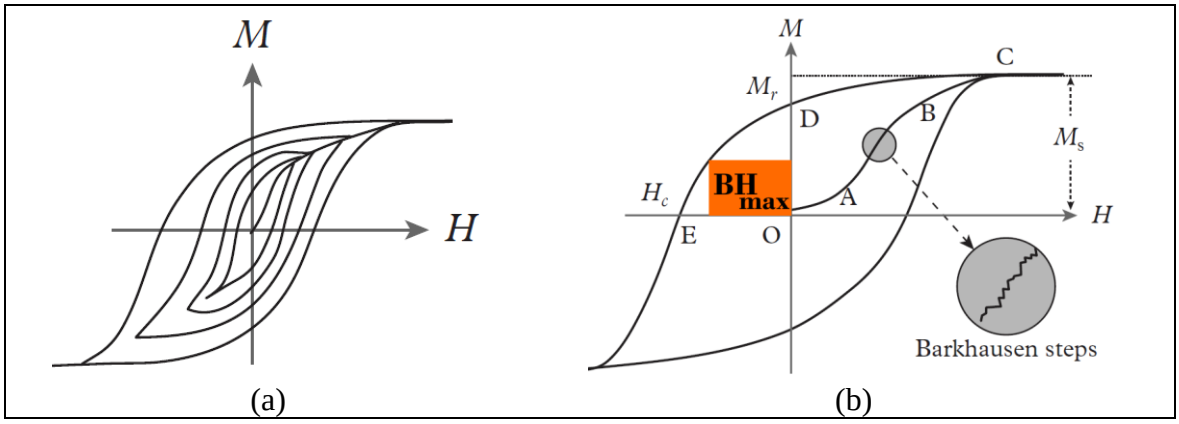


Figure 3.25. Characteristics of ferromagnetic materials (a) Minor loops (b) Hysteresis curve

The magnetization curve of ferromagnetics is composed of several regions with distinct magnetic properties. The reversible portion of the curve, OA, can be retraced if a magnetic field is applied and then reduced to zero. The irreversible domain wall motion region is denoted as AB. The region BC refers to the point where all the domains align themselves along the applied field direction, leading to complete saturation magnetization, M_s. After saturating the material in any direction, if the magnetic field is gradually reduced to zero, the magnetization is not reduced to zero. This value of magnetization at zero field, denoted as M (H=0), is referred to as remanence or remanent magnetization, M_r. If the direction of the field is now reversed and its strength gradually increases to some well-defined value in the opposite direction, the magnetization is once again reduced to zero. This negative value of the applied field at which M=0 is known as the intrinsic coercivity, H_{ci}. The second quadrant of the hysteresis curve, segment DE, is known as the demagnetizing curve.

There are two types of B-H curves for PMs: intrinsic and normal. The intrinsic B-H curve is a theoretical curve that represents the magnetic properties of the PMs individual magnetic domains. It assumes that all of the domains are aligned in the same direction, which is not the case in a real magnet. This curve shows the maximum magnetic flux density that can be achieved in a magnet. The normal B-H curve, on the other hand, represents the magnetic properties of the entire magnet, taking into account the distribution of magnetic domains within the magnet [288]. This curve is obtained by measuring the magnetic properties of the entire magnet using a magnetometer. The normal B-H curve is always below the intrinsic curve because it takes into account the effects of domain wall motion and other factors that limit the maximum magnetic flux density that can be achieved in a real magnet.

Maximum energy product

The maximum energy product BH_{max} is a crucial parameter used to assess the magnetic energy density that a magnet can store. It is obtained by multiplying the magnetic field strength (H) and the magnetic flux density (B) at the point where the magnet delivers its maximum energy output. Essentially, it signifies the magnetic field strength per unit volume that a magnet can generate. Higher BH_{max} in PMs results in stronger magnetic fields, enabling operation at specific points on the B-H curve with minimal dimensions. BH_{max} is not the sole factor that determines PM performance. Other crucial parameters such as microstructure, coercivity, remanence, and temperature stability also play a critical role.

Permeability and retentivity

Ferromagnetics are extensively utilized in engineering applications owing to their high permeability, which facilitates the generation of high magnetic inductions with relatively low magnetic fields. It is worth noting that only a few elements in the periodic table, such as iron, cobalt, nickel, and certain lanthanides, exhibit ferromagnetism and are of immense technological significance. Ferromagnetics are notable for their high relative permeability.

However, unlike paramagnets, the permeability of a ferromagnet does not remain constant as a function of the magnetic field. Consequently, to fully characterize the properties of ferromagnetics, it is necessary to measure the magnetic induction B as a function of H over a continuous range of H, resulting in a hysteresis curve. Typically, the initial relative permeabilities of ferromagnetics lie in the range of 10 to 10^5 [289]. The highest values are found in special alloys, such as Metglas, permalloy, and supermalloy, which are nickel-iron alloys and are useful as flux concentrators.

Ferromagnetics are highly valued for their remarkable ability to be magnetized, allowing them to retain their magnetization even after the magnetic field is removed. This property is widely recognized, as many individuals have likely experienced magnetizing pieces of iron using a permanent magnet. This distinguishes ferromagnetics from paramagnets, which, although they acquire a magnetic moment when exposed to an applied field H, are unable to maintain their magnetization once the field is removed.

Effect of temperature on permanent magnets

When a PM exceeds its critical temperature (T_c) or maximum operating temperature (T_{max}), the thermal energy can overcome the energy holding the magnetic domains in place, causing random orientation. This leads to a reduction in the magnetic field strength and magnetic flux density, which can result in demagnetization. If the temperature is high enough, the PM can lose all of its magnetization and become nonmagnetic. This critical temperature is known as the Curie temperature. At this temperature, both the coercivity and remanence become zero, and the permeability drops suddenly. Therefore, it is crucial to design PMs that can operate within their intended temperature range to prevent demagnetization. Table 3.6 presents the Curie temperatures of commonly used PMs [245].

Table 3.6. Curie temperature comparison of permanent magnets

Permanent Magnet Type	Curie Temperature (°C)	Working Temperature (°C)	Residual Flux Density (B_r)
AlNiCo	860	540	1,15
Ferrit (Ceramic)	450	200	0,4
SmCo	800	350	1
NdFeB	350	200	1,2

Demagnetization

Demagnetization is the process of reducing or eliminating the magnetic properties of a material. The magnetization of a material is due to the alignment of its magnetic domains, which are regions where the magnetic moments of atoms are aligned. Demagnetization occurs when the magnetic domains become disordered or disrupted, resulting in a loss of magnetic field strength. PMs, which are designed to retain their magnetic field strength indefinitely, can also undergo demagnetization under certain conditions, including exposure to high temperatures, mechanical stress, volume loss, and exposure to external magnetic fields that are in opposition to the PMs' own field [290].

Heat: Demagnetization due to an increase in temperature is a common phenomenon. As the temperature of a magnet approaches its Curie point, the level of demagnetization also increases. The extent of demagnetization is greatly influenced by the material and grade of the magnet and is explained by its demagnetization curve.

Collision and loss of volume: Collisions with other objects can also cause demagnetization in permanent magnets. Repeated impacts, such as those caused by hammering, can disrupt the atom movements and alter the alignment of the magnet's north and south poles, leading to its demagnetization.

Conflicting magnetic fields: Permanent magnets can also lose their magnetism due to exposure to external magnetic fields. When an external magnetic field surrounds the magnet, it can exert a demagnetizing force and cause damage to the magnet.

Permeance coefficient

The permeance coefficient, P_c, is a parameter that determines the PM operating point on the B-H curve, and is defined as the ratio of magnetic flux density to magnetic field strength at the operating point. P_c is crucial in determining the amount of flux available in a magnetic circuit, and thus the amount of work done. The P_c value is typically designed to be close to one, which is at or near the maximum energy product of the PM, but for applications such as EMs, a P_c above one should be selected to reduce the demagnetization risk.

P_c is calculated using the geometry of the magnet, with thicker magnets operating higher on the demagnetization curve and thinner magnets falling farther down the curve. As the aspect ratio of length to diameter is reduced, the magnet operates at a lower operating point and becomes more susceptible to demagnetization [277]. Figure 3.26 shows the second quadrant demagnetization curve for a typical NdFeB magnet.

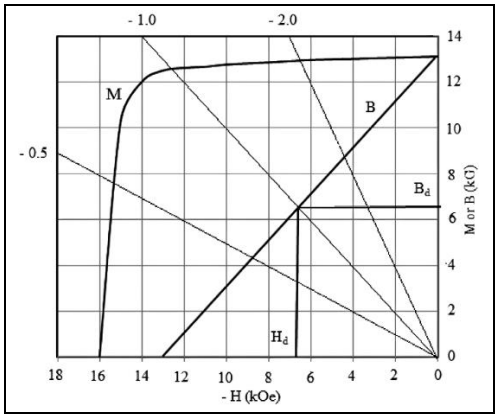


Figure 3.26. Permeance coefficient definition [277]

Rare-earth permanent magnets

In the past two decades, high-energy and permanent induction magnet materials have played a significant role in the current importance of magnets in EMs. These materials, known by the general formulas NdFeB and SmCo, exhibit superior properties compared to other magnets. Rare earth PMs are alloys formed between 3d-transition metals with strong magnetic properties such as Iron (Fe), Cobalt (Co), Cerium (Ce), Paraseodium (Pr), Neodymium (Nd) and Samarium (Sm), which belong to the 4f-transition series and are also called Lanthanides [245]. Table 3.7 presents a comparison between NdFeB and SmCo.

Table 3.7. Comparison of rare-earth permanent magnets, NdFeB and SmCo

Specification	NdFeB	SmCo
Working Temperature	< 200°C (EH)	< 350°C
Flux Loss at Higher Temperature	% 0,11 B_r/C°	% 0,03 B_r/C°
Environmental Preference	Need coating because of the oxidation problem	No need coating
Hydrogen-Rich Atmosphere	Hydrogenation risk	No hydrogenation risk
Cost	Lower	Higher
Radiation Environment	Particularly vulnerable to gamma rays	Stable in radiated environments
Mechanical Strength	Very strong, not fragile	Weak and fragile
High Space Requirements	Higher fields and energy	Lower fields and energy
Aerospace Applications	Preferred at low altitudes	Preferred at high altitudes
Saline, Open Sea, Acidic, Alkaline Environment	Should be coated	Stable in saline environment
Coatings	Suitable	No need coating
Ion Vapor Deposition (IVD)	Suitable	Not convenient

Coating types

SmCo magnets, although inherently resistant to corrosion, do not always need to be coated for protection. Nonetheless, it is a common practice to coat them with a thin layer of material due to their brittleness and proneness to corrosion. The protective layer on SmCo magnets serves to prevent corrosion and provide insulation between the magnets and any other materials that they may come into contact with. Furthermore, the coating can improve the adhesion of the magnet to other materials when used in assemblies or systems. In contrast, NdFeB magnets usually require coating against corrosion and rust, as they are not intrinsically corrosion-resistant. The coating additionally helps to prevent a reduction in the magnetic field due to the volume loss of the magnet alloy material. Several types of coatings can be used, such as nickel, zinc, gold, epoxy, plastic, and Teflon. Among these, epoxy is the most commonly used type for aerospace, as shown in red in Figure 3.27 [265].

Plating / Coating	Indoor Use	Abrasion Resistance	Humidity	Water	Salty Air	Salt Water	Glue	Thickness
Nickel (Ni-Cu-Ni)	Excellent	Good	Good	Bad	Bad	Bad	Bad	10-20 Microns
Zinc (Zn)	Excellent	Excellent	Excellent	Good	Good	Bad	Good	8-10 Microns
Gold (Ni-Cu-Au)	Excellent	Good	Good	Bad	Bad	Bad	Bad	10-20 Microns
Black Enoxy (Ni-Cu-BE)	Superior	Bad	Superior	Superior	Excellent	Excellent	Good	15-25 Microns
Raw Epoxy (BE)	Superior	Good	Superior	Superior	Excellent	Excellent	Superior	10-20 Microns
Plastic (ABS)	Superior	Superior	Superior	Superior	Superior	Superior	Excellent	>800 Microns
Teflon® (PTFE)	Superior	Superior	Superior	Superior	Superior	Superior	Bad	250-500 Microns
Everlube-6155®	Superior	Superior	Superior	Superior	Superior	Superior	Good	8-25 Microns
Xylan®	Superior	Superior	Superior	Superior	Superior	Superior	Good	15-30 Microns
Parylene	Superior	Superior	Superior	Superior	Superior	Superior	Good	15-30 Microns

Figure 3.27. Commercial coating types of permanent magnets [265]

Magnetic orientation

A magnet exhibits the characteristic of being magnetized in various directions. The schematic diagrams shown in Figure 3.28 serve to demonstrate the diverse magnetic orientations that can be attained during the PM manufacturing process [291].

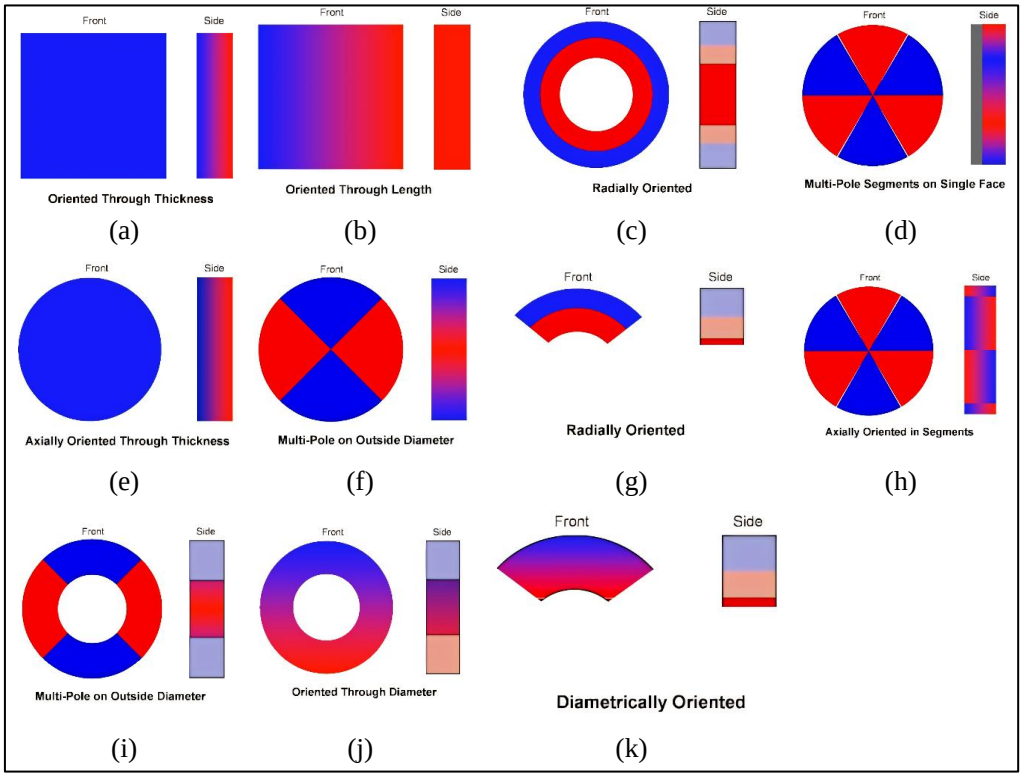


Figure 3.28. Orientations (a) Through thickness (b) Through length (c) Radially (d) Multipole (e) Axially (f) Outside diameter (g) Radially in segments (h) Axially in segments (i) Single face (j) Through diameter (k) Diametrically [291]

Future permanent magnets

The straightforward approach to enhance PM properties would be to discover a new intermetallic phase with a saturation magnetization greater than $Nd_2Fe_{14}B$ and a comparable magnetocrystalline anisotropy and Curie temperature. Some of the most interesting potential PM materials that are currently being investigated are summarized in Table 3.8 [288].

Table 3.8. Compound list as possible permanent magnets [288]

Material	B_r		$H_{c,i}$		BH_{max}	
	kG	T	kO_e	kA/m	MGO_e	kJ/m^3
L10-MnA1 (alloy)	5-6	0,5-0,6	2-4	159-318	5-8,8	40-70
L10-MnA1 (particles)	2,5-5	0,25-0,5	3,6-5,6	286-446	4,8	38
MnBi (powder)	2,5	0,25	19-12	1512-1671	1,75	14
MnBi (Bonded)	5	0,5	11	875	7,5	60
Zn2Co11 (ribbon)	6	0,6	2	159	5,3	42
HfCo2 (ribbon)	7	0,7	2	159	4,4	35
HfCo2 (particle)	9	0,9	4,5	358	12,6	100

Recently, SmFeN and integrated powder (IP) magnets have been developed as a new family of PMs. The SmFeN compound has all the necessary requirements for a PM, including high saturation magnetization, large magnetocrystalline anisotropy field, and high Curie temperature [291]. The IP magnet is a unique and innovative encapsulated magnet type that provides high magnetic strength, eco-friendliness, and cost savings in production, material, finishing, assembly, and better tolerance [292]. It is also highly corrosion-resistant due to sealed enclosure, making it an ideal option for exposure to chemicals, water, and gases. Commercial rare-earth PMs are listed in Figure 3.29 [288].

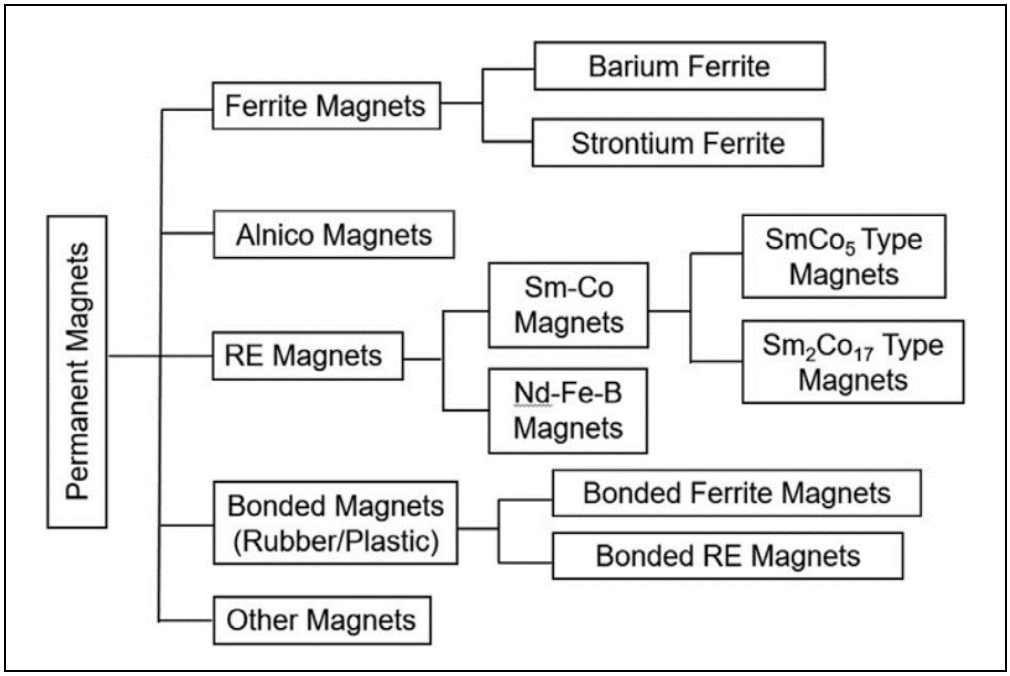


Figure 3.29. Commercial rare-earth permanent magnets [288]

3.3.5. Materials utilized in magnetic couplers

The yokes in magnetic couplers are typically made of magnetically soft steel, which is a type of metallic alloy as shown in Figure 3.30 with their composition [266, 293].

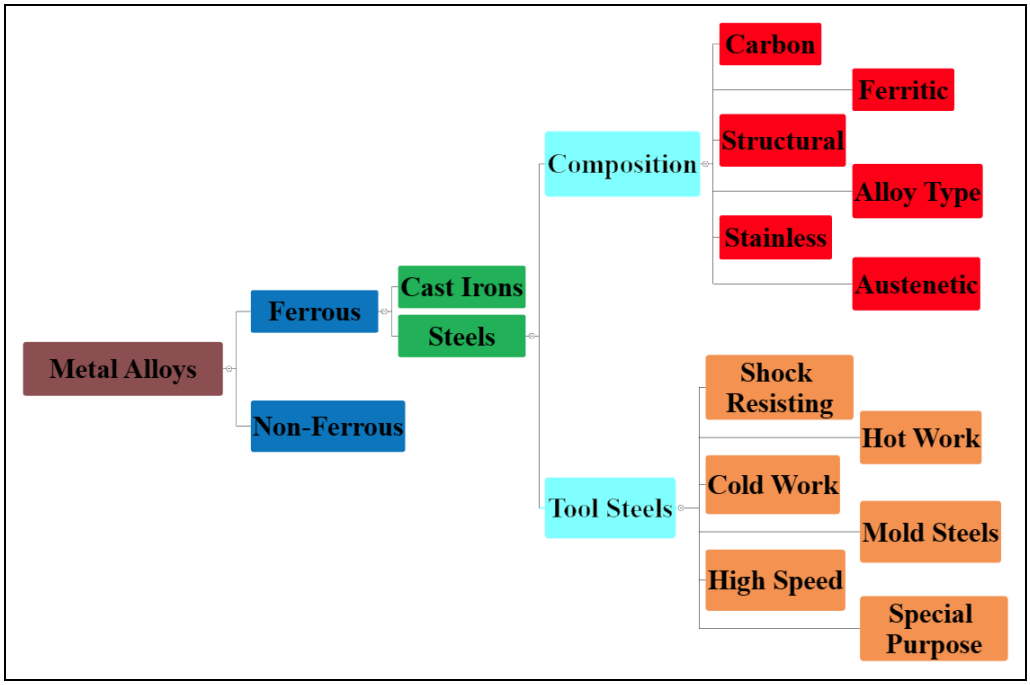


Figure 3.30. Magnetic coupler yoke materials

The selection of rotor core materials should consider four primary qualifications: saturation level, core losses, cost, and manufacturability [294-296]. Oriented steels have higher magnetic permeability and lower core losses, but are less cost-effective and reproducible due to limited availability. Magnetic stainless steel has lower losses and saturation points than carbon steel, but similar mass densities. Nonmagnetic stainless steel is a preferred material for retaining sleeves as it provides easy access and protects PMs from centrifugal forces at high speeds [245].

A static seal shroud is used to provide a barrier between the rotors, preventing leakage of the fluid being transferred and protecting the magnetic assembly from external contamination [269]. The materials used in MCs are listed in Table 3.9.

Table 3.9. List of the materials used in magnetic couplers

Rotor Yoke	Permanent Magnets	Protective Cover	Containment Shrould	Shafts
Electric Steel	NdFeB/SmCo	Stainless Steel	Nonferrous	Nonmagnetics
Carbon Steel	Ferrite/Ceramic	Fibres	Hastelloy	Magnetics
Metals	Alnico	Plastics	Oxide ceramics	Alloys

4. ANALYTICAL DESIGN AND MODELLING OF SYNCHRONOUS MAGNETIC COUPLERS AND PERMANENT MAGNET STARTER/GENERATORS WITH CONTROL STRATEGIES

The chapter elucidates the stator and rotor reference frames that are crucial components of the S/G vector control structure, detailing their role in machine operation. Furthermore, the chapter provides an extensive overview of the analytical design equations of synchronous magnetic couplers and permanent magnet Starter/Generators, methods, and approaches for various control structures, equipping the reader with the knowledge required to achieve optimal design outcomes. This chapter is a valuable resource for professionals seeking an inclusive understanding of the latest techniques and technologies employed in the S/G industry. Likewise, this chapter provides a rigorous exploration of the analytical design methods and approaches used in the magnetic coupler of contactless torque transmission between S/G stages. The chapter examines the essential principles of MC and the factors that affect its performance and efficiency. It also examines design methodology approaches to enhance the coupling efficiency, performance, and reliability of S/G systems.

4.1. Analytical Design Methodologies of Magnetic Couplers

Modelling the stored energy in permanent magnets (PMs) and the force between PMs is an important step in deriving an analytical model of magnetic couplers. This is because the stored energy in PMs determines the maximum amount of energy that can be transferred between the magnet and other components in a magnetic coupler system. The force between PMs is also a critical parameter that must be modelled in order to derive an analytical model of magnetic couplers. This force determines the torque that can be transmitted between the magnets and the amount of energy that can be transferred between them. The analytical model can be used to quickly predict the performance of the magnetic coupler under varying operating conditions.

4.1.1. Stored energy in permanent magnets

A thorough understanding of the energy stored in magnetic circuits is crucial for comprehending their operation. Although PMs are a ubiquitous element in various magnetic circuits, there is some degree of ambiguity regarding the energy stored in PMs.

Obtaining a comprehensive understanding of this energy is of great importance to researchers and engineers working in fields that require the use of PMs, such as in the design of motors and generators, magnetic bearings, and magnetic storage devices. Additionally, a thorough comprehension of the stored material is vital for predicting the magnet's response to transient and steady-state conditions and for estimating its efficiency and performance.

By considering of the electrical energy input into an ideal solenoid, it is possible to derive the standard definition for the magnetic energy of a material in which B and H are parallel. This definition can be expressed as a volume integral in Eq. 4.1 [297].

$$W = \int \left(\int_0^B H(B_1)\, d(B_1) \right) dv \tag{4.1}$$

where $W, B_1,$ and v are the stored energy, integration variable, and volume respectively. The lower limit of energy density integration is arbitrary when calculating force from the stored energy derivative with respect to displacement [298]. However, for a modern rare earth magnet, which acts along its linear demagnetization characteristic with a slope $\mu_0\mu_r$, it is more appropriate to select the lower limit as the remanence B_r, as shown in Figure 4.1.

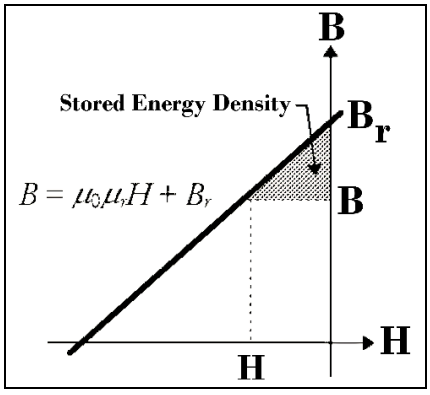


Figure 4.1. Stored energy density in PMs [297]

When integrating along the demagnetization line, both the magnetic field strength H and the differential of the magnetic induction ΔB are negative. However, by defining Eq. 4.2, the energy stored in a magnet with a keeper, or one with H=0 and positive and symmetrical H on either side of H=0, is zero. Eq. 4.3 illustrates the force of a simple idealized permanent magnet circuit with no electrical energy input [299].

This choice of zero energy is not only convenient under the condition of partial demagnetization, but is also grounded in sound physical reasoning [297]:

- Removing the keeper causes an increase in energy as work is done on the system.
- Zero energy is consistent with the conventional definition of energy in an unmagnetized material.
- Stored energy is generally considered to be positive.
- Only easily recoverable energy can be considered, with the exclusion of energy associated with crystal structure, and energy dissipated as heat during magnetization.

$$W = \int \left(\int_{B_r}^{B} H(B_1)\, d(B_1) \right) dv \qquad (4.2) \qquad F = -\frac{dW}{dx} \qquad (4.3)$$

where F and dx are the exerted force and axial displacement, respectively.

Figure 4.2 depicts an idealized simple magnetic circuit consisting of a magnet with a linear demagnetization curve, and serves to verify the energy-force relationship.

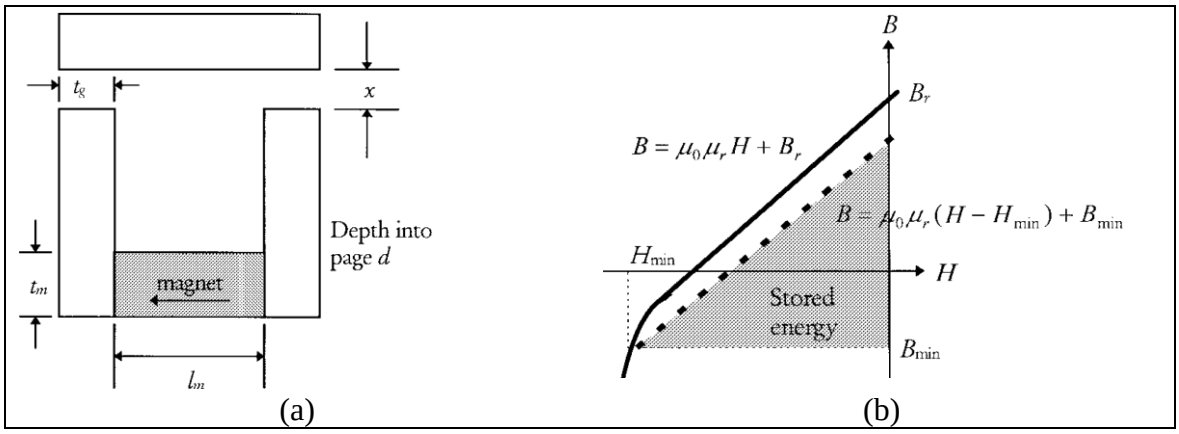


Figure 4.2. (a) Model with a PM and ideal iron (b) Ideal PM demagnetization curve [297]

Neglecting fringing and leakage, and assuming ideal iron with infinite permeability and nonsaturating properties, the PM satisfies the following equation [297]:

$$B_m = \mu_0 \mu_r H_m + B_r \qquad (4.4)$$

where $B_m, H_m, \mu_0, \mu_r,$ and B_r are the PM flux density, PM field intensity, free-space permeability, relative permeability, and residual flux density, respectively.Using Ampere's law and flux conservation for a zero-length air gap, the following equations are obtained.

$$\frac{B_g}{\mu_0} 2x + H_m l_m = 0 \quad (4.5) \qquad B_g t_g = B_m t_m \quad (4.6)$$

where B_g and l_m are the air gap flux density and magnet length, respectively. By solving Eq. 4.4-Eq.4-6, the following results are obtained.

$$B_g = \frac{B_r l_m t_m}{2 t_m x \mu_r + t_g l_m} \quad (4.7) \qquad B_m = \frac{B_r l_m t_g}{2 t_m x \mu_r + t_g l_m} \quad (4.8)$$

The total magnetic energy for an ideal iron is zero, resulting in the summation of energy contributions solely from the air gaps. Substituting Eq. 4.7 and Eq. 4.8 confirms that the force obtained from Eq. 4.3, using the energies specified in Eq. 4.9 and Eq. 4.10, is equivalent to the product of the total gap area and recognized magnetic force per unit area.

$$W_g = 2(x t_g d) \frac{1}{2} \frac{B_g^2}{\mu_0} \quad (4.9) \qquad W_m = (l_m t_m d) \frac{1}{2} \mu_0 \mu_r H_m^2 \quad (4.10)$$

$$F = -\frac{d}{dx}\left(W_g + W_m\right) = -(2 t_g d) \frac{B_g^2}{2\mu_0} \quad (4.11)$$

where $W_g, t_g, \mathrm{W_m}, \mathrm{t}_m,$ and d are the stored energy in the air gap, air gap width, stored energy in the PM, width of the PM, and model depth, respectively. However, in practice, the demagnetization or recoil curve for a real PM is not linear. Nevertheless, for modern rare earth magnets, it is a close enough approximation to be approximated by a constant.

However, if the magnet is subjected to an excessive demagnetizing field or high temperature, it will partially demagnetize. The magnet will subsequently operate along a recoil line that is approximately parallel to the original demagnetization curve with close μ_r, as described by Eq. 4.12. It is crucial to note such phenomena for a comprehensive analysis of magnetic circuits in advanced applications.

$$B = \mu_0 \mu_r (H - H_{min}) + B_{min} \quad (4.12)$$

where B_{min} and H_{min} are the minimum flux density experienced by the PM and the corresponding magnetic field intensity, respectively as shown in Figure 4.2.

Thus, for any point located on the new recoil line, the energy stored per unit volume in the PM can be described by Eq. 4.13. The utilization of H to express energy eliminates the necessity of accounting for the variation in B_r. The energy enclosed by the dotted and solid lines in Figure 4.2 corresponds to the energy responsible for demagnetization and is primarily lost as heat, commonly referred to as hysteresis loss.

The energy in the form of Eq. 4.13 is applicable to any linear material, including the case when a component of H is applied in the direction perpendicular to the magnetization direction in a magnet [297].

$$\frac{W}{v} = -\frac{1}{2} H[(B_{min} - \mu_0 \mu_r H_{min}) - B] = \frac{1}{2} \mu_0 \mu_r H^2 \quad (4.13)$$

4.1.2. Force between permanent magnets

The use of the magnetic pole theory method and a seminumerical integration method enables an effective calculation of the force exerted between two magnets [300, 301]. Under magnetic pole theory, a parallelepipedical magnet of dimensions (a,b,c) can be conceptualized as two charged planes, S_{1+} and S_{1-} [302]. The former is charged with positive magnetic charges, while the latter with negative magnetic charges, as depicted in Figure 4.3.

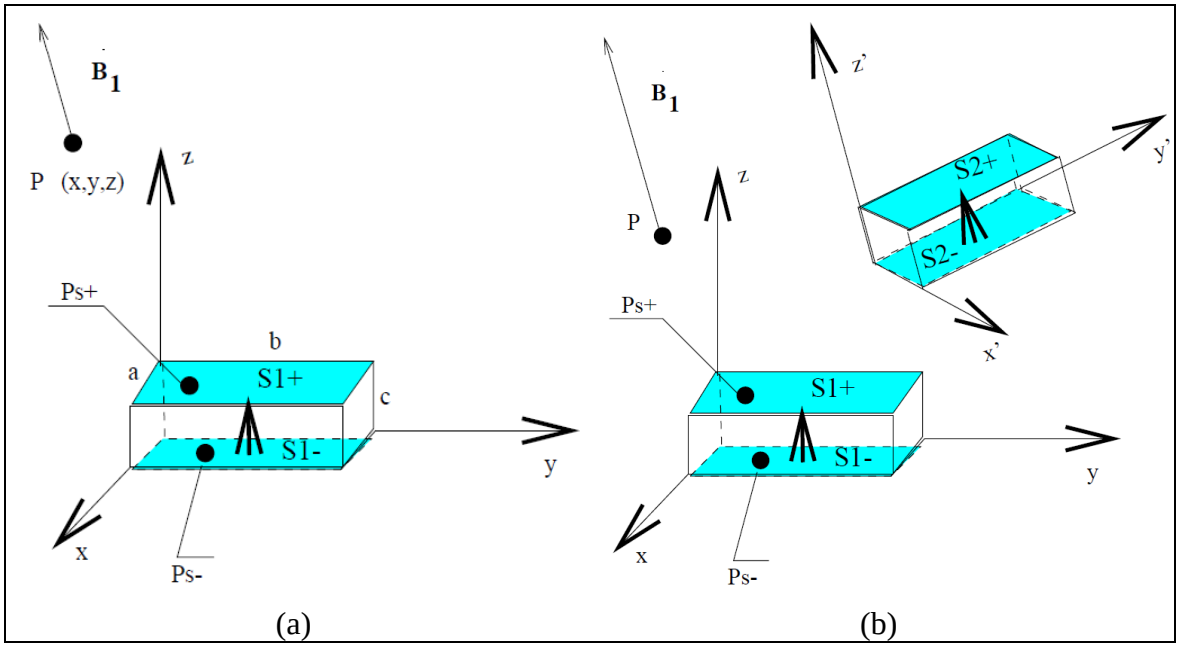


Figure 4.3. (a) Permanent magnet field (b) Force between two PMs [302]

Each plane has a charge density of $\overline{J}.\overline{n}$, where $\overline{J}$ represents the material magnetization and $\overline{n}$ denotes the surface normal vector. Consequently, the magnetic induction created by a magnet at a given P point (x,y,z) in free space is a superposition of each field, as follows:

$$\overline{B_1} = \iint_{S_{1+}} \frac{J}{4\pi} \frac{\overline{P_S^+ P}}{\overline{P_S^+ P}^3} dS_{1+} - \iint_{S_{1-}} \frac{J}{4\pi} \frac{\overline{P_S^- P}}{\overline{P_S^- P}^3} dS_{1-} \tag{4.14}$$

Expressing the equation analytically in all three axes yields the following equations [303].

$$B_{1x}(x,y,z,a,b,c,J_0) = \frac{J}{4\pi} \ln \left[\frac{N_x(x,y,z,a,b,c) N_x(x,y,z,0,0,c) N_x(x,y,z,a,0,0) N_x(x,y,z,0,b,0)}{N_x(x,y,z,a,0,c) N_x(x,y,z,0,b,c) N_x(x,y,z,a,b,0) N_x(x,y,z,0,0,0)} \right] \tag{4.15}$$

$$B_{1y}(x,y,z,a,b,c,J_0) = \frac{J}{4\pi} \ln \left[\frac{N_y(x,y,z,a,b,c) N_y(x,y,z,0,0,c) N_y(x,y,z,a,0,0) N_y(x,y,z,0,b,0)}{N_y(x,y,z,a,0,c) N_y(x,y,z,0,b,c) N_y(x,y,z,a,b,0) N_y(x,y,z,0,0,0)} \right] \tag{4.16}$$

$$B_{1z}(x,y,z,a,b,c,J_0) = -\frac{J}{4\pi} \begin{bmatrix} N_z(x,y,z,a,b,c) - N_z(x,y,z,a,b,0) \\ -N_z(x,y,z,a,0,c) + N_z(x,y,z,a,0,0) \\ -N_z(x,y,z,0,b,c) + N_z(x,y,z,0,b,0) \\ N_z(x,y,z,0,0,c) - N_z(x,y,z,0,0,0) \end{bmatrix} \tag{4.17}$$

$$N_x(x,y,z,a,b,c) = b - y + \sqrt{(x-a)^2 + (y-b)^2 + (z-c)^2} \tag{4.18}$$

$$N_y(x,y,z,a,b,c) = a - x + \sqrt{(x-a)^2 + (y-b)^2 + (z-c)^2} \tag{4.19}$$

$$N_z(x,y,z,a,b,c) = \tan^{-1}\frac{(a-x)(b-y)}{(c-z)\sqrt{(x-a)^2 + (y-b)^2 + (z-c)^2}} \tag{4.20}$$

The forces between two magnets in any spatial orientation can be inferred from the field produced by the first magnet on the charged planes of the second magnet, as shown in Figure 4.3. Therefore, the forces between two magnets in free space can be expressed as follows.

$$\bar{F} = \iint_{S_{2+}} \frac{J}{\mu_0}\overline{B_1} dS_{2+} - \iint_{S_{2+}} \frac{J}{\mu_0}\bar{B} dS_{2+} \tag{4.21}$$

4.1.3. Analytical calculation of synchronous active radial magnetic couplers

Magnetic couplers (MCs) are classified into two main groups: synchronous and asynchronous. This classification is based on the rotor speeds and magnetic field variations that occur in response to the load, which enhances the versatility. The magnetization direction of PMs offers a further layer of classification. This provides distinct design options for radial and axial orientations, which can fulfil specific requirements for various applications. Additionally, MCs can be categorized based on their interaction types, such as active, reactive, eddy-current, and hysteresis. This categorization is crucial for designing and optimizing the MC performance for specific applications, as highlighted in Section 3.2.

Aerospace Starter/Generator applications rely heavily on the use of synchronous magnetic couplers due to their crucial role in achieving a smooth transfer of torque between the piston engine and the Starter/Generator shafts, resulting in reduced noise and vibration, as well as improved control of Starter/Generator operations. Furthermore, synchronous MCs offer advantages over asynchronous couplers, including higher efficiency, greater torque density, and improved power transfer control, making them ideal for applications where precise synchronization and high performance are needed.

By using synchronous types, maintenance requirements are reduced and the service life of the system is prolonged, leading to cost savings and overall improved system performance.

In low-speed aerospace applications, axial MCs are typically preferred over radial MCs due to their higher torque density. In high-speed aerospace applications, such as Starter/Generators, axial magnetic couplers can pose significant challenges due to the high contact pressures required to transfer torque at high speeds, resulting in increased heat and wear. Additionally, the larger and heavier structure of axial couplers can be disadvantageous in aerospace applications where weight and space are critical factors.

In contrast, the use of radial MCs in aerospace applications is highly effective due to several advantages over axial couplers. Radial couplers offer greater efficiency, reliability, and compactness in high-speed applications compared to axial couplers. They also operate with lower contact pressures, reducing wear and heat generation, and can be designed to be lightweight and compact, ideal for weight and space-critical applications.

Radial couplers can reduce vibration and noise generated during operation and accommodate misalignments and angular offsets between the PE and the S/G, ensuring efficient torque transfer. In addition, the ease of maintenance and repair of radial couplers is crucial in minimizing downtime and performing maintenance quickly and efficiently.

Synchronous radial MCs can be categorized into two groups: active and reactive couplers, as illustrated in Figure 4.4. An active magnetic coupler (AMC) consists of PMs inserted into both rotors. On the other hand, a reactive magnetic coupler (RMC) has PMs mounted on only one-half of the rotor, while the other half is made of steel in the form of PMs.

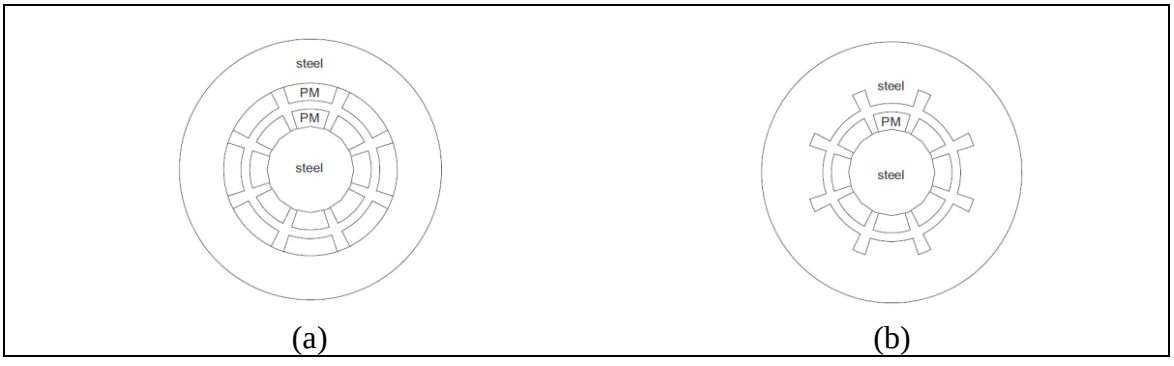


Figure 4.4. Simple synchronous MCs (a) Active type (b) Reactive type [304]

The AMC has a significantly higher maximal mechanical torque, which is a key characteristic of AMCs, compared to the RMC [304]. The torque change period for the RMC is half that of the AMC. These findings indicate that the AMC is generally better suited for use. However, in environments where the temperature can exceed 200°C, the PM quality is compromised, leading to a loss of their attraction and repulsion forces. In such cases, it is advisable to use the RMC, which is also preferred when mechanical torque is not critical. Since RMCs use fewer PMs, they are also more cost-effective. After a thorough evaluation of all the factors discussed above, the synchronous active radial magnetic coupler topology has been deemed the most suitable choice for the thesis.

Analytical approaches such as Virtual Work [205], Maxwell Stress [305], Coulombian [306], Monte Carlo [307], 3D semi-analytical [206], and analytical magnetic field methods [204] are regarded as fast and straightforward methods to estimate the preliminary design dimensions of magnetic couplers.

Despite their usefulness, conventional methods for calculating the transmitted torque of MCs have high margins of error. This is due to various assumptions made during the calculations, such as the homogeneity of PM magnetization, large model length, average air gap radius compared to PM thickness and air gap length, increase in torque with increasing pole numbers, and unsaturated rotor materials with high permeability. Analytical calculations involving these effects can also be laborious and complicated. However, utilizing the Virtual Work approach and analytical subdomain method, which is based on the Maxwell stress tensor, can provide fast and useful analytical calculations for the transmitted torque of MCs.

Analytical subdomain method based on the Maxwell Stress Tensor

The subdomain analytical method is based on the resolution of Laplace's and Poisson's equations in the air-gap and PM subdomains, respectively, which provides a fast and accurate calculation of the transmitted torque in AMCs, as illustrated in Figure 4.5 [208].

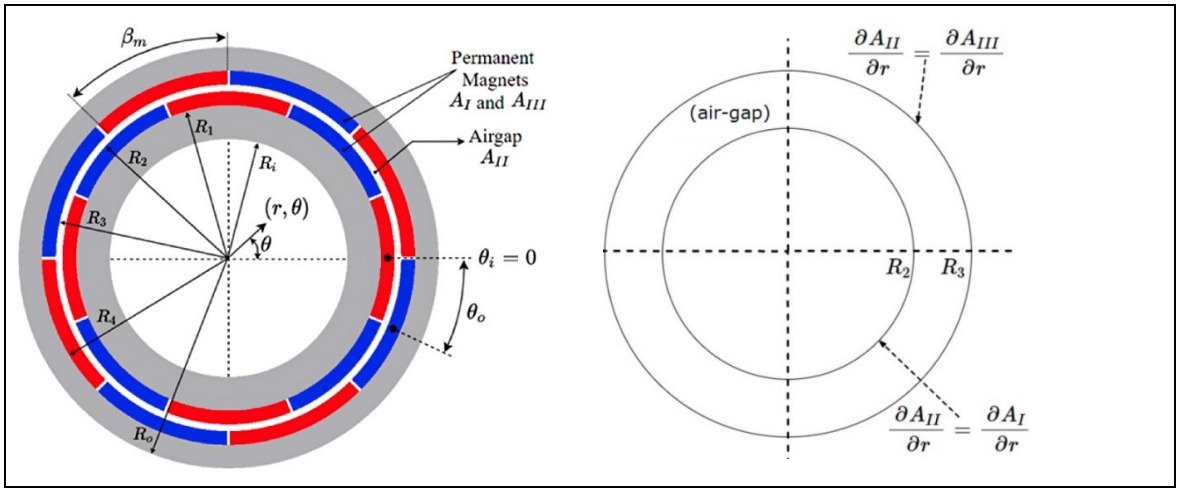


Figure 4.5. Parameters of synchronous active radiallly oriented magnetic couplers [208]

where R_i, R_1, R_2, R_3, R_4, R_o, l_a, p, l_m, B_m, l_{out}, l_s and B_r are the inner radius of the back iron, inner radius of the inner PM, outer radius of the inner PM, inner radius of outer PM, outer radius of outer PM, outer radius of outer back iron, air gap length, pole-pair, thickness of PMs, openings of PMs, outer diameter, active part length, and PM remanence, respectively.

The 2D analytical method assumes a cylindrical geometry and neglects end effects. The back iron is assumed to have infinite permeability, and the magnetic field is perpendicular to it. PMs are assumed to have a relative permeability of 1 and are radially magnetized [308].

The determination of the flux density distribution is achieved through the use of the solutions obtained from the vector potential in the air-gap, as described by the following equations:

$$B_{IIr}(r,\Theta) = \frac{1}{r}\frac{\partial A_{II}}{\partial \Theta} \qquad (4.22) \qquad B_{II\Theta}(r,\Theta) = -\frac{\partial A_{II}}{\partial r} \qquad (4.23)$$

The aforementioned equations denote that the air gap flux density distributions $B_{\mathrm{II}r}(r,\Theta)$ and $B_{\mathrm{II}\Theta}(r,\Theta)$ are a function of the radial distance (r) and angle (Θ) in polar coordinate representation. ∂A_{II} is the vector potential in the air gap. The flux density distribution components can also be expressed using the following equations obtained by rearranging the above equations:

$$B_{IIr}(r,\Theta) = -\sum_{n=1}^{\infty}\left(A_n^{II}\frac{nr^n}{r} + B_n^{II}\frac{nr^{-n}}{r}\right)\sin(n\Theta) + \sum_{n=1}^{\infty}\left(C_n^{II}\frac{nr^n}{r} + D_n^{II}\frac{nr^{-n}}{r}\right)\sin(n\Theta) \quad (4.24)$$

$$B_{II\Theta}(r,\Theta) = -\sum_{n=1}^{\infty}\left(A_n^{II}\frac{nr^n}{r} - B_n^{II}\frac{nr^{-n}}{r}\right)\cos(n\Theta) - \sum_{n=1}^{\infty}\left(C_n^{II}\frac{nr^n}{r} - D_n^{II}\frac{nr^{-n}}{r}\right)\sin(n\Theta) \quad (4.25)$$

The coefficients of the vector potential, $A_n^{II}, B_n^{II}, C_n^{II}, D_n^{II}$, are determined by using the relationship between the boundary conditions and the potential functions. These boundary conditions and potential functions are reported in [208]. This version separates the explanation of the coefficients from the reference to the potential functions, making it easier to follow the logical progression of the sentence. Ultimately, the transmitted torque can be calculated by implementing the Maxwell stress tensor method as follows:

$$T = \frac{l_s r_{mean}}{\mu_0}\int_0^{2\pi}[B_{IIr}(r_{mean},\Theta)B_{II\Theta}(r_{mean},\Theta)]d\Theta \quad (4.26)$$

The total model active length is denoted by l_s. The radius of the middle of the air gap is represented by r_{mean}, as depicted in Figure 4.5. r_{oi} and r_{io} correspond to the inner rotor outer radius and outer rotor inner diameter, respectively.

Virtual work method

The force and torque exerted on a single pole of the synchronous active radial MC can be effectively evaluated by calculating the work done during small axial and angular displacements from their initial positions. The representative model is shown in Figure 4.6 [201]. The configuration typically includes two rotating parts: an inner and an outer rotors.

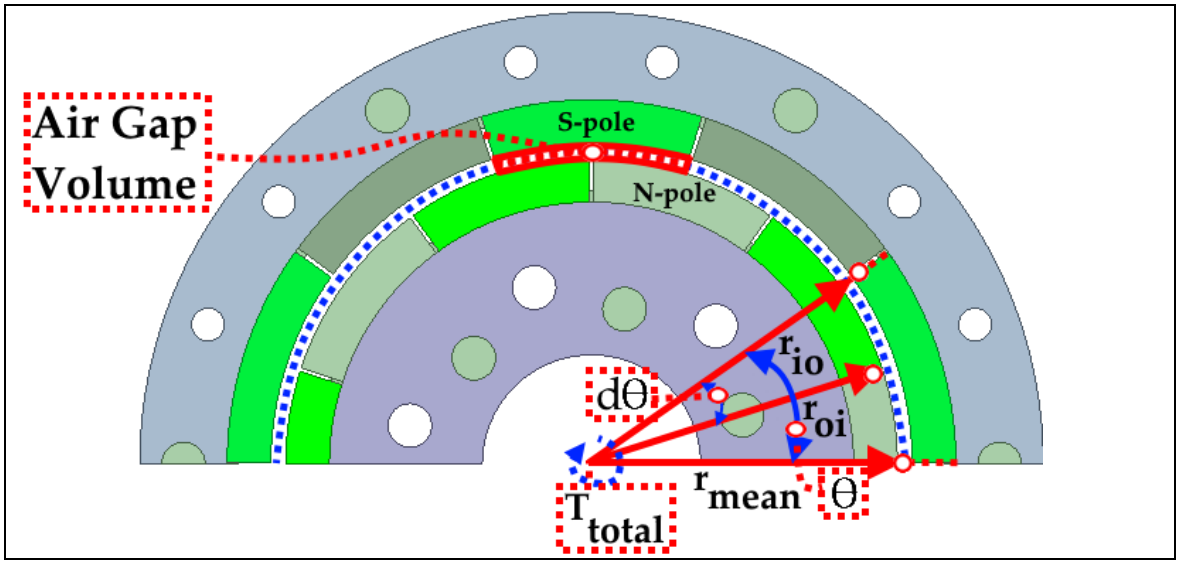


Figure 4.6. Synchronous active radial MC model for analytical calculations [201]

where r_{oi}, r_{io}, r_{mean} are the inner rotor outer radius, outer rotor inner diameter, and middle of the air gap, respectively. The energy stored in the air gap can be obtained by the following:

$$W_{f1} = \frac{(B_{g1})^2 (V_{ag})}{2\mu_0} \quad (4.27) \qquad W_{f2} = \frac{(B_{g2})^2 (V_{ag2})}{2\mu_0} \quad (4.28)$$

where B_{g1}: effective air gap flux density at zero torque angle (T)

W_{f1}: stored energy at minimum energy position (J)

V_{ag}: air gap volume at zero torque angle (m^3)

W_{f2}: stored energy at the specific torque angle of dθ (J)

V_{ag2}: air gap volume at the specific displacement (m^3)

Assuming that the total flux remains constant when a pole is displaced relative to its opposite pole by an axial distance dx or angular distance dΘ, it becomes concentrated in the air gaps, as seen in Eq. 4.30.

Θ and dΘ represent pole the angle and small angular displacement in radians. x and dx represent pole arc length and small axial displacement in meters, respectively, as shown in Figure 4.7. The air gap area at dΘ and dx can be calculated using Eq. 4.30.

$$B_{g1}A_1 = B_{g2}A_2 \quad (4.29)$$

$$A_2 = A_1 * \frac{(\Theta - d\Theta)}{\Theta} = A_1 * \frac{(x - dx)}{x} \quad (4.30)$$

The resulting flux density and air gap volume can be expressed as follows:

$$B_{g2} = \frac{(B_{g1}) * \Theta}{(\Theta - d\Theta)} = \frac{(B_{g1}) * x}{(x - dx)} \quad (4.31)$$

$$V_{ag2} = V_{ag} * \frac{(\Theta - d\Theta)}{\Theta} = V_{ag} * \frac{(x - dx)}{x} \quad (4.32)$$

Thus, the increase in energy can be expressed as follows:

$$W_{f2} = \frac{(B_{g2})^2(V_{ag2})}{2\mu_0} = \frac{(B_{g1})^2(V_{ag}) * \Theta}{2\mu_0(\Theta - d\Theta)} = \frac{(B_{g1})^2(V_{ag}) * x}{2\mu_0(x - dx)} \quad (4.33)$$

The air gap area and volume at zero position and small displacement are seen in Figure 4.7.

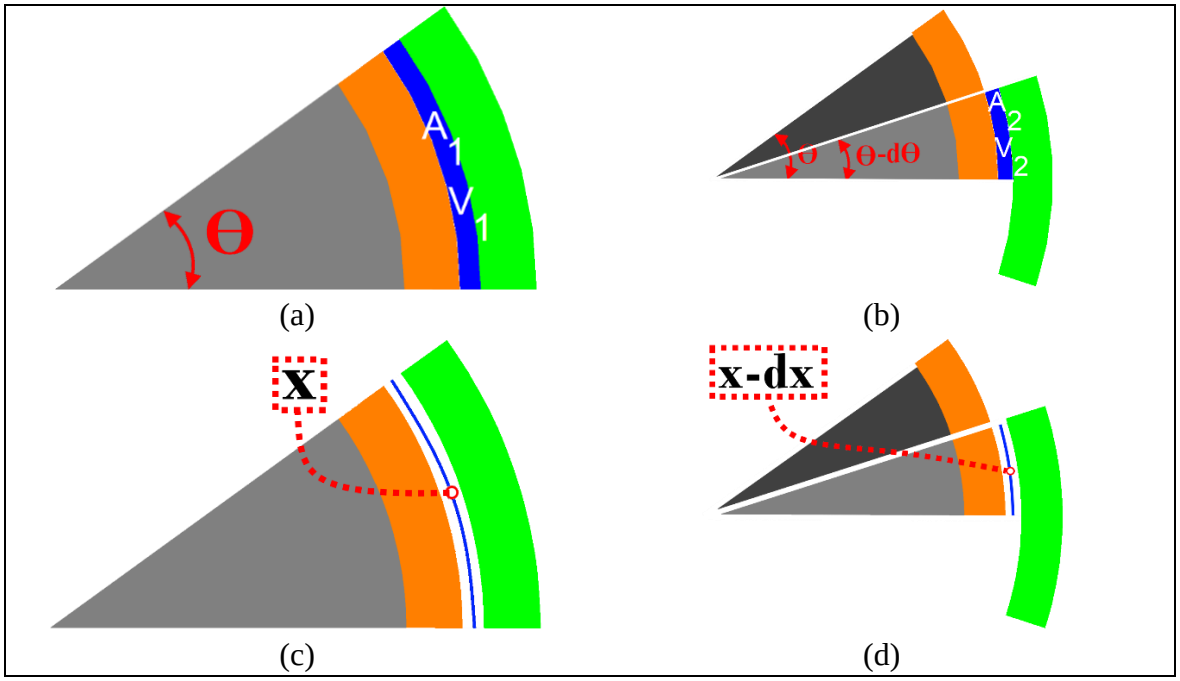


Figure 4.7. Air gap area and volume at (a) Torque angle of zero (b) Torque angle of Θ (c) Axial displacement of zero (d) Axial displacement of dx

A_1 and A_2 are the air gap area at zero torque angle and torque angle of dΘ respectively.

V_{ag1},V_1 and V_{ag2},V_2 are the air gap volume at zero torque angle and torque angle of dϴ respectively. The energy increase, dW, resulting from the displacement of the pole by a distance dx or dϴ is equivalent to the work done, and can be represented as follows:

$$dW = W_{f2} - W_{f1} = \frac{(B_{g1})^2(V_{ag}) * d\Theta}{2\mu_0(\Theta - d\Theta)} = \frac{(B_{g1})^2(V_{ag}) * dx}{2\mu_0(x - dx)} \tag{4.34}$$

The force acting on a single pole can be determined using the Virtual Work principle, as expressed in Eq. 4.35 [309]. This method involves evaluating the change in stored energy within the air gap resulting from a small axial displacement between the poles. The torque can similarly be calculated by replacing the axial displacement (x-dx) in the equation with the angular displacement (ϴ-dϴ) [265].

$$F_{single_pole} = \frac{dW}{dx} = \frac{(B_{g1})^2(V_{ag})}{2\mu_0(x - dx)} \tag{4.35}$$

$$T = \frac{dW}{d\Theta} \tag{4.36}$$

$$T_{single_pole} = \frac{dW}{d\Theta} = \frac{(B_{g1})^2(V_{ag})}{2\mu_0(\Theta - d\Theta)} \tag{4.37}$$

where F_{single_pole}: exerted force on a single-pole (N)

dW: stored energy change in the air gap (J)

x: pole arc length (m)

dx: small displacement distance of a pole (m)

T: torque exerted on a single-pole (N)

The total force and torque acting on the rotors are evaluated with respect to the Effective Air Gap (EAG), which is determined based on the total number of poles, 2p. The EAG is determined as the midpoint of the air gap and is utilized to calculate the force and torque on the rotors, as expressed below:

$$F_{total_pole} = \frac{dW}{dx} = \frac{(B_{g1})^2(V_{ag})}{2\mu_0(x - dx)} * (2p) \tag{4.38}$$

$$T_{total_pole} = \frac{dW}{d\Theta} = \frac{(B_{g1})^2(V_{ag})}{2\mu_0(\Theta - d\Theta)} * (2p) \tag{4.39}$$

The critical angle, denoted as $\Theta_{critical}$ (in mechanical degrees, Mdeg), is the angle at which the maximum torque is achieved, corresponding to an electrical angle (Edeg) of 90°. The critical angle and maximum torque are also referred to as the maximum torque angle and pullout torque, respectively. Mdeg and Edeg represent the mechanical and electrical degrees, respectively. The critical angle can be calculated using Eq. 4.40, as shown below.

$$\theta_{critical,Mdeg} = \frac{360^\circ}{(2p) * 2} \quad (4.40) \qquad \theta_{Edeg} = \frac{(2p)}{2} * \theta_{Mdeg} \quad (4.41)$$

In magnetic couplers, if the critical torque angle is exceeded, the magnetic coupling between the two rotors is lost, and the coupler stops transmitting power. This is because the magnetic forces can no longer overcome the mechanical forces that are trying to separate the rotors. In other words, the coupler experiences magnetic pullout, which is a failure mode in which the magnetic attraction between the rotors is no longer sufficient to maintain synchronization and torque transmission. This can cause the magnetic coupler to experience torque ripple, which can result in noise and vibration. Therefore, it is important to operate magnetic couplers within their designed torque limits to ensure efficient and reliable operation.

The value of permanent magnet embrace (β), as defined in Eq. 4.42, is a crucial parameter affecting the output torque of magnetic couplers.

$$\beta = \frac{\alpha_{pole_arc}}{\alpha_{pole_pitch}} \quad (4.42)$$

Pole embrace, the ratio of the pole arc to the pole pitch, is depicted in Figure 4.8 (a) [201].

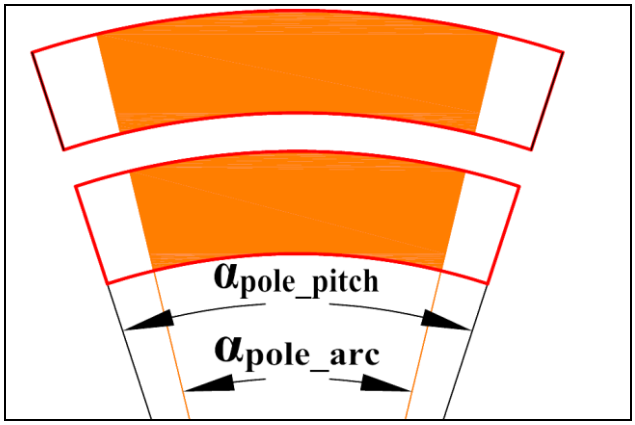


Figure 4.8. Definition of PM embrace

Wider embrace of PMs result in higher mechanical torque for magnetic couplers [265]. Research shows that wider permanent magnets, which correspond to a higher pole embrace ratio (β), cause the mechanical torque to take on a trapezoidal shape [41]. In MCs, similar to EMs, the flux density in the yoke needs to be considered, given as follows [225]:

$$h_{yoke} = \frac{\pi * R_4 * \beta * 2}{(2p)} \frac{B_{PM}}{B_{yoke}} = \frac{\pi * (R_5 - h_{yoke}) * \beta * 2}{(2p)} \frac{B_{PM}}{B_{yoke}} \quad (4.43)$$

where R_4, R_5, and h_{yoke} represent the radius of the inner and outer surfaces of the outer half coupler and the thickness of the rotor yokes, respectively, as illustrated in Figure 4.9. A smaller number of poles results in a more distinct trapezoidal shape of the mechanical torque. This effect is further amplified by an increase in the yoke thickness, h_{yoke}, as the pole number decreases.

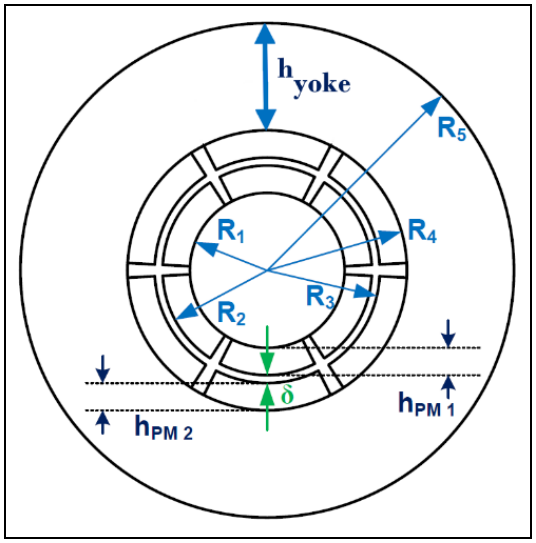


Figure 4.9. Definition of MC dimensions

Analytical solutions can also be utilized to determine the initial dimensions necessary for the efficient design of modulated and nonmodulated magnetic gear [310-313] and magnetic gears assisted electric machines [271, 314].

While analytical calculations may suggest a linear relationship between variables, nonlinear effects of magnet embrace, magnet offset, number of poles, rotor yoke thickness, and effective air gap radius can be better understood through numerical analysis. The following section provides an in-depth description of the relevant analyses conducted for thesis study.

4.2. Mathematical Modelling of BLDC

In the context of PM Starter/Generators, it is important to understand the types of permanent magnet machines used in these systems. Permanent magnet brushless machines can be divided into two categories based on the control types: brushless DC machines (BLDCs) and permanent magnet synchronous machines (PMSMs), as detailed in Section 3.1.

Table 4.1 compares the ideal characteristics of BLDCs with concentrated windings, which are typically powered with trapezoidal waveforms, and PMSMs with sinusoidal windings, which are typically powered with sinusoidal waveforms, as illustrated in Figure 4.10 [315].

Traditionally, a distributed winding configuration has been utilized as the prevailing approach for the stator winding configuration in three-phase systems, with the objective of generating a sinusoidal flux within the air gap. Nevertheless, there has been a discernible shift in recent times towards the adoption of concentrated windings in PMSMs. Despite the inherent drawback of a concentrated winding, which results in a less sinusoidal magnetomotive force distribution when compared to a distributed winding, the adoption of concentrated windings in PMSMs has gained prominence in recent years due to several compelling advantages. These include heightened power density, improved overall efficiency, reduced end turns, increased slot-fill factor, cost-effectiveness achieved through segmented stator structures, minimized cogging torque, the ability to facilitate flux weakening, and enhanced fault tolerance [316].

Table 4.1. Ideal characteristic comparison of BLDC and PMSM

Parameters	BLDC	PMSM
Flux linkage	Nonsinusoidal (Trapezoidal)	Sinusoidal
Back EMF	Trapezoidal	Sinusoidal
Stator current	Six-step	Sinusoidal
Phase energies	Two phases at any time	Three phases all time
Output torque	High ripple	Low ripple

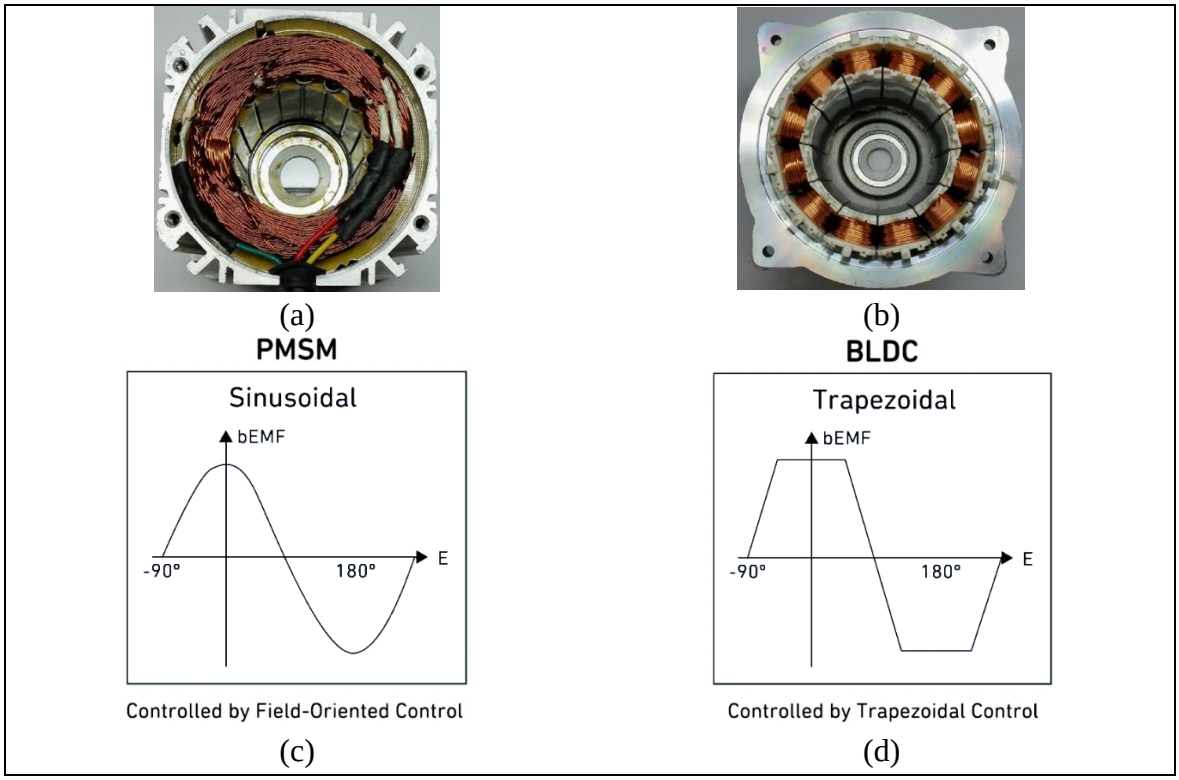


Figure 4.10. (a) PMSM with distributed winding (b) BLDC with concentrated winding

Both machines can be used in S/G applications, and the choice depends on factors such as power, efficiency, and cost. A thorough understanding of their characteristics is crucial for successful S/G system design.

Starter/Generator in starter and motor mode can be operated as BLDC or PMSM. These topologies offer notable advantages compared to other options, such as brushed DC, wound rotor, reluctance, and induction motors. Here are the key points that emphasize the possibility and benefits of utilizing BLDC or PMSM motors in starter mode:

High Starting Torque: BLDC and PMSM motors exhibit the ability to deliver substantial torque even at low speeds, which is crucial for effectively starting the piston engine.

Speed Control: BLDC and PMSM motors can be precisely controlled using advanced motor control techniques. This allows for optimal speed management during the motor mode.

Compact and Lightweight Design: BLDC and PMSM motors possess a compact and lightweight construction, making them highly suitable for integration into UAVs.

Efficiency and Energy Savings: Both BLDC and PMSM motors are known for their high efficiency, leading to enhanced energy utilization and reduced fuel consumption.

Durability and Maintenance: The brushless nature of BLDC and PMSM motors eliminates the need for brushes, thereby reducing wear and maintenance requirements.

Control Flexibility: BLDC and PMSM motors offer flexible control options, allowing for precise management of motor speed, torque, and position.

Figure 4.11 depicts a schematic of a simple three-phase star and delta connected BLDC motor with phase currents [317].

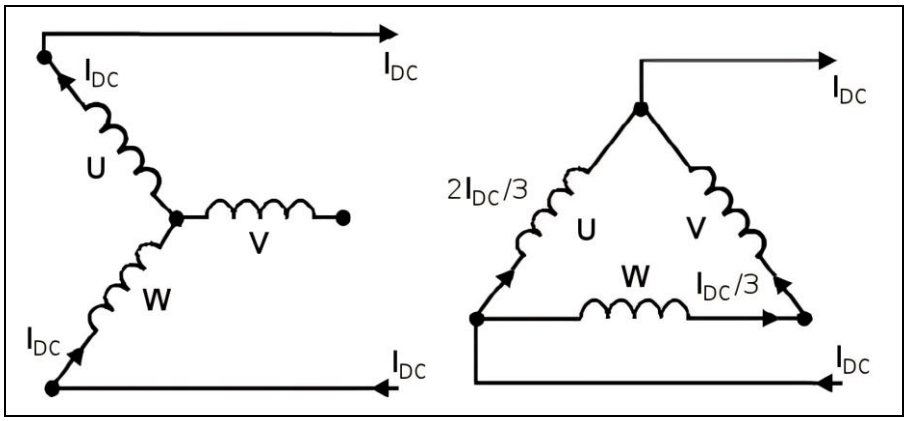


Figure 4.11. Three-phase BLDC motor (a) Star connected (b) Delta connected

$$V_a = R_a i_a + \frac{d\psi_a}{dt} \qquad V_b = R_b i_b + \frac{d\psi_b}{dt} \qquad V_c = R_c i_c + \frac{d\psi_c}{dt} \tag{4.44}$$

where R_a, R_b, R_c : Phase resistances in ohm
V_a, V_b, V_c : Phase voltages in volt
i_a, i_b, i_c : Phase current in ampere
ψ_a, ψ_b, ψ_c : Flux linkages in weber

$$\psi_a = L_a i_a + L_{ab} i_b + L_{ac} i_c + \psi_{am} \tag{4.45}$$

$$\psi_b = L_b i_b + L_{ba} i_a + L_{bc} i_c + \psi_{bm} \tag{4.46}$$

$$\psi_c = L_c i_c + L_{ca} i_a + L_{cb} i_b + \psi_{cm} \tag{4.47}$$

where L_a, L_b, L_c : Self inductances in henry

L_{ab}, L_{ac}, L_{ba}, L_{bc}, L_{ca}, L_{cb} : Mutual inductances of phases in henry

ψ_{am}, ψ_{bm}, ψ_{cm} : Flux linked with each phase due to PMs in weber

When equations Eq. 4.44-4.47 are written in matrix form, the following equation is obtained:

$$\begin{bmatrix} V_a \\ V_b \\ V_c \end{bmatrix} = \begin{bmatrix} R_a & 0 & 0 \\ 0 & R_b & 0 \\ 0 & 0 & R_c \end{bmatrix} \begin{bmatrix} i_a \\ i_b \\ i_c \end{bmatrix} + \frac{d}{dt} \begin{bmatrix} L_a & L_{ab} & L_{ac} \\ L_{ba} & L_b & L_{bc} \\ L_{ca} & L_{cb} & L_c \end{bmatrix} \begin{bmatrix} i_a \\ i_b \\ i_c \end{bmatrix} + \frac{d}{dt} \begin{bmatrix} \psi_{am} \\ \psi_{bm} \\ \psi_{cm} \end{bmatrix} \tag{4.48}$$

The rate of change of the flux linkages created by the PMs in each phase is equivalent to the induced back electromotive force (EMF) in the winding. Assuming no changes in the rotor reluctances, the self-inductances (L) and mutual inductances (M) of each phase are assumed to be similar. It is also assumed that the winding resistances are equal. When the three phases are connected in a wye configuration without a neutral point, the sum of the currents in the three phases is zero. Therefore, the above equation can be expressed as follows [318].

$$\begin{bmatrix} V_a \\ V_b \\ V_c \end{bmatrix} = \begin{bmatrix} R & 0 & 0 \\ 0 & R & 0 \\ 0 & 0 & R \end{bmatrix} \begin{bmatrix} i_a \\ i_b \\ i_c \end{bmatrix} + \frac{d}{dt} \begin{bmatrix} \mathrm{L-M} & 0 & 0 \\ 0 & \mathrm{L-M} & 0 \\ 0 & 0 & \mathrm{L-M} \end{bmatrix} \begin{bmatrix} i_a \\ i_b \\ i_c \end{bmatrix} + \begin{bmatrix} e_a \\ e_b \\ e_c \end{bmatrix} \tag{4.49}$$

The electromagnetic torque equation, derived from the back electromotive forces (EMFs) and coenergy, is expressed as shown in Equations 4.50 and 4.51, respectively:

$$T_e = \frac{e_a i_a + e_a i_a + e_a i_a}{w_{rm}} \qquad T_e = \frac{2p}{2} \frac{\partial W_c(\Theta_{re})}{\partial \Theta_r} \tag{4.50}$$

where 2p : Pole numbers

W_c : Coenergy

Θ_{re} : Rotor position in electrical degree

w_{rm} : Rotor angular speed in mechanical degree

In surface-mounted PMMs, the direct and quadrature axis inductances are nearly equal. As a result, L and the energy stored in the PM (W_{PM}) are independent of the rotor position (Θ_r).

$$W_c(\Theta_{re}) = \frac{1}{2}[i_a \quad i_b \quad i_c]L\begin{bmatrix} i_a \\ i_b \\ i_c \end{bmatrix} + [i_a \quad i_b \quad i_c]\begin{bmatrix} \psi_m \sin\Theta_{re} \\ \psi_m\left(\sin\Theta_{re} - \frac{2\pi}{3}\right) \\ \psi_m\left(\sin\Theta_{re} + \frac{2\pi}{3}\right) \end{bmatrix} + W_{pm} \tag{4.51}$$

$$T_e = \frac{2p}{2}\frac{\partial W_c(\Theta_{re})}{\partial\Theta_{re}} = \frac{2p}{2}[i_a \quad i_b \quad i_c]\frac{\partial}{\partial\Theta_r}\begin{bmatrix} \psi_m \sin\Theta_{re} \\ \psi_m\left(\sin\Theta_{re} - \frac{2\pi}{3}\right) \\ \psi_m\left(\sin\Theta_{re} + \frac{2\pi}{3}\right) \end{bmatrix} \tag{4.52}$$

$$T_e = \frac{(2p)\psi_m}{2}\left[i_a\cos\Theta_{re} + i_b\left(\cos\Theta_{re} - \frac{2\pi}{3}\right) + i_c\left(\cos\Theta_{re} + \frac{2\pi}{3}\right)\right] \tag{4.53}$$

T_e and T_L are the electromagnetic torque and torque load, respectively. B is the viscous friction coefficient. If the mechanical equation is implemented as shown below:

$$T_e = J\frac{dw_{rm}}{dt} + Bw_{rm} + T_L \tag{4.54}$$

Through conversion of above equations, the mechanical differential equations are obtained.

$$w_{re} = \frac{2p}{2}w_{rm} \qquad \Theta_{re} = \frac{2p}{2}\Theta_{rm} \tag{4.55}$$

$$\frac{2}{2p}\frac{dw_{re}}{dt} = \frac{(2p)}{2J}\frac{\partial W_c}{\partial\Theta_{re}} - \frac{B}{J}\frac{2}{(2p)}w_{rm} - \frac{1}{J}T_L \tag{4.56}$$

$$\frac{dw_{re}}{dt} = \frac{(2p)^2}{4J}\frac{\partial W_c}{\partial\Theta_{re}} - \frac{B}{J}w_{rm} - \frac{(2p)}{2J}T_L \tag{4.57}$$

$$\frac{d\Theta_{re}}{dt} = w_{re} \tag{4.58}$$

4.3. Mathematical Modelling of Starter/Generator

In the realm of PMSMs, two distinct rotor configurations have gained prominence: surface mounted and interior mounted, as discussed in Section 3. Surface mount types (SPMSMs) do not possess inherent reluctance torque. The rotor structure of an SPMSM consists of magnets mounted on the rotor surface, providing a concentrated magnetic field.

It interacts with the stator windings to generate torque primarily through MMF. Reluctance torque, which arises from the variation in magnetic reluctance between the rotor and stator, is not a significant factor in SPMSM. Thus, SPMSMs exhibit a reduced stator winding inductance, resulting in equivalent d-axis and q-axis inductances.

Interior mount types (IPMSMs) utilize a rotor design incorporating magnets and salient rotor poles, resulting in variable air gaps between the rotor and stator during motor rotation. IPMSMs exhibit varying d and q-axis inductances depending on the magnet arrangement. In parallel topology, magnets are positioned along the d-axis, resulting in higher q-axis inductance compared to the d-axis. In perpendicular topology, the q-axis inductance is lower than the d-axis. This difference in inductance creates magnetic saliency, enabling IPMSMs to harness reluctance torque, particularly in the case of a right torque angle drive [319].

Figure 4.12 illustrates the armature current phasor position in the d-q coordinate system, indicating the operating modes of the synchronous machine as an overexcited or underexcited generator, as well as an overexcited or underexcited motor, depending on the quadrant of the armature current [285].

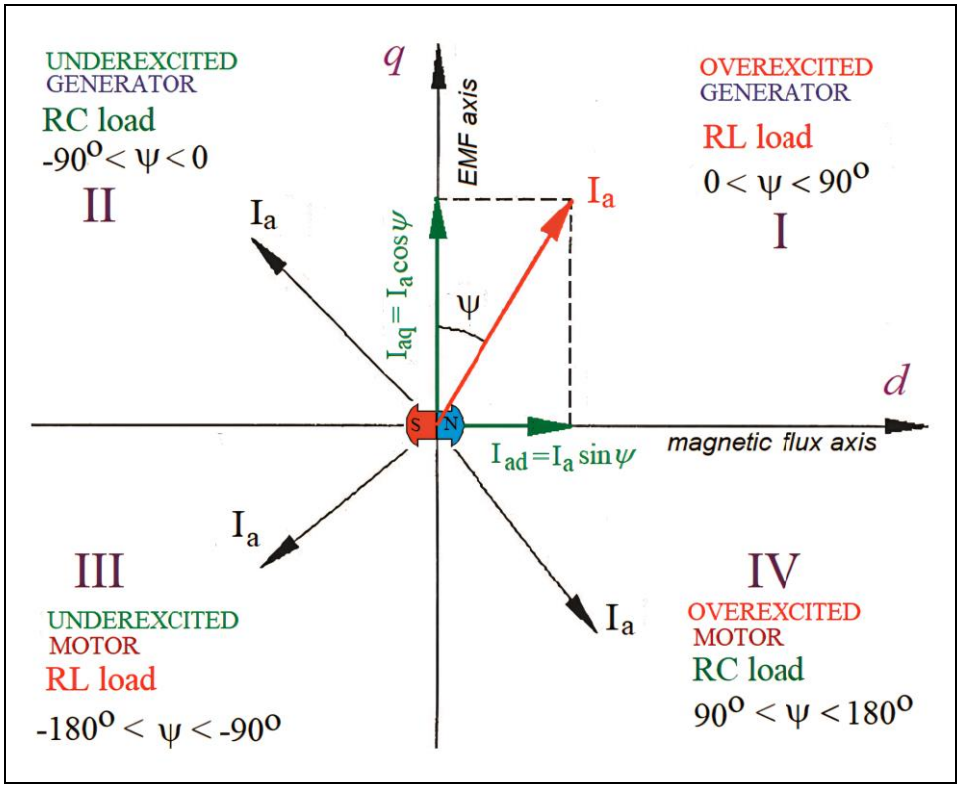


Figure 4.12. Armature current I_a in d-q reference system and PMSM operation modes [285]

In the PMSM equivalent circuit shown in Figure 4.30, it is customary to employ two arrow systems for the motor mode, as shown in Eq. 4.59 and generator mode as shown in Eq. 4.60.

$$E_f = U_1 + I_a R_1 + \mathrm{j} I_{ad} X_{sd} + \mathrm{j} I_{aq} X_{sq} = U_1 + I_{ad}(R_1 + jX_{sd}) + I_{aq}(R_1 + jX_{sq}) \quad (4.59)$$

$$U_1 = E_f + I_a R_1 + \mathrm{j} I_{ad} X_{sd} + \mathrm{j} I_{aq} X_{sq} = E_f + I_{ad}(R_1 + jX_{sd}) + I_{aq}(R_1 + jX_{sq}) \quad (4.60)$$

where $I_a = I_{ad} + I_{aq}$

$I_{ad} = I_a \sin\psi$

$I_{aq} = I_a \cos\psi$

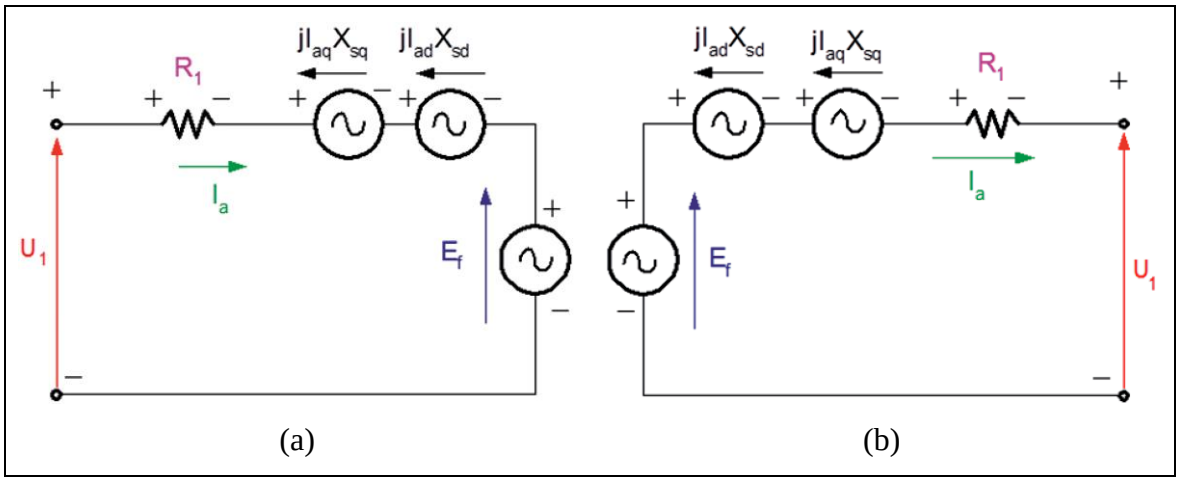


Figure 4.13. PMSM equivalent circuit (a) Motor notation (b) Generator notation [285]

Phasor diagrams for synchronous generators utilize the generator arrow system, where an overexcited generator supplies inductive current and reactive power to the line. The same arrow system can be used for motors, but the motor arrow system is more convenient. For underexcited motors, the d-q coordinate system is rotated by 180° to represent the 3rd quadrant as the position of the 1st quadrant. The phasor diagram, using the motor arrow system, illustrates a load current (I_a) lagging behind the vector U_1 by the angle ϕ, indicating an underexcited motor. At this angle, the motor induces a capacitive current component ($I_a \sin\Psi$) relative to the input voltage U_1. An overexcited motor draws a leading current from the circuit and supplies reactive power [320].

4.3.1. Mathematical model of SPMSM

The mathematical modelling of the 3-phase SPMSM, as illustrated in Figure 4.14, involves the following assumptions [321]:

- The three-phase stator winding is distributed symmetrically in space, disregarding the discrete properties of its structure. As a result, the MMF generated by the stator windings in the air gap is assumed to be sinusoidal, along with the induced EMF.
- The internal permeability of the PM is assumed to be the same as that of air, and the excitation EMF produced in the air gap is assumed to have a sinusoidal distribution.
- Various factors such as iron loss, terminal effects, and magnetic saturation are neglected, and the rotor is assumed to have an infinite constant permeability.
- The motor parameters are assumed to be unaffected by temperature and load effects, and there is no damper winding on the rotor.

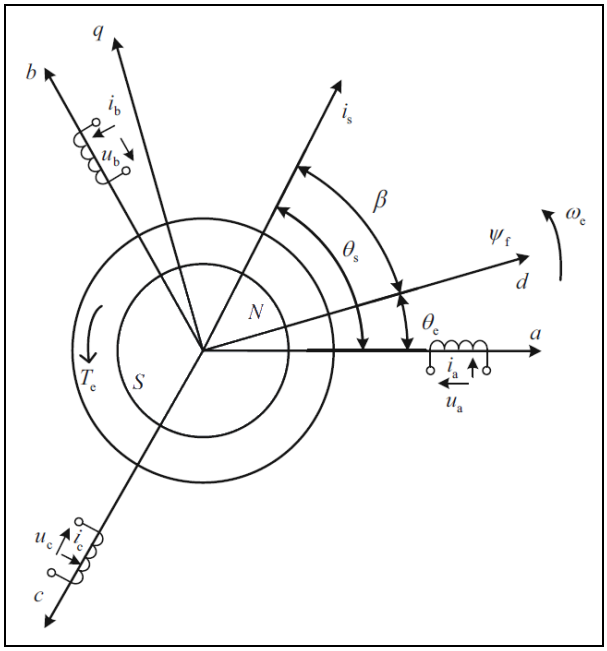


Figure 4.14. SPMSM model [321]

$$\begin{bmatrix} u_a \\ u_b \\ u_c \end{bmatrix} = \begin{bmatrix} R_s & 0 & 0 \\ 0 & R_s & 0 \\ 0 & 0 & R_s \end{bmatrix} \begin{bmatrix} i_a \\ i_b \\ i_c \end{bmatrix} + \frac{d}{dt} \begin{bmatrix} \psi_a \\ \psi_b \\ \psi_c \end{bmatrix} \tag{4.61}$$

$$\begin{bmatrix}\psi_a\\ \psi_b\\ \psi_c\end{bmatrix} = L_{abc}\begin{bmatrix}i_a\\ i_b\\ i_c\end{bmatrix} + \psi_f\begin{bmatrix}\cos(\Theta_e)\\ \cos\left(\Theta_e - \frac{2\pi}{3}\right)\\ \cos(\Theta_e + 2\pi/3)\end{bmatrix}\begin{bmatrix}i_a\\ i_b\\ i_c\end{bmatrix} = \begin{bmatrix}\psi_{fa}\\ \psi_{fb}\\ \psi_{fc}\end{bmatrix} + \begin{bmatrix}L_a & M_{ab} & M_{ac}\\ M_{ba} & L_b & M_{bc}\\ M_{ca} & M_{cb} & L_c\end{bmatrix}\begin{bmatrix}i_a\\ i_b\\ i_c\end{bmatrix} \quad (4.62)$$

where ψ_a, ψ_b, ψ_c : Flux linkage of three phase a, b, c

$\psi_{fa}, \psi_{fb}, \psi_{fc}$: PM flux linked of three phase a, b, c

ψ_f : Rotor flux vector

R_s : Stator winding resistance

The self-inductance and mutual inductances of the a-b-c winding are considered constant and independent of the rotor position.

$$M_{ab} = M_{ba} = M_{ac} = M_{ca} = M_{bc} = M_{cb} = L_m \cos 120 = -\frac{1}{2}L_m \quad (4.63)$$

$$\psi_a = \left(L_{s\sigma} + \frac{3}{2}L_{m1}\right) i_a + \psi_{fa} = (L_{s\sigma} + L_m)i_a + \psi_{fa} = L_S i_a + \psi_{fa} \quad (4.64)$$

$$\psi_s = (L_{s\sigma} i_s) + L_m i_s + \psi_f = L_s i_s + \psi_f \quad (4.65)$$

where $L_m i_s$: Produced by is corresponding to armature field

$L_{s\sigma} i_s$: Flux leakage produced by i_s

ψ_s : Stator flux vector

i_s : Stator current composed of i_a, i_b, i_c

By considering $\psi_f = \left(\psi_f e^{j\theta_e}\right)$ and assuming the amplitude of the variable is constant in the steady-state condition, the voltage vector form can be obtained as follows:

$$\dot{U}_s = R_s \dot{I}_s + jw_e L_s \dot{I}_s + jw_e \dot{\psi}_f = R_s \dot{I}_s + jw_s L_s \dot{I}_s + \dot{E}_0 \quad (4.66)$$

By observing the phasor diagram of the SPMSM, as shown in Figure 4.15, the electromagnetic torque of the surface mount S/G can be determined.

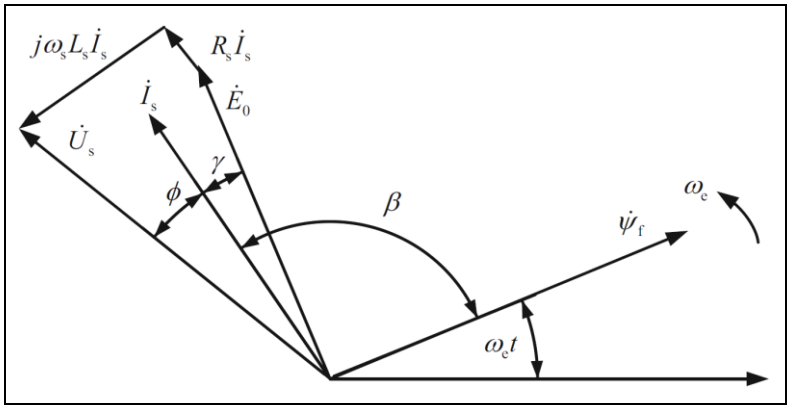


Figure 4.15. Phasor diagram of SPMSM [321]

$$T_e = (2p)\psi_f i_s \sin\beta = (2p)\psi_f \, x \, (i_s) \tag{4.67}$$

In vector control, the control parameters used are the amplitude of the stator current vector i_s and the space phase angle β with respect to ψ_f. In the sinusoidal steady state, this is equivalent to controlling the amplitude of the stator current phasor and the phase angle β.

4.3.2. Mathematical model of IPMSM

In an IPMSM, the air gap is not uniform, resulting in variations in the armature reaction magnetic field due to the difference in the space phase angle β, as depicted in Figure 4.16.

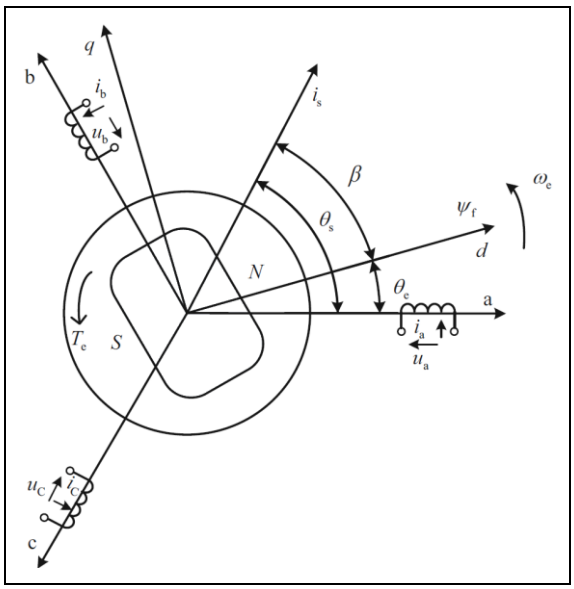


Figure 4.16. IPMSM model

The voltage equation and the flux linkage equation of the three-phase winding in the IPMSM have a similar form to that of the SPMSM, as illustrated in the above equations. However, due to the nonuniform air gap in the IPMSM, the self-inductances and mutual inductances of the phase windings become periodic functions with respect to the rotor position [322].

$$\begin{cases} L_a = L_{s0} + L_{s2}\cos(2\theta_e) \\ L_b = L_{s0} + L_{s2}\cos 2\left(\theta_e - \frac{2\pi}{3}\right) \\ L_c = L_{s0} + L_{s2}\cos 2\left(\theta_e + \frac{2\pi}{3}\right) \end{cases} \tag{4.68}$$

$$\begin{cases} M_{ab} = M_{ba} = -M_{s0} + M_{s2}\cos 2\left(\theta_e + \frac{2\pi}{3}\right) \\ M_{bc} = M_{cb} = -M_{s0} + M_{s2}\cos(2\theta_e) \\ M_{ca} = M_{ac} = -M_{s0} + M_{s2}\cos 2\left(\theta_e - \frac{2\pi}{3}\right) \end{cases} \tag{4.69}$$

where L_{s0} : Average magnitude of self inductance
L_{s2} : Second harmonic of self inductance
M_{s0} : Average magnitude of mutual inductance
M_{s2} : Second harmonic of mutual inductance

The inductances along the α-β axes in an IPMSM remain periodic functions of the rotor position. By applying the Park transformation, these inductances are transformed into the d-q coordinate frame [323]. In the d-q coordinate frame, the voltage equation, flux linkage, and inductance matrix can be expressed as follows:

$$\begin{bmatrix} u_d \\ u_q \end{bmatrix} = R_s \begin{bmatrix} i_d \\ i_q \end{bmatrix} + \frac{\mathrm{d}}{dt}\begin{bmatrix} \psi_\alpha \\ \psi_\beta \end{bmatrix} + w_e \begin{bmatrix} -\psi_q \\ \psi_d \end{bmatrix} \tag{4.70}$$

$$\begin{bmatrix} \psi_d \\ \psi_q \end{bmatrix} = L_{dq} \begin{bmatrix} i_d \\ i_q \end{bmatrix} + \begin{bmatrix} \psi_f \\ 0 \end{bmatrix} \tag{4.71}$$

$$L_{dq} = \begin{bmatrix} \mathrm{L}_d & 0 \\ 0 & \mathrm{L}_q \end{bmatrix} \tag{4.72}$$

$$\dot{U}_s = R_s\dot{I}_s + jw_sL_d\dot{I}_d + jw_sL_q\dot{I}_q + \dot{E}_0 \tag{4.73}$$

where u_d : d-axis stator voltage component
u_q : q-axis stator voltage component
i_d : d-axis stator current component

i_q : q-axis stator current component

ψ_d : d-axis stator flux component

ψ_q : q-axis stator flux component

L_{dq} : d-q axis inductance matrices

By observing the phasor diagram of the IPMSM, as shown in Figure 4.17, the electromagnetic torque of the interior mount S/G can be determined.

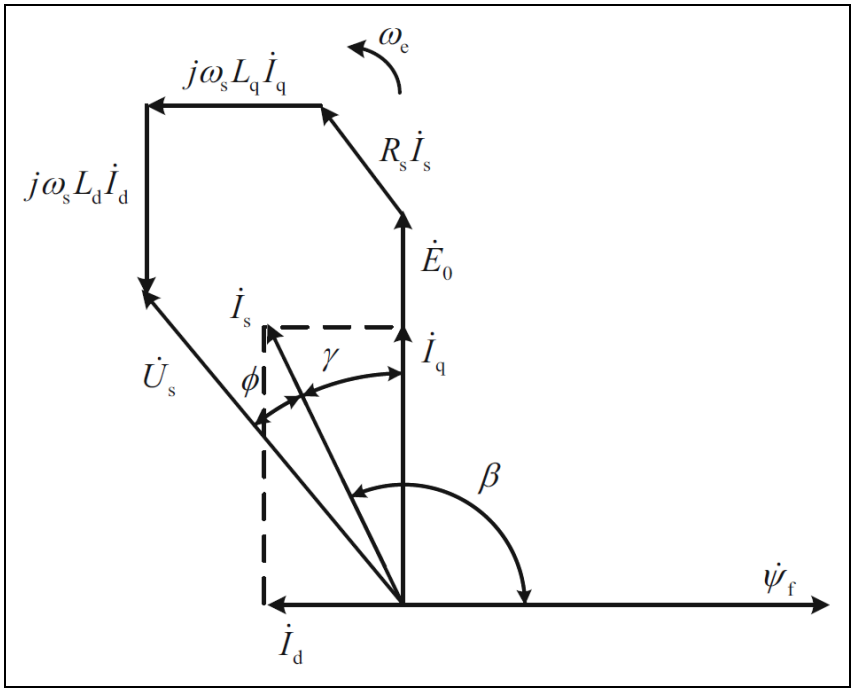


Figure 4.17. Phasor diagram of IPMSM [321]

$$T_e = \frac{3}{2}(2p)\left[\psi_f i_q + \left(L_d - L_q\right) i_d i_q\right] \quad T_e = J\frac{dw_r}{dt} + Bw_r + T_L \tag{4.74}$$

However, the utilization of surface mounted permanent magnet (SMPM) rotors in Starter/Generators brings notable benefits in terms of design flexibility, efficient production, and cost-effectiveness, leading to their widespread adoption, as discussed in detail in Section 3.1. However, one limitation of this rotor design is the magnets' vulnerability to centrifugal forces, which can potentially damage the rotor. To address this concern, incorporating non-magnetic materials on the rotor surface can significantly enhance the robustness of surface magnet rotors, ensuring their reliable operation in demanding aerospace environments.

4.4. Reference Frame Transformation of PM Starter/Generators

Reference frame transformation, specifically the d-q transformation, is employed to convert the commonly used three-phase abc variables in AC systems into orthogonal d-q variables. This transformation is applied in control strategies to simplify analysis and enable independent control of specific components, such as the flux-producing and torque-producing components of the S/G. Figure 4.18 illustrates these variables, where the direction of the abc variables aligns with the magnetic axes of their respective windings [324].

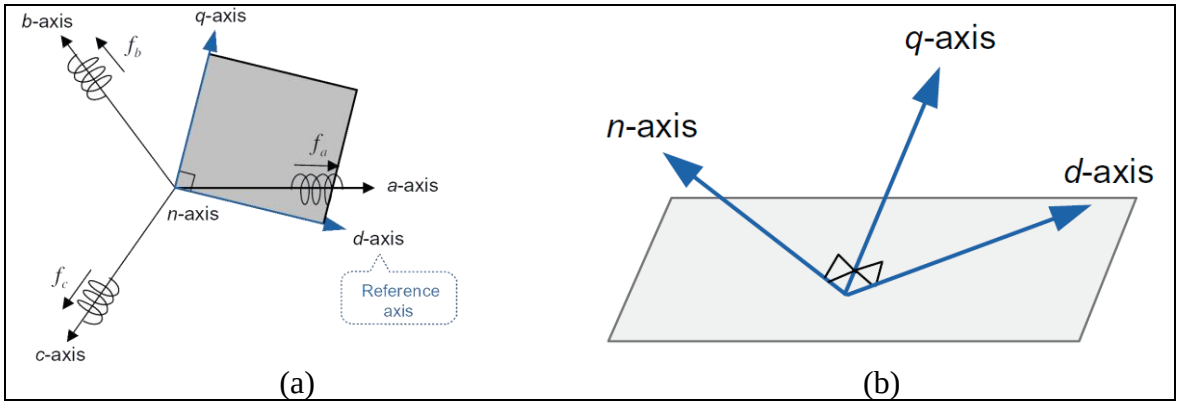


Figure 4.18. Reference frame notation (a) abc coordinates (b) d-q axes [324]

In the reference frame transformation involves three axes: the d-axis, q-axis, and n-axis. The d-axis represents the direction of the magnetic flux in the machine and serves as the reference axis in vector control. The flux-producing component of the motor current is aligned along the d-axis. The q-axis is positioned 90° electrical degrees ahead of the d-axis. It represents the direction where the torque-producing component of machine current or the back-EMF is aligned in vector control. The n-axis is orthogonal to both the d-axis and q-axis. It is not directly associated with the mechanical output power of the motor but is relevant to losses.

The d-q coordinate system can be rotated at any desired speed, but there are two commonly used reference frames. The first is the synchronously rotating reference frame, also known as the synchronous reference frame, which rotates at the speed of the rotating magnetic field. This reference frame is denoted by the d^e-q^e axes. The second is the rotor reference frame, which rotates at the speed of the rotor itself. This reference frame is denoted by the d^r-q^r axes. These two reference frames provide different perspectives and are used in various control strategies and analyses in AC systems.

The angle θ, which represents the deviation between the rotating reference frame and the stationary reference frame, is subject to variation over time. Mathematically, this angle θ can be obtained by integrating the angular velocity ω of the rotating reference frame. For instance, the notation "i^{e}_{ds}" signifies the stator current along the d-axis in the synchronously rotating reference frame.

$$\theta = \int w(\tau)d\tau + \theta(0) \tag{4.75}$$

The transformation of any reference frame into different types of reference frames can be achieved by adjusting the rotation speed. This conversion is known as the generalized rotating transformation. The reference frame transformation can be readily achieved using matrix forms or complex vectors, facilitating a straightforward conversion process.

4.4.1. Matrix form reference frame transformation

Figure 4.19 illustrates the conversion of the three-phase abc variables into dqn variables within the stationary reference frame. The reference frame transformation can be understood as the orthogonal projection of the three-phase abc variables (f_a, f_b, f_c) onto the d-q axis in the stationary reference frame (d^s-q^s axes). The frame of reference can rotate at an angular velocity ω. Therefore, the transformation of the three-phase stationary abc variables into dqn variables in an arbitrary reference frame rotating at a speed ω and the transformation matrix, T(θ) is defined as follows [324]:

$$f^{w}_{dqn} = T(\theta)f_{abc} \tag{4.76}$$

where $f_{dqn} = [f_d f_q f_n]^T$ $f_{abc} = [f_a f_b f_c]^T$

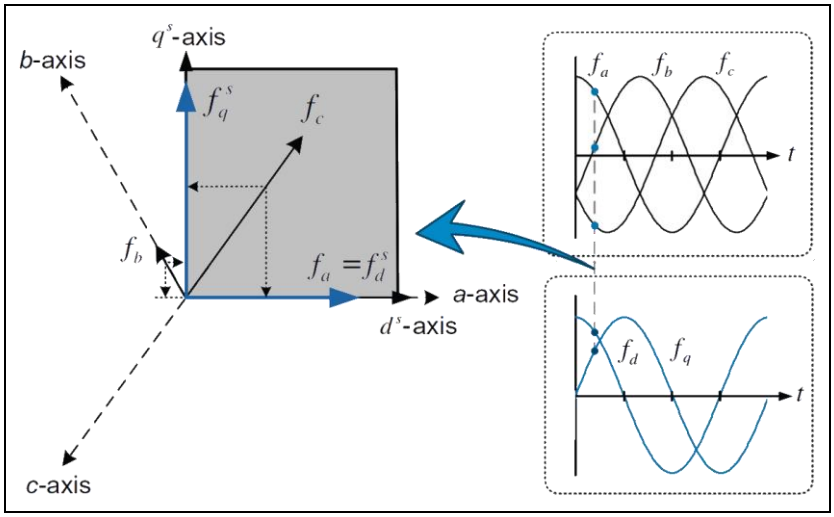


Figure 4.19. Stationary reference frame transformation [324]

$$T(\theta) = \frac{2}{3}\begin{bmatrix} \cos\theta & \cos\left(\theta - \frac{2}{3}\pi\right) & \cos\left(\theta + \frac{2}{3}\pi\right) \\ -\sin\theta & -\sin\left(\theta - \frac{2}{3}\pi\right) & -\sin\left(\theta + \frac{2}{3}\pi\right) \\ \frac{1}{2} & \frac{1}{2} & \frac{1}{2} \end{bmatrix} \tag{4.77}$$

In the case of using a coefficient of 2/3, the magnitude of the dq variables is exactly the same as that of the abc variables. This transformation is known as the magnitude invariance transformation. However, the power and torque calculated in the dqn variables become 2/3 smaller compared to those calculated in the abc variables. On the other hand, when employing a coefficient of √(2/3), the power remains the same value in both reference frames. This transformation is referred to as the power invariance transformation.

4.4.2. ABC into dqn variables transformation in the stationary reference frame

By setting θ=0 in Eq. 4.76, the transformation of the three-phase abc variables into dqn variables in the stationary reference frame is obtained. This transformation is referred to as Clark's transformation. The equations for this transformation are as follows [324]:

$$f_{dqn}^{s} = T(0) f_{abc} = \frac{2}{3}\begin{bmatrix} 1 & -\frac{1}{2} & -\frac{1}{2} \\ 0 & \frac{\sqrt{3}}{2} & -\frac{\sqrt{3}}{2} \\ \frac{1}{\sqrt{2}} & \frac{1}{\sqrt{2}} & \frac{1}{\sqrt{2}} \end{bmatrix}\begin{bmatrix} f_a \\ f_b \\ f_c \end{bmatrix} \tag{4.78}$$

$$f_d^s = \frac{2f_a - f_b - f_c}{3} \qquad f_q^s = \frac{1}{\sqrt{3}}(f_b - f_c) \qquad f_n^s = \frac{2(f_a + f_b + f_c)}{3} \tag{4.79}$$

In the stationary reference frame, dqn variables are arithmetically related to abc variables. Specifically, if the sum of the abc variables in a balanced three-phase system with no neutral connection is zero ($f_a+f_b+f_c=0$), then the n-axis variable (f^s_n) is zero. Consequently, the d^s-axis variable (f^s_d) is equal to the phase a-axis variable (f_a). In this scenario, the dq variables are reduced as follows:

$$f_d^s = f_a \qquad f_n^s = 0 \qquad f_q^s = \frac{1}{\sqrt{3}}(f_b - f_c) \tag{4.80}$$

The inverse transformation of the dqn variables in the stationary reference frame back into abc variables can be expressed as follows:

$$f_d^s = f_a \qquad f_b = -\frac{1}{2}f_d^s + \frac{\sqrt{3}}{2}f_q^s \qquad f_c = -\frac{1}{2}f_d^s - \frac{\sqrt{3}}{2}f_q^s \tag{4.81}$$

4.4.3. Transformation between reference frames

To analyse Synchronous Generators (S/Gs), it is often necessary to perform variable transformations between different reference frames, as depicted in Figure 4.20.

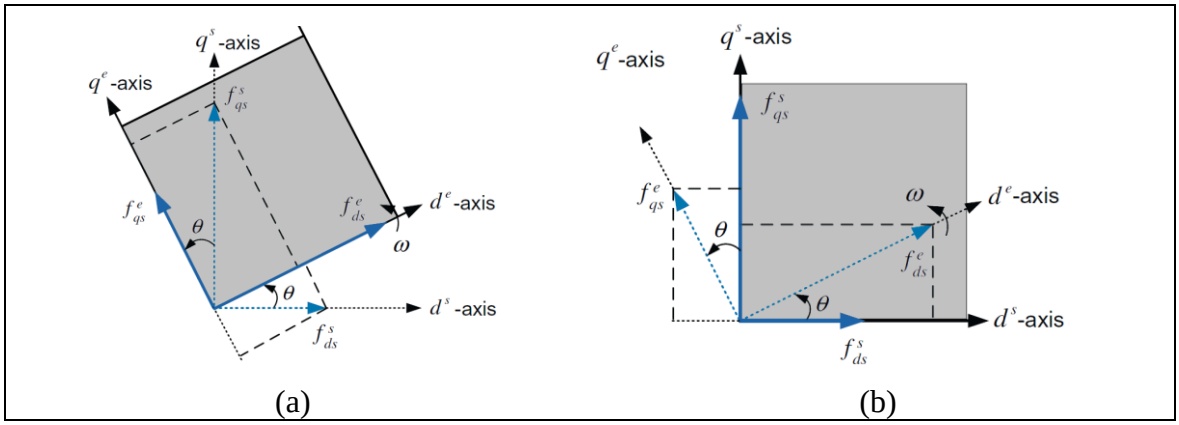


Figure 4.20. Transformations (a) Stationary into rotating (b) Rotating into stationary [324]

Park's transformation is a commonly used method to convert variables from the stationary reference frame to the rotating reference frame. The transformation is expressed as follows:

$$f^e_{dqn} = R(\theta) f^s_{dqn} = \begin{bmatrix} cos\ \theta & \sin\theta & 0 \\ -\sin\theta & cos\ \theta & 0 \\ 0 & 0 & 1 \end{bmatrix} \begin{bmatrix} f^s_d \\ f^s_q \\ f^s_n \end{bmatrix} \tag{4.82}$$

When the variable n is equal to zero,f^s_n=0, Eq. 4.82 can be expressed as separate equations as follows:

$$f^e_d = f^s_d cos\,\theta + f^s_q \sin\theta \qquad f^e_q = -f^s_d \sin\theta + f^s_q cos\,\theta \tag{4.83}$$

Similarly, the inverse transformation can be expressed as follows:

$$f^s_d = f^e_d cos\,\theta - f^e_q \sin\theta \qquad f^s_q = f^e_d \sin\theta + f^e_q cos\,\theta \tag{4.84}$$

4.4.4. Complex vector reference frame transformation

Any three-phase quantity can be represented by a complex space vector, denoted as f_{abc}, in the complex plane as shown in Figure 4.21. This representation enables the analysis of the three-phase system as a whole, providing a comprehensive view rather than considering individual phases separately.

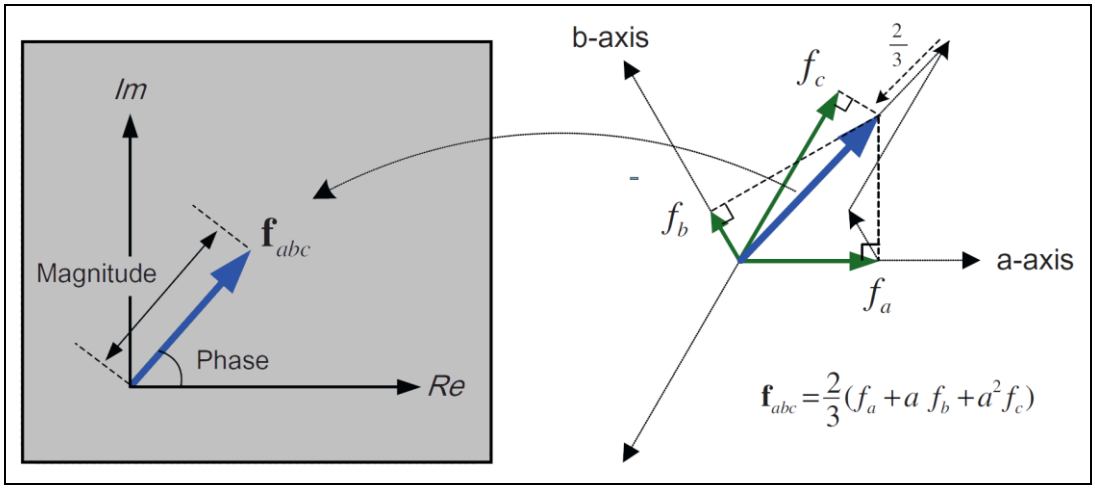


Figure 4.21. Complex space vector

Notably, a space vector differs from a phasor, which represents the amplitude and phase of a sine wave in steady-state conditions. The complex space vector is defined as follows [324]:

$$f_{abc} = \frac{2}{3}(f_{abc} + f_{abc} + f_{abc}) \qquad a = e^{j(2\pi/3)} \qquad a^2 = e^{j(4\pi/3)} \tag{4.85}$$

The complex space vector, representing a three-phase quantity, rotates at the same angular velocity ω_e as the three-phase quantities themselves, as illustrated in Figure 4.22.

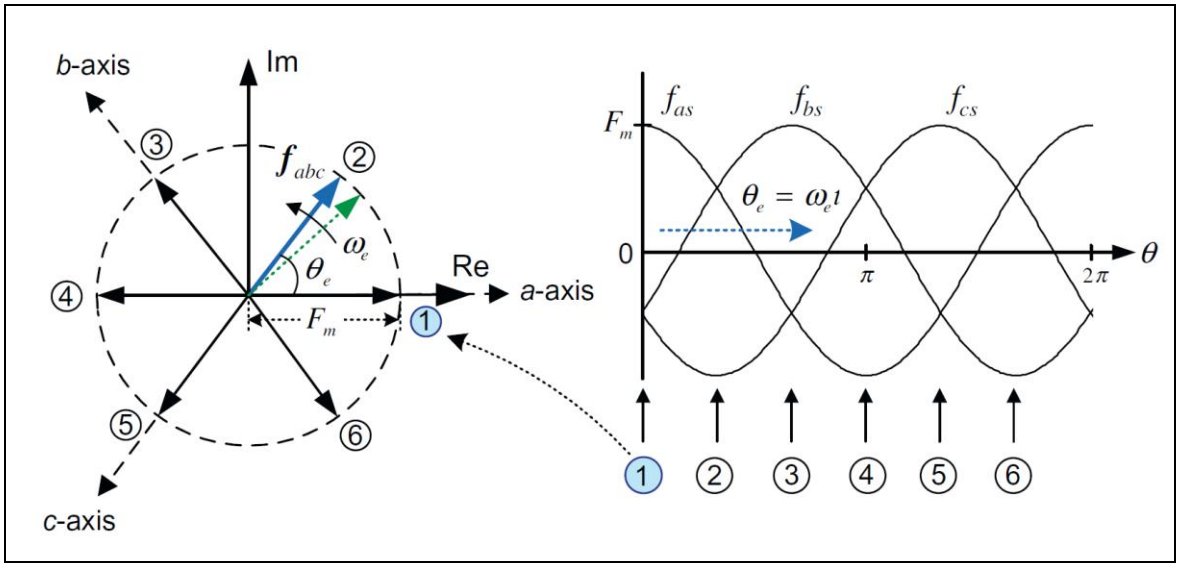


Figure 4.22. Complex space vector with three-phase quantities [324]

When comparing the complex plane with the dq coordinate system discussed earlier, it is observed that both systems possess similar orthogonal coordinates. Specifically, the real axis and imaginary axis in the complex plane correspond to the d-axis and q-axis in the stationary reference frame. Therefore, the space vector f_{abc} is considered equivalent to the vector f^{s}_{dq} in the stationary reference frame, which comprises the components along the d- and q-axes.

$$f_{dq}^{s} = f_{d}^{s} + jf_{q}^{s} \tag{4.86}$$

However, since the dq-axis can rotate at any angular velocity, it is necessary to examine the relationship between a space vector and a vector in the dq-axes rotating at a specific angular velocity. A vector f^{ω}_{dq} in an arbitrary reference frame rotating at a speed ω in Figure 4.23 can be expressed as follows:

$$f_{dq}^{w} = f_{d}^{w} + jf_{q}^{w} \tag{4.87}$$

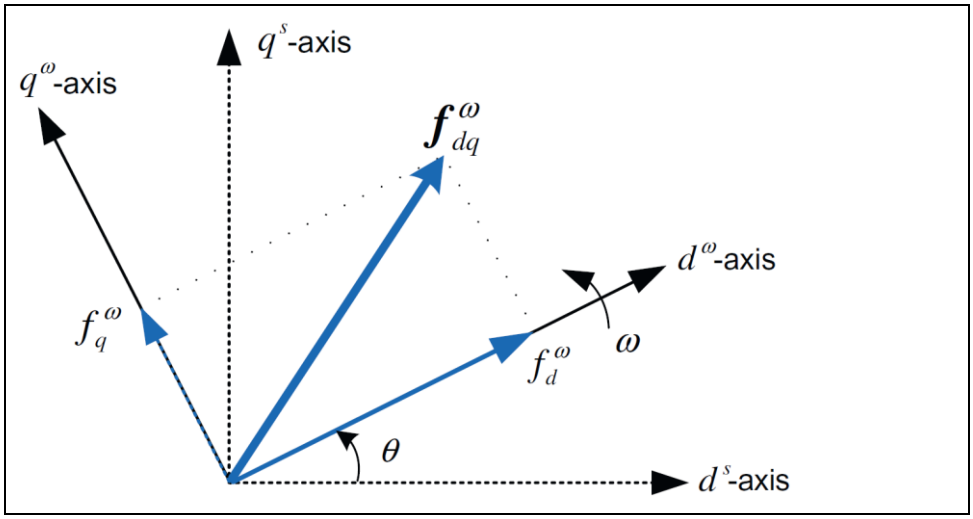


Figure 4.23. Rotating vector in an arbitrary reference frame [324]

$$f_{d}^{w} = \frac{2}{3}\left[f_{a}cos\,\theta + f_{b}cos\left(\theta - \frac{2}{3}\pi\right) + f_{c}cos\left(\theta - \frac{4}{3}\pi\right)\right] \tag{4.88}$$

$$f_{q}^{w} = \frac{2}{3}\left[f_{a}\sin\Theta + f_{b}\sin\left(\theta - \frac{2}{3}\pi\right) + f_{c}\sin\left(\theta - \frac{4}{3}\pi\right)\right] \tag{4.89}$$

$$f_{dq}^{w} = \frac{2}{3}\left[f_a(\cos\Theta - j\sin\Theta) + f_b\left(cos\left(\theta - \frac{2}{3}\pi\right) - j\sin\left(\theta - \frac{2}{3}\pi\right)\right)\right.$$
$$\left. + f_c\left(cos\left(\theta - \frac{4}{3}\pi\right) - j\sin\left(\theta - \frac{4}{3}\pi\right)\right)\right] \quad (4.90)$$
$$= \frac{2}{3}[f_a + af_a + a^2 f_a]e^{-j\Theta} = f_{abc}e^{-j\Theta}$$

When θ=0, the space vector fabc is equivalent to the vector f^{s}_{dq} in the d-q axis of the stationary reference frame. In the rotating reference frame with angular velocity $\omega=\omega_e$, a vector fωdq can be expressed as follows:

$$f_{dq}^{s} = f_{abc}e^{-j0} = f_{abc} \qquad f_{dq}^{e} = f_{abc}e^{-j\Theta_e} = f_{dq}^{s}e^{-j\Theta_e}$$
$$\Theta_e = \int w_e(t)dt + \Theta(0) \quad (4.91)$$

The instantaneous power can be expressed in terms of the complex vector as follows:

$$P = \frac{3}{2}Re[V_{abc}I_{abc}{}^{*}] = \frac{3}{2}Re\left[V_{dq}^{w}I_{dq}^{w\,*}\right] \quad \text{Note: * is the conjugate} \quad (4.92)$$

4.4.5. Torque equation of the Starter/Generator in the d-q axes

The input power can be expressed in the d-q axes as follows:

$$P_{in} = \frac{3}{2}\left(v_{ds}^{r}i_{ds}^{r} + v_{qs}^{r}i_{qs}^{r}\right) \quad (4.93)$$

By substituting the voltage and flux linkage equations [325-329] into Eq. 4.93, it is obtained:

$$P_{in} = \frac{3}{2}\left(\left(R_s i_{ds}^{r} + \frac{d\lambda_{ds}^{r}}{dt} - w_r\lambda_{qs}^{r}\right)i_{ds}^{r} - \left(R_s i_{qs}^{r} + \frac{d\lambda_{qs}^{r}}{dt} + w_r\lambda_{ds}^{r}\right)i_{qs}^{r}\right) =$$
$$\frac{3}{2}\left(R_s\left(i_{ds}^{r2} + i_{qs}^{r2}\right) + i_{ds}^{r}\frac{d\lambda_{ds}^{r}}{dt} + i_{qs}^{r}\frac{d\lambda_{qs}^{r}}{dt} + w_r\emptyset_f i_{qs}^{r} + w_r\left(L_{ds} - L_{qs}\right)i_{ds}^{r}i_{qs}^{r}\right) \quad (4.94)$$

Stator Copper Loss | Magnetic Energy Variation | Mechanical Outpu Power P_{out}

$$T_e = \frac{(2p)}{2}\frac{3}{2}\left(\emptyset_f i_{qs}^r + \left(L_{ds} - L_{qs}\right) i_{ds}^r i_{qs}^r\right) \quad (4.95)$$

Magnet Torque — Reluctance Torque

Eq. 4.95 indicates that the developed torque of a PM Starter/Generator is composed of two components. The first term represents the magnet torque generated by the PMs, while the second term represents the reluctance torque resulting from saliency. In an SPMSM with a cylindrical rotor and equal d-q axis inductances (Lds=Lqs), there is no reluctance torque.

In the field of PMSM control, there are several vector control modes for PM S/Gs that offer distinct strategies for achieving desired performance characteristics [321, 330-332]. These include the I_d=0 vector control mode, which focuses on maintaining the zero direct current component in the machine to minimize losses and improve efficiency. Another mode is maximum torque per ampere (MTPA) control, which aims to maximize the torque output for a given current input, optimizing the machine's torque production capabilities. Additionally, there is the flux weakening control mode, which allows the machine to operate beyond its rated speed by reducing the magnetic flux, enabling higher rotational speeds. These vector control modes, among others, provide flexible control strategies to meet specific operational requirements and enhance the overall performance of electric machines.

4.5. Performance Comparison of BLDC and PMSM

BLDC and PMSM motors, despite their resemblances in stator and rotor configurations, demonstrate distinct performance variations due to factors including back-EMF characteristics, intended applications, and driving techniques. These dissimilarities give rise to variations in efficiency, torque output, speed range, and control precision, thereby differentiating the performance of BLDCs and PMSMs. A comparative analysis of these performance aspects is presented in Table 4.2 [333-336].

Table 4.2. Performance comparison of BLDC and PMSM

Features	BLDC	PMSM
Machine Categorization	Synchronous	Synchronous
Supply-Fed	DC current	AC current
Back-EMF	Trapezoidal (Generally)	Sinusoidal (Generally)
Drive Method	Commutation	Control Algorithms
Phase Conduction	Two phases	Three phases
Torque Ripple	High	Low
Harmonic Order	Low order harmonics	Fewer harmonics
Core Loss	High due to the harmonics	Low
Switching Loss	Low	High
Complexity in Control	Simple	Complex
Ease of Control	Easy	Complex
Noise Level	High	Low
High Speed Performance	Good	Poor
Torque per Peak Current	High	Low
Torque per RMS Current	Low	High
Cost	Low	High
Efficiency	Low	High
Maintanence Cost	Low	High
Overload Capacity	<120%	<150%
Starting Torque	Medium	High

The ideal torque-speed curves of the BLDC, SPMSM and IPMSM exhibit distinctive characteristics, as illustrated in Figure 4.24 [337, 338].

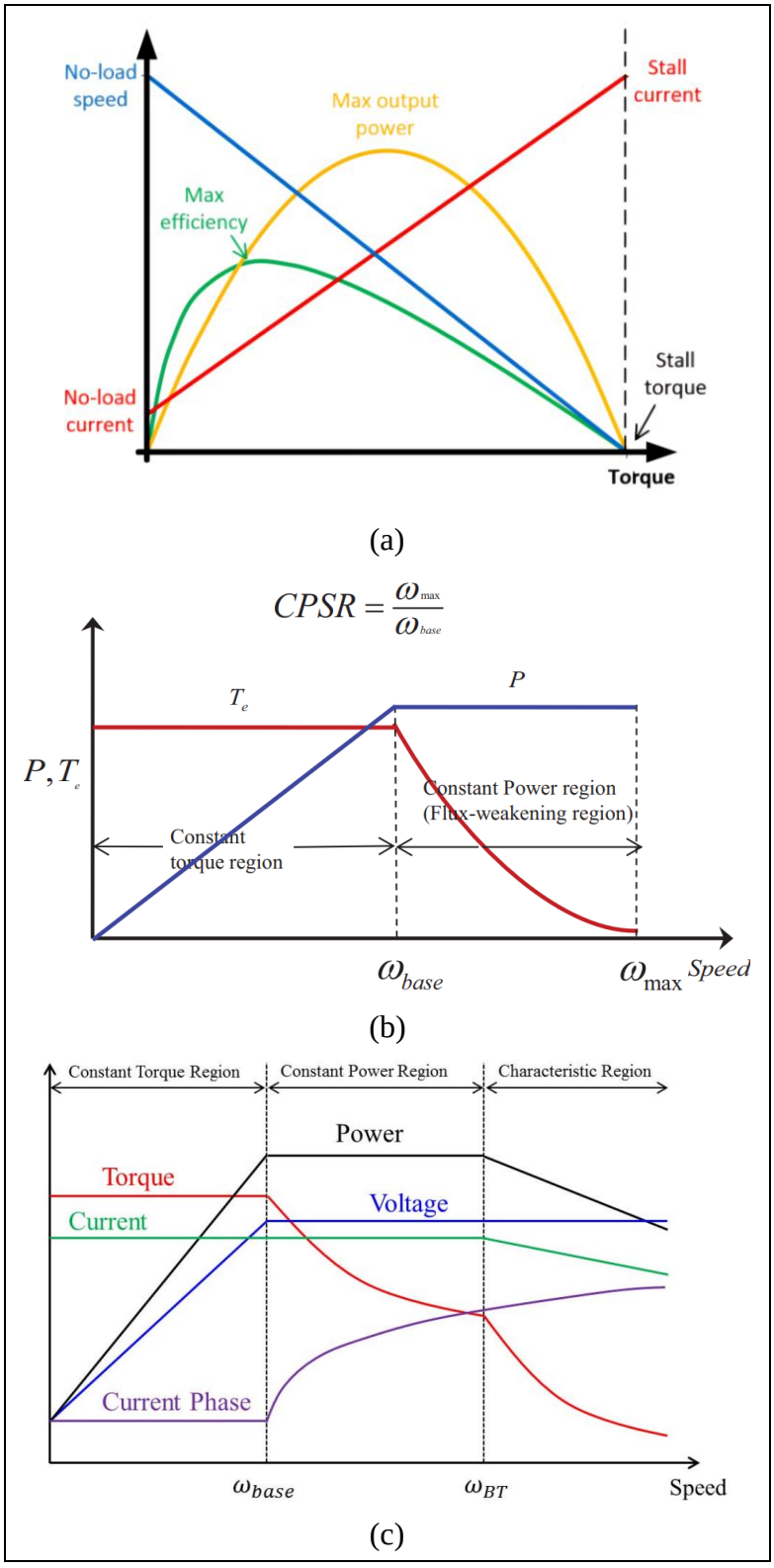


Figure 4.24. General ideal torque speed characteristics (a) BLDC [339] (b) SPMSM [340] (c) IPMSM [337]

The torque ripple characteristics of the BLDC and PMSM are illustrated in Figure 4.25. These plots provide insights into the behavior of the machines under different operating conditions and can help evaluate the performance in terms of torque fluctuations.

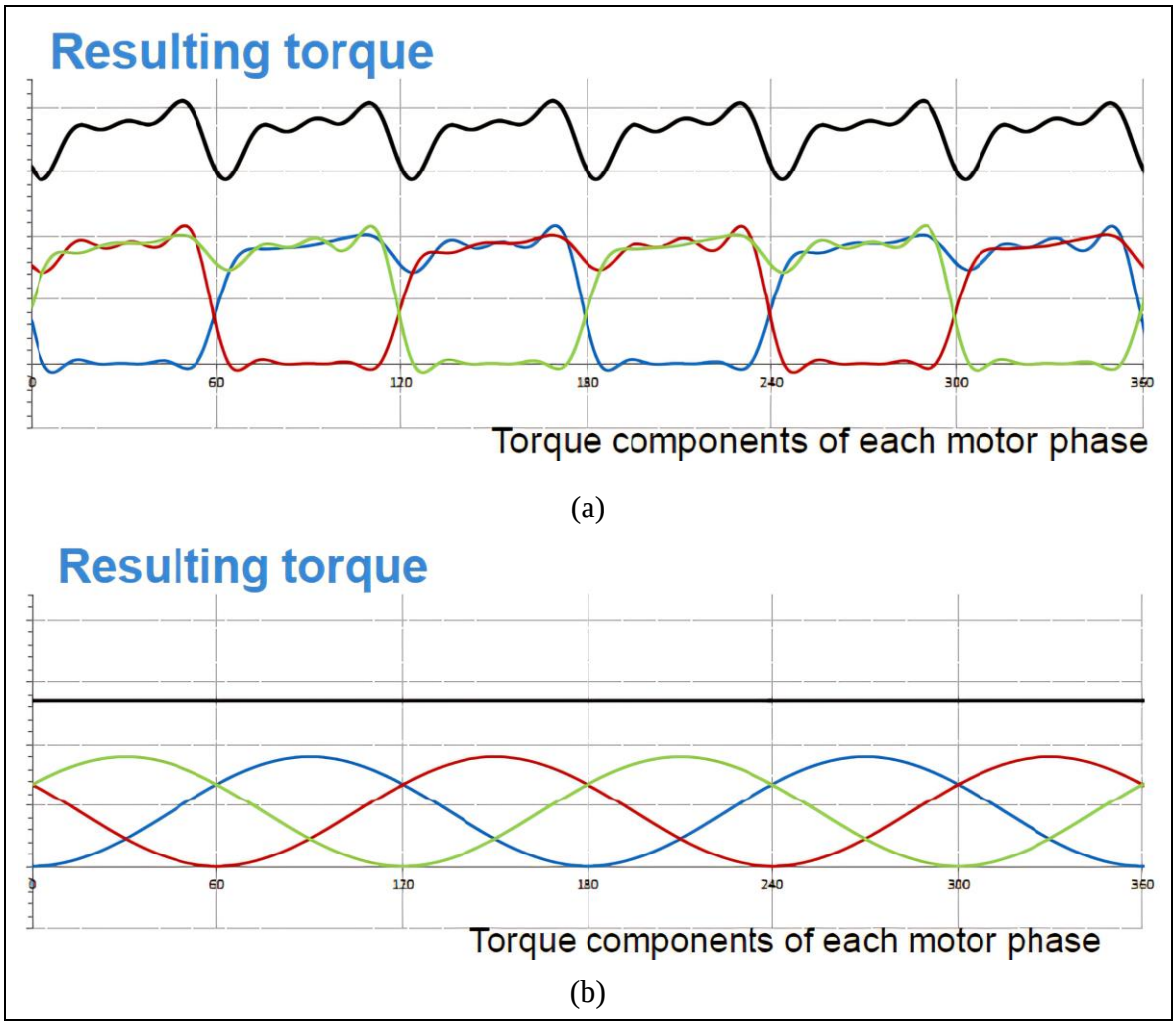


Figure 4.25. Ideal model torque ripple comparison (a) BLDC (b) PMSM [341]

On the other hand, radial flux permanent magnet machines (PMMs) are favored over axial flux structures for high-speed direct-drive starter/generator applications due to their smaller diameter and longer rotor, which generate smaller rotor stresses and enable higher speeds. They can incorporate effective protection methods to prevent damage to delicate permanent magnets at high speeds, which is not possible with axial flux structures. On the other hand, axial flux structures with larger rotor diameters and shorter lengths lead to increased rotor surface speeds and higher stresses, resulting in higher maintenance costs and reduced machine continuity. Hence, it is crucial to perform a detailed investigation of radial flux PMMs to make informed design decisions in high-speed direct-drive S/G applications.

4.6. Control Strategies for Permanent Magnet Starter/Generators

In the design of permanent magnet Starter/Generators, it is critical to have a deep understanding of the driver strategies and switching methods to ensure optimal performance and efficiency. This is because the driver strategy has a significant impact on the control of the S/G, which directly affects its output power, efficiency, and reliability. In addition, it affects the machine performance, as well as the overall system cost. The appropriate driver strategy should be chosen early in the design to meet the specific application requirements, which can include high starting torque, high efficiency, low noise, and low weight.

The driver strategy can be achieved through various control techniques, such as commutation, scalar control, vector control, direct torque control, and field-oriented control, as detailed in Figure 4.26 [247, 342]. Each control technique has advantages and disadvantages, which must be carefully evaluated to select the most appropriate strategy.

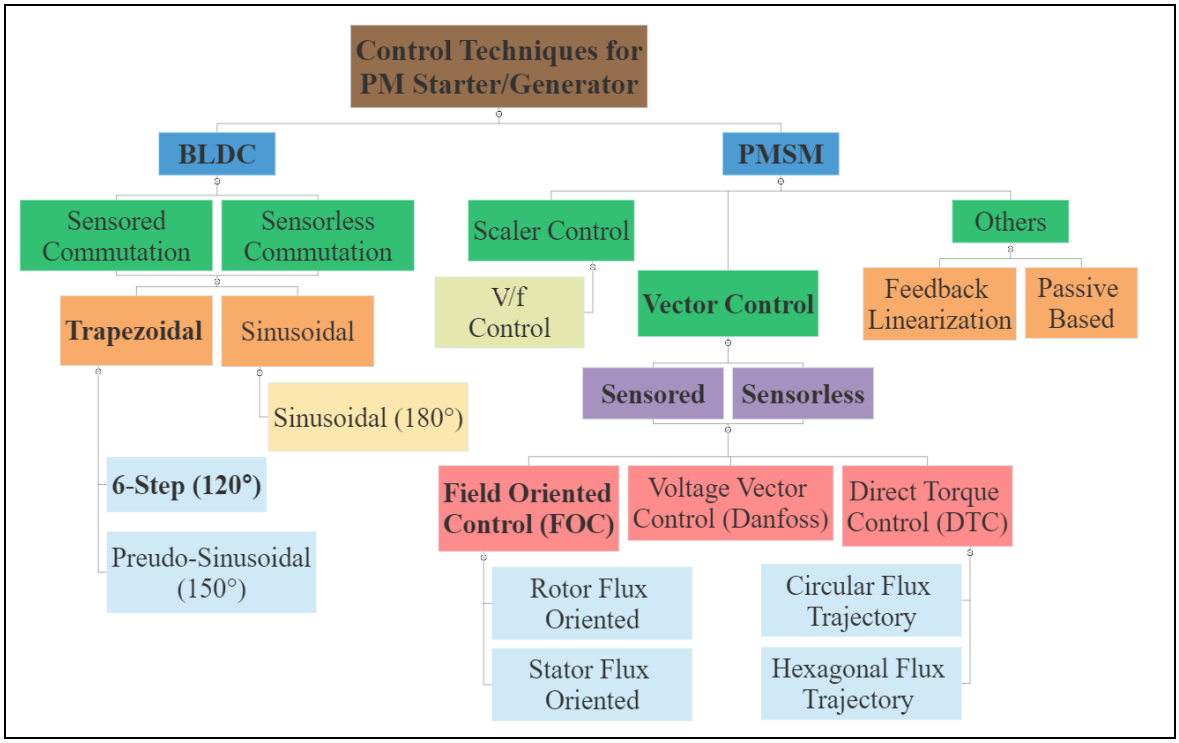


Figure 4.26. Control strategies for Starter/Generators

The scalar control technique is a simplified control approach that relies on a model that is only applicable to steady states. This method involves controlling the magnitude and frequency of voltage, current, and flux linkage space vectors.

However, due to its limitations, the scalar control technique is not suitable for transient performance and is not recommended for PMSMs that lack damper winding [247]. To achieve stable operation, a stabilization loop must be formed using either rotor speed perturbation, input power, DC-link current perturbation, or flux and power angle stabilizing loop. Therefore, scalar control is only suitable for applications that do not require high dynamic performance.

On the other hand, the vector control technique is a more advanced approach that allows for precise control of the position, magnitude, and frequency of voltage, current, and flux space vectors [343]. This technique can be divided into three categories: Field Oriented Control (FOC), Direct Torque Control (DTC), and Voltage Vector Control (VVC+).

The FOC technique uses frame transformation of the machine equation in a PM flux rotating frame, allowing decoupled control of stator current components, indirectly controlling motor flux and torque. It involves d-q axis current controllers for decoupled drive control. DTC enables direct control of motor flux and torque without the need for inner current control loops. Although DTC can achieve good dynamic performance, it suffers from several disadvantages, such as a requirement for fast sampling time, the need for two hysteresis controllers, variable switching frequency behavior, and higher ripples in torque and flux.

VVC+ control, developed by Danfoss Drive, is a promising approach that results in good steady-state and transient performance of PMSM drives. VVC+ controls the voltage impressed on the motor with respect to both amplitude and angle using a vector concept based on a steady-state motor model. It offers advantages such as the absence of feedback position or speed sensors, a simple control algorithm, less computation, and improved transient response compared to the scalar control method.

The stabilization of the PMSM is achieved by measuring the change in input power, and the reference speed is proportionally varied according to this power variation.

The current controller compensates for machine parameter mismatch, temperature drift of stator resistance, and other unmodelled factors. If all machine parameters are correct, the output of the controller will not depend on the load, and the d-axis current is kept at the desired value at steady state, depending on the control strategy, Maximum Torque Per Ampere (MTPA) or Constant Stator Flux Control (CSFC).

FOC and six-step commutation are two important control techniques used in the control of aerospace three-phase Starter/Generators. FOC is a widely used technique that enables precise control of the torque and speed. It allows independent control of the magnetic field and torque components, which improves the overall efficiency and performance. Six-step commutation, on the other hand, is a simpler control technique that is commonly used in applications where high precision is not needed. Stator currents are switched in a sequence of six steps to generate a rotating magnetic field that drives the rotor. Commutation is determined using sensors or sensorless methods based on the rotor position. It is relatively simple and cost-effective, but it may not provide the same level of control precision as FOC.

Both techniques have their advantages and limitations, and the choice of use depends on the application. FOC is often used in high-performance applications such as aerospace and electric vehicle propulsion systems, while six-step commutation is more commonly used in lower performance applications such as fans, pumps, and industrial equipment.

Types of rotor position sensors for permanent magnet brushless machines

The determination of rotor positions in brushless PMM is accomplished through the utilization of position sensors, which include Hall sensors, incremental or absolute encoders, and resolvers, as illustrated in Figure 4.27. These sensors are designed to detect the position of the rotor field, thereby enabling the identification of the rotor shaft's position [321].

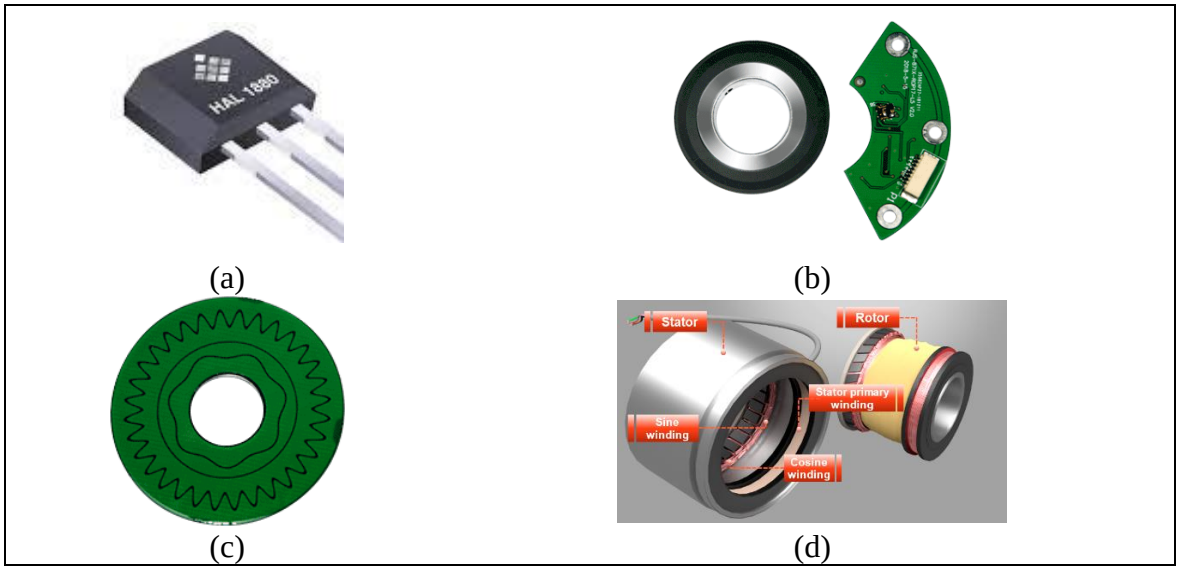


Figure 4.27. Rotor position sensors (a) Hall sensor (b) Incremental encoder (c) Absolute encoder (d) Resolver

4.6.1. 6-Step commutation in starter and motor mode

The marvel of a BLDC motor lies in the synchronized interaction of rotor permanent magnet field with a magnetic field generated by a DC voltage across its stator coils. For seamless rotation, the stator magnetic field needs to be rotated sequentially, with each phase current switching in sync with the machine back EMF as a function of rotor position. At each position, a constant current multiplies the back EMF's constant part, yielding the machine output torque. However for this synchronization and commutation sequence to be identified, the rotor position must be known at fixed angular intervals, as shown in Figure 4.28 [344].

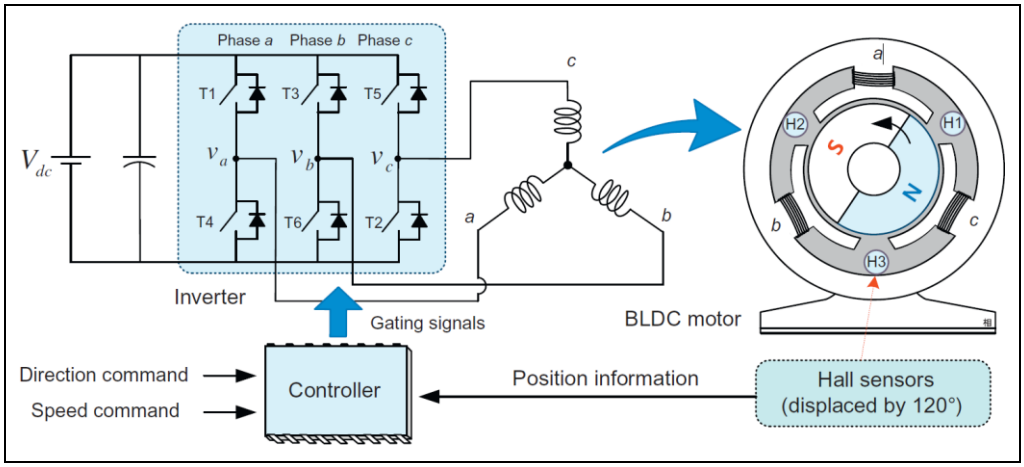


Figure 4.28. Driver system of BLDC motor [344]

The rotor position can be determined through the utilization of position sensors, including encoders, resolvers, and Hall sensors. Alternatively, a sensorless method can detect the position of the rotor field and therefore the position of the rotor shaft.

Hall effect sensored control

The implementation of Hall sensors in sensing the rotor position of BLDC motors has gained significant popularity over the use of encoders and resolvers. This can be attributed to several factors, including the simplicity and cost-effectiveness of Hall sensors compared to encoders and resolvers. Additionally, Hall sensors do not require physical contact with the rotor shaft and do not suffer from mechanical wear, making them more reliable in the long run. The use of Hall sensors offers a practical and efficient solution for BLDC rotor position sensing. The position of Hall sensors determines the output type: either 60° or 120° phase shift. Combining these signals from three sensors can determine the exact commutation sequence.

Hall sensors are classified into analog and digital types, as shown in Figure 4.29. Analog sensors produce a continuous voltage output proportional to the magnetic field strength with higher resolution and sensitivity. Digital sensors are simpler to use, as they output a digital signal, but lack the precision of analog sensors. Analog sensors require additional signal circuitry to convert output to a digital format to be processed by a microcontroller [345].

On the other hand, digital Hall sensors output a digital signal that is either high or low depending on the presence of a magnetic field. They are cost-effective and easy to implement, making them commonly used in position sensing for brushless DC motors [346].

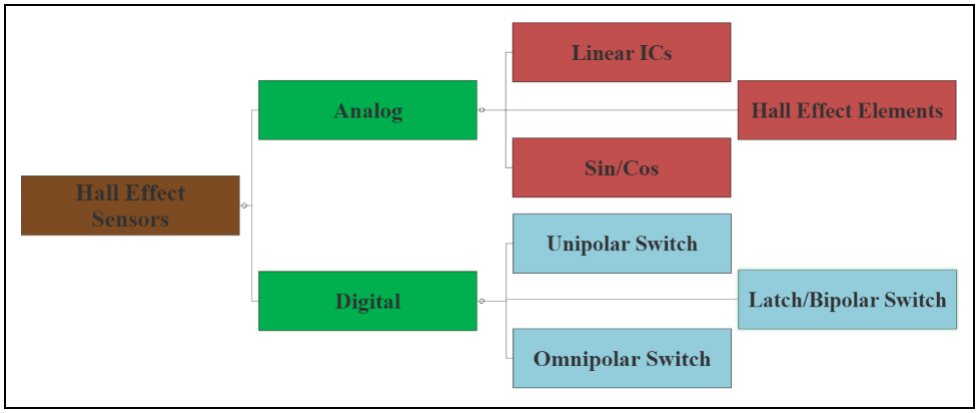


Figure 4.29. Types of Hall sensors

The unipolar switch is an active sensor that operates in only one magnetic pole spectrum, north or south, and is primarily used for position sensing. As depicted in Figure 4.30 (a), both B_{OP} and B_{RP} will be activated with the same magnetic pole. However, a minimum hysteresis is required to prevent unwanted toggling caused by variations in the magnet.

The Latch/Bipolar switch is an active sensor that is activated with one magnetic field and deactivated with the opposite field, as shown in Figure 4.30 (b). The operating point and release point have the same absolute values but opposite signs, with B_{OP} = - B_{RP}. Both thresholds are symmetrical and centered around 0 mT. Due to its operational characteristics, the latch-type Hall effect sensor is widely used for rotor position sensing in BLDC motors.

Omnipolar sensors, as demonstrated in Figure 4.30 (c), are active in both the North and South magnetic fields. They are commonly used to detect changes in both spectra. B_{OP_S} and B_{RP_S} are parameters that identify the South Pole operating and release points, while B_{OP_N} and B_{RP_N} refer to the North Pole parameters.

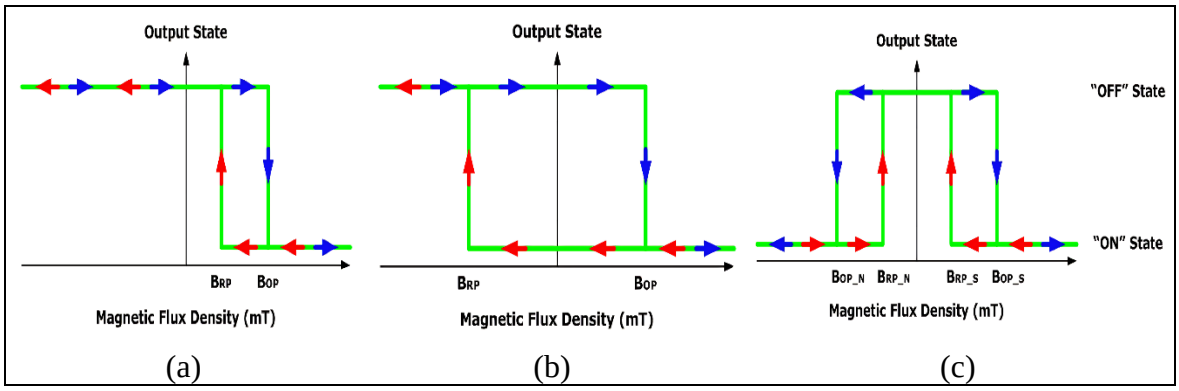


Figure 4.30. Hall sensor types (a) Unipolar (b) Latch/Bipolar (c) Omnipolar

The commutation sequence of a three-phase BLDC motor driver circuit with 120°E for counterclockwise rotation is shown in Figure 4.31. °E represents the electrical degree. Three Hall sensors (a, b, c) are mounted on the stator at 120°E intervals, while the three phase windings are arranged in a star formation. With every 60°E rotation, one of the Hall sensors changes its state, taking six steps to complete a whole electrical cycle.

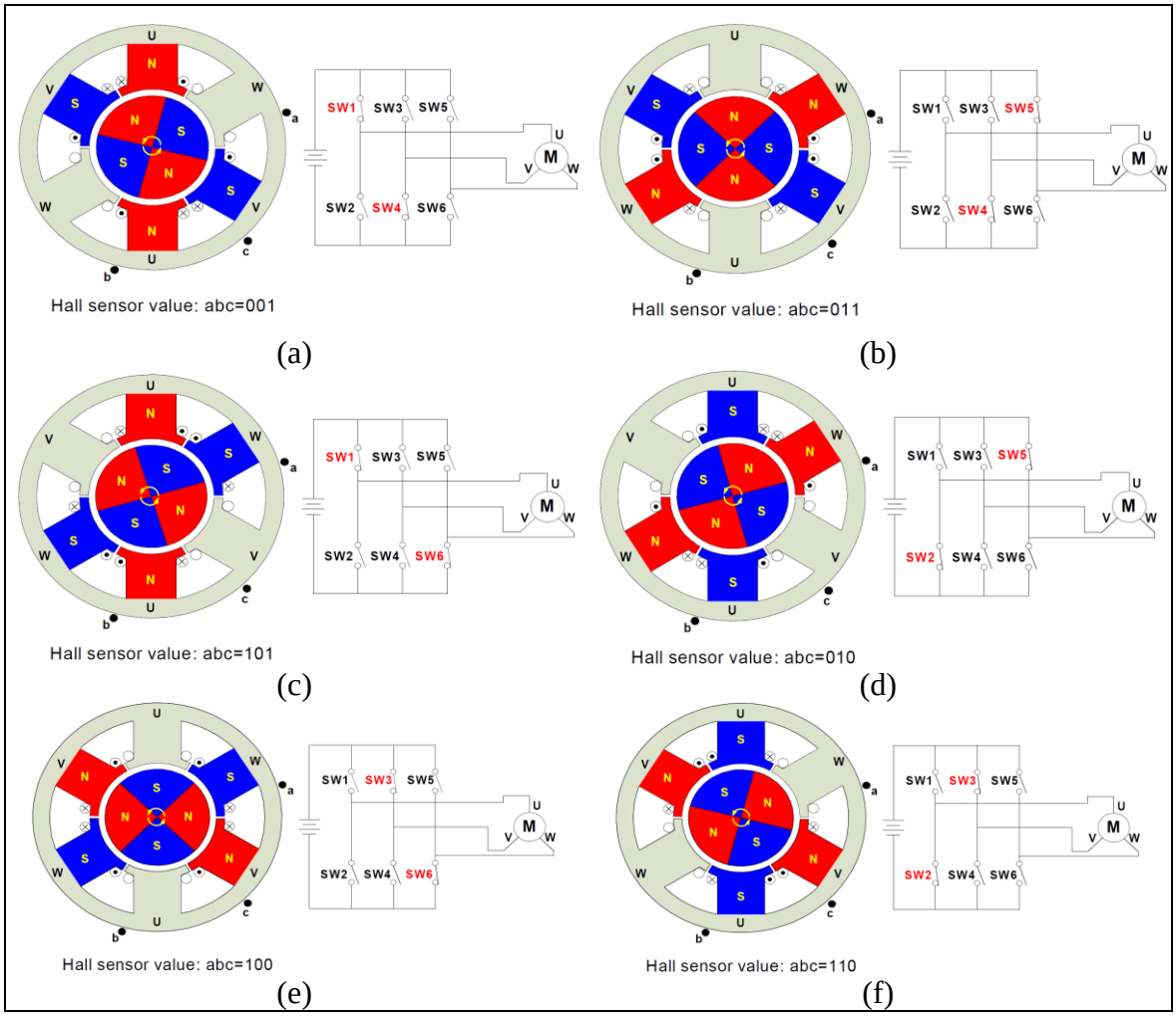


Figure 4.31. Commutation sequence logic of three-phase BLDC [346]

In synchronous mode, the phase current switching updates every 60°, with one motor terminal driven high, another driven low, and the third left floating for each step. Therefore, during each step, only two phases are conducted. The number of signal cycles needed to complete a mechanical rotation is determined by the number of rotor pole pairs. Every rotor pole pair requires one signal cycle in one mechanical rotation.

Sensorless control

In some applications where only variable speed control is required, and system dynamics are not too demanding, position sensors can be eliminated to reduce cost and motor size. Sensorless communication is particularly useful in dusty or oily environments where motors are hard to access and only require occasional cleaning.

Some control methods provide enough information to estimate rotor position with sufficient precision for synchronous phase current operation, thus enabling a PM brushless drive that requires only electrical measurements, called a sensorless drive.

There are several techniques to obtain the position information of the BLDC motor [347]:

- Back EMF detection,
- Stator third harmonic voltage detection,
- Conducting interval of freewheeling diodes connected in antiparallel with solid-state switch detection,
- Measurement of inductance variation, terminal voltages and currents.

One of the most commonly used sensorless control strategies is based on back electromotive forces or back-EMFs, which eliminates the need for position sensors such as Hall sensors to commutate the signal [348]. The back-EMF of an unused phase is an efficient and cost-effective method to obtain the commutation sequence in star windings.

However, since back-EMF is zero at standstill and proportional to speed, the measured terminal voltage, which has a large signal-to-noise ratio, cannot detect zero crossing at low speeds. As a result, the low-speed performance of back-EMF-based sensorless methods is limited, and an open loop starting strategy or back-EMF amplifiers are necessary [349].

There are two primary methods for sensing back-EMF in BLDC motors: direct back-EMF detection and indirect back-EMF detection [350]. Direct back-EMF detection techniques involve sensing the back-EMF of the floating phase and detecting its zero crossing by comparing it with the neutral point voltage. However, such methods are prone to high common mode voltage and high frequency noise due to the pulse width modulation (PWM) drive, thereby necessitating the use of low pass filters and ADCs, as shown in Figure 4.32. Direct back-EMF detection techniques can be classified as back-EMF zero crossing detection (ZCD) or terminal voltage sensing, and PWM strategies.

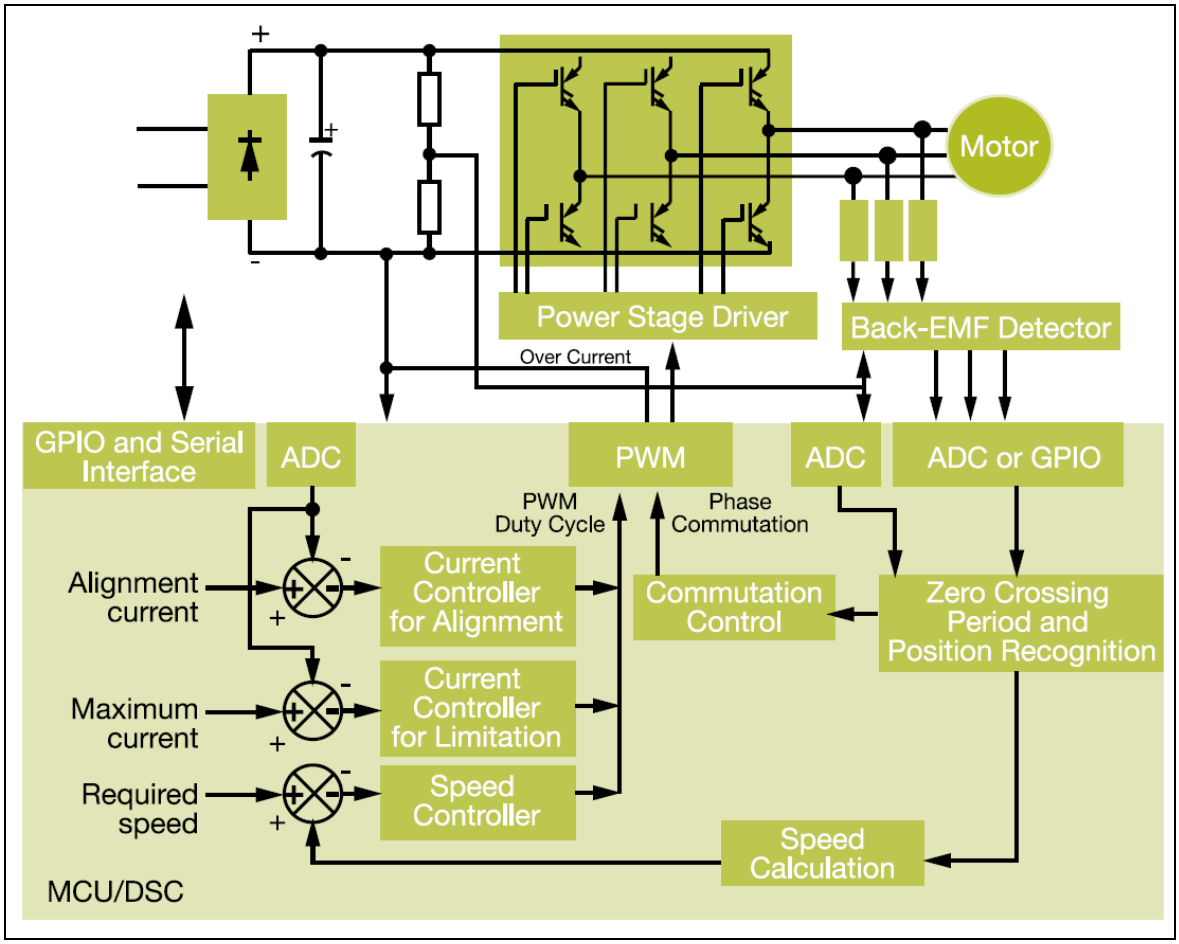


Figure 4.32. Block scheme of the sensorless back-EMF based BLDC driver

Indirect back-EMF detection methods are employed to reduce switching noise. This is because filtering introduces commutation delay at high speeds, while attenuation reduces signal sensitivity at low speeds. Examples of indirect back-EMF detection methods include back-EMF integration, third harmonic voltage integration, and free-wheeling diode conduction or terminal current sensing.

4.6.2. Field oriented control (FOC) of starter/generator

FOC, shown in Figure 4.33, is a control technique employed to regulate the direct and quadrature axis current, i_d and i_q, with the objective of achieving the desired torque. Eq. 4.95 represents the torque as a function of the current components. By independently controlling i_d and i_q, it becomes possible to optimize the Maximum Torque Per Ampere (MPTA) ratio, thereby minimizing the current required for a specific torque and maximizing the efficiency.

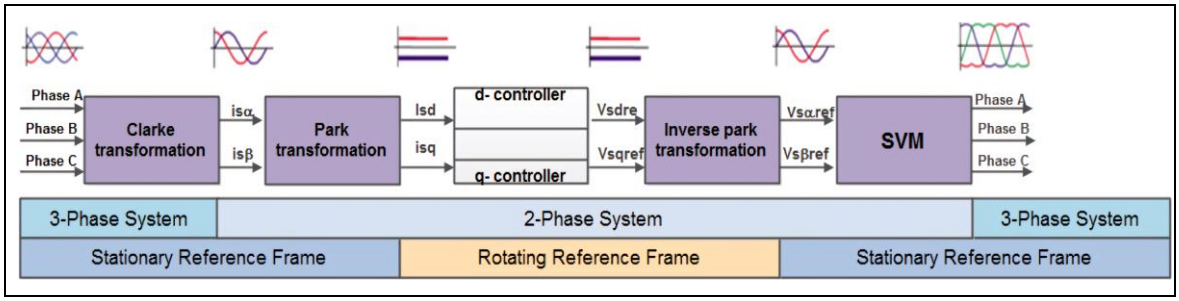


Figure 4.33. General principle of Field Oriented Control (FOC)

In the case of a nonsalient machine, where L_d=L_q, implementing control is relatively straightforward. According to Eq. 4.95, a nonsalient machine cannot generate any reluctance torque. As a result, i_d does not influence torque production and needs to remain zero at all times to achieve MPTA. Consequently, the torque curves in the dq reference frame are linear, and the trajectory for MPTA lies along the quadrature axis.

Conversely, for a salient machine with Ld≠Lq, implementing control becomes more challenging since the S/G generates both electromechanical and reluctance torque. Consequently, the torque as a function of current in the dq reference frame is no longer linear. To achieve MPTA, it is necessary to calculate the minimum distance from the origin to the curve representing the desired torque. Thus, accurate determination of the S/G rotor position becomes a critical parameter for FOC. Indirect FOC (IFO) is commonly employed, which utilizes a mechanical sensor, such as an incremental or absolute resolver (sin/cos), coupled to the motor's shaft for position sensing. Alternatively, Direct FOC (DFO) estimates the position from the flux or back-EMF vector [351].

Another significant parameter is the variation in inductance values, L_d and L_q, which constantly change during operating conditions due to saturation effects.

Sensored field oriented control

FOC can be implemented using either a sensor or a sensorless approach. However, for applications that require high precision control, sensored control is generally preferred. The key differentiation between sensor-based and sensorless FOC resides in the manner of rotor position and speed detection. Sensored FOC employs external sensors, such as encoders or resolvers, to directly measure the rotor position and speed, as shown in Figure 4.34.

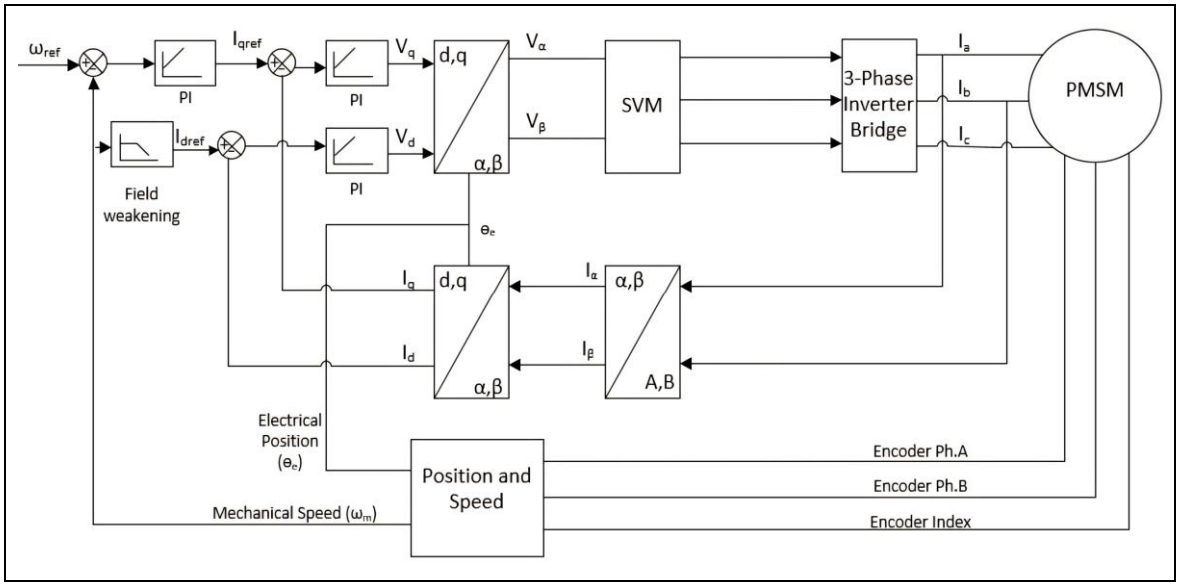


Figure 4.34. Block diagram of sensored FOC

The control process can be summarized as follows [352]:

Measurement of Stator Currents: The three-phase stator currents are measured, and for an S/G with balanced windings, only two currents need to be measured.

Conversion to a Stationary Two-Axis System: The measured three-phase currents (i_a, i_b, i_c) are converted to a stationary two-axis system. This conversion, called the Clarke transform, yields time-varying quadrature current values (i_α, i_β), as observed from the stator perspective.

Alignment with Rotor Flux: The stationary two-axis coordinate system is rotated to align with the rotor flux using a transformation angle determined during the previous control loop iteration. This transformation, called the Park transform, yields the quadrature current values (i_d, i_q) in the rotating coordinate system. Under steady-state conditions, i_d and i_q remain constant. I_{sq} is associated with torque, while I_{sd} is linked to flux. Setting I_{sdref} to zero establishes a direct proportionality between torque and current.

PI Controllers: The error signals are fed into Proportional-Integral (PI) controllers. The outputs of the controllers generate the voltage vectors (v_d, v_q) to be applied to the S/G.

Angle Measurement: A new angle is measured from the encoder input. This angle guides the FOC algorithm in determining the placement of the next voltage vector.

Transformation Back to Stationary Frame: The outputs (v_d, v_q) from the PI controllers are transformed back to the stationary reference frame using the new angle. This transformation, called the Inverse Park transform, calculates the next quadrature voltage values (v_α, v_β).

PWM Duty Cycle Calculation: The (v_α, v_β) values are used to calculate the new Pulse-Width Modulation (PWM) duty cycle values, which generate the desired voltage vector.

Switching: To determine the switching sequence of the upper three power transistors in an inverter, specifically a voltage source inverter (VSI), generally Space Vector Modulation (SVPWM) is employed. SVPWM ensures that the inverter generates the appropriate output voltage waveform to achieve the desired control objectives in the FOC system [353].

Mechanical Speed Calculation: The mechanical speed (ω_m) and I_{qref} are calculated after each discrete PWM cycle.

The FOC in software is generally implemented within the ADC interrupt service routine, running at the same rate as the PWM frequency, after data conversion is completed.

Sensorless field oriented control

Sensorless FOC is commonly used in applications where the inclusion of external sensors for rotor position and speed detection is impractical. The control processes are fundamentally similar in nature. Sensorless FOC utilizes mathematical models and internal motor measurements to estimate the rotor position.

The sensorless techniques can be classified into two primary categories based on their approach to deriving the rotor position, as depicted in Figure 4.35 [324]. The first group utilizes the back-EMF, which carries information about the rotor speed. In this approach, the rotor position is obtained through the utilization of estimators or observers that employ mathematical equations specific to the S/G. The second group derives the rotor position by leveraging the inherent characteristics of the S/G itself. This technique involves injecting a specialized signal into the S/G to extract the position-dependent characteristics. Typically, a high-frequency voltage is employed as the special signal.

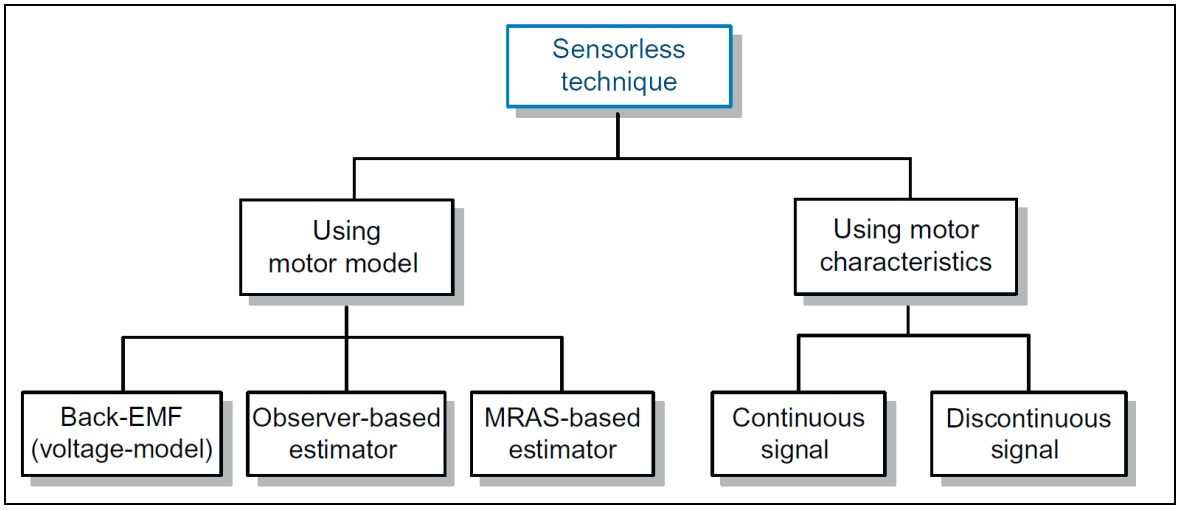


Figure 4.35. Types of sensorless FOC [324]

It is customary to divide the position estimation of S/Gs into two primary groups: back EMF-based methods and saliency-based methods, as illustrated in Figure 4.36. This categorization is justified partly due to the distinct factors that influence each group. Back EMF relies on the rotor motion, while saliency is a characteristic of the S/G structure [322].

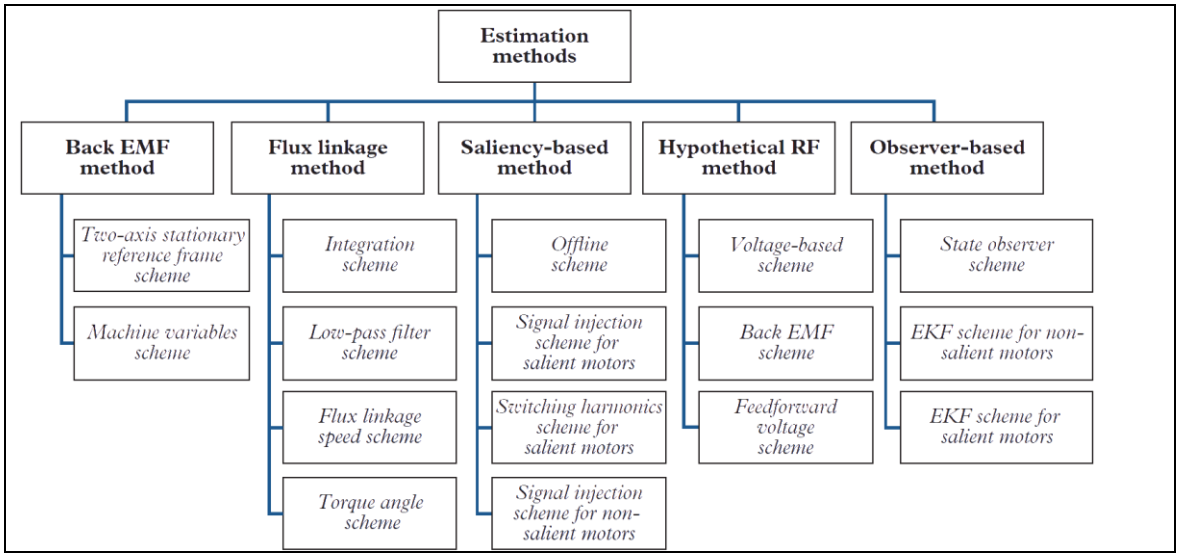


Figure 4.36. Position and speed estimation methods for sensorless FOC [322]

However, as research in this area has expanded, confining the methods solely to these categories has become challenging. One reason is the implementation of back-EMF and saliency methods using different techniques, which appear to be more crucial than the categories themselves.

For instance, observer-based estimation is capable of utilizing both back-EMF and saliency methods and has emerged as a significant category for position and speed estimation.

Another reason is that they do not fit into either of the traditional categories. Hypothetical position estimation serves as an example. In fact, the wide diversity of position and speed estimation methods, along with their overlapping characteristics, makes categorization a difficult task. Nevertheless, despite these challenges, attempting to categorize the methods provides a broader perspective of the field, aiding in the understanding of their fundamental principles before delving into specific details.

On the other hand, the necessity of conducting comparisons between control algorithms arises from the imperative to methodically evaluate and discern the best and most efficient approach for attaining desired control objectives [354]. Through comprehensive assessments and comparisons, as shown in Figure 4.37, valuable insights are garnered pertaining to the individual merits and limitations of different algorithms, encompassing aspects such as their inherent strengths, performance attributes, computational demands, resilience to uncertainties, and applicability to specific domains.

Control				Advantages	Disadvantages
Sinusoidal	Scalar			Simple control scheme	Control is not optimal, not suitable for tasks where the variable load, loss of control is possible
	Vector	Field oriented control	With position sensor	Smooth and precise setting of the rotor position and motor rotation speed, large control range	Requires rotor position sensor and powerful microcontroller inside the control system
			Without position sensor	No rotor position sensor required. Smooth and precise setting of the rotor position and motor rotation speed, large control range, but less than with position sensor	Sensorless field oriented control over **full speed range** is possible only for PMSM with salient pole rotor, a powerful control system is required
		Direct torque control		Simple control circuit, good dynamic performance, wide control range, no rotor position sensor required	High torque and current ripple
Trapezoidal	Open loop			Simple control scheme	Control is not optimal, not suitable for tasks where the variable load, loss of control is possible
	Closed loop	With position sensor (Hall sensors)		Simple control scheme	Hall sensors required. There are torque ripples. It is intended for control of PMSM with trapezoidal back EMF, when controlling PMSM with sinusoidal back EMF, the average torque is lower by 5%.
		Without sensor		More powerful control system required	Not suitable for low speed operation. There are torque ripples. It is intended for control of PMSM with trapezoidal back EMF, when controlling PMSM with sinusoidal back EMF, the average torque is lower by 5%.

Figure 4.37. Comparison of vector control algorithms [354]

4.6.3. Pulse width modulation strategies

The emergence of different circuit configurations has gained significant popularity and caught the attention of researchers. Three-phase voltage-fed Pulse Width Modulation (PWM) inverters have recently gained traction in aerospace applications. The rising popularity of these inverters can be attributed to their ability to generate output voltage waveforms with low switching frequencies, high efficiency and low distortion level. The two-level inverter is currently the most commonly used topology due to its simplicity and cost-effectiveness. Higher-level structures are primarily utilized in high-voltage applications and will not be discussed extensively in this thesis.

PWM techniques have revolutionized the field of power electronics by providing versatile control strategies for voltage source inverters. In the realm of S/G voltage source inverters, a range of PWM techniques has emerged, each offering unique characteristics and advantages.

These techniques are designed to meet specific requirements, allowing engineers to optimize inverter performance specific to the application at hand. Figure 4.38 explores the classification of various PWM techniques [355].

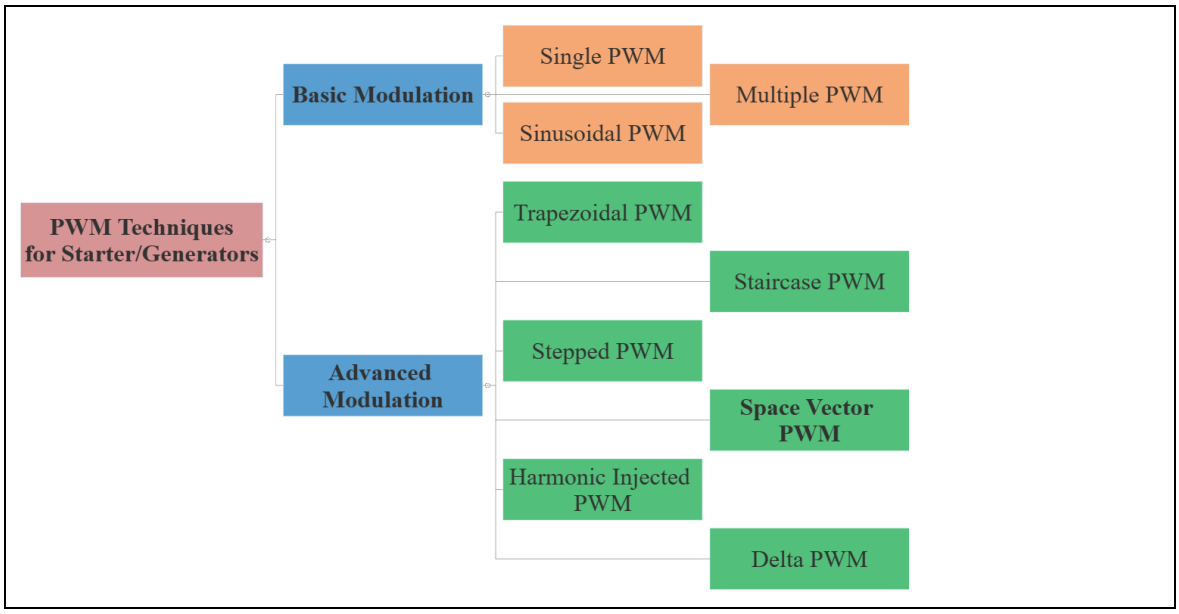


Figure 4.38. Classification of PWM techniques

In particular, the Space Vector PWM (SVPWM) has garnered substantial interest in recent times. It offers a higher magnitude of fundamental output voltage compared to sinusoidal PWM. Table 4.2 summarizes the performance comparison of PWM techniques [356, 357].

Table 4.3. Performance comparison of PWM techniques

	THD	Complexity	Efficiency	Dynamic Response
PWM	High	Simple	Low	Slower
SPWM	Moderate	Simple	Moderate	Slower
SVPWM	Low	Complex	High	Moderate
Phase Disposition PWM	Moderate	Moderate	Low	Moderate
Simple Boost Control	Low	Complex	High	High
Phase Shifted PWM	Low	Complex	Very High	High

4.6.4. Space vector PWM

The SVPWM method is widely recognized as an effective approach for PMSM drive applications, as it generates PWM control signals in a three-phase inverter.

The switches employed in the inverter circuit, such as Mosfets or IGBTs, are illustrated in Figure 4.39. When the upper switches (S1, S3, S5) are ON, they are equal to 1, while the lower switches (S2, S4, S6) are equal to 0 when they are OFF. The output voltage can be determined by considering the ON and OFF states of the switches [358].

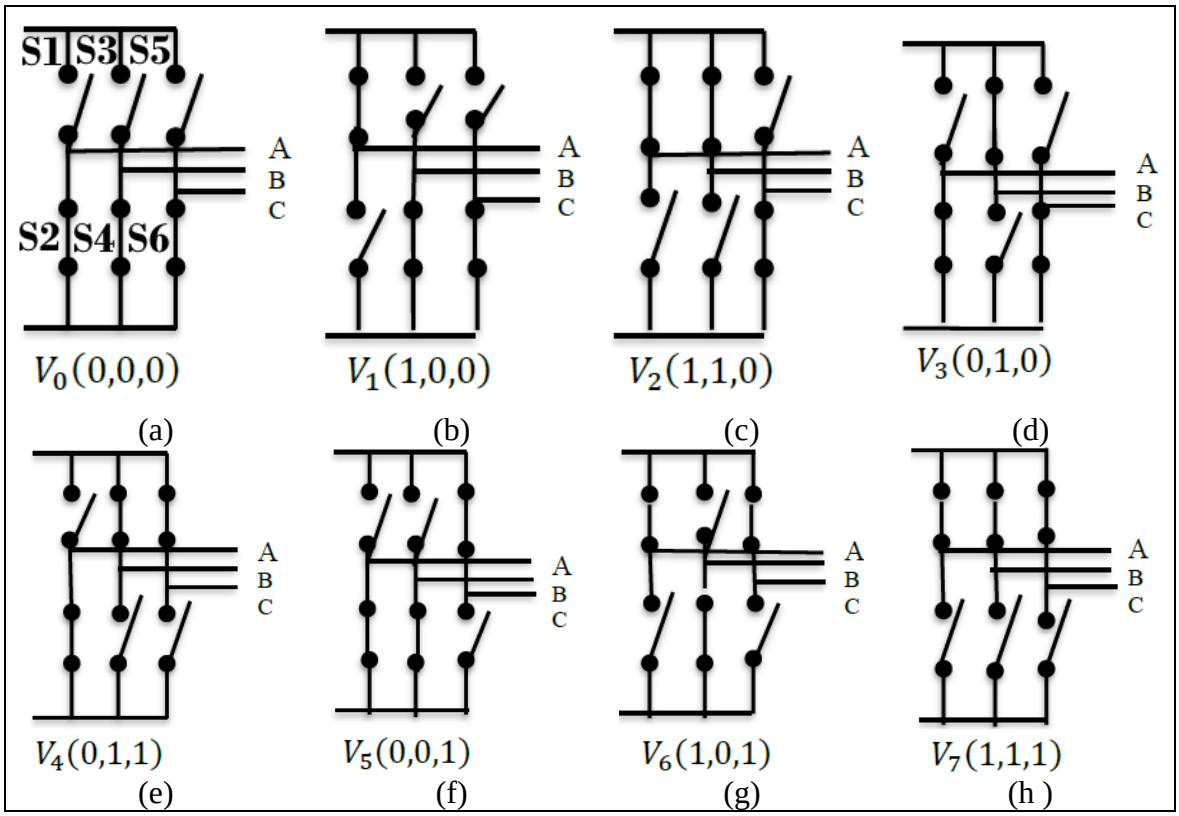


Figure 4.39. Switching states of SVPWM (a) $V_0(0,0,0)$ (b) $V_1(1,0,0)$ (c) $V_2(1,1,0)$ (d) $V_3(0,1,0)$ (e) $V_4(0,1,1)$ (f) $V_5(0,0,1)$ (g) $V_6(1,0,1)$ (h) $V_7(1,1,1)$ [358]

The three-phase inverter produces eight switching vectors as a result of the switching partners. Among these vectors, two are zero vectors (V0, V7), while the remaining six are nonzero vectors (V1, V2, V6). When the zero vectors are utilized in the inverter, the currents of the S/G will be zero. Table 4.4 provides an illustration of the eight switching vectors, output line-to-neutral voltages, and output line-to-line voltages.

Table 4.4. Switching vectors and sectors

Voltage Vectors	Switching Vectors			Line to Neutral Voltage			Line to Line Voltage		
	S_1	S_3	S_5	V_{an}	V_{bn}	V_{cn}	V_{ab}	V_{bc}	V_{ca}
V0	0	0	0	0	0	0	0	0	0
V1	1	0	0	$2/3V_{dc}$	$-1/3V_{dc}$	$-1/3V_{dc}$	V_{dc}	0	$-V_{dc}$
V2	1	1	0	$1/3V_{dc}$	$1/3V_{dc}$	$-2/3V_{dc}$	0	V_{dc}	$-V_{dc}$
V3	0	1	0	$-1/3V_{dc}$	$2/3V_{dc}$	$-1/3V_{dc}$	$-V_{dc}$	V_{dc}	0
V4	0	1	1	$-2/3V_{dc}$	$1/3V_{dc}$	$1/3V_{dc}$	$-V_{dc}$	0	V_{dc}
V5	0	0	1	$-1/3V_{dc}$	$-1/3V_{dc}$	$2/3V_{dc}$	0	$-V_{dc}$	V_{dc}
V6	1	0	1	$1/3V_{dc}$	$-2/3V_{dc}$	$1/3V_{dc}$	V_{dc}	$-V_{dc}$	0
V7	1	1	1	0	0	0	0	0	0

Table 4.4 displays the switching vectors and sectors. The sectors are separated by 60 degrees. For instance, the reference voltage vector is positioned in sector 1.

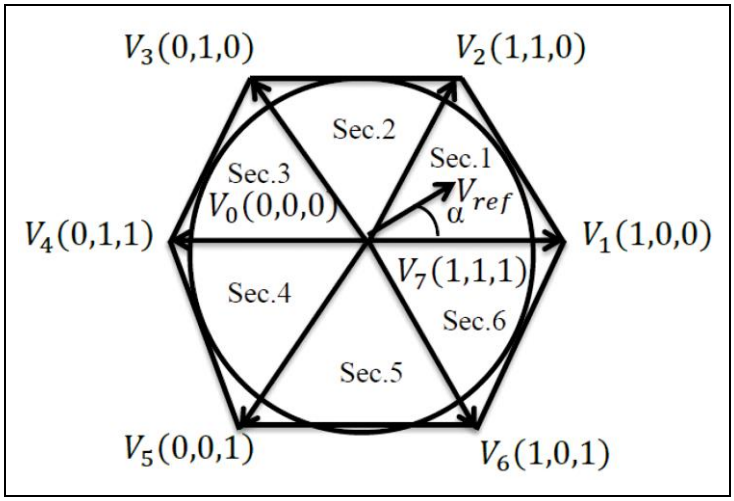


Figure 4.40. Exploration of the space vector diagram [358]

The significant advantage of SVPWM techniques lies in their ability to generate higher output voltage levels compared to other PWM techniques, as demonstrated in Table 4.5 [334]. This capability makes SVPWM highly advantageous for applications where a robust high voltage capability is essential.

This capability contributes to the improved performance, efficiency, and reliability of power electronic systems, making SVPWM a preferred choice in various aerospace and industrial energy conversion applications.

Table 4.5. Comparison of voltage produced by different PWM techniques

Voltage	$V_{L\text{-}Lrms} / V_s$	Relative to 6-Step Commutation
6-step 120°	$\frac{3}{\sqrt{2}\pi} = 0{,}675$	0,8660
6-step 180°	$\frac{\sqrt{6}}{\pi} = 0{,}780$	1
Hexagon tracking	$\frac{3\sqrt{6}}{\pi^2} = 0{,}7446$	0,9545
Circle tracking	$\frac{1}{\sqrt{2}} = 0{,}707$	0,9069
Maximum linear range of Sine/Triangle (SPWM)	$\frac{\sqrt{3}}{2\sqrt{2}} = 0{,}612$	0,7854
Sine/Triangle with 3rd harmonic injection (SVPWM)	$\frac{1}{\sqrt{2}} = 0{,}707$	0,9069

4.6.5. Control Approaches for Starter, Motor and Generator Modes of S/Gs

Figure 4.41 illustrates the typical operating performance curve of an aircraft piston engine and defines the operational regions of the S/G. In conventional UAV systems, an external drive mechanism is needed to initiate the startup of the piston engine, as they lack internal starters. Additionally, these systems rely on large battery packs to fulfil their electrical system requirements.

The integration of the MEA concept with UAV systems has revolutionized their operational efficiency by incorporating an S/G with the piston engine. This integration enables the S/G to effectively fulfil crucial functions within the system.

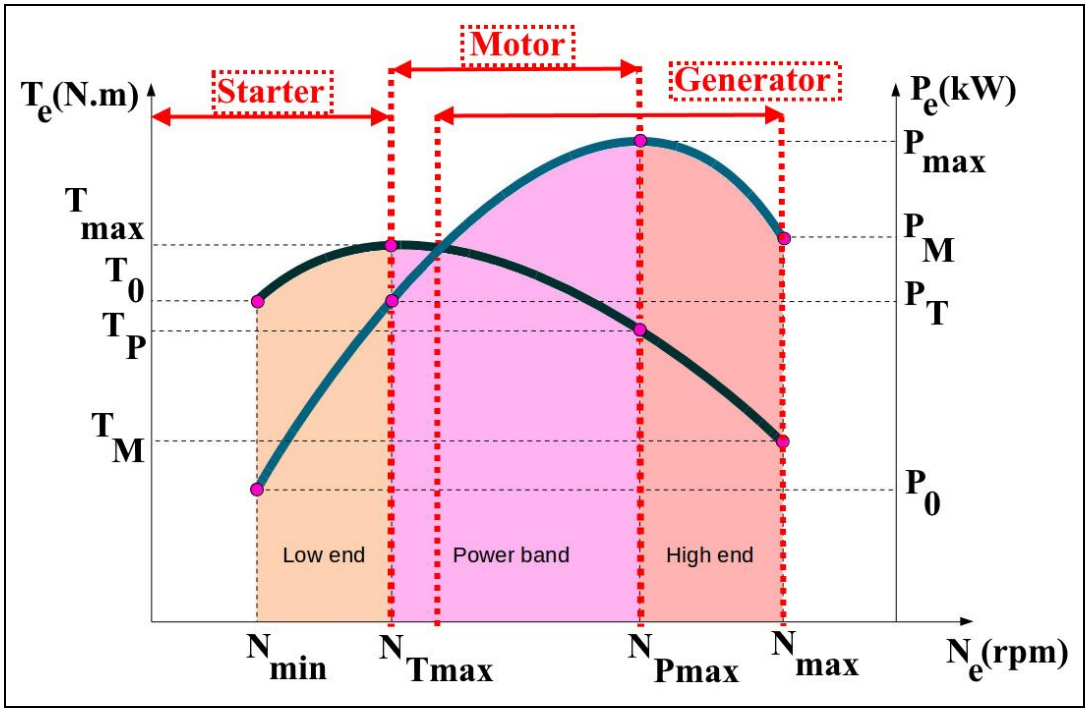


Figure 4.41. Operational zone of modes for aerospace Starter/Generator

Primarily, S/G serves as the initial drive mechanism to initiate the PE in the starting mode. Subsequently, during the motor mode, the S/G seamlessly transitions into generator mode, facilitating the charging of the battery group that powers the electronic system while the engine is running and the UAV is cruising. Figure 4.42 illustrates the simple configuration of the inverter/converter stage of the S/G for both motor and generator modes [31].

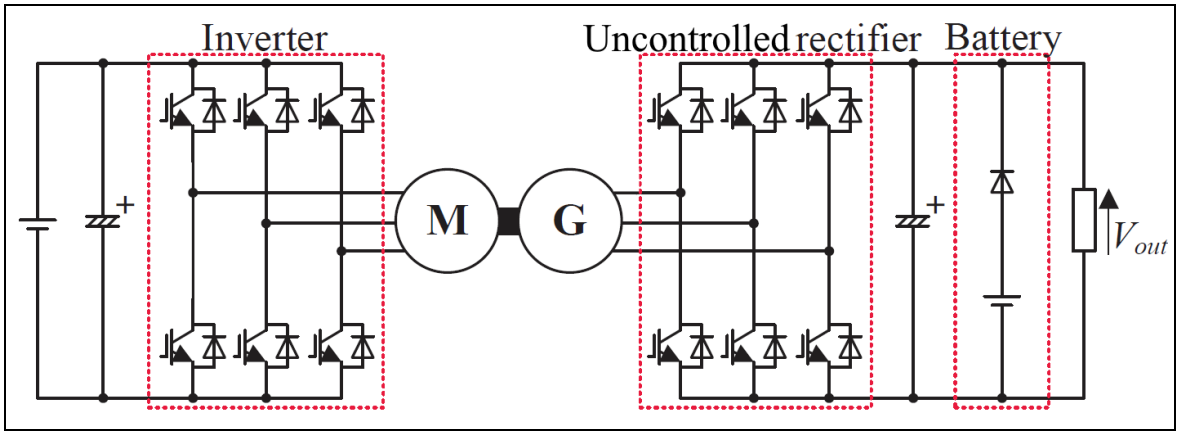


Figure 4.42. Simple configuration of the inverter/converter stage of Starter/Generator

The 3-phase two-level inverter topology is employed for both the motor and starting modes of the S/G.

This topology allows for efficient and controlled power delivery to the S/G, ensuring smooth operation and reliable starting of the engine. It also enables the conversion of DC power from the battery into AC power for the S/G in motor or starting modes.

In the generator mode of the S/G, an uncontrolled rectifier topology is typically used to convert the AC power generated by the S/G into DC power. This DC power can be used to charge the battery or power other electrical systems in the UAV. The uncontrolled converter topology provides a straightforward and cost-effective solution for power conversion in generator mode. In addition to uncontrolled converter topologies, there are also controlled inverter/converter topologies available for both the motor and generator modes of the S/G. One example is the bidirectional converter, shown in Figure 4.43, which offers improved control and flexibility in managing power flow during generator operation. These controlled rectifiers provide benefits such as enhanced power quality, better control over the generated power, and improved regulation and stability.

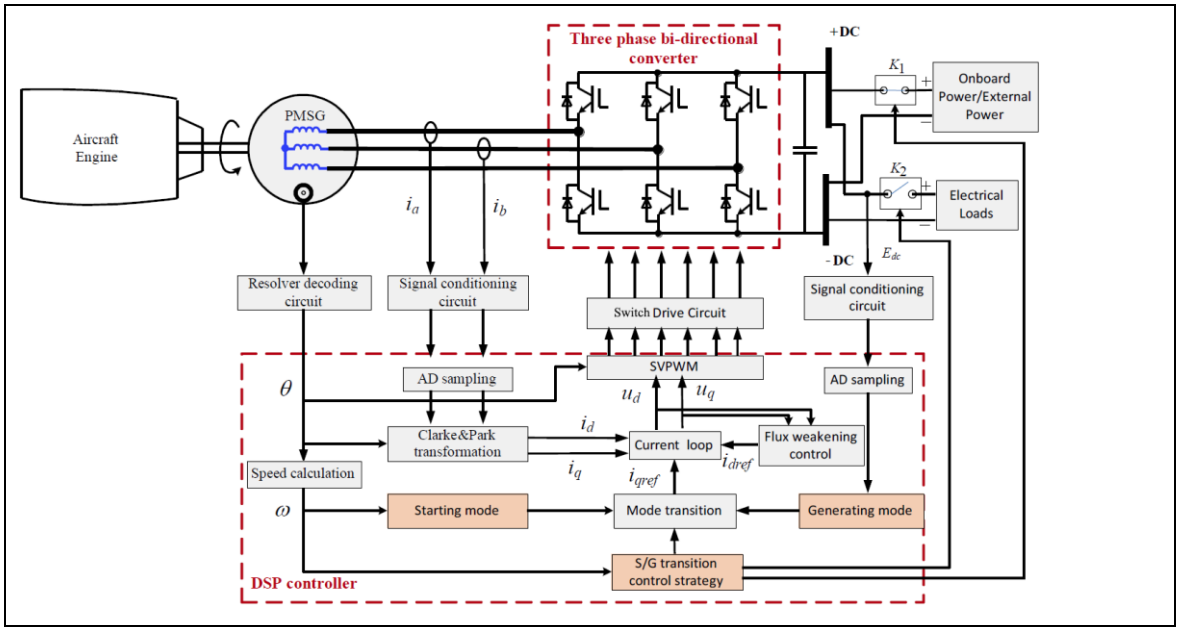


Figure 4.43. Block scheme of the S/G using bidirectional converter topology [12]

The advanced control system of the S/G, as depicted in Figure 4.43, comprises the S/G, a bidirectional converter, a DSP controller, a switch drive circuit, and more.

During the starting mode, the S/G is initially powered by an onboard or ground power supply.

Once the S/G reaches the cut-off speed, switch K1 is activated, stabilizing the DC voltage. At this point, switch K2 is turned on to deliver power to the load. In the starting mode, a vector control strategy with $i_d=0$ is employed for effective control of the S/G performance, particularly at low speeds. In the generating mode, the AC power generated by the S/G is converted into DC power using an uncontrolled full-bridge rectifier. This DC power is utilized to supply the load or charge the battery [12].

4.7. Analytical Design Equations of Inrunner Radial BLDC Starter/Generator

There are various methods to determine the distribution of magnetic fields in the air gap of permanent magnet machines (PMMs). Simple analytical equations can be used for straight-forward geometries to calculate the magnetic field. However, for complex structures such as axial flux PMSMs, a realistic field analysis typically requires FEM studies. Nevertheless, it is possible to reasonably approximate the field distribution using analytical models [359].

The analytical magnetic S/G model provides a rapid evaluation tool for analysing S/G performance in steady-state conditions. It enables easier optimization of different parameters while maintaining reliability. For the analytical analysis of a magnetic circuit, flux paths and reluctances must be defined for each component. In PMMs, this task is relatively straightforward as the presence of magnets determines the flux paths. The flux naturally follows the magnetization direction of the magnets within the poles and splits into two paths towards adjacent poles, as illustrated in Figure 4.44.

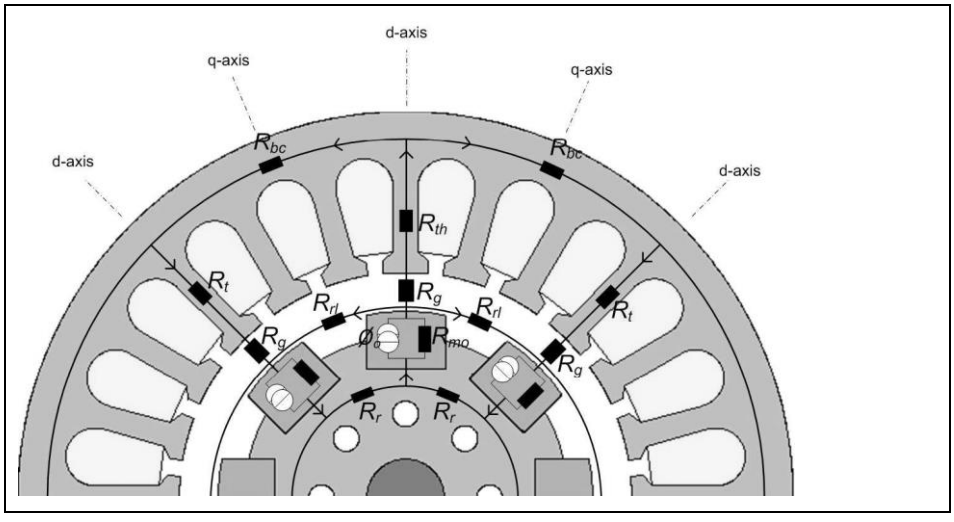


Figure 4.44. 2D magnetic circuit model illustration of surface mount PMMs [359]

where ϕ_0 : Permanent magnet flux

R_{m0} : Internal reluctance of permanent magnet

R_{rl} : Reluctance of the flux path in the rotor between adjacent poles.

R_g : Magnetic reluctance of equivalent air gap

R_{th} : Tooth path reluctance

R_{bc} : Stator yoke reluctance

R_r : Rotor yoke reluctance

Taking into account the machine cross section depicted in Figure 4.44, it can be observed that the machine comprises 8-poles. The magnetic flux originating from the rotor surface crosses over to the stator and divides into two equivalent sections. Each section travels in the opposite direction, traversing the air gap towards the adjacent rotor pole. The flux follows a closed path between two adjacent poles. Additionally, some magnetic flux jumps from one magnet to the next in the air gap without passing through the stator, as indicated by R_{rl} in Figure 4.45. This flux is commonly referred to as magnet or rotor leakage flux [360]. It is worth noting that the flux paths illustrated in Figure 4.44 repeat for every pole, allowing for modelling of a single pole to characterize the PM motor. Stator slot leakage is neglected in this analysis. The arrows on the lines in the figure denote the direction of the flux.

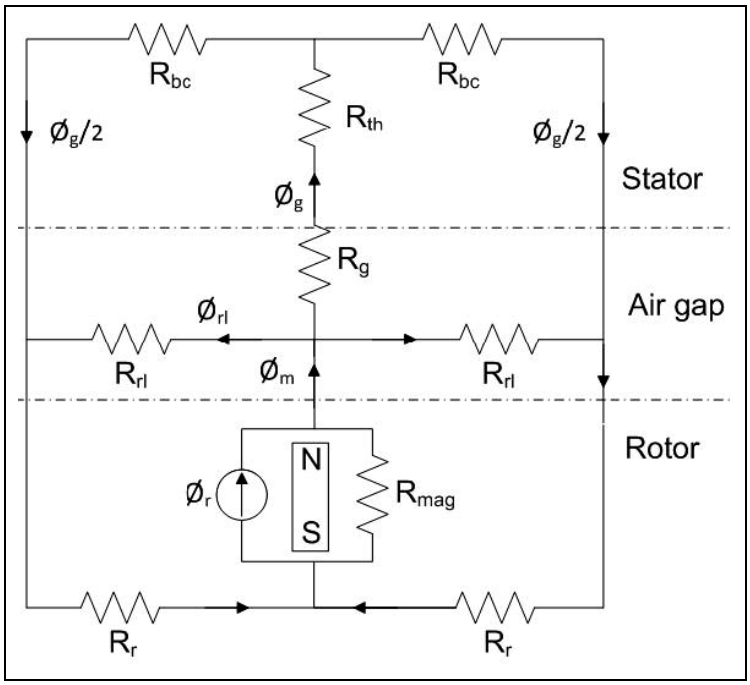


Figure 4.45. One-pole magnetic circuit model of surface mount PMMs [359]

The flux leaving the magnets splits into leakage flux and air gap flux. To determine the actual air gap flux, it is necessary to determine the reluctances associated with these two paths. However, estimating the rotor leakage paths and explicitly defining leakage reluctances is a challenging task. Instead, an empirical approach using a leakage factor is commonly employed in analytical models [361]. For surface and inset magnet motors, the leakage flux typically accounts for up to 10% of the air gap flux and can be modelled by introducing a leakage factor that multiplies the air gap reluctance, $R_{rl} = k_{rl}R_g$ [362]. The presented model can be utilized to determine the mean or rms value of flux density in the air gap. For a more detailed flux distribution analysis , the utilization of FEM is often necessary. The analytical design process typically commences by defining both the dependent and independent design parameters. The dependent design parameters are directly influenced by the independent design parameters and are the key characteristics or outputs of the system under consideration. On the other hand, the independent design parameters are the variables that can be adjusted by the designer to achieve specific design goals [363].

4.7.1. Calculation of direct dependent variables

The calculation of the desired output torque and corresponding input current, phase current, coil current, and input power in the ideal case can be determined using the following equations that provide a clearer understanding of the process involved [334, 360, 363].

$$T_{out} = \frac{P_{out}}{w_m} \qquad w_m = 2\pi * rps \qquad rps = \frac{rpm}{60} \tag{4.96}$$

$$P_{in} = \frac{P_{out}}{\eta_d} \tag{4.97}$$

$$I_t = \frac{P_{in}}{V_{DC}} \tag{4.98}$$

$$I_{ph,peak} = I_t \tag{4.99}$$

$$I_{ph,rms} = \sqrt{\frac{2}{3}} I_{ph,peak} \tag{4.100}$$

$$I_c = \frac{I_{ph}}{N_p} \tag{4.101}$$

where T_{out} : Rated output torque (N)

P_{out} : Rated output power (kW)

w_m, w_e : Rated mechanical angular speed (rad/s)

rpm : Revolution per minute

rps : Revolution per second

η_d : Desired efficiency (%)
P_{in} : Rated input power (kW)
I_{ph} : Phase current (A)
I_t : Average terminal current (A)
I_c : Coil current (A)
N_p : Number of parallel path in winding
V_{DC} : Input DC voltage

4.7.2. Calculation of the back-EMF

Output equations play a crucial role in the design and dimensioning of EMs, enabling to calculate of important machine dimensions. The equation establishes a relationship between the input electrical power, output mechanical power, and various machine parameters.

To derive the output equation of the S/G, the first step is to calculate the back-EMF using the following equations in linear magnetic properties:

$$E_{ph} = \frac{d\lambda}{dt} = \frac{d\lambda}{d\Theta_e}\frac{d\Theta_e}{dt} = \frac{d\lambda}{d\Theta_e} w_e = \frac{d\lambda}{d\Theta_e} w_m * \frac{N_m}{2} \quad (4.102)$$

$$\lambda_{max} = k_w * N_{tph} * \emptyset_p \quad (4.103)$$

$$E_{ph} = \frac{2\lambda_{max}}{\pi} * w_m * \frac{N_m}{2} \quad (4.104)$$

where E_{ph} : Induced phase back-EMF (V)
λ : Flux linkage (Wb)
θ_e : Electrical degree (rad)
N_m, (2p) : Number of poles
N_{tph} : Number of effective turns per phase
k_w : Winding factor
ϕ_p : Pole flux (Wb)

Flux linkage and back-EMF as a function of rotor position are illustrated in Figure 4.46.

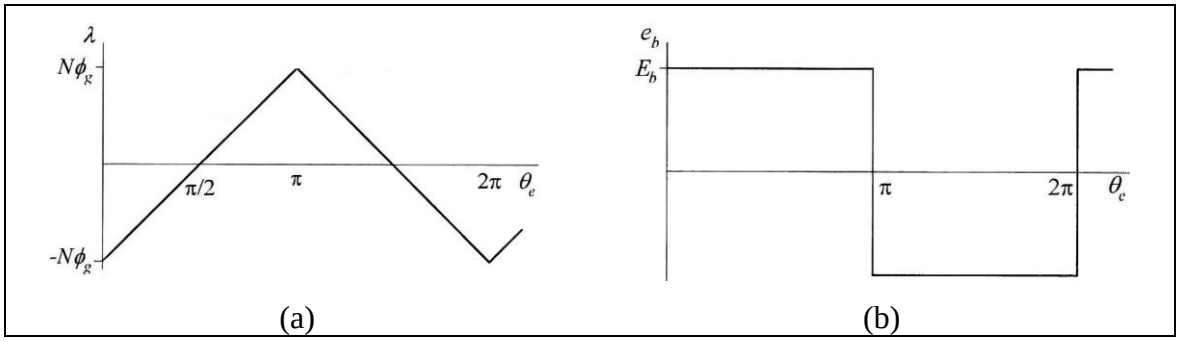


Figure 4.46. (a) Flux linkage (b) Back-EMF as a function of rotor [360]

To improve the accuracy of the back-EMF equation mentioned above and align it with the real case, a correction is applied, as depicted in Eq. 4.105 and Figure 4.47.

$$k_s = \frac{m_{line1}}{m_{line2}} \geq 1 \qquad k_s = \frac{E_{ph,max}}{(2\lambda_{max})/T_s/2} = \frac{E_{ph,max}}{(4\lambda_{max})f_s} \tag{4.105}$$

$$E_{ph} = k_s * \frac{2\lambda_{max}}{\pi} w_m * \frac{N_m}{2} \tag{4.106}$$

where k_s : Slope factor

T_s / f_s : Time period / Rated frequency of phase current

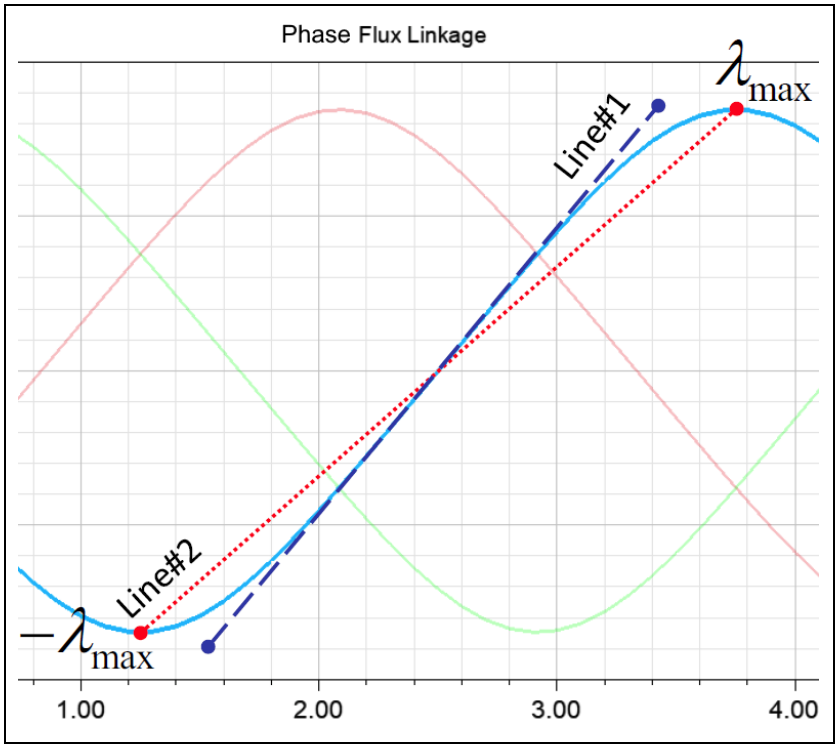


Figure 4.47. Phase flux linkage in real operation [363]

4.7.3. Calculation of the magnetic and electric loadings

The magnetic and electric loadings play a crucial role in the design of S/Gs because they significantly impact the efficiency, performance, and overall operational characteristics of the machines. Proper consideration and optimization of these loadings are essential for achieving desired outcomes in terms of energy conversion, power output, and reliability. The magnetic and electric loadings are calculated using the following equations:

$$B_{av} = \frac{N_m \emptyset_p}{\pi DL} \qquad \emptyset_p = \frac{B_{av} * \pi DL}{N_m} \tag{4.107}$$

$$E_{ph} = k_s k_w N_{tph} B_{av} * \pi DL * 2(rps) \tag{4.108}$$

$$ac = \frac{2 * \frac{N_s}{3} * 2N_{tc} * I_{c,peak}}{\pi D} = \frac{4N_{tph} * I_{ph,peak}}{\pi D} \tag{4.109}$$

where B_{av} : Specific magnetic loading (T)
[Average of the flux density in the middle of air gap]
D : Stator bore diameter (m)
L, L_{stk} : Stack length (m)
ac : Specific electric loading (kA/m)
N_s : Stator slot number

The selection of specific magnetic and electric loadings is a critical aspect, which is depicted in Table 4.6 and Table 4.7, considering the types of machine and cooling in italics [336].

Table 4.6. Selection of specific magnetic loading for BLDC

	Flux Density, B (T)		
	Salient-Pole Synchronous Machines	Nonsalient-Pole Synchronous Machines	*DC Machines*
Air gap	0,85-1,05	0,8-1,05	*0,6-1,1*
Stator yoke	1-1,5	1,1-1,5	*1,1-1,5*
Stator tooth	1,6-2	1,5-2	*1,6-2*
Rotor tooth	1,6-2	1,5-2	*1,8-2,2*
Rotor yoke	1-1,5	1,3-1,6	*1-1,5*
Pole core	1,3-1,8	1,1-1,7	*1,2-1,7*

Table 4.7. Selection of specific electric loading for BLDC

<table>
<tr><td rowspan="3"></td><td rowspan="3">Salient-Pole Synchronous Machines</td><td colspan="3">Nonsalient-Pole Synchronous Machines</td><td rowspan="3">DC Machines</td></tr>
<tr><td colspan="2">Indirect Cooling</td><td rowspan="2">Direct Cooling</td></tr>
<tr><td>Air</td><td>Hydrogen</td></tr>
<tr><td>A (kA/m)</td><td>35-65</td><td>30-80</td><td>90-110</td><td>150-200</td><td>25-65</td></tr>
<tr><td></td><td>Armature Winding</td><td>Armature Winding</td><td>Armature Winding</td><td>Armature Winding</td><td>Armature Winding</td></tr>
<tr><td rowspan="4">J (A/mm^2)</td><td rowspan="4">4-6,5</td><td rowspan="4">3-5</td><td rowspan="4">4-6</td><td>Water Cooling</td><td rowspan="2">4-9</td></tr>
<tr><td>7-10</td></tr>
<tr><td>Hydrogen Cooling</td><td>Pole Winding</td></tr>
<tr><td>6-13</td><td>2-5,5</td></tr>
<tr><td rowspan="2">J (A/mm^2)</td><td>Field-Winding Multi-Layer</td><td>Field-Winding</td><td>Field-Winding</td><td rowspan="4"></td><td>Compensating Winding</td></tr>
<tr><td>2-3,5</td><td>3-5</td><td>3-5</td><td>3-4</td></tr>
<tr><td rowspan="2">J (A/mm^2)</td><td>Field-Winding Single-Layer</td><td colspan="2">Water Cooling</td><td></td></tr>
<tr><td>2-4</td><td colspan="2">13-18</td><td></td></tr>
</table>

4.7.4. Calculation of the developed power and output equation

By incorporating the magnetic and electric loadings, the developed power and the output equation of the S/G can be derived as follows:

$$P_{out} = 2E_{ph}i_{ph} \qquad P_{out} = 2 * k_s k_w N_{tph} B_{av} * \pi DL * 2(rps) * i_{ph} \tag{4.110}$$

$$P_{out} = (k_s * k_w * \pi^2 * B_{av} * ac) * D^2 L * (rps) = G * D^2 L * (rps) \tag{4.111}$$

where G : Output equation [coefficient] (J/m^3 or N.m/m^3)

4.7.5. Calculation of main dimensions

The aspect ratio plays a significant role in the segregation of the stator bore diameter and stack length within the output power equation of S/Gs. It refers to the ratio of the stack length to the pole pitch and is a critical parameter in the design and optimization of EMs. The proper selection of the aspect ratio of the model determines the degree of elongation in length. the D^2L product determines the size of the motor and thus its power and torque density.

$$D^2L = \frac{P_{out}}{G * (rps)} \tag{4.112}$$

$$ar = \frac{L}{\tau_p} \qquad \tau_p = \frac{\pi D}{(2p)} \tag{4.113}$$

$$D = \sqrt[3]{\frac{(2p) * D^2L}{ar * \pi}} \tag{4.114}$$

where ar : Aspect ratio

τ_p : Pole pitch (m)

(2p), N_m : Pole number

4.7.6. Calculation of total flux, pole flux and stator tooth flux

To calculate the detailed stator and rotor dimensions, it is necessary to calculate the total flux and pole flux first. These calculations are essential steps in the design process of S/Gs and provide crucial information for determining the appropriate dimensions.

$$\emptyset_{total} = B_{av} * \pi DL \qquad \emptyset_p = \frac{\emptyset_{total}}{(2p)} \tag{4.115}$$

$$\emptyset_{st} = \frac{\emptyset_{total}}{N_s} \tag{4.116}$$

where $\emptyset_{total}$: Total air gap flux (Wb)

$\emptyset_{st}$: Stator tooth flux (Wb)

4.7.1. Calculation of stator dimensions

Through the calculation of the total flux and pole flux, it becomes possible to accurately determine the dimensions of the stator. The dimensions of the stator, including the stator slot dimensions, are depicted in Figure 4.48 [363].

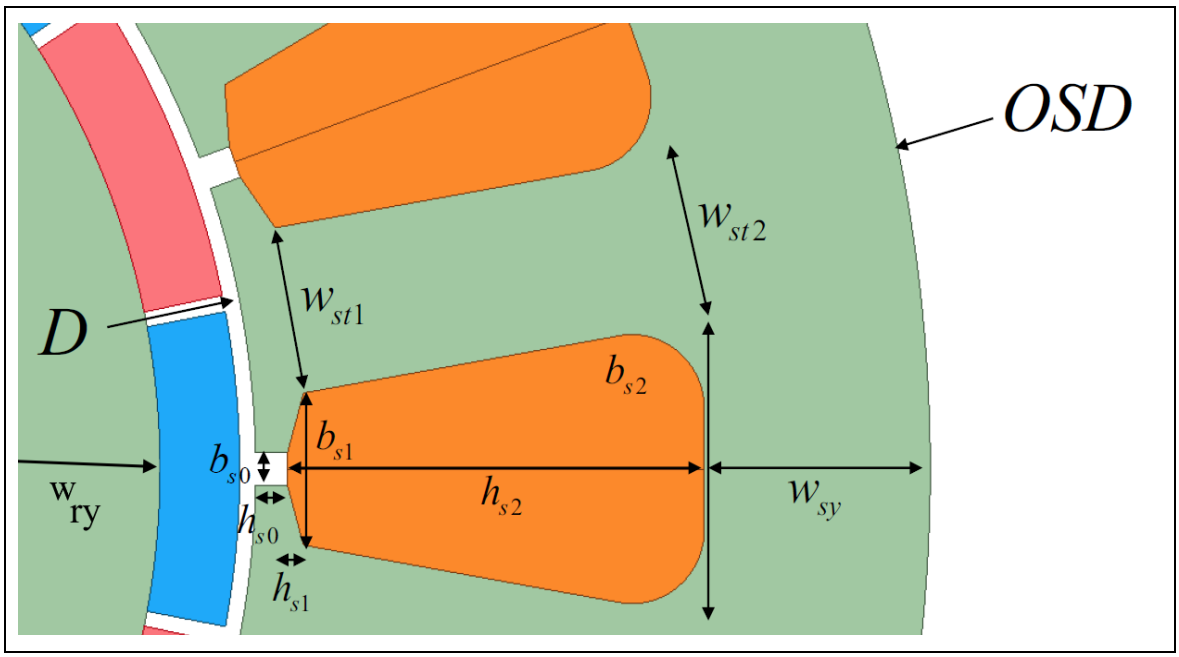


Figure 4.48. Stator slot dimensions

The stator slot dimensions in Figure 4.48 are calculated using the following equations:

$$\gamma_{wst} = \frac{w_{st2}}{w_{st1}} \qquad w_{st2} = \gamma_{wst} * w_{st1} \tag{4.117}$$

$$\emptyset_{st} = B_{st} * w_{st1} * L * k_i \tag{4.118}$$

$$b_{s1} = 2\left(\tan(\pi/N_s) * \left(\frac{D}{2} + h_{s0} + h_{s1}\right) - \frac{w_{st1}/2}{\cos(\pi/N_s)}\right) \tag{4.119}$$

$$\frac{\emptyset_p}{2} = B_{sy} * w_{sy} * L * k_i \qquad \frac{\emptyset_p}{2} = B_{ry} * w_{ry} * L * k_i \tag{4.120}$$

$$\alpha_s = \frac{2\pi}{N_s} \tag{4.121}$$

$$b_{s2} = 2\left(\tan(\alpha_s/2) * \left(\frac{D}{2} + h_{s0} + h_{s1} + h_{s2}\right) - \frac{w_{st2}/2}{\cos(\alpha_s/2)}\right) \tag{4.122}$$

where γ_{wst} : Ratio of the stator tooth width at tail to at tip
w_{st1} : Stator tooth width at tip (m)
w_{st2} : Stator tooth width at tail (m)
w_{sy} : Width of stator yoke (m)
w_{ry} : Width of rotor yoke (m)
B_{st} : Maximum permitted flux density in stator tooth (T)
B_{sy} : Maximum permitted flux density in stator yoke (T)
B_{ry} : Maximum permitted flux density in rotor yoke (T)
k_i : Stacking factor (iron insulation factor)
b_{s1} : Slot openning width (m)
h_{s0} : Slot openning height (m)
h_{s1} : Height of tooth shoe (m)
α_s : Stator slot pitch angle (rad)

4.7.7. Calculation of back-EMF

To calculate the number of turns in the stator winding, it is necessary to first calculate the phase back-EMF. This step allows us to determine the appropriate number of turns required to achieve the desired voltage and performance characteristics.

$$\gamma_{emf} = \frac{E_{ph}}{V_{DC}/2} \tag{4.123}$$

$$E_{ph} = k_s * k_w * N_{tph} * \emptyset_{total} * 2(rps) \tag{4.124}$$

$$N_{tph} = N_{tc} * \frac{N_s}{m} * \frac{1}{N_p} \tag{4.125}$$

where N_{tph} : Number of effective turns per phase
N_{tc} : Number of turns per coil
N_s : Number of stator slots
m : Number of phases
γ_{emf} : Initial back-EMF calculation constant
(γ_{emf} <1, for motor mode of S/G)
(γ_{emf} >1, for generator mode of S/G)

4.7.8. Calculation of the stator slot area

Now, with the calculation of the number of turns per coil, it becomes possible to determine the stator slot area, as shown in Figure 4.49.

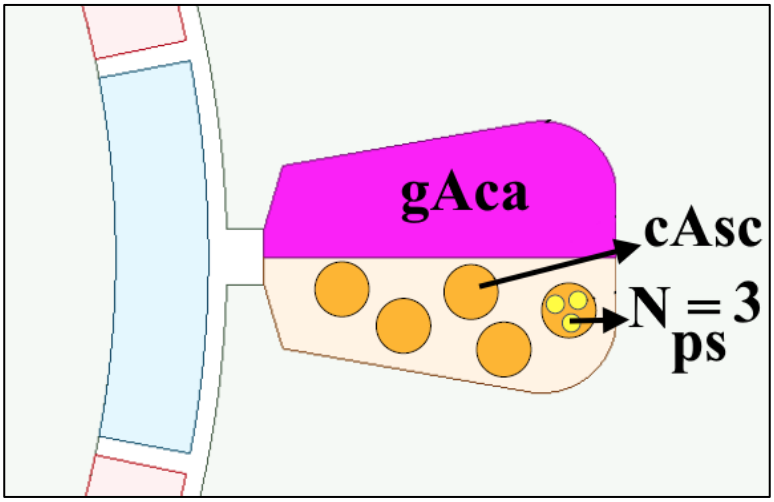


Figure 4.49. Slot area explanation

By accurately calculating the stator slot area, efficient winding placement, proper insulation, and effective cooling can be ensured, ultimately contributing to the optimal performance and reliability of the machine.

$$cAca = N_{tc} * cAsc \qquad gAca = \frac{cAsc}{K_f} \qquad cAsc = \frac{I_c}{J_{sw}} \tag{4.126}$$

$$2 * gAca = \frac{(b_{s1} + b_{s2})}{2} * h_{s2} \tag{4.127}$$

where cAca : Copper area of coil arm (m^2)
cAsc : Copper area of single conductor (m^2)
gAca : Gross area of coil arm (m^2)
K_f : Fill factor (0-1)
J_{sw} : Permitted maximum armature current density (A/m^2)

4.7.9. Rough calculation of permanent magnet dimensions

In the field of magnet design, as shown in Figure 4.50, various calculation methods exist, including rough calculation and magnetic equivalent circuit calculation methods, which are commonly used for initial estimations and detailed analysis, respectively.

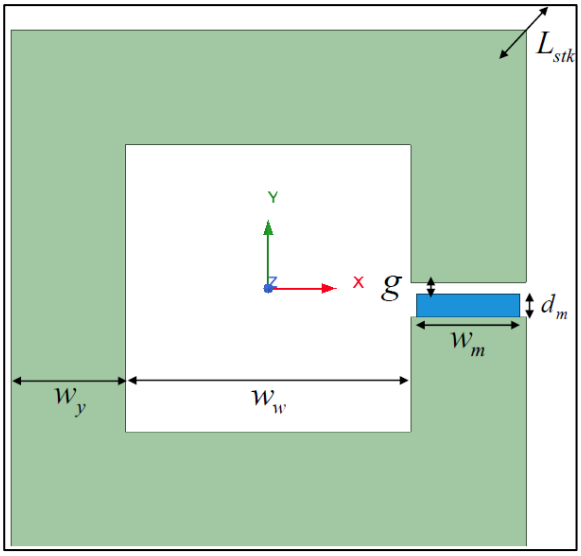


Figure 4.50. Calculation approach for the rough method for magnet design

In the rough method, the desired average magnetic flux density in the air gap is approximated by adjusting the width and depth of the permanent magnet using the following equations.

$$\gamma_m = \frac{\alpha_m}{\alpha_p} = \frac{\alpha_m}{2\pi/(2p)} \tag{4.128}$$

$$A_m = w_m * L_{stk} \qquad A_g = w_g * L_{stk} \qquad \gamma_m = \frac{w_m}{w_y} \leq 1 \tag{4.129}$$

$$\emptyset = B_m * A_m * k_l = B_g * A_g \qquad \emptyset_{magnet} = B_m * A_m \tag{4.130}$$

$$\int H.dl = 0 = H_m * d_m = -H_g * g * k_r \tag{4.131}$$

$$B_m * w_m * k_l = B_g * w_g \qquad H_m * d_m = -H_g * g * k_r \tag{4.132}$$

$$B_m = \frac{B_g * w_g}{w_m * k_l} = \frac{B_g}{\gamma_m * k_l} \tag{4.133}$$

$$B_m = \mu_m H_m + B_r \qquad \mu_m = -\frac{B_r}{H_c} \qquad \mu_r = \frac{\mu_m}{\mu_0} \tag{4.134}$$

$$H_m = -\frac{H_g * g * k_r}{d_m} = -\frac{B_g * g * k_r}{\mu_0 * d_m} \tag{4.135}$$

$$\frac{B_g}{\gamma_m * k_l} = \mu_m * \left(-\frac{B_g * g * k_r}{\mu_0 * d_m}\right) + B_r \tag{4.136}$$

$$B_g = \frac{\gamma_m * k_l * B_r}{1 + \mu_r * \left(\frac{\gamma_m * k_l * g * k_r}{d_m}\right)} \tag{4.137}$$

$$d_m = \frac{B_g * \mu_r * \gamma_m * k_r * k_l * g}{\gamma_m * k_l * B_r - B_g} \tag{4.138}$$

where γ_m : Embrace of permanent magnet (0-0,9)
α_m : Arc angle of permanent magnet (rad)
$\emptyset_{total}$: Total flux generated by permanent magnet (Wb)
α_p : Rotor pole pitch angle (rad)
A_m : Cross-sectional area of permanent magnet (m^2)
A_g : Cross-sectional area of air gap (m^2)
w_m : Width of the permanent magnet (m)
w_g : Width of the air gap (m)
g : Air gap length (m)
d_m : Depth of the permanent magnet (m)
H_m : Magnetic field of permanent magnet (kA/m)
B_m : Flux density of permanent magnet (T)
μ_r : Relative permeability
k_r : Reluctance factor (1-1,3)
k_l : Leakage factor (0,8-1)
B_r : Residual flux density of permanent magnet (T)
B_g : Flux density in the air gap (T)
w_w : Width of the C-core window
w_y : Width of the core yoke

4.7.10. Magnetic equivalent circuit calculation of permanent magnet dimensions

Another method commonly used to calculate the magnet dimensions is the magnetic equivalent circuit, as shown in Figure 4.51. This method involves treating the PMs as an equivalent magnetic circuit and leveraging circuit analysis to estimate its dimensions.

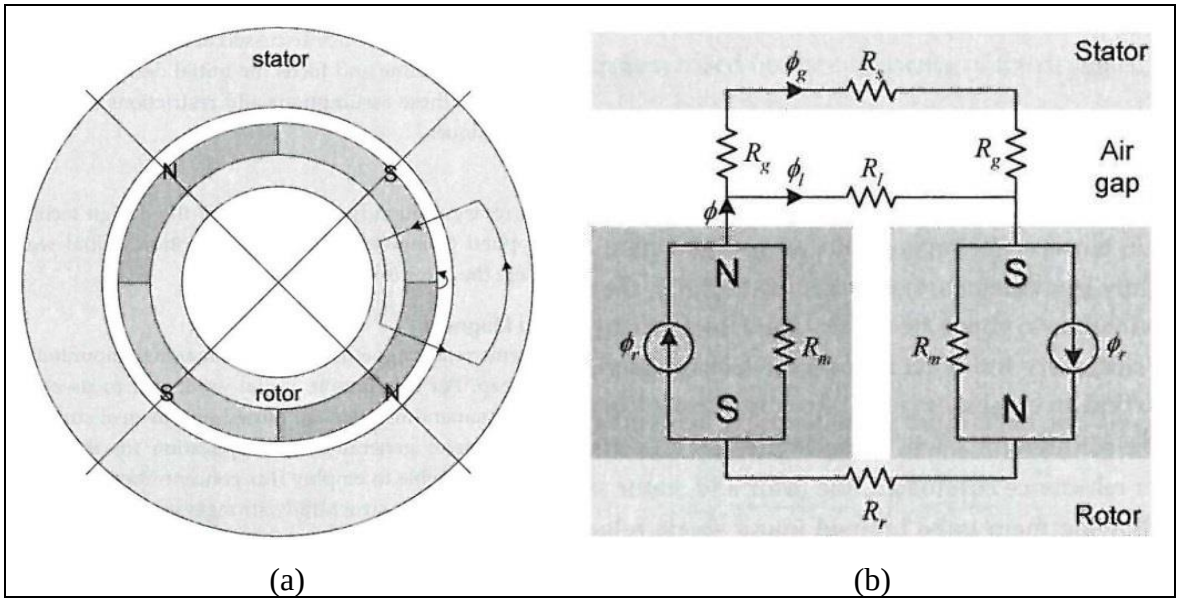


Figure 4.51. 4-pole machine exploration (a) Model (b) Magnetic equivalent circuit [360]

$$\phi_g = k_l \phi_{magnet} = \frac{k_l}{1 + k_r * \left(\frac{\mu_r * g * A_m}{l_m A_g}\right)} \tag{4.139}$$

$$B_g = \frac{k_l C_\phi}{1 + k_r * \frac{\mu_r}{P_c}} B_r \tag{4.140}$$

$$C_\phi = \frac{A_m}{A_g} \qquad P_c = \frac{l_m}{(g * C_\phi)} \tag{4.141}$$

where ϕ_g : Air gap flux (Wb)

ϕ_{magnet} : Total flux generated by magnet cross air gap (Wb)

ϕ_{total} : Flux of permanent magnet (Wb)

l_m : Depth of the permanent magnet (m)

C_ϕ : Flux concentration factor

P_c : Permeance coefficient

Figure 4.52 proposes a method for the proper selection of the permeance coefficient [364]. It defines the depth of the magnet compared to the air gap length.

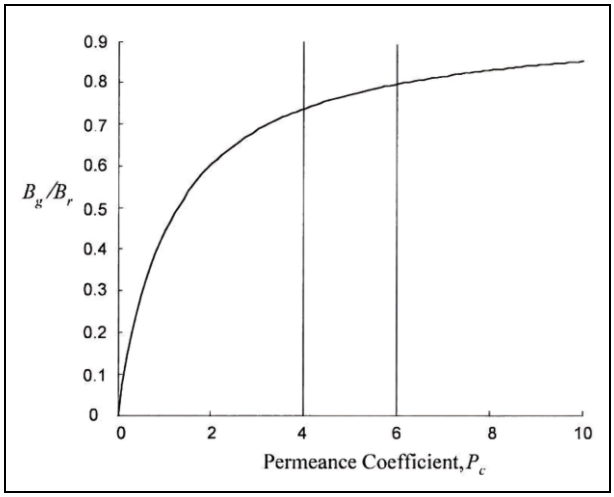


Figure 4.52. Selection of permeance coefficient [364]

4.7.11. Updating process of the design parameters

In analytical design outputs, certain parameters such as the number of effective turns in each phase and the number of turns in a single coil may be calculated as fractional values. However, in practical motor design, these values need to be updated to integers. This adjustment ensures that the machine electrical and mechanical properties align with real-world manufacturing requirements and constraints.

The procedure involves several steps to ensure practical design considerations. First, the number of turns per coil is converted to a fixed integer value to facilitate the winding arrangement and manufacturing feasibility. Next, the number of effective turns in each phase is also adjusted to a fixed integer value to align with practical manufacturing constraints. Subsequently, the machine stack length is updated by modifying the total air gap flux value. This step is essential as it ensures that the magnetic circuit design remains consistent and accounts for the updated winding configuration. By adjusting the stack length, the magnetic flux distribution is appropriately maintained, contributing to the desired performance characteristics of the machine. The following equations yield the updating procedure:

$$E_{ph} = k_s k_w N_{tph} * \emptyset_{total} * 2(rps) \tag{4.142}$$

$$\emptyset_p = \frac{B_{av} * \pi DL}{(2p)} \qquad \frac{\emptyset_{p,new}}{\emptyset_{p,old}} = \frac{L_{new}}{L_{old}} \tag{4.143}$$

$$\emptyset_{total,new} = \frac{E_{ph}}{k_s * k_w * N_{tph,new} * 2(rps)} \quad (4.144)$$

where $\emptyset_{(p,new)}$: Updated pole flux (Wb)
$\emptyset_{(p,old)}$: Old pole flux (Wb)
$\emptyset_{(total,new)}$: Updated total air gap flux (Wb)
$N_{(tph,new)}$: Updated number of effective turns per phase
L_{new} : Updated stack length (m)
L_{old} : Old stack length (m)

4.7.12. Coil and phase resistance

The next step involves calculating the coil and phase resistance, which is crucial for evaluating ohmic losses, as follows [336]:

$$R_{c,T} = N_{tc} * \rho_T * \frac{L_{mt}}{cAsc} \quad (4.145)$$

$$\rho_T = \rho_{20}\left(1 + \alpha_T(T_{amb} + T_r - 20)\right) \quad (4.146)$$

$$R_{ph} = R_c * \frac{N_s}{m} * \frac{1}{{N_p}^2} \quad (4.147)$$

$$L_{mt,distributed} = 2l + 2{,}4W + 0.1 \quad (4.148)$$

$$L_{mt,concentrated} = 2 * L_{stk} + 4 * L_{end} + \pi\left(\frac{b_{s1} + b_{s2}}{2}\right) + 2\left(\frac{w_{s1} + w_{s2}}{2}\right) \quad (4.149)$$

where $R_{c,T}$: Coil resistance (ohm)
ρ_T : Material resistivity at operating temperature (ohm-meter)
$L_{mt,distributed}$: Mean turn length for distributed winding scheme (m)
$L_{mt,concentrated}$: Mean turn length for concentrated winding scheme (m)
ρ_{20} : Material resistivity at 20 celcius (ohm-meter)
α_T : Temperature coefficient for stator winding resistance
T_{amb} : Ambient temperature (celcius)
T_r : Temperature rise (celcius)
R_{ph} : Phase resistance (ohm)

4.8. Analytical Design Equations of Inrunner Radial PMSM Starter/Generator

The analytical design approach for PMSMs shares similarities with that of BLDCs due to their common underlying principles. Both motor types employ PMs for generating magnetic fields and utilize similar mathematical equations for performance analysis and design. However, there are differences in the driving methods and the number of conducting phases at each driving step, as discussed in Section 4.5. This section focuses on the distinctive factors between the analytical design equations for PMSMs to avoid repetition [365].

4.8.1. Calculation of direct dependent variables

$$T_{out} = \frac{P_{out}}{w_m} \; ; \; w_m = 2\pi * rps \qquad rpm = \frac{120 * f}{(2p)} \; ; \; rps = \frac{rpm}{60} \tag{4.150}$$

$$P_{in} = \frac{P_{out}}{\eta_d} \tag{4.151}$$

$$S_{in} = \frac{P_{out}}{\eta_d * \cos(\emptyset)} \tag{4.152}$$

$$Q_{in} = S_{in} * \sqrt{1 - \cos(\emptyset)^2} \tag{4.153}$$

$$I_t = \frac{P_{in}}{\sqrt{3} V_t \cos(\emptyset)} \tag{4.154}$$

$$I_{ph} = \begin{cases} I_t : Star\ connection \\ \frac{I_t}{\sqrt{3}} : Delta\ connection \end{cases} \tag{4.155}$$

$$V_{ph} = \begin{cases} \frac{V_t}{\sqrt{3}} : Star \\ V_t : Delta \end{cases} \tag{4.156}$$

$$I_c = \frac{I_{ph}}{N_p} \tag{4.157}$$

$$V_{ph} = \frac{V_c * N_{cpph}}{N_p} \tag{4.158}$$

$$N_{cpph} = \begin{cases} \frac{N_s}{2m} : Single\ Layer \\ \frac{N_s}{m} : Double\ Layer \end{cases} \tag{4.159}$$

$$\gamma_{emf} = \frac{E_{ph}}{V_{ph}} \tag{4.160}$$

$$S_{in} = 3 * V_{ph} * I_{ph} \tag{4.161}$$

$$S_{in} = 3 * \frac{E_{ph}}{\gamma_{emf}} * I_{ph} \tag{4.162}$$

where T_{out} : Rated output torque (N)

P_{out} : Rated output power (kW)

w_m : Rated mechanical angular speed (rad/s)

rpm : Revolution per minute

rps : Revolution per second

η_d : Desired efficiency (%)

P_{in}	:	Rated input active power (kW)
S_{in}	:	Rated input apperant power (VA)
Q_{in}	:	Rated input reactive power (VAR)
I_{ph}	:	Phase current (A)
I_t	:	Input terminal current (A)
I_c	:	Coil current (A)
N_p	:	Number of parallel path in winding
V_t	:	Input terminal voltage (V)
V_{ph}	:	Input phase voltage
N_{cpph}	:	Number of coils per phase
N_s	:	Number of stator slots
γ_{emf}	:	(γemf <1, for motor mode of S/G) (γemf >1, for generator mode of S/G)
(2p)	:	Number of poles
f, f_s	:	Rated frequency of supply (Hz)
cos(∅)	:	Desired power factor
m	:	Number of phases
E_{ph}	:	Induced phase back-EMF (V)

4.8.2. Calculation of the back-EMF

The calculation of the induced back-EMF voltage in PMSMs differs from that in BLDCs. It is typically determined using the equations specific to synchronous operation, as follows:

$$E_{ph} = 4{,}44 * f_s * N_{tph} * k_w * \emptyset_p \tag{4.163}$$

$$N_{tph} = N_{tc} * N_{cpph} * \frac{1}{N_p} \tag{4.164}$$

$$k_w = k_d * k_p * k_{skew} \tag{4.165}$$

$$S_{in} = 3 * \frac{4{,}44 * f_s * N_{tph} * k_w * \emptyset_p}{\gamma_{emf}} * I_{ph} \tag{4.166}$$

where N_{tph} : Number of effective turns per phase

N_{tc} : Number of turns per coil

k_w : Winding factor

k_d : Distribution factor

k_p : Pitch factor

k_{skew} : Skew factor

ϕ_p : Pole flux (Wb)

4.8.3. Winding factor

The winding factor for a specific winding configuration quantifies the ratio of flux linked by that winding in comparison to the flux that would have been linked by a single-layer, full-pitch, nonskewed integer-slot winding with the same number of turns and one slot per pole per phase, as shown in Figure 4.53.

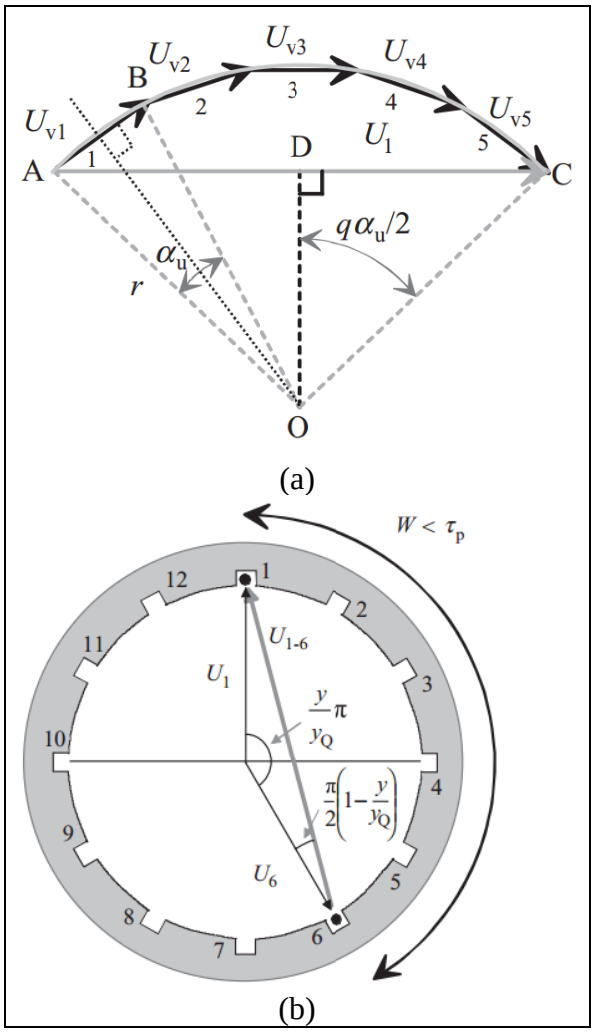
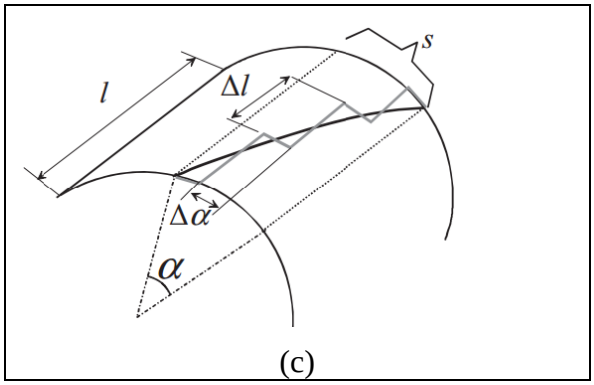


Figure 4.53. Winding factor (a) Distribution factor (b) Pitch factor (c) Skew factor [336]



(c)

Figure 4.53. (continued) Winding factor (a) Distribution factor (b) Pitch factor (c) Skew factor [336]

$$k_{dv} = \frac{\sin\left(v\frac{q\alpha_u}{2}\right)}{\mathrm{q}\sin\left(v\frac{\alpha_u}{2}\right)} \tag{4.167}$$

$$k_{pv} = \sin\left(v\frac{W}{\tau_p}\frac{\pi}{2}\right) = \sin\left(v\frac{y}{y_Q}\frac{\pi}{2}\right) \tag{4.168}$$

$$k_{sqv} = \frac{\sin\left(v\frac{s}{\tau_p}\frac{\pi}{2}\right)}{v\frac{s}{\tau_p}\frac{\pi}{2}} = \frac{\sin\left(v\frac{S_{sp}}{\mathrm{mq}}\frac{\pi}{2}\right)}{v\frac{S_{sp}}{\mathrm{mq}}\frac{\pi}{2}} \tag{4.169}$$

$$q = \frac{N_s}{m * (2p)} \tag{4.170}$$

$$\alpha_u = \frac{2\pi}{N_s} \tag{4.171}$$

$$y_Q = \frac{N_s}{(2p)} \tag{4.172}$$

where k_{dv} : Distribution factor at v^{th} harmonic component

k_{pv} : Pitch factor at v^{th} harmonic component

k_{sqv} : Skewing factor at v^{th} harmonic component

v : v^{th} harmonic component

α_u : Stator slot pitch angle (rad)

q : Number of stator slots per pole per phase

y_Q : Pole pitch (m)

S_{sp} : Skewing denoted as the number of slot pitches

s Skewing denoted as the number of pole pitches

The distribution factor accounts for the arrangement of winding coils in multiple slots within each phase. Due to the phase difference between the induced EMFs in different slots, the phasor sum of these EMFs is less than their numerical sum [366].

The pitch factor accounts for the partial winding arrangement commonly used in electrical machines, where individual turns are reduced to shorten the end-turn length, resulting in incomplete coverage of a full pole-pitch, also known as chorded winding.

The skew factor accounts for the angular twist in the winding, which leads to an angular spread and a reduction in the EMF. Squirrel-cage induction motors and permanent magnet synchronous machines often have their stator slots or rotor skewed by one slot-pitch to minimize the winding factor harmonics introduced by stator slotting.

4.8.4. Calculation of the magnetic and electric loadings

The calculation of specific magnetic loading in PMSMs follows an approach similar to that in BLDCs. On the other hand, the calculation of specific electric loading in PMSMs differs from that in BLDCs. Table 4.8 and Table 4.9 provide the selection process, taking into consideration the machine type and cooling method in italics [336].

Table 4.8. Specific magnetic loading for SPMSM

	Flux Density, B (T)	
	Salient-Pole Synchronous EM	*Nonsalient-Pole Synchronous EM*
Air gap	0,85-1,05	*0,8-1,05*
Stator yoke	1-1,5	*1,1-1,5*
Stator tooth	1,6-2	*1,5-2*
Rotor tooth	1,6-2	*1,5-2*
Rotor yoke	1-1,5	*1,3-1,6*
Pole core	1,3-1,8	*1,1-1,7*

Table 4.9. Specific electric loading for SPMSM

<table>
<tr><td rowspan="2"></td><td rowspan="2">Salient-Pole Synchronous Machines</td><td colspan="3">Nonsalient-Pole Synchronous Machines</td></tr>
<tr><td colspan="2">Indirect Cooling</td><td rowspan="2">Direct Cooling</td></tr>
<tr><td>Air</td><td>Hydrogen</td></tr>
<tr><td>A
(kA/m)</td><td>35-65</td><td>30-80</td><td>90-110</td><td>150-200</td></tr>
<tr><td></td><td>Armature Winding</td><td>Armature Winding</td><td>Armature Winding</td><td>Armature Winding</td></tr>
<tr><td>J
(A/mm^2)</td><td>4-6,5</td><td>3-5</td><td>4-6</td><td>Water Cooling</td></tr>
<tr><td rowspan="3">J
(A/mm^2)</td><td>Field-Winding Multi-Layer</td><td>Field-Winding</td><td>Field-Winding</td><td>7-10</td></tr>
<tr><td rowspan="2">2-3,5</td><td rowspan="2">3-5</td><td rowspan="2">3-5</td><td>Hydrogen Cooling</td></tr>
<tr><td>6-13</td></tr>
<tr><td rowspan="2">J
(A/mm^2)</td><td>Field-Winding Single-Layer</td><td colspan="2">Water Cooling</td><td rowspan="2"></td></tr>
<tr><td>2-4</td><td colspan="2">13-18</td></tr>
</table>

Specific magnetic loading involves determining the magnetic flux density in the air gap and evaluating the magnet dimensions and properties to achieve the desired magnetic loading. The specific electric loading is determined by considering factors such as the current density, winding fill factor, and slot area. It quantifies the electric loading on the machine windings and and heat dissipation capabilities of the machine which determines the overall efficiency.

$$B_{av} = \frac{(2p)\emptyset_p}{\pi DL} \tag{4.173}$$

$$ac = \frac{3 * 2 * N_{tc} * N_{cpph} * I_c}{\pi D} \tag{4.174}$$

where B_{av} : Specific magnetic loading (T)
[Average of the flux density in the middle of air gap]
D : Stator bore diameter (m)
L, L_{stk} : Stack length (m)
ac : Specific electric loading (kA/m)
ϕ_p : Pole flux (Wb)

4.8.5. Calculation of the developed power and output equation

By incorporating the magnetic and electric loadings, the developed power and the output equation of the S/G can be derived. This equation serves as a fundamental representation of the machine performance characteristics.

$$\frac{P_{out}}{\eta_d * \cos(\emptyset)} = \left(\frac{1{,}11 * \pi^2 * k_w * B_{av} * ac}{\gamma_{emf}}\right) D^2 L * (rps) \tag{4.175}$$

$$P_{out} = \left(\frac{1{,}11 * \pi^2 * k_w * B_{av} * ac * \eta_d * \cos(\emptyset)}{\gamma_{emf}}\right) D^2 L * (rps) \tag{4.176}$$

$$P_{out} = G * D^2 L * (rps) \tag{4.177}$$

$$G = \left(\frac{1{,}11 * \pi^2 * k_w * B_{av} * ac * \eta_d * \cos(\emptyset)}{\gamma_{emf}}\right) \tag{4.178}$$

where G : Output equation [coefficient] (J/m^3 or N.m/m^3)

4.8.6. Calculation of main dimensions

The D^{2}L product, which refers to the product of the stator bore diameter and the stack length, has a direct influence on the size, power, and torque density of the machine. This product provides valuable insights into the overall dimensions and capabilities of the machine, as it combines both the radial and axial dimensions. The aspect ratio is a crucial factor in determining the relationship between the stator bore diameter and stack length within the output power equation of S/Gs. It represents the ratio of the stack length to the pole pitch.

$$D^2 L = \frac{P_{out}}{G * (rps)} \tag{4.179}$$

$$ar = \frac{L}{\tau_p} \qquad \tau_p = \frac{\pi D}{(2p)} \tag{4.180}$$

$$D = \sqrt[3]{\frac{(2p) * D^2 L}{ar * \pi}} \tag{4.181}$$

where ar : Aspect ratio

τ_p : Pole pitch (m)

(2p), N_m : Pole number

4.8.7. Calculation of total flux, pole flux and stator tooth flux

The calculation of total flux, pole flux, and stator tooth flux for SPMSM Starter/Generators follows a similar approach to that discussed in Section 4.10.6 for BLDCs. The principles and equations outlined in that section can be applied to SPMSM S/Gs.

4.8.8. Calculation of stator dimensions

The calculation of stator dimensions for SPMSM follows a similar approach to that discussed in Section 4.10.7 for BLDCs. The design principles and equations discussed in that section can be applied to SPMSMs with some modifications specific to the motor type.

The knowledge and methodologies provided in Section 4.10.7 can be adapted to the specific requirements and characteristics of SPMSM S/Gs, allowing for accurate and efficient design calculations. By utilizing this approach, optimal performance and proper integration of the stator dimensions are ensured.

$$\emptyset_{st,max} = B_{st} * w_{st1} * L * k_i \tag{4.182}$$

$$\emptyset_{st,max} = \int B.ds = \int_{-\frac{\pi}{N_s}}^{\frac{\pi}{N_s}} B_r(\theta) * \frac{D}{2} d\theta * L \tag{4.183}$$

$$B_r(\theta) = B_M \cos\left(\frac{(2p)}{2}\theta\right) = \frac{\pi}{2} B_{av} \cos\left(\frac{(2p)}{2}\theta\right) \tag{4.184}$$

$$\emptyset_{st,max} = \frac{B_{av} * \pi DL}{(2p)} * \sin\left(\frac{\pi(2p)}{2N_s}\right) = \emptyset_p * \sin\left(\frac{\pi(2p)}{2N_s}\right) \tag{4.185}$$

where $\emptyset_{st,max}$: Maximum permitted flux density in the stator tooth (Wb)

B_M : Maximum value of the radial component of the flux densiny (T)

B_r : Radial component of flux density (T)

4.8.9. Calculation of the number of turns

The calculation of the number of effective turns per phase and the number of turns per coil differs between PMSM and BLDC, as shown by the following equations:

$$N_{tph} = \frac{E_{ph}}{4{,}44 * f * k_w * \emptyset_p} \tag{4.186}$$

$$N_{tph} = N_{tc} * N_{cpph} * \frac{1}{N_p} \tag{4.187}$$

where N_{tph} : Number of effective turns per phase
N_{tc} : Number of turns per coil
N_{cpph} : Number of coils per phase

4.8.10. Calculation of the stator slot area

In SPMSMs, the calculation of the stator slot area follows a similar approach to that of BLDCs. After determining the copper area of a single conductor (cAsc), it is recommended to consult the SWG or AWG table to ensure the model aligns with real-world applications.

$$cAca = N_{tc} * cAsc \qquad gAca = \frac{cAsc}{K_f} \qquad cAsc = \frac{I_c}{J_{sw}} \tag{4.188}$$

$$gAss = \frac{(b_{s1} + b_{s2})}{2} * h_{s2} \tag{4.189}$$

where cAca : Copper area of coil arm (m^2)
cAsc : Copper area of single conductor (m^2)
gAca : Gross area of coil arm (m^2)
gAss : Gross area of stator slot (m^2)
K_f : Fill factor (0-1)
J_{sw} : Maximum stator current density (A/m^2)

The update process begins with the copper area of a single conductor wire (cAsc), which is obtained from existing industrial conditions. Next, the copper area of the coil arm (cAca) and fill factor (K_f) are adjusted to derive the updated gross area of the coil arm (gAca).

Subsequently, the corresponding new Gross area of the stator slot (gAss) is calculated, and the values of h_{s2} and b_{s2} are updated accordingly.

4.8.11. Rough and magnetic equivalent circuit methods to calculate PM dimensions

The rough and magnetic equivalent circuit methods are commonly used to estimate the dimensions of PMs in both PMSMs and BLDCs. These methods are similar in their approach due to similar rotor topologies and provide a way to determine the appropriate dimensions of the PMs, as detailed in Sections 4.10.10 and 4.10.11.

In the rough method, the PM dimensions are estimated based on simplified assumptions and empirical relationships. This method takes into account factors such as the desired magnetic flux density, air gap length, and motor performance requirements. By using these parameters, along with considerations for saturation and demagnetization effects, an approximate estimation of the PM dimensions can be obtained.

The magnetic equivalent circuit method is a more detailed approach that involves modelling the magnetic circuit of the machine. The machine is divided into magnetic equivalent circuits, with each circuit representing different components such as the stator, rotor, and PMs. By considering the magnetic properties of these components, along with the machine operating conditions and desired performance characteristics, the dimensions of the PMs can be determined through iterative calculations or optimization techniques. Both methods aim to find the optimal dimensions for the PMs that satisfy the desired radial component of the average air gap flux density requirements while taking into account factors such as magnetic saturation, demagnetization, and efficiency. The fundamental principles of these methods in PMSMs and BLDCs remain similar in both motor types.

4.8.12. Carter factor

In manual calculations of the magnetic voltage across an air gap, it is necessary to simplify the geometry of the air gap. Typically, both the stator and rotor surfaces in a machine have slots, where the flux density decreases at the slot opening, as shown in Figure 4.54.

This makes it challenging to accurately determine the average flux density of the slot pitch between the stator and rotor.

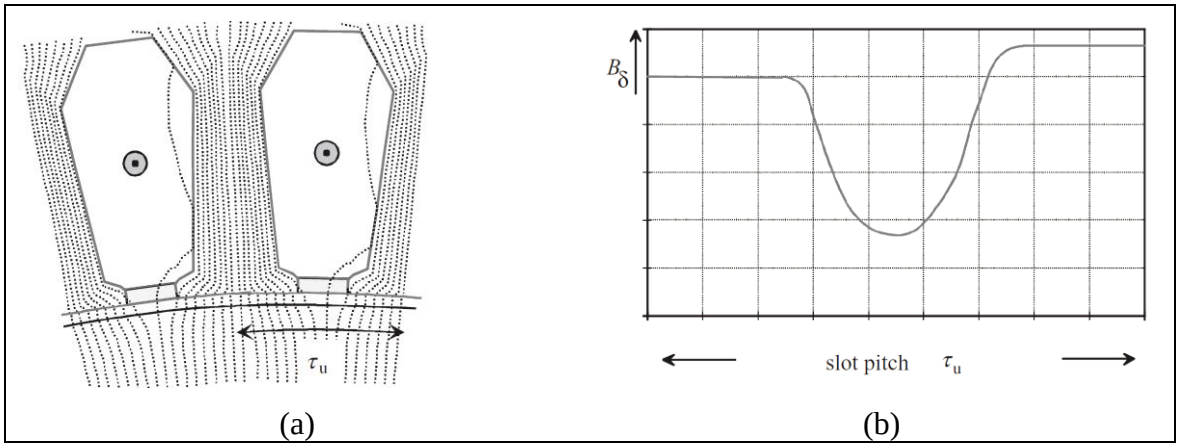


Figure 4.54. (a) Flux diagram under a stator slot along one slot pitch (b) The behavior of the air-gap flux density along a slot pitch [336]

However, F.W. Carter proposed a solution in 1901 known as Carter's principle. According to this principle, the air gap length, denoted as δ, is considered longer than its physical measure by a factor called the Carter factor (K_c), as shown in the following equations [365]:

$$K_c = \frac{1}{1 + 5\frac{l_g}{W_s}} \tag{4.190}$$

$$R = \frac{l_g}{\mu_0 A} = \frac{l_g}{\mu_0 L y_s} \tag{4.191}$$

$$R = \frac{l_g}{\mu_0 A} = \frac{l_g}{\mu_0 L W_t} = \frac{l_g}{\mu_0 L (y_s - W_s)} : Approximation \tag{4.192}$$

The initial correction assumes a smooth rotor surface, replacing the real flux density curve with a rectangular function. This approximation ensures that the flux density remains constant under the teeth and is zero at the slot opening. In other words, the shaded areas S1+S1 in Figure 4.55 are equal to S2, defining the equivalent slot opening [336].

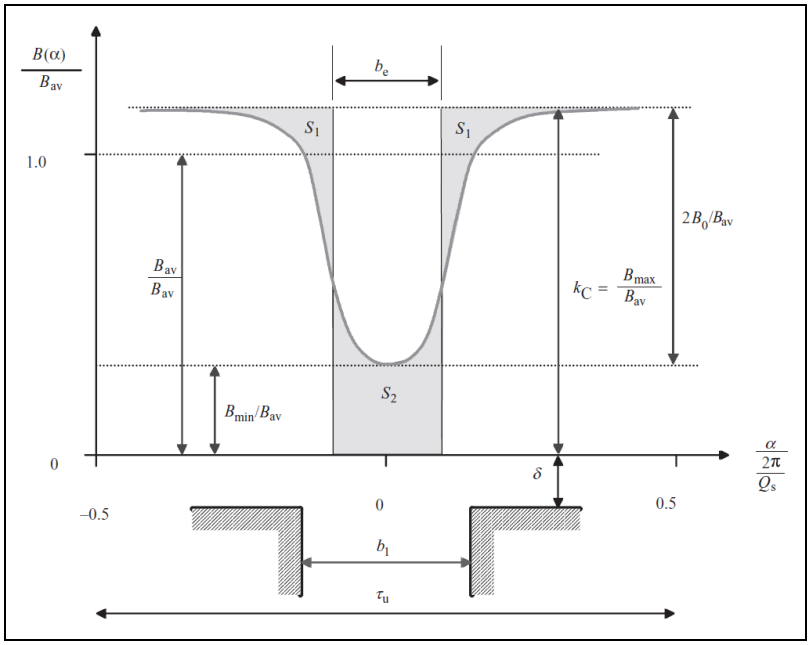


Figure 4.55. Distribution of air-gap flux density at a distance of one slot pitch

The Carter factor is utilized to incorporate the influence of stator slot openings, which contribute to an increase in the reluctance of the air gap. Calculating the effects of slot openings in a closed-slotted stator is relatively straightforward, as depicted in Figure 4.56.

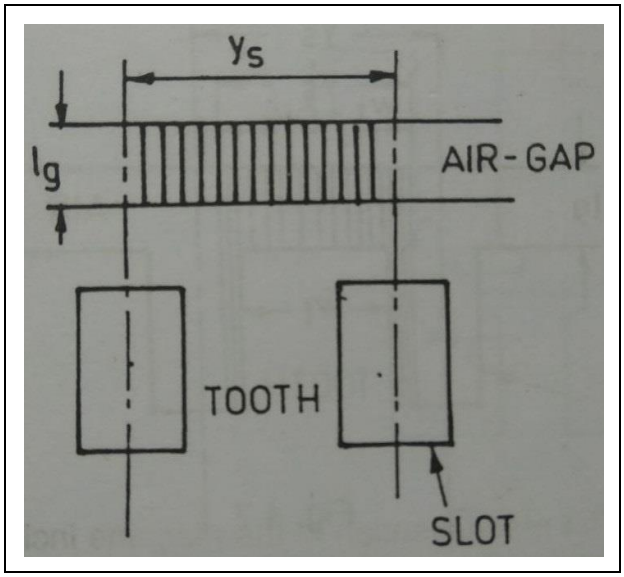


Figure 4.56. Carter factor for closed-slotted stator type

However, for an open-slotted stator, the task becomes complex, as illustrated in Figure 4.57.

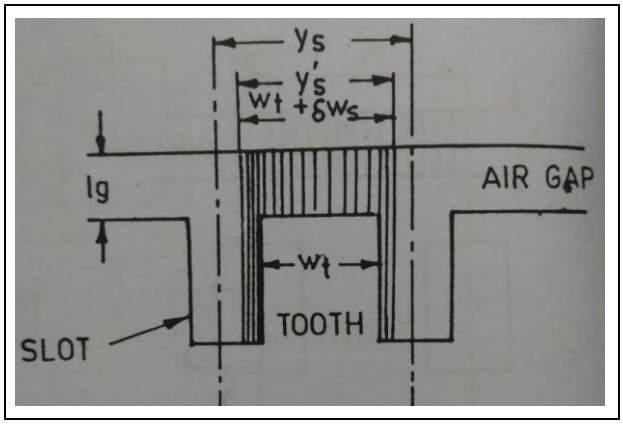


Figure 4.57. Carter factor for open-slotted stator type

To analyse and understand these effects, the following assumed equations can be derived.

$$y_s' = W_t + \delta W_s = W_t + \delta W_s + W_s - W_s \tag{4.193}$$

$$y_s' = y_s - (1-\delta)W_s \qquad y_s' = y_s - K_{cs}W_s \tag{4.194}$$

$$K_{cs} = \frac{1}{1 + 5\frac{l_g}{W_s}} : Improved\ approximation \tag{4.195}$$

$$K_{gs} = \frac{R_{slot,open}}{R_{slot,closed}} = \frac{\frac{l_g}{\mu_0 L(y_s - K_{cs}W_s)}}{\frac{l_g}{\mu_0 L y_s}} = \frac{y_s}{(y_s - K_{cs}W_s)} \tag{4.196}$$

$$K_{cs} = \frac{(K_{gs} - 1) * (W_s - W_t)}{K_{gs} * W_s} \tag{4.197}$$

where

	K_c	:	Carter factor
	l_g	:	Air gap length (m)
	W_s	:	Width of slot (m)
	W_t	:	Width of tooth (m)
	R	:	Air gap reluctance (H^{-1})
	A	:	Stator tooth area (m^2)
	L	:	Stack length (m)
	y_s	:	Slot pitch (m)
	y_s'	:	Effective slot pitch (m)
	K_{cs}	:	Carter factor of stator core
	K_{gs}	:	Gap contraction factor
	δ	:	Coefficient

4.8.13. Calculation of air gap flux based on the open-slotted type stator

The basic calculation to investigate the Carter effect on the air gap flux density in open-slotted stator types, as illustrated in Figure 4.58, is performed using the following steps:

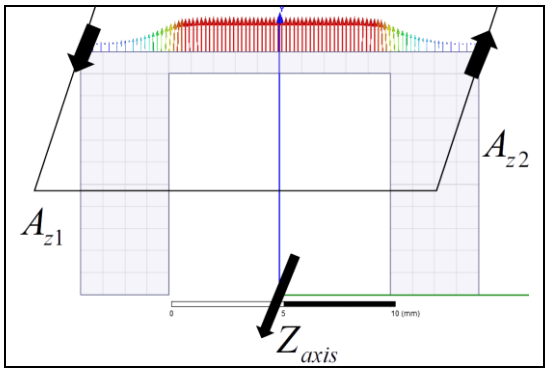


Figure 4.58. Air gap flux density over open-slotted stator [365]

$$\emptyset_{st} = B_{st,av} * (W_t + W_s) L_{stk} = (A_{z1} - A_{z2}) L_{stk} \tag{4.198}$$

$$A_{z1} = \frac{B_{st,av} * (W_s + W_t)}{2} \qquad A_{z2} = -A_{z1} \tag{4.199}$$

where $\emptyset_{st}$:

$B_{st,av}$:

A_{z1} : Magnetic vector potential at point of z1

A_{z2} : Magnetic vector potential at point of z2

4.8.14. Updating process of the design parameters

In analytical design, some parameters, such as effective turns per phase and turns per coil may be fractional. In practical machines, values are adjusted to integers to meet manufacturing requirements. First, the number of turns per coil is converted to a fixed integer value to facilitate manufacturing. Next, the number of effective turns per phase is also adjusted to a fixed integer value. Subsequently, the machine stack length is modified based on the total air gap flux value. The following equations outline the updating procedure:

$$E_{ph} = 4{,}44 * f_s * N_{tph} * k_w * \emptyset_p \tag{4.200}$$

$$\emptyset_p = \frac{B_{av} * \pi DL}{(2p)} \qquad \frac{\emptyset_{p,new}}{\emptyset_{p,old}} = \frac{L_{new}}{L_{old}} \tag{4.201}$$

$$\emptyset_{p,new} = \frac{E_{ph}}{4{,}44 * f_s * N_{tph,new} * k_w} \tag{4.202}$$

where $\emptyset_{(p,new)}$: Updated pole flux (Wb)

$\emptyset_{(p,old)}$: Old pole flux (Wb)

$N_{(tph,new)}$: Updated number of effective turns per phase

L_{new} : Updated stack length (m)

L_{old} : Old stack length (m)

4.8.15. Coil and phase resistance with mean turn length

The approach to calculate coil and phase resistance, as well as the mean turn length, is similar in both PMSMs and BLDCs. The mean turn length, representing the average wire length in a single coil turn, is used to determine the coil and phase resistance. By multiplying the mean turn length by the wire resistivity, the resistance values can be obtained. This approach allows for consistent analysis of the electrical characteristics in both machine types.

5. DESIGN AND OPTIMIZATION OF THE PROPOSED MAGNETICALLY COUPLED STARTER/GENERATOR (DCSG)

This chapter presents a comprehensive overview of the analytical and finite element method-based 2D and 3D numerical analyses conducted on the proposed Magnetically Coupled double stage Starter/Generator. The focus is specifically on both the independent and dependent design of magnetic couplers and Starter/Generators. In addition, this section presents a pivotal component in the form of analytical design and numerical FEM verifications of the retaining sleeve or the containment shroud, which offers a practical solution to a common problem faced in S/Gs. It plays a critical role in the research presented, addressing the potential displacement of the magnetic coupler inner rotor and S/G rotor magnets due to centrifugal force at high speeds.

Additionally, the chapter illuminates the numerical-based analysis software and tools utilized, comparing their efficacy with other software within the field. Finally, the chapter employs both classical and nature-inspired optimization techniques to meticulously refine the final model, significantly enhancing its performance and reliability. This chapter plays a pivotal role in advancing the understanding of the DCSG and provides engineers with essential tools and knowledge to design high-performance hybrid UAVs.

5.1. Overview of Proposed DCSG Model

The thesis workout introduces a smart modular hybrid propulsion system and its management method, designed to enhance efficiency, reduce total system weight, decrease fuel consumption, and increase flight time, particularly for combustion engined aircraft. Section 2 provides a comprehensive overview of the system's contributions to science.

The developed propulsion system incorporates a combustion engine along with multiple modular magnetically coupled Starter/Generator stages that can operate as generators and/or motors. By individually managing all the drive elements, optimal operating ranges can be achieved for both the combustion engine and the modular DCSG stages, catering to various power requirements. Furthermore, the thesis delves into the enhancements made to the system's robustness and reliability in the event of a failure.

Special attention is given to the implementation of magnetic couplers between the piston engine and Starter/Generator stages, aiming to ensure seamless operation and continuity even under challenging circumstances. By integrating these magnetic couplers, the system's fault tolerance and ability to withstand potential failures are significantly improved. Detailed analysis and findings regarding the system's enhanced functionality in failure scenarios are presented in Section 2. The overall system block scheme is depicted in Figure 5.1, providing a visual representation of the system's configuration and components. The system is also accompanied by a TR patent and registration number 2020 22757.

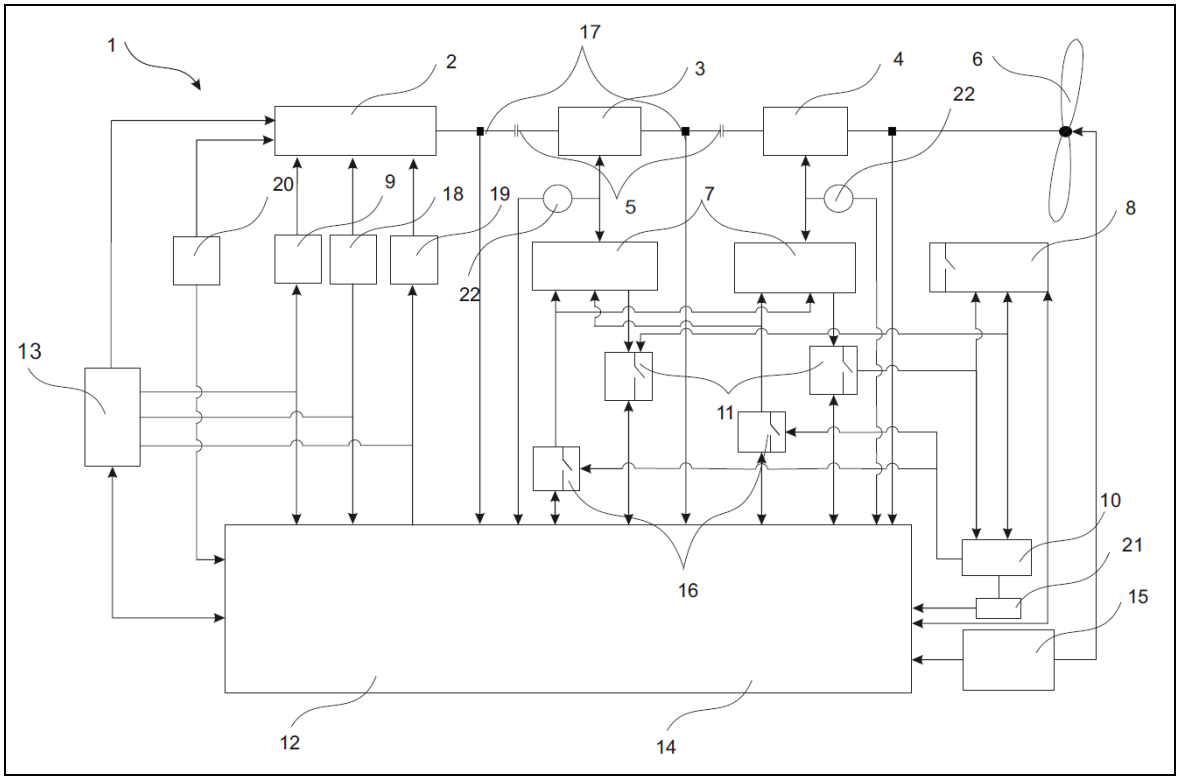


Figure 5.1. Advanced block scheme of the proposed multiple modular DCSG system

where

1	:	Drive system	12	:	Intelligent control unit
2	:	Combustion engine	13	:	External motor controller
3	:	First stage DCSG	14	:	Built-in digital motor controller
4	:	Second stage DCSG	15	:	Propeller pitch controller
5	:	Modular magnetic couplers	16	:	Buck/Boost converter
6	:	Load (Propeller)	17	:	Encoder or speed/position sensor
7	:	Bidirectional converter	18	:	Fuel controller
8	:	Load braking unit	19	:	Ignition controller

9	:	Gas control	20	:	Ambient value measurement unit
10	:	Battery	21	:	Battery measurement unit
11	:	Charging unit	22	:	Current sensors of stages

Figure 5.2 depicts the 3D model of the DCSG structure, which is further explored and analysed in detail within the thesis study.

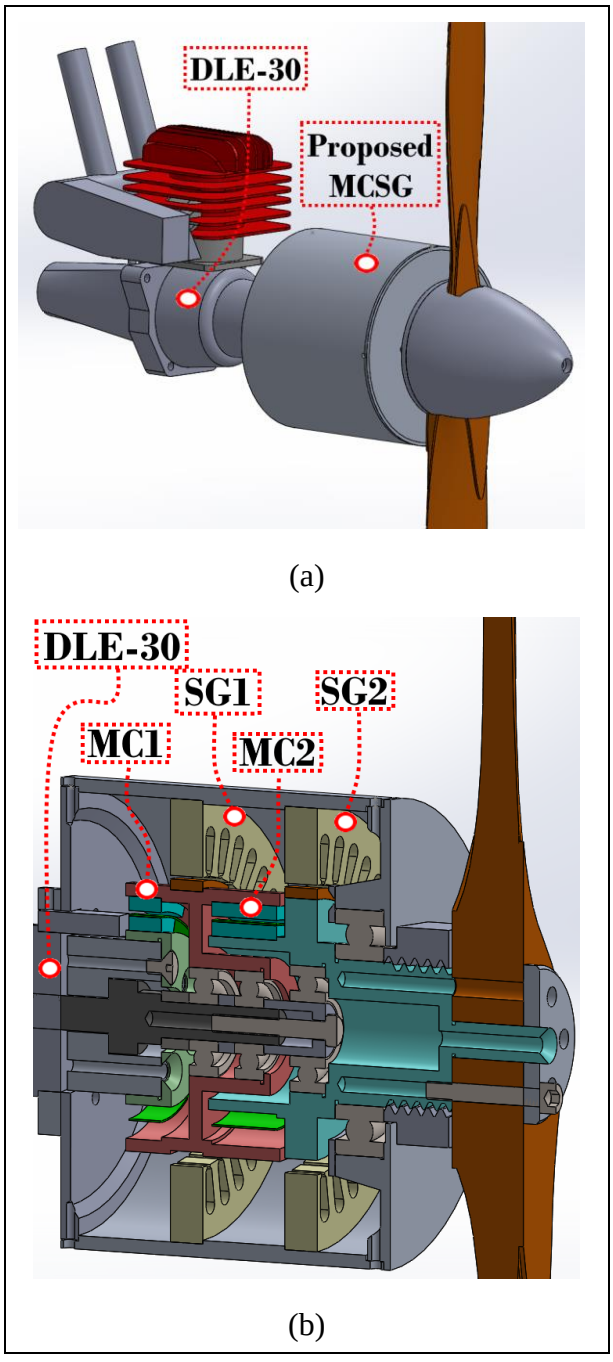


Figure 5.2. Proposed DCSG model workout in the thesis (a) Full 3D model of DCSG structure for DLE-30 (b) Split 3D model of DCSG structure for DLE-30

The thesis primarily concentrates on the analytical and numerical design aspects, as well as the 2D and 3D FEM analysis, optimization, prototype fabrication, and testing of the magnetic coupler and Starter/Generator stages within the smart modular system.

5.2. Design Parameters and Hybridization Rate

The determination of design parameters for the magnetically coupled double-stage Starter/Generator (DCSG) structure is a crucial aspect, dependent on several factors. These factors include the shaft structure and power of the piston engine used in the UAV system, the desired hybridization rate of the UAV, and the propeller selection. The shaft structure of the piston engine directly influences the inner rotor diameters of the magnetic coupler stages, and consequently, the inner rotor diameters of the Starter/Generator stages. The hybridization ratio plays a significant role in determining the required torque values for both the magnetic coupler and Starter/Generator stages within the system.

In addition, the choice of propeller significantly impacts the effective operating zone, which represents the region where the propeller functions optimally and generates thrust. It is important to ensure that the outer diameter of the DCSG system does not exceed the diameter at which the active region of the propeller begins. The maximum outer diameter of the Starter/Generator stages and the DCSG system are thereby affected. Consequently, each DCSG system needs to be customised to meet the specific design requirements; failure to do so will inevitably result in a loss of efficiency.

The central focus of this thesis revolves around the development of a system specifically designed to facilitate the conversion of a conventional mini-scale UAV equipped with a DLE-61 engine into a 50% hybrid UAV. The proposed hybridization entails the removal of the existing conventional engine and the subsequent integration of the DLE-30 engine along with the DCSG system into the UAV. This strategic modification aims to optimize the UAV operational efficiency and performance by leveraging the benefits of hybrid technology.

Furthermore, to delve into the various system responses regarding magnetic torque transmission, the magnetic coupler design is expanded to encompass an additional hybrid UAV configuration, distinct from the one involving the DLE-30 engine.

In this particular configuration, a conventional mini-scale UAV originally equipped with a 3W-70R2 engine is substituted with a 3W-55XI engine, accompanied by the integration of the DCSG system, resulting in a 40% hybridization rate. The identical MC model can also be implemented for the 3W-70R2 engine. Figure 5.3 provides a visual representation of the piston engines with their shaft dimensions where the magnetic couplers are utilized.

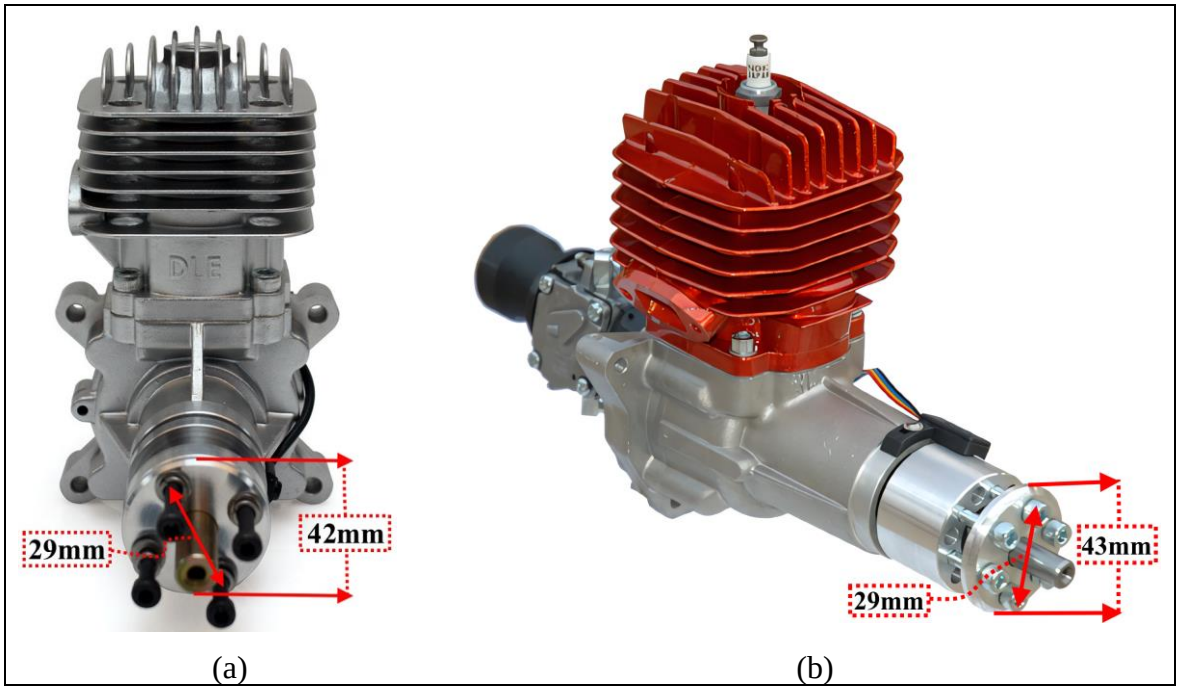


Figure 5.3. The shaft dimensions of the (a) DLE-30 engine (b) 3W-55XI engine

5.2.1. Determination of the inner rotor mounting dimensions of the magnetic couplers

Considering that the DLE-30 and 3W-55XI engine have flange diameters of 42 mm and 43 mm with connection points measuring 29 mm, respectively, it is essential for the magnetic coupler inner rotor flange points to align with the same diameter. Additionally, if the magnetic coupler inner rotor yoke material directly interfaces with the DLE-30 engine shaft, the inner diameter of the magnetic coupler inner rotor must be 42 mm.

5.2.2. Determination of the maximum outer diameter of the DCSG with housing

The hybrid system incorporating the DLE-30 engine is designed to utilize 19x8 propellers, while the hybrid system featuring the 3W-55XI engine employs 24x8 propellers.

In cases where the magnetic coupler inner rotor does not have a direct connection with the DLE-30 shaft, it becomes crucial to meticulously determine the outer diameter of the MC in coordination with the S/G design. This meticulous consideration is undertaken to ensure the proper positioning of the DCSG outside the propeller active area, where torque is generated, as shown in Figure 5.4 [367]. By strategically placing the DCSG outside this region, the risk of interference or disruption to the operation of the propeller is effectively minimized. On the other hand, exceeding the active zone of the propeller can lead to a reduction in torque due to aerodynamic interference, increased turbulence, and inefficient power transfer [368].

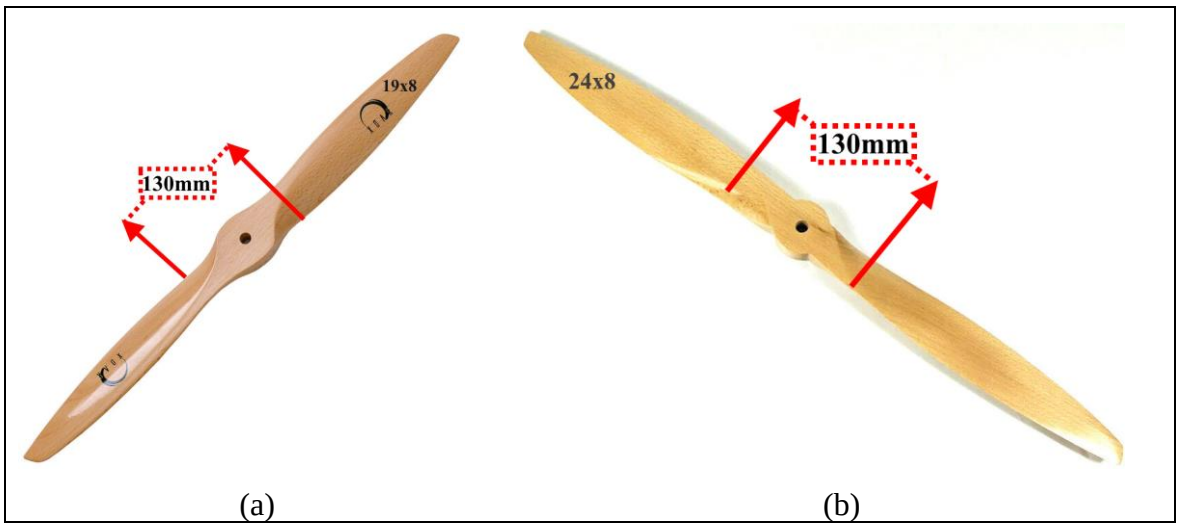


Figure 5.4. Propeller for (a) DLE-30 (b) 3W-55XI

To ensure that the DCSG system remains within the active zone of the propeller, it is imperative to maintain an outer diameter of approximately 130 mm. This requirement is reinforced by the findings presented in Sections 4.10 and 4.11, which highlight the significance of minimizing power losses associated with the BLDC and PMSM outputs while maximizing torque density and unit volume power density. Therefore, the outer diameter of the DCSG, including the housing, is constrained to 130 mm to uphold the desired performance parameters. This limitation imposes a maximum outer diameter of 74 mm for the MC stages, ensuring compliance with the specified restriction.

In the pursuit of performance enhancements, increasing the length of the system can present challenges in terms of preserving structural integrity, ensuring optimal weight distribution, and maintaining aerodynamic efficiency. No mandatory axial length limitations exist, but prioritizing a compact and concise system design is prudent to address potential issues.

5.2.3. Torque and speed requirements of DCSG stages based on hybridization rate

The determination of torque and speed requirements for magnetic couplers of the DCSG stages is dependent on the performance data of the piston engine when paired with an appropriate propeller. These data serve as a crucial basis for understanding the engine characteristics, including its torque output and rotational speed. On the other hand, the performance data of piston engines can vary depending on the specific propeller with which they are paired. Different propellers have distinct characteristics that can influence the engine performance in terms of torque, speed, and overall efficiency.

The torque and speed requirements for the Starter/Generator are determined by considering both the performance values of the piston engine and the hybridization ratio. By analysing the performance characteristics of the engine, such as its torque output and rotational speed, in conjunction with the desired level of hybridization, the specific requirements for the S/G can be accurately determined. The DCSG stages are illustrated in Figure 5.5.

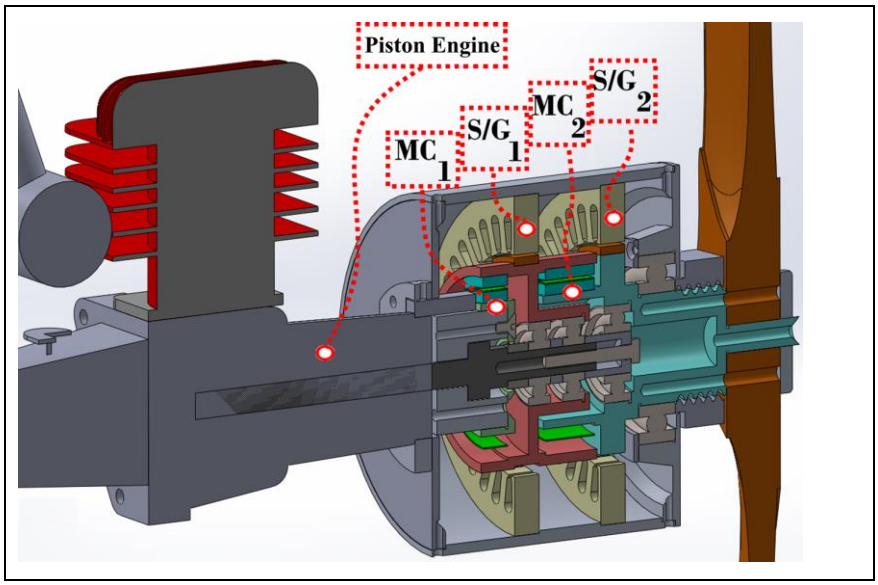


Figure 5.5. Stages of the DCSG model

Through a careful analysis of the engine performance data in tandem with the desired system performance, precise torque and speed requirements for the DCSG stages can be derived. This process is essential because it allows for the customization of the DCSG design to meet the system-specific demands while ensuring the attainment of optimal performance and efficiency.

Table 5.1 presents the maximum performance data for the DLE-30 engine paired with a 19x8 propeller and the 3W-55XI engine paired with a 24x8 propeller.

Table 5.1. Maximum performance data of DLE-30 with a 19x8 propeller and 3W-55XI with a 24x8 propeller

Brand	Diameter (")	Pitch	Blades	Speed (rpm)	Thrust (kg.f)	Torque (N.m)	Power (kW)
DLE-30	19	8	2	7250	6	3.3	2.5
3W-55XI	24	8	2	6250	11.5	4.3	2.8

Table 5.2 summarizes the performance requirements of the DCSG stages, taking into consideration the hybridization rate, working speed and torque capability of the engines.

Table 5.2. Torque and speed requirement of DCSG stages for DLE-30 and 3W-55XI

	DLE-30 Hybrid	3W-55XI Hybrid
Maximum piston engine speed (rpm)	7250	6500
Maximum piston engine torque (N.m)	3.3	4.4
Maximum piston engine power (kW)	2.5	3
Aspect ratio for each stages of MC	1.2	
Safety factor for each stages of MC	1.2	
Hybridization rate based on 1-Stage DCSG (%)	50	40
MC1, minimum torque requirement (N.m)	4.75	6.4
SG1, minimum torque requirement (N.m)	Motor / Generator Mode: 2.1 / 2.2	
MC2, minimum torque requirement (N.m)	6.9	8.5
SG2, minimum torque requirement (N.m)	Motor / Generator Mode: 2.1 / 2.2	
Rated speed of DCSG, motor mode (rpm)	4500	
Rated speed of DCSG, generator mode (rpm)	5500	
Propeller maximum transferable torque (N.m)	9	10.6

To ensure a robust and reliable system, a factor of safety of 1.2 was incorporated for each stage of the DCSG.

Additionally, an aspect ratio of 1.2, representing the FEM design error rate factor, was considered. By incorporating these factors, the minimum requirements for the system were established, aiming to mitigate potential turbulence and adverse effects.

Conducting thorough testing, the operating speed ranges for the DLE-30 engine were evaluated within the range of 1600-7250 rpm, while the 3W-55XI engine exhibited operating speed ranges of 2000-6250 rpm. The required minimum torque density is 18.5 N.m/kg. Taking these factors into account, the designs of the DCSG stages are meticulously crafted to adhere to these established values. This ensures that the DCSG stages are optimized to meet the required torque density, operating speed ranges, and others, thus aligning with the performance requirements set forth by the UAV manufacturer. The design scheme block diagram is presented in Figure 5.6, illustrating the overall interconnections of the system.

5.3. Design Methodology

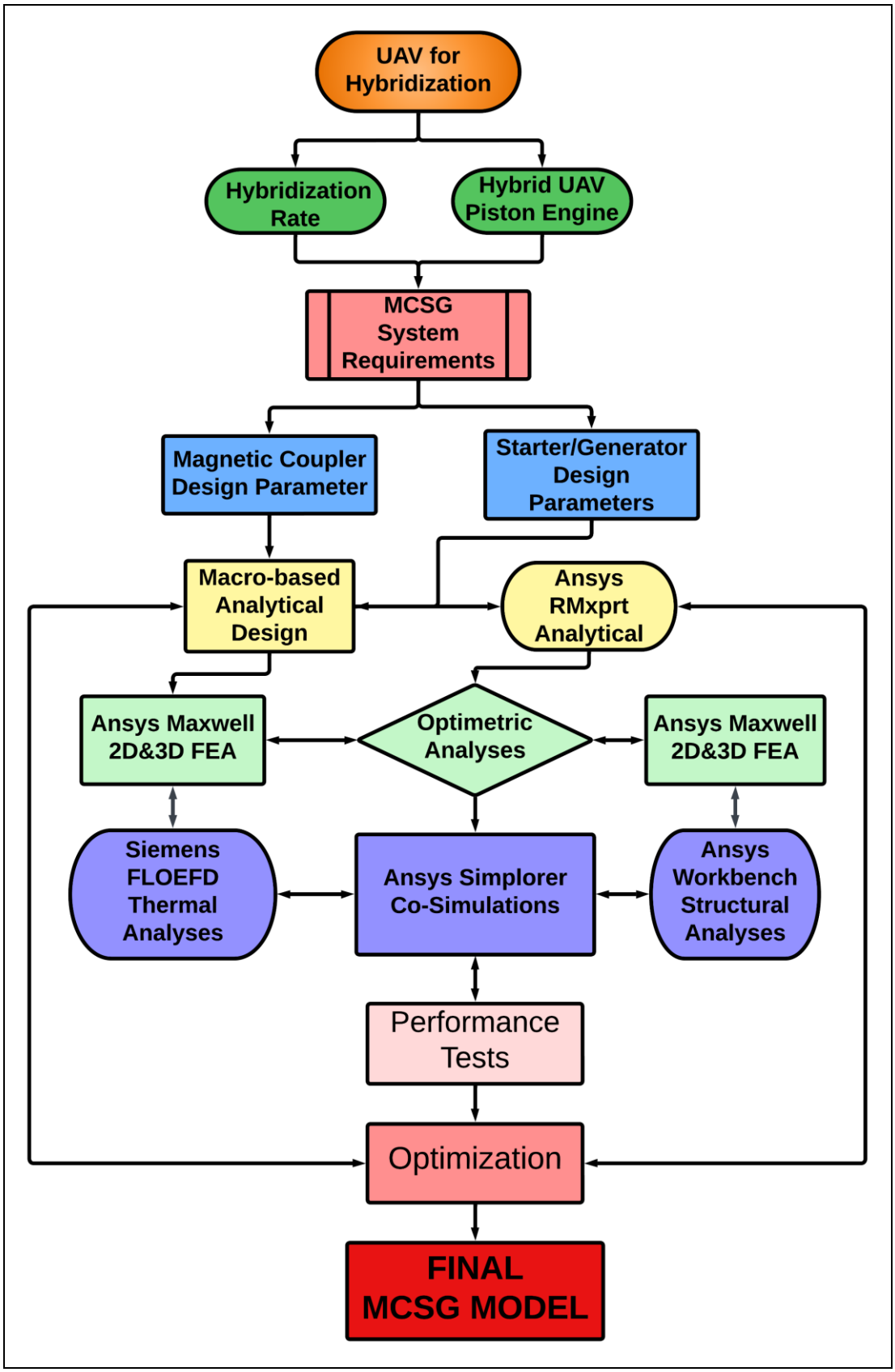


Figure 5.6. Design flowchart of the DCSG system

The design process of the double stage magnetically coupled Starter/Generator (DCSG) structure involved macrobased analytical designs of the Magnetic Coupler (MC) and Starter/Generator (S/G) utilizing Octave. For the S/G, analytical sensitivity analysis was conducted using Ansys RMxprt. To further analyse and optimize the electromagnetic performance of both the MC and S/G stages, electromagnetic FEM analyses were carried out using Ansys Maxwell 2D and 3D v2022R1.

Thermal Computational Fluid Dynamics (CFD) analyses were performed to assess the thermal behavior of the DCSG structure, as well as the magnetic coupler and Starter/Generator stages, employing Siemens FloEFD v2021.R2. Additionally, structural FEA was conducted using Ansys Workbench. CAD drawings of the entire model were created using Solidworks v2017. These comprehensive analyses and design tools were employed to ensure a well-informed and optimized DCSG structure.

Ansys RMxprt, offers versatility in the preliminary dimensioning of electrical machines, providing a wide range of machine design templates, power electronics, and control circuit options. Additionally, it enables the solution of more intricate circuits by seamlessly transferring them to the Simplorer interface. This capability expedites the design and optimization process, leveraging analytical calculations within the solution. With its extensive features, the software facilitates accelerated and efficient design and optimization.

Ansys Maxwell 2D and 3D, is a powerful and interactive software designed to solve a wide range of electromagnetic problems using the FEM. This high-performance software efficiently addresses electrostatic, magnetostatic, eddy current, and transient problems. By utilizing Maxwell equations within a finite space domain and incorporating appropriate boundary conditions, the software effectively tackles these complex problems. Moreover, designers have the flexibility to input initial conditions to further extend the solution when needed, enhancing the versatility and adaptability of the software [369].

Simcenter FLOEFD is a comprehensive CFD software with multiphysics capabilities that is seamlessly integrated within CAD environments. This powerful tool caters to the needs of both designers and analysts, providing a streamlined workflow. By frontloading fluid flow simulation and thermal analysis and utilizing native CAD geometry, it significantly reduces development time by an impressive 65-75% when compared to traditional CFDs [370].

The design process for the magnetically coupled double stage Starter/Generator (DCSG) system begins with the selection of the UAV to be hybridized, followed by determining the hybridization ratio and selecting a compatible piston engine for the hybrid UAV. The main topology of the DCSG system is established based on the performance values obtained by testing the new piston engine of the hybrid UAV. Subsequently, design parameters for both the magnetic coupler (MC) and the Starter/Generator (S/G) stages are determined. Detailed information regarding the MC and S/G topologies, the eligible materials, and the power electronics system is detailed in Section 3 of the document. To avoid redundancy, these details are not reiterated here. Interested readers are encouraged to refer to Section 3 for comprehensive insights into these aspects of the system design.

Macrobased analytical design is conducted for both the magnetic coupler and Starter/Generator stages, with initial dimensions entered into the Ansys analytical analysis environment. The Ansys RMxprt module is utilized for analytical analysis of the S/G stages, while the magnetic coupler stages are directly incorporated into the 2D and 3D Finite Element Method (FEM) analysis environment.

Detailed 2D and 3D FEM analyses are performed using Ansys Maxwell 2D and 3D, incorporating optimization assignments and analysis to obtain approximately optimal design parameters. The resulting model is cosimulated with the power electronics system using Ansys Simplorer, and thermal and structural analyses are conducted using Siemens FLOEFD software and Ansys Workbench, respectively.

If the model fails the thermal and structural analyses, the 2D and 3D optimetric analyses are repeated based on new data. Performance tests are carried out on the problem-free model using a direct-dynamic test system. If the model fails the performance tests, cosimulations are re-evaluated. Finally, the optimized final model is achieved through optimization techniques, considering objective functions such as maximum efficiency, minimum weight, or maximum torque density.

This comprehensive design process ensures that the DCSG system is thoroughly analysed, optimized, and validated to meet the desired performance objectives while considering thermal, structural, and functional requirements. The design methodology flow is depicted in Figure 5.7, illustrating the sequential steps and processes involved in the design.

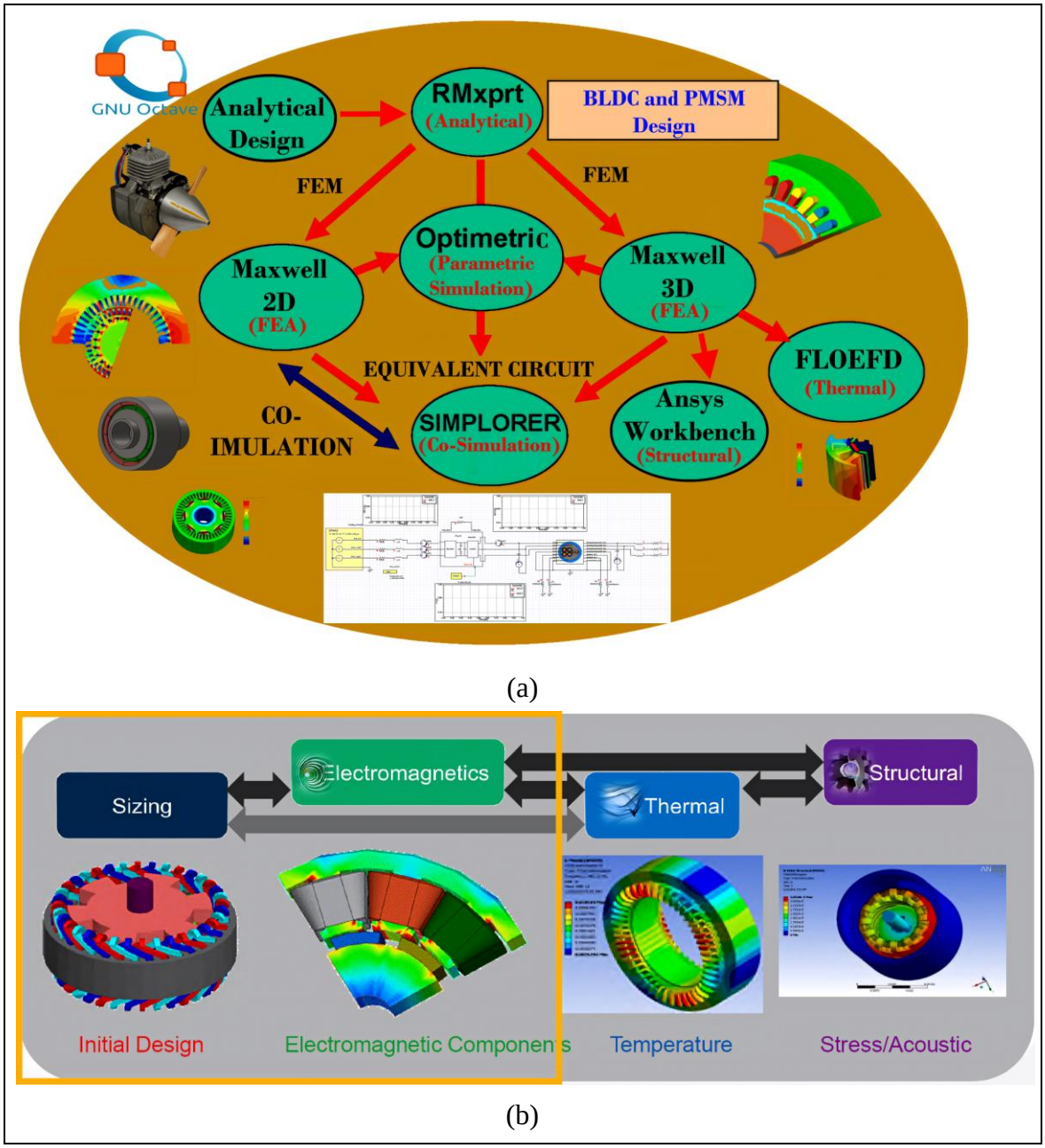


Figure 5.7. Design scheme of DCSG system (a) Design methodology (b) Design flowchart

5.4. Design of Active Radial Magnetic Couplers for DLE-30 and 3W-70R2 Engine

The comprehensive system model comprises several components, including the outer rotor yoke (1), outer rotor permanent magnets (2), retaining sleeve and air gap (3), inner rotor permanent magnets (4), inner rotor yoke (5), stamp (6), piston engine shaft (7,8), piston engine stationary body (9), and S/G parts (10) [265]. These components are illustrated in Figure 5.8 (a), which shows a single stage of the DCSG.

The synchronous MC is designed to meet one-to-one speed requirements, and the radial type is preferred among synchronous types due to its cylindrical shaft motion.

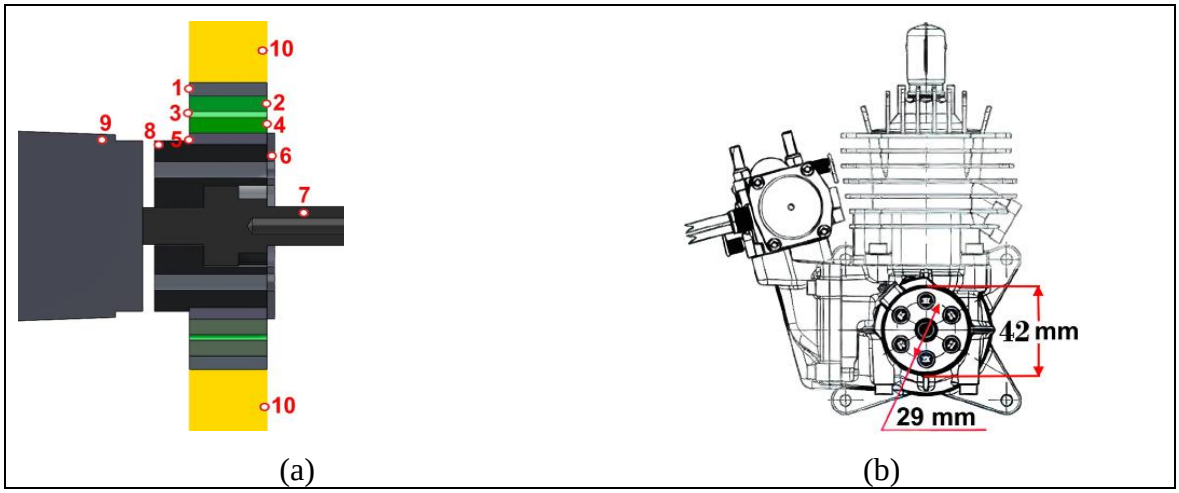


Figure 5.8. Magnetic coupler stage for DLE-30 and 3W-70R2 (a) Model (b) Dimensions

In addition to the design parameters outlined in Table 5.2, the consideration of turbulence and correction factors becomes imperative in mitigating disturbances such as sudden G-turns and weather-related overloads. Hence, an initial selection of a correction factor of 1.2 and a turbulence coefficient of 1.1 is incorporated. As a result, the minimum torque requirements for the magnetic couplers are adjusted to 10 N.m and 20 N.m for the first (MC_1) and second (MC_2) stages of couplers, respectively, as described in Figure 5.5. These updated torque values are denoted as the maximum or pullout torque within the design.

5.4.1. Analytical design based on the Virtual Work method

The force acting on a single pole can be determined by applying the Virtual Work principle [309], as expressed in Eq. 5.1. This principle takes into account the change in stored energy within the air gap caused by a small axial displacement between the poles. Similarly, the torque can be calculated by substituting the axial displacement (x-dx) in the equation with the angular displacement (Θ-dΘ) [265].

$$F_{single_pole} = \frac{dW}{dx} = \frac{(B_{g1})^2(V_{ag})}{2\mu_0(x - dx)} \qquad T = \frac{dW}{d\Theta} \tag{6.1}$$

where F_{single_pole}: force exerted on a single-pole (N)

dW: change in stored energy in the air gap (J)

B_{g1}: effective air gap flux density (T) – [the fundamental component]

V_{ag}: volume of air gap (m^3)

μ_0: permeability of free space (4π10^-7 H/m)

x: pole arc length (m)

dx: small displacement distance of a pole (m)

T: torque exerted on a single-pole (N)

If the force acting on a pole and the small displacement distance are known, the required air gap volume can be determined by assuming an initial air gap magnetic flux density of 0.6 T to prevent demagnetization of the permanent magnets. Based on this assumption, analytical calculations, summarized in Table 2, are performed using the critical angle.

Table 5.3. Analytical calculations for preliminary dimensions

Virtual Work Method	Analytical Virtual Work Method	
Output	8-pole	10-pole
Air gap volume, required	3427 mm^3	2192 mm^3
Length of the model, required	12.12 mm	7.75 mm
(x-dx), equals dx at critical angle	11.78 mm	9.42 mm
(Θ-dΘ), equals dΘ at critical angle	0.3925 rad.	0.314 rad.
Critical angle	22.5 (Mdeg)	18 (Mdeg)
Force on EAG based on a single pole	41.67 N	33.33 N
Total force on EAG based on total pole number	333.33 N	
Preliminary Design Assumptions		
Effective air gap radius		30 mm
Average air gap flux density		0.6 T
Air gap length/Retaining sleeve thickness		1/0.5 mm
Pullout torque, required		10 N.m
Magnet grade		N48H-60deg

In this case, (x-dx) is directly equal to dx, and similarly, (Θ-dΘ) is directly equal to dΘ. Here, Θ represents the mechanical angle of a pole, and dΘ represents the small angular displacement in radians. Figure 5.9 shows the Virtual Work method parameter definitions.

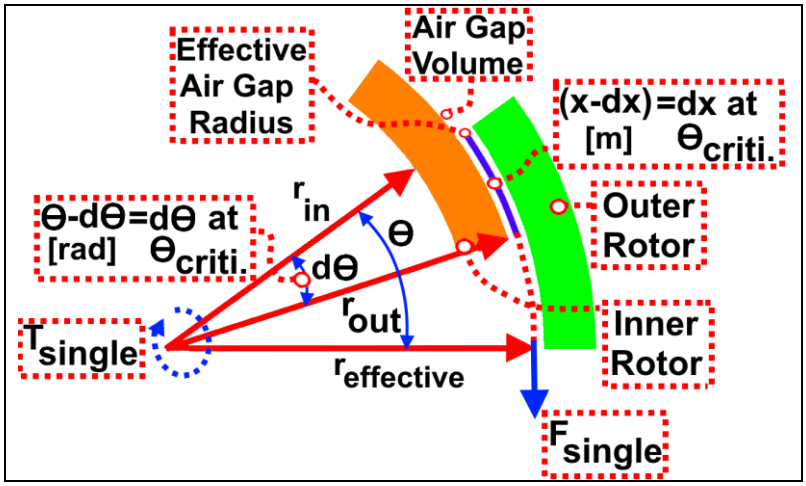


Figure 5.9. Definition of parameters for Virtual Work method

The air gap volume refers to the space between the outer rotor inner diameter and the inner rotor outer diameter. If the inner rotor is directly mounted on the piston engine shaft, the inner diameter of the inner rotor (r_{in}) can be at least 42 mm, as shown in Figure 5.8. The effective air gap, which is the middle of the air gap, is denoted by the effective air gap radius ($r_{effective}$) in analytical calculations of force or torque on the rotors, as depicted in Figure 5.9.

Considering the thickness of the inner rotor yoke and magnets, reffective is initially chosen as 30 mm. The sleeve thickness is assumed to be 0.5 mm based on experience. As a result, the total air gap clearance with the air gap is 1.5 mm. Accordingly, the corresponding inner rotor outer diameter and outer rotor inner diameter are found to be 29.25 mm and 30.75 mm, respectively. The critical angle ($\Theta_{critical,Mdeg}$), calculated as shown in Eq. 6.1, corresponds to an electrical angle (Θ_{Edeg}) of 90°, where the pullout torque is obtained.

$$\theta_{critical,Mdeg} = \frac{360^\circ}{(2p) * 2} \qquad \theta_{Edeg} = \frac{(2p)}{2} * \theta_{Mdeg} \tag{6.2}$$

Here, Mdeg and Edeg represent the mechanical and electrical degrees, respectively, and (2p) denotes the total number of poles. For a 10-pole configuration, the values for Θ and $\Theta_{critical}$ are 36 Mdeg and 18 Mdeg, respectively. For an 8-pole configuration, the values for Θ and Θcritical are 45 Mdeg and 22.5 Mdeg, respectively. The corresponding values for Θ and dΘ at the critical angle in radians are depicted in Figure 5.9, with 0.628 and 0.314 for 10-poles, and 0.785 and 0.3925 for 8-poles, respectively.

Similarly, at the critical angle, the pole arc length and small displacement distance are determined to be 18.85 mm and 9.42 mm for the 10-pole configuration, and 23.56 mm and 11.78 mm for the 8-pole configuration, respectively. The total force is the force exerted on the Effective Air Gap (EAG) used to calculate the force on the rotors, taking into account the total number of poles. Considering that a torque of 10 N.m is needed, the ideal total force is calculated as 333.33 N by determining the effective air gap radius ($r_{effective}$). Consequently, the force exerted on a single pole is 33.33 N for the 10-pole configuration and 41.67 N for the 8-pole configuration. The respective air gap volumes are calculated as 2192 mm^3 for the 10-pole configuration and 3427 mm^3 for the 8-pole configuration. As a result, the required model length is determined to be 7.75 mm for the 10-pole configuration and 12.12 mm for the 8-pole configuration, as shown in Table 5.3.

5.4.2. Optimetric design approach based on Maxwell 2D magnetostatic FEA

The Maxwell 2D solutions employed in this thesis utilize optimetric assignments and sensitivity tools. The magnetic coupler model is fully parameterized, allowing for multiparameter analyses to investigate the impact of various variables. FEM is a robust and accurate technique utilized to calculate the maximum transferrable torque or pullout torque at the critical angle. By applying a denser mesh as depicted in Figure 5.10 (a) for critical areas such as the air gap, the analysis error is reduced by approximately 10%.

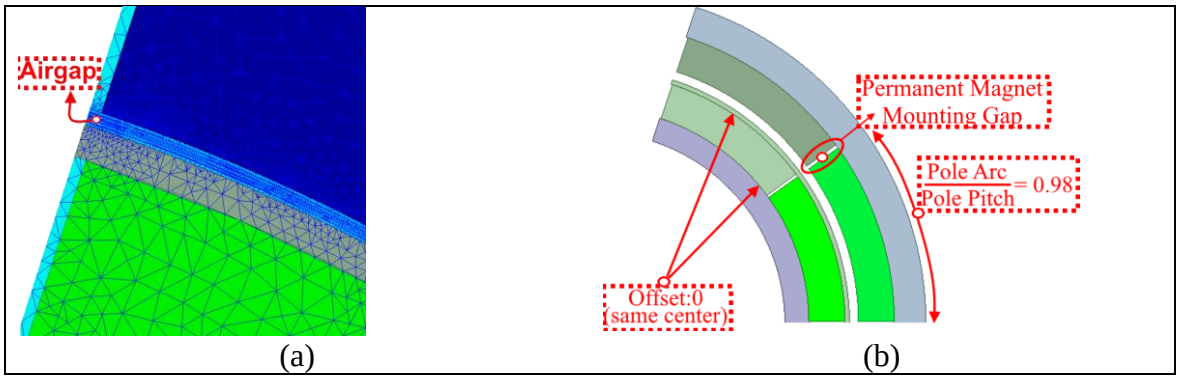


Figure 5.10. (a) Mesh distribution of model (b) Pole embrace and pole arc offset definition

FEAs are performed using two solution types: transient for the dynamic state and magnetostatic for the static state. To facilitate assembly and production requirements, the pole embrace and offset are set to 0.98 and 0, respectively, as illustrated in Figure 5.10 (b).

The embrace refers to the ratio of the pole arc to the pole pitch, while the offset defines the concentricity of the permanent magnets.

5.4.3. Pullout torque investigation based on outer diameter and length

The design process should commence from the outer rotor and progress towards the inner rotor, deviating from the conventional method, primarily due to limitations imposed on the outer rotor outer diameter. In Figure 5.11 (a), the pullout torque is examined by altering both the coupler length and the outer rotor outer diameter. The outer rotor outer diameter is adjusted within the range of 66 mm (minimum possible) to 74 mm (maximum) at the critical angle, considering a 10-pole configuration. Meanwhile, the coupler length varies between 9 mm and 13 mm. Furthermore, Figure 5.11 (b) presents an analysis of the torque density based on the outer rotor outer diameter, with a fixed coupler length of 10 mm.

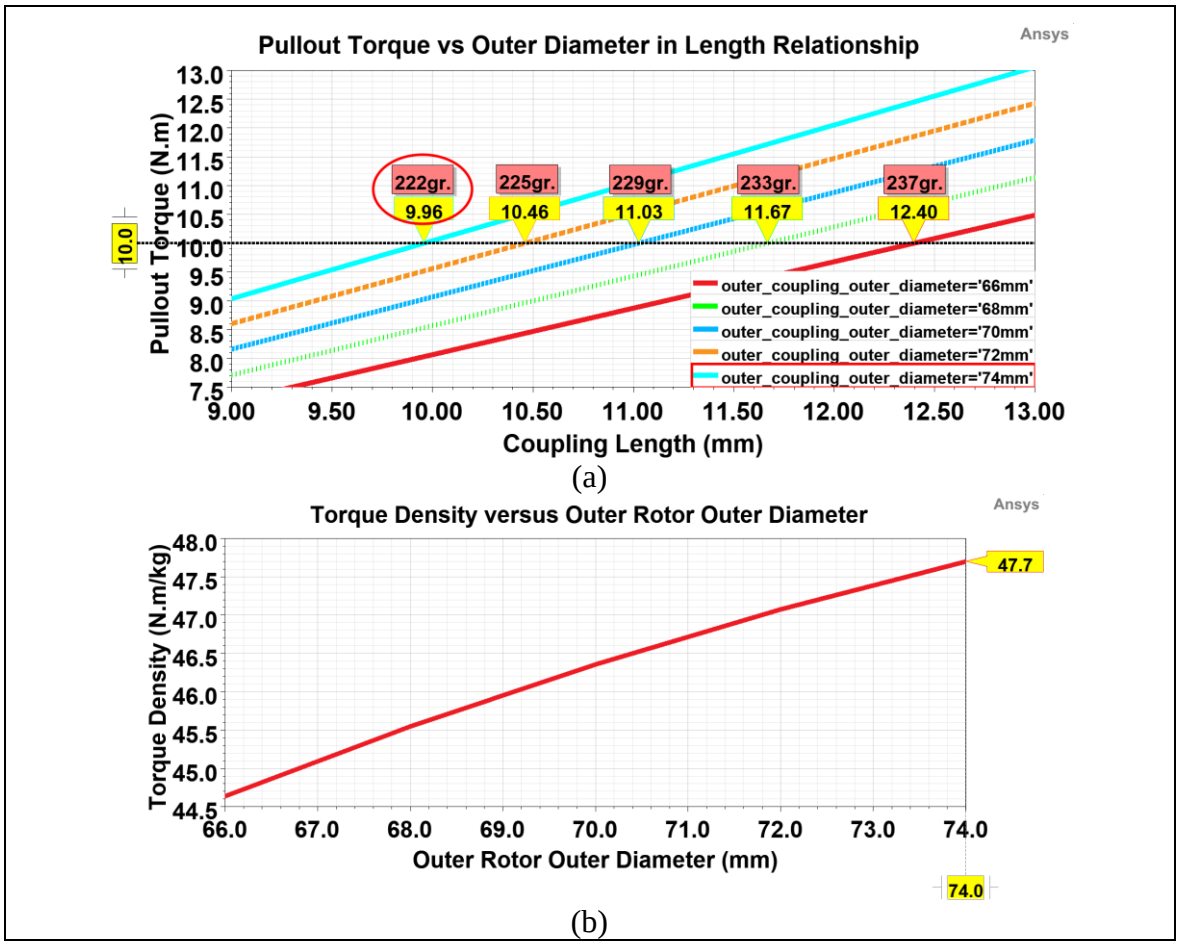


Figure 5.11. (a) Pullout torque in outer diameter and length (b) Torque density depending on the outer diameter of the outer rotor

In Figure 5.11 (a) and (b), specific dimensions are assigned to the components involved. The thicknesses of the PMs, rotor yokes, retaining sleeve, and air gap length are uniformly set at 4 mm, 4 mm, 0.5 mm, and 1 mm, respectively. Taking into account the mounting points, the minimum feasible inner diameter of the inner rotor is determined to be 31 mm. Consequently, the corresponding minimum outer diameter of the inner rotor yoke is 39 mm, while the inner diameter of the outer rotor PMs measures 50 mm.

However, considering the achievement of maximum torque density at the highest outer rotor outer diameter, as depicted in Figure 5.11 (b), an outer diameter of 74 mm and a corresponding length of 10 mm are selected. Maintaining the outer diameter of the outer rotor near the limits has a beneficial impact on the operation of the piston engine. It enhances mechanical strength and contributes to the flywheel effect.

5.4.4. Determination of the PM thickness based on the static pullout torque

The static torque, also known as locked-rotor torque, refers to the torque exerted by the system when it is in a locked-rotor state. Figure 5.12 investigates the static pullout torque for various thicknesses of inner and outer PMs. It is evident that the desired torque can be attained with different magnet thicknesses. However, for the sake of assembly convenience and practical aspects, a thickness of 4 mm is preferred for both the inner and outer PMs. This preference is indicated by the red markers in Figure 5.12, as it ensures that the required torque can be achieved without compromising the ease of assembly and manufacturability.

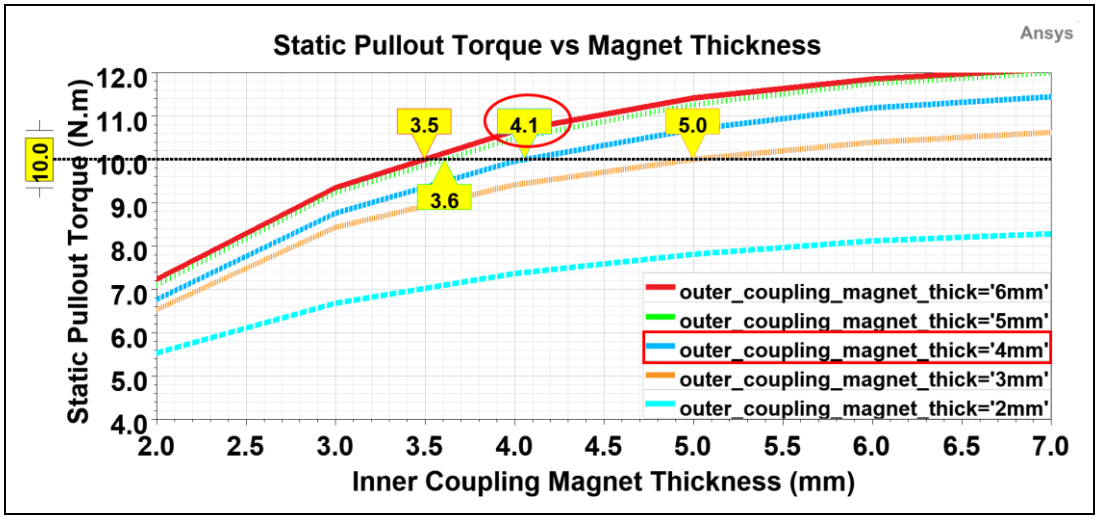


Figure 5.12. Static pullout torque with respect to changes in PM thickness

5.4.5. Locked-rotor torque investigation based on torque angle

The torque angle is the mechanical angle between the inner and outer rotor d-axes during the loading of the MCs. It represents the transferable torque through the MCs and determines the overload capacity of the system. Figure 5.13 investigates the locked-rotor torque as it varies with the torque angle. At the critical angle, a maximum torque of 10.15 N.m is achieved, satisfying the requirements. MCs are typically operated close to the critical angle to achieve high torque density. However, it should be noted that operating at the exact critical angle may render the coupler susceptible to turbulence-induced desynchronization. In aviation applications, it is advisable to provide the pullout torque slightly below the critical angle or consider coefficients that account for the effects of turbulence. This ensures reliable operation and mitigates potential issues arising from turbulent conditions.

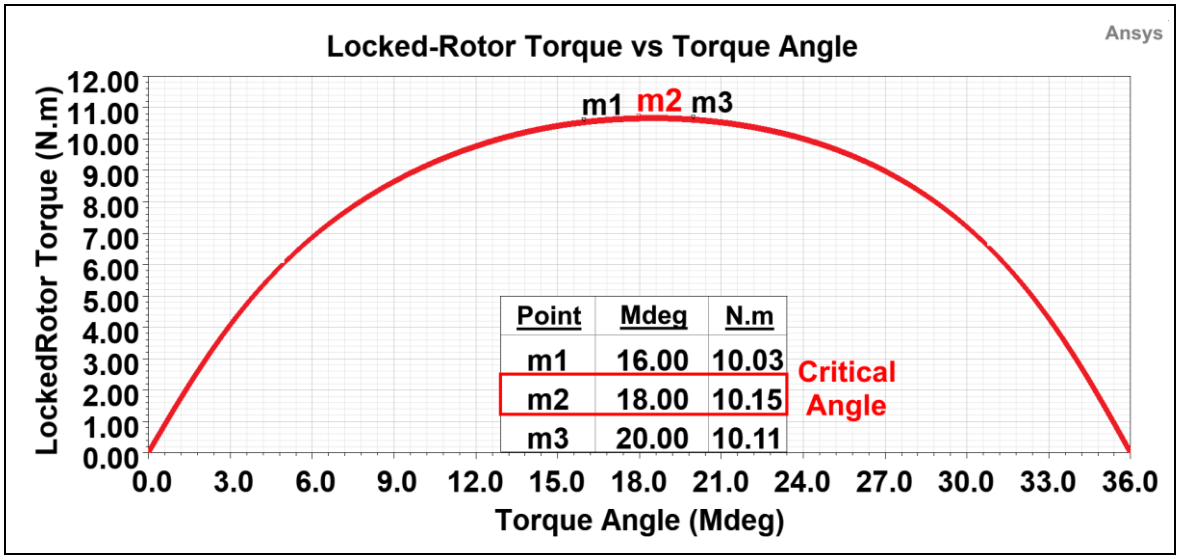


Figure 5.13. Locked-rotor torque depending on torque angle

5.4.6. Rotor yoke thickness determination

The thickness of the rotor yokes plays a significant role in determining the torque output of the system. It directly impacts the average air gap flux density by influencing the total reluctance. Additionally, the rotor yokes are constrained by the outer diameter limitation, which in turn affects the effective air gap radius and ultimately the torque density through variations in the rotor diameters. Through analysis, as depicted in Figure 5.14, it has been determined that the optimal thicknesses for the rotor yokes are 3.5 mm and 3 mm.

These values are highlighted in red in the below figure. Selecting minimum yoke thicknesses meets the maximum torque requirement while minimizing the overall weight.

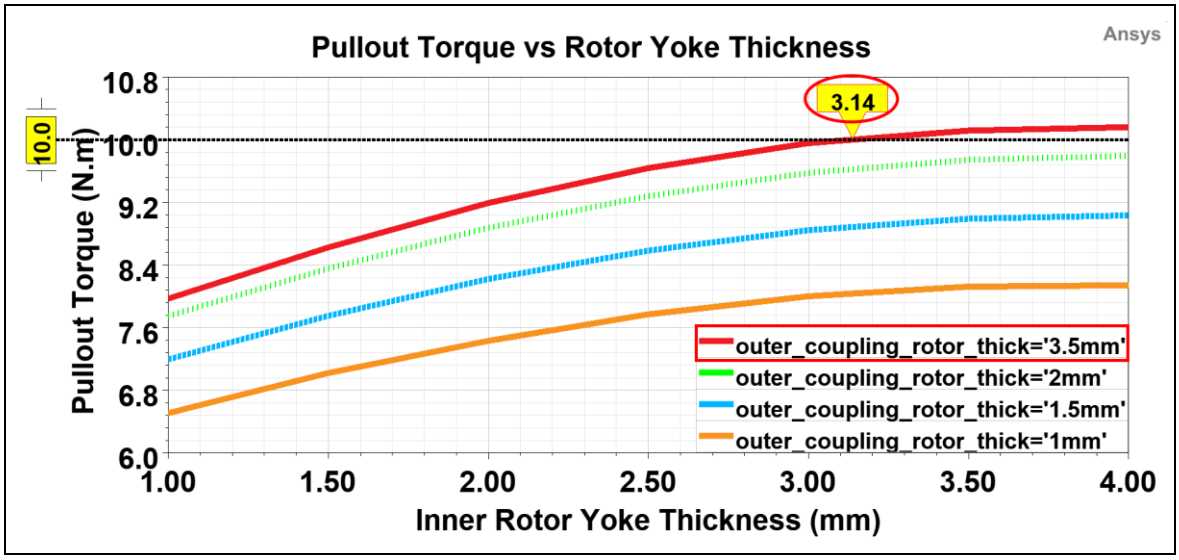


Figure 5.14. Pullout torque with respect to changes in rotor yoke thickness

It is worth noting that in yokeless designs, where the use of magnetic materials is restricted, achieving the same torque would necessitate thicker PMs. Therefore, the utilization of yokes allows for a more efficient and lightweight design, resulting in improved performance.

Figure 5.15 (a) and (b) examine the magnetic flux density and distribution, respectively. Efforts can be made to reduce leakage fluxes by optimizing the embrace and magnet housing, as seen in red in Figure 5.15 (b). In coupler applications, utilizing Steel1020 for rotor yokes can be more advantageous than electrical steels due to its high saturation level of 2.5 T.

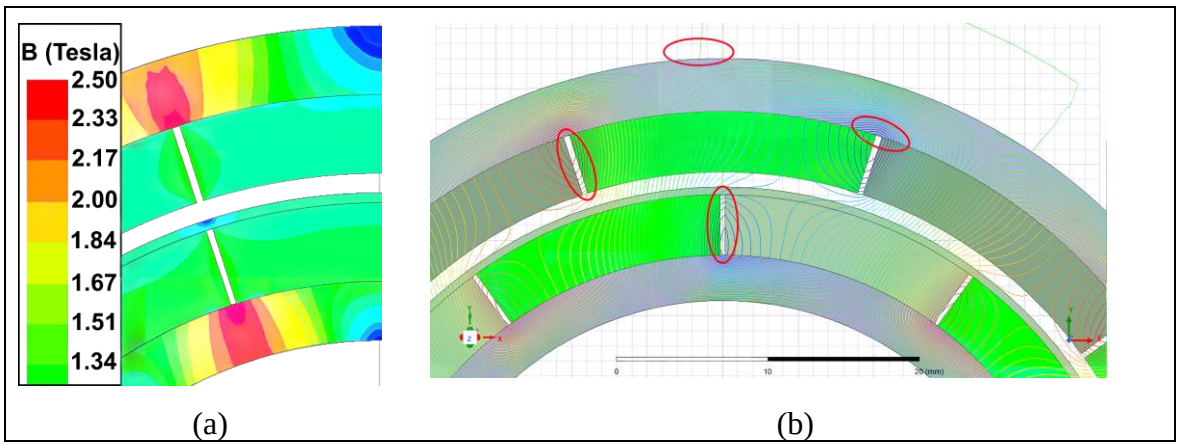


Figure 5.15. (a) Flux density of rotor yokes (b) flux distribution for the 10-pole configuration

Operating at saturation points may not always result in higher torque density but can lead to lower weight. The air gap flux density at no-load and full-load conditions is analysed in Figure 5.16, showing a decrease as the MC is loaded but remaining below saturation.

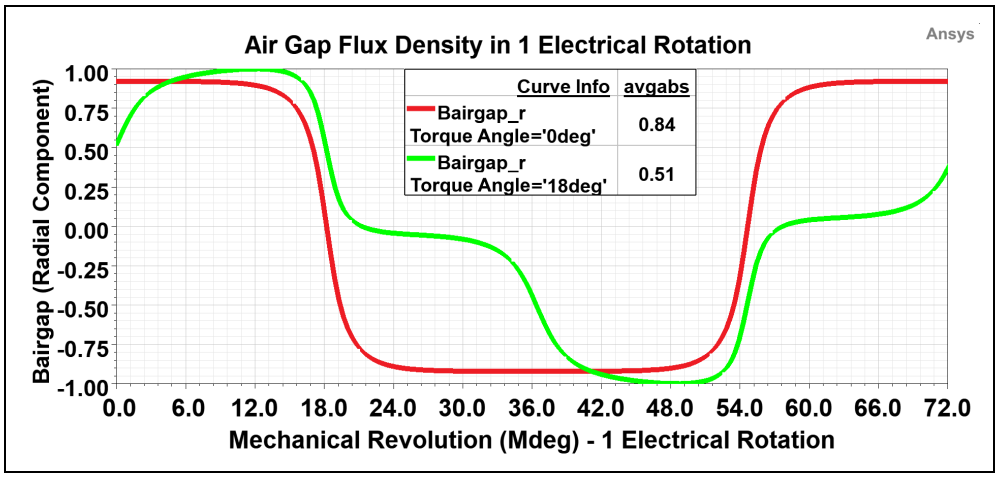


Figure 5.16. Air gap flux density distribution at no-load and full-load

5.4.7. Investigation of the magnetic coupler model length

To achieve higher torque within the outer diameter limitation, the length of the MC needs to be increased, enabling modular operation. Figure 5.17 demonstrates that doubling the length results in approximately double the torque. Therefore, the second magnetic coupler is designed with a model length of 20 mm to accommodate the desired torque increase.

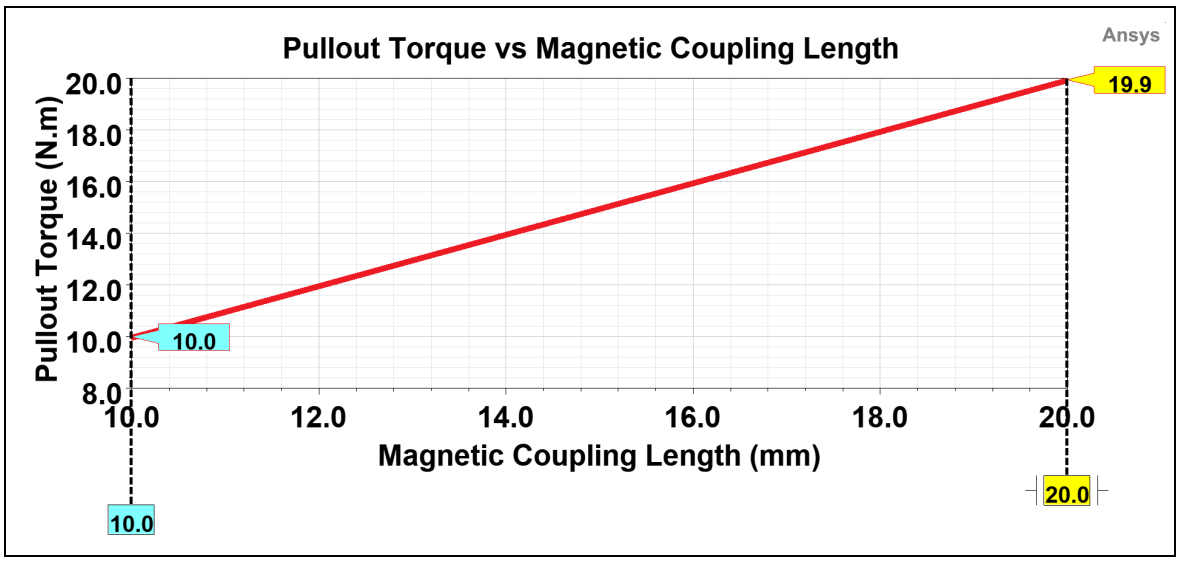


Figure 5.17. Pullout torque depending on coupler length

5.4.8. Determination of the pole numbers based on pullout torque

In synchronous magnetic couplers with a 1:1 speed conversion ratio, the torque is influenced by the number of rotor poles. Increasing the pole number enhances the torque by increasing the air gap flux density, up to a point where leakage fluxes become dominant. Additionally, the presence of mounting and weight reduction holes in the rotor impacts the selection of the pole number at which maximum torque is achieved.

As depicted in Figure 5.18, the pullout torque is attained when the number of poles is 18. However, a higher pole number also implies increased challenges in mounting, particularly for the outer rotor magnets. Considering the balance between torque requirements and practical considerations, a pole number of 10 is chosen because it meets the system torque and weight requirements to a satisfactory degree. If 8 poles were to be used, the model length would need to be increased by 20% to achieve the required torque, resulting in an approximate 23% increase in total weight.

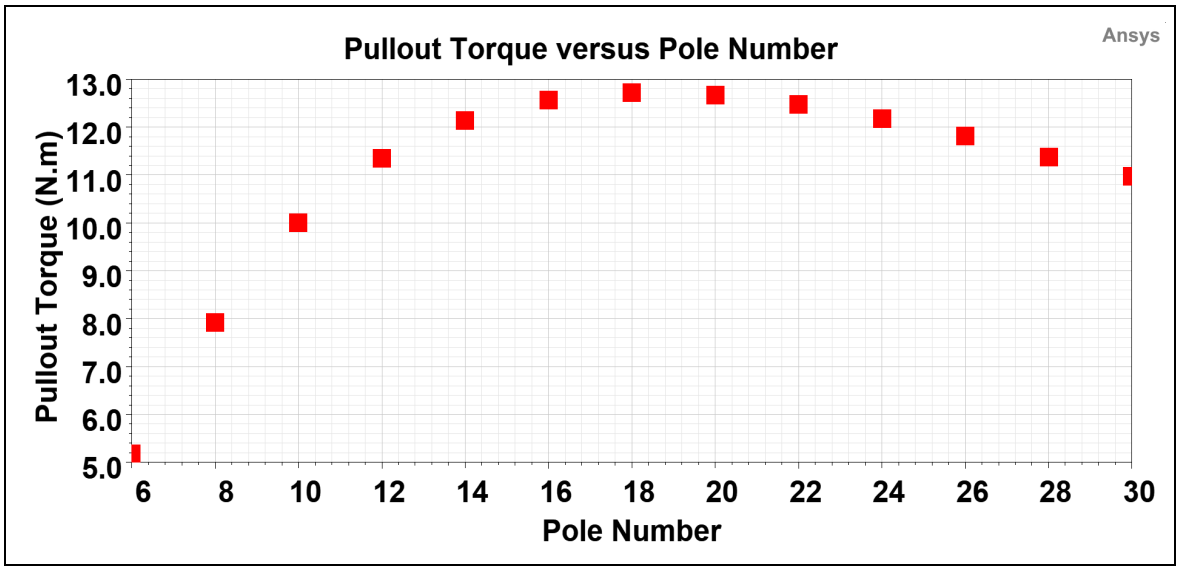


Figure 5.18. Pullout torque depending on the number of poles

5.4.9. Optimetric design approach based on Maxwell 2D transient FEA

The dynamic behavior of the MC is investigated using Maxwell transient simulation, taking into account the moment of inertia, mechanical losses, and the type of load applied.

To ensure realistic analyses, the model is created in Solidworks, and the moments of inertia for the inner and outer rotors are determined to be 0.34 kg·cm² and 1.55 kg·cm², respectively. Mechanical losses, including bearing losses, windage, and friction losses, are typically estimated to be between 2% and 4% of the output power in the absence of a computational fluid dynamics (CFD) solution, similar to rotating electric machines. In this study, a 3% mechanical loss is assumed, resulting in a total mechanical loss of 0.000478 W/(rad/sec)².

Dynamic torque tests are conducted using N48H magnets at a temperature of 60°C, which allows for effective cooling in the dynamic state. This leads to a 5% higher torque per unit volume compared to static torque due to the higher residual flux density of the PMs at lower temperatures. Transient simulations are performed directly at the critical angle with high precision and low time-steps, considering mechanical revolutions. The pullout torque, accompanied by torque ripple, is obtained for the case without a retaining sleeve Figure 5.19 (a). However, when a sleeve is utilized, the pullout torque is reduced by approximately 10.5% due to the dominant eddy current losses Figure 5.19 (b). In this scenario, increasing the model length by approximately 12% is necessary to achieve the same torque. Due to the different moments of inertia of the rotors, instant load changes result in torque ripple during dynamic torque transmission.

The torque fluctuations are measured at 0.1% and 0.15% for the cases without and with the sleeve, respectively, under instant load variation Figure 5.19 (a) and (b). In synchronous MCs, the torque ripple remains minimal until the critical angle. Without considering dynamic modelling, transient simulations would result in constant torque Figure 5.19 (c).

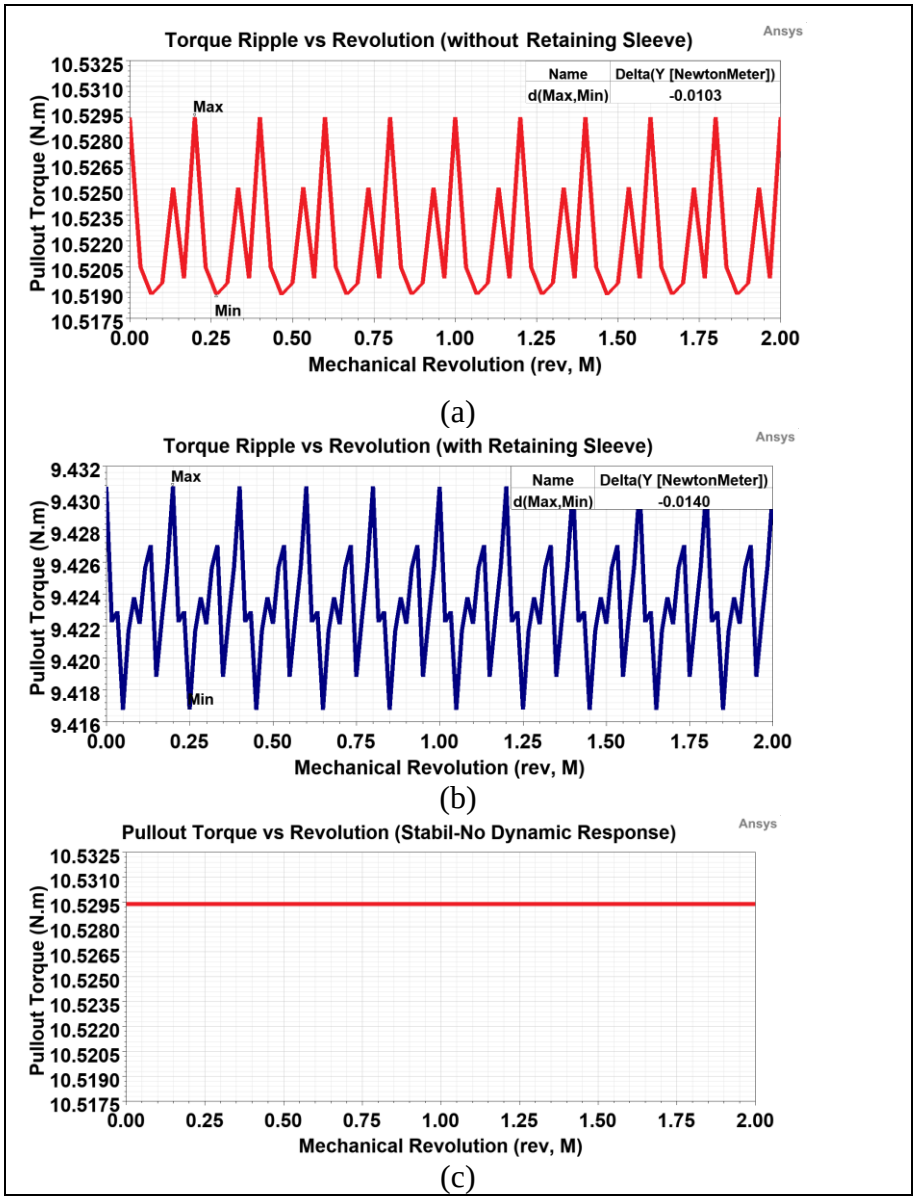


Figure 5.19. (a) Dynamic torque without sleeve at critical angle (b) Dynamic torque with sleeve at critical angle (c) Torque ignoring dynamic model at critical angle

5.4.10. Repulsive torque examination at loss of synchronization

Analysing the torque during the Loss of Synchronization (LoS) between the coupler rotors is crucial for system protection against overloads, especially in aerospace applications where the system should be operated by the Starter/Generator during LoS events. Two scenarios can lead to LoS: piston shaft malfunction or exceeding the pullout torque of the magnetic coupler.

When the piston shaft is undisturbed, LoS caused by overload results in the piston shaft and inner rotor of the MC running at idle speed (e.g., 2000 rpm for a 3W-70 engine), while the outer rotor runs at near idle speed. To analyse this scenario, the inner rotor is rotated at 2000 rpm, and the outer rotor is rotated at 2100 rpm, just above the idle speed. Figure 5.20 (a) illustrates that the attraction torque in this case is -0.6 N.m. The effect at different speeds is further examined in Figure 5.20 (b).

Alternatively, in the event of a locked piston engine shaft and inner rotor due to shaft failure, LoS analysis is conducted by setting the inner rotor speed to 0 and rotating the outer rotor at different operating speeds at the critical angle. As depicted in Figure 5.20 (b), the attraction torque is -0.52 N.m for the minimum operating speed and -0.72 N.m for the maximum operating speed in this scenario. Further investigation can be carried out on a skewed model to reduce the attraction torque [371, 372]. However, decreasing the attraction torque by implementing skewing may also result in a decrease in the maximum torque per unit volume.

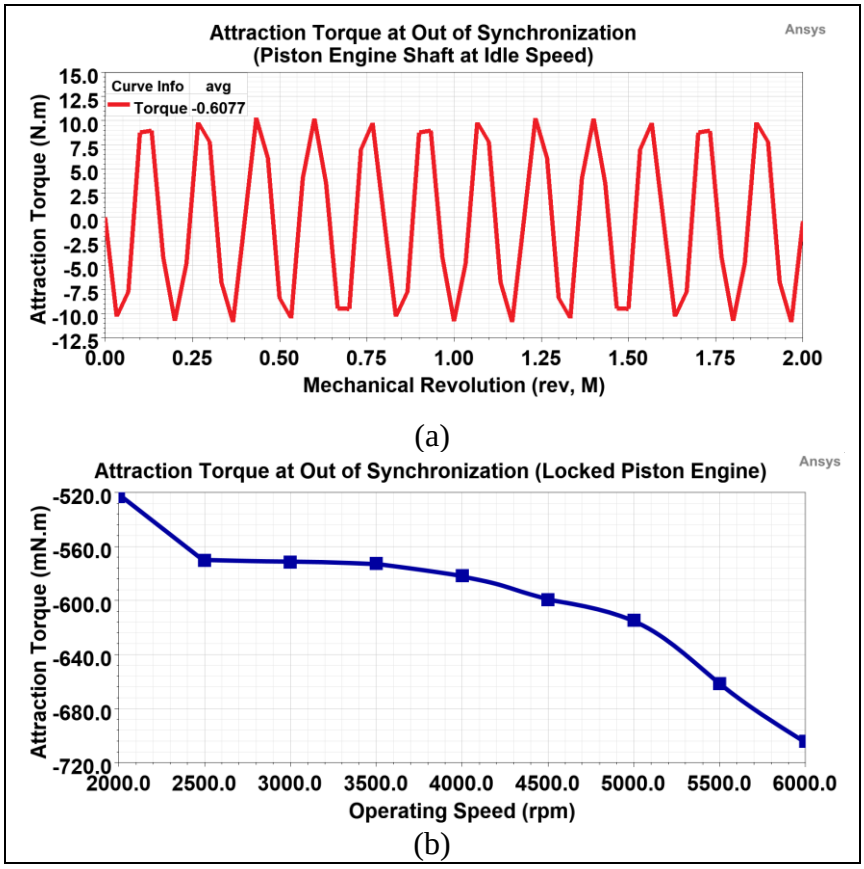


Figure 5.20. (a) Attraction torque at out of synchronization if piston shaft is not locked (b) Attraction torque at out of synchronization if piston shaft is locked

5.4.11. Parameter tuning based on Maxwell 3D optimization techniques

The optimum dimensions of the magnetic coupler, obtained from Maxwell 2D optimetric simulations, are further analysed using optimization techniques in Maxwell 3D. Various objectives can be considered, such as maximizing torque per permanent magnet volume, maximizing torque per total weight, or minimizing cost per volume. However, in hybrid UAV applications, there is often a requirement for a minimum weight that meets the system's specifications.

To reduce optimization time, the 3D model is divided into one-fifth using symmetry features. Several applicable optimization techniques, including Sequential Nonlinear Programming (SNLP), Genetic Algorithm (GA), and Multi-Objective Genetic Algorithm (MOGA) [373, 374], can be employed in magnetic couplers. The results of these optimization techniques are summarized in Table 5.4.

However, it should be noted that the prototypes are fabricated based on the dimensions obtained from sensitivity analyses in Table 5.4. This approach takes into account production tolerances and measurable dimensions, even if the maximum torque density is not achieved. This ensures practicality and feasibility in the fabrication process.

Table 5.4. Design parameters obtained by using Maxwell 3D optimization techniques

Design Parameters	Optimization Technique			Sensitivity* Analyses
	SNLP	GA	MOGA	
Inner PM thickness (mm)	4.1	4.49	4.026	4*
Outer PM thickness (mm)	3.93	4.25	3.79	4*
Inner yoke thickness (mm)	2.57	2.61	2.525	3*
Outer yoke thickness (mm)	3.03	3.02	3.028	3.5*
Optimum Model Dimensions				
Inner diameter of inner rotor (mm)	42			
Outer diameter of inner PMs (mm)	56			
Inner diameter of outer PMs (mm)	59			
Outer diameter of outer rotor (mm)	74			
Air gap volume of final model (mm^3)	2709.6			
Length of the final model (mm)	10			
Cost Function Outputs				
Average torque (N.m)	10.2	10.95	10.24	10.5
Total coupler weight (gr)	194	205	195	207
Torque density (N.m/kg)	52.58	53.41	52.51	50.72
Elapsed time (min.)	150	270	210	15
* Optimum values obtained from the sensitivity analyses.				

5.4.12. Magnetic coupler efficiency and losses based on Maxwell 3D FEA

Calculating losses in magnetic couplers analytically can be challenging; however, numerical methods provide an effective solution. Magnetic coupler losses encompass various components, including rotor core losses, permanent magnet losses, retaining sleeve losses, and mechanical losses. Ansys Maxwell offers a reliable approach to calculate core losses, which comprise hysteresis, eddy-current, and excess losses. These losses can be evaluated using the following equation [375]:

$$p_{loss} = \mathrm{k}_h * f * B^2 + k_c * f^2 * B^2 + k_e * f^{1.5} * B^{1.5} \quad (6.3)$$

where k_h: hysteresis loss coefficient of material
f: frequency of air gap flux density
B: absolute average of air gap flux density
k_c: eddycurrent loss coefficient of material
k_e: eddycurrent loss coefficient of material

Under ideal conditions in synchronous couplers, where the inner and outer rotors rotate at the same speed, there is no induction of eddy currents on the PMs and the retaining sleeve.

However, due to load disturbances, high vibrations, and torque ripple from the natural operation of the piston engine, the torque angle frequently fluctuates. Consequently, in addition to hysteresis losses [376], eddy-current losses [377] arise as a result of induced eddy currents. These losses are converted into heat, gradually raising the temperature of the PMs. If not mitigated, they can significantly reduce the residual flux density of the PMs and the transmitted torque. Excess losses occur due to the eddy current generated by the displacement of magnetic domain walls.

Figure 5.21 (a), (b), (c), and (d) investigate the losses in the magnetic coupler, including rotor core losses, hysteresis losses of PMs, eddy-current losses of PMs, and eddy-current and hysteresis losses of the sleeve. These losses are analysed based on the torque angle at the maximum operating speed for the optimal coupler configuration of 10-poles and 10 N.m.

In Ansys Maxwell 3D, the efficiency of the magnetic coupler is analysed in two cases. Similar to Maxwell 2D simulations, dynamic effects are incorporated through the "Model-Motion Setup-Consider Mechanical Transient" settings. The losses and efficiency are evaluated under the following conditions:

Losses and efficiency at the critical angle for different operating speeds: By setting the inner rotor speed to zero and limiting the positive rotation of the outer rotor at various operating speeds from a torque angle of zero to the critical angle, the losses and efficiency at the critical angle are determined. Figure 5.21 (e) presents the coupler efficiency as a function of operating speed at the critical angle.

Losses and efficiency at maximum operating speed for different torque angles: By setting the inner rotor speed to zero and limiting the positive rotation of the outer rotor at maximum operating speed from a torque angle of zero to different torque angles, the losses and efficiency at the maximum operating speed are obtained. Figure 5.21 (f) illustrates the efficiency as a function of torque angle at maximum operating speed.

Based on the analysis, the coupler efficiency is found to be 93.8% at the maximum speed and critical angle, while it reaches 96.9% at the minimum torque angle and minimum speed. These efficiency values provide valuable insights into the performance and energy conversion capabilities of the magnetic coupler system.

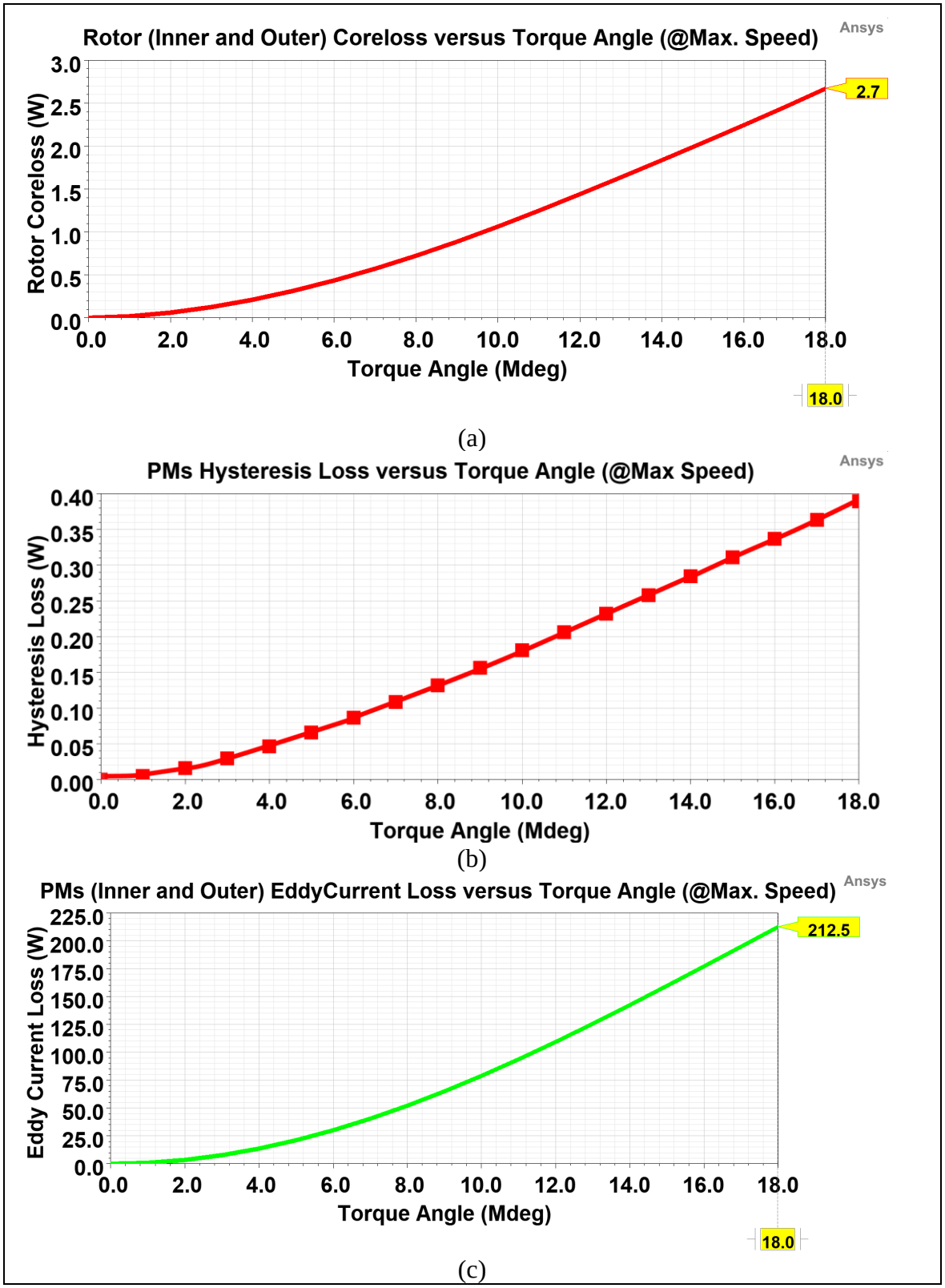


Figure 5.21. (a) Rotor core loss depending on torque angle (b) Hysteresis loss of PMs depending on torque angle (c) Induced eddy-current loss of PMs depending on torque angle (d) Induced eddy-current and hysteresis loss of retaining sleeve (e) Coupler efficiency at critical angle depending on operating speed (f) Coupler efficiency at maximum speed depending on torque angle

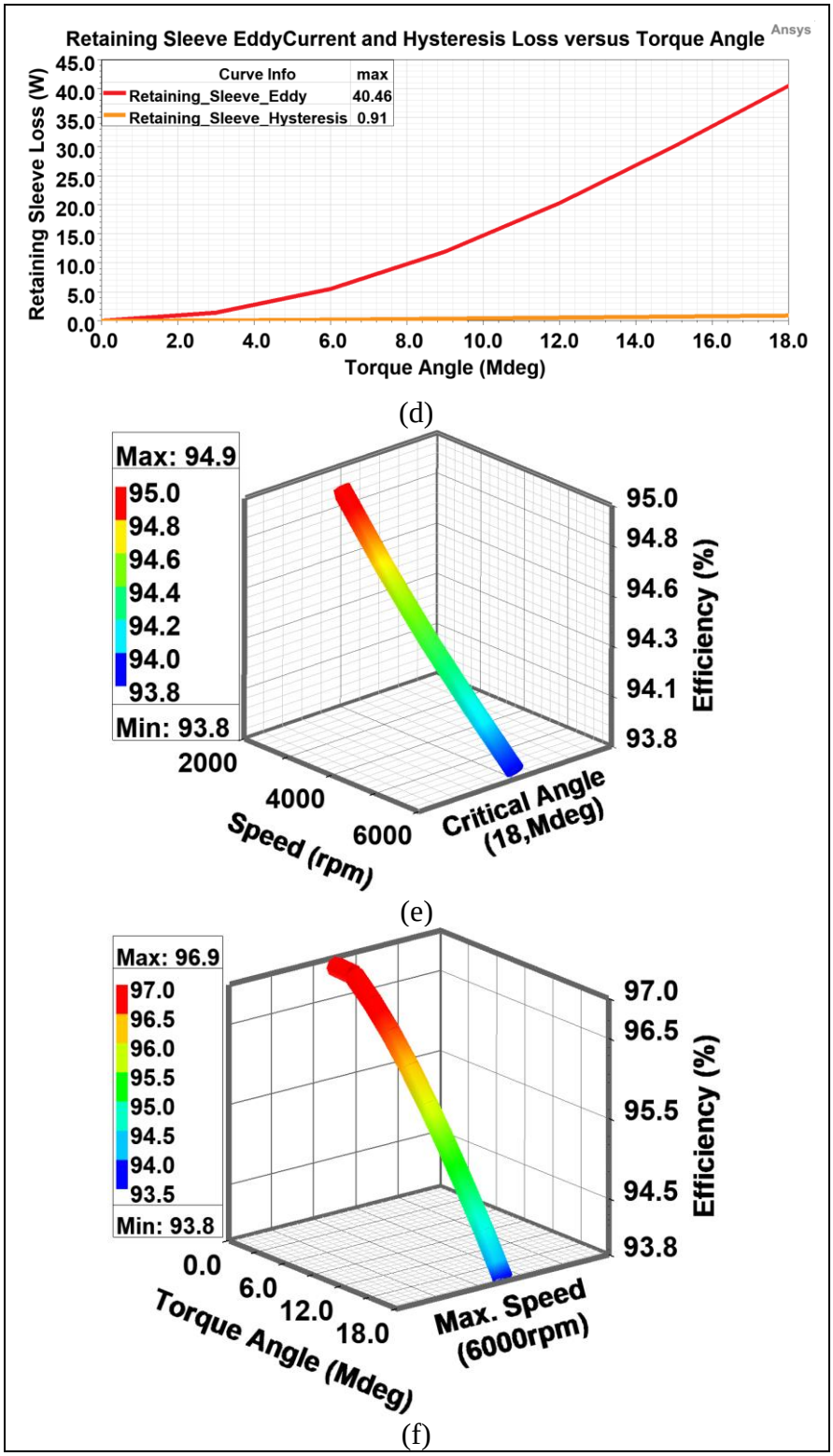


Figure 5.21. (continued) (a) Rotor core loss depending on torque angle (b) Hysteresis loss of PMs depending on torque angle (c) Induced eddy-current loss of PMs depending on torque angle (d) Induced eddy-current and hysteresis loss of retaining sleeve (e) Coupler efficiency at critical angle depending on operating speed (f) Coupler efficiency at maximum speed depending on torque angle

5.4.13. Design of the retaining sleeve or bandage

When operating at speeds exceeding 3600 rpm, commonly referred to as high speed, it becomes necessary to utilize a retaining sleeve to prevent the magnets from dislodging from the rotor surface due to the significant centrifugal force. A suitable material for the sleeve is nonmagnetic stainless steel 316L, which possesses favorable properties listed in Table 5.5.

Table 5.5. Properties of Steel316L used in the analytical design of the retaining sleeve

Properties	Value	Unit
Mass density	8000	kg/m^3
Tensile strength, ultimate/yield	515/205	MPa
Young's modulus (Elasticity modulus)	193000	MPa
Poisson's ratio	0.25	
Magnetic permeability	1.02	

Although the sleeve thickness can be promptly determined through optimetric analyses in Maxwell 2D, preliminary dimensions can also be estimated by conducting analytical calculations based on centrifugal pressure and tangential stress [378]. The analytical results, based on the inner rotor dimensions depicted in Figure 5.22 (a), are summarized in Table 5.6 and subsequently verified through Ansys structural analysis, as illustrated in Figure 5.22 (b).

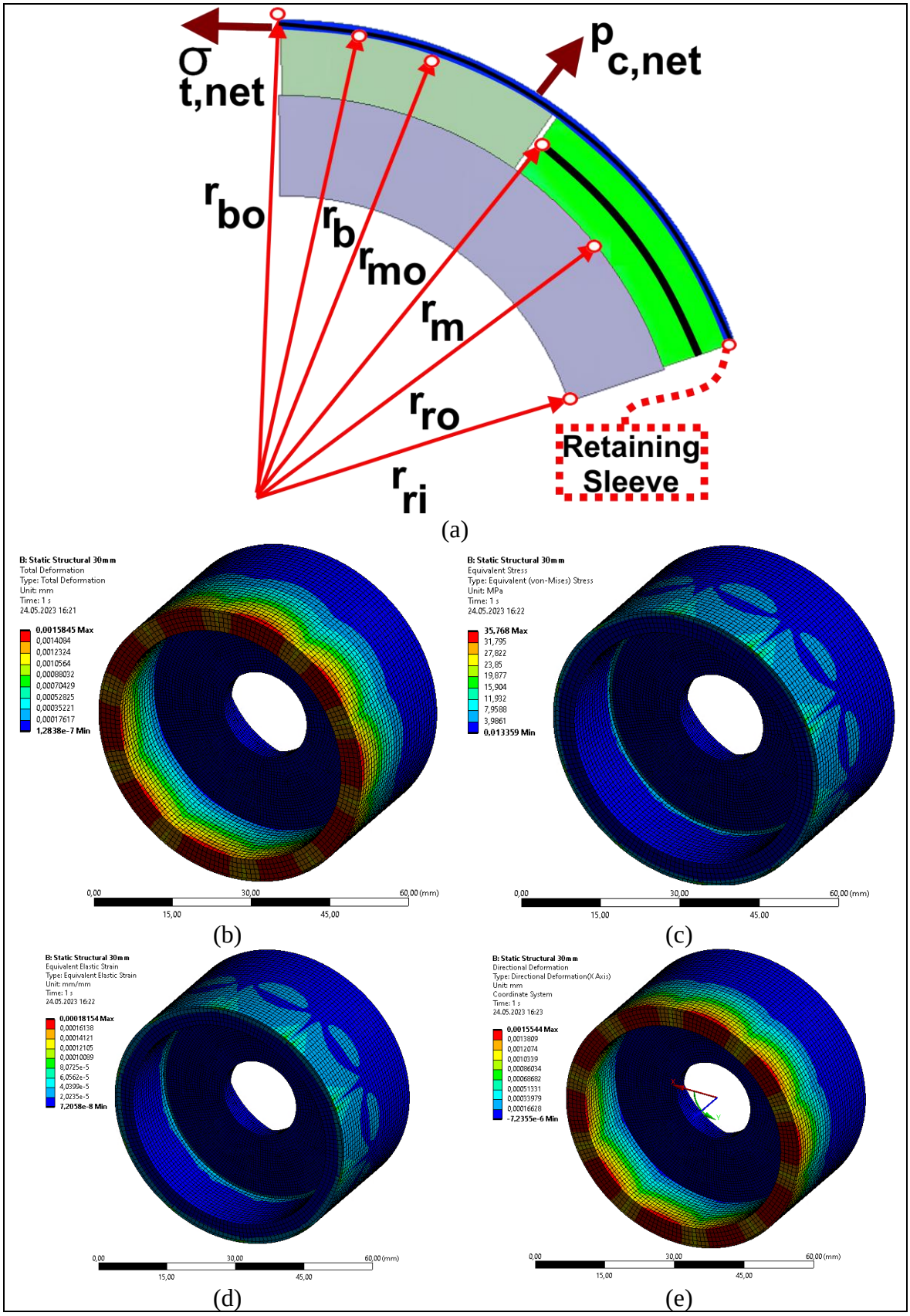


Figure 5.22. (a) Inner rotor parameters (b) Sleeve total deformation (c) Sleeve equivalent stress (d) Sleeve elastic strain (e) Sleeve X-axis directional deformation

Structural analyses were conducted considering their respective maximum operating speeds of 7250 rpm for DLE-30 and 6250 rpm for 3W-55XI. Figure 5.22 presents the results for the 30 mm magnetic coupler model, showcasing maximum deformation and stress to avoid cluttering the image with excessive details. Additionally, the equivalent elastic strain and directional deformation along the X-axis are depicted in Figure 5.22 (d) and (e), respectively.

Analytical design of the retaining sleeve

The determination of the minimum sleeve thickness involves satisfying two fundamental conditions, even when the adhesive effect is disregarded:

1. The residual contact pressure between the magnets and the rotor core must remain positive during overspeed conditions, as expressed by Eq. 6.4.

$$p_{\mathrm{c}} = (p_{\mathrm{c,prestress}} - p_{w,m} - p_{w,b}) > 0 \tag{6.4}$$

where $p_{w,b}$: centrifugal force on sleeve shell — MPa

$p_{w,m}$: centrifugal force on magnets — MPa

$p_{c,prestress}$: contact pressure due to interference fit of sleeve onto magnets — MPa

p_c: $residual\ contact\ pressure$ — MPa

Eq. 6.5 and Eq. 6.6 provides the calculations for the centrifugal forces acting on the sleeve and magnets, which contribute to the reduction of residual contact pressure.

$$p_{w,b} = r_{\mathrm{b}} * \rho_b * w_{overspeed}^2 * h_{\mathrm{b}} \tag{6.5}$$

where $p_{w,b}$: centrifugal force on sleeve — MPa

r_{b}: $mean\ radius\ of\ sleeve\ shell$ — m

ρ_b: $mass\ density\ of\ sleeve\ shell$ — kg/m^3

$w_{overspeed}$: $angular\ velocity, at\ over\ speed$ — rad/s

h_{b}: $thickness\ of\ sleeve\ shell$ — m

$$p_{w,m} = r_m * \rho_m * w_{overspeed}^2 * h_m \tag{6.6}$$

where $p_{w,m}$: centrifugal force on magnet — MPa

r_m: $mean\ radius\ of\ magnets$ — m

ρ_m: $mass\ density\ of\ magnets$ kg/m^3

h_m: $thickness\ of\ magnets$ m

Eq. 6.7 and Eq. 6.8 are utilized to evaluate the contact pressure and prestress resulting from the interference fit between the sleeve shell and the magnets.

$$p_{c,prestress} = \sigma_{t,prestrees} * \frac{(r_{bo}^2 - r_{mo}^2)}{(r_{bo}^2 + r_{mo}^2)} \tag{6.7}$$

where
$\sigma_{t,prestrees}$: prestress due to interference fit of sleeve onto magnets MPa

r_{bo}: $sleeve\ shell\ outer\ radius$ m

r_{mo}: $magnet\ outer\ radius$ m

$$\sigma_{t,prestrees} = E * \frac{\Delta D}{2 * r_b} \tag{6.8}$$

where
E: Young's modulus MPa

ΔD: $sleeve\ undersize$ m

2. The stress within the retaining sleeve must remain below the maximum tolerable tangential stress, as outlined by Eq. 6.9.

$$\sigma_t = \left(\sigma_{t,prestrees} + \sigma_{t,w}\right) < \sigma_{t,max} \tag{6.9}$$

where
$\sigma_{t,w}$: tangential stress due to sleeve rotation MPa

$\sigma_{t,max}$: maximum tangential stress MPa

σ_t: $stress\ inside\ sleeve\ shell$ MPa

The tangential stress resulting from the rotation of the retaining sleeve shell, characterized by a mass density of ρ_b, can be estimated using Eq. 6.10 [245, 379, 380].

$$\sigma_{t,w} = \rho_b * w_{overspeed}^2 * r_b^2 \tag{6.10}$$

The analysis confirms that the residual contact pressure at overspeed, p_c, remains positive, and the stress inside the retaining sleeve, σ_t, is well below the ultimate tensile stress of the Steel316L material listed in Table 5.5. This is further validated through numerical Ansys structural analysis, as depicted in Figure 5.22 (b).

To determine the minimum required sleeve thickness, analytical equations are applied incrementally, starting from 0.05 mm with 0.05 mm step intervals. It is found that a sleeve thickness of 0.24 mm satisfies the conditions for contact pressure, while a thickness of 0.28 mm is sufficient to meet the tangential stress requirements, considering the safety factor.

However, it is practically challenging to obtain or process materials with such thin thicknesses. Considering production feasibility and incorporating a safety factor of 2, a sleeve thickness of 0.5 mm is deemed a practical and suitable choice [265]. Table 5.6 summarizes the analytical design parameters and dimensions of the retaining sleeve.

Table 5.6. Summary of the analytical design of the retaining sleeve

DESIGN INPUTS			
r_{ri}	Inner radius of inner rotor	21	mm
r_{ro}	Outer radius of inner rotor	24	mm
r_m	Mean radius of permanent magnet	26	mm
r_{mo}	Outer radius of permanent magnet	28	mm
r_b	Mean radius of retaining sleeve	28.25	mm
r_{bo}	Outer radius of retaining sleeve	28.5	mm
ΔD	Sleeve undersize	0.1	mm
γ_{over}	Overspeed factor	1.5	
γ_{safety}	Safety factor	2	
DESIGN OUTPUTS			
Residual Contact Pressure at Overspeed			
Centrifugal force on sleeve	$p_{w,b}$	0.14	MPa
Centrifugal force on a magnet	$p_{w,m}$	1.01	MPa
Contact pressure (due to interference fit of sleeve)	$p_{c,prestress}$	6.27	MPa
Residual contact pressure	p_c	5.12	MPa
Stress Inside Retaining Sleeve Shell			
Tangential stress (due to rotation of sleeve)	$\sigma_{t,w}$	8.17	MPa
Prestress (due to interference fit of sleeve)	$\sigma_{t,prestress}$	354	MPa
Stress inside retaining sleeve shell	σ_t	362	MPa
Determination of Retaining Sleeve Thickness			
Minimum required thickness of retaining sleeve, based on contact pressure	$h_{b,min,pressure}$	0.24	mm
Minimum required thickness of retaining sleeve, based on tangential stress	$h_{b,min,stress}$	0.28	mm
Selected thickness of retaining sleeve	$h_{b,selected}$	0.5	mm

5.5. Design of Active Radial Magnetic Couplers for a 3W-55XI Engine

The utilization of the proposed magnetic couplers (MCs) in hybrid UAVs incorporating piston engines (PE) and starter/generator (S/G) units is of significant importance due to their ability to safeguard the UAV, particularly in challenging scenarios involving excessive loading and shaft lock-up, as discussed in detail in Section 2. In such critical situations, the S/G operates in motor mode, enabling the UAV to maintain its flight mission or safely land by exploiting the loss of synchronization between the inner and outer rotors of the MC.

While this loss of synchronization may appear problematic in conventional machine designs, the adoption of MCs confers a substantial advantage in terms of protecting hybrid UAVs from potential breakage.

In the hybrid UAV configuration with the 3W-55XI piston engine, the coupler is mounted on the engine shaft using a coupler rotor, as depicted in Figure 5.23 over single stage of the DCSG. This arrangement allows for efficient power transmission and integration of the MC with the engine system. Similar to the model with DLE-30 and the 3W-70R2 hybrid model, the design parameters are listed in Table 5.2 [201].

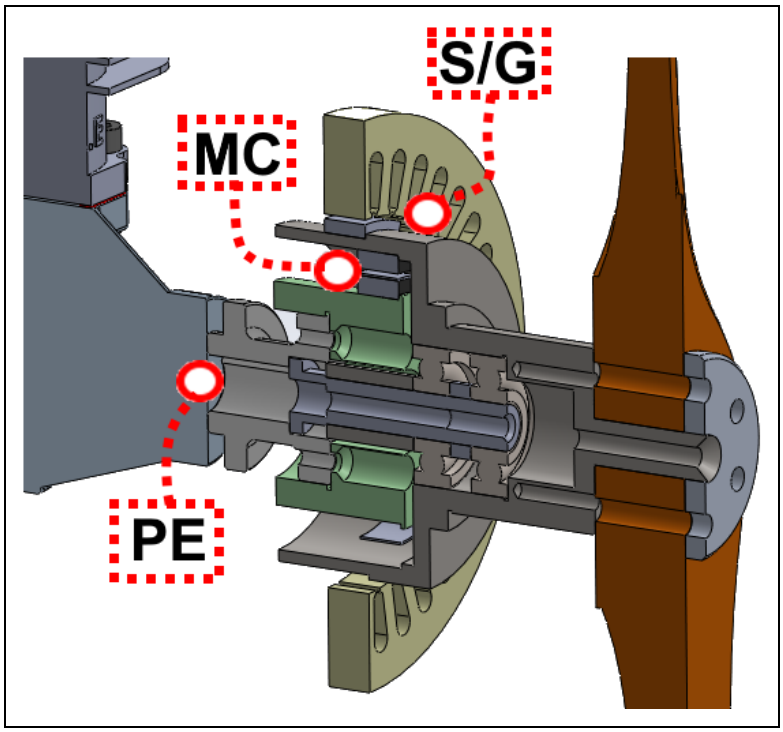


Figure 5.23. 3D drawing of the single-stage DCSG model

5.5.1. Determination of the minimum outer diameter of the inner rotor

In this configuration, to enhance the safe operation of the hybrid UAV, the magnetic coupler features a direct connection between the inner rotor and the flange of the piston engine, as indicated by the red marking in Figure 5.24 (a).

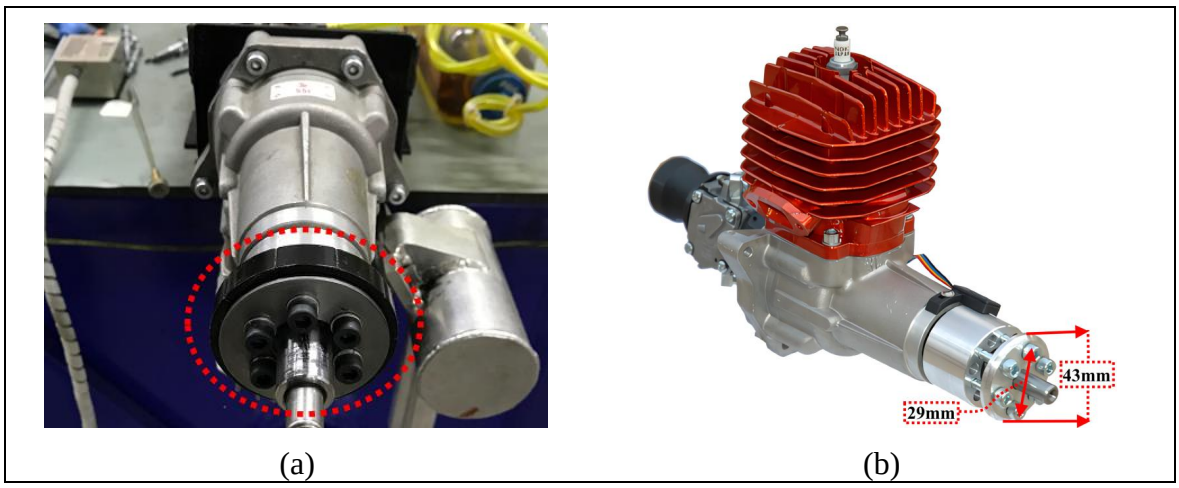


Figure 5.24. Mounting illustration of the (a) Inner rotor; (b) Inner flange

The design of the MC follows a unique approach, starting from the inner rotor and progressing towards the outer rotor. This methodology is necessitated by the diameter limitations of the inner flange in the 3W-55XI PE, as illustrated in Figure 5.24 (b). By leveraging this design constraint, the outer rotor of the MC also serves as the rotor of the S/G, maximizing the utilization of available space and resources. The proposed cylindrical MC model consists of an inner and outer rotor (1,7), weight reduction holes (2,9), mounting holes (3,8), PM housings (4,10), and PMs (5,6), as depicted in Figure 5.25 (a).

In Figure 5.25 (b), the torque angle (θ) represents the mechanical angle between the d-axes of the inner and outer rotors when the MC is under load. The critical or maximum angle [304] is calculated using Eq. 6.2 and corresponds to 90°E. The critical angle for a 10-pole configuration is 18 Mdeg and 0.314 radians. Initial sizing is performed using Virtual Work method and summarized in Table 2 for the 10-pole configuration at the critical angle, where (Θ-dΘ) is directly equal to dΘ. The value of Θ is 36 Mdeg and 0.628 radians for 10-poles.

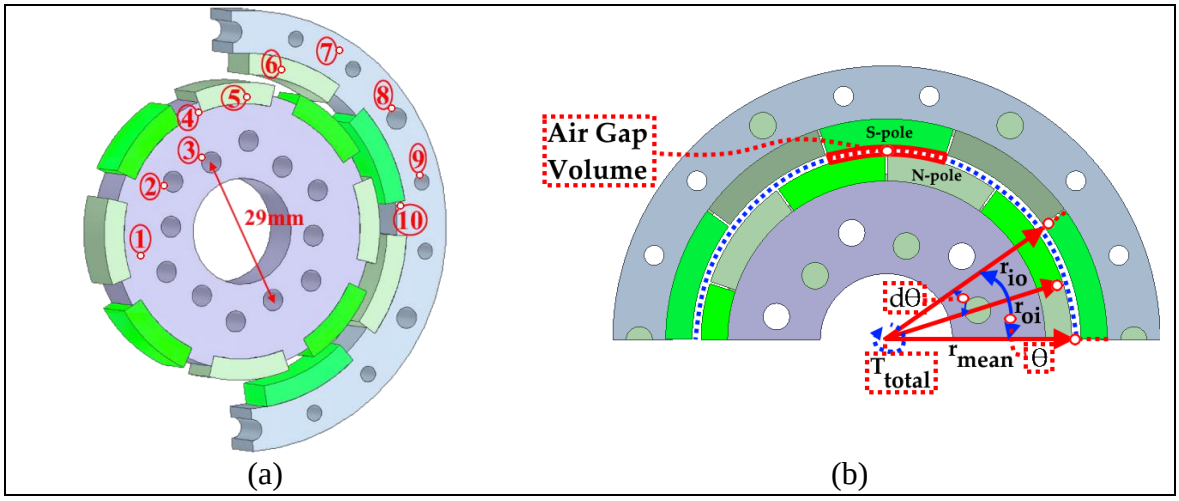


Figure 5.25. Magnetic coupler model definitions of (a) Parameters (b) Materials

The respective air gap volume is calculated to be 1289.5 mm^3. Due to the mounting hole diameters on the flange, the bore diameter of the inner rotor is determined to be 29 mm, as shown in Figure 5.25 (a). Likewise, the outer diameter of the inner rotor is set to a minimum of 43 mm for the model. Considering the thickness of the rotor yokes and PMs, the initial selection for r_{mean} is 27.5 mm. Assuming an air gap length of 1.5 mm, the outer diameter of the inner rotor and the inner diameter of the outer rotor are calculated as 26.75 mm and 28.25 mm, respectively. Consequently, the corresponding model length is determined to be 5 mm.

Table 5.7. Analytical design calculations by virtual work approach for preliminary sizing

Design Outputs	10-Pole Configuration
Air gap volume, minimum required	1289.5 mm^3
Length of the model, based on r_{mean}	5 mm
(Θ-dΘ), dΘ at critical torque angle	0.314 rad.
Critical torque angle	18 (°M)
Design Assumptions	
Middle of the air gap radius, r_{mean}	27.5 mm
Average air gap flux density	0.65 T
Air gap length	1.5 mm

5.5.2. Correlation of effective air gap diameter based on 2D FEA

The analysis begins with a 10-pole configuration to determine the appropriate effective air gap diameter and model length that would meet the required torque and torque density. The analysis considers a minimum effective air gap diameter of 45 mm, accounting for the air gap and yoke thicknesses. The effective air gap is defined as the midpoint of the air gap. Figure 5.26 explores the pullout torque across a range of effective air gap diameters and model lengths. The specified pullout torque of 6.9 N.m can be achieved with a minimum effective air gap diameter of 47 mm and a model length of 10 mm. Alternatively, a minimum model length of 6 mm is sufficient with an effective air gap diameter of 67 mm.

The relationship between the effective air gap diameter and the length of the MC significantly impacts the system inertia and transferrable torque in the hybrid UAV. Opting for a higher effective air gap diameter allows for increased system inertia and facilitates modular construction for higher torque transmissions. Consequently, an effective air gap diameter of 57.5 mm, nearing the upper limit of the range, is selected. On the other hand, the linear increase in model length corresponds to an almost proportional increase in pullout torque such that the required torque of 6.9 N.m can be achieved with a minimum coupler length of 7.4 mm. However, for enhanced manufacturability and greater tolerance to disturbances, a length of 10 mm is chosen, resulting in a pullout torque of 9.4 N.m. This updated torque requirement will be referred to hereafter.

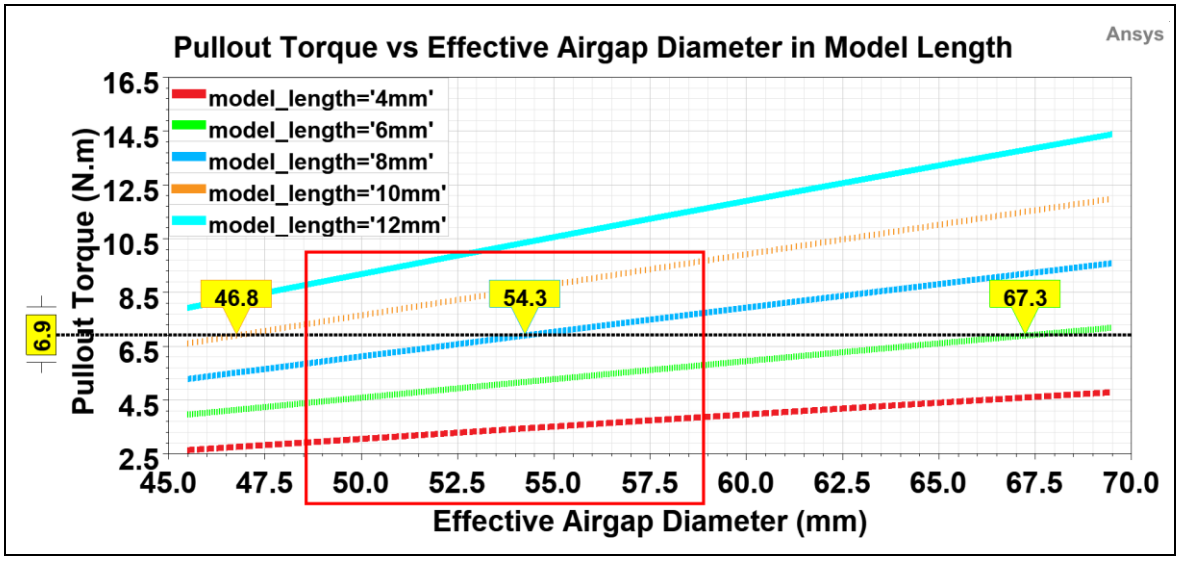


Figure 5.26. Pullout torque versus effective air gap length in model length

5.5.3. Investigation of optimum pole number based on 2D FEA

The pole number configuration of the rotors plays a vital role in determining the transmitted torque and, consequently, the torque density. Opting for a pole number of 10 for both the inner and outer rotors proves to be the optimal choice, as it yields the highest pullout torque for this configuration, as depicted in Figure 5.27 (a). Figure 5.27 (b) explores the feasibility and impracticability of different inner and outer rotor pole number configurations in terms of torque density. Torque density represents the pullout torque per unit weight in N.m/kg.

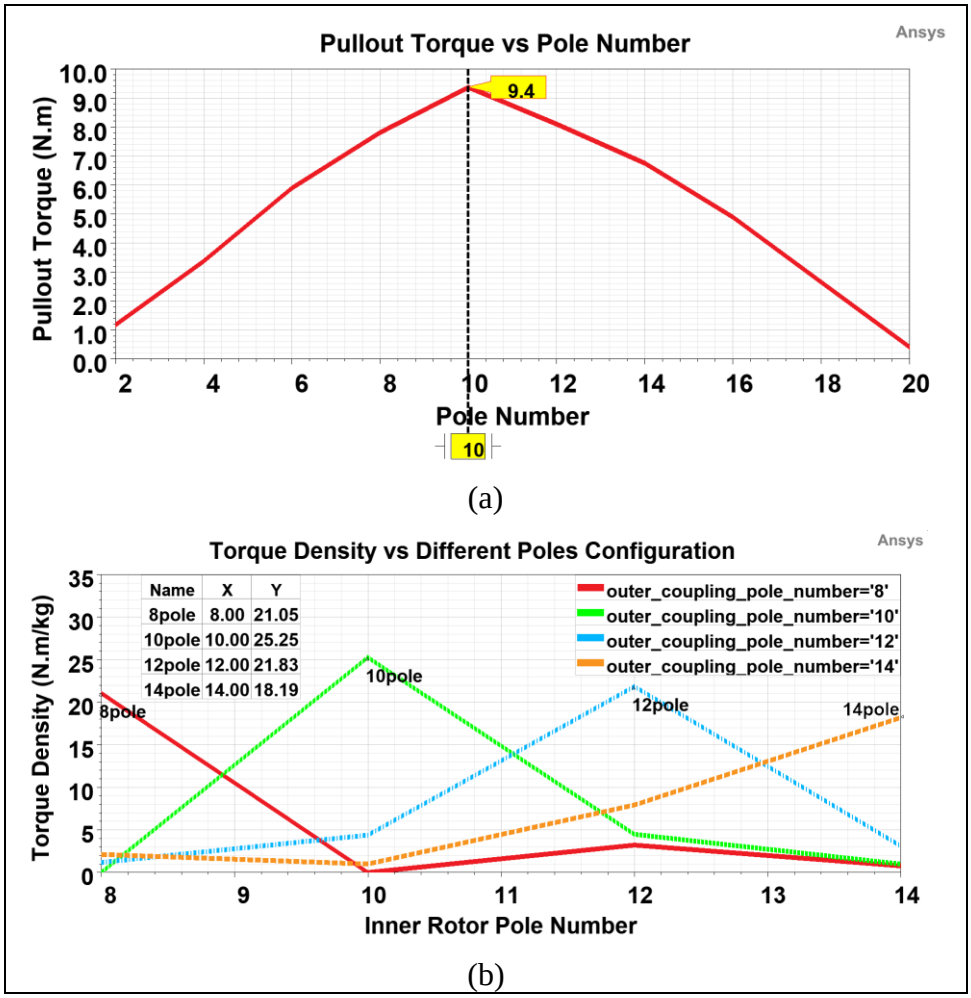


Figure 5.27. (a) Torque vs same pole number (b) Torque density vs different pole number

It is observed that the torque density experiences a significant decline when there is a mismatch in the pole numbers of the inner and outer rotors. However, with a well-designed modulator in the air gap, it is feasible to have different numbers of poles on both rotors. This realization gives birth to the concept of magnetic gears.

5.5.4. Investigation of the PM embrace and offset effect based on 2D FEA

Pole embrace refers to the ratio of the pole arc to the pole pitch. In some cases, the arched PMs may not be perfectly concentric with the rotor, leading to a nonuniform air gap. This offset between the center of the bottom and top of the PM arc is known as the pole arc offset. While the embrace significantly influences the pullout torque, the impact of the offset is relatively limited. An embrace value of 0.98, indicated by the red marker in Figure 5.28 (a), offers a higher torque density. However, the pole arc offset is generally not preferred because it tends to have a negative effect on the output torque, as shown in Figure 5.28 (b), unless specifically required for situations such as cogging torque. Consequently, the maximum pullout torque is achieved by maximizing the embrace and minimizing the offset.

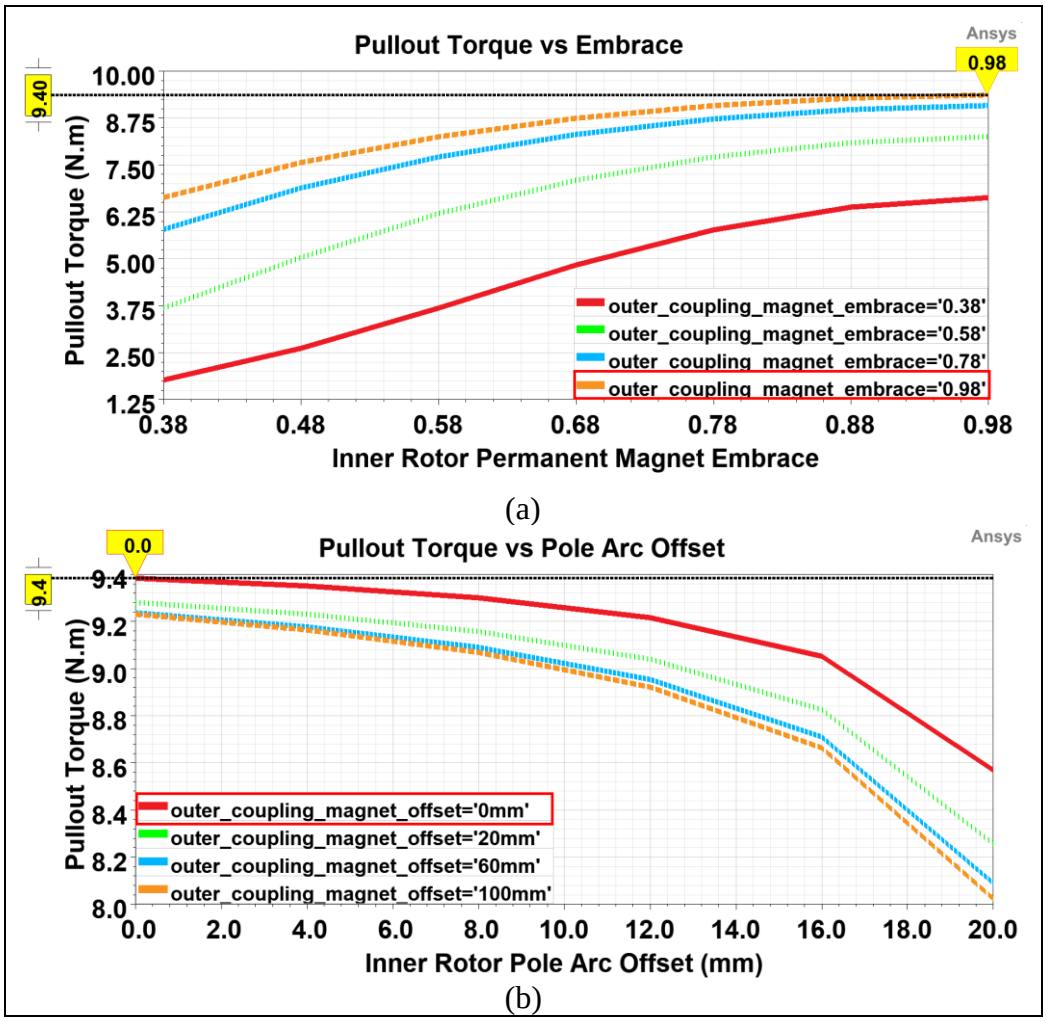


Figure 5.28. Pullout torque versus: (a) PM embrace (b) PM offset

5.5.5. Effect of PM type, grade, and temperature on pullout torque based on 2D FEA

The grade, type, orientation, and operating temperature of PMs play a crucial role in the design of MCs. Figure 5.29 examines the implications of these factors for the 10-pole configuration at a critical angle. Figure 5.29 (a) demonstrates that the pullout torque increases with higher PM grades. Conversely, Figure 5.29 (b) reveals that SmCo magnets can withstand higher temperatures and harsher conditions, but their energy density is lower than that of NdFeB magnets, resulting in a lower pullout torque for the same PM thickness.

Regarding the magnetization, Figure 5.29 (c) shows that it has minimal effect on the pullout torque. However, the operating temperature of the PMs has a significant impact, as depicted in Figure 5.29 (d). Radially oriented N48H magnets are preferred for improved accessibility.

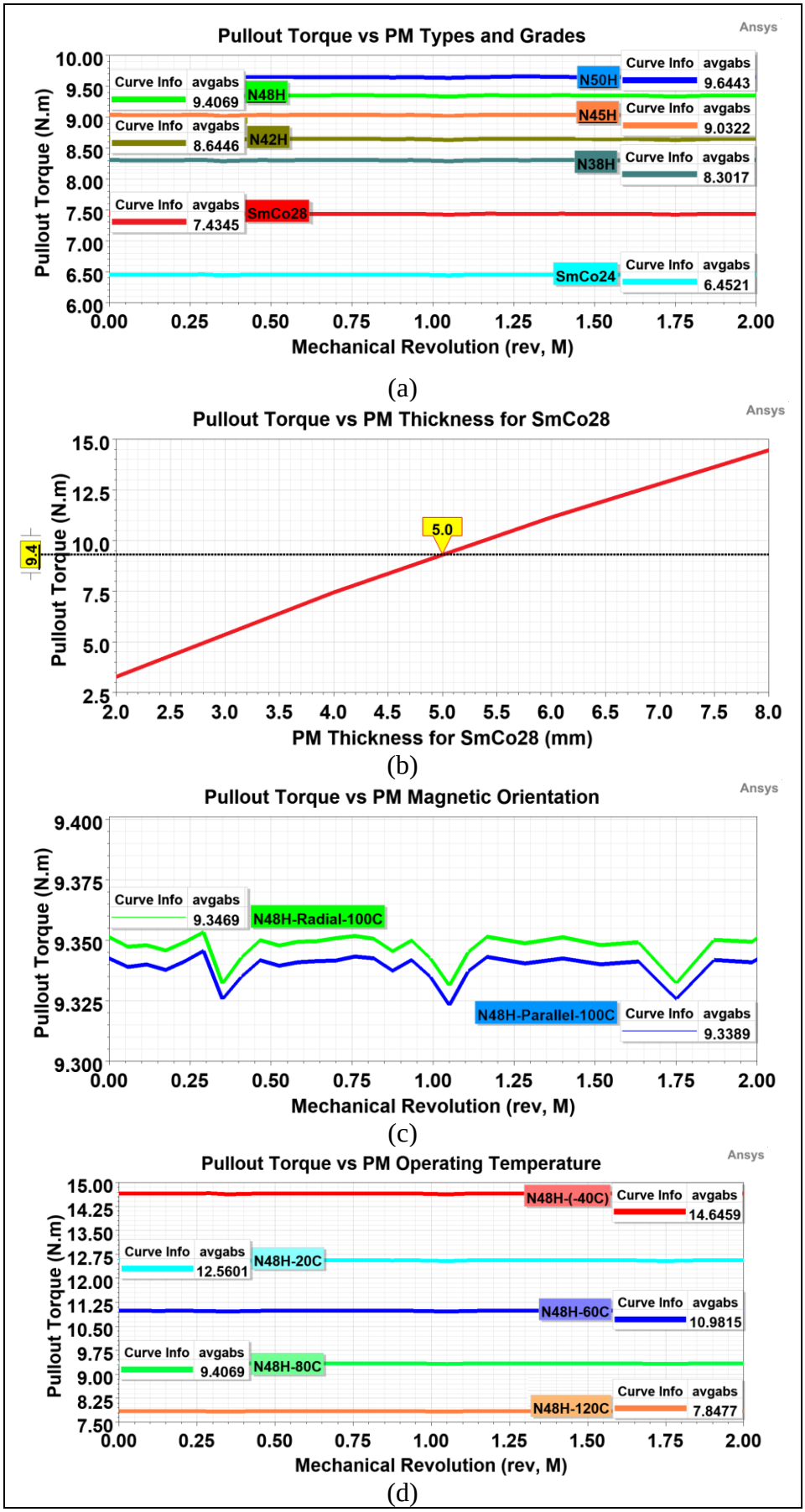


Figure 5.29. Effect of PMs based on (a) Grade (b) Type (c) Orientation (d) Temperature

5.5.6. Investigation of negative torque at loss of synchronization based on 2D FEA

The loss of synchronization (LoS) occurs when the rotational synchronization between the rotors is disrupted due to exceeding the torque limit and critical torque angle caused by a malfunction in the PE shaft. In such cases, while the drive system is sustained by the S/G, it is essential to analyse and account for the negative torque exerted by the rotors to determine the power limits of the S/G, considering safety factors. In the 2D simulation, the LoS torque is evaluated by setting the inner rotor speed to 0 rpm and varying the speed of the outer rotor.

In the experimental setup, the LoS torque is measured by immobilizing the inner rotor to prevent its rotation and gradually rotating the outer rotor at different speeds using a speed source. As depicted in Figure 5.30, the LoS torque at maximum speed is recorded as -0.61 N.m in the 2D simulation and -0.6 N.m in the test results.

The slight variations in the results can be attributed to the sensitivity of the sensors and the higher moment of inertia of the test bench in comparison to the dynamic model of the UAV utilized in the simulations.

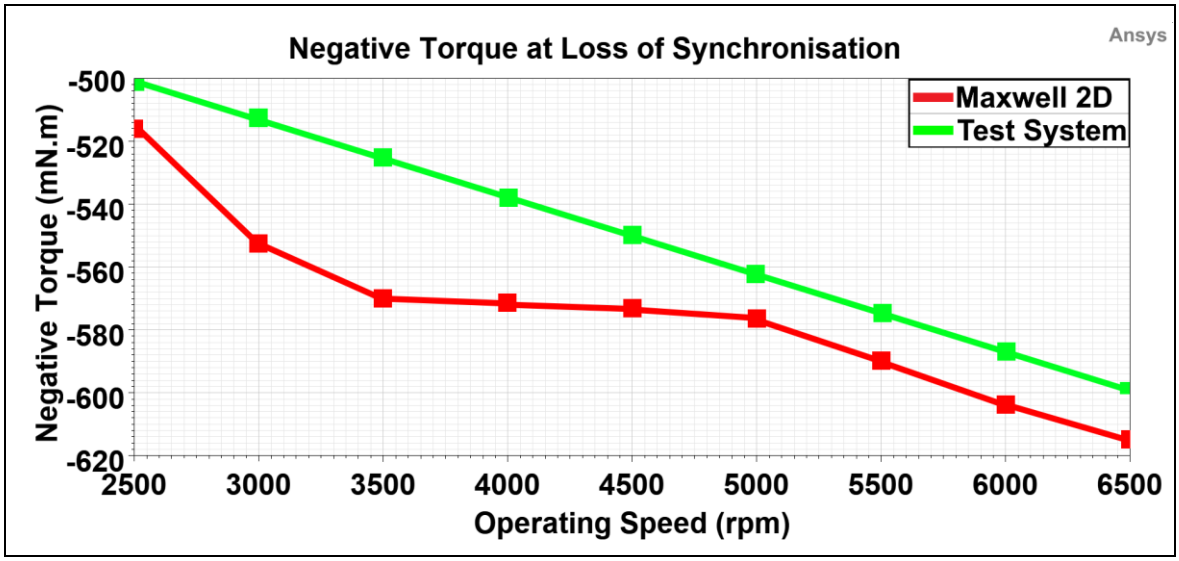


Figure 5.30. Negative torque at loss of synchronization depending on operating speed

5.5.7. Static locked-rotor torque and transient torque ripple analyses

The locked-rotor or static torque represents the torque capability of the coupler and can be evaluated for different pole numbers, depending on the torque angle, as seen in Figure 5.31 (a). In the 10-pole configuration, the maximum static torque is achieved, reaching 9.4 N.m. During dynamic operation, the torque transmission in response to instantaneous load variations introduces torque ripple in MCs due to the varying moments of inertia of the rotors and the flywheel effect, as depicted in Figure 5.31(b).

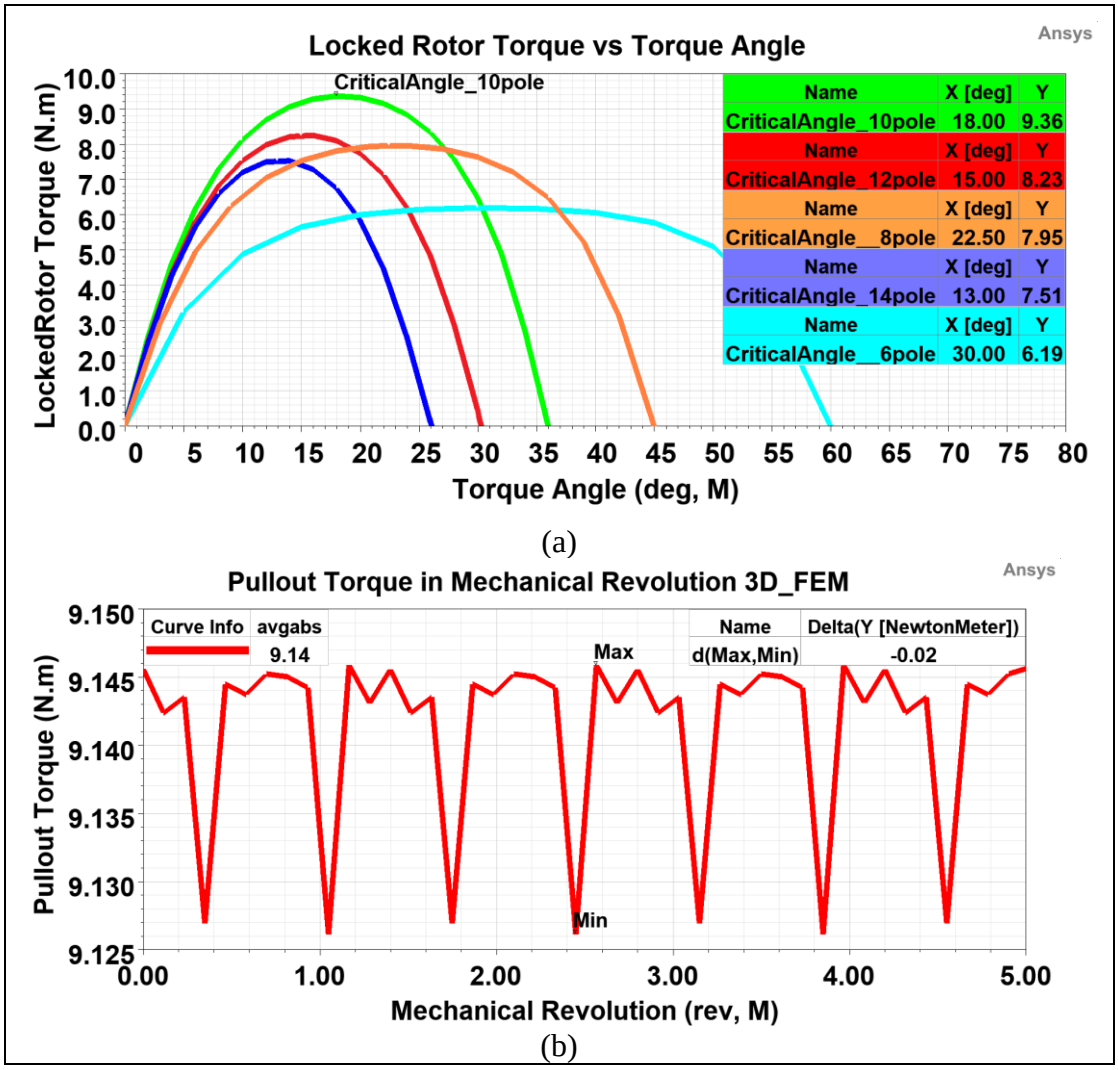


Figure 5.31. (a) Locked-rotor torque versus torque angle (b) Torque ripple in revolutionM

5.5.8. Investigation of different rotor materials

While electrical steel offers lower core losses in synchronous MCs, it does not provide a significant advantage in the proposed model due to its limited volume. Additionally, if electrical steel is preferred, it would lead to a higher yoke thickness due to its lower saturation point. However, certain exceptional cases, such as military applications, may necessitate the use of nonmagnetic materials like Steel-316, resulting in a yokeless design.

In such situations, it becomes essential to increase the thickness of the PMs to prevent a substantial drop in torque, which can be approximately 60%, as depicted in Figure 5.32. For the production of MCs, Steel-1020 is commonly utilized as the rotor material.

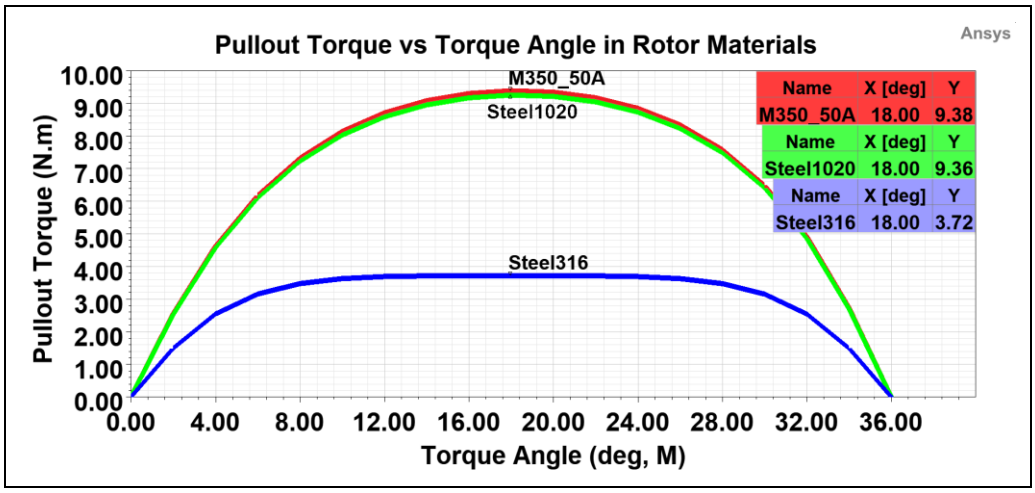


Figure 5.32. Investigation of the effect of different rotor materials on torque

5.5.9. Study of pullout torque depending on misalignment length

To assess the worst-case scenario, it is crucial to analyse the reduction in pullout torque resulting from misalignment length, which occurs when the propeller forces the system forward, leading to the inability to generate thrust in the event of severe bearing failure. Figure 5.33 (a) provides a visual representation of the misalignment itself. As the misalignment increases, the torque decreases accordingly. Figure 5.33 (b) illustrates the relationship between the pullout torque and misalignment length.

The test results and simulations show agreement, but slight discrepancies may arise due to challenges in precisely adjusting the misalignment length in the test system.

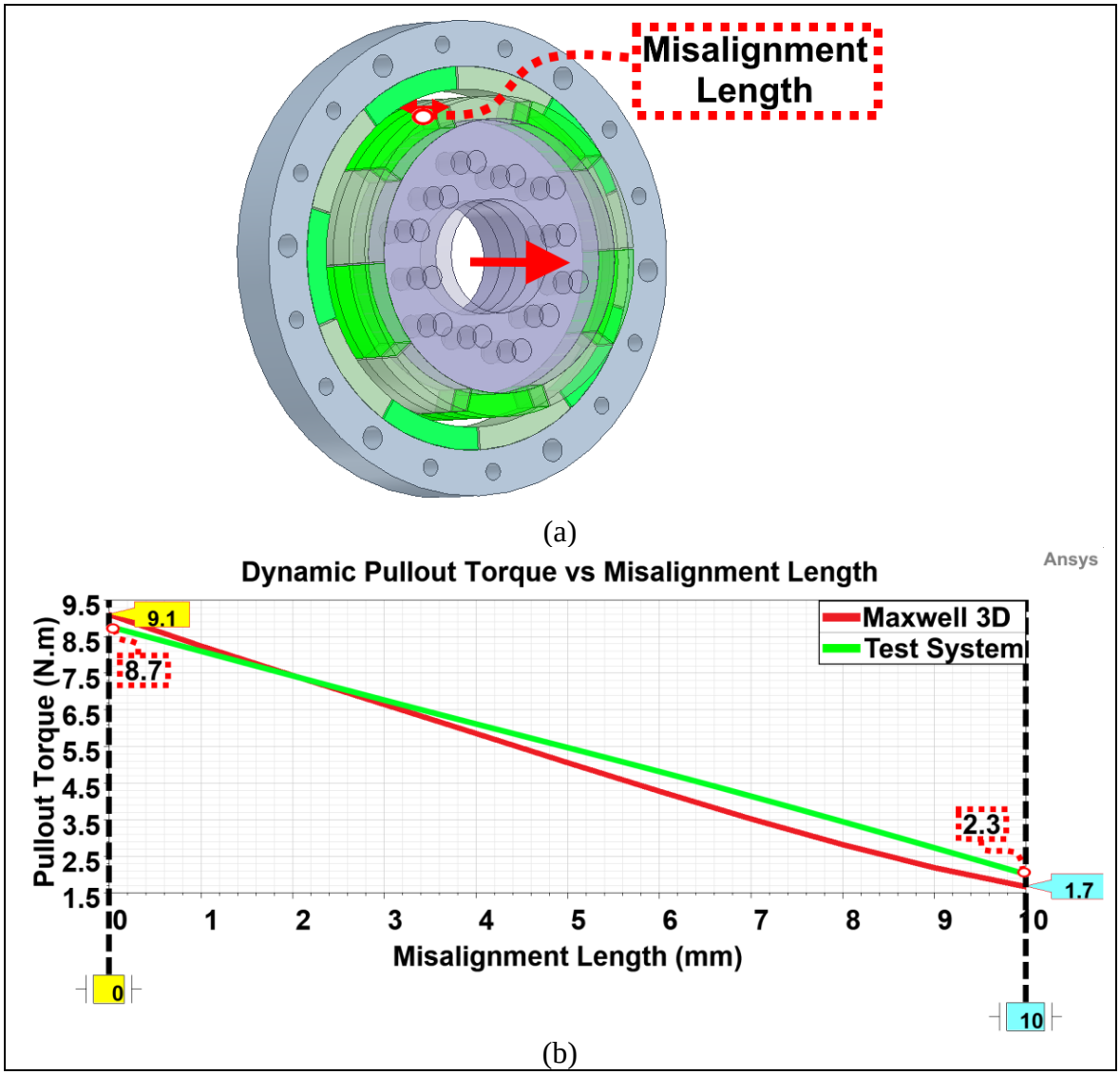


Figure 5.33. (a) Misalignment exhibition (b) Pullout torque versus misalignment length

5.6. Design of Starter/Generator

The Starter/Generator design, similar to the magnetic coupler design, follows a structured approach that begins with a macrobased analytical calculation. This calculation helps determine the initial dimensions needed for the Ansys Maxwell input. The flowchart outlining the design process is presented in Figure 5.6.

The analytical calculations for both motor mode and generator mode operation of the Starter/Generator (S/G) are similar. In the motor mode of S/G, the design is based on Field-Oriented Control (FOC) strategy and Space Vector Pulse Width Modulation (SVPWM) switching technique, as described in Section 4.8.

Simultaneously, the permanent magnet synchronous motor (PMSM) model is utilized to drive the Starter/Generator in starter mode using the 6-step commutation technique outlined in Section 4.7. Consequently, separate analyses employing FOC and 6-step commutation are performed concurrently.

The importance of using the 6-step commutation technique rather than the FOC strategy in the starter mode when initiating the start-up of a piston engine lies in its ability to provide higher torque at low speeds and ease of control, ensuring reliable and prompt engine start, as well as its superior response characteristics in the face of load variations, making it adaptable to rapid changes in engine load during the start-up process; additionally, its simplicity and robustness make it easier to implement and maintain, while its reduced sensitivity to parameter variations guarantees stable and reliable operation even in challenging conditions, and its compatibility with MCUs optimizes integration and control, making the 6-step commutation technique an advantageous choice for achieving consistent and efficient engine starting performance.

The design process for generator mode is similar to that of the motor mode but the performance rating is slightly different. However, in S/G generator mode, the winding calculations are conducted based on the uncontrolled rectifier, as explained in detail in Sections 4.6 and 4.9, different than in motor mode. Integration of S/G structure to the piston engine over a single-stage DCSG is illustrated in Figure 5.34. The unique constraints of each UAV necessitate the implementation of a system-based DCSG model to achieve optimal torque density, despite the availability of certain market products. Figure 5.34 illustrates the rotor flange connections and the outer diameter limitations of the single-stage DCSG [41].

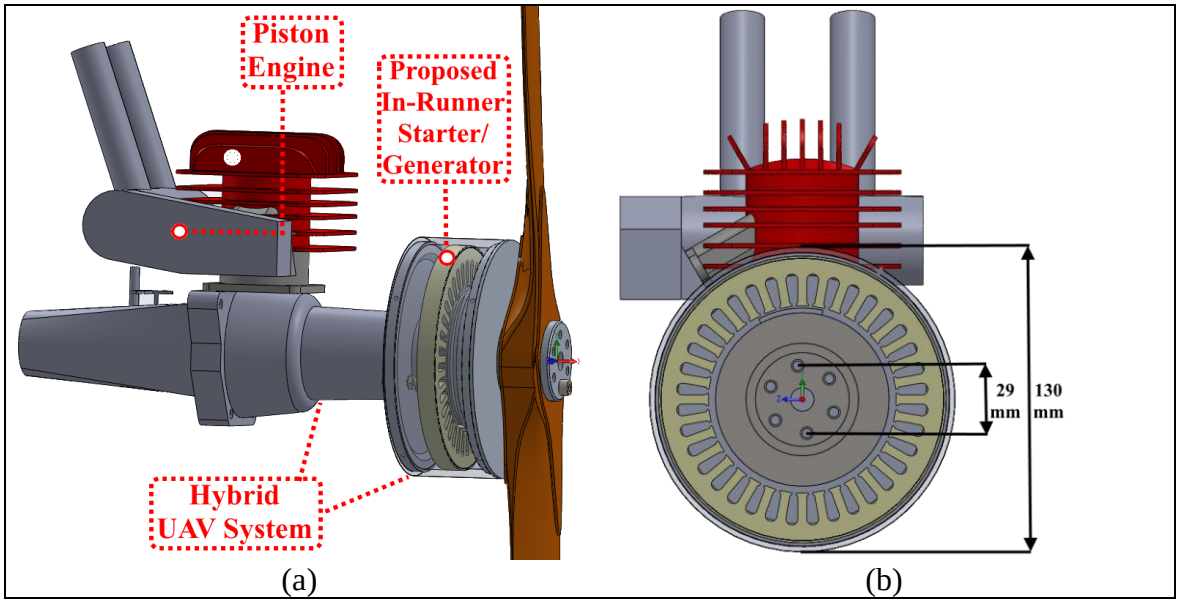


Figure 5.34. (a) Single-stage DCSG integration (b) Integration dimensions

The performance values are analysed separately to accommodate the varying operating speeds between the motor and generator modes. While small UAV systems typically utilize a 28 VDC battery pack, the DCSG is specifically designed for a 48 VDC DC bus inverter. In generator mode, when the operating speed falls below the nominal value, the S/G charges an additional 28 VDC battery group. Table 5.8 serves as a reminder of the design parameters.

Table 5.8. Design data and constraint summary of the Starter/Generator stages

Motor Mode Performance Data		
Design Parameter	Value	Unit
Rated torque	2.1	N.m
Rated speed	4500	rpm
DC bus voltage	48	VDC
Operational speed range	3500-5000	rpm
Generator Mode Performance Data		
Design Parameter	Value	Unit
Rated output power	1250	W
Rated speed	5500	rpm
Generated phase voltage, min.	15	VAC-rms
Operational speed range	4500-6500	rpm
Constraints		
Outer diameter limit, including case	130	mm
Maximum model length, excluding the case	25	mm
Total weight, excluding case and covers	1.5	kg

The control method for the S/G stages of the DCSG is FOC. In the motor mode of S/Gs, the DC bus voltage is 48 VDC, and the switching technique employed is SVPWM. Based on these parameters, the motor mode $V_{L\text{-}L}$(rms) value is calculated as 34 VAC (48 VDC×0,707), as shown in Table 4.5. However, when the duty cycle ratio of the DCSG driver switch reaches 0.95, the motor $V_{L\text{-}L}$(rms) is adjusted accordingly to 32 VAC (34 VAC×0,95). Hence, the number of turns for the motor mode is determined based on this adjusted value.

5.6.1. Operating points of Starter/Generator based on working modes

Figure 4.41 depicts the common torque and speed characteristics of a conventional piston engine employed in aviation applications. However, for mini-small scale UAVs, customised piston engines are utilized to enhance performance. The performance of these UAVs is also inherently reliant on the specific customization of the piston engine and the choice of propeller. Furthermore, these specialized piston engines often demonstrate distinct operating characteristics that deviate from the conventional torque-speed graphs observed in conventional piston engines. Consequently, it is imperative to directly measure the torque, speed, and thrust values of the piston engine through a dedicated direct method test system.

Figure 5.35 (a) and (b) showcase the output power and specific fuel consumption obtained from the direct-test system, illustrating the performance for both the DLE-30 and the 3W-55XI piston engines employed in this particular context. These figures provide valuable insights into the characteristics and performance capabilities of the respective engines, serving as essential references for the integration and optimization of the DCSG model.

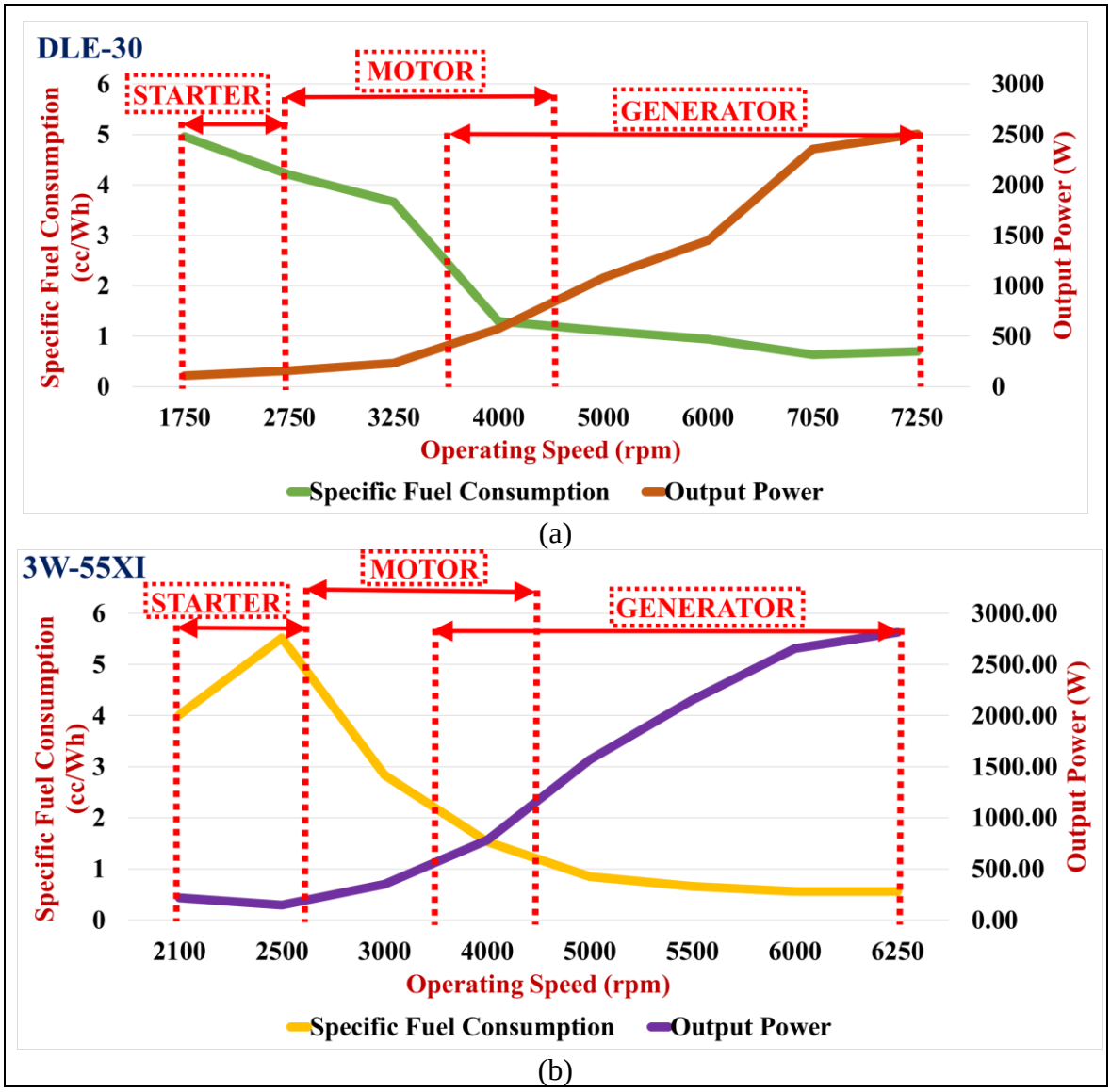


Figure 5.35. Output power and specific fuel consumption curves of (a) DLE-30 with 19x8 wooden propeller (b) 3W-55XI with 24x8 wooden propeller

Fundamental principle of DCSG is based on an efficieny-tracking approach. Specifically, the DCSG serves as the primary propulsion source in situations where the piston engine demonstrates inefficiency and high specific fuel consumption. Conversely, when the piston engine operates efficiently with low specific fuel consumption, it becomes the primary power source, while the DCSG charges the battery pack. Additionally, as described in Section 2, during scenarios such as G-turns, climbing, sudden manoeuvring, and turbulence, both the piston engine and the DCSG work in tandem to provide propulsion capabilities.

The designed DCSG stages have been tailored to achieve compatibility with the DLE-30 and 3W-55XI piston engines employed in various UAV systems, requiring no modifications.

To achieve this, consistent operating regions have been established.The starter mode operates within the range of 1750-2750 rpm, the motor mode operates within 2750-4500 rpm, and the generator operating zones span 3500-7250 rpm. These predefined ranges allow for effortless integration and optimal utilization of the DCSG stages across diverse systems.

5.6.2. Determination of duty-cycle for S/G stages in the DCSG model

The duty cycle, as defined by the IEC standards [381], establishes the operational conditions of the EMs. The duty cycle class of the DCSG in this model is classified as S8, indicating continuous operation with periodic variations in load, as shown in Figure 5.36.

This duty cycle plays a pivotal role in determining the current density and electrical-magnetic specific loadings during the analytical design process. Failure to meet the duty cycle conditions can lead to excessive heat generation and potentially result in performance values below their rated capabilities.

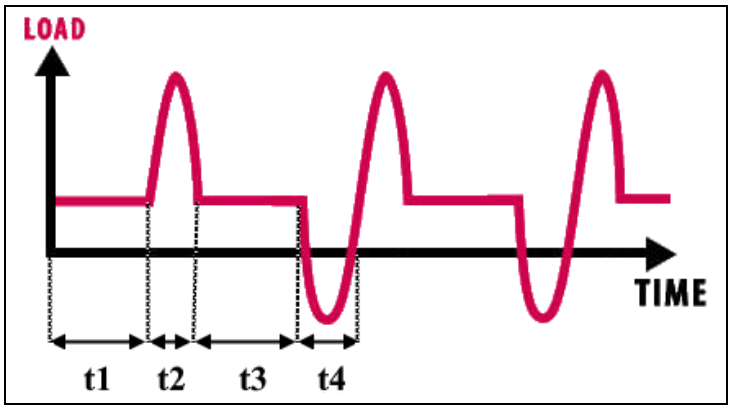


Figure 5.36. Determination of duty-cycle of S/G stages

The electromagnetic design process of the S/G commences with analytical calculations, where initial dimensions are provided as input for sensitivity analysis using Ansys RMxprt. The finely tuned analytical structure, adjusted for sensitivity, is then modelled in Maxwell 2D to perform multiobjective FEA, aiming to identify optimal design values. The optimized model, based on FEM, is further simulated in Maxwell 3D to generate efficiency and torque maps. To minimize the solution time, the S/G model is divided based on the symmetry ratio. Stator and permanent magnet materials are selected as M250-35A and N38SH, respectively.

The preliminary dimensions are derived utilizing the PMSM design equations in Section 4.8. The analytical design incorporates independent variables, which are outlined in Table 5.9.

Table 5.9. Independent variables of analytical design

Adjustable Independent Variables	Analytical-Accepted	RMxprt-Calculated	Maxwell FEA-Calculated
Specific magnetic loading, T	0.68	0.65	0.63
Electric loading, kA/m	30	26	24
Current density, A/mm^2	6	7	8.1
Stator tooth flux density, T	1.5	1.46	1.44
Stator yoke flux density, T	1.4	1.3	1.3
Rotor yoke flux density, T	1.1	1	0.95

In the analytical design phase, the specific magnetic and electrical loadings, initially accepted at the onset of the design, are presented in the "Analytical" column. Upon concluding the final design, the data obtained from the RMxprt and the results obtained from the Maxwell FEA are consolidated in the same table to facilitate a comprehensive comparison. The design outputs are summarized in Table 5.10.

Table 5.10. Comparison of Starter/Generator design methods

Design Outputs	Analyses Methodologies		
	Analytical	RMxprt Sensitivity	Maxwell 2D-FEM
D^2L, rotor volume product, cm^3	115	105	96
Stator tooth width-parallel, mm	4.77	4.49	3.83
Stator yoke width, mm	8.05	7.58	7.5
Rotor yoke width, mm	10.45	9.85	9
PM thickness, mm	2.3	2.7	3
Efficiency, %	84	87	90
Weight of active parts, kg	1.6	1.45	1.3
Torque density, N*m/kg	1.4	1.5	1.65

In the analytical design, the initial efficiency of 84% was enhanced to 87% through RMxprt analytical optimization. Furthermore, with Maxwell FEM optimizations, the efficiency further improved to 90%.

5.6.3. RMxprt sensitivity analyses for stator Slot/Pole number combinations

Sensitivity analyses play a crucial role in examining how changes in independent variables influence dependent variables within a given set of assumptions. In the context of the design process, the ratio of stator slots to pole numbers holds significance because it impacts key factors such as the winding factor and the occurrence of space harmonics resulting from the distribution of ampere-conductors. By increasing the ratio, the winding factor improves while the presence of space harmonics diminishes. However, it is important to note that an increase in the number of poles can introduce complexities in the driver structure due to higher voltage frequencies that need to be handled.

Figure 5.37 offers a valuable depiction that delves deeper into the implications of different slot and pole combinations. This figure provides a comprehensive analysis of various combinations in terms of their efficiency, frequency, copper loss, weight of active parts, and torque density. These parameters are critical considerations in the design process. Among the combinations evaluated, the variation of 36 slots and 8 poles is specifically chosen based on accumulated experience and expertise, warranting further investigation and analysis.

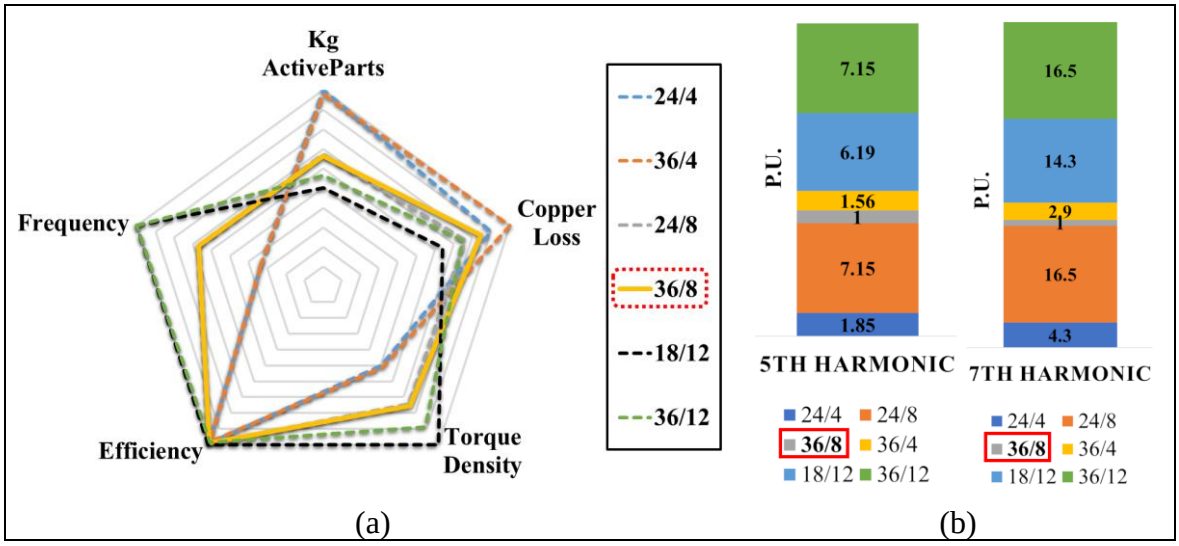


Figure 5.37. Stator slot and pole number selection (a) Parameters (b) Space harmonics

5.6.4. Stator bore diameter and stack length separation based on RMxprt

Stator bore diameter and model length determination takes into account various constraints. Figure 5.38 illustrates that as the model length decreases, the weight also decreases.

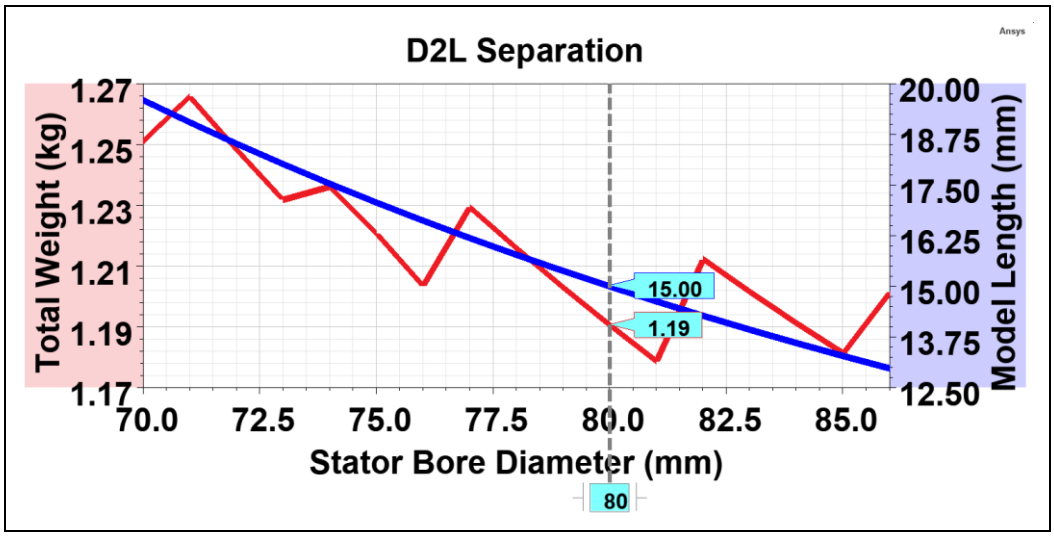


Figure 5.38. Stator bore diameter and model length separation

However, opting for a shorter length can lead to production and winding challenges. To strike a balance, a stack length of 15 mm is chosen, considering the design limitations outlined in Table 5.8 and the requirement for an adequate end-span length of the coils.

Moreover, efforts have been made to maximize the specific loadings to enhance power density. Consequently, a stator bore diameter of 80 mm is selected, and the resulting current density and electric loadings are presented in Table 5.9.

5.6.5. Stator and rotor yoke thickness determination based on RMxprt

The determination of the stator yoke thickness aims to achieve a magnetic operating point close to saturation while minimizing weight. Based on this objective, a stator yoke thickness of 7.5 mm is selected. Likewise, for the rotor yoke, a thickness of 9 mm is chosen. These values, depicted in Figure 5.39, are carefully determined to optimize the magnetic performance of the system, taking into account weight considerations.

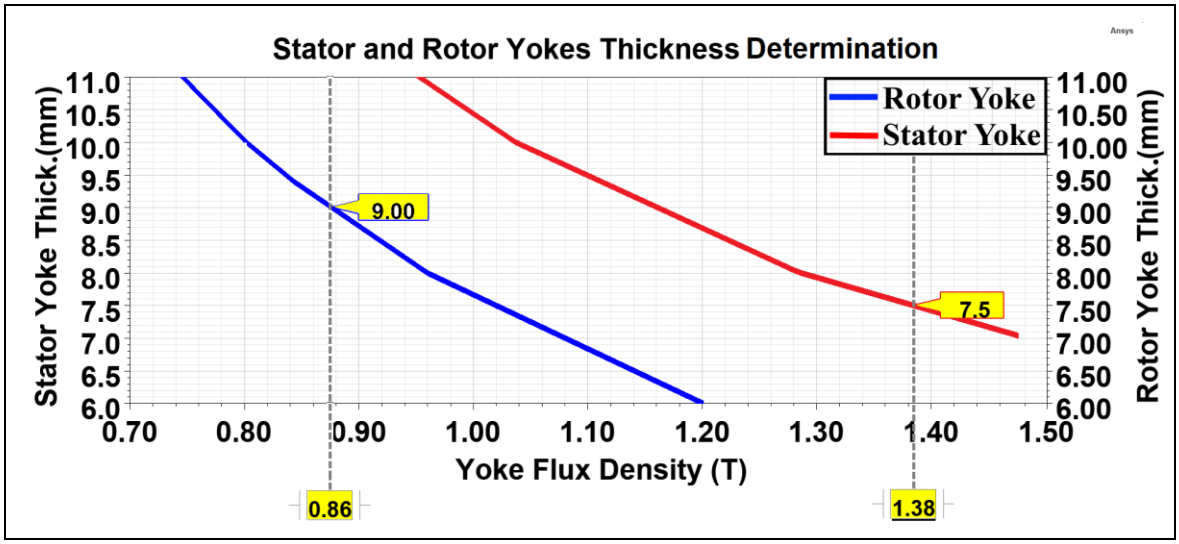


Figure 5.39. Thickness of stator and rotor yokes determination

The flux density distribution, as depicted in Figure 5.40, showcases the magnetic characteristics of the model. It is observed that the model operates well below but close to the saturation points, indicating that the magnetic field strength is within the desired range throughout the system. This ensures efficient and reliable performance without compromising the integrity of the components.

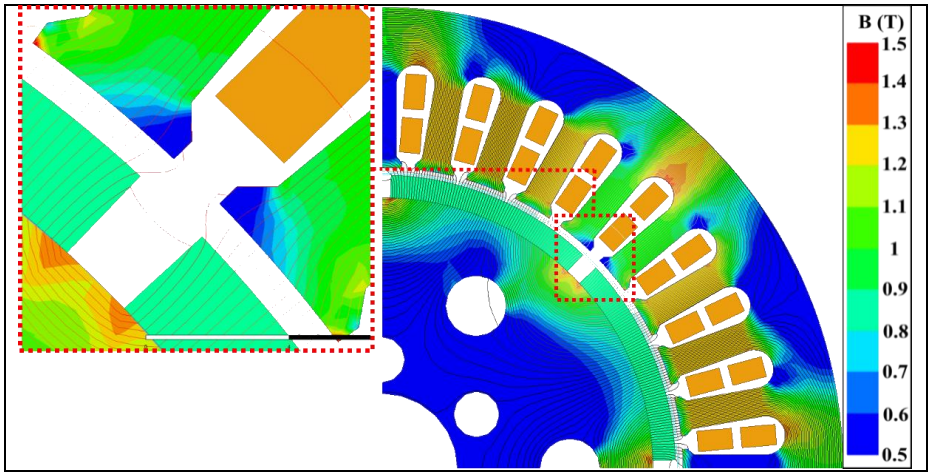


Figure 5.40. Magnetic flux density distribution of the stator and rotor

5.6.6. Air gap clearance investigation based on RMxprt

Figure 5.41 illustrates that increasing the air gap length leads to a higher specific electrical loading, while maintaining the same output coefficient. This observation highlights the importance of carefully selecting the air gap length to optimize the system performance.

On the other hand, it is important to note that when determining the air gap length, the consideration of a retaining sleeve becomes crucial to mitigate the impact of high centrifugal forces on the permanent magnets at elevated speeds. For the specified hybrid UAV application, an air gap length of 1 mm is chosen. Additionally, a stainless steel containment shroud, with a thickness of 0.4 mm, is initially utilized to provide structural support.

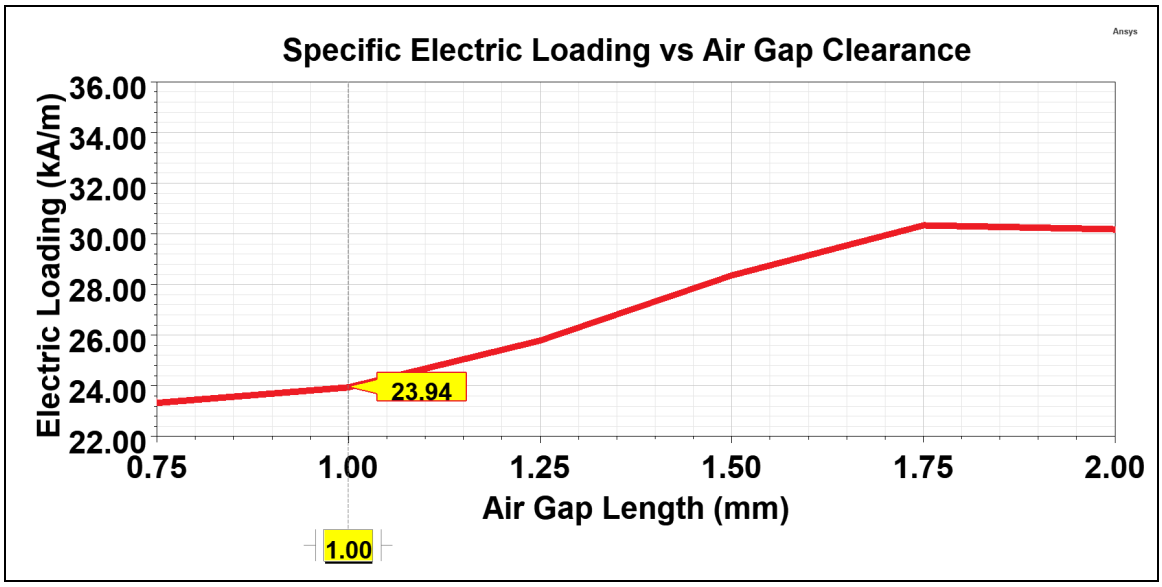


Figure 5.41. Air gap determination based on specific electric loading

5.6.7. Determination of the thickness of permanent magnets based on RMxprt

The thickness of the PMs plays a crucial role in determining the average air gap flux density and output power of the system. Figure 5.42 demonstrates that the optimal air gap average flux density is achieved with a magnet thickness of 3 mm. It is important to note that increasing the magnet thickness beyond this point may lead to material saturation, while decreasing the thickness may result in lower magnetic loading. Therefore, careful consideration is given to selecting the appropriate magnet thickness to strike a balance between achieving the desired flux density and maximizing the overall output power.

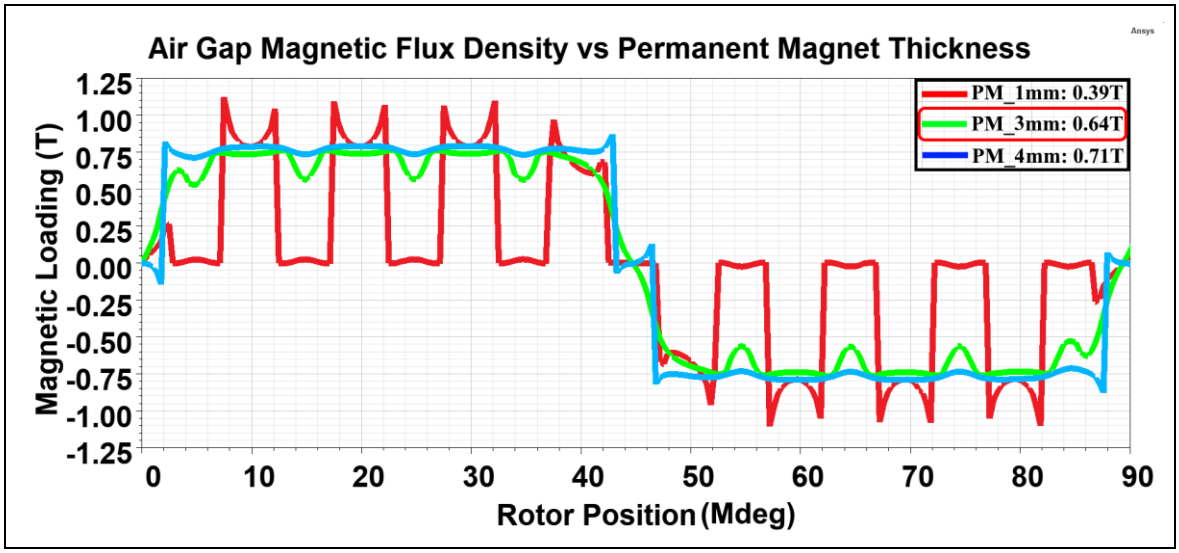


Figure 5.42. Air gap determination based on specific electric loading

5.6.8. Permanent magnet temperature effect on dynamic torque based on RMxprt

Figure 5.43 depicts the impact of temperature variations of the PMs on the dynamic torque. The torque ripple for the system is observed to be 0.11 N.m. In the context of the analysis, the terms Mdeg and Edeg correspond to the mechanical and electrical angles, respectively.

To minimize torque ripples, additional techniques such as skewing can be employed on either the stator or the PMs, as suggested in reference [382]. The analysis takes into account the worst-case operating conditions of the S/G, where the PMs reach a temperature of 120 degrees Celsius. By considering these extreme conditions, the design can be optimized to ensure reliable and stable performance even under challenging scenarios. The detailed demagnetization analyses are performed using 2D FEA, as discussed in the following results.

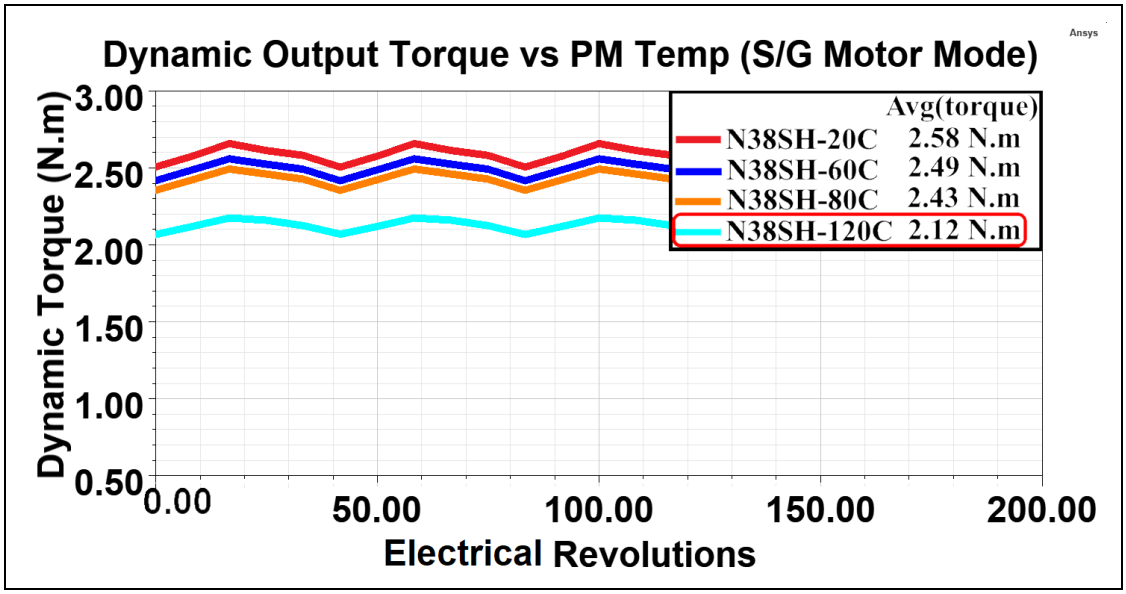


Figure 5.43. Dynamic output torque versus magnet temperature changes

5.6.9. Determination of the Carter and Leakage factor based on 2D FEA

As mentioned in Section 4.8.12, the Carter factor is employed to account for the impact of stator slot openings, which results in increased air gap reluctance. The evaluation of slot opening effects in a closed-slotted stator is a relatively straightforward process. The Carter factor for the single stage of the S/G is shown in Figure 5.44.

The Carter factor for this model was determined to be 0.26, considering the slot-opening structure of the S/G stage. This factor is utilized to estimate the effective air gap length, which is taken into account during both analytical and numerical sensitivity analyses.

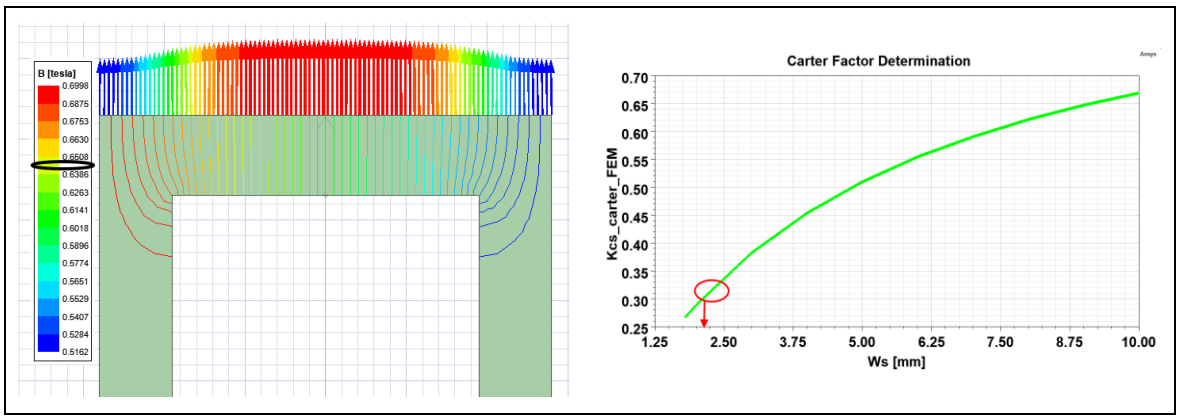


Figure 5.44. Carter factor determination of the single-stage Starter/Generator of the DCSG

Special attention should be given to the design of the stator and rotor, as the air gap flux density decreases with increasing leakage factor, as depicted in Figure 5.45.

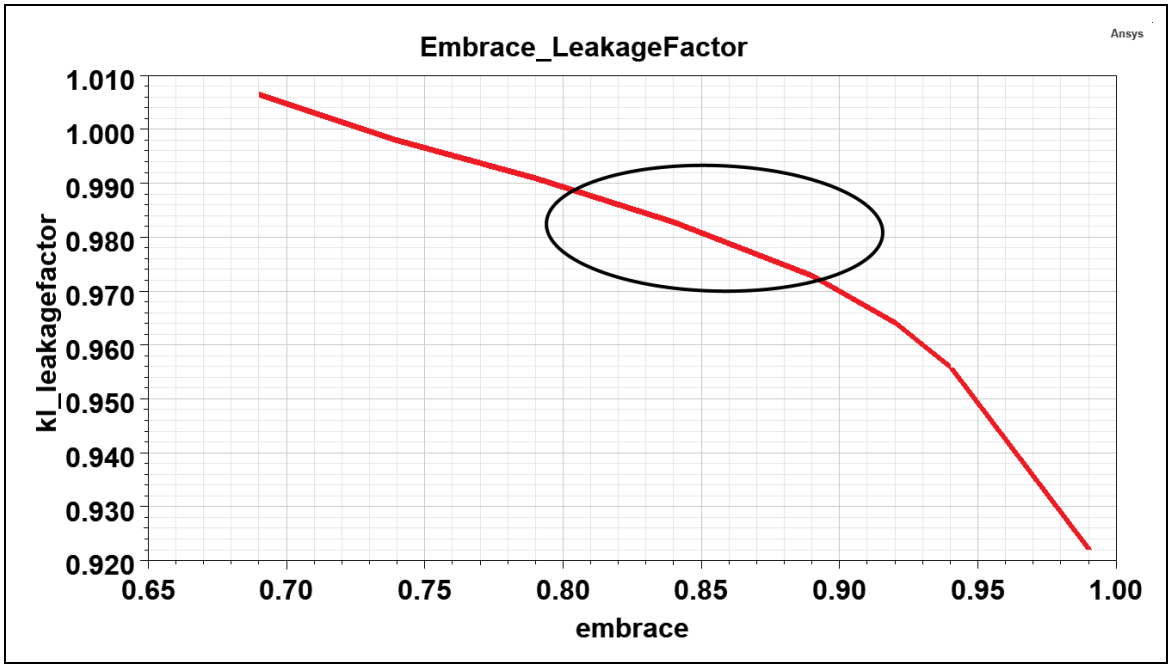


Figure 5.45. Leakage factor of the single-stage S/G

5.6.10. d-axis alignment of the stator and rotor

One notable vector control mode is the I_d=0 vector control, as discussed in Section 4.4.5, which aims to minimize losses and improve efficiency by maintaining the zero direct current component in the machine. To implement this control strategy, it is crucial to align the d-axis of the rotor with the phase windings. Figure 5.46 illustrates the alignment angle of 7.5 mechanical degrees, indicating the optimal orientation of the rotor and Phase A windings. By ensuring this alignment, the magnetic field generated by the PMs interacts effectively with the stator windings, enabling precise control of the Starter/Generator.

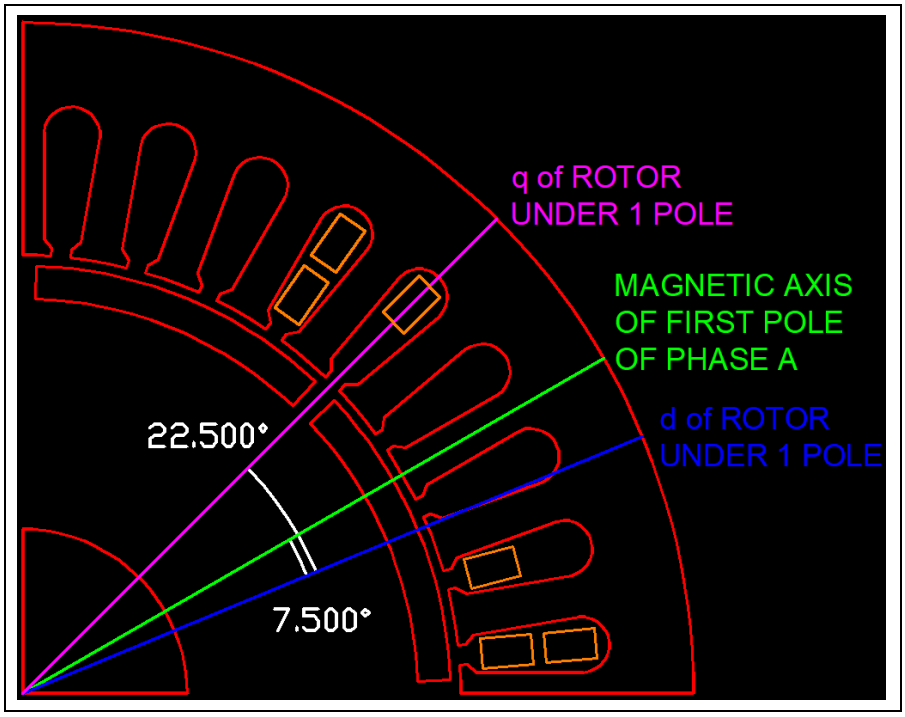


Figure 5.46. Rotor alignment mechanical angle illustration

5.6.11. Demagnetization study based on 2D FEA

The demagnetization study is an essential analysis conducted to ensure the safe and reliable operation of permanent magnet synchronous motors (PMSMs). PMSMs rely on permanent magnets to generate the magnetic field necessary for motor operation. However, under certain operating conditions, such as high temperatures or excessive external magnetic fields, there is a risk of demagnetization, which can lead to a loss of machine performance or even complete failure, as analysed analytically in Figure 5.43.

The purpose of the demagnetization study is to assess the S/Gs susceptibility to demagnetization and determine the safe operating limits. This study involves evaluating the magnetic properties of the PMs used in S/Gs and analysing their response to various operating conditions. One important scenario is when the torque angle is set to 180 electrical degrees, as depicted in Figure 5.47. At this torque angle, the stator winding current aligns precisely with the rotor d-axis, resulting in a demagnetizing effect on the PMs. This configuration can lead to a reduction in the magnetic field strength of the magnets.

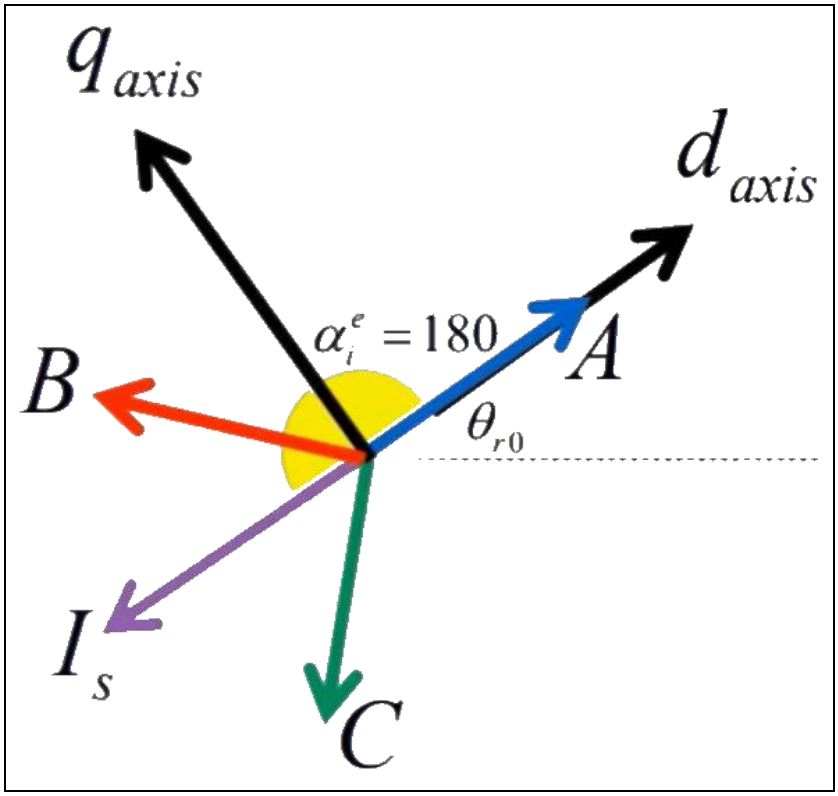


Figure 5.47. Demagnetization study approach [365]

The worst-case scenario involves identifying the operating conditions that pose the highest risk of demagnetization. This includes considering factors such as maximum temperature and maximum external magnetic field that may affect the PM properties. On the other hand, the over-case scenario explores the demagnetization behaviour under extreme conditions that exceed the normal operating limits. The demagnetization study takes into account both worst-case and overcase scenarios, as shown in Figure 5.48 (a) and (b), respectively.

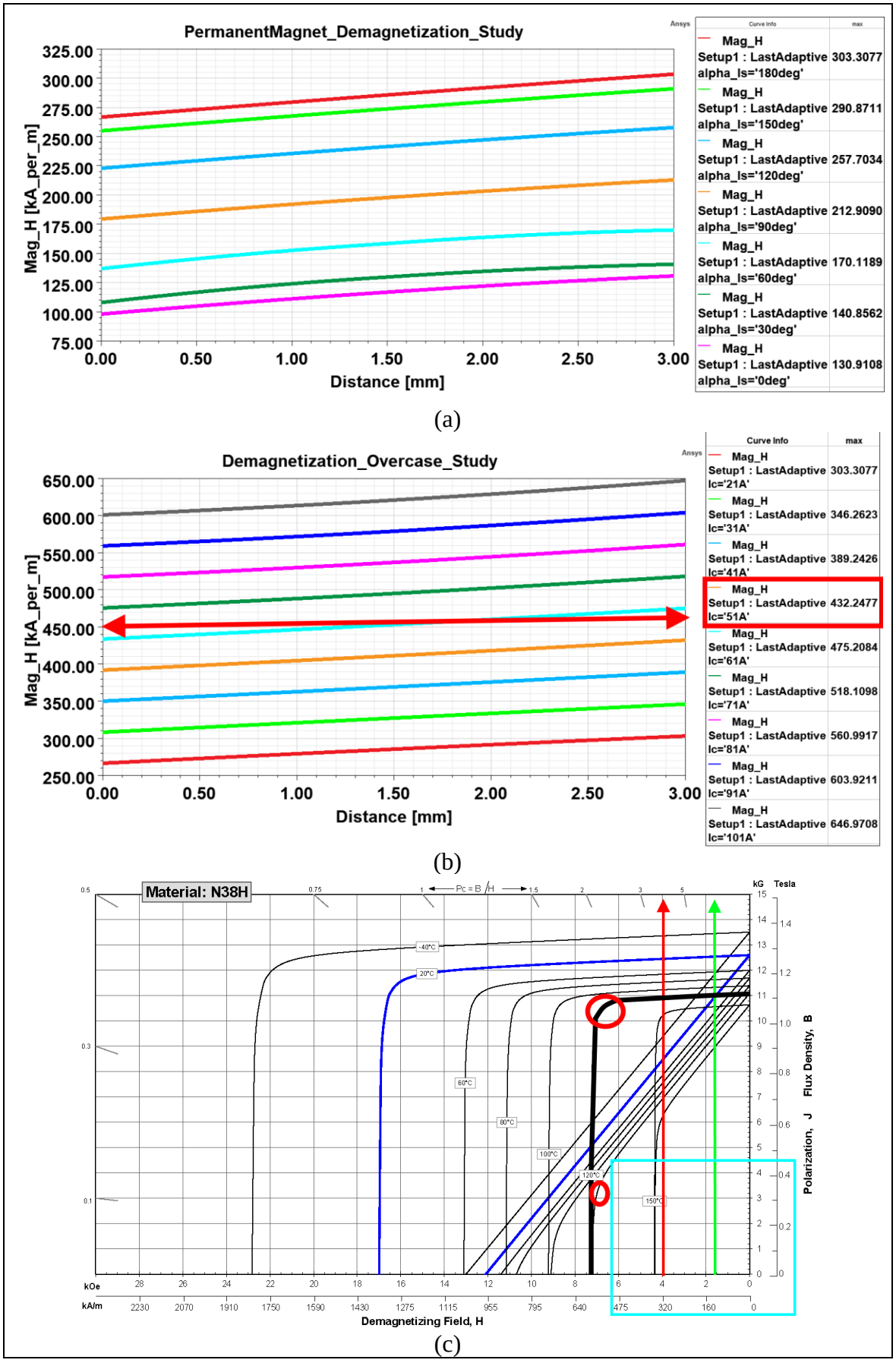


Figure 5.48. Demagnetization study (a) Worst-case (b) Overcase

Upon examination of Figure 5.48 (c), it is evident that the S/G stages operate safely below the demagnetization point even under worst-case operating conditions. Furthermore, Figure 5.48 (b) provides detailed information on the overstate criteria, revealing that the demagnetization limit occurs at 50 A when the torque angle is set to 180 Edeg.

To safeguard the S/Gs against demagnetization, precautionary measures are necessary in the driver against short circuits. Techniques such as employing a 50 A fast fuse or semiconductor current protection can be implemented to mitigate the risk of demagnetization. These protective measures serve to ensure the integrity and longevity of PMs.

It is important to note that in the event of demagnetization, the upper surfaces of the magnets tend to be more susceptible than the entire magnet, as depicted in Figure 5.49. This characteristic allows for the safe landing of the UAV even in cases of potential overloading, as the high specific electrical loading is sustained only for a brief duration.

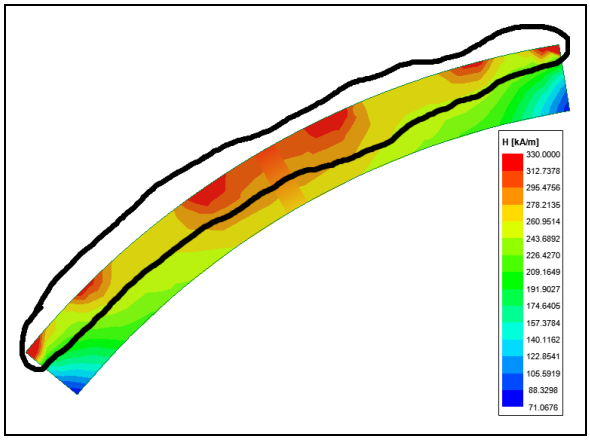


Figure 5.49. Demagnetization over the surface of the PMs in the overcase situation

5.6.12. Matching specific magnetic loading based on 2D FEA

In the initial analytical design of the S/G stages, the absolute average of the radial component of the air gap flux density or specific magnetic loading of 0.68 T was assumed. However, subsequent 2D FEA analysis, as shown in Figure 5.50 revealed an average air gap flux density of 0.64 T, indicating a slight deviation from the initial assumption. To bridge the gap between the analytical and numerical designs, the analytical calculations were revised, incorporating the updated value of 0.64 T instead of the initial 0.68 T.

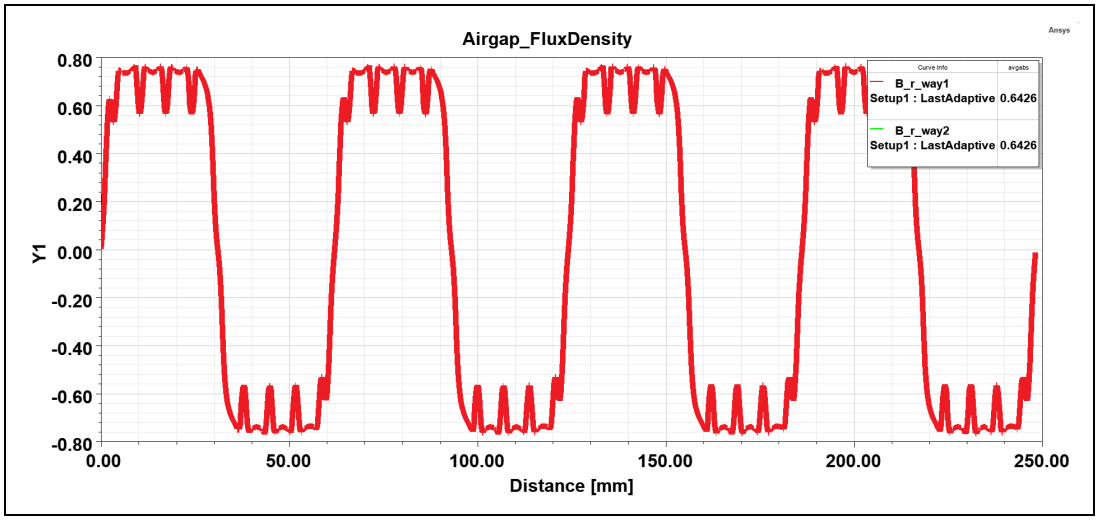


Figure 5.50. Determination of the specific magnetic loading based on 2D FEA

5.6.13. Static torque investigation in motor mode based on 3D FEA

The static torque refers to the torque produced by the DCSG fed by the rated current when it is in a stationary, steady-state or locked-rotor condition, without any rotational motion [201]. Static torque is an essential parameter for drive control in motor mode, as it helps in maintaining stable operation and achieving desired performance characteristics. Figure 5.51 illustrates that the FOC strategy, utilizing the i_d=0 approach, achieves the highest output torque when the torque angle is set to 90 Edeg. This arrangement presents a 90 Edeg phase shift between the stator and rotor fields, ensuring that the q-axis of the rotor aligns with the axis of the stator current, resulting in maximum output torque.

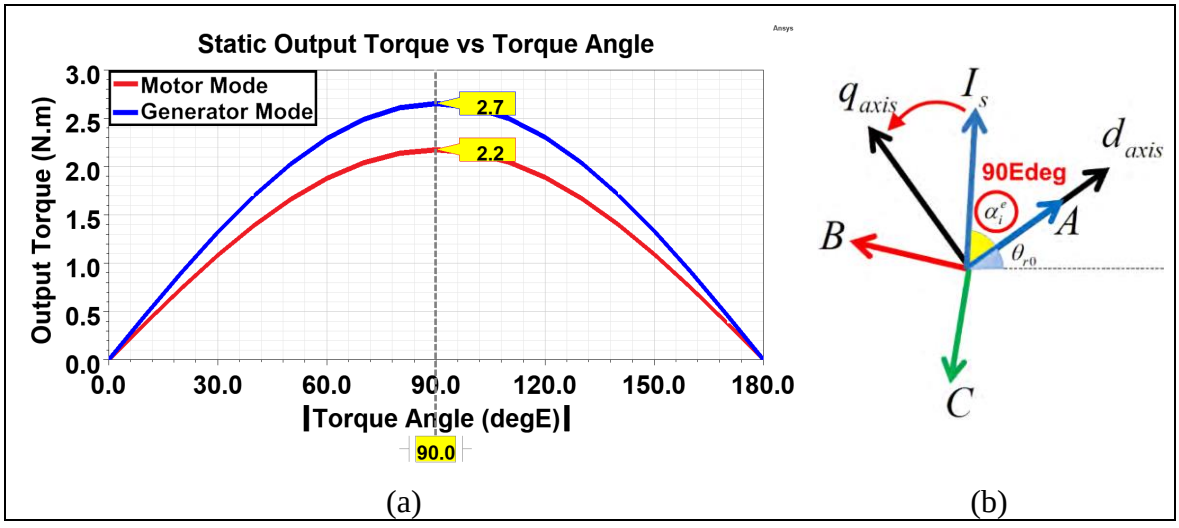


Figure 5.51. (a) Static torque examination versus absolute torque angle (b) i_d=0 control

5.6.14. Induced Back-EMF voltages in generator mode based on 3D FEA

Despite the similarity in output torques between the motor mode and generator mode S/G stages, their winding structures and number of turns differ due to their respective operational characteristics. In the motor mode, the S/G stage directly draws power from the 48 VDC battery group. However, in generator mode, the 24 or 48 VDC battery group is charged. Therefore, it is essential for the induced phase voltages to reach a level that enables charging of the 24/48 VDC LiPo or LiFePo4 battery group after rectification. Notably, considering the generator mode operating range of 3500-7250 rpm, the winding structure needs to be tailored to the minimum speed of 3500 rpm. Figure 5.52 (a) and (b) illustrate the induced back-EMF depending on winding turn numbers for the minimum and maximum speeds.

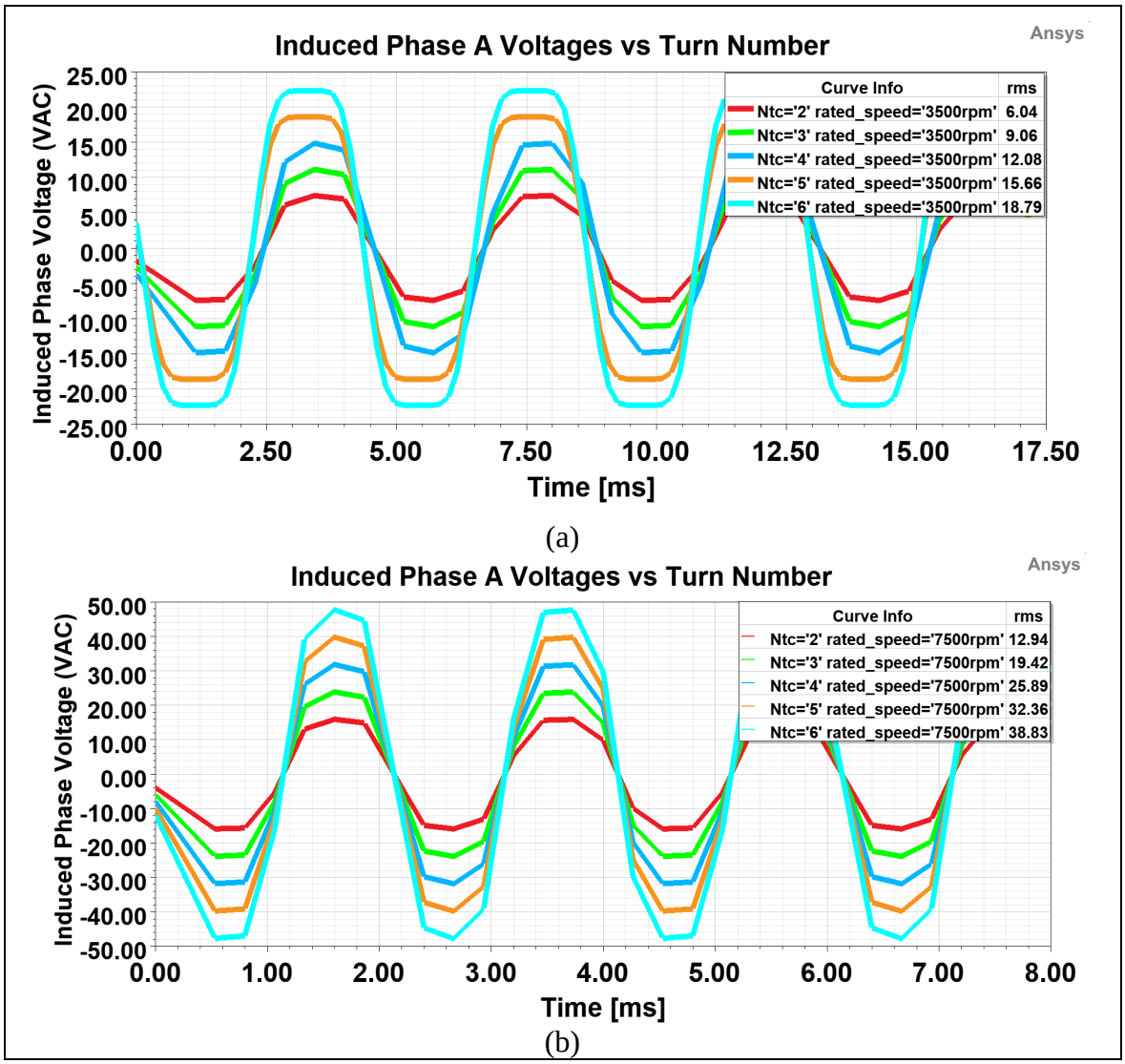


Figure 5.52. Induced back EMF at (a) Minimum speed (b) Maximum speed

Figure 5.53 (a) and (b) depict the output of the full-wave rectifier and output voltages depending on various input voltages based on the battery equivalent circuit, respectively. To ensure efficient charging of the 48 VDC battery pack at high speeds and the 24 VDC battery pack at low speeds, the number of windings was carefully determined to be 4. On the other hand, the number of turns in motor mode was computed as 3 using an analytical method and subsequently corroborated through rigorous analysis utilizing 2D FEM.

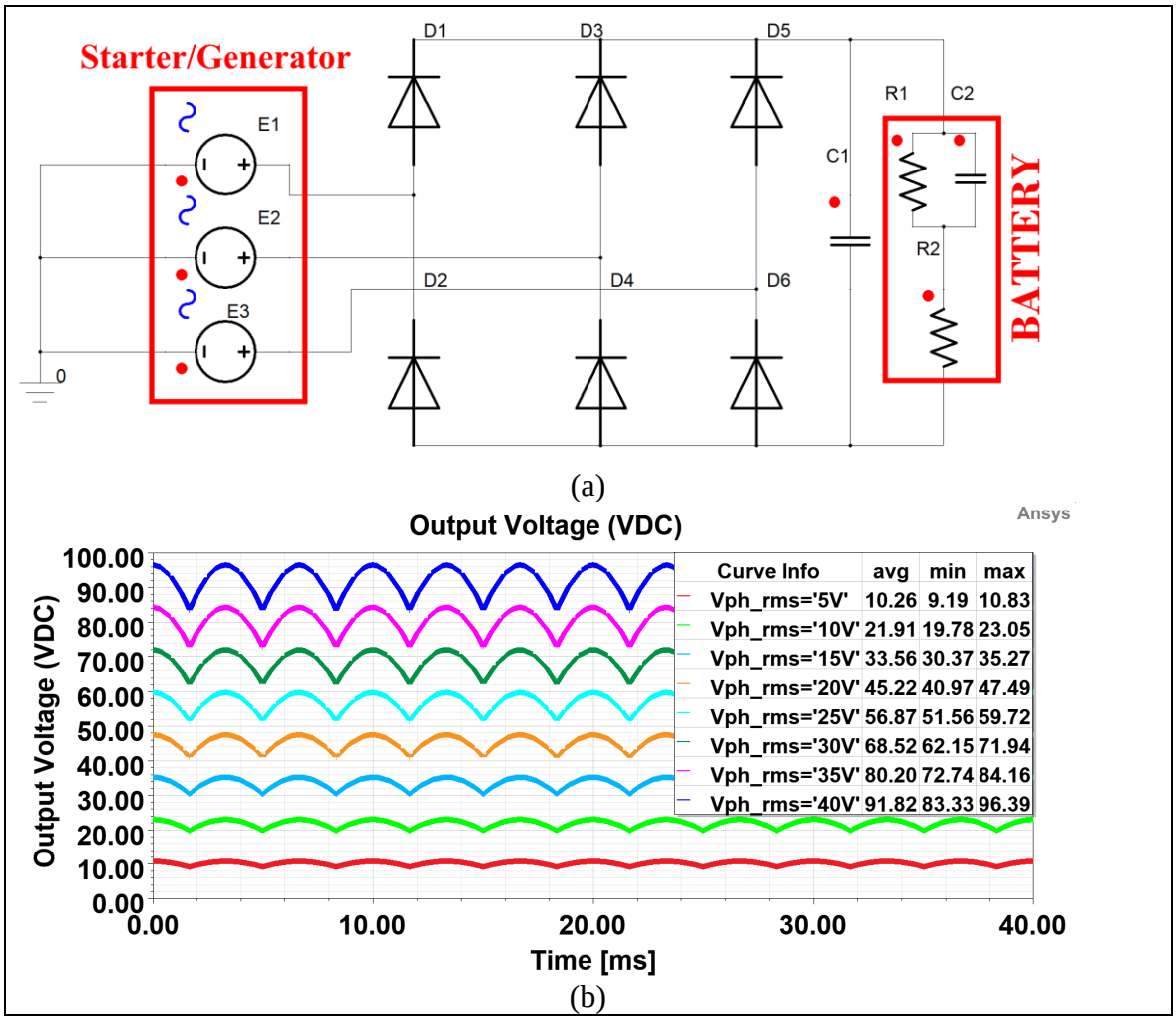


Figure 5.53. Output of the full-wave rectifier depending on different input voltages

5.6.15. Stator slot fill factor

The slot fill factor (FF) is determined by dividing the conductor area by the total slot area, as seen in Eq. 6.3. It represents the proportion of the slot area occupied by conductors.

For instance, a slot fill factor of 0.5 indicates that half (50%) of the slot area is taken up by the conductors, while the remaining is allocated to conductor insulation, slot insulation, and the necessary gaps between the conductors and the slot sides, as illustrated in Figure 5.54.

$$FF = \frac{NA_{wb}}{A_s} \tag{6.11}$$

where N: Total number of turns in the slot
A_{wb}: Wire cross-sectional area without enamel
A_s: Stator slot cross-sectional area

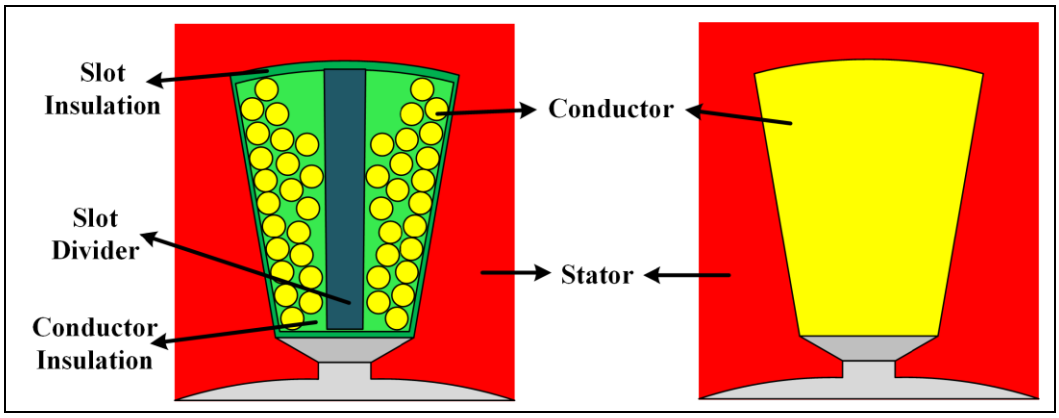


Figure 5.54. Stator slot fill factor [383]

The fill factor is influenced by various factors such as the type of winding (distributed or concentrated), the stator manufacturing method, and the winding technique employed. In the case of factory or automatic machine winding, the FF is typically kept below 45% to accommodate the insertion of needles and other winding components between the stator slots. For manual winding techniques, the FF is maintained below 60% for distributed winding and below 55% for concentrated winding.

However, advancements in stator design, such as segmented structures, allow for higher FF values of up to 70%. In the case of the proposed DCSG model, where the stages of S/Gs have a distributed winding pattern, the FF is targeted to be within the range of 55-60%. Deviating from this range can result in difficulties during the winding process and reduced heat transfer due to excessive slot filling.

5.6.16. Winding Scheme

To facilitate the identification of desirable windings, it becomes necessary to make certain assumptions to focus and delimit the scope of pole and slot count combinations, as well as winding layouts. The following assumptions were taken into consideration in this context [360]:

- The motor comprises three phases and only balanced windings are considered.
- All slots are full and the slot number in 3-ph machine is always a multiple of three.
- Each slot accommodates two coil sides which is double layer winding.
- Number of slots per pole per phase is assumed to be either less than or equal to two.
- All coils possess an equal number of turns and span the same number of slots.

The objective in the winding arrangement is to position coils with a span of S in slot pairs, aiming for minimal angular separation between relative midpoints at approximately 0°E and 180°E. The coil span and winding symmetry are presented in Eq. 6.12 and Eq. 6.13 [360].

$$S = \max\left(fix\left(\frac{N_s}{N_m}\right), 1\right) \pm p_f \qquad (6.12)$$

$$\mathrm{GCD}(Q_s, \frac{(2p)}{2}) \qquad (6.13)$$

where S: Coil span

N_s: Stator slot number

N_m: Number of poles

p_f: Pitch factor

Coils situated close to 0°E are wound in one direction, while coils near 180°E are wound in the reverse or opposite direction. This distinction is made due to the opposite direction of magnet flux at 180°E. Table 5.11 presents the selected phase A coil angles in the S/G stages.

Table 5.11. Coil angles of phase A in the S/G stages

PHASE A				
COIL NUMBER	COIL	SLOT ANGLE	SLOT IN	SLOT OUT
1	1	0	1	5
2	10	0	10	14
3	19	0	19	23
4	28	0	28	32
5	6	20	10	6
6	15	20	19	15
7	24	20	28	24
8	33	20	1	33
9	5	-20	9	5
10	14	-20	18	14
11	23	-20	27	23
12	32	-20	36	32

5.6.17. Dynamic torque and torque ripple exploration based on 2D and 3D FEA

The dynamic torque of an S/G refers to the torque produced by the S/G in motor or starting mode during dynamic or transient operating conditions. During dynamic operation, the S/G experiences variations in torque due to changes in load, speed, or control inputs. These variations can be caused by factors such as acceleration, deceleration, sudden changes in load torque, or adjustments in motor control parameters [384]. In the motor mode, the S/G employs an FOC structure, depicted in Figure 5.55 (a). Conversely, during the starter mode, the S/G utilizes a 6-step commutation control structure, illustrated in Figure 5.55 (b).

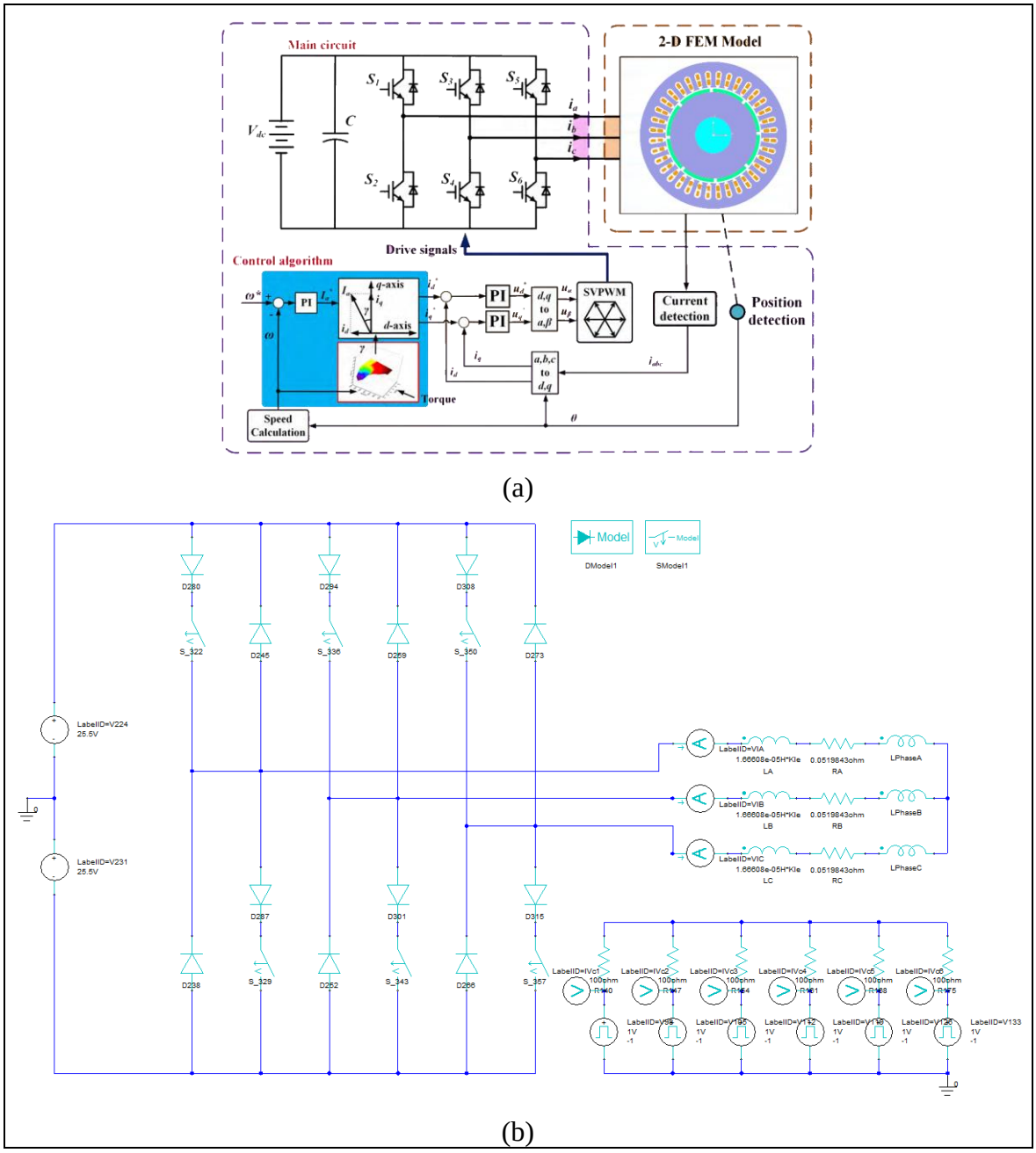


Figure 5.55. Control schematics of the S/G staqes in (a) Motor mode (b) Starter mode

The dynamic torque of the S/G is influenced by several factors, including the machine mechanical and electrical characteristics, the control strategy employed, and the machine moment of inertia and damping effects. To accurately analyse and predict the dynamic torque behavior of the S/G, dynamic models and control algorithms are utilized.

The analysis of output torques for motor mode and starter mode can be found in Figure 5.56 (a) and (b), respectively. In motor mode, despite the S/G stage with the FOC strategy having a lower maximum torque, the torque ripple remains relatively low at 5%.

However, in Starter mode, although the S/G with a 6-step strategy achieves a higher torque, the torque ripple is significantly higher, reaching 35%. Torque ripple is calculated as the difference between the maximum and the minimum torque, divided by the average torque.

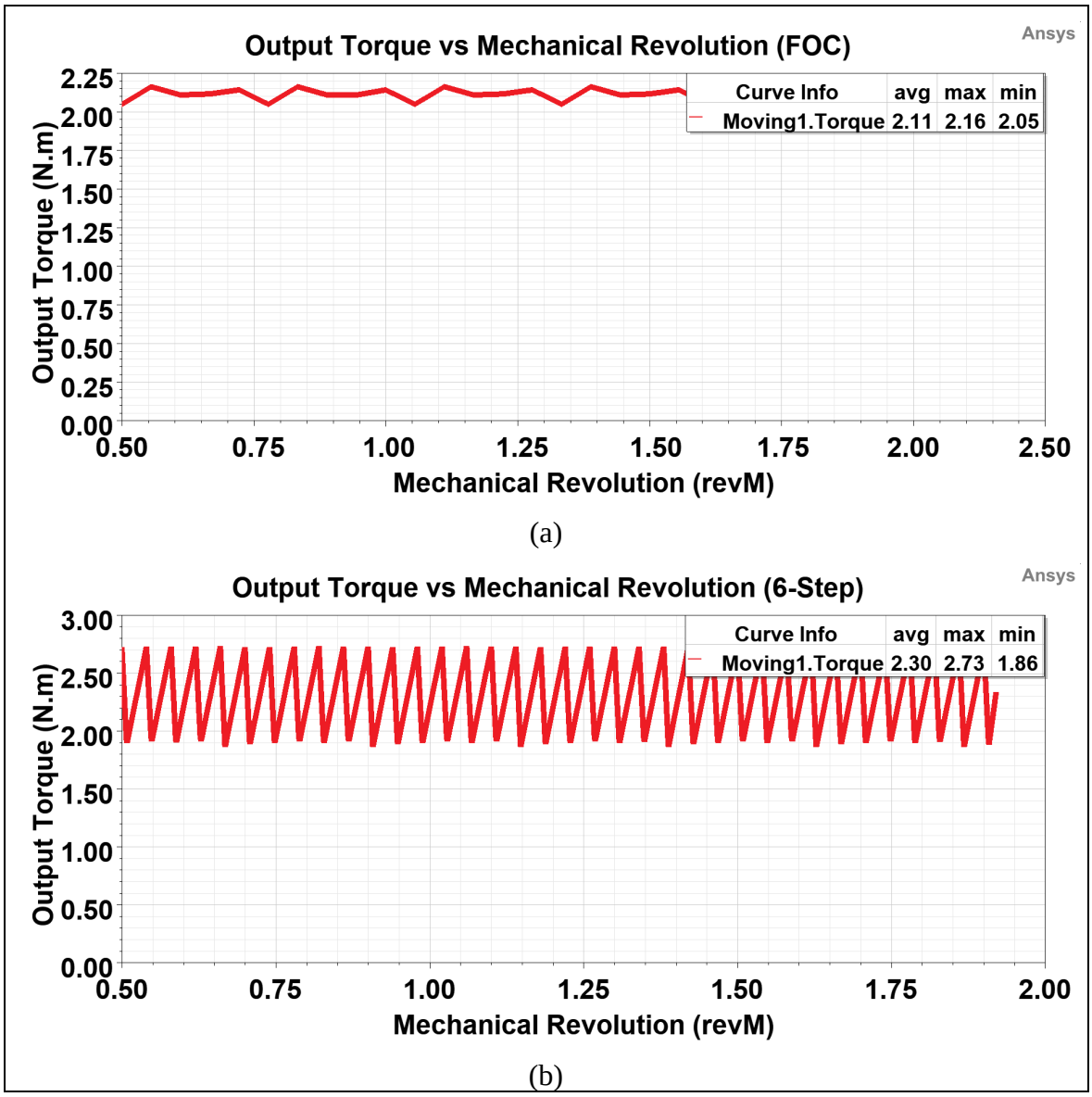


Figure 5.56. Output torque examination (a) Motor mode (FOC) (b) Starter mode (6-step)

5.6.18. Investigation of cogging torque and skew techniques

In permanent magnet motors (PMMs), the cogging torque refers to a detrimental component that affects the average torque. It arises from the interaction between the structure of the magnets, either mounted on or inside the rotor surface, and the structure of the stator teeth when there is no excitation in the winding.

The cogging torque occurs due to changes in the magnetic field caused by the movement of magnets within the rotor.

Figure 5.57 illustrates the cogging torque analysis for the S/Gs. The peak-peak value of the cogging torque is measured to be 18 mN.m. Given the low cogging torque value for hybrid UAVs, skew techniques are unnecessary because the impact on the system would be minimal.

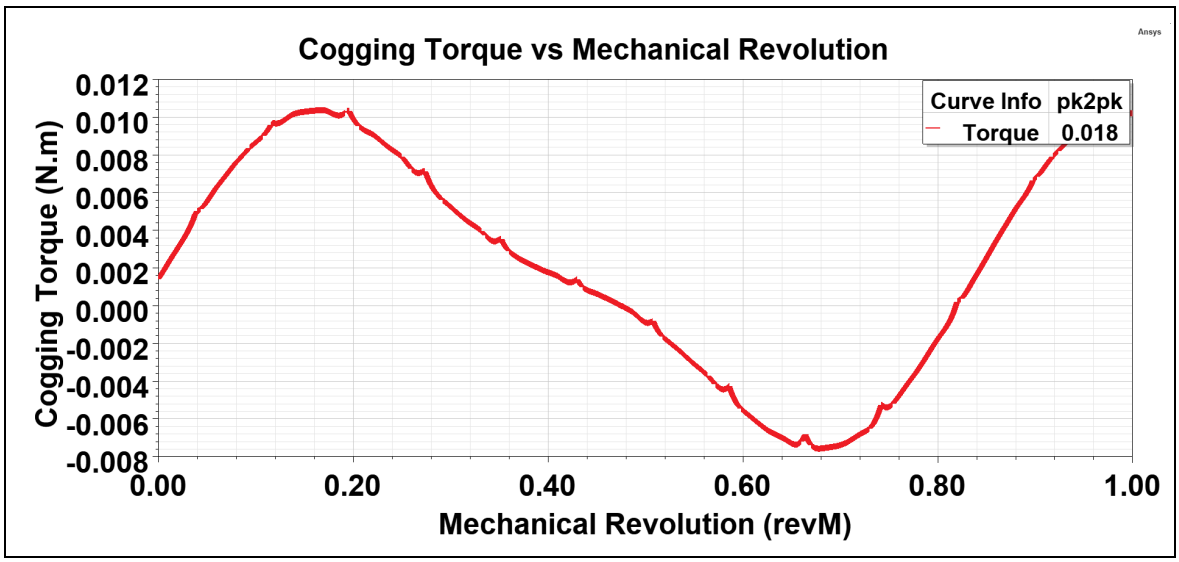


Figure 5.57. Cogging torque investigation of the S/Gs stages

The quality of the output torque directly influences the performance of PMMs and is a crucial consideration in machine design. Torque ripple in electric machines can stem from various sources, including cogging torque, PWM current harmonics, nonideal EMC waveform, and fluctuations in the DC bus.

At low speeds, torque ripple can result in undesirable variations in speed, vibration, and acoustic noise. Minimizing cogging torque, which is a primary contributor to torque ripple in PMMs, is particularly important in low-speed precision applications. However, at high speeds, the inertia of the system can help filter out torque ripples [385]. The literature suggests various techniques, as illustrated in Figure 5.58, to reduce the cogging moment in radial flux permanent magnet synchronous motors [386, 387].

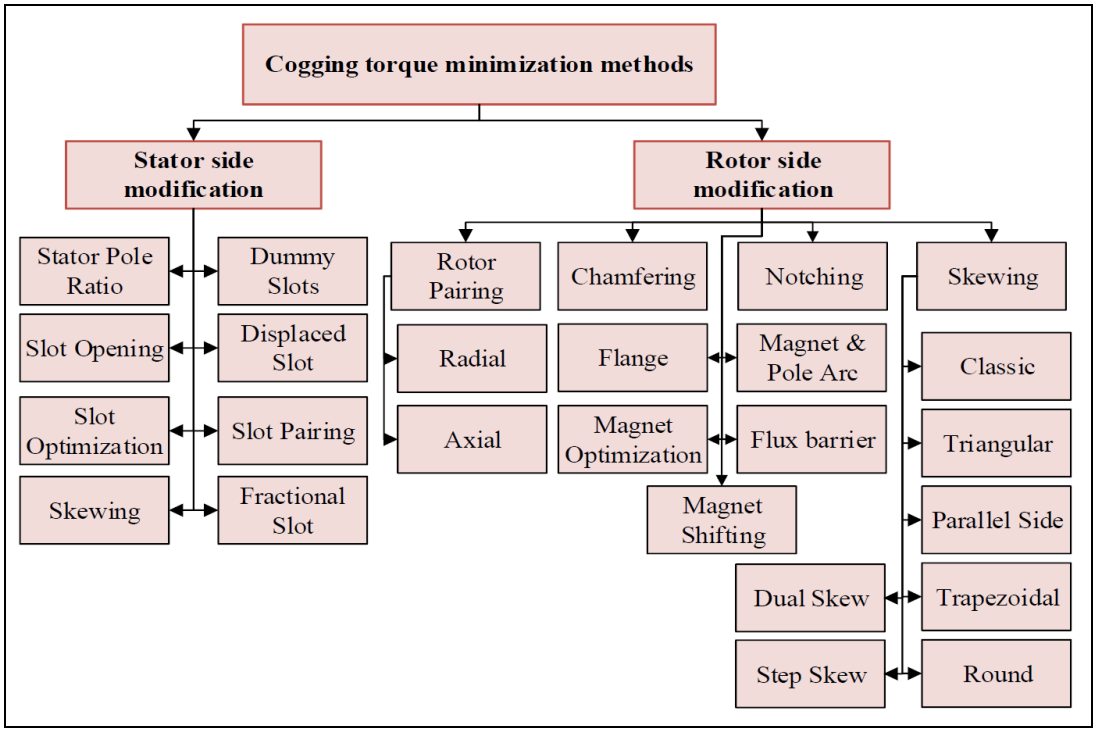


Figure 5.58. Skew techniques for minimization of cogging torque and torque ripple [387]

Figure 5.59 demonstrates the effect of applying the skew technique. While it effectively reduces torque ripple, it also results in a reduction of the maximum output torque. Consequently, the decision to implement skew techniques should be based on the specific application requirements and considerations.

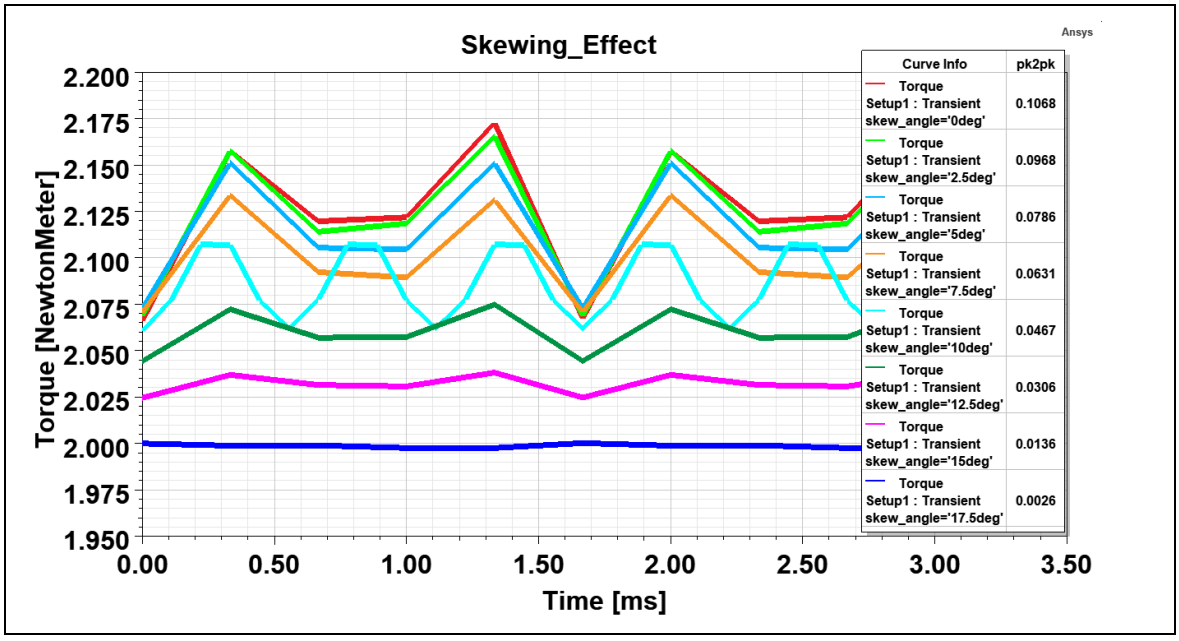


Figure 5.59. Effect of the skew for the S/G stages

5.6.19. Investigation of the losses and efficiency of S/Gs based on 3D FEA

Analytically calculating losses can be a challenging task, but numerical methods provide an effective means of calculation. Starter/Generator losses encompass core losses, permanent magnet losses, retaining sleeve losses, copper losses, mechanical losses, and additional losses, as shown in Figure 5.60.

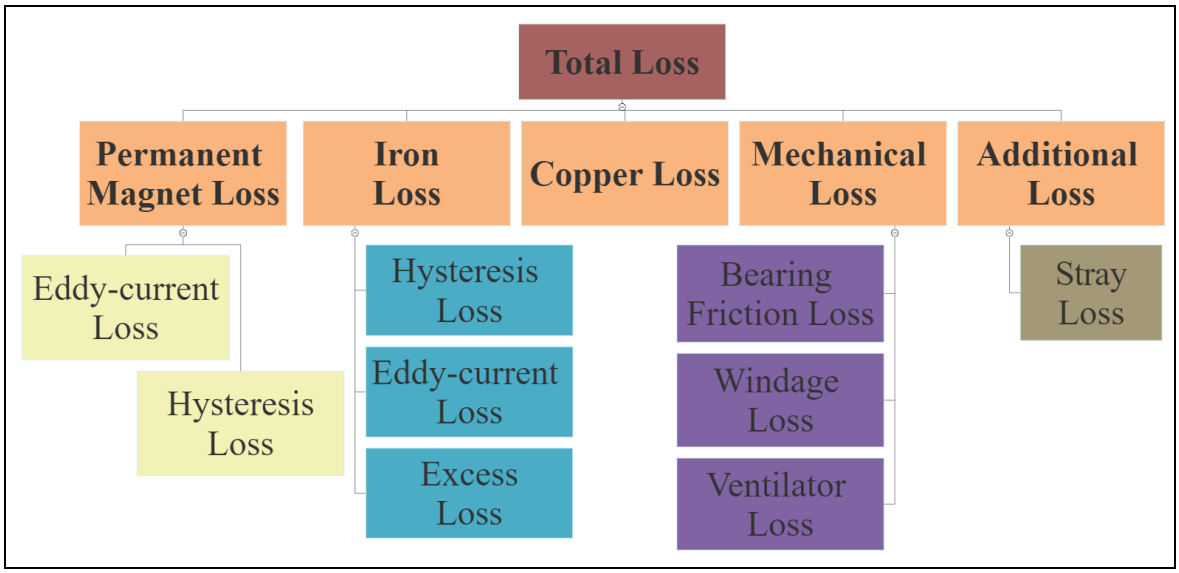


Figure 5.60. Loss table of Starter/Generator

Copper losses occur in the stator windings and are influenced by resistance and current, as shown in Eq. 6.14 [375]. They are categorized as frequency dependent or frequency independent. Frequency independent losses are determined by wire dimensions (length and cross-sectional area) and the material used. Frequency-dependent losses increase with higher frequencies due to the skin effect, which restricts the current-carrying area. To mitigate this effect, larger-diameter wires are divided into multiple separate wires. However, excessive wire division can lead to increased resistance due to the proximity effect.

$$P_{cu} = \mathrm{m} * \mathrm{R}_{AC} * I_{ph}^2 \; ; \qquad \mathrm{R}_{ac} = k_R * \mathrm{R}_{dc} \tag{6.14}$$

where p_{cu}: Copper loss

R_{ac}: AC resistance

k_r: AC resistance factor

R_{dc}: DC resistance

Core losses encompass hysteresis losses, eddy current losses, and additional losses and are calculated in Ansys Maxwell as in Eq. 6.5 [265]. Iron losses are weight-dependent and rely on frequency and maximum flux density. To minimize losses, soft magnetic materials with minimal hysteresis curves, such as electrical sheets, are employed. Iron losses are mainly concentrated in the stator and rotor.

$$p_{loss} = \mathrm{k}_h * f * B^2 + k_c * f^2 * B^2 + k_e * f^{1.5} * B^{1.5} \tag{6.15}$$

where k_h: $hysteresis\ loss\ coefficient\ of\ material$

f: $frequency\ of\ air\ gap\ flux\ density$

B: $absolute\ average\ of\ air\ gap\ flux\ density$

k_c: $eddycurrent\ loss\ coefficient\ of\ material$

k_e: $excess\ loss\ coefficient\ of\ material$

Eddy currents emerge when the magnetic flux within the stator fluctuates. These currents generate losses and heat within the stator. To reduce eddy current losses, the stator is divided into insulated laminations, effectively mitigating these losses. Thinner laminations further decrease eddy current losses [388]. Although losses in magnets are typically small, they are critical because magnets generally have limited temperature resistance. The selection of the retaining sleeve thickness requires careful consideration due to its impact on the air gap length, torque density, and induced eddy-current losses. Detailed analysis of eddy-current losses is crucial because they contribute to increased magnet temperature, leading to a reduction in the residual flux density of the magnets [377].

Changes in the magnetic field can induce wall displacements, resulting in additional losses, also known as excess losses. Estimating stray losses can be challenging, but they generally amount to approximately 1%. Mechanical losses encompass friction losses and ventilation losses. Friction losses depend on the speed and occur in components such as bearings. Proper lubrication of bearings helps minimize friction losses. Ventilation losses occur in electric motors with nonround rotors and are influenced by the speed at which the motor operates.

Extensive analysis of losses and efficiency for the Starter/Generator stages has been conducted using 3D FEA. To present the efficiency in a clear manner, Figure 5.61 illustrates the efficiency of both motor and generator modes considering the losses.

The analysis reveals an efficiency of 90% in motor mode and 92% in generator mode. The 2D and 3D final models of S/Gs are illustrated in Figure 5.61 (a) and (b), respectively.

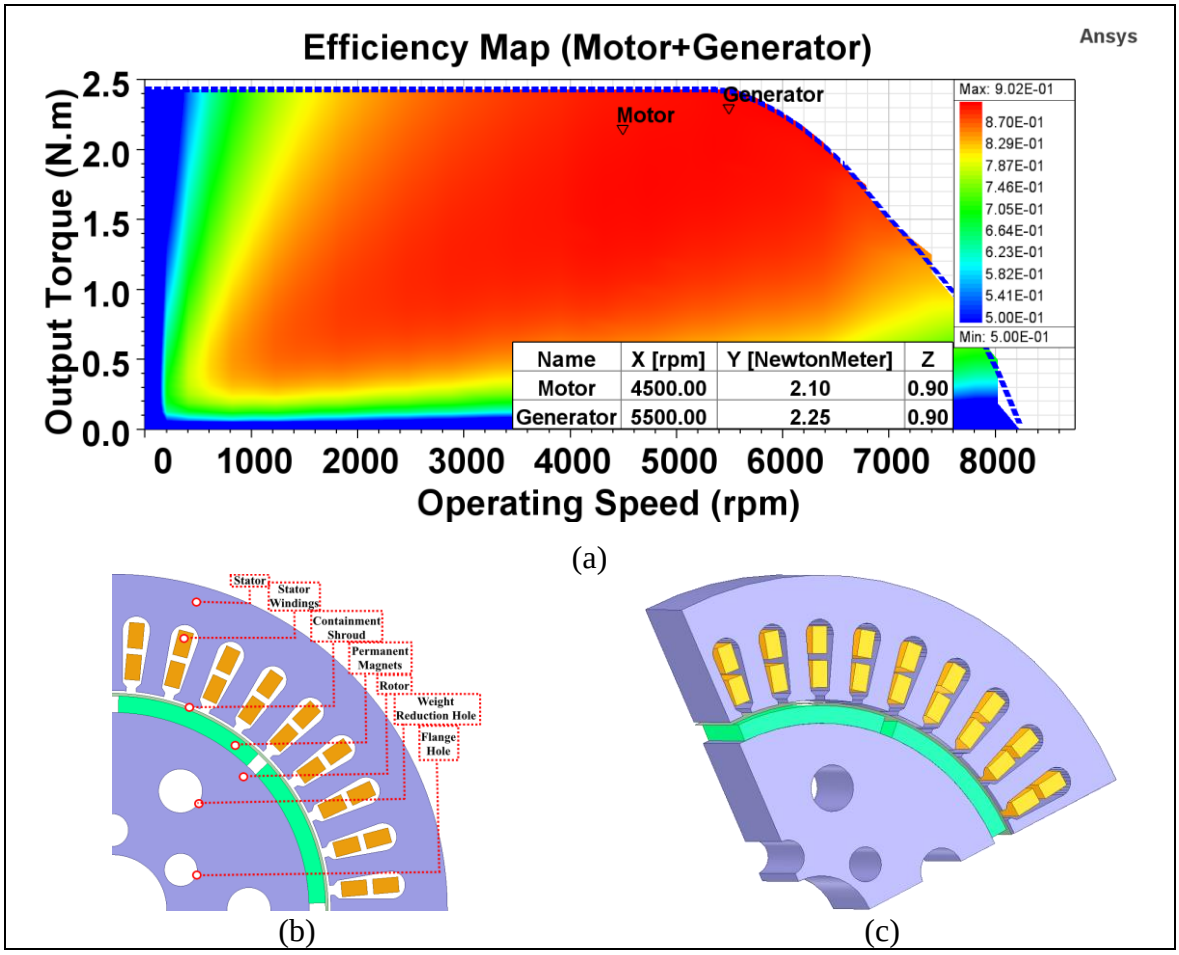


Figure 5.61. (a) Efficiency map in motor and generator mode (b) 2D model (c) 3D model

5.6.20. Retaining sleeve design for Starter/Generator stages

The design of the retaining sleeve for the S/G stages can be carried out analytically, as outlined in Section 5.4.13, following a similar approach used for magnetic couplers. The summarized results of the S/G sleeve design based on 7500 rpm are presented in Table 5.12.

Table 5.12. Retaining sleeve design for Starter/Generator

DESIGN OUTPUTS			
Residual Contact Pressure at Overspeed			
Centrifugal force on sleeve	$p_{w,b}$	0,31	MPa
Centrifugal force on a magnet	$p_{w,m}$	1,87	MPa
Contact pressure (due to interference fit of sleeve)	$p_{c,prestress}$	3,24	MPa
Residual contact pressure	p_c	1,05	MPa
Stress Inside Retaining Sleeve Shell			
Tangential stress (due to rotation of sleeve)	$\sigma_{t,w}$	24,69	MPa
Prestress (due to interference fit of sleeve)	$\sigma_{t,prestress}$	254,45	MPa
Stress inside retaining sleeve shell	σ_t	279,15	MPa
Determination of Retaining Sleeve Thickness			
Minimum thickness of retaining sleeve (contact pressure)	$h_{b,min,pressure}$	0,34	mm
Minimum thickness of retaining sleeve (tangential stress)	$h_{b,min,stress}$	0,38	mm
Selected thickness of retaining sleeve	$h_{b,selected}$	0.4	mm

5.6.21. Optimization of the Starter/Generator

The dimensions of the optimal S/G for motor and generator modes, obtained through Maxwell 2D optimetric simulations, are subjected to microanalysis using optimization techniques in Maxwell 3D. To streamline the optimization process and reduce computational time, the 3D model is divided into one-fifth sections by employing symmetry features.

Various optimization techniques are employed for S/Gs, leveraging tools such as Sequential Nonlinear Programming (SNLP), Genetic Algorithm (GA), and Multi-Objective Genetic Algorithm (MOGA) within Ansys Maxwell [369]. These techniques are selected based on their effectiveness in achieving the desired design objectives. Figure 5.62 provides a comprehensive overview of the optimization techniques utilized and their respective applications within the context of Ansys Maxwell. These techniques allow for efficient design, enabling the identification of optimal dimensions that satisfy the given objectives.

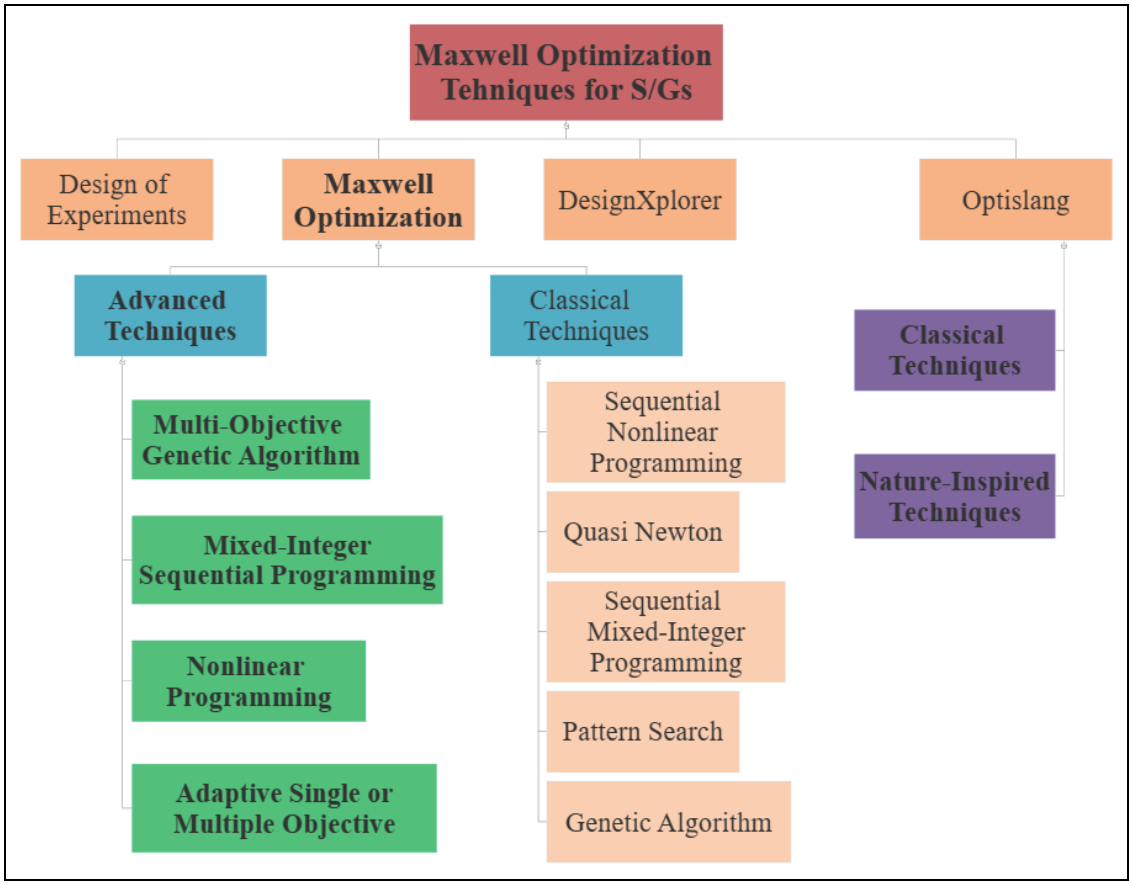


Figure 5.62. Applicable optimization techniques using Ansys Maxwell

The objectives of the optimization process typically include maximizing torque per PM volume, maximizing torque per total weight, and minimizing cost per volume. However, it is crucial to consider the minimum weight requirements for hybrid UAV applications. The results obtained from the optimization process for the S/G stages are summarized in Figure 5.63 for further analysis and evaluation.

Design Parameters	Parametrization Techniques			Optimization Techniques			Selected Design Parameters
	Statics Tool	Optimetrics Tool	Tuning Tool	SNLP (Sequential NonLinear Programming)	GA (Genetic Algorithm)	MOGA (Multi-Objective Genetic Algorithm)	
S/G Magnet Thickness (mm)	2.5 - 3.5	2.75 - 3.25	2.8 - 3.1	2.96	3.1	2.98	3mm
S/G Magnet Embrace	0.8 - 1	0.85 - 0.95	0.87 - 0.93	0.89	0.93	0.94	0.92
S/G Slot Height (mm)	9 - 10.5	9.2 - 10.2	9.5 - 10	9.66	9.82	9.75	9.7
S/G Model Depth	10 - 20	12 - 17	13 - 16	14.7	15.3	14.9	15
S/G Stator Winding Conductor/Slot in Motor	6 - 14	6 - 12	6 - 10	10	8	9	6
S/G Stator Winding Conductor/Slot in Generator	6 - 14	6 - 12	6 - 10	10	9	10	8
Cost Function Outputs							
Output Torque in Motor (N.m)	1.8 - 2.4	1.9 - 2.3	2 - 2.2	2.23	2.18	2.25	2.1
Output Torque in Generator (N.m)	1.8 - 2.4	1.9 - 2.3	2 - 2.2	2.23	2.18	2.25	2.2
Total S/G Mass in Motor (gr)	1000 - 1350	1050 - 1250	1100 - 1200	1165	1202	1194	1180
Total S/G Mass in Generator (gr)	1000 - 1350	1050 - 1250	1100 - 1200	1165	1202	1194	1200
Torque/Mass Ratio	1.8 - 1.77	1.8 - 1.84	1.82 - 1.83	1.91	1.82	1.88	1.78
Analyses Time							
Elapsed Time (min.)	25	40	65	150	270	210	

Figure 5.63. Optimization of the Starter/Generator stages

5.7. Field Weakening Control of Starter/Generator

As discussed in Section 2.7, the double-stage magnetically coupled Starter/Generator (DCSG) offers several advantages, including the ability to enhance the speed and altitude of the UAV by pushing the Starter/Generator stages beyond their rated speeds using the field weakening control technique during mission conditions that do not demand high thrust, such as cruising or diving. The design and field-weakening capability of the DCSG also enable a reduction in propeller diameter, enhancing high-speed performance and extended range.

The principle of field weakening involves controlling the excitation flux by adjusting the armature current flowing through the field winding. The torque produced is the result of the armature current and the excitation flux.

The induced voltage is directly proportional to the speed and flux. During low speeds, the rated current and rated flux are used to generate the rated torque. Both the voltage and output power increase linearly with speed [389].

The rated speed or base speed is reached when the voltage equals the rated voltage, which is defined as the maximum voltage provided by the drive. To achieve speeds higher than the rated speed, the flux needs to be reduced or weakened while keeping the voltage constant at the rated value. This results in an inverse relationship between torque and speed, allowing the output power to remain constant beyond the base speed, as shown in Figure 5.64.

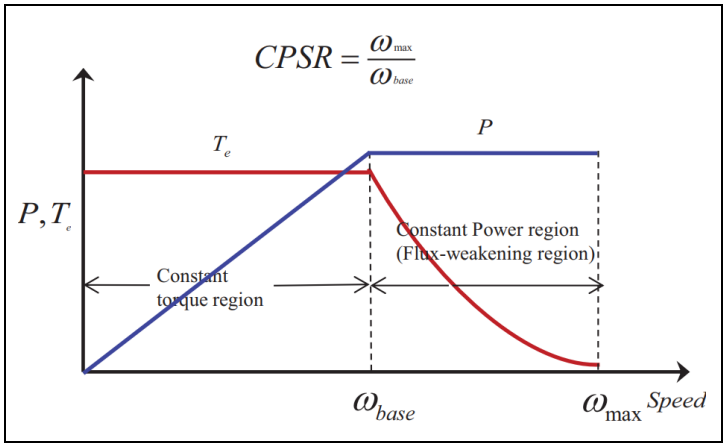


Figure 5.64 General ideal torque speed curve of surface mount Starter/Generator [340]

The control of the total flux in the d-axis for field-weakening, is achieved by introducing a negative d-axis current I_d to counteract the fixed excitation field from the PMs by adjusting the torque angle. Figure 5.65 illustrates the phasor diagram depicting the S/G operations at different speeds of below rated speed, at rated speed, and beyond rated speed.

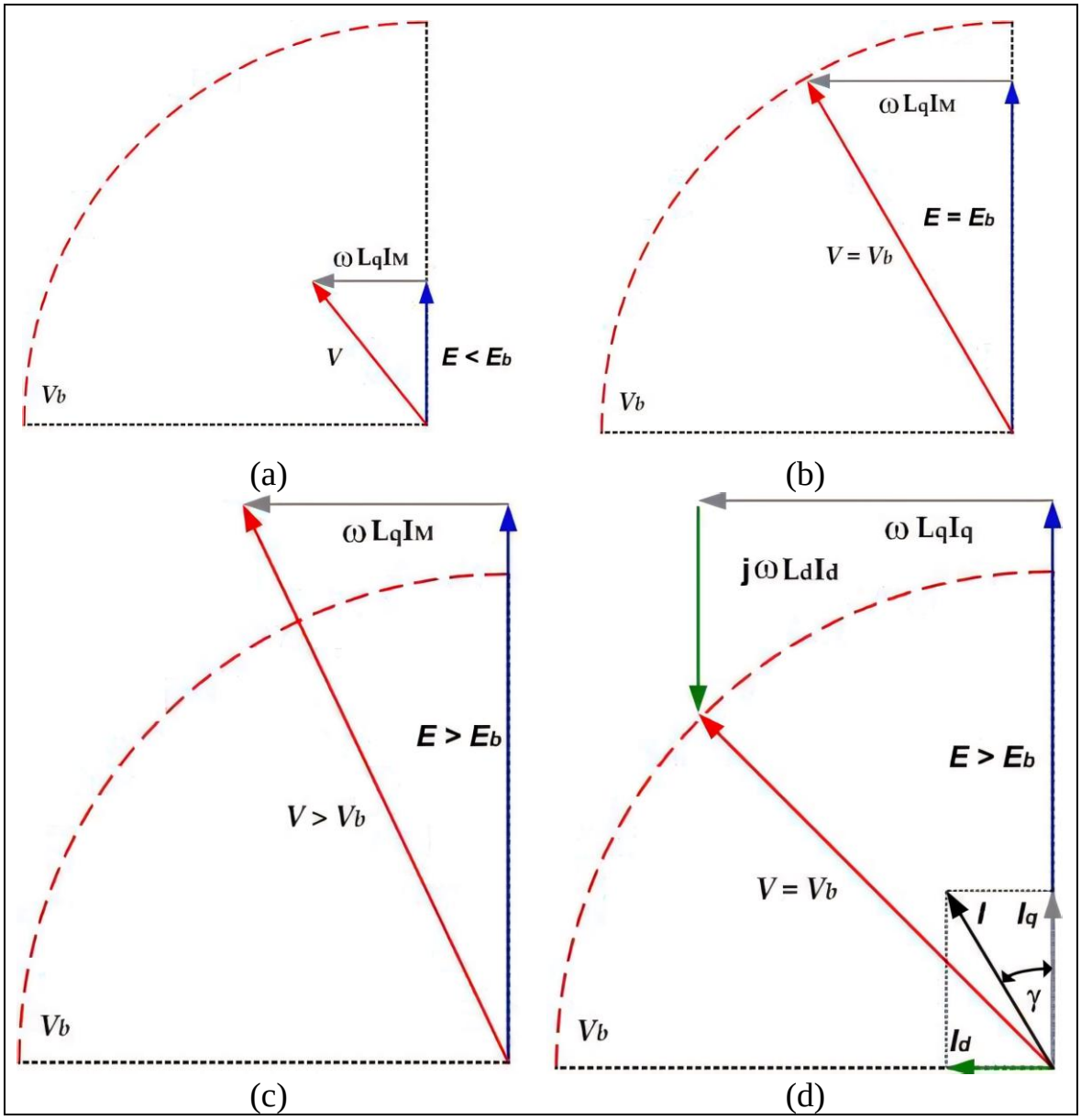


Figure 5.65. S/G Phasor diagram in ideal operating conditions (a) At low speed (b) At rated speed (c) Beyond rated speed without I_d (not-feasible) (d) Beyond rated speed with I_d [389]

The field weakening performance of the SPMSM is limited due to the nonvarying dq-axis inductance. In contrast, the field weakening of the IPMSM relies on the difference between the dq-axis inductance values, allowing for better control and adjustment of the flux weakening capability.

Due to the reduced effective air gap, the small inductance SPMSMs limit their capability for flux-weakening during high-speed operations.

Conversely, IPMSMs exhibit higher d-axis inductance compared to an equivalent SPMSM, which grants them a significant advantage in flux-weakening operations.

To address the high-speed operation of permanent magnet synchronous motors (PMSMs), three distinct methods can be employed for flux-weakening control: the feedforward method, which derives current commands required for high-speed operation from steady-state voltage equations; the feedback method, which obtains current commands from voltage feedback; and a combination of these two techniques. [324].

Hence, in hybrid UAV applications that necessitate field-weakening, interior-mount rotor topologies may be preferred due to their ease of flux attenuation, among other reasons.

6. PROTOTYPING AND TESTING OF DCSG SYSTEM

The chapter meticulously outlines the IEC and IEEE recommended testing procedure for the prototyped MCs and S/G stages, which are carried out separately in a specially designed direct-dynamic test system. The chapter also provides valuable insights into the integrated system tests conducted on the test stand and piston engine to showcase the performance of the entire system. As a result, the chapter presents a double-stage magnetically coupled S/G structure that significantly improves system performance while also providing single-stage magnetically coupled and direct-drive S/G structures for comparative purposes. The knowledge gained from the testing procedures and results in this chapter is essential for advancing the understanding of DCSG and designing reliable systems for piston engines. The findings presented in this chapter offer invaluable information for engineers and researchers seeking to enhance the performance and efficiency of such systems.

6.1. Prototyping Approach of Double Stage Magnetically Coupled Starter/Generator

As explained in the preceding sections, the double-stage magnetically coupled Starter/Generator (DCSG) structure comprises two stages: the first stage and the second stage magnetic couplers, as well as the first stage and second stage Starter/Generators. Each stage of the S/G can function as both a motor and a generator. Additionally, the DCSG system retains all the advantages of a single-stage system.

While conducting tests on the piston engine within the DCSG structure to determine torque, power and efficiency, it can be challenging to measure these parameters directly. Therefore, thrust and speed measurement tests are typically conducted on hybrid piston engine tests. Based on the collected thrust data, the output torque, power and efficiency can be calculated for both static and dynamic states. However, it is necessary to know the performance characteristics of each S/G stage and magnetic coupler individually.

Consequently, during the development of the DCSG structure, a motor model, a direct-mounted single-stage structure for testing each stage, a magnetically coupled single-stage structure, a direct-mounted double-stage structure and a magnetically coupled double-stage structure are created. The production scheme chart is presented in Figure 6.1 for reference.

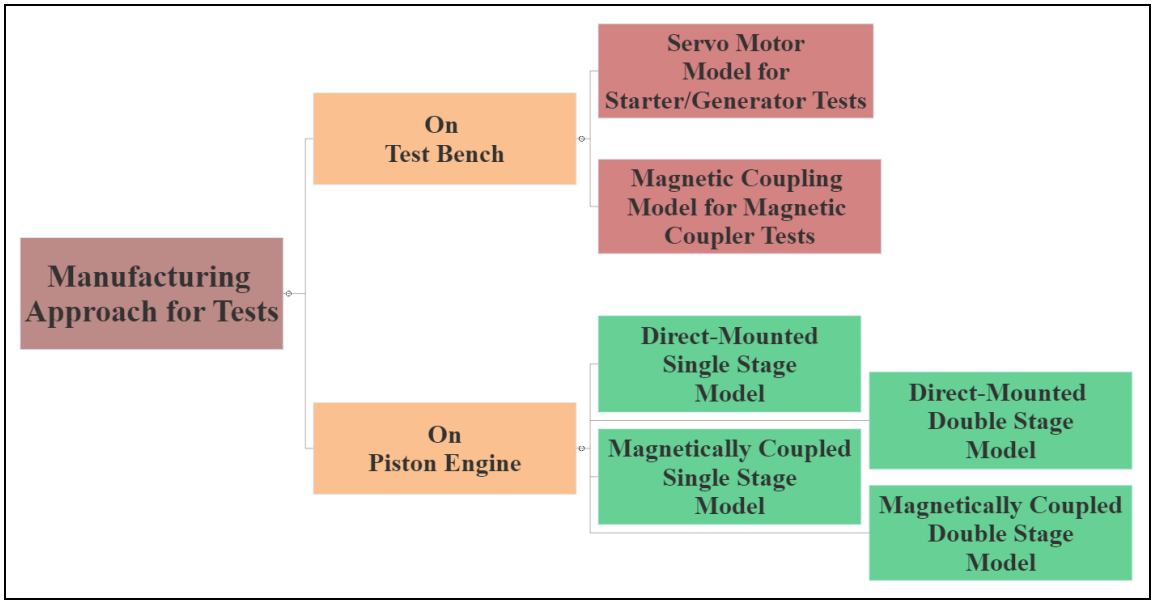


Figure 6.1. Organization scheme of system manufacturing for performance tests

6.1.1. Test bench setup based on torque measurement for MCs and S/Gs

The establishment of a test bench based on the torque measurement allowed for separate testing of the Starter/Generator stages and magnetic couplers. Figure 6.2 (a) and (b) provides an illustration of the test setup employed for the magnetic coupler tests, while Figure 6.2 (c) showcases the dedicated test bench utilized for the tests of Starter/Generator stages. In Figure 6.2 (d), the measurement board is depicted, which serves as the collection point for the sensors and indicators. While test bench components generally fulfil similar functions, the loading technique and torque/speed transmitter may vary depending on the maximum torque value of the device-under-test (DUT) [201, 265].

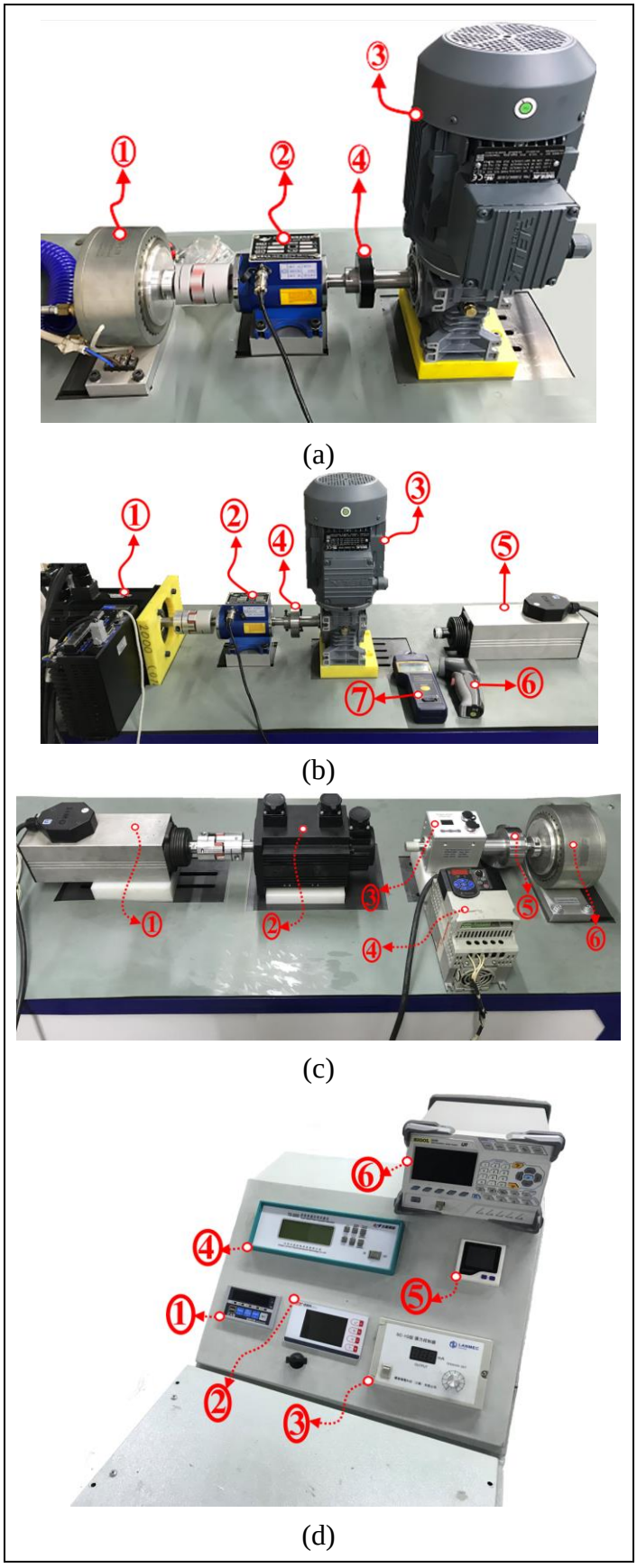


Figure 6.2. Direct dynamic bench: (a) Magnetic couplers with servo (b) Magnetic couplers for hysteresis (c) Starter/Generator with hysteresis (d) Measurement panel

The magnetic coupler test system, depicted in Figure 6.2 (a) and (b), will now be elucidated. The test bench comprises a servo motor (1) in (a) and a hysteresis brake (1) in (b), both serving as load components. Furthermore, the system incorporates a torque/speed transmitter (2), a geared asynchronous motor (3), magnetic couplings under test (4), a high-speed spindle motor (5), and a laser thermometer (6). The operational principle of the test system entails the gradual loading of the magnetic coupling, driven by the asynchronous motor, through the utilization of either the servo motor or the hysteresis brake operating in torque mode. The servo motor provides a higher torque capability as a load, whereas the hysteresis brake exhibits greater brake sensitivity despite its limited torque capability. Concurrently, the transmitted torque and speed are dynamically measured via the torque/speed sensor. The temperature of the magnetic coupling is obtained using the laser thermometer. Additionally, the speed can be manually measured through the employment of a speed transmitter (7). The test system shown in Figure 6.2 (a) is employed for torque tests lower than 5 N.m, whereas the system depicted in Figure 6.2 (b) is utilized for torque tests exceeding 5 N.m.

Similar to the magnetic coupler tests, Figure 6.2 (c) illustrates the direct measurement test system utilized for the Starter/Generator stages. The efficiency of the Starter/Generator can be determined by calculating the ratio of output power to input power. International electrotechnical standards (IEC) define several methods to obtain the efficiency [390]:

Direct Measurement Method: This method involves directly measuring the S/G input power and output power under different load conditions using specialized instruments. The load on the S/G shaft can be applied through either a brake system or by loading a calibrated generator. By comparing the measured values, the efficiency of the S/G can be obtained. Tests conducted using the direct measurement method often yield more accurate results.

Indirect Measurement Method: In this approach, the efficiency is determined by summing all the losses during the no-load condition and estimating the output power accordingly. This method offers the advantage of testing S/G units without the need for an engine shaft braking system, making it applicable to certain scenarios where direct measurement is not feasible.

Regenerative Measurement Method: The regenerative method involves connecting two identical motors to each other, with one operating as a motor and the other as a generator.

By measuring the input and output power of these motors, the efficiency of the S/G can be determined. This method is particularly suitable for testing high-power S/Gs.

Starter/Generator stages, produced as servo motors, are connected to the test system to facilitate performance testing independently of the propeller test system. In Figure 6.2 (c), S/G (2) serves as the DUT and is linked to spindle motor (1) for conducting back-emf tests and to torque transmitter (3) for performing loading tests. This connection is achieved using specially designed magnetic couplers (5), replacing the mechanical couplings mentioned earlier. The magnetic couplers provide protection to the S/G (2), torque transmitter (3), and hysteresis brake (6) shafts, shielding them from adverse conditions such as high load, sudden load variations, vibrations, and misalignment.

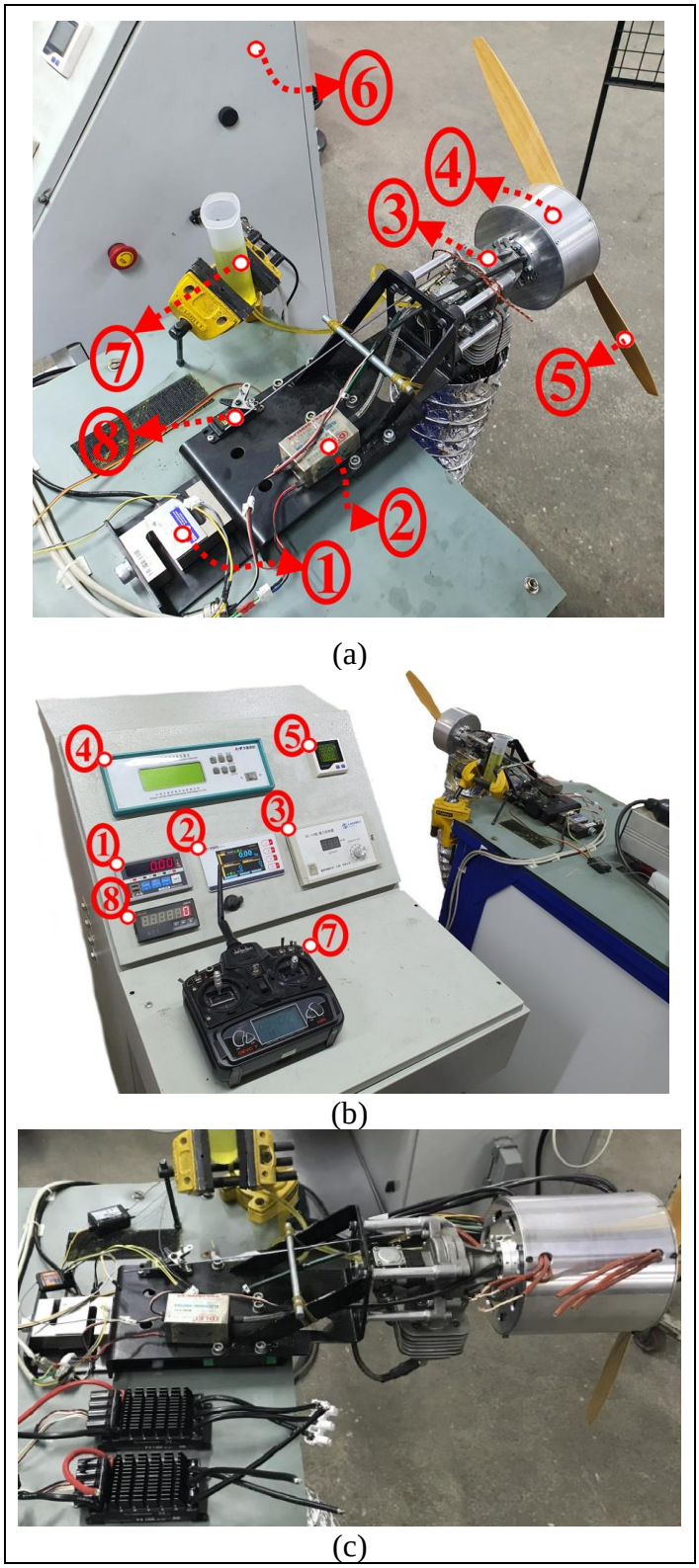
For the back-EMF tests, the S/G (2) operates in generator mode, driven by the spindle motor (1), with the rotational speed gradually adjusted using the VFD driver (4). The back-EMF voltages are then captured and analysed using an oscilloscope. In the loading tests, S/G (2) functions in motor mode. Using Field-Oriented Control (FOC) or the 6-step driving technique, S/G (2) is incrementally loaded by the hysteresis brake (6) during operation. Simultaneously, the torque/speed transmitter (3) measures and records the output power and output speed of the system. Additionally, the input power of S/G (2) is measured by the bidirectional DC energy analyser (5) located on the measurement panel. The efficiency of S/G (2) is calculated by dividing the output power to the input power. The temperature of S/G (2) is monitored and displayed by datalogger (6) through the use of a positive temperature coefficient (PTC) sensor placed among the windings.

Figure 6.2 (d) showcases the measurement panel, where various parameters are measured and displayed by indicators, including the DUT output speed (2), DUT output torque (2), DUT temperature (6), DUT output power (2), loaded torque (3), and induction motor input power (5). Furthermore, all the data are collected through RS485 serial communication.

6.1.2. Propeller bench setup based on thrust measurement

Following the individual performance tests of the magnetic coupler and S/G stages within the DCSG structure, an integrated hybrid performance testing approach was adopted by incorporating the thrust measurement-based propeller test system, as depicted in Figure 6.3.

This system was specifically implemented to conduct comprehensive performance evaluations in conjunction with the piston engine.



(a)

(b)

(c)

Figure 6.3. Propeller test bench for (a) Single DCSG (b) Sensor panel (c) Double DCSG

Double-stage magnetically coupled Starter/Generator (DCSG) thrust tests are conducted using the test system depicted in Figure 6.3 (a). This hybrid system is composed of various components, including the ignition (2), propeller (5), piston engine (3), and DCSG (4). Throttle adjustment is achieved remotely (7) through a servo motor (8), while the generated thrust is measured and displayed by the power measurement panel (6) using a load cell (1). To facilitate effective endurance tests, a scaled fuel tank (7) is utilized. The obtained thrust values are further analysed and correlated with static and dynamic calculations to estimate the torque and power output of the piston engine.

Figure 6.3 (b) showcases the measurement panel, where various parameters are measured and displayed by indicators, including the hybrid UAV output thrust in kg (1), hybrid UAV output speed (8) and DUT temperature by datalogger and thermal camera.

6.2. Prototyping and Testing of Magnetic Couplers

6.2.1. for 3W-55XI

Table 6.1 presents a summary of the different MC designs derived from simulations. Within the constraints of the system, the optimal design is achieved, with the corresponding optimum parameters denoted by an asterisk. It is important to note that the measurement of the inner rotor outer diameter and outer rotor inner diameter includes the PM thickness [201].

Table 6.1. Dimension and performance list of various MCs in summary

Pole Number	8-Pole				10-Pole *	
Embrace	0.6	0.8		0.98	0.8	0.98 *
PM Thickness	3 mm	4 mm		4 mm	4 mm *	
Grade of PM	N48H	N45H	N48H	N48H	N48H *	
Outer rotor outer diameter	79 mm	83 mm		83 mm *		
Outer rotor inner diameter	57 mm	59 mm		59 mm *		
Inner rotor outer diameter	54 mm	56 mm		56 mm *		
Inner rotor inner diameter	20 mm	20 mm		20 mm *		
Air gap length	1.5 mm	1.5 mm		1.5 mm *		
Effective air gap diameter	55.5 mm	57.5 mm		57.5 mm *		
Model length	10 mm	10 mm		10 mm *		
Total weight (gr)	320	350	351	370	352	371
Dynamic torque (N.m)	3.9	6.9	7.2	7.5	8.1	8.7
Torque density (N.m/kg)	12.2	19.7	20.5	20.3	23	23.45

Figure 6.4 encompasses a range of MCs that have been manufactured, featuring distinct design parameters. Figure 6.4 visually presents a selection of these MCs, with the upper and lower sections highlighting the outer and inner rotors of the coupler, respectively.

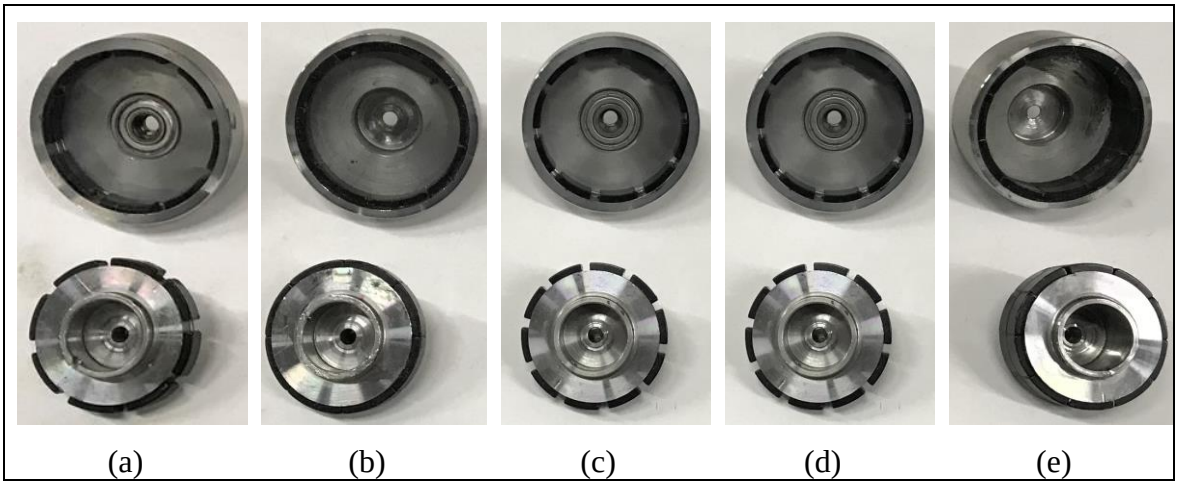


Figure 6.4. Various MC productions of: (a) 8-pole/0.8-embrace/3 mm-PM thickness/10 mm length; (b) 8-pole/0.98-embrace/4 mm-PM thickness/10 mm length; (c) 10-pole/0.8-embrace/4 mm-PM thickness/10 mm length; (d) 10-pole/0.98-embrace/4 mm-PM thickness/10 mm length; (e) 10-pole/0.98-embrace/4 mm-PM thickness/20 mm length

The utilization of the direct test method yields more precise results because it dynamically measures key MC parameters such as output torque and output speed through a torque/speed transmitter. Figure 6.5 (a) depicts the installation of the MC within the direct dynamic test system, while Figure 6.5 (b) showcases its installation on the PE and propeller. This approach ensures accurate and real-time measurements for precise performance analysis.

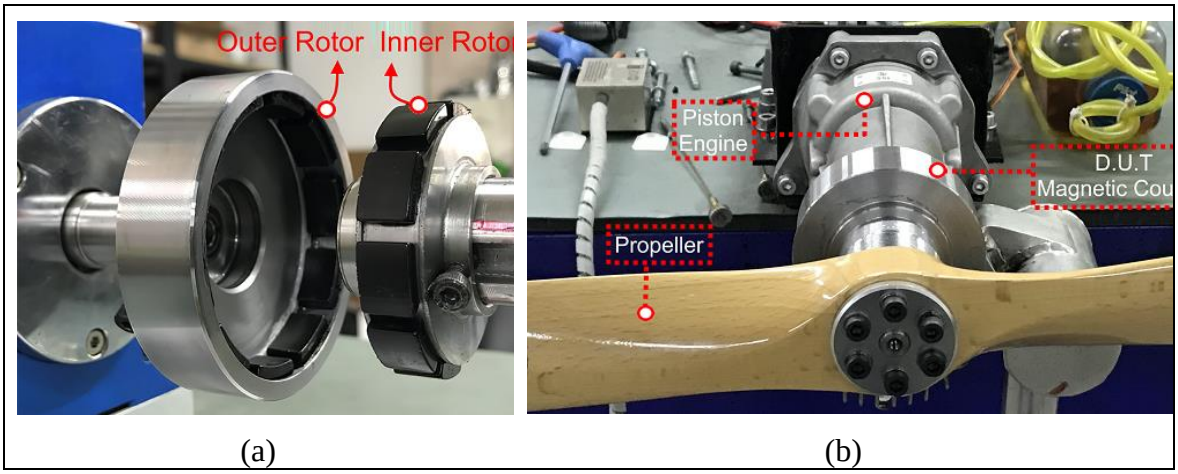


Figure 6.5. Assembly of (a) MC for dynamic tests (b) MC with piston engine and propeller

Magnetic coupler tests designed for 3W-55XI were conducted using Figure 6.2 (a). During the locked-rotor or static test, the shaft is subjected to a substantial load imposed by the hysteresis brake, rendering it immobile. The torque is measured by gradually adjusting the load based on the torque angle, while recording the corresponding data. Figure 6.6 (a) presents the outcomes of the static test conducted at a critical torque angle, utilizing a 10 mm coupler length for configurations characterized by higher torque density. Conversely, Figure 6.6 (b) showcases the results obtained for a lower torque density configuration.

The maximum locked-rotor torque is observed in the configuration featuring 10 poles and a 0.98-embrace, as indicated by the black marker in Figure 6.6 (a). However, when comparing the same configuration with 8 poles, a reduction of approximately 14% in the maximum locked-rotor torque is noted, as indicated by the blue marker in Figure 6.6 (a).

Additionally, an examination of the influence of the model length reveals that doubling the length leads to an almost twofold increase in the locked-rotor torque. These findings underscore the significant impact of configuration parameters, such as the pole number and embrace, as well as the model length on the locked-rotor torque performance.

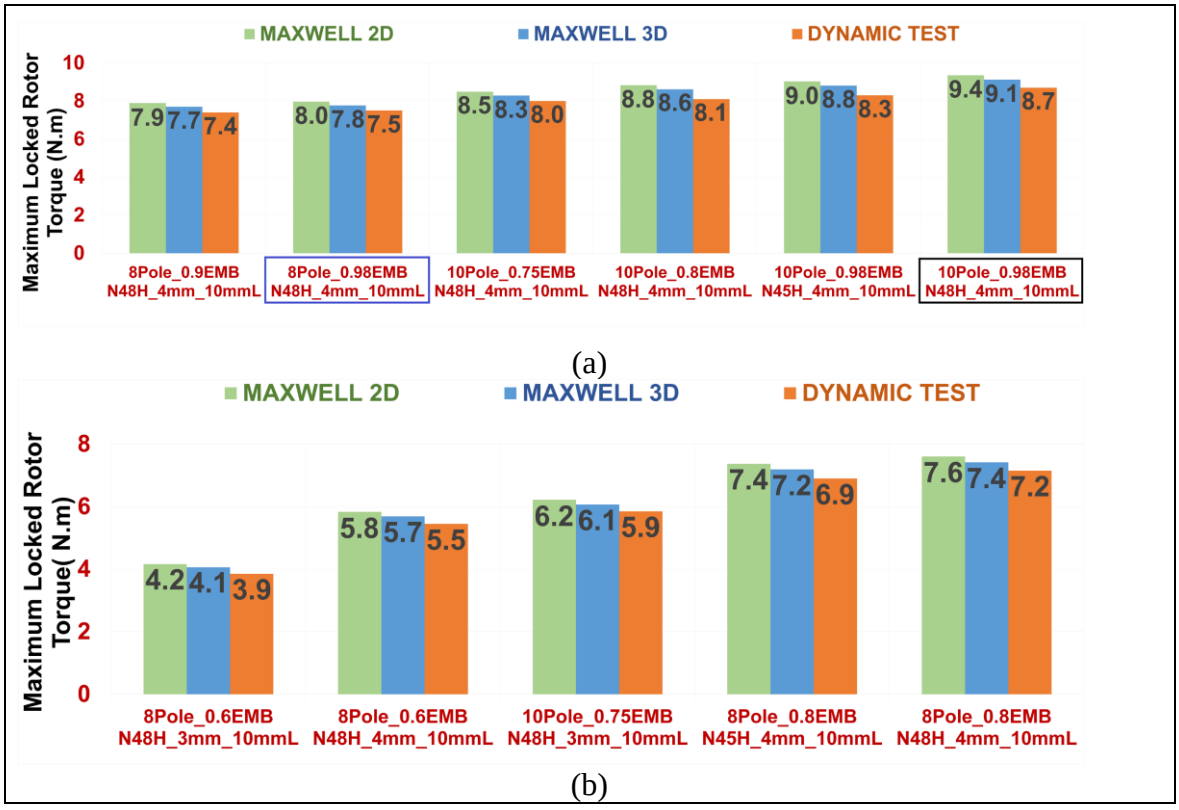


Figure 6.6. Locked-rotor test results of (a) Higher torque density (b) Lower torque density

The locked-rotor and dynamic test results exhibit a consistent correlation, allowing for the focus on plotting the results for the optimal design configuration of 10 poles, 0.98-embrace, and 10 mm length. This selection aims to maintain clarity and avoid visual clutter in the presentation of the data. Figure 6.7 (a) provides a comparison of the time-dependent results obtained from the Maxwell 2D and 3D simulations, as well as the dynamic tests. The average dynamic pullout torque values derived from the 2D and 3D simulations are recorded as 9.35 N.m, 9.15 N.m, and 8.7 N.m, respectively. Figure 6.7 (b) showcases the static torque results obtained at different torque angles. At the critical angle of 18 Mdeg, the maximum static torque values obtained from the Maxwell 2D and 3D simulations, as well as the static tests, are documented as 9.32 N.m, 9.11 N.m, and 8.72 N.m, respectively. These findings highlight the agreement between the simulation and test results, further validating the accuracy.

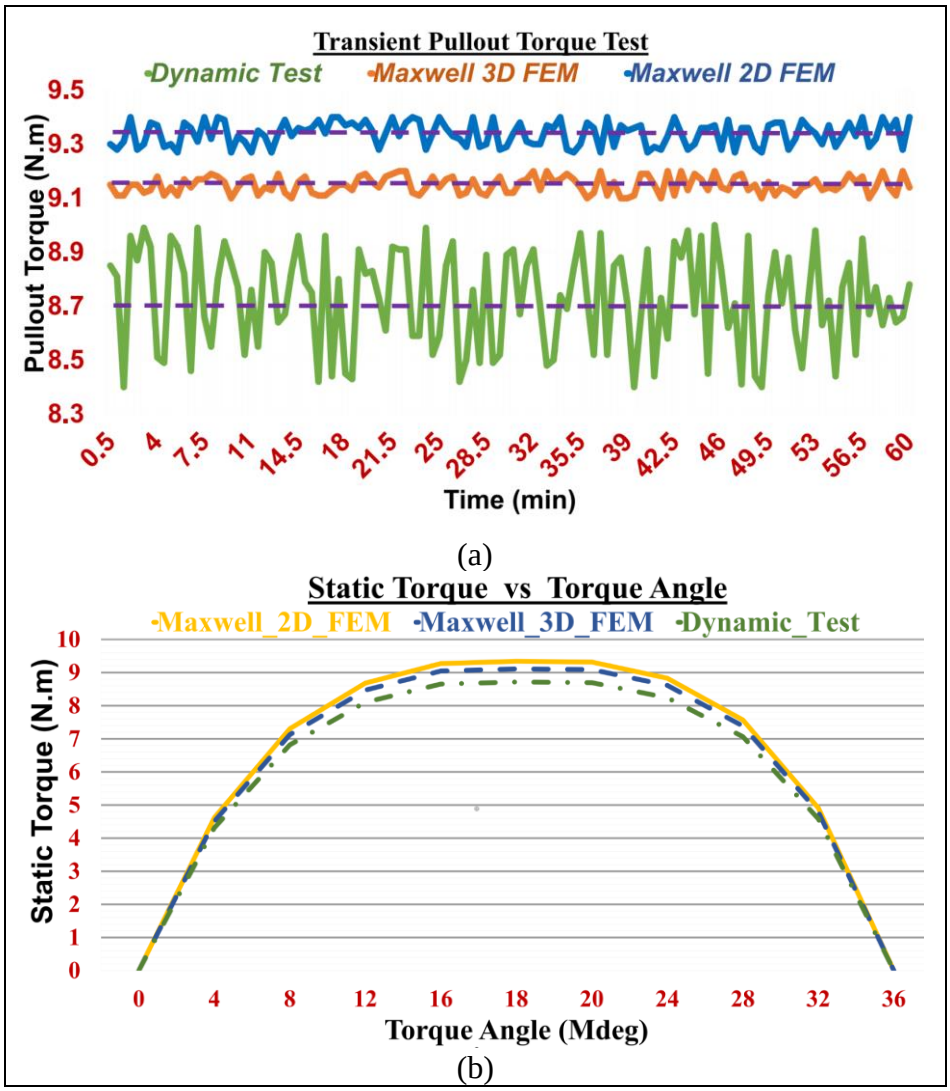


Figure 6.7. Test results of the 10-pole, 0.98-embrace, and 10 mm length model (a) Pullout torque in transients (b) Static torque versus torque angle in magnetostatics

The Maxwell simulations exhibit a high level of agreement with the test results, demonstrating their accuracy and reliability. The numerical simulations demonstrate an acceptable margin of error compared to the test results, with an 8% deviation for Maxwell 2D and a 4.5% deviation for 3D, without considering the safety factor. To achieve a more effective design, it is recommended to introduce a correction coefficient in the initial stage of the numerical design, accounting for the observed differences or margin of error.

Considering the inclusion of a safety factor, the Maxwell 2D and 3D simulations, on average, yield results that are 14% and 9% higher, respectively, than the direct dynamic test results for the proposed model. Based on these observations, it is suggested to apply a correction coefficient of 1.2 for the Maxwell 2D simulations and 1.1 for the Maxwell 3D simulations when utilizing MCs in hybrid UAVs.

By incorporating these correction coefficients, the simulation results can be aligned more closely with the experimental test results, ensuring a more reliable and accurate design approach for the implementation of MCs in hybrid UAV systems.

6.2.2. for DLE-30 or 3W-70R2

Magnetic coupler tests were conducted on the DLE-30 and 3W-70R2 piston engines, similar to the 3W-55XI, utilizing Figure 6.2 (b). The locked-rotor tests involve immobilizing the outer rotor of the magnetic coupler using excessive torque adjustment of the servo motor. For high torque tests, the MCs are driven at a speed of 250 rpm. Additionally, high-speed tests are conducted on the test bench using the spindle motor (5). The torque angle is measured by absolute hall encoders on both the load servo motor and drive asynchronous motor. Loctite648 serves as the adhesive material for permanent magnets, and the retaining sleeve material is excluded, leaving an air gap of 1.5 mm with the sleeve [265].

While the output torque and speed are measured, calculating efficiency requires a second torque/speed transmitter to measure input torque and speed. Due to the absence of suitable testing facilities, dynamic plotting of efficiency was not possible. However, based on data obtained from other test results, the actual efficiency graph could be estimated using the proposed correction factor in conjunction with the numerical efficiency graph.

Figure 6.8 (a) presents the results of the pullout torque and temperature obtained from dynamic tests conducted on a magnetic coupling with a length of 10 mm. The average pullout torque recorded during the dynamic tests was 8.9 N.m, while it was 10.5 N.m for transient Maxwell 2D and 9.9 N.m for transient Maxwell 3D analyses.

Similarly, Figure 6.8 (b) illustrates the dynamic test results of the MCs with a length of 20 mm. These data confirm that doubling the length leads to an almost twofold increase in the pullout torque. The results from Maxwell 2D and 3D transient dynamic analyses align closely with the test results. Dashed lines indicate the average values of the obtained results.

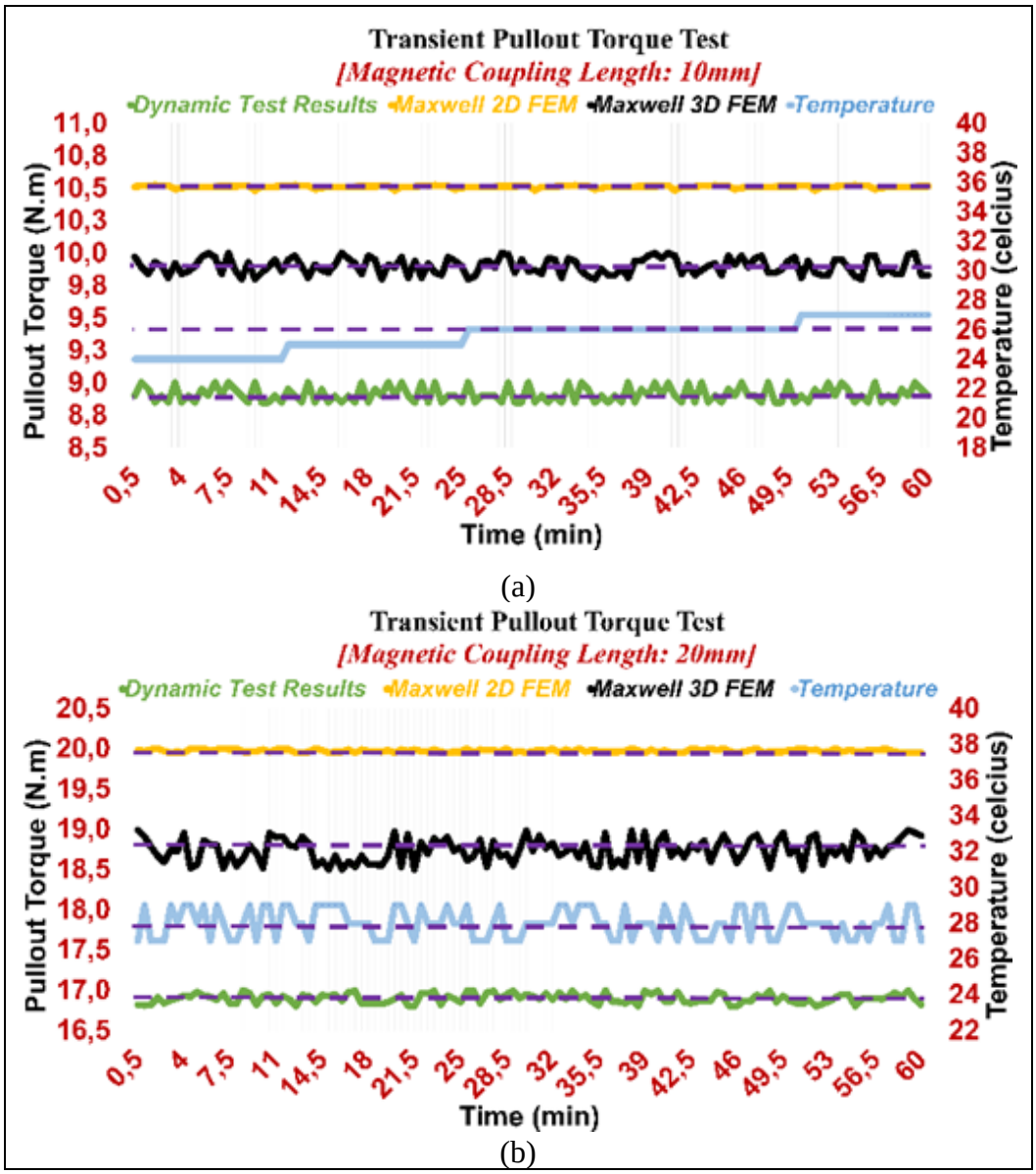


Figure 6.8. Transient pullout torque test results for MC with 20 mm length

In Maxwell 3D, torque simulations in the transient dynamic state exhibit torque fluctuations during sudden load changes. This is attributed to the moment of inertia of the coupler, mechanical losses represented by the damping factor, and the characteristics of the applied load, all of which are modelled in the analysis. The 3D modelling and layout of the test bench are accomplished using Solidworks v2017 software to ensure precise production. The test components are manufactured with high precision using CNC machines, and their assembly is meticulously performed. Special attention is given to ensuring that the coupler rotors fit snugly and rest on the bearing flanges, ensuring concentricity and alignment of the axes. The torque/speed transmitter and temperature sensor, KTY84-130, used in the tests are calibrated by an internationally accredited organization [391]. The tests are repeated three times at different intervals, and the average values are utilized for the graphs.

During dynamic tests, the servo motor employed in torque mode endeavors to maintain the load at the maximum torque point of the magnetic coupling, utilizing position information from the encoder and current information from the driver. However, fluctuations in torque results are observed on the test bench due to the unstable load caused by the moment of inertia of the servo motor, the mechanical imbalances between the servo and the torque sensor, and the low sensitivity of the torque sensor. Figure 6.9 compares the locked-rotor torque results obtained from the Virtual Work method, numerical Maxwell 2D and 3D simulations, and the test bench.

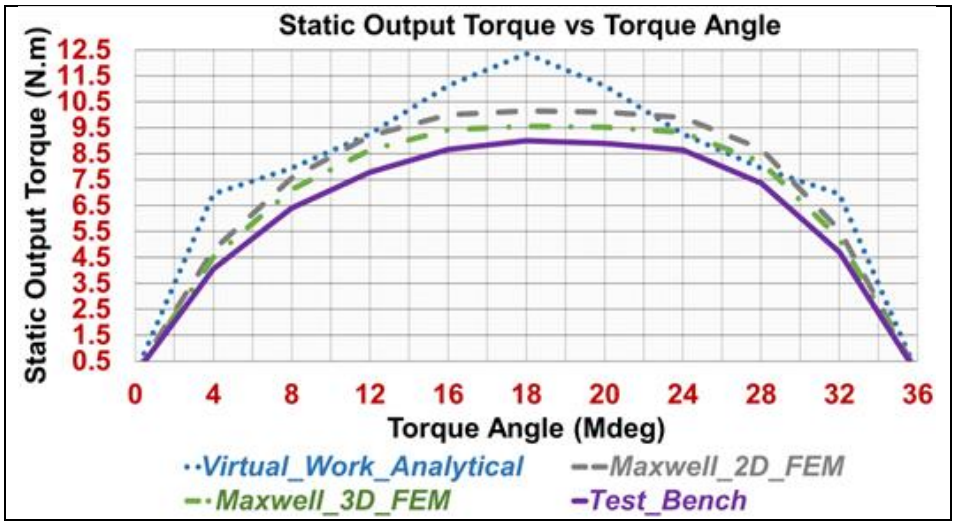


Figure 6.9. Static torque results of the optimum model depending on the torque angle

The analytical Virtual Work method utilized the optimum values determined in Table 5.4, considering factors such as manufacturability and accessibility. Eq. 6.1 was employed to calculate the torque corresponding to various torque angles. Within the synchronous zone which is before the critical angle, the torque increases as the torque angle increases until reaching the critical angle, where it reaches its maximum value. In the asynchronous zone following the critical angle, the torque angle and output torque decrease as the reference is taken from the subsequent incoming PM with opposite polarity. However, the system becomes unstable in the asynchronous region, leading to a loss of synchronization. Additionally, the torque is zero at the minimum energy position, occurring at rest.

The static torque at the critical angle is as follows: 9 N.m for static tests, 10.15 N.m for static Maxwell 2D, 9.56 N.m for static Maxwell 3D, and 12.35 N.m for the Virtual Work method. The static test results on the test bench incorporate a torque angle variation of 4 mechanical degrees to minimize errors associated with torque angle readings using an encoder.

For more realistic results, the magnet temperature is updated to 80°C in the magnetostatic analysis from the initial 60°C considered in the transient analysis. This update accounts for cooling difficulties encountered during the steady state of the system, enabling exploration of torque deviations dependent on static and dynamic states. However, as these effects cannot be replicated on the test bench, the static and dynamic results exhibit close agreement.

Analytical methods are commonly used for preliminary design under ideal conditions, primarily relying on basic parameters and desired output values. Consequently, nonlinearities inherent in material behavior are not typically taken into account. Variables such as leakage fluxes, cross-coupling effects, core losses, thermal effects, and eddy losses are disregarded in these calculations. On the other hand, analytical calculations that incorporate these effects can be complex and time-consuming. FEM provides a practical approach, offering high accuracy by precisely defining the material nonlinear properties.

Finally, the correction factor coefficient allows the design methods to reduce errors and yield results that closely align with practical observations [212]. Based on the correlation of analytical calculations, Maxwell FEA, and the results obtained from the dynamic test system, a correction factor of 1.39 is proposed for the Virtual Work method, 1.18 for Maxwell 2D, and 1.11 for Maxwell 3D.

6.3. Prototyping and Testing of Starter/Generator Stages as a Servo Motor

The Starter/Generator stages are designed as servo motors to facilitate dynamic performance tests of the DCSG system. Figure 6.10 showcases the production parts and the final model, providing a visual representation of the manufacturing process.

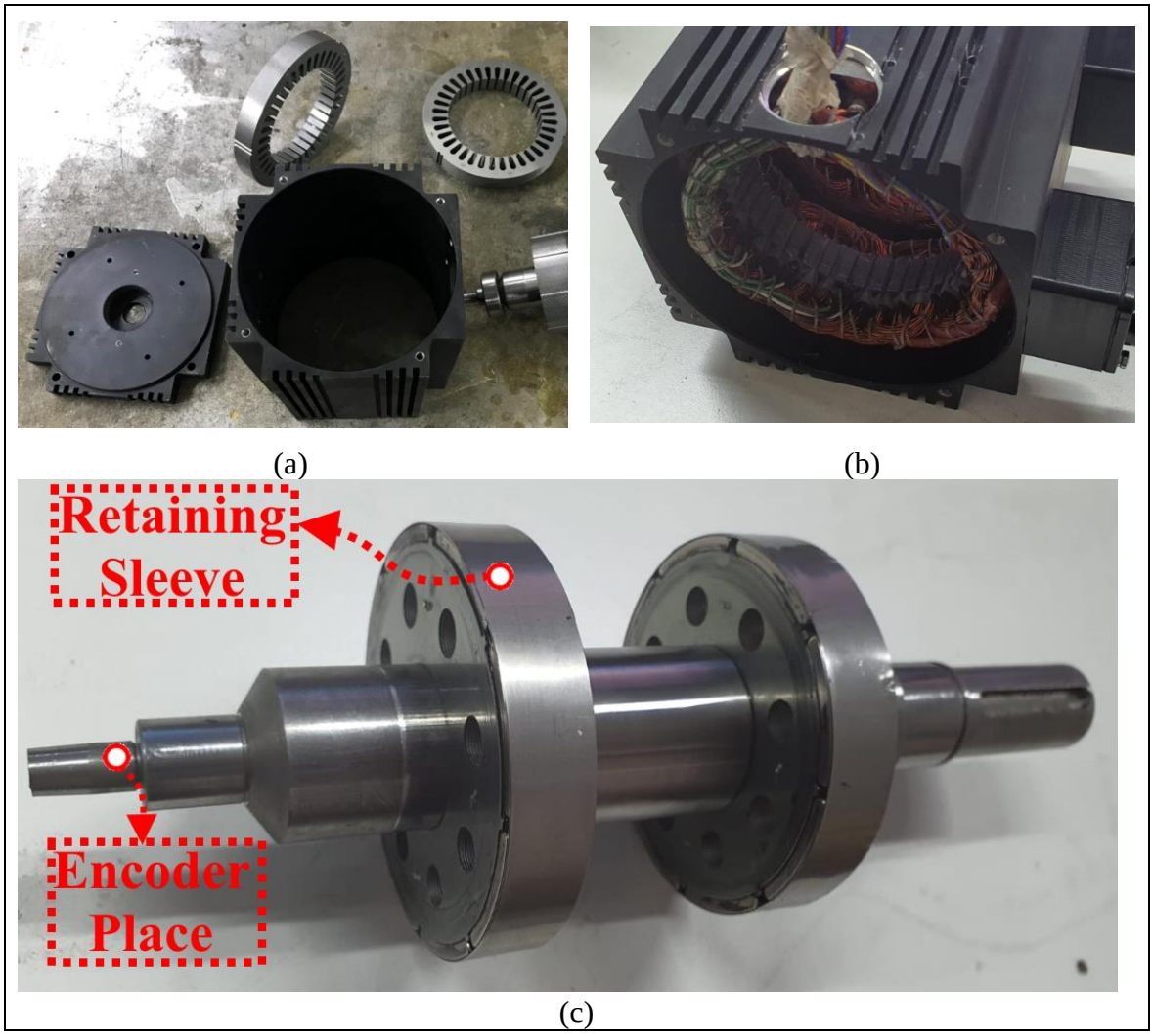


Figure 6.10. Manufacturing of (a) Housing, flanges, stators (b) Windings (c) Shaft, rotors, sleeve (d) 3D model (e) Servo Starter/Generator (f) 0-3 kW Load bank for tests

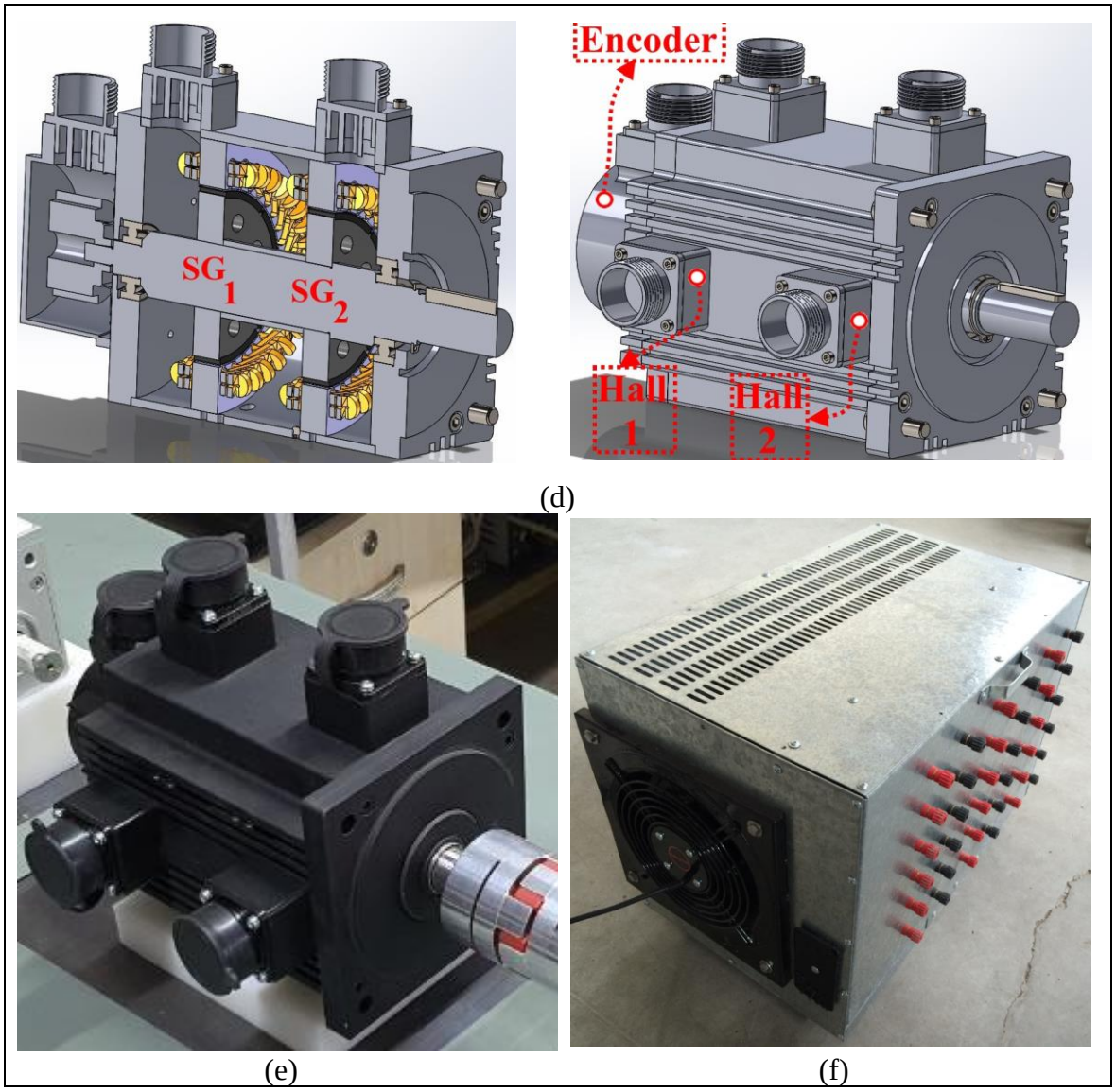
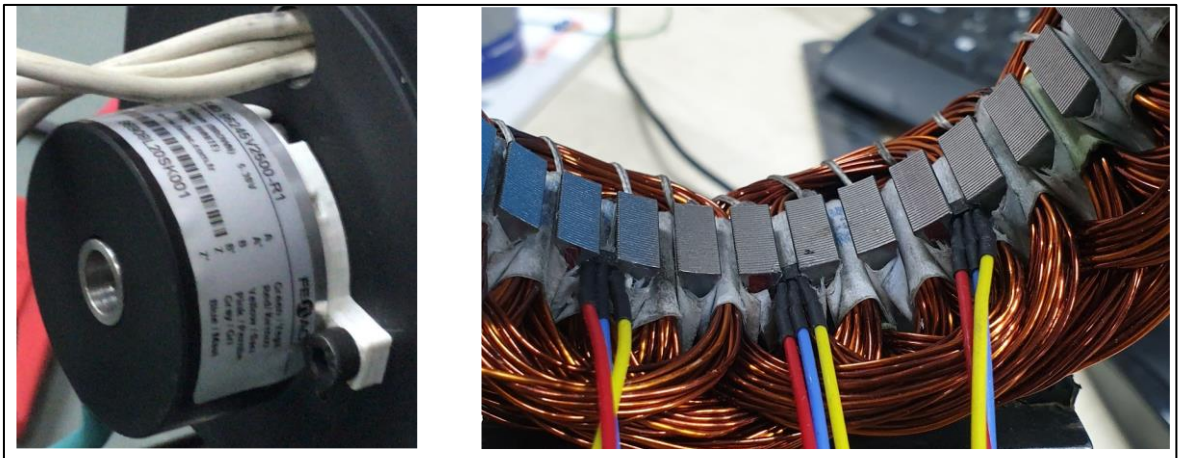


Figure 6.10. (continued) Manufacturing of (a) Housing, flanges, stators (b) Windings (c) Shaft, rotors, sleeve (d) 3D model (e) Servo Starter/Generator (f) 0-3 kW Load bank for tests

Table 6.2 presents an overview of the production methods utilized. To evaluate performance using both FOC-based and 6-step-based driving techniques, a servo motor model equipped with an incremental encoder and hall sensor was developed. Figure 6.11 (a) displays the layout of the hall sensor, while Figure 6.11 (b) illustrates the encoder layout.

Table 6.2. Manufacturing methods for servo Starter/Generator model

Material Description	Material	Manufacturing Mehod	Assembly Method
Housing	AL7000 series	CNC 5-Axis	Set-screw bracing
Front Bearing Flange	AL6061	CNC 5-Axis	Snug-Tight
Back Bearing Flange	AL6061	CNC 5-Axis	Snug-Tight
Stator	M250-35A	Wire-cutting	Heating (oven/warmers)
Rotor	M250-35A	CNC Lathe	Heating (oven/warmers)
Shaft	Steel316L	CNC Lathe	Heating (oven/warmers)
Permanent Magnets	N38SH	Mould	with Adhesive
Retaining Sleeve	Steel316L	Roll-weld	Snug-Tight



(a) (b)

Figure 6.11. Driving methods (a) FOC with encoder (b) 6-step with Hall sensor or sensorless

6.3.1. Hall sensor placement

In 6-step drive control, there are two types: with sensors and without sensors. In sensorized speed control applications, the position of the rotor is easily detected using Hall effect sensors. Additionally, optical sensors (encoders) and zero crossing detectors can also be utilized [392].

When selecting a sensing element, the magnitude of rotor angular displacement, the allocated distance for the sensor, the required precision and accuracy of control, the maximum power expected to be drawn by the sensor element, and the ability to produce the sensor element in series need to be considered.

Hall effect sensors are positioned at 60° or 120° electrical angles on the stator or rotor. Considering our drive model for Starter/Generator stages, Hall effect sensors are placed between the stator teeth at 120° Edeg. In the case of the S/G with 36 stator slots, each slot corresponds to 10 Mdeg and 40 Edeg. In the case of placing three hall sensors with a spacing of 120 electrical degrees, the placement angles of the sensors are determined by counting three slots after the first hall sensor for the second hall sensor, and the subsequent three slots for the third hall sensor. This arrangement ensures the proper functioning of the system.

$$\alpha_{hall,E} = \frac{180*(2p)}{N_s} \tag{6.16}$$

where $\alpha_{hall,E}$: Electrical angle of hall sensors

Ns/(2p) : Number of stator slots / poles

Performance tests were conducted utilizing the test system depicted in Figure 6.2 (c), detailed in Section 6.1.1. The data were gathered through the measurement panel shown in Figure 6.2 (d). A summary of the test methods is shown in Figure 6.12 [393-397].

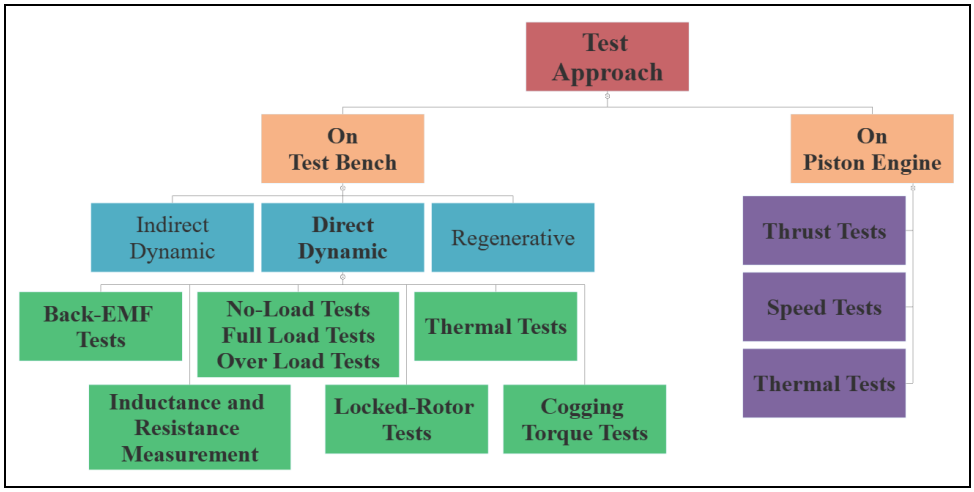


Figure 6.12. Summary of the test methods for direct-dynamic and propeller test systems

6.3.2. Back-EMF Voltage and Rectification

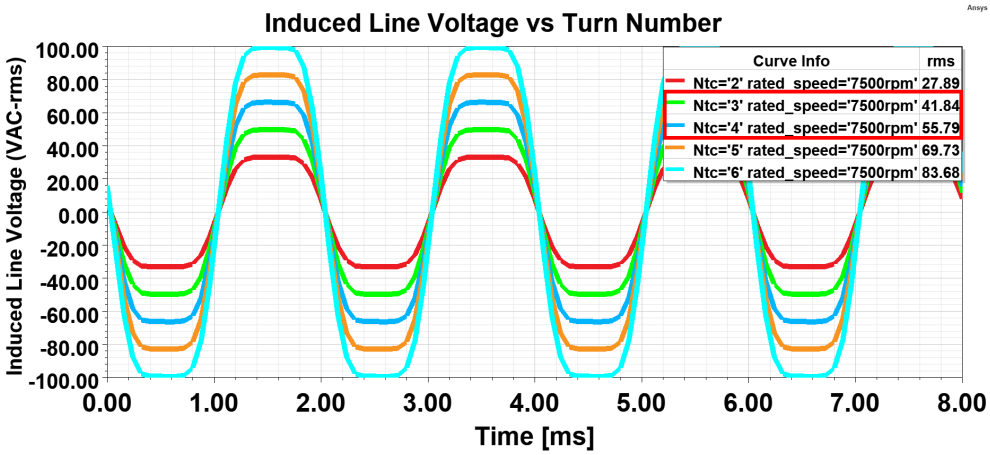
Back-EMF tests were conducted by rotating S/G at various speeds using the spindle motor while ensuring the S/G was de-energized. The back-EMF constant, which can have different definitions in the literature and is important for DCSG driver based on FOC, was determined by calculating the ratio of the rms value of the line-line voltage to the speed expressed in kRPM [398]. It is 5,4 for motor mode and 7,3 for generator mode, as presented in Table 6.3. Additionally, Figure 6.13 provides a comparison of the analysed and tested back-EMF for phase A and full-wave diode rectified DC bus voltage at the maximum speed of 7500 rpm.

Table 6.3. Back-EMF constant calculation for motor and generator modes

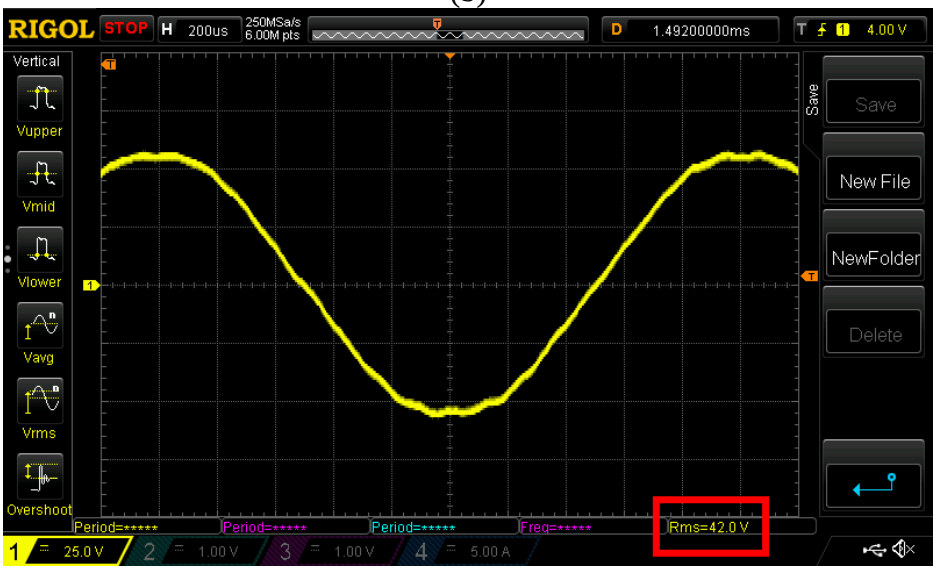
No	VAC-Line (rms) Motor Mode	VAC-Line (rms) Generator Mode	Measured Speed (rpm)	Ke (Motor)	Ke (Generator)
1	9,40	12,63	1750	5,37	7,22
2	13,50	18,13	2500	5,40	7,25
3	19,00	25,52	3500	5,43	7,29
4	24,40	32,78	4500	5,42	7,28
5	30,00	40,30	5500	5,45	7,33
6	35,00	47,01	6500	5,38	7,23
7	40,20	54,00	7500	5,36	7,20



(a)

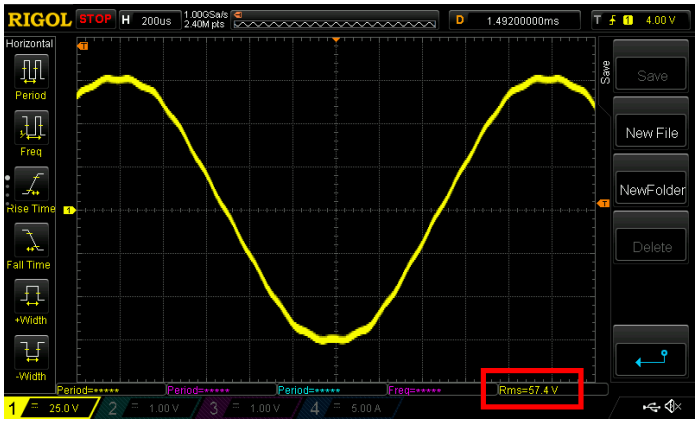


(b)



(c)

Figure 6.13. (a) Test bench back-EMF (b) FEA vs turn number (c) Motor mode back-EMF (d) Generator mode back-EMF (e) Rectified DC voltage for generator mode



(d)



(e)

Figure 6.13. (continued) (a) Test bench back-EMF (b) FEA vs turn number (c) Motor mode back-EMF (d) Generator mode back-EMF (e) Rectified DC voltage for generator mode

6.3.3. Calculation of the d and q inductances

In SMPM, the synchronous inductances tend to be nearly equal. This is primarily due to the nature of the machine, which results in consistent reluctance across all positions within the motor. Consequently, the magnetic field distribution remains relatively uniform, resulting in similar synchronous inductances throughout the machine. In practical scenarios, magnetic circuits are susceptible to saturation as the current levels rise. This effect is particularly pronounced when the current component I_q is increased, leading to a reduction in the value of the synchronous inductance L_q [391]. Conversely, the current component I_d is typically kept at zero or maintained at a negative value (a technique known as flux-weakening) in the majority of operating conditions, thereby minimizing the likelihood of L_d saturation. Hence, the saturation of L_d is infrequently encountered.

To measure the d-axis inductance accurately, follow the steps outlined below:

- Begin by aligning the rotor with phase A. Connect phase A to the positive potential (+), while grounding phases B and C (-).
- Ensure that the rotor shaft is securely locked to prevent any rotational movement.
- Apply a negative step voltage to the SG. Ground phase A (-) and connect phases B and C to the positive terminal (+). The applied current is typically 10% of the rated current.
- A current probe is employed to measure and capture the step response of the current. This step response provides valuable information for calculating the inductance.
- Calculate L_d using the measured data obtained from the step response analysis.

To accurately measure the q-axis inductance, follow the step-by-step guide provided below:

- Start by aligning the rotor with the q-axis. Connect phase B to the positive (+) of the voltage source while grounding phase C (-). Keep the phase A terminal floating.
- Ensure that the rotor shaft is securely locked in place, as the current step response in the q-axis can generate torque, which may cause unwanted rotational movement.
- Generate a current step response in this specific configuration: Connect phase A to the positive potential (+) of the voltage source while grounding phases B and C.
- Utilize the measured data from the step response analysis to calculate the q-axis inductance (L_q) using the same method employed for calculating L_d.

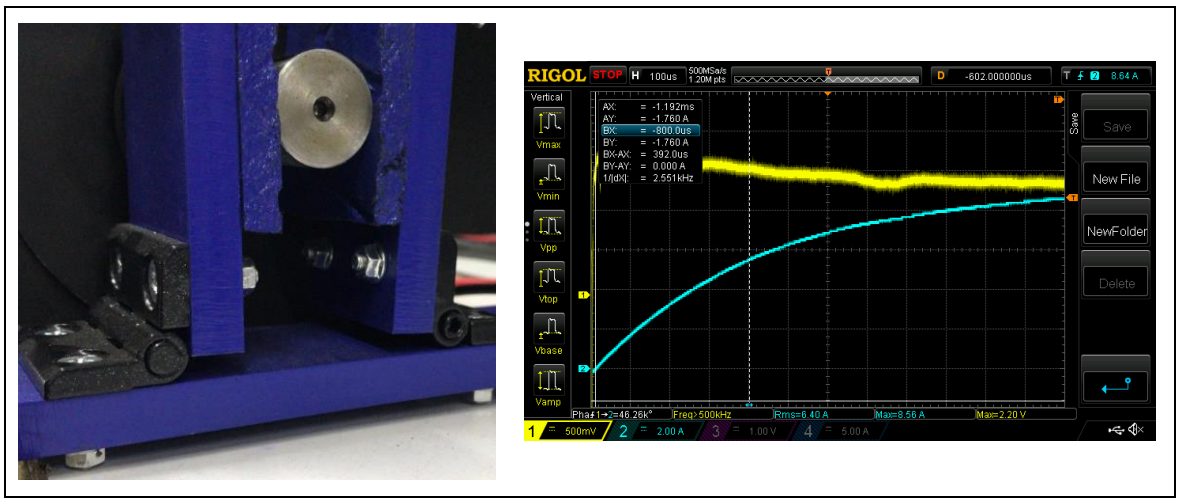


Figure 6.14. (a) Shaft locking method (b) Inductance measurement

$$i_{(d\ or\ q)} = \frac{2V}{3R_{phase}}\left(1 - e^{-t/\tau}\right) \qquad \tau = \frac{L_{(d\ or\ q)}}{R_{equivalent}} \tag{6.17}$$

L_d and L_q are 45 uH for motor mode and 75 uH for generator mode. R_{phase} is 150 mΩ for motor mode and 200 mΩ for generator mode. The measurements are made at 1 kHz.

6.3.4. Dynamic load-tests

The dynamic tests of the starter/generator stages were conducted using the test system described in Figure 6.2 (c), focusing on 100% nominal loading values while also considering other loading levels. The S/G stages were subjected to a hysteresis load, bringing them to their rated speed after being run at idle, and then loaded with the rated load. The results, depicted in Figure 6.15, illustrate the performance under full loading conditions, with hysteresis brake loads set at 2,1 N.m for motor mode and 2,2 N.m for generator mode.

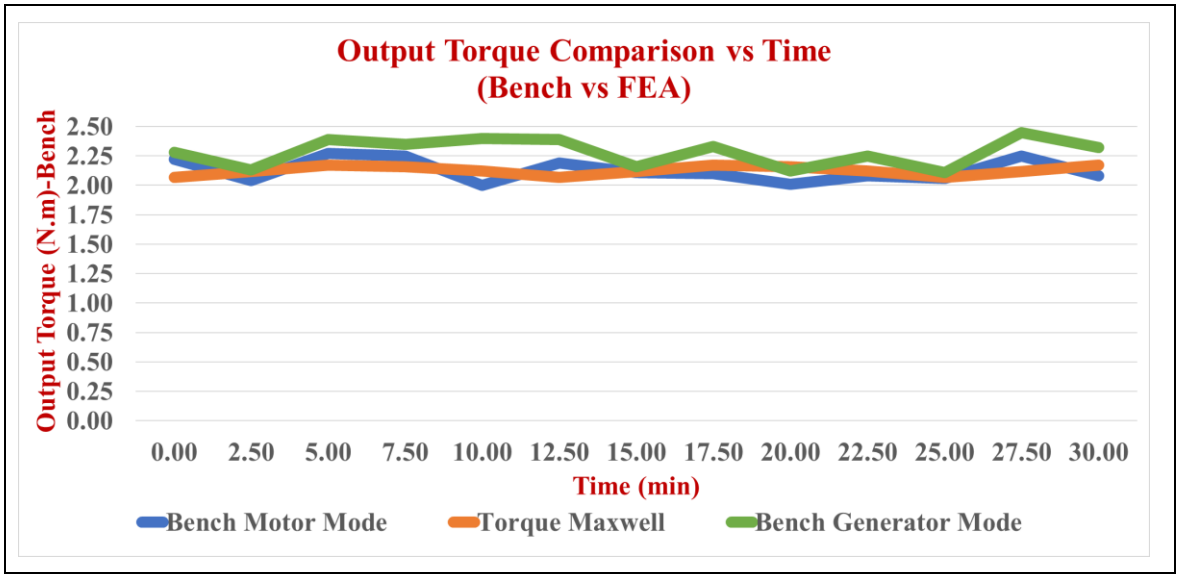


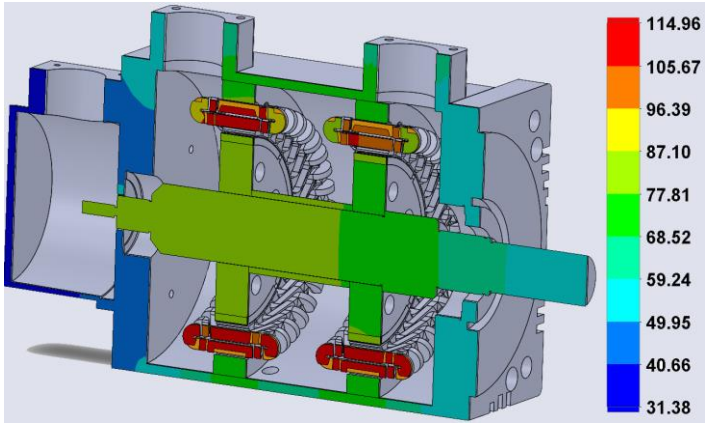
Figure 6.15. Output torque comparison of motor motor, generator mode and FEA

Comparing the analysis results with the test system findings, a close correlation can be observed. There is a disparity in torque ripple, with the FEA indicating 4% while the test system results show approximately 10%. This difference could be attributed to factors such as measurement accuracy and variable load conditions caused by the hysteresis brake.

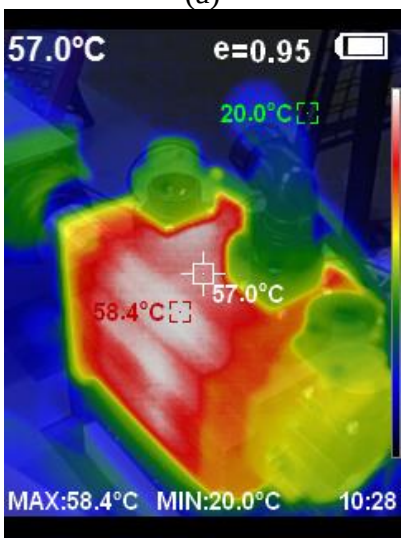
Additionally, another notable distinction is the current density. The RMxprt analytical design suggests a current density of 7 A/mm^2, whereas the 2D FEM analysis indicates 8 A/mm^2, and the test results demonstrate 10 A/mm^2.

This variance can be attributed to the need for higher current in practice to achieve the desired torque output for the S/G stages, surpassing the originally designed specifications. The current value falls within the safe range, ensuring reliable operation under the S8 duty cycle and high-altitude conditions.

On the other hand, thermal analysis of the S/G stage in generator mode under full load operating conditions was conducted using Siemens FloEFD CFD, and the corresponding thermal images of the real system are presented in Figure 6.16 (a) and (b).



(a)



(b)

Figure 6.16. S/G thermal issues in generator mode (a) FloEFD CFD (b) Real time thermal

The maximum temperature observed on the winding sides reaches approximately 110°C, while the permanent magnets reach around 80°C on FloEFD CFD, as shown in Figure 6.16 (a). However, based on the data from the test system, the maximum temperature observed during 30 minutes of operation at full load in S/G generator mode is approximately 60°C.

Real-time thermal imaging has the disadvantage of providing low accuracy in regard to in-machine temperature measurement. It is noteworthy that the winding temperatures of the S/G remain well within a maximum of 60°C, even when subjected to an ambient environment with a 1 m^3/s air flow. Considering that the S/G duty cycles are S8, the obtained temperatures are well within the safe operating range. Therefore, these findings provide confidence in the thermal performance and operational reliability of the S/G stages.

6.3.5. Locked-Rotor or static tests in overload conditions

Locked rotor or static tests play a crucial role in determining the maximum torque capacity of S/G stages. These tests involve applying a high torque load to the hysteresis brake and subsequently operating the S/G stages (motor and generator) in both motor modes while measuring the torque.

The static test results, shown in Figure 6.17, consistently exceed the values obtained from dynamic tests. This disparity arises from the fact that dynamic tests are conducted at rated values, whereas static tests are carried out at maximum load conditions. However, acquiring static torque values can be challenging due to the torque angle dependency in static tests conducted on the test bench. To simplify the analysis, a torque angle assumption of 90 Edeg, based on the i_d=0 approach in the FOC driver, is made. These static test results are then compared with FEA analysis, as depicted in Figure 6.17.

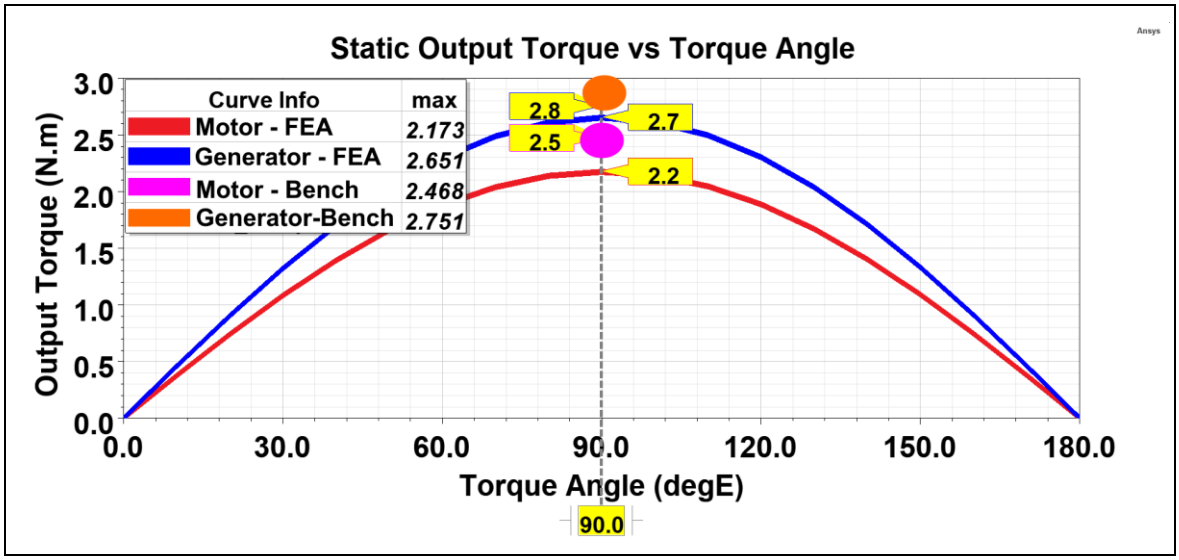


Figure 6.17. Static torque test comparison

6.3.6. Cogging torque tests

Using the test system illustrated in Figure 6.2 (b), the cogging torque was assessed. In this setup, the de-energized S/G was subjected to rotational motion in both clockwise and counterclockwise directions by the load servo motor operating in speed and torque mode. The resulting output torque, known as the cogging torque, was measured and is depicted in Figure 6.18 (b). This analysis provided valuable insights into the cogging behavior of the S/G, facilitating a better understanding of its operational characteristics.

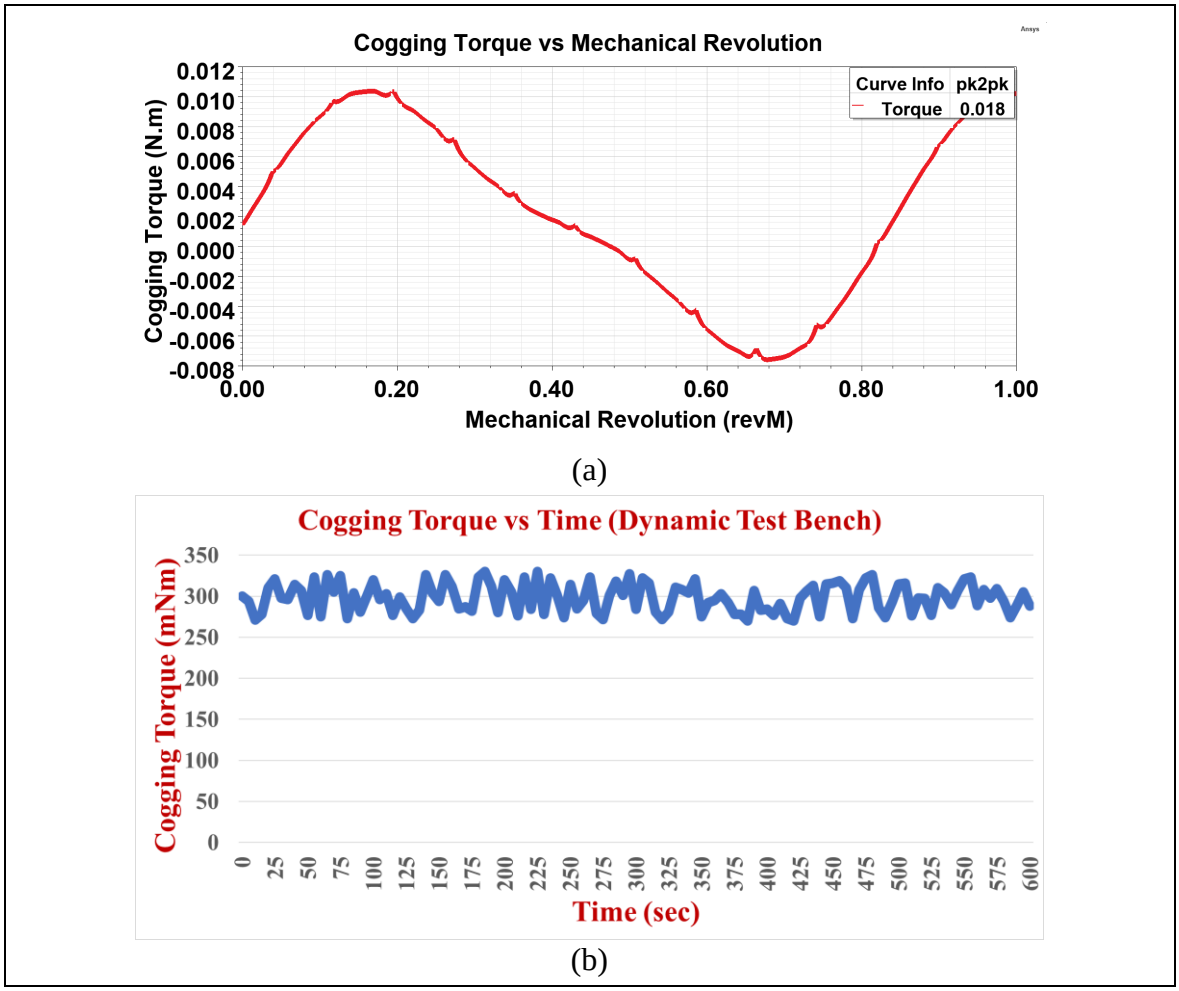


Figure 6.18. Cogging torque determination (a) Maxwell FEA (b) Test bench

In the analysis values, the peak-to-peak cogging torque is approximately 180 mNm, as shown in Figure 6.18 (a), whereas during the tests, the average cogging torque measures around 300 mNm, as shown in Figure 6.18 (b). This difference can be attributed to various factors, such as the influence of the magnetic coupler employed in the shaft connections of the test system and the accuracy of the torque/speed transmitter used for measurements.

6.3.7. Efficiency calculation

Efficiency calculations were carried out by conducting rated load tests on the S/G stages designed for motor and generator mode, utilizing a BLDC-based driver at bus voltages of 48 VDC and 51 VDC, respectively. The output power was determined by measuring the speed and torque, while the input power was calculated as the product of the input DC voltage and current using a power analyser.

Figure 6.19 presents the obtained values for the ratio of output power to input power, reflecting the corresponding efficiency values.

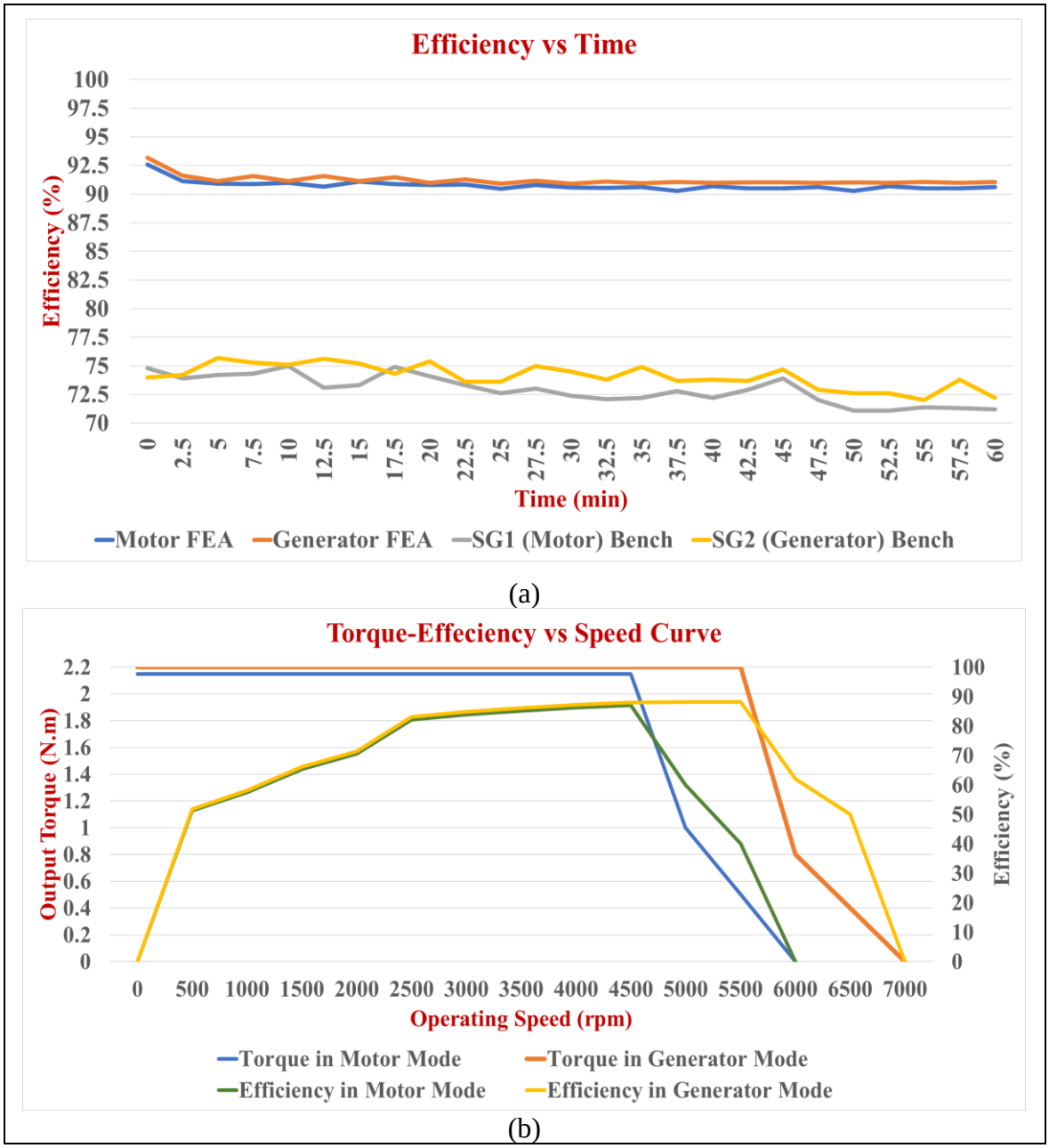


Figure 6.19. (a) Efficiency comparison of FEA and test results (b) Torque-Speed-Efficiency curve of S/G in motor and generator modes

Remarkably, the efficiencies of the S/G stages operating in motor mode and generator mode exhibit close proximity. However, it should be noted that the efficiency derived from the bench was lower than those obtained through analysis, primarily due to the analysis overlooking the driver efficiency.

The efficiency study was conducted after operating the S/G stages for a maximum duration of 60 minutes, as per the operating time of the UAV.

Upon reviewing Figure 6.19, the FEM analysis indicates a motor mode efficiency of 90% and a generator mode efficiency of 92%. In contrast, the test results demonstrate a motor mode efficiency of 74% and a generator mode efficiency of 76%. However, considering the typical efficiency range of BLDC drives, which is approximately 85%, an estimated motor mode S/G efficiency of 87% and generator mode S/G efficiency of 88% can be calculated.

Figure 6.19 (b) illustrates the torque-speed and efficiency-speed curves. By analysing this graph and calculating the fuel consumption based on the power generated by the piston engine, the efficiency of the DCSG system can be accurately determined.

6.4. Fuel Tests of DLE-30

A fuel test was conducted specifically on the DLE30, as shown in Figure 6.20, to compare the test fuel and flight time of the hybridized system with and without the DCSG structure. During the cruise state, which constitutes approximately 60% of the flight time, the operating speed ranges between 3500 and 4000 rpm, while the fuel consumption is estimated to be around 500-750 cc/h. It allows for performance comparison with and without the DCSG.

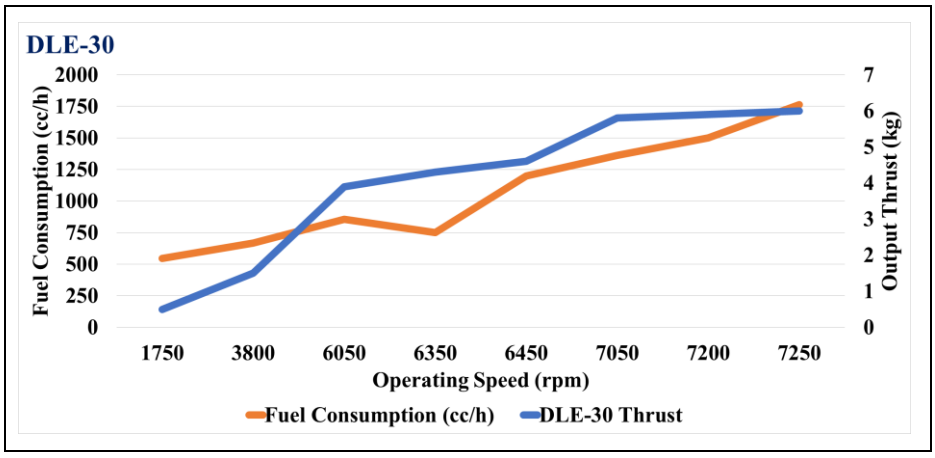


Figure 6.20. DLE-30 fuel consumption and thrust test

6.5. Prototyping and Testing of Double Stage Magnetically Coupled S/G (DCSG)

The proposed DCSG structure incorporates the advantages and contributions discussed in Section 2, in addition to the benefits of a single-stage design. The DCSG system presents four distinct configurations: single stage direct-mounted S/G, single stage magnetically coupled S/G, double stage direct-mounted S/G, and double stage magnetically coupled S/G.

6.5.1. Prototyping of the single-stage model

In Figure 6.21. (a), the direct-mounted single-stage structure comprises the S/G rotor and engine shaft (2), a single-stage S/G stator (1), and a housing (3). Likewise, in Figure 6.21. (b), the magnetically coupled structure consists of a single-stage magnetic coupler (2), S/G rotor-shaft (3), single-stage S/G stator (1), and housing (4).

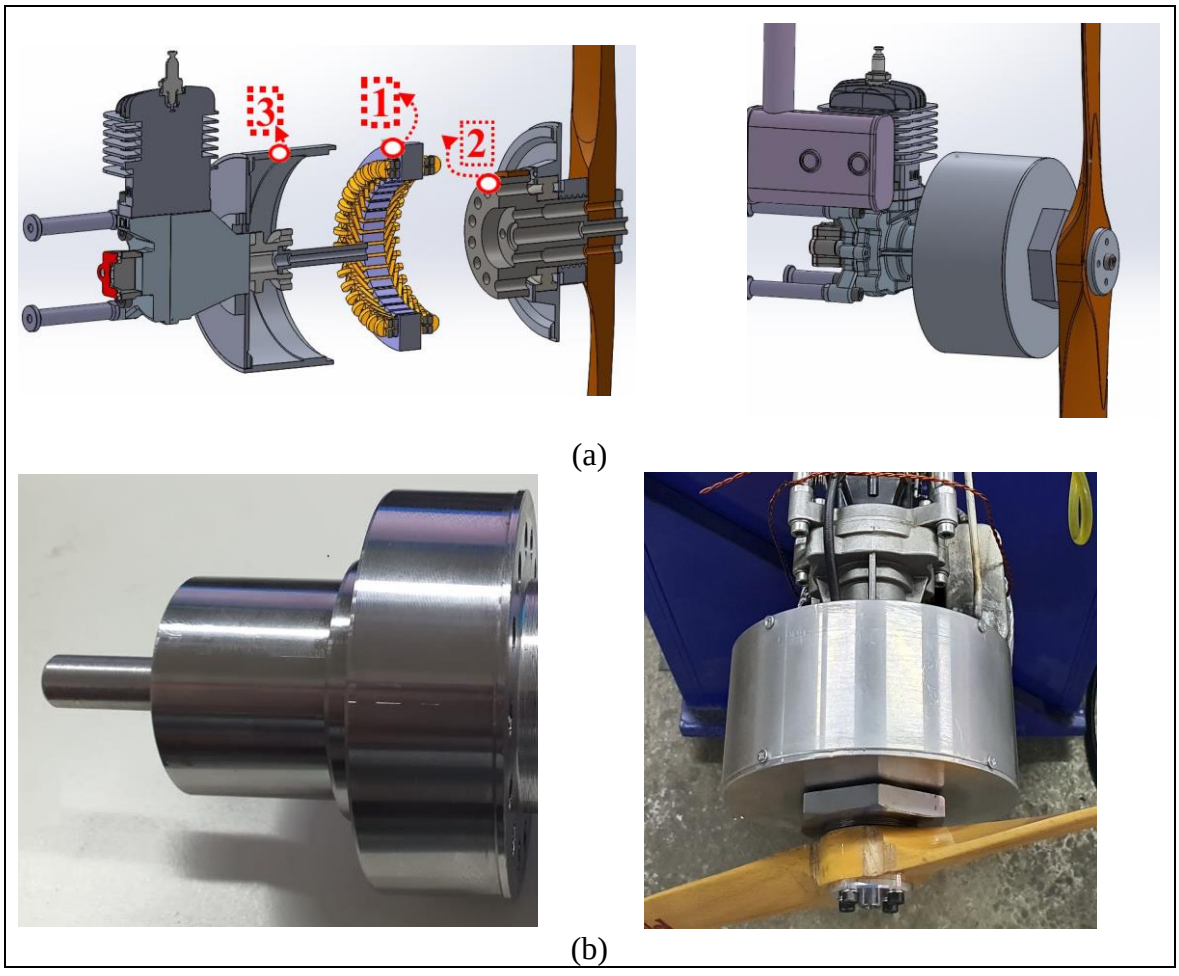
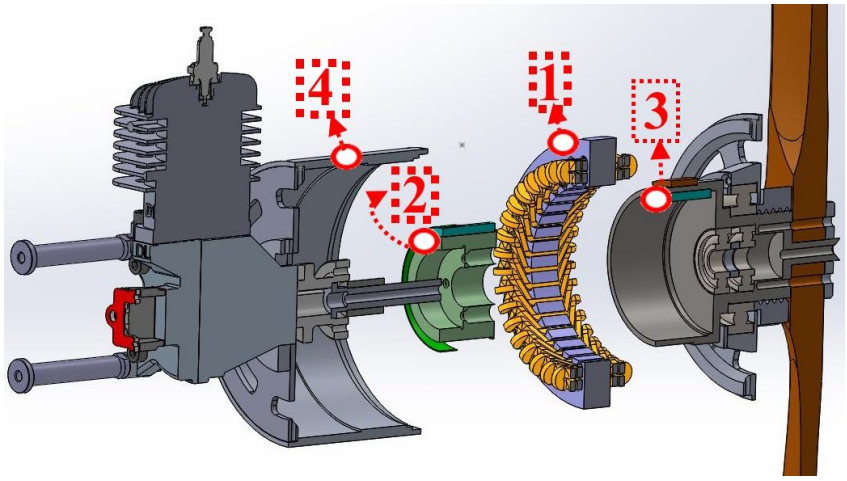
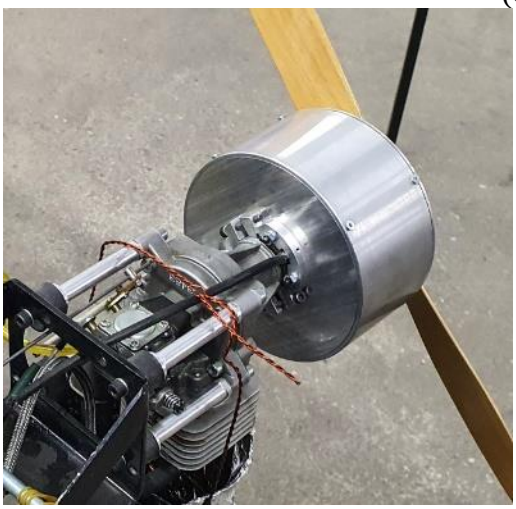
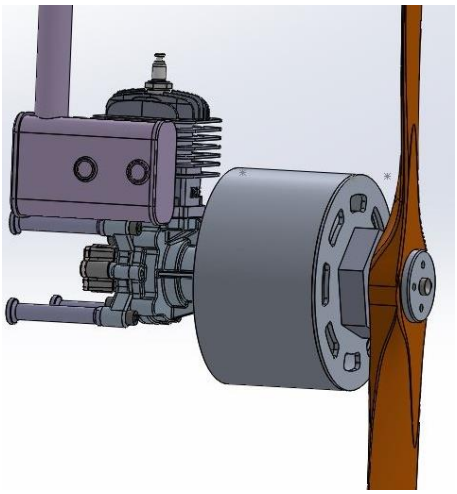


Figure 6.21. Single stage S/G model (a) Direct-mounted cross-section (b) Direct-mounted 3D (c) Magnetically coupled cross-section (d) Magnetically coupled 3D



(c)





(d)

Figure 6.21. (continued) Single stage S/G model (a) Direct-mounted cross-section (b) Direct-mounted 3D (c) Magnetically coupled cross-section (d) Magnetically coupled 3D

6.5.2. Prototyping of the double-stage model

In Figure 6.22 (a), the direct-mounted double-stage model comprises the first stage S/G stator (1), first stage magnetic coupler and S/G rotor (2), second stage magnetic coupler and S/G rotor (3), second stage S/G stator (4), second stage S/G rotor, and housing (6). Likewise, in Figure 6.22 (b), the magnetically coupled model consists of the first stage S/G stator (1), second stage S/G stator (2), S/G rotor and engine shaft (3), and housing (4).

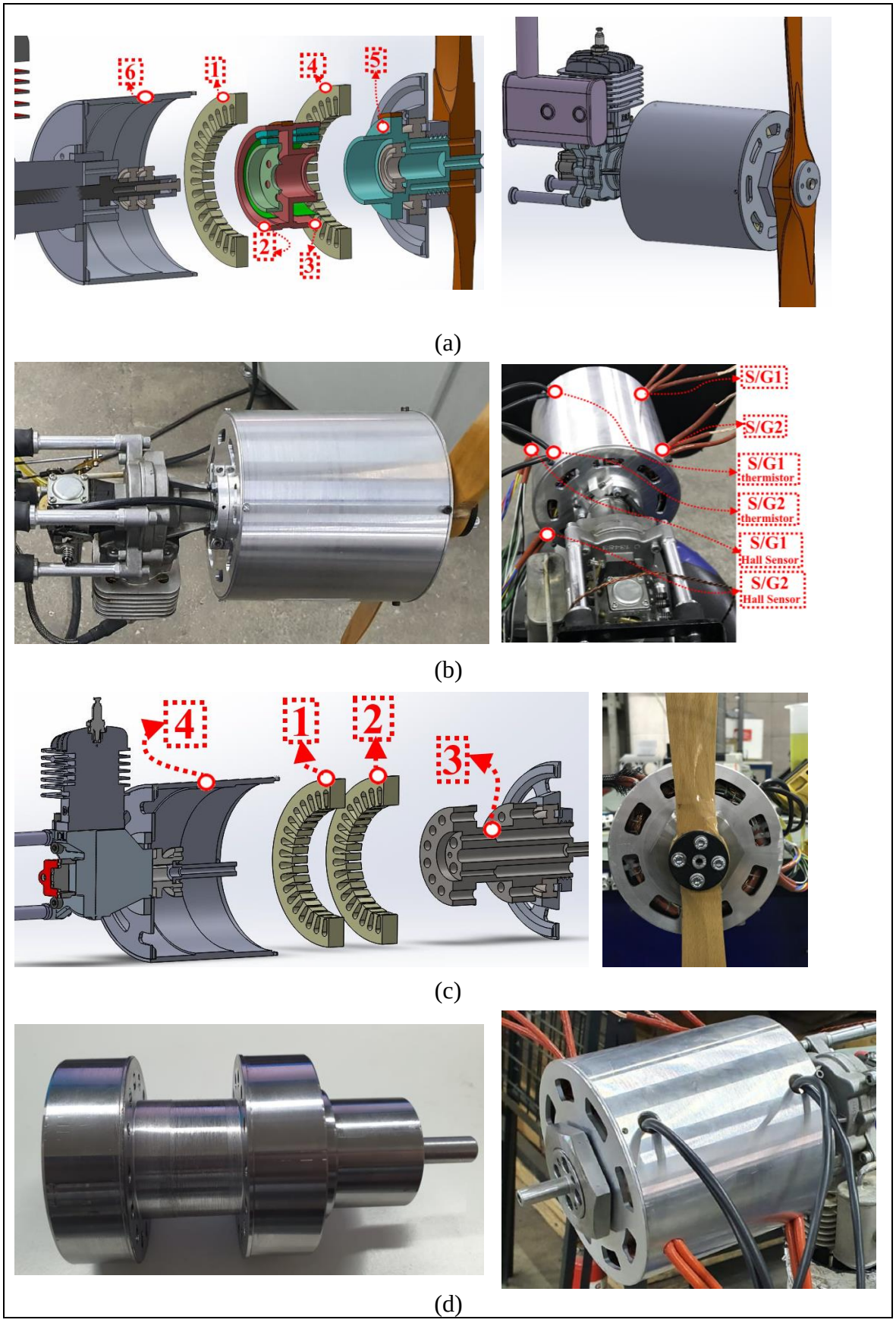


Figure 6.22. Double stage S/G model (a) Direct-mounted cross-section (b) Direct-mounted 3D (c) Magnetically coupled cross-section (d) Magnetically coupled 3D

6.5.3. Total weight of the models with configurations

Table 6.4 lists the output power and the weight of the sample piston engines with a brand of 3W for reference. Table 6.5 lists the manufacturing and assembly methods of the proposed model, including the four configurations, along with their respective weights.

Table 6.4. Comparison of the weight and output power of different piston engines

Piston Engine Weight (gr) and Output Power (kW)							
	DLE30	3W-55	3W-170XI	3W-210XI	3W-275XI	3W-342i	3W-684i
Weight (gr)	1200	1800	4100	6000	7100	8900	16500
Power (kW)	2.5	2.8	14	15	19	23	45

Table 6.5. Total weight of the DCSG model with configurations

Material	Weight (gr)							
	Double Coupled		Single Coupled		Double Direct		Single Direct	
	DLE30	3W55	DLE30	3W55	DLE30	3W55	DLE30	3W55
Housing	510		250		510		250	
Front-Flange	150		150		150		150	
Bearing	200		200		200		200	
End-Flange	100		100		100		100	
Stator with windings	1800		900		1900		900	
Rotor with magnets	1900	1750	900	800	1600	1450	750	650
Driver	220		220		220		220	
Power (kW)	2.5		1.25		2.5		1.25	
Total Weight (gr)	4880	4730	2720	2620	4680	4530	2570	2470

6.6. Thermal Analyses of DCSG with Magnetic Couplers and Starter/Generators

Thermal analysis plays a paramount role in the comprehensive understanding and effective management of permanent magnet double-stage magnetically coupled Starter/Generators, as it encompasses a range of critical aspects, including accurate temperature estimation, optimal design of cooling systems, selection of suitable materials, and the optimization of machine efficiency and performance.

By conducting thorough thermal analyses, it is empowered to gain insights into the intricate temperature distribution within the machine, enabling them to identify potential overheating risks, prevent insulation degradation, minimize winding resistance, and ensure the long-term reliability and operational stability of DCSGs in diverse applications such as aerospace, electric vehicles and industrial machinery, robotics, and renewable energy systems.

Within this context, the significance of thermal analysis becomes evident as it covers a holistic examination of the entire system, encompassing the four configurations, alongside the magnetic coupler and Starter/Generator stages.

6.6.1. Thermal analyses of magnetic coupler stages

Thermal analyses were conducted to evaluate the performance and temperature characteristics of the magnetic couplers in various configurations designed for the DLE-30 and 3W-55XI piston engines with 10 mm and 30 mm coupler lengths under different operating conditions.These analyses, depicted in Figure 6.23, were performed using Siemens FloEFD CFD software at ambient temperature.

The simulations accounted for an assumed ambient air flow rate of 1 m^3/sec in static steady-state conditions, enabling a comprehensive assessment of heat dissipation and thermal management within the magnetic couplers for accurate temperature estimation and the identification of potential overheating risks.

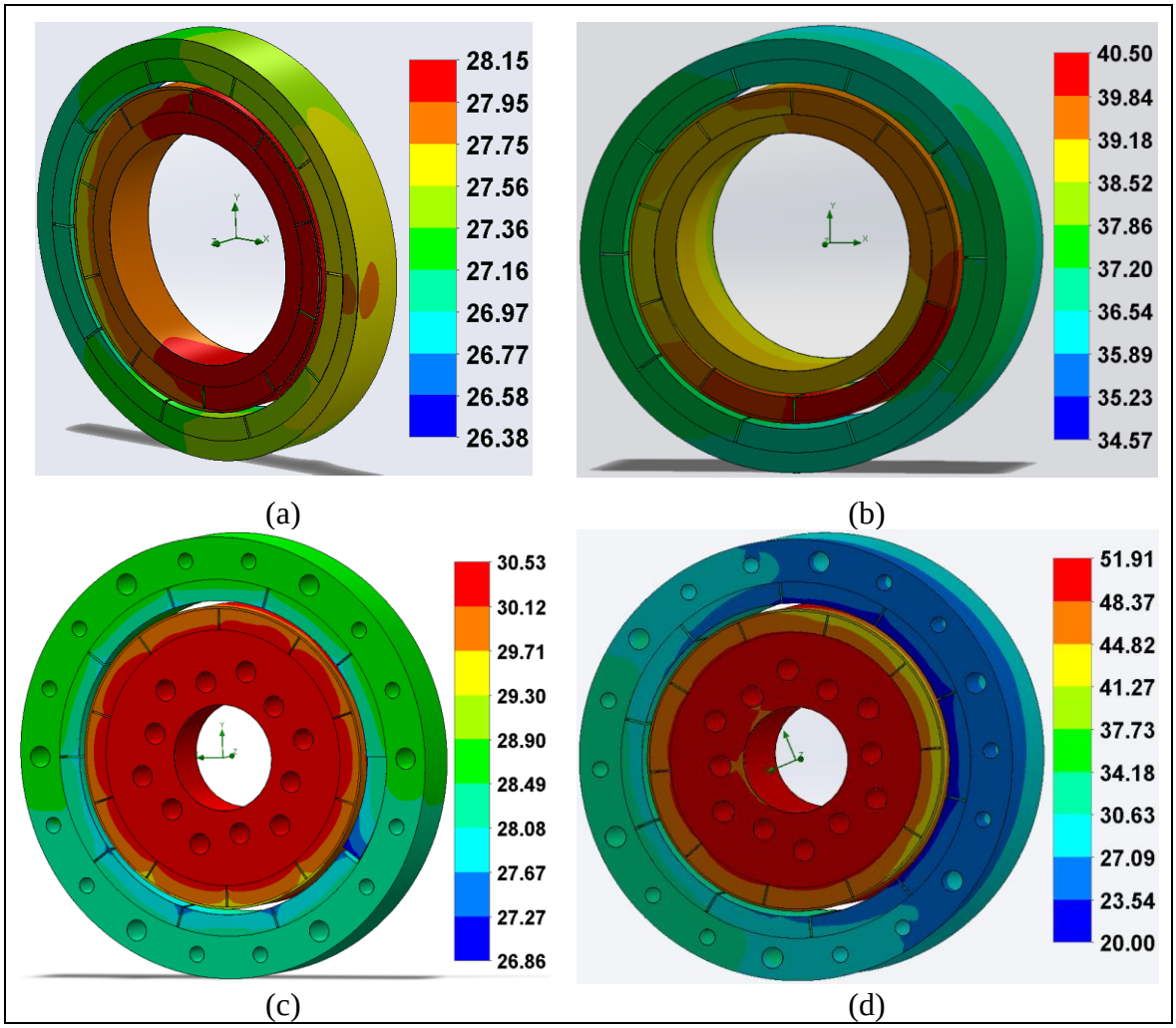


Figure 6.23. Thermal analyses of MCs for DLE-30 and 3W-55XI engines with lengths of (a) DLE-30, 10 mm (b) DLE-30, 30 mm (c) 3W-55, 10 mm (d) 3W-55, 30 mm

Upon detailed examination of Figure 6.23, noteworthy observations arise regarding the maximum temperatures attained by the couplers under investigation. Specifically, the coupler with a 10 mm length exhibits a maximum temperature of 31°C, while the coupler with a 30 mm length reaches a maximum temperature of 52°C.

Notably, these coupler designs were specifically tailored for worst-case conditions. However, the crucial insight gleaned from the thermal analysis is that the obtained temperature results remain below the critical threshold of 80°C for materials, which signifies that the risk of demagnetization is effectively mitigated. Consequently, these findings offer reassurance regarding the robustness and operational integrity of the coupler designs under consideration.

6.6.2. Thermal analyses of Starter/Generator stages

In the context of thermal analysis for the Starter/Generator (S/G) stages, the focus was primarily on the generator mode, given its higher output power compared to the motor mode, which is expected to yield lower temperatures. Similar to the MCs, the S/G thermal analyses were conducted at ambient temperature, specifically for worst-case operating conditions.

The winding temperatures of the S/G remain well within a maximum of 60°C, even when subjected to an ambient environment with a 1 m^3/s air flow, as shown in Figure 6.24. Magnet temperatures remain comfortably within the safe operating range, with readings confined to the 40°C range. These temperatures assure the longevity of the S/G under diverse conditions.

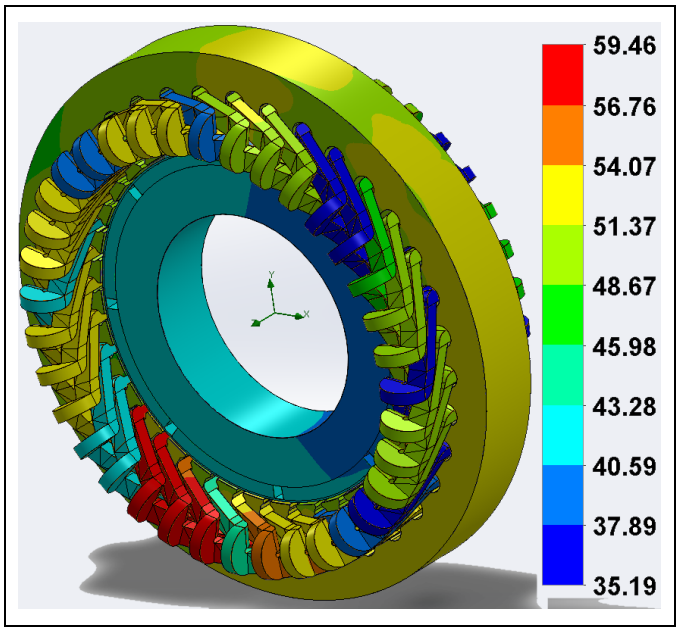


Figure 6.24. Thermal analyses of S/G in generator mode: Worst-case in ambiant flow

6.7. Fuel Consumption and Flight Time Comparison of Hybrid UAV with DCSG model

In novel hybrid UAV applications, the propulsion system incorporates both a fueled piston engine and an electric-fed Starter/Generator. To evaluate the efficiency and specific fuel consumption (SFC) of this hybrid propulsion system, the approach of thermal efficiency, also referred to as fuel conversion efficiency, is utilized [399, 400]. The specific fuel consumption is determined by the reciprocal of the product between the efficiencies characterizing the energy conversion process and the specific calorific value of the fuel.

During the fuel-to-power conversion within the piston engine, the process exhibits inefficiencies, with only approximately one-fourth of the fuel potential energy being converted into power at the flywheel [401].

The remaining energy is dissipated as waste heat through the exhaust or transferred to the surrounding air or water. This ratio between the actual power produced and the potential power is defined as the engine thermal efficiency.

The thermal efficiency, alternatively known as the fuel conversion efficiency, quantifies the ratio of work generated per cycle to the amount of fuel energy supplied per cycle that can be released through combustion. Its mathematical representation, in a simplified form, is provided in Equation 6.2.

$$\eta_t = \frac{1}{SFC * Q_{HV}} \tag{6.18}$$

where η_t : Thermal efficiency of the piston engine
SFC : Specific fuel consumption
Q_{HV} : Net heating value of the fuel (35MJ/kg for gasoline)

For the comparison of fuel consumption and flight time in the proposed system, a 50% hybridization of the UAV propulsion system is conducted by implementing the proposed DCSG model with a combination of the conventional 3W-55XI engine. The battery pack capacity of 48 VDC 10 Ah LiPo and the fuel tank size remain unchanged from the conventional setup. The propellers are kept the same. The conventional 3W-55XI UAV has a specified flight time of 1 hour. The operation of the DCSG stages as motor and/or generator is determined based on the engine SFC, as depicted in Figure 6.25.

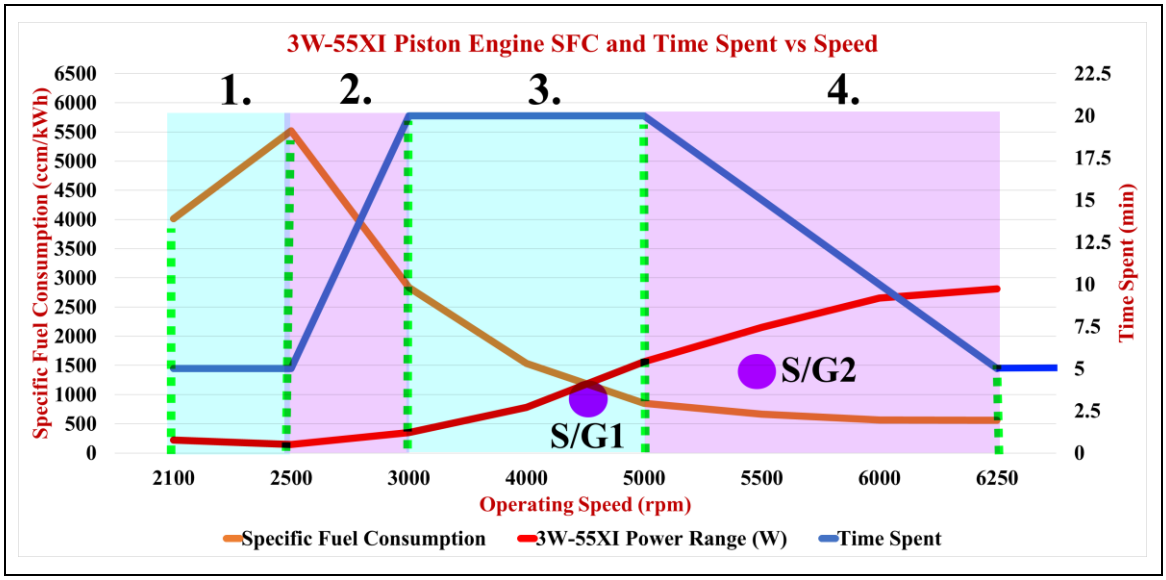


Figure 6.25. 3W-55XI piston engine SFC and time spent curve

The DCSG system consists of two Starter/Generator stages designated S/G1 and S/G2. The flight profile is divided into distinct zones as follows:

Zone 1: Lasting for 5 minutes, this marks the heating phase of the piston engine for starting where the DCSG initiates the piston engine or the idle operation.

Zone 2: Extending for about 10 minutes, this zone corresponds to diving and landing missions. Due to the high SFC in this zone, the piston engine is either silenced or running at low throttle. The propulsion system is predominantly supported by S/G1 during this period.

Zone 3: In this zone, both the piston engine and S/G1 share the load of the propulsion system. In sudden situations such as manoeuvres, G-tun, or turbulence, S/G2 engages in engine mode alongside S/G1. Both the engine and S/G1 can work at full-rate during take-off.

Zone 4: Within this zone, the piston engine and S/G1 operate at full capacity based on the power requirements, while S/G2 consistently functions as a generator. By incorporating S/G1 as an additional source in motor mode, the overall propulsion system efficiency is enhanced. Additionally, both the engine and S/G1 can work at full-rate during take-off.

In essence, organizing the system to align with the working zone of maximum efficiency contributes to an overall improvement in the propulsion efficiency, as shown in Table 6.6.

Table 6.6. Hybrid UAV working zone and thrust ratio determination

Operating Speed (rpm)	Required Power (W)	Piston Thrust Ratio	SG1 Thrust Ratio	SG2 Thrust Ratio	S/G1 Mode	S/G2 Mode
2000	90	10%	90.00%	0.00%	Motor	-
2500	150	25%	75.00%	0.00%	Motor	-
3000	260	30%	70.00%	0.00%	Motor	Generator
4000	730	35%	65.00%	0.00%	Motor	Generator
5000	1240	60%	40.00%	0.00%	Motor	Generator
5500	1600	40%	0.00%	60.00%	Generator	Motor
6000	2160	75%	0.00%	25.00%	Generator	Motor
6500	3000	90%	0.00%	10.00%	Generator	Motor

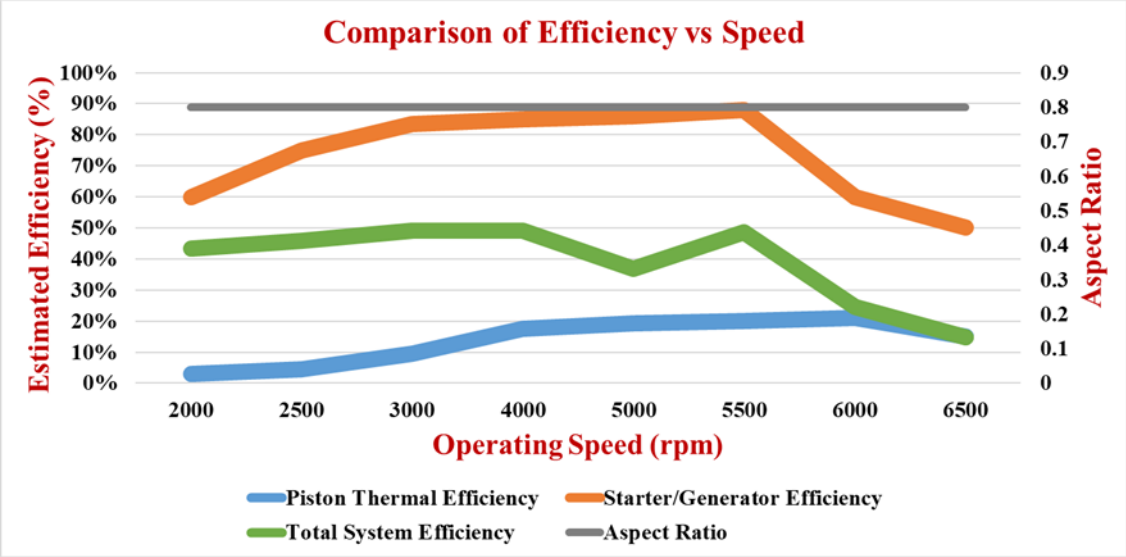


Figure 6.26. Efficiency comparison, piston engine, S/G and overall system

Based on the propeller test system shown in Figure 6.3, the data obtained with the hybrid DCSG system are summarized in Figure 6.26. The comparison of flight time between the conventional and hybrid systems was conducted under the same conditions of LiPo battery pack and fuel tank. The propulsion system efficiency has been improved from 20% to 45%.

Although the DCSG system has a high torque capacity, to make a direct comparison, the propulsion system power is taken based on the power consumed in the conventional system. The flight time and specific fuel consumption were evaluated by simulating the time spent in the operating zones shown in Figure 6.27, considering throttle settings in the test bench, and calculating the total achieved flight time in the test system.

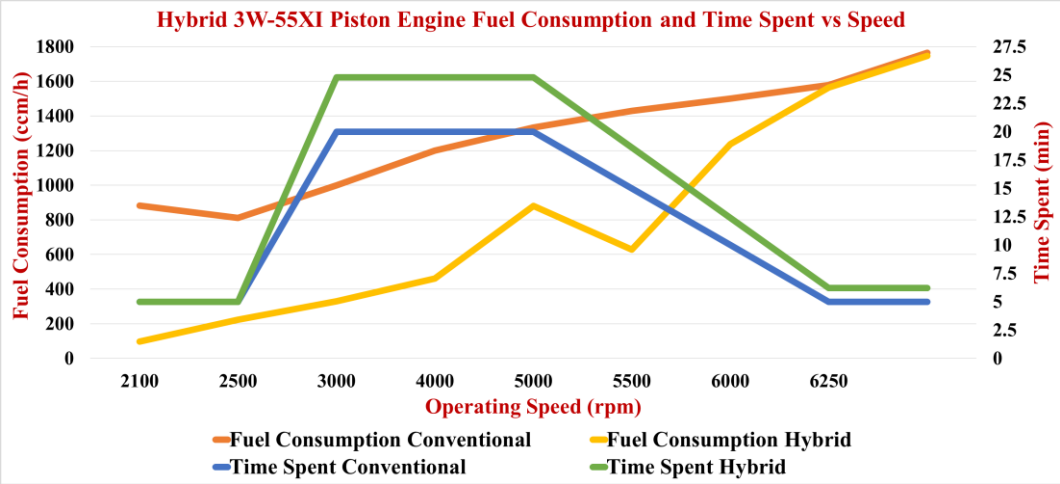


Figure 6.27 Optimizing the fuel consumption and flight time of hybrid UAVs

Analysing Figure 6.27 reveals that, under the same operating conditions and with the DCSG structure in the designated mission areas and thrust ratios, the total flight time increased by 24% despite the increased weight of the UAV. This significant improvement can be attributed to the high efficiency of the electric-fed DCSG system. Additionally, the fuel consumption during flight time has been reduced from 11500 cc/h in the conventional UAV to 7170 cc/h with the DCSG system, resulting in a remarkable fuel reduction of 37%.

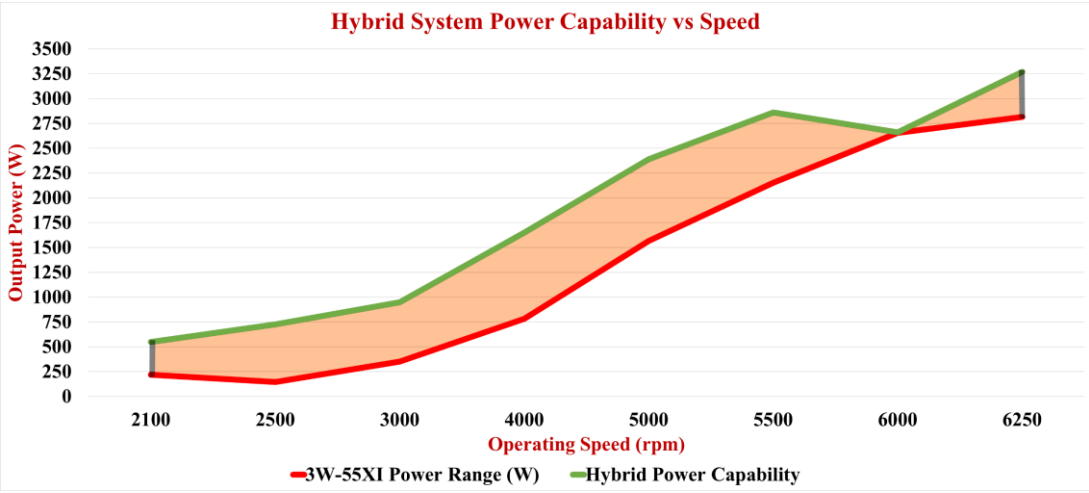


Figure 6.28. Hybrid system power capability vs conventional system

Moreover, as depicted in Figure 6.28, the DCSG system significantly enhances the instantaneous power generation capability by approximately 75% during cruise operating conditions within the 3000-5000 rpm range. This increase adds to the system reliability, particularly in critical scenarios such as sudden manoeuvring, turbulence, and climbing.

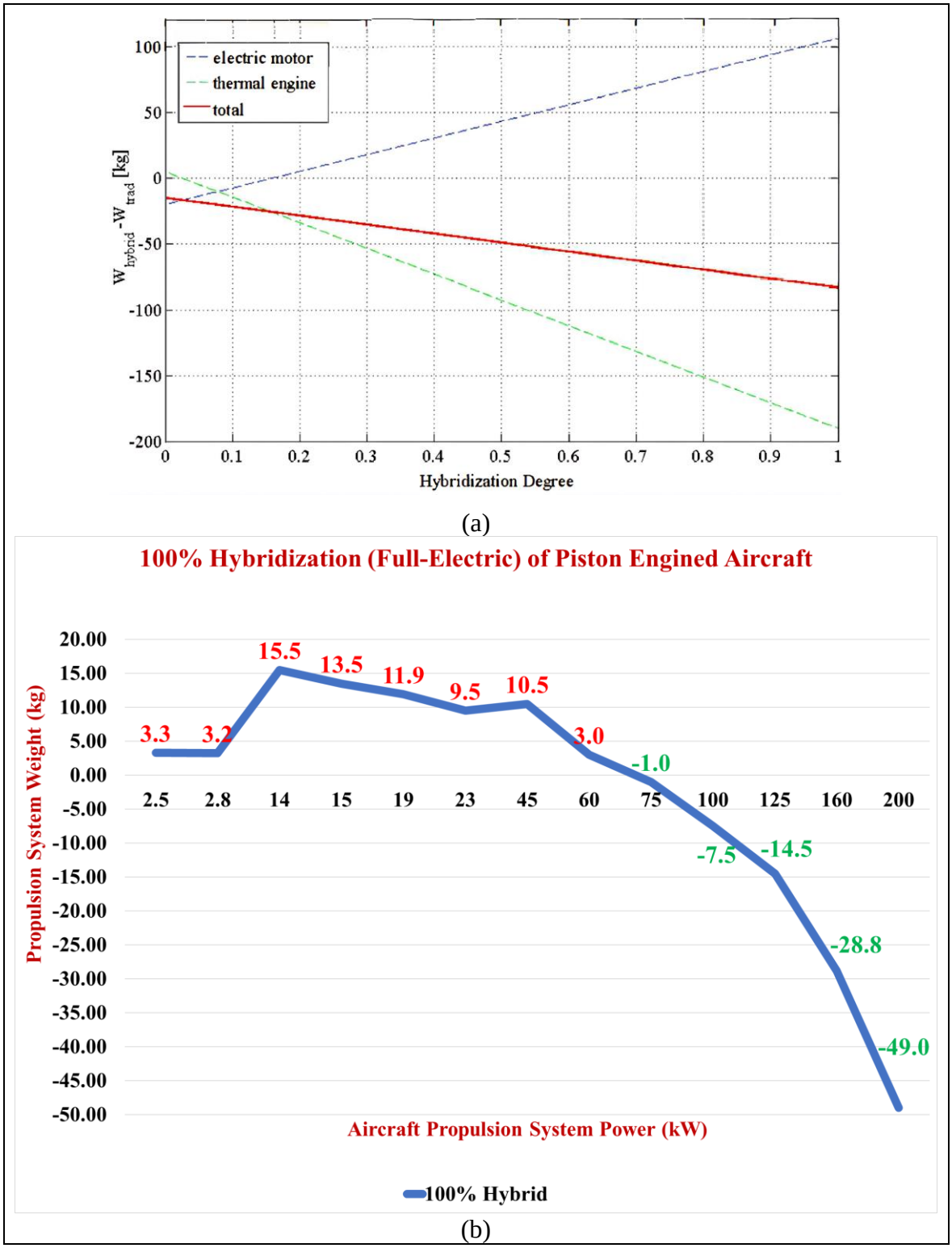
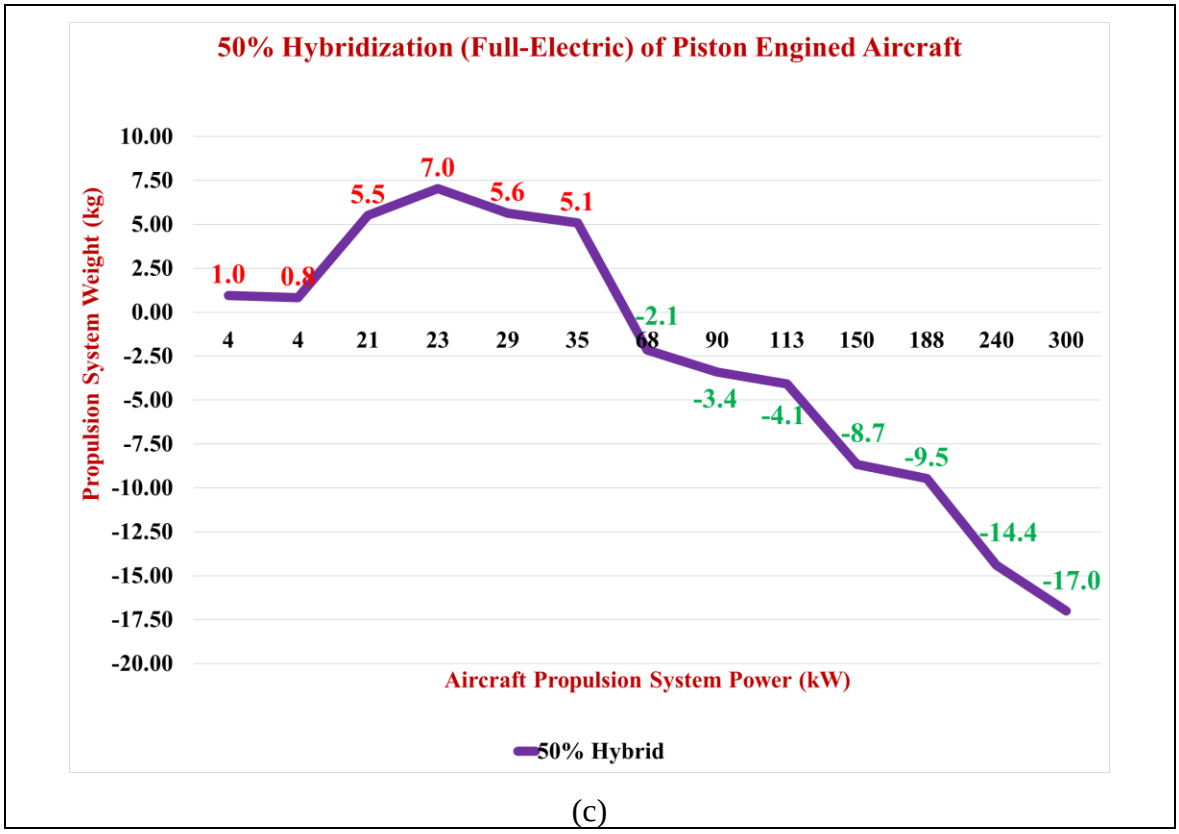


Figure 6.29. Weight reduction with (a) 100 kW piston prop aircraft versus hybridization rate (b) DCSG at 100% hybridization (c) DCSG at 50% hybridization



(c)

Figure 6.29. (continued) Weight reduction with (a) 100 kW piston prop aircraft versus hybridization rate (b) DCSG at 100% hybridization (c) DCSG at 50% hybridization

The applicability of hybrid systems to medium and high-altitude high-endurance UAVs offers the potential for reduced system weight, as demonstrated in Figure 6.29 [19]. Furthermore, Figures 6.30 and 6.31 provide a comparison of the performance and propulsion characteristics between the hybrid DCSG models and the conventional system, respectively.

Upon analysing the figures, it is evident that the conventional system exhibits a flight duration of 60 minutes, whereas the implementation of a single DCSG extends the flight time to 67.8 minutes, and the utilization of dual DCSG further extends it to 74.4 minutes. Additionally, the fuel consumption experiences a reduction from 11499 cc/h in the conventional system to 9470 cc/h with the single DCSG and even further to 7168 cc/h with the dual DCSG. In contrast, the system weight undergoes an increase from 1800 grams in the conventional system to 2620 grams with the implementation of a single DCSG, and significantly rises to 4730 grams with the use of dual DCSGs. Despite the fact that the productions were carried out for proof of concept purposes, the dual DCSG model is expected to exhibit greater effectiveness with the implementation of weight reduction holes.

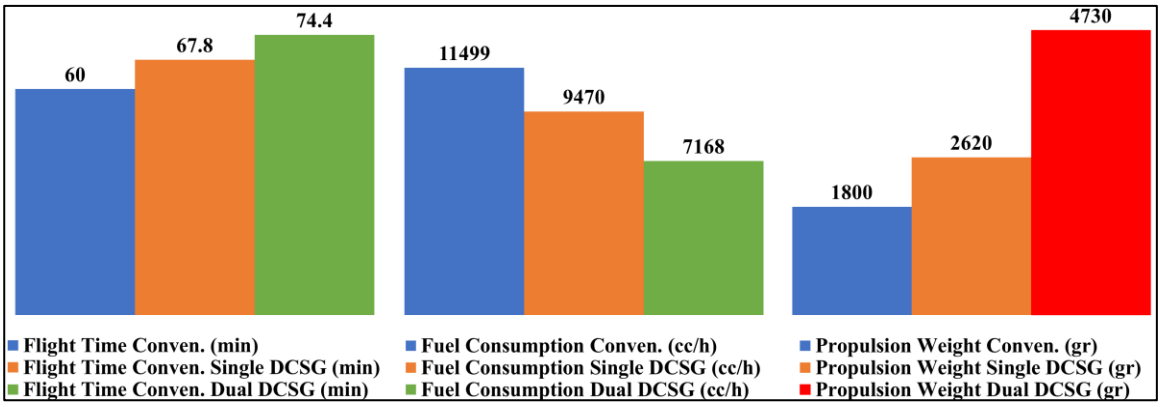


Figure 6.30. Performance comparison of DCSG structures versus conventional systems

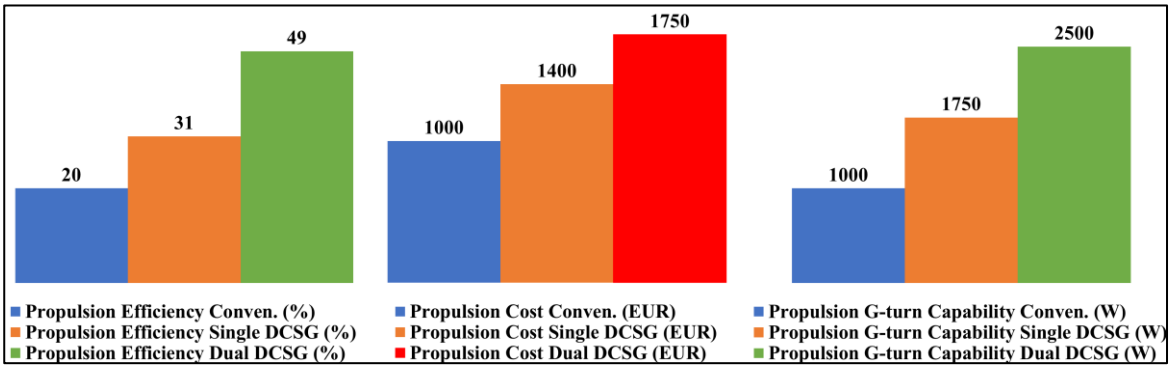


Figure 6.31. Propulsion comparison of DCSG structures versus conventional systems

6.7.1. Thermal operation of novel DCSG model

The thermal analysis of the presented DCSG model diverged from that of the coupler and S/G stages, as it was specifically conducted under engine and propeller operating conditions. In this scenario, the propeller was set to rotate at a cruise speed of 4500 rpm, while the piston engine temperature was established as 75°C based on the obtained thermal test data. On the other hand, Figure 6.26 illustrates the variations in the piston engine thermal efficiency, S/G efficiency, and system efficiency with respect to the total thrust ratio.

The thermal analysis results for the DCSG structure are depicted in Figure 6.32 (a) for the model equipped with ventilation ducts on the front and rear flanges and Figure 6.32 (b) for the model lacking ventilation ducts but featuring fins on the housing. In the air ducted model, the maximum temperature is observed at the windings, reaching approximately 70°C.

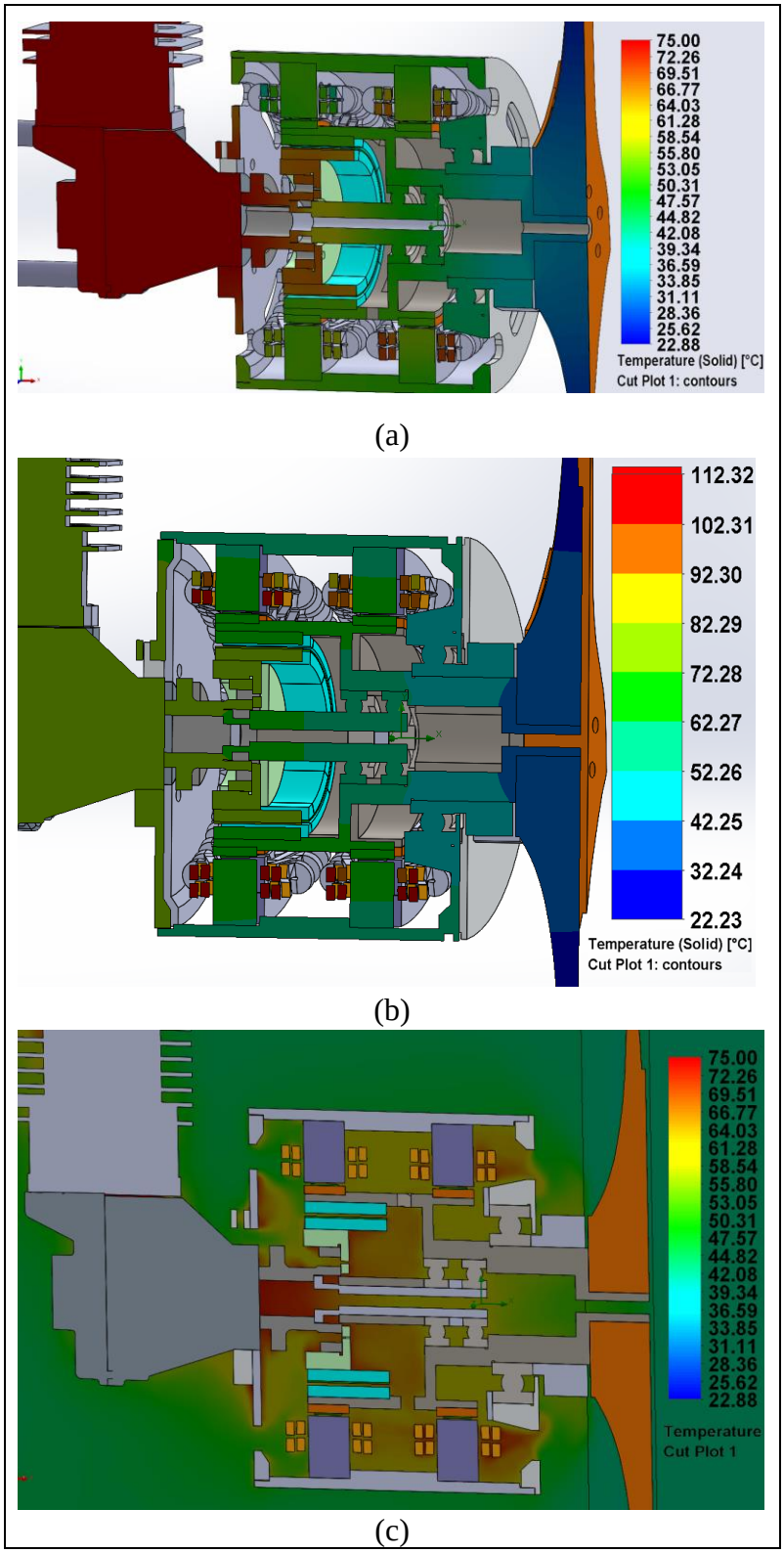


Figure 6.32. Thermal analyses of DCSG model (a) with cooling slots on front and back flanges (b) with fins on housing (c) air flow temperature

However, in the finned version, cooling becomes slightly more challenging, leading to winding temperatures rising to approximately 110°C. Nevertheless, the permanent magnet temperatures remain within the safe zone, approximately 60°C. Furthermore, Figure 6.32 (c) presents a depiction of the temperature distribution of the air flow within the model.

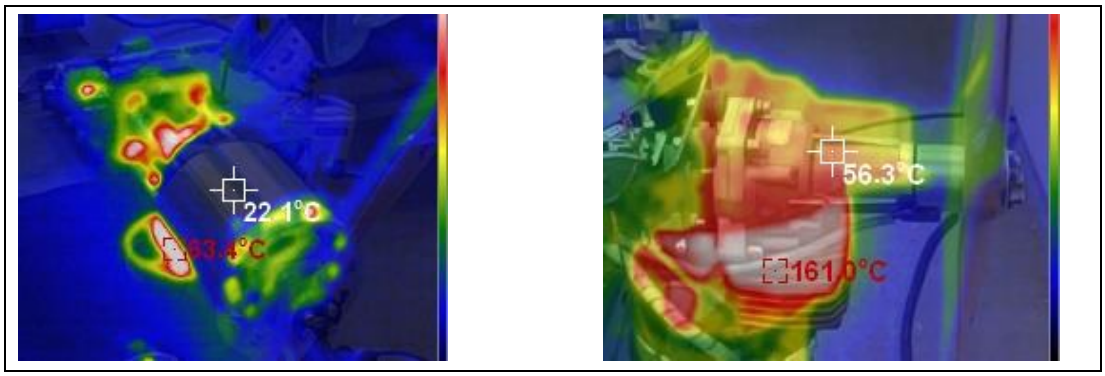


Figure 6.33. Temperature monitoring (a) at cruise speed (b) at rest after 1 hour operation

The CFD analysis indicates winding temperatures ranging between 75-100°C at 4500 rpm cruise operation. However, real-time tests demonstrate lower temperatures. This disparity arises due to the steady-state operating conditions considered in CFD analysis, while the DCSG stages operate under S8 duty cycle conditions, resulting in lower temperature values. As depicted in Figure 6.33, the hybrid UAV exhibits a piston engine temperature of 60°C during cruise operations, whereas the DCSG structure remains approximately 25°C.

6.8. Operating both Starter/Generator Stages in Motor Mode

Implementing a series connection of the Starter/Generator (S/G) stages in motor modes without a suitable Phase-Locked Loop (PLL) system presents various challenges in achieving efficient synchronization and load sharing between the units, leading to noticeable amplification of torque ripple. The absence of a reliable PLL mechanism hinders the precise alignment of phase and frequency among the S/G stages, causing irregularities in torque production and undermining the smooth operation of the system. As a consequence, the increased torque ripple adversely impacts the overall performance and efficiency of the S/G stages, while also introducing mechanical stresses and vibrations that can potentially compromise the longevity of system components.

In series motor mode, the S/G stages operating in motor mode have lower nominal operating speeds. Each stage is designed to deliver a constant torque of 2.1 N.m with the aid of the FOC-based driver. Ideally, when both stages are combined in the system, the torque capability should reach 4.2 N.m. However, upon analysing Figure 6.34, it is observed that the maximum torque produced is 3.9 N.m, accompanied by a torque ripple of approximately 20%. Torque ripple is quantified by computing the difference between the maximum and minimum torque values and subsequently dividing it by the average torque. This discrepancy suggests that there is room for improvement in the speed algorithm and PLL implementation within the drive system to enhance the torque output and minimize the ripple effect.

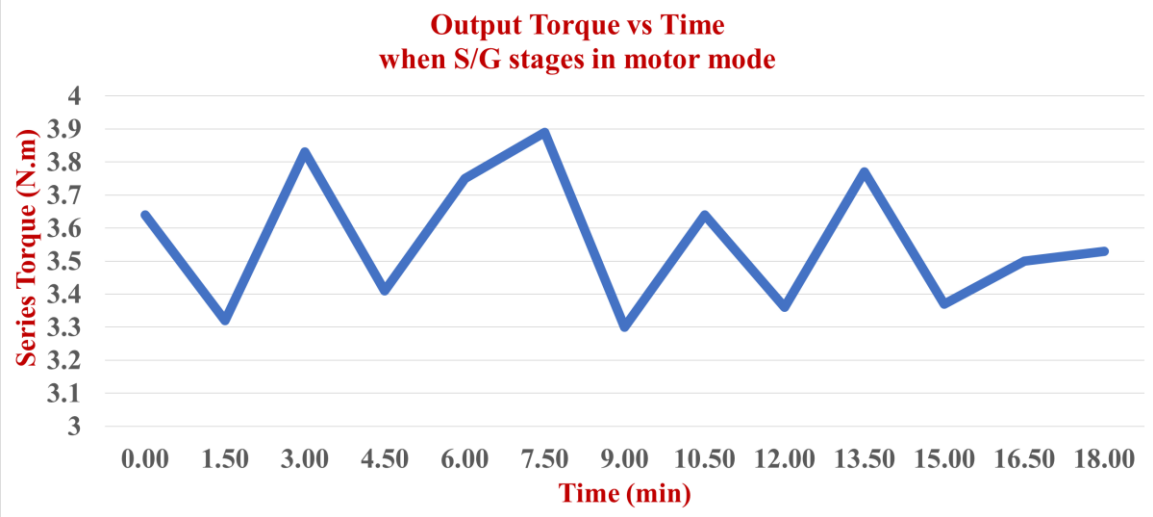


Figure 6.34. Output torque with torque ripple in motor modes of both S/G stages

7. CONCLUSIONS – FUTURE RESEARCH

The chapter carefully outlines the final arguments and findings of the thesis, while also engaging in a discussion regarding potential future work that can build on the research presented in this thesis. The insights gained from this chapter offer significant value to researchers, professionals, and engineers seeking to advance the field of magnetically coupled S/G especially for piston engines. The chapter's recommendations provide a clear direction for future research and development, encouraging the continued exploration of innovative designs and novel technologies to improve system performance and reliability. It provides a vital contribution to the field of S/G by consolidating the key findings of this thesis and providing valuable insights for future research and development efforts.

Magnetic couplers for the 3W-55XI piston engine

The design and testing of magnetic couplers for the 3W-55XI piston engine provide valuable insights into the impact of various design parameters on active cylindrical MCs, achieved through multi-objective simulations based on FEMs. The magnetic design was optimized using optimetric and tuning tools in Ansys Maxwell. Increasing the number of poles yields a maximum torque density up to a certain threshold. The configuration of a 10-pole and 0.98-embrace demonstrates the highest pullout torque, surpassing the 8-pole configuration by 18%. Enhancing the embrace leads to increased output torque, with a 20% increase resulting in a 7.5% boost in torque density. Decreasing the embrace to below 0.6 nearly halves the output torque. Introducing an offset reduces the transmitted torque by a maximum of 10%. PMs with lower residual flux density yield reduced pullout torque, with NdFeB PMs exhibiting higher torque density compared to SmCo couplers. Doubling the air gap length results in a 13% reduction in pullout torque. Decreasing PM and yoke thickness significantly diminishes torque density. Operating the MC close to the saturation point minimizes the system weight. For testing, a direct-type dynamic test system was established for transient and locked-rotor tests, while a thrust test system was utilized for force tests of the MC on the PE. Exceeding the critical torque angle leads to loss of synchronization between the inner and outer rotors. The torque fluctuation during load changes is approximately 0.25%, and the loss of synchronization torque at maximum speed is -0.61 N.m. The magnetic coupler efficiency exceeds 94% at maximum speed.

While the Maxwell 2D FEM results are higher than the 3D and dynamic tests, they still exhibit reasonable agreement within an error margin. Test results differ by 8% with Maxwell 2D results and 4.5% with 3D results due to density variations in adaptive meshes, inclusion of end-leakage effects in 3D FEM, and temperature assignments. Consequently, a correction coefficient of 1.2 for Maxwell 2D and 1.1 for Maxwell 3D is proposed. This comprehensive examination of active cylindrical MCs contributes to their potential utilization in various applications such as robotics, hydraulics, automotive, medical, and pumps.

Magnetic couplers for the DLE-30 or 3W-70R2 piston engine

The specific design of the magnetic coupler for the DLE-30 or 3W-70R2 piston engine contributes to an optimal design study of active synchronous magnetic couplings using a multiobjective analysis approach. Initial analytical calculations are based on the Virtual Work method, while the magnetic design is performed in Ansys Maxwell 2D using optimetric solutions and in Maxwell 3D utilizing sensitivity analyses and optimization techniques such as SNLP, GA, and MOGA. Considering manufacturability, a 10-pole configuration is preferred, providing a 17% higher torque density compared to an 8-pole configuration. Torque fluctuations are measured at 0.1% without a retaining sleeve and 0.15% with the sleeve. Operating the system at saturation points ensures meeting the requirements with minimum weight. Loss of synchronization is calculated to result in an average attraction torque of -0.6 N.m, suggesting the need for skew work in S/G applications. Static structural analysis of the retaining sleeve, designed to protect permanent magnets from contact pressure and tangential stress, confirms its robustness. Magnetic couplings are manufactured with lengths of 10 mm and 20 mm, with doubling the stack length corresponding to an almost twofold increase in torque. The proposed modular stack structure offers ease of production due to the limitation of the outer diameter, deviating from the traditional method. A direct dynamic test system is implemented for magnetic couplings, conducting full load, overload, and locked-rotor tests. The dynamic and static test results closely correlate with the outputs of Maxwell 2D and 3D FEM simulations. Experimental static results reveal a 37% absolute error for the Virtual Work method in analytical calculations. However, the presence of errors, 13% for 2D FEM and 6% for 3D FEM, underscores the importance of numerical simulations in aviation applications. The test results also provide insights into the safety factor and turbulence coefficient.

At the critical angle, the total rotor core losses amount to 2.7 W, PM hysteresis losses are 0.40 W, the induced eddy-current losses on the magnets are 212.5 W, sleeve hysteresis loss is 0.91 W, and induced eddy-current loss of the sleeve is 40.46 W. Among these losses, PMs and eddy current losses induced on the sleeve have the most significant impact. The coupling efficiency at maximum operating speed and critical angle is 93.8%, while at minimum torque angle and minimum operating speed, it reaches 96.9%. The study introduces a correction factor of 1.39 for the Virtual Work method, 1.18 for Maxwell 2D, and 1.11 for Maxwell 3D, enabling realistic design opportunities. Thus, it can be concluded that the modular design of magnetic couplings is valid and can be safely adapted to various applications.

Double stage magnetically coupled Starter/Generator (DCSG)

The DCSG system optimizes propulsion system efficiency by utilizing one or two stages as motor during high thrust requirements like climbing, when the piston engine consumes more fuel. Conversely, during low thrust requirements such as cruising and diving, when the UAV consumes less fuel, one or two stages of the high-efficiency DCSG function as generators to charge the system battery group. This approach reduces the overall fuel consumption of the piston engine while efficiently charging the batteries, thereby increasing flight time.

To ensure operational continuity, the DCSG model incorporates specially designed magnetic couplers between the engine and the first stage S/G, as well as between the first and second S/G stages, effectively isolating all shafts. In the event of a shaft failure, one or more S/G stages can continue operating as motors, enabling the UAV to complete its mission.

Dynamic tests of the Starter/Generator stages were conducted using a direct-dynamic test system, achieving full loading conditions with the S/G capable of providing 2.1 N.m in motor mode and 2.2 N.m in generator mode. The analysis results closely align with the findings from the test system. Even when exposed to an ambient environment with a 1 m^3/s air flow, the winding temperatures of the S/G remain well within the maximum of 60°C. FEM analysis indicates a motor mode efficiency of 90% and a generator mode efficiency of 92%. However, the test results demonstrate slightly lower values with a motor mode efficiency of 74% and a generator mode efficiency of 76%. It is worth noting that the typical efficiency range of BLDC drives is approximately 85%, suggesting an estimated motor mode S/G efficiency of 87% and generator mode S/G efficiency of 88%.

The DCSG system provides a significant weight advantage compared to conventional UAVs, depending on the total propulsion power and hybridization ratio. However, this weight reduction benefit may not be as applicable to UAVs with less than 40 HP.

A comparison of flight time between conventional and hybrid systems was conducted using the same LiPo battery pack and fuel tank conditions. The propulsion system efficiency has been improved from 20% to 45% with the implementation of the DCSG model in designated mission areas and thrust ratios. Consequently, the total flight time increased by 24% despite the increased weight of the UAV. Moreover, fuel consumption during flight time decreased from 11500 cc/h in the conventional UAV to 7170 cc/h with the DCSG system, resulting in a significant fuel reduction of 37%. The DCSG model also significantly enhances the instantaneous power generation capability by approximately 75% during cruise operating conditions within the 3000-5000 rpm range. Additionally, a single-stage magnetically coupled Starter/Generator, represented by production images in Figure 6.22, underwent similar investigations to the DCSG system. However, the benefits achieved were found to be 55% lower compared to the double-stage DCSG model.

Advantages

In addition, the DCSG design takes into account the propeller dead-zone, resulting in a negligible 2% reduction in thrust generated by the piston engine when the DCSG system is not in operation. This minor reduction in thrust has minimal impact on the overall performance of the propulsion system. This study emphasizes the importance of considering kickback torque during piston engine startup in magnetic coupler design. A modular design approach was adopted, considering the different torque values between the 1st and 2nd stages of the magnetic coupler.

While the 1st stage MC demonstrated higher torque transmission capabilities with an 18 or 20 pole ratio, a decision was made to opt for 10 poles due to ease of production and assembly. However, it was found that the 10-pole MC was insufficient to overcome the initial starting kickback torque. To address this challenge, the length of the 1st stage MC was doubled to meet the torque requirements while considering production and assembly constraints. Although this solution increased the weight of the UAV by approximately 350 grams, it successfully resolved the torque-related issue.

Disadvantages

The DCSG system, operating in a master/slave configuration as detailed in Section 2, ensures a high level of system reliability. However, in the unlikely event of an extreme failure resulting in the inoperability of the DCSG system, propeller test system data reveal a 30% decrease in the flight time, primarily due to the increased weight. To mitigate such risks, it is important to monitor the performance of the DCSG system using speed or current sensors. Gathering relevant information from these sensors allows for determining whether the DCSG system is functioning properly or not. This knowledge can then be incorporated into the mission scenario, enabling informed decisions on whether the UAV should continue its mission or take appropriate measures based on the operational conditions.

One notable drawback is the cost associated with the DCSG system. For instance, while the 3W-55XI piston engine used in this study costs approximately 1000 EUR, the production cost of the DCSG system amounts to 750 EUR. This represents an approximate 75% increase in system cost, which may raise concerns in industrial applications. However, in specialized fields such as the military and defense industry, where longer flight times and reduced fuel consumption hold significant value, the benefits of the DCSG system outweigh the cost considerations. In Start/Stop mode, which is generally required for flight at high speeds, the extended flight time is reduced by 20% because the piston engine consumes some oil-mixed fuel to maintain piston engine lubrication.

While the torque ripple generated by the series-connected S/G stages may be lower compared to that of the piston engine, it is still crucial to incorporate a suitable Phase-Locked Loop (PLL) system to ensure optimal comfort and performance of the overall system. In the proposed DCSG system, complete implementation of a PLL is not employed when both S/G stages are operated in motor mode, resulting in torque ripple. The torque ripple can be obtained by testing the servo Starter/Generator model on a dynamic test bench.

Future research

Future research directions for the proposed double-stage magnetically coupled Starter/Generator (DCSG) are outlined below:

- Investigate the feasibility of utilizing alloy materials to further reduce the weight of the DCSG system, thereby enhancing its overall efficiency.
- Explore and test new manufacturing techniques that can effectively reduce the weight of the DCSG system while maintaining its performance and reliability.
- Develop and implement an improved Phase-Locked Loop (PLL) application to minimize torque ripple when both stages of the DCSG system are operated as motors.
- Investigate the feasibility and potential benefits of incorporating new generation semiconductor drivers, such as SiC and GaN, in the DCSG drive system, with a focus on their impact on weight reduction.
- Study the IPMSM topology in addition to the studied SPMSM topology, analysing their contributions to power density and exploring the benefits of reluctance torque.
- Evaluate the operability and performance of the hybrid UAV at high speeds by leveraging the field-weakening feature offered by the IPMSM topology.
- Investigate the impact of coating materials such as gold and platinum on the lifetime and performance of NdFeB magnets, exploring their potential benefits for the DCSG system.
- Examine the effect of the piston engine start/stop feature on the flight time of the hybrid UAV during its operational duties.
- Assess the impact of regenerative braking on fuel consumption in the DCSG system and explore its potential for further improving efficiency.
- Investigate the effectiveness and reliability of measuring vibrations generated by the piston engine and using the DCSG stages to dampen those vibrations, thereby enhancing the safety and reliability of the hybrid UAV.
- Explore the applicability and adaptability of the DCSG system for medium and long-altitude UAVs, assessing its potential benefits in different operational scenarios.
- Conducting performance tests and weight studies with LiPo and LiOn battery types with higher C values other than the LiFePo4 battery group.
- Attempting to reduce the size of the propeller with the ability to reach higher speeds with DCSG stages in the IPMSM topology using flux-weakening.
- Investigating specific fuel consumption reduction for smaller fuel tanks.
- The impact of the DCSG model, which will be lightweighted through borehole drilling, on the system will be examined.
- An effort will be made to decrease the length of the S/G stages from 15 mm to 10 mm by increasing the specific electrical loading, which is one of the design parameters.

REFERENCES

1. Petritoli, E., Leccese, F., and Ciani, L. (2018). Reliability and maintenance analysis of unmanned aerial vehicles. *Sensors (Basel)*, 18(9), 1-16.

2. International Air Transport Association. (2019). Aircraft technology roadmap to 2050. *IATA*, Geneva, 10-45.

3. Austin, R. (2010). *Unmanned Aircraft Systems: UAVs Design, Development and Deployment*. New York: Wiley, 1-365.

4. Wargo, C. A., Church, G. C., Glaneueski, J., and Strout, M. (2014). *Unmanned aircraft systems (UAS research and future analysis).* IEEE Aerospace Conference 2014, Big Sky, Toronto, 1-16.

5. Birch, N. T. (2000). 2020 Vision: The prospects for large civil aircraft propulsion. *Aeronautical Journal*, 104(1038), 347-352.

6. Bojoi, R., Cavagnino, A., Miotto, A., Tenconi, A., and Vaschetto, S. (2010). *Radial flux and axial flux PM machines analysis for more electric engine aircraft applications.* 2010 IEEE Energy Conversion Congress and Exposition, Georgia, 1672-1679.

7. Muehlbauer, K. and Gerling, D. (2010). *Two-generator-concepts for electric power generation in More Electric Aircraft Engine.* The XIX International Conference on Electrical Machines - ICEM 2010, Rome, 1-5.

8. Wenping, C., Mecrow, B. C., Atkinson, G. J., Bennett, J. W., and Atkinson, D. J. (2012). Overview of electric motor technologies used for more electric aircraft (MEA). *IEEE Transactions on Industrial Electronics,* 59(9), 3523-3531.

9. Yeoh, S. S., Yang, T., Tarisciotti, L., Hill, C. I., Bozhko, S., and Zanchetta, P. (2016). *More electric aircraft Starter-Generator system with utilization of hybrid modulated model predictive control.* International Conference on Electrical Systems for Aircraft, Railway, Ship Propulsion and Road Vehicles and International Transportation Electrification Conference, Nottingham, 1-6.

10. Liu, Y., Mo, D., Nalianda, D., Li, Y., and Roumeliotis, I. (2022). Review of more electric engines for civil aircraft. *International Journal of Aeronautical and Space Sciences,* 23(4), 784-793.

11. Noland, J. K., Leandro, M., Suul, J. A., and Molinas, M. (2020). High-power machines and Starter-Generator topologies for more electric aircraft: A technology outlook. *IEEE Access,* 8, 130104-130123.

12. Zhang, Z., Huang, J., Jiang, Y., Geng, W., and Xu, Y. (2017). Overview and analysis of PM Starter/Generator for aircraft electrical power systems. *CES Transactions On Electrical Machines and Systems,* 1(2), 1-15.

13. Jiang, M., Salmon, J., and Knight, A. M. (2009). *Design of a permanent magnet synchronous machine for a flywheel energy storage system within a hybrid electric vehicle.* IEEE International Electric Machines and Drives Conference, San Francisco, 1736-1742.

14. Aksugür, M. (2010). *Preliminary design, build and flight testing of a VTOL tailsitter unmanned aerial vehicle with hybrid propulsion system*, M.Sc. Thesis, Istanbul Technical University Aeronautics and Astronautics Engineering, Istanbul, 1-111.

15. Schoemann, J. (2014). *Hybrid-electric propulsion systems for small unmanned aircraft*, Ph.D. Thesis, Technische Universitat München, Munchen, 1-188.

16. Saikumar, A. K., Avinash, B., and Vamsikrishna., C. (2015). Conceptual design of hybrid UAV. *International Journal of Engineering Research and Technology,* 4, 1-7.

17. Silva, H. L. and Gil, A. A. (2017). *Hybrid-electric aircraft: Conceptual design, structural and aeroelastic analyses*, Bachelor Thesis, Universidade Federal de Uberlandia Faculdade de Engenharia Mecanica, Uberlandia, 1-123.

18. Tejaswini, R., Ranjitha, G., Mythri, L., and Chaithra, Y. H. (2022). Conceptual design of hybrid electric aircraft. *International Journal of Scientific Development and Research,* 7(7), 1-10.

19. Fusaro, R. (2016). The advantages of a hybrid piston prop aircraft. *Aviation,* 20(2), 85-97.

20. Ibrahim, R. A. (2018). *Market and cost analysis of hybrid-electric aircraft*, M.Sc. Thesis, Politecnico di Milano Aeronautical Engineering, Milano, 1-117.

21. Nagy, A. (2019). Electric aircraft - present and future. *Production Engineering Archives,* 23(23), 36-40.

22. Sahoo, S., Zhao, X., and Kyprianidis, K. (2020). A review of concepts, benefits, and challenges for future electrical propulsion-based aircraft. *Aerospace,* 7(4), 1-69.

23. Miller, J. M., Stefanovic, V., Ostovic, V., and Kelly, J. (2001). *Design considerations for an automotive integrated Starter-Generator with Pole-Phase Modulation.* Conference Record of the 2001 IEEE Industry Applications Conference, Chicago, 2366-2373.

24. Mudannayake, C. P. and Rahman, M. F. (2003). *An integrated Starter Alternator for the 42 V PowerNet.* The Fifth International Conference on Power Electronics and Drive Systems (PEDS), Montreal, 648-653.

25. Nuscheler, R. (2003). *Two concepts of Starter-Generator-Machines for 8 to 12 cylinder combustion engines.* IEEE IEMDC'03: IEEE International Electric Machines and Drives Conference, Madison, 194-199.

26. Friedrich, G., Chedot, L., Biedinger, J. M., and Macret, P. (2005). *Integrated Starter Generator: Need of an optimal design and control approach. Application to a permanent magnet machine.* IEEE International Conference on Electric Machines and Drives, 2005., San Antonio, 1529-1534.

27. Liu, J. B., Hu, J. G., and Xu, L. Y. (2004). *Design and control of a kilo-amp DC/AC inverter for integrated Starter-Generator (ISG) applications.* Conference Record of the 2004 IEEE Industry Applications Conference, Seattle, 2754-2761.

28. Liu, J. (2005). *Modeling, analysis and design of integrated starter generator system based on field oriented controlled induction machines*, Ph.D. Thesis, The Ohio State University Graduate School of The Ohio State University, Ohio, 1-204.

29. Luchache, D. D., Horga, V., Albu, M., and Ratoi, M. (2006). *Indirect field oriented control of an integrated Starter Generator.* IECON 2006 - 32nd Annual Conference on IEEE Industrial Electronics, Paris, 5107-5112.

30. Chedot, L., Friedrich, G., Biedinger, J.-M., and Macret, P. (2007). Integrated Starter Generator: The need for an optimal design and control approach. Application to a permanent magnet machine. *IEEE Transactions on Industry Applications,* 43(2), 551-559.

31. Itoh, J., Kawamura, K., Koshikizawa, H., and Abe, K. (2018). *Control strategy for Starter Generator in UAV with micro jet engine.* International Power Electronics Conference 2018 (IPEC-Niigata 2018 -ECCE Asia), Niigata, 1567-1574.

32. Friedrich, G. and Girardin, A. (2009). Integrated Starter Generator. *IEEE Industry Applications Magazine*, 15, 26-34.

33. Bhangu, B. S. and Rajashekara, K. (2014). Electric Starter Generators: Their integration into gas turbine engines. *IEEE Industry Applications Magazine,* 20, 14-22.

34. European Technical Standard Order, (2013). *Engine driven direct current generator/starter generator,* ETSO-C56bA1.

35. Sharma, A., Capoor, G. K., and Chattopadhyay, A. B. (2015). *Advanced aircraft electrical systems to enable an all-electric aircraft.* 2015 International Conference on Electrical Systems for Aircraft, Railway, Ship Propulsion and Road Vehicles (ESARS), Aachen, 1-6.

36. Singh, R., Lal, R., Ranganath, M., and Chaudhary, R. (2014). Failure of piston in IC engines: A review. *International Journal of Modern Engineering Research,* 4(9), 1-10.

37. Australian Transport. (2016). Engine failures and malfunctions in light aeroplanes 2009-2014, investigation number AR-2013-107. *Australian Transport Safety Bureau*, Australia, 1-38.

38. Shah, J. B. (2019). Overheating of aircraft engine cylinders, *ASM Failure Analysis Case Histories: Air and Spacecraft*, 1-3.

39. Gurugubelli, S., Kuna, S. K., and Gowravarapu, K. (2022). Analysıs of piston failure: A review. *International Research Journal of Modernization in Engineering Technology and Science,* 04(11), 1-14.

40. Hall, R., Jack, A. G., Mecrow, B. C., and Mitcham, A. J. (2005). *Design and initial testing of an outer rotating segmented rotor switched reluctance machine for an aero-engine shaft-line-embedded Starter/Generator.* IEEE International Conference on Electric Machines and Drives, 2005, San Antonio, 1870-1877.

41. Arslan, S., Iskender, I., and Navruz, T. S. (2022). *Optimal design of an in-runner direct-drive synchronous permanent magnet Starter/Generator for UAVs.* 2022 International Symposium on Multidisciplinary Studies and Innovative Technologies (ISMSIT), Ankara, 543-548.

42. He, T., Zhu, Z., Eastham, F., Wang, Y., Bin, H., Wu, D., Gong, L., and Chen, J. (2022). Permanent magnet machines for high-speed applications. *World Electric Vehicle Journal,* 13(1), 1-38.

43. Rhyu, S.-h., Khaliq, S., Baek, C.-W., and Ha, Y.-C. (2020). Optimal design and static performance analysis of permanent magnet coupling for chemical pump application. *Journal of Magnetics,* 25(1), 64-69.

44. Akcay, Y., Giangrande, P., Gerada, C., and Galea, M. (2020). *Comparative analysis between axial and coaxial magnetic couplings.* The 10th International Conference on Power Electronics, Machines and Drives (PEMD 2020), Nottingham, 385-390.

45. Akcay, Y., Giangrande, P., and Galea, M. (2020a). *Design, analysis and dynamic performance of radial magnetic coupling.* 2020 23rd International Conference on Electrical Machines and Systems (ICEMS), Hamamatsu, 222-227.

46. Akcay, Y., Giangrande, P., and Galea, M. (2020b). *A novel magnetic coupling configuration for enhancing the torque density.* 2020 23rd International Conference on Electrical Machines and Systems (ICEMS), Hamamatsu, 228-233.

47. Krasil’nikov, A. Y. and Krasil'nikov, A. A. (2011). Calculation of losses in current-conducting screen in sealed machines and devices due to loose packing of magnets in half-clutches of magnetic clutch. *Chemical and Petroleum Engineering,* 47, 392-397.

48. Balachandran, A., Boden, M., Sun, Z., Forrest, S. J., Ede, J. D., and Jewell, G. W. (2019). Design, construction, and testing of an aero-engine starter-generator for the more-electric aircraft. *The Journal of Engineering,* 2019(17), 3474-3478.

49. Yuan, W. Q., Liu, Y., Li, D., and Meng, G. Y. (2014). Research on overloading protection of permanent magnetic coupler in coal mine. *Advance Materials Development and Applied Mechanics,* 597, 492-497.

50. Mathee, A. (2017). *Development of a magnetic gear for dry-cooling power plant applications,* M.Sc. Thesis, Stellenbosch University Faculty of Engineering, Stellenbosch, 1-132.

51. Sun, X., Hu, Q., Yan, L., Chen, Y., Zhang, K., and Qu, J. (2019). A magnetic torque optimization method for a hydraulic - magnetic coupling-drive cuttings cleaning tool. *Natural Gas Industry B,* 6(4), 374-383.

52. Yılmaz, M. E. (2022). *Yeni nesil teknolojilerden insansız hava aracı ve özel hayatın gizliliğinin korunması*, M.Sc. Thesis, Hacettepe Üniversitesi Kamu Hukuku, Ankara, 1-115.

53. Prisacariu, V. (2017). The history and the evolutıon of UAVs from the beginning till the 70s. *Journal of Defense Resources Management*, 8(1), 1-9.

54. Sonawane, U. and Mustafi, N. N. (2020). Design and Development of Small Engines for UAV Applications, *Advanced Combustion Techniques and Engine Technologies for the Automotive Sector*. s. 231-246.

55. Demircan, A. (2016). *Aerodynamic and structural design and analysis of an electric powered mini UAV*, M.Sc. Thesis, Middle East Technical University Aerospace Engineering, Ankara, 1-199.

56. Abdallah, R. (2019). *Reliability approaches in networked systems: Application on unmanned aerial vehicles*, Ph.D. Thesis, Universite Bourgogne Franche-Comte Sciences pour I'Ingenieur, Bourgogne, 1-139.

57. Karaaslan, S. (2021). *İnsansız hava araçları akustik yön kestirimi*, Yüksek Lisans Tezi, Hacettepe Üniversitesi Elektrik ve Elektronik Mühendisliği, Ankara, 1-137.

58. Lawhorn, D. (2021). *Electric power systems and components for electric aircraft*, Ph.D. Thesis, University of Kentucky College of Engineering, Kentucky, 1-190.

59. Constantine Dario. (2020). The future of the drone economy. *Levitate Capital*, California, 20-150.

60. Barnhart, R. K., Marshall, D. M., and Shappee, E. (2021). *Introduction to unmanned aircraft systems*. New York: CRC Press, 1-214.

61. Chodnicki, M., Siemiatkowska, B., Stecz, W., and Stepien, S. (2022). Energy efficient UAV flight control method in an environment with obstacles and gusts of wind. *Energies*, 15(10), 1-31.

62. Montmany Cardo, J. (2022). *Design and simulation of a microgrid used in a more electric aircraft*, M.Sc. Thesis, Catalunya University Industrial Engineering, Catalunya, 1-69.

63. Darryll Pines, Felipe Bohorquez. (2008). Unmanned aerial Vehicles: an Overview. *INSIDE GNSS*, New Jersey, 1-8.

64. Özdemir, U. (2015). *Dikey iniş kalkış yapabilen sabit kanatlı insansız hava aracı tasarım, üretimi ve uçuş testleri*, Ph.D. Thesis, İstanbul Teknik Üniversitesi Uçak ve Uzay Mühendisliği, İstanbul, 1-204.

65. Dhaliwal, S. S. (2009). *Control of an unconventional double-ducted fan VTOL UAV for obstructed environments using the MARC system*, M.Sc. Thesis, University of Calgary Department of Mechanical and Manufacturing Engineering, Calgary, 1-167.

66. Elmeseiry, N., Alshaer, N., and Ismail, T. (2021). A detailed survey and future directions of unmanned aerial vehicles (UAVs) with potential applications. *Aerospace*, 8(12), 1-29.

67. Abdelhafez, A. and Forsyth, A. J. (2009). *A review of more-electric aircraft.* Aerospace Sciences & Aviation Technology, Military Technical College, Kobry Elkobbah, 1-13.

68. Batgi, S. (2019). *Bölgesel denetim amaçlı insansız hava aracı (İHA) tasarımı ve imalatı*, Yüksek Lisans Tezi, Erciyes Üniversitesi Sivil Havacılık, Erciyes, 1-87.

69. Singhal, G., Bansod, B. S., and Mathew, L. (2018). *Unmanned aerial vehicle classification, applications and challenges: A review*. Preprints, India, 1-19.

70. Valavanis, K. P. and Vachtsevanos, G. J. (2014). *Handbook of Unmanned Aerial Vehicles*. New York: Springer, 1-3015.

71. European Union Aviation Safety Agency, Official Journal of the European Union, *Easy Access Rules for Unmanned Aircraft Systems (Regulations EU 2019/947 and 2019/945)*, 2022.

72. Federal Aviation Administration (1989). *Federal aviation regulations*. Washington, D.C.: U.S. Dept. of Transportation, 46-88.

73. Rossi, N. (2018). *Conceptual design of hybrid-electric aircraft*, M.Sc. Thesis, Politecnico di Torino Aeronautical Engineering, Torino, 1-111.

74. Jia, Y. (2016). *Induction generator based more electric architectures for commercial transport aircraft*, Ph.D. Thesis, The University of Texas Electrical Engineering, Texas, 1-137.

75. Brown, S. P. (2017). *Design and optimization of a 1 kW hybrid powertrain for unmanned aerial vehicles*, M.Sc. Thesis, Oregon State University Mechanical Engineering, Oregon, 1-125.

76. Buticchi, G., Wheeler, P., and Boroyevich, D. (2022). The More-Electric Aircraft and beyond. *Proceedings of the IEEE*, Toronto,1-15.

77. Neuberger, B. M. (2017). *An exploration of commercial unmanned aerial vehicles (UAVs) through life cycle assessments*, M.Sc. Thesis, Rochester Institute of Technology Department of Industrial and Systems Engineering, Rochester, 1-68.

78. Tom, L., Khowja, M., Vakil, G., and Gerada, C. (2021). Commercial aircraft electrification-current state and future scope. *Energies*, 14(24), 1-29.

79. Shahmoradi, J., Talebi, E., Roghanchi, P., and Hassanalian, M. (2020). A comprehensive review of applications of drone technology in the mining industry. *Drones*, 4(3), 1-25.

80. Ducard, G. J. J. and Allenspach, M. (2021). Review of designs and flight control techniques of hybrid and convertible VTOL UAVs. *Aerospace Science and Technology*, 118, 1-26.

81. Adu-Gyamfi, Appiah, B., and Good, C. (2022). Electric aviation: A review of concepts and enabling technologies. *Transportation Engineering,* 9, 1-14.

82. Bozhko, S., Hill, C. I., and Yang, T. (2018). More-electric aircraft: systems and modeling, In *Encyclopedia of Electrical and Electronics Engineering*. New York: Wiley, 1-31.

83. Reyes, A. (2018). *Design and development of an UAV with hybrid flight capabilities*, M.Sc. Thesis, Centro De Investigaciones Optomechatronics, Spanish, 1-69.

84. Benzaquen, J., He, J., and Mirafzal, B. (2021). Toward more electric powertrains in aircraft: Technical challenges and advancements. *CES Transactions On Electrical Machines and Systems,* 5(3), 177-193.

85. Insight. (2018). 07-Electrical power systems. *ATI,* Cranfield, 1-16.

86. Geiss, I. (2020). *Sizing of the series hybrid-electric propulsion system of general aviation aircraft*, Ph.D. Thesis, University of Stuttgart Faculty of Aerospace Engineering and Geodesy, Stuttgart, 1-172.

87. Nguyen Duy, V. (2020). Review on the hybrid-electric propulsion system and renewables and energy storage for unmanned aerial vehicles. *International Journal of Electrochemical Science*, 5296-5319.

88. Krznar, M., Piljek, P., Kotarski, D., and Pavkovic, D. (2021). Modeling, control system design and preliminary experimental verification of a hybrid power unit suitable for multirotor uavs. *Energies,* 14(9), 1-24.

89. Mbarki, S. (2019). *The innovation of electric and hybrid aircraft*, Tesi di Laurea, Universita degli Studi di Napoli "Federico II" Facolta di Ingegneria e Scienze di Base, Dipartimento di Ingegneria Industriale, Naples, 1-62.

90. Yiğit, E. (2020). *Mikro/mini sınıf bir İHA'nın elektrikli itki sisteminin matematiksel modellenmesi ve deneysel doğrulanması*, M.Sc. Thesis, Anadolu Üniversitesi Uçak Gövde Motor Bakım, Eskişehir, 1-159.

91. Aircraft Electrical Propulsion. (2018). Onwards and upwards. *Roland Berger*, London, 12-23.

92. Zhang, T. (2019). *Design, analysis and validation of a silver gull inspired hybrid UAV*, Ph.D. Thesis, University of Technology Sydney Faculty of Engineering and Information Technology, Sydney, 1-202.

93. Fleckenstein. (2019). Electric aircraft working group. *WSDOT,* Olympia, 1-3.

94. Yezeguelian, A. and Isikveren, A. T. (2020). Methods to improve UAV performance using hybrid-electric architectures. *Aircraft Engineering and Aerospace Technology,* 92(5), 685-700.

95. Adamski, M. (2017). Analysis of propulsion systems of unmanned aerial vehicles. *Journal of Marine Engineering & Technology,* 16(4), 291-297.

96. Pornet, C. and Isikveren, A. T. (2015). Conceptual design of hybrid-electric transport aircraft. *Progress in Aerospace Sciences,* 79, 114-135.

97. Richard Nelson, Donald Dix. (2003). Development of engines for unmanned air vehicles: some factors to be considered. *Institute For Defense Analyses*, Virginia, 1-91.

98. Rasmussen, J., Nielsen, J., Garcia-Ruiz, F., Christensen, S., Streibig, J. C., and Lotz, B. (2013). Potential uses of small unmanned aircraft systems (UAS) in weed research. *Weed Research,* 53(4), 242-248.

99. A. Mohammed, A., Shinkafi, A. A., Isah, A., Ajayi, J. A., Pedro, P. T., Asooto, B. C., Ejakita, J. O., and Johnson-Anamemena, N. (2022). Prospects and challenges of propulsion technologies of unmanned aerial vehicles: A review. *Nigerian Journal of Technology,* 40(6), 1-9.

100. Military Air Systems. (2007). Electrically driven general systems for UAV's: RTO-MP-AVT-145. *MAS*, Munich, 2-7.

101. Pham, K. L., Leuchter, J., Bystricky, R., Andrle, M., Pham, N. N., and Pham, V. T. (2022). The study of electrical energy power supply system for UAVs based on the energy storage technology. *Aerospace,* 9(9), 1-29.

102. Bill Canis. (2015). Unmanned aircraft systems (UAS): Commercial outlook for a new industry. *Congressional Research Service*, Washington, 1-17.

103. Dinç, A., Taher, R., Moayyedian, M., Bushehri, A., Alruwayeh, A., Alsaeedi, A., Alali, A., and Alsarraf, F. (2021). A performance review of a high altitude long endurance drone. *International Journal of Progressive Sciences and Technologies (IJPSAT)*, 24(1), 1-8.

104. Kahveci, M. and Can, N. (2017). İnsansiz hava araçları: Tarihçesi, tanımı, dünyada ve Türkiye'deki yasal durumu. *Selcuk University Journal of Engineering ,Science and Technology*, 5(4), 511-535.

105. Fioriti, M., Vaschetto, S., Corpino, S., and Premoli, G. (2020). Design of hybrid electric heavy fuel MALE ISR UAV enabling technologies for military operations. *Aircraft Engineering and Aerospace Technology*, 92(5), 745-755.

106. Yun, J., Cho, S., Liu, H. C., Lee, H. W., and Lee, J. (2015). *Design of electromagnetic field of permanent magnet generator for VTOL series-hybrid UAV.* 18th International Conference on Electrical Machines and Systems (ICEMS 2015), Pattaya, 83-86.

107. Pastrone, D., Suleman, A., and Obertino, D. (2021). *Hybrid-electric propulsion system,* M.Sc. Thesis, Politecnico di Torino Aerospace Engineering, Torino, 1-109.

108. Jian, L. and Chau, K. T. (2010). Design and analysis of a magnetic-geared electronic-continuously variable transmission system using finite element method. *Progress in Electromagnetics Research-pier*, 107, 47-61.

109. Haselbach, F., Newby, A., and Parker, R. (2015). *Next generation of large civil aircraft engines - Concepts & Technologies.* 11th European Turbomachinery Conference, Madrid, 23-27.

110. Boukoberine, M. N., Zhou, Z., and Benbouzid, M. (2019). A critical review on unmanned aerial vehicles power supply and energy management: Solutions, strategies, and prospects. *Applied Energy*, 255, 1-56.

111. Karamanli, İ. A. (2018). *Model insansız hava aracı üretimi*, M.Sc. Thesis, Karabuk University Makine Mühendisliği, Karabük, 1-85.

112. Gu, C., Zhang, H., Buticchi, G., Sala, G., Galassini, A., Papadopoulos, S., and Degano, M. (2018). *Multi-port power conversion systems for the More-Electric-Aircraft.* IECON 2018 - 44th Annual Conference of the IEEE Industrial Electronics Society, Washington, 5553-5558.

113. Leonardi, F. and Degner, M. (2001). *Integrated Starter Generator based HEVs: A comparison between low and high voltage systems.* IEEE International Electric Machines and Drives Conference (IEMDC 2001), Massachusetts, 622-628.

114. Finger, D. F. (2020). *Methodology for multidisciplinary aircraft design under consideration of hybrid-electric propulsion technology*, Ph.D. Thesis, RMIT University School of Engineering College of Science, Engineering and Health, Melbourne, 1-271.

115. Papaoikonomou, D. (2014). *Design of a high speed induction Starter/Generator for aerospace applications comparison with PM machine*, M.Sc. Thesis, Delft University of Technology Faculty of Electrical Engineering, Mathematics and Computer Science, Delft, 1-147.

116. Bojoi, R., Cavagnino, A., Cossale, M., and Tenconi, A. (2014). *Multiphase Starter Generator for 48v mini-hybrid powertrain: Design and testing.* 2014 International Symposium on Power Electronics, Electrical Drives, Automation and Motion (Speedam), Ischia, 1319-1324.

117. Yeoh, S. S. (2016). *Control strategies for the more electric aircraft Starter-Generator electrical power system*, Ph.D. Thesis, University of Nottingham, Nottingham, 1-261.

118. Aslan, B., Semail, E., Korecki, J., and Legranger, J. (2011). *Slot/pole combinations choice for concentrated multiphase machines dedicated to mild-hybrid applications.* IECON 2011: 37th Annual Conference on IEEE Industrial Electronics Society, Victoria, 3698-3703.

119. Dalamagkidis, K., Valavanis, K. P., and Piegl, L. A. (2008). On unmanned aircraft systems issues, challenges and operational restrictions preventing integration into the National Airspace System. *Progress in Aerospace Sciences,* 44(7-8), 503-519.

120. Andersson, F. (2018). *Integrated Generator for use in aircraft engines*, M.Sc. Thesis, Lund University Department of Energy Sciences, Scandinavia, 1-74.

121. Asaei, B., Farhangi, S., and Fayazi, A. (2007). *Intelligent energy management in a vehicle with integrated Starter Alternator.* IEEE Vehicle Power and Propulsion Conference, California, 597-604.

122. Diab, A., Rashed, M., Li, J., Gerada, C., and Bozhko, S. (2018). *Performance analysis of PMSM for high-speed Starter-Generator system.* IEEE International Conference on Electrical Systems for Aircraft, Railway, Ship Propulsion and Road Vehicles & International Transportation Electrification Conference 2018 (ESARS-ITEC), Nottingham, 1-7.

123. Elbuluk, M. E. and Kankam, M. D. (1996). Potential Starter/Generator technology for future aerospace application. *IEEE Aerospace and Electronic Systems Magazine*, 11(10), 17-24.

124. Gaines, T. L., Auer, P. J., Lane, G. H., and Wissinger, J. A. (2005). *More Electric Aircraft Starter-Generator Multi-Speed Transmission System*. US Patent No.: US007481062B2.

125. Hajek, V., Mach, M., and Hysek, R. (2014). *Starter-Generator.* 2014 Ninth International Conference on Ecological Vehicles and Renewable Energies (EVER), Monte-Carlo, 1-6.

126. Bojoi, R., Cavagnino, A., Tenconi, A., and Vaschetto, S. (2016). Control of shaft-line-embedded multiphase Starter/Generator for aero-engine. *IEEE Transactions on Industrial Electronics*, 63(1), 641-652.

127. Miljkovic, D. (2011). *Fault detection for aircraft piston engine by exhaust noise analysis.* 2011 Proceedings of the 34th International Convention MIPRO, Opatija, 756-761.

128. Bhangu, B. S. and Rajashekara, K. (2011). *Control strategy for electric starter generators embedded in gas turbine engine for aerospace applications.* 2011 IEEE Energy Conversion Congress and Exposition (ECCE), Arizona, 1461-1467.

129. Davis, R. I. and Lorenz, R. D. (2003). Engine torque ripple cancellation with an integrated starter alternator in a hybrid electric vehicle: Implementation and control. *IEEE Transactions on Industry Applications*, 39(6), 1765-1774.

130. Keiyinci, S. and Aydin, K. (2021). Conceptual design of fuel cell based hybrid unmanned air vehicle. *European Mechanical Science*, 5(1), 14-20.

131. Cheng, S. K., Pei, W. L., Chai, F., and Cui, S. M. (2003). *The torque pulsation analysis of a Starter Generator with concentrated windings based-hybrid electric vehicles.* IEEE International Electric Machines and Drives Conference, San Francisco, 218-221.

132. Zharkov, M. A. and Sidorov, V. E. (2019). *Electric starter system for launching a gas turbine aircraft engine.* 20th International Conference of Young Specialists on Micro/Nanotechnologies and Electron Devices (EDM 2019), Erlagol, 700-704.

133. Colton, J., Patterson, D., and Hudgins, J. L. (2008). *Design of a low-cost and efficient integrated Starter-Alternator.* 4th IET Conference on Power Electronics, Machines and Drive, York, 357-361.

134. Bogusz, P., Korkosz, M., Powrozek, A., Prokop, J., and Wygonik, P. (2015). *An analysis of properties of the bldc motor for unmanned aerial vehicle hybrid drive.* International Conference on Electrical Drives and Power Electronics (EDPE 2015), Slovakia, 458-464.

135. Cheng, M., Chau, K. T., and Chan, C. C. (2001). Design and analysis of a new doubly salient permanent magnet motor. *IEEE Transactions on Magnetics*, 37(4), 3012-3020.

136. Chau, K. T., Cheng, M., and Chan, C. C. (2002). Nonlinear magnetic circuit analysis for a novel stator doubly fed doubly salient machine. *IEEE Transactions on Magnetics*, 38(5), 2382-2384.

137. Mellor, P. H., Burrow, S. G., Sawata, T., and Holme, M. (2003). *A wide speed range permanent magnet generator for future embedded aircraft generation systems.* IEEE International Electric Machines and Drives Conference, Chicago, 1308-1313.

138. Mudannayake, C. P. and Rahman, M. F. (2004). *A study of the transient behavior of a 42 V prototype integrated Starter Alternator for sudden load changes.* 30th Annual Conference of IEEE Industrial Electronics Society (IECON 2004), Husan, 1694-1699.

139. Cai, D. W. (2004). *Comparison and review of electric machines for integrated Starter Alternator applications.* Conference Record of the 2004 IEEE Industry Applications Conference, Seattle, 386-393.

140. Abdelhafez, A. A. and Yousef, A. M. (2019). *Machine topology for integral starter-generator in more-electric aircraft.* Proceedings of 2019 International Conference on Innovative Trends in Computer Engineering (Itce 2019), Egypt, 526-533.

141. Arumugam, P., Dusek, J., Aigbomian, A., Vakil, G., Bozhko, S., Hamiti, T., Gerada, C., and Fernando, W. (2014). *Comparative design analysis of permanent magnet rotor topologies for an aircraft Starter-Generator.* IEEE International Conference on Intelligent Energy and Power Systems 2014 (IEPS), Kharkiv, 273-278.

142. El-Refaie, A. M. (2005). *High speed operation of permanent magnet machines*, Ph.D. Thesis, University of Wisconsin-Madsion Electrical and Computer Engineering, Wisconsin, 1-596.

143. Mudannayake, C. P. and Rahman, M. F. (2006). *Control design of an induction machine based integrated Starter Alternator for 42 V PowerNet.* Conference Record of the 2006 IEEE Industry Applications Conference, 41st IAS Annual Meeting, Illinois, 1585-1592.

144. Hasan, S. M. N., Husain, I., Veillette, and R. J., C., J. E. (2007). *A PM brushless DC Starter/Generator system for a series-parallel 2x2 hybrid electric vehicle.* Conference Record of the 2007 IEEE Industry Applications Conference 42th IAS Annual Meeting, New Orleans, 1686-1693.

145. Fang, Z. X., Wang, Y., Shen, J.-X., and Huang, Z. (2008). *Design and analysis of a novel flux-switching permanent magnet Integrated-Starter-Generator.* 4th IET Conference on Power Electronics, Machines and Drives, York, 106-110.

146. Leuchter, J., Bauer, P., Rerucha, V., and Hajek, V. (2009). Dynamic behavior modeling and verification of advanced Electrical-Generator set concept. *IEEE Transactions on Industrial Electronics,* 56(1), 266-279.

147. Muratoğlu, A. (2019). *Design, modeling and control of a hybrid UAV,* M.Sc. Thesis, Middle East Technical University Aerospace Engineering, Ankara, 1-151.

148. Legranger, J., Friedrich, G., Vivier, S., and Mipo, J. C. (2010). Combination of finite-element and analytical models in the optimal multidomain design of machines: Application to an interior permanent-magnet Starter Generator. *IEEE Transactions on Industry Applications,* 46(1), 232-239.

149. Jurkovic, S. and Strangas, E. G. (2011). Comparison of PMAC machines for Starter-Generator application in a series hybrid-electric bus. *International Journal of Vehicular Technology,* 2011, 1-11.

150. Niu, X.-w., Schofield, N., and Al-Adsani, A. S. (2012). *Comparison of 3- and 9-phase brushless PM drive systems for aerospace actuation.* 6th IET International Conference on Power Electronics, Machines and Drives (PEMD 2012), Bristol, 1-2.

151. Friedrich, G., Vivier, S., Khlissa, R., Benkara, K. E., and Assaad, B. (2013). *Determination of rotor-stator heat exchange coefficients in the case of totally enclosed machines: Application to an integrated Starter-Generator.* 2013 IEEE Energy Conversion Congress and Exposition (ECCE), Colorado, 1526-1533.

152. Zeaiter, A. (2020). *Thermal modeling and cooling of electric motors: Application to the propulsion of hybrid aircraft,* Ph.D. Thesis, ISAE-ENSMA Ecole Nationale Superieure Mecanique et d'Aerotechique Poitiers, Chasseneuil-du-Poitou, 1-240.

153. Rocca, A. l., Pickering, S. J., Eastwick, C. N., and Gerada, C. (2014). *Enhanced cooling for an electric Starter-Generator for aerospace application.* 7th IET International Conference on Power Electronics, Machines and Drives (PEMD 2014), Manchester, 1-7.

154. Alnajjar, M. and Gerling, D. (2015). *Model predictive control of six-phase variable frequency electrically excited Starter Generator for more electric aircraft.* IEEE 11th International Conference on Power Electronics and Drive Systems (PEDS 2015), Sydney, 23-28.

155. Salihu, S. M., Misron, N., Mariun, N., Othman, M. L., and Hanamoto, T. (2016). A novel double-stator permanent magnet generator ıntegrated with a magnetic gear. *Progress In Electromagnetics Research M,* 49, 69-80.

156. Hosad, D. M., M, C., R, B., and Ranjit, S. (2017). An integrated Starter-Generator and winding configuration for hybrid vehicles. *Ijireeice,* 5(2), 62-67.

157. Kong, Y., Lin, M., Guo, R., Li, N., and Xu, D. (2018). Design and optimization of an outer-rotor permanent magnet synchronous machine with an amorphous stator core. *IEEE Transactions on Applied Superconductivity,* 28(3), 1-5.

158. Nøland, J. K., Leandro, M., Suul, J. A., Molinas, M., and Nilssen, R. (2019). *Electrical machines and power electronics for Starter-Generators in more electric aircrafts: A technology review.* IECON 2019 - 45th Annual Conference of the IEEE Industrial Electronics Society, Lisbon, 6994-7001.

159. Wei, J., Xu, H., Zhou, B., Zhang, Z., and Gerada, C. (2019). An integrated method for three-phase AC excitation and high-frequency voltage signal injection for sensorless starting of aircraft Starter/Generator. *IEEE Transactions on Industrial Electronics,* 66(7), 5611-5622.

160. Ismagilov, F. R., Finkelberg, L. A., Vavilov, V. E., Yamalov, I. I., Farrakhov, D. R., Kostyuchenkov, A. N., Sayakhov, I. F., Baryshnikov, S. I., Pronin, E. A., and Gulin, A. (2021). *Creation of an integrated Starter-Generator for the aircraft piston engine-demonstrator APD-500.* 2021 International Conference on Electrotechnical Complexes and Systems (ICOECS), Ufa, 584-591.

161. Wang, R., Liu, W. G., Meng, T., Jiao, N. F., Han, X., Sun, C. H., and Yang, Y. (2022). Rotor position estimation method of brushless electrically excited synchronous Starter/Generator based on multistage structure. *IEEE Transactions on Power Electronics,* 37(1), 364-376.

162. Bajec, P., Voncina, D., Miljavec, D., and Nastran, J. (2004). *Bi-directional power converter for wide speed range integrated starter-generator.* 2004 IEEE International Symposium on Industrial Electronics, Ajaccio, 1117-1122.

163. Bozhko, S., Yang, T., Le Peuvedic, J.-M., Arumugam, P., Degano, M., La Rocca, A., Xu, Z., Rashed, M., Fernando, W., Hill, C. I., Eastwick, C., Pickering, S., Gerada, C., and Wheeler, P. (2018). Development of aircraft electric Starter–Generator system based on active rectification technology. *IEEE Transactions on Transportation Electrification,* 4(4), 985-996.

164. Calzo, G. L., Zanchetta, P., Gerada, C., Gaeta, A., and Crescimbini, F. (2015). *Converter topologies comparison for more electric aircrafts high speed Starter/Generator application.* 2015 IEEE Energy Conversion Congress and Exposition (ECCE), Quebec, 3659-3666.

165. Calzo, G. L., Zanchetta, P., Gerada, C., Lidozzi, A., Degano, M., Crescimbini, F., and Solero, L. (2014). *Performance evaluation of converter topologies for high speed Starter/Generator in aircraft applications.* IECON 2014 - 40th Annual Conference of the IEEE Industrial Electronics Society, Dallas, 1707-1712.

166. Dai, W., Xiu, T., Wang, H., and Yan, Y. (2006). *Control of a novel dual stator doubly salient aircraft engine Starter-Generator.* 37th IEEE Power Electronics Specialists Conference, Korea, 1-5.

167. NTRS - NASA Technical Reports Server. (2017). Overview of NASA electrified aircraft propulsion research for large subsonic transports. *NASA,* Washington D.C., 1-20.

168. Civil Aviation Safety Authority (2014). *Airworthiness Approval of Avionics Equipment,* Appendix 1: Existing Avionics Standards, 1-7.

169. Ramirez, D. C. and Suarez Sanchez, M. A. (2016). *Hybrid Power System for Piston Engine Aircrafts*. ES Patent No.: ES2500015A1.

170. Turan, A. (2017). *Yakıt motorlu dronlarda elektrik motorları ile denge kontrolü*. TR Patent No.: TR201708206A2.

171. Beddok, S. and Bazet, J.-M. (2017). *Transmission Assembly for an Aircraft and a Helicopter*. FR Patent No.: US20170175856A1.

172. Klemen, D., Wilson, E., and Ross, C. A. (2015). *Dual Redundant Motor/ Generator for an Engine*. US Patent No.: US20150180309A1.

173. Chantriaux, E. and Chretien, P. (2014). *Aircraft comprising a distributed electric power unit with free wheels*. FR, AU Patent No.: US20140203739A1.

174. Moulon, F., Mercier-Calvairac, and Ma.Ux, D. L. (2017). *Hybrid propulsion system for a multi-engine aircraft*. FR Patent No.: US20170247114A1.

175. Roggemans, E. and Logeais, J.-F. (2014). *Hybrid power supply architecture for supplying mechanical power to a rotor and managed from the on-board network of a rotorcraft*. FR Patent No.: US20140013751A1.

176. Eric, M. and Bruno, E. (2013). *Combined power unit for E.G. Car, has electric machine mechanically connected to output shaft of unit and electrically connected to electrical energy management pack for charging electric machine or supplying charge by electric machine*. FR Patent No.: FR2986566A1.

177. Xu, M., Anghel, C., and Scherzinger, W. (2011). *Single stage starter/generator with rotor quadrature ac excitation*. US Patent No.: US007915869B2.

178. Taneja, D. N., Huang, H., Kettering, P., Centerville, Z., Springboro, W., and Abbas, A. M. (2010). *Dual-structured aircraft engine starter/generator*. US Patent No.: US007687928B2.

179. Ullrich Masberg, R., Thomas Pels, O., Klaus-Peter, Z. C., Andreas Grindl, M., and Bernhard Hoffmann, S. (2001). *Starter/generator for an internal combustion engine, especially an engine of a motor vehicle*. DE Patent No.: US006177734B1.

180. Wergifosse, E. D. (2012). *Turbine engine starter/generator, and method for the control thereof*. FR Patent No.: US20120211981A1.

181. Stout, E. D., Duddeck, W. M., Pearson, W. T., and Xu, M. (2006). *Dual-rotor, single input/output starter-generator*. US Patent No.: US20060087123A1.

182. Davis, J. A., Davis, I. C., and Hurzook, F. A. (2012). *Multistage variable reluctance motor/generator*. CA Patent No.: US20120212094A1.

183. Ahner, P., Schustek, B., Ackermann, D., Eisenhardt, O., and Schenk, S. R. (1997). *Starter for an internal combustion engine*. DE Patent No.: US006098584A.

184. Glennon, T. F. and Rockford, I. (1997). *PMG main engine starter/generator*. US Patent No.: US005929537A.

185. Harmon, F. G., Hiserote, R. M., Rippl, M. D., and Ausserer, J. K. (2012). *Parallel hybrid-electric propulsion systems for unmanned aircraft*. US Patent No.: US20120209456A1.

186. Cirigliano, D., Frisch, A. M., Liu, F., and Sirignano, W. A. (2018). Diesel, spark-ignition, and turboprop engines for long-duration unmanned air flights. *Journal of Propulsion and Power*, 34(4), 878-892.

187. Çoban, S. and Oktay, T. (2018). Unmanned aerial vehicles (UAVs) according to engine type. *Journal of Aviation*, 2, 1-8.

188. Zhang, B., Song, Z., Zhao, F., and Liu, C. (2022). Overview of propulsion systems for unmanned aerial vehicles. *Energies*, 15(2), 1-25.

189. Saeed, A. S., Younes, A. B., Cai, C., and Cai, G. (2018). A survey of hybrid unmanned aerial vehicles. *Progress in Aerospace Sciences*, 98, 91-105.

190. Capata, R., Marino, L., and Sciubba, E. (2014). A hybrid propulsion system for a high-endurance UAV: Configuration selection, aerodynamic study, and gas turbine bench tests. *Journal of Unmanned Vehicle Systems*, 2(1), 16-35.

191. Mohsan, S. A. H., Othman, N. Q. H., Li, Y. L., Alsharif, M. H., and Khan, M. A. (2023). Unmanned aerial vehicles (UAVs): Practical aspects, applications, open challenges, security issues, and future trends. *Intelligent Service Robotics*, 16(1), 109-137.

192. Saeed, A. S., Younes, A. B., Islam, S., Dias, J., Seneviratne, L., and Cai, G. W. (2015). *A review on the platform design, dynamic modeling and control of hybrid UAVs.* 2015 International Conference on Unmanned Aircraft Systems (ICUAS'15), Denver, 806-815.

193. Zhang, H., Song, B. F., Wang, H. F., and Xuan, J. L. (2019). A method for evaluating the wind disturbance rejection capability of a hybrid UAV in the quadrotor mode. *International Journal of Micro Air Vehicles*, 11, 1-19.

194. Linda Werfelman. (2018). Tracking engine troubles. *FSF*, Virginia, 2-4.

195. Grachev, P. Y., Strizhakova, E. V., and Tabachinskiy, A. S. (2017). *Starter-Generator design and analysis of Start/Stop processes for HEVs.* 2017 International Conference on Industrial Engineering, Applications and Manufacturing (Icieam), Chelyabinsk, 1-4.

196. Ismagilov, F. R., Vavilov, V. E., and Gusakov, D. V. (2018). *High-speed Starter-Generator for aerospace applications: Design and initial testing.* XIII International Conference on Electrical Machines (ICEM 2018), Alexandroupoli, 2593-2599.

197. Schmidhofer, A., Pisek, P., Bouvier, S., Gerbis, R., Kohlhauser, M., and Weidenholzer, G. (2013). *Design aspects of low cost electric machines used for highly integrated Starter-Generator systems.* 2013 World Electric Vehicle Symposium and Exhibition (EVS27), Barcelona, 1-7.

198. Huang, J., Shan, F., Xiong, R., Shao, Y., and Luo, J. (2021). *Energy-efficient UAV flight planning for a general poi-visiting problem with a practical energy model.* 2021 International Conference on Computer Communications and Networks (ICCCN), Manchester, 1-10.

199. Jarrah, K., Alali, Y., Lalko, A., and Rawashdeh, O. (2022). Flight time optimization and modeling of a hybrid gasoline–electric multirotor drone: An experimental study. *Aerospace*, 9(12), 1-24.

200. Fügenschuh, A., Müllenstedt, D., and Schmidt, J. (2021). Flight Planning for Unmanned Aerial Vehicles. *Military Operations Research*, 26(3), 49-71.

201. Arslan, S., Iskender, I., and Navruz, T. S. (2023). Finite element method-based optimisation of magnetic coupler design for safe operation of hybrid UAVs. *Aerospace*, 10(2), 1-22.

202. Yonnet, J. P., Hemmerlin, S., Rulliere, E., and Lemarquand, G. (1993). Analytical Calculation of Permanent-Magnet Couplings. *IEEE Transactions on Magnetics*, 29(6), 2932-2934.

203. Ravaud, R., Lemarquand, G., Lemarquand, V., and Depollier, C. (2009). Permanent magnet couplings: Field and torque three-dimensional expressions based on the coulombian model. *IEEE Transactions on Magnetics*, 45(4), 1950-1958.

204. Choi, J.-Y., Shin, H.-J., Jang, S.-M., and Lee, S.-H. (2013). Torque analysis and measurements of cylindrical air-gap synchronous permanent magnet couplings based on analytical magnetic field calculations. *IEEE Transactions on Magnetics*, 49(7), 3921-3924.

205. Carpentier, A., Galopin, N., Chadebec, O., Meunier, G., and Guerin, C. (2014). Application of the virtual work principle to compute magnetic forces with a volume integral method. *International Journal of Numerical Modelling: Electronic Networks, Devices and Fields*, 27(3), 418-432.

206. Li, K., Bird, J. Z., and Acharya, V. M. (2017). Ideal radial permanent magnet coupling torque density analysis. *IEEE Transactions on Magnetics*, 53(6), 1-4.

207. Hogberg, S., Mijatovic, N., Holboll, J., Jensen, B. B., and Bendixen, F. B. (2014). *Parametric design optimization of a novel permanent magnet coupling using finite element analysis.* IEEE Energy Conversion Congress and Exposition 2014 (ECCE), Pittsburgh, 1465-1471.

208. Akcay, Y., Giangrande, P., Tweedy, O., and Galea, M. (2021). Fast and accurate 2D analytical subdomain method for coaxial magnetic coupling analysis. *Energies*, 14(15), 1-18.

209. Lubin, T., Mezani, S., and Rezzoug, A. (2014). Experimental and theoretical analyses of axial magnetic coupling under steady-state and transient operations. *IEEE Transactions on Industrial Electronics*, 61(8), 4356-4365.

210. Canova, A., Freschi, F., Gruosso, G., and Vusini, B. (2005). Genetic optimisation of radial eddy current couplings. *COMPEL - The International Journal for Computation and Mathematics in Electrical and Electronic Engineering,* 24(3), 767-783.

211. Lubin, T., Vahaj, A. A., and Rahideh, A. (2020). Design optimisation of an axial-flux reluctance magnetic coupling based on a two-dimensional semi-analytical model. *IET Electric Power Applications,* 14(5), 901-910.

212. Wu, W., Lovatt, H. C., and Dunlop, J. B. (1997). Analysis and design optimisation of magnetic couplings using 3D finite element modelling. *IEEE Transactions on Magnetics,* 33, 4083-4094.

213. Ose, B. and Pugachov, V. (2011). The influence of pole pair number and magnets' width on mechanical torque of magnetic coupler with rounded permanent magnets. *Scientific Journal of Riga Technical University,* 29, 1-4.

214. Sun, K., Shi, J., Cui, W., and Meng, G. (2021). Theoretical computational model for cylindrical permanent magnet coupling. *Electronics,* 10(16), 1-20.

215. Zhuo, M., Zina, Z., and Yize, S. (2015). 3-D analysis for the torque of permanent magnet coupler. *IEEE Transactions on Magnetics,* 51(4), 1-8.

216. Ziolkowski, M. and Brauer, H. (2010). Fast computation technique of forces acting on moving permanent magnet. *IEEE Transactions on Magnetics,* 46(8), 2927-2930.

217. Ose-Zala, B., Onzevs, O., and Pugachov, V. (2013). Formula synthesis of maximal mechanical torque on volume for cylindrical magnetic coupler. *Electrical, Control and Communication Engineering,* 3(1), 37-43.

218. Chen, Y., Fu, W. N., Ho, S. L., and Liu, H. (2014). A quantitative comparison analysis of radial-flux, transverse-flux, and axial-flux magnetic gears. *IEEE Transactions on Magnetics,* 50(11), 1-4.

219. Dolisy, B., Mezani, S., Lubin, T., and Leveque, J. (2015). A new analytical torque formula for axial field permanent magnets coupling. *IEEE Transactions on Energy Conversion,* 30(3), 892-899.

220. Atallah, K., Calverley, S. D., and Howe, D. (2004). Design, analysis and realisation of a high-performance magnetic gear. *IEE Proceedings - Electric Power Applications,* 151(2), 135-143.

221. Benarous, M. and Trezieres, M. (2019). Design of a cost-effective magnetic gearbox for an aerospace application. *The Journal of Engineering,* 2019(17), 4081-4084.

222. Ho, S. L., Niu, S., and Fu, W. N. (2010). Transient analysis of a magnetic gear integrated brushless permanent magnet machine using circuit-field-motion coupled time-stepping finite element method. *IEEE Transactions on Magnetics,* 46(6), 2074-2077.

223. Wang, S., Guo, Y. C., Wang, P. Y., and Li, D. Y. (2017). Study on torque calculation for hybrid magnetic coupling and influencing factor analysis. *3D Research,* 8(1), 1-12.

224. Li, Y., Hu, Y., Song, B., Mao, Z., and Tian, W. (2019). Performance analysis of conical permanent magnet couplings for underwater propulsion. *Journal of Marine Science and Engineering*, 7(6), 1-17.

225. Ose-Zala, B., Jakobsons, E., and Suskis, P. (2012). The use of magnetic coupler instead of lever actuated friction clutch for wind plant. *Electronics and Electrical Engineering*, 18(10), 13-16.

226. Niemenmaa, A., Salmia, L., Arkkio, A., and Saari, J. (2010). Modeling motion, stiffness, and damping of a permanent-magnet shaft coupling. *IEEE Transactions on Magnetics*, 46(8), 2763-2766.

227. Mei, Y. and Luo, J. (2022). Influence of eccentric arc design at the rotor on the electromagnetic performance of a permanent-magnet synchronous motor. *Iranian Journal of Science and Technology, Transactions of Electrical Engineering*, 47(1), 23-33.

228. Fontchastagner, J., Lefevre, Y., and Messine, F. (2009). Some co-axial magnetic couplings designed using an analytical model and an exact global optimization code. *IEEE Transactions on Magnetics*, 45(3), 1458-1461.

229. Kim, S. H., Shin, J. W., and Ishiyama, K. (2014). Magnetic bearings and synchronous magnetic axial coupling for the enhancement of the driving performance of magnetic wireless pumps. *IEEE Transactions on Magnetics*, 50(1), 1-4.

230. Tallerico, T. F., Scheidler, J. J., and Cameron, Z. A. (2019). *Electromagnetic mass and efficiency of magnetic gears for electrified aircraft.* AIAA/IEEE Electric Aircraft Technologies Symposium (EATS 2019), Indianapolis, 1-25.

231. Tallerico, T., Cameron, Z. A., and Scheidler, J. J. (2019). *Design of a magnetic gear for Nasa's vertical lift quadrotor concept vehicle.* AIAA/IEEE Electric Aircraft Technologies Symposium (EATS 2019), Indianapolis, 1-21.

232. Gregor Puchhammer. (2014). Magnetic gearing versus conventional gearing in actuators for aerospace applications. *NASA*, Washington D.C., 3-6.

233. Charpentier, J. F., Fadli, N., and Jennane, J. (2003). Study of ironless permanent magnet devices being both a coupling and an axial bearing for naval propulsion. *IEEE Transactions on Magnetics*, 39(5), 3235-3237.

234. Moosavian, A., Najafi, G., Ghobadian, B., and Mirsalim, M. (2017). The effect of piston scratching fault on the vibration behavior of an IC engine. *Applied Acoustics*, 126, 91-100.

235. Arslan, S. (2020). *Akıllı modüler hibrit tahrik sistemi ve bunun yönetim yöntemi*. TR Patent No. 2020/22757. Turkish Patent and Trademark Office.

236. Ganev, E. (2014). Selecting the best electric machines for electrical power-generation systems: High-performance solutions for aerospace more electric architectures. *IEEE Electrification Magazine, 2,* 13-22.

237. van der Geest, M., Polinder, H., Ferreira, J. A., and Zeilstra, D. (2013). Machine selection and initial design of an aerospace Starter/Generator. *2013 International Electric Machines & Drives Conference*, 196-203.

238. Arsalan, H. and Iman, S. (2021). A comprehensive review on high speed permanent magnet motors and their modern applications. *Electromechanical Energy Conversion Systems (EECS)*, 1(2), 1-7.

239. Song, Z. X., Liu, C. H., and Zhao, H. (2019). *Comparative analysis of slotless and coreless permanent magnet synchronous machines for electric aircraft propulsion.* 2019 22nd International Conference on Electrical Machines and Systems (ICEMS 2019), Harbin, 5554-5559.

240. Mekri, F., Ben Elghali, S., and Benbouzid, M. E. (2013). Fault-tolerant control performance comparison of three and five-phase PMSG for marine current turbine applications. *Ieee Transactions on Sustainable Energy*, 4(2), 425-433.

241. Nounou, K., Benbouzid, M., Marouani, K., Charpentier, J. F., and Kheloui, A. (2018). Performance comparison of open-circuit fault-tolerant control strategies for multiphase permanent magnet machines for naval applications. *Electrical Engineering*, 100(3), 1827-1836.

242. Laksar, J., Cermak, R., and Hruska, K. (2021). Challenges in the electromagnetic design of multiphase machines: Winding and equivalent circuit parameters. *Energies*, 14(21), 1-19.

243. Yaskawa Electric America. (2009). General purpose permanent magnet motor drive without speed and position sensor. *YASKAWA*, Waukegan, 2-4.

244. Borisavljevic, A. (2012). *Limits, Modeling and Design of High-Speed Permanent Magnet Machines*, Ph.D. Thesis, Technische Universiteit Delft, Delft, 1-238.

245. Arslan, S. (2014). *Design and analysis of high speed permanent magnet generator*, M.Sc. Thesis, Gazi University Electrical and Electronics Engineering, Ankara, 1-173.

246. Dannier, A. (2018). Chapter: Overview of Main Electric Subsystems of Zero-Emission Vehicles. In Alessandro Serpi. *Propulsion Systems*. IntechOpen.

247. Dwivedi, S. K., Laursen, M., and Hansen, S. (2010). *Voltage vector based control for PMSM in industry applications.* IEEE International Symposium on Industrial Electronics (ISIE 2010), Bari, 3845-3850.

248. Shao, L. Y., Navaratne, R., Popescu, M., and Liu, G. P. (2021). Design and construction of axial-flux permanent magnet motors for electric propulsion applications-a review. *IEEE Access*, 9, 158998-159017.

249. Sakunthala, S., Kiranmayi, R., and Mandadi, P. N. (2017). *A study on industrial motor drives: Comparison and applications of PMSM and BLDC motor drives.* 2017 International Conference on Energy, Communication, Data Analytics and Soft Computing (ICECDS), Chennai, 537-540.

250. Dorrell, D. G., Hsieh, M.-F., Popescu, M., Evans, L., Staton, D. A., and Grout, V. (2011). A review of the design issues and techniques for radial-flux brushless surface and internal rare-earth permanent-magnet motors. *IEEE Transactions on Industrial Electronics,* 58(9), 3741-3757.

251. Ocak, C., Uygun, D., Cetinceviz, Y., Demir, E., and Gungor, Y. (2012). *Performance aspects and verifications of in-runner and out-runner permanent magnet synchronous generator designs of the same magnet structure for low speed wind systems.* 2012 11th International Conference on Environment and Electrical Engineering, Venice, 440-445.

252. Bayraktar, H. C. and Balik, H. H. (2015). The control of brushless DC motors. *International Journal of Electronics, Mechanical and Mechatronics Engineering,* 5, 919-932.

253. Yılmaz, K. (2009). *Comparison of axial flux and radial flux brushless DC motor topologies for control moment gyroscope wheel applications,* M.Sc. Thesis, Middle East Technical University Electrical and Electronics Engineering, Ankara, 1-213.

254. Slutskiy, D., Aung, S. H., and Basnet, S. (2022). *Comparison of axial and radial flux permanent magnet machines.* 2022 North American Power Symposium (NAPS), Salt Lake City, 1-6.

255. Hao, Z., Ma, Y. Y., Wang, P. Y., Luo, G., and Chen, Y. S. (2022). A review of axial-flux permanent-magnet motors: Topological structures, design, optimization and control techniques. *Machines,* 10(12), 1-20.

256. Cosovic, M. and Smaka, S. (2015). *Design of initial topology of interior permanent magnet synchronous machine for hybrid electric vehicle.* IEEE International Electric Machines & Drives Conference (IEMDC 2015), Idaho, 1658-1664.

257. Zheng, J. Q., Zhao, W. X., Ji, J. H., and Liu, G. H. (2015). *Design and comparison of interior permanent-magnet machines for hybrid electric vehicles.* 2015 IEEE International Conference on Applied Superconductivity and Electromagnetic Devices (ASEMD), Shanghai, 234-235.

258. Sadeghi, S., Isfahani, A. H., Mirsalim, M., and Asaei, B. (2008). *Optimal design of permanent magnet synchronous machines for hybrid electric vehicles.* Proceedings of the 11th International Conference on Optimization of Electrical and Electronic Equipment, Brasov, 1-81.

259. Özçıra, S. (2007). *Sabit mıknatıslı senkron motorun kontrol yöntemleri ve endüstriyel uygulamaları*, M.Sc. Thesis, Yıldız Teknik Üniversitesi Fen Bilimleri Enstitüsü, İstanbul, 1-102.

260. Du, G. H., Li, N. M., Zhou, Q. X., Gao, W. T., Wang, L., and Pu, T. (2022). Multi-physics comparison of surface-mounted and interior permanent magnet synchronous motor for high-speed applications. *Machines,* 10(8), 1-20.

261. Abroshan, A., Hasanzadeh, S., and Fard, J. R. (2022). Multi-objective optimization of a V-type line-start PM motor based on parameter stratification and RSM. *Electrical Engineering,* 1-10.

262. Eker, M., Zoehra, B., and Akar, M. (2023). Experimental performance verification of radial and axial flux line start permanent magnet synchronous motors. *Electrical Engineering*, 1-10.

263. Karami, M., Mariun, N., Mehrjou, M. R., Ab Kadir, M. Z. A., Misron, N., and Radzi, M. A. M. (2014). Static eccentricity fault recognition in three-phase line start permanent magnet synchronous motor using finite element method. *Mathematical Problems in Engineering*, 2014, 1-13.

264. Jr., N. C. V. (2019). *Transferring power through a magnetic couple*, Bachelor Thesis, Linfield University Applied Physics, Oregon, 1-61.

265. Arslan, S., Iskender, I., and Navruz, T. S. (2023). FEM-based optimal design and testing of synchronous magnetic coupling for aerospace Starter/Generator applications. *Engineering Science and Technology, an International Journal*, 41, 1-14.

266. Ose-Zala, B. (2015). *Design optimization of cylindrical magnetic coupler based on calculations of magnetic field*, Ph.D. Thesis, Riga Technical University Power and Electrical Engineering, Riga, 1-139.

267. Li, X., Chau, K. T., Cheng, M., and Hua, W. (2013). Comparison of magnetic-geared permanent-magnet machines. *Progress in Electromagnetics Research-pier*, 133, 177-198.

268. Niu, S. and Mao, Y. (2016). A comparative study of novel topologies of magnetic gears. *Energies*, 9(10), 1-10.

269. Ravaud, R. and Lemarquand, G. (2009). Magnetic couplings with cylindrical and plane air gaps: Influence of the magnet polarization direction. *Progress in Electromagnetics Research B*, 16, 333-349.

270. Kang, H., Choi, J., Cho, H., and Kim, J. (2014). Comparative study of torque analysis for synchronous permanent magnet coupling with parallel and halbach magnetized magnets based on analytical field calculations. *IEEE Transactions on Magnetics*, 50(11), 1-4.

271. Topet, G. and Dehez, B. (2019). *Structural strength evaluation and comparison of laminated ferromagnetic pole structures in magnetic gears, using 3D-FEM*, M.Sc. Thesis, Universite Catholique de Louvain Ecole Polytechnique de Louvain, Louvain-la-Neuve, 1-92.

272. Filippini, M. (2019). *Magnetic gears numerical modelling and optimization*, Ph.D. Thesis, Universit`a degli Studi di Padova Department of Industrial Engineering, Padova, 1-171.

273. Gerber, S. (2015). *Evaluation and design aspects of magnetic gears and magnetically geared electrical machines*, Ph.D. Thesis, Stellenbosch University Department of Electrical and Electronic Engineering, Stellenbosch, 1-196.

274. Cooke, G. (2018). *Magnetically geared electrical machines*, Ph.D. Thesis, The University of Sheffield Department of Electrical and Electronic Engineering, Sheffield, 1-243.

275. Frandsen, T. V. (2016). *Motor integrated permanent magnet gear*, Ph.D. Thesis, Aalborg Universitet Det Teknisk-Naturvidenskabelige Fakultet, Aalborg, 1-260.

276. Mukerji, S. K., Khan, A. H., and Singh, Y. (2015). *Electromagnetics for Electrical Machines*. Taylor & Francis Group, 1-433.

277. Kurt, Ü. (2006). *Eksenel akılı sürekli mıknatıslı senkron makinalar için yeni tasarım modeli geliştirme*, Ph.D. Thesis, Ondokuz Mayıs Üniversitesi Elektrik-Elektronik Mühendisliği, İzmir, 1-115.

278. Gieras, J. F. (2008). *Advancements in electric machines*. New York: Springer, 1-283.

279. Ocak, C. (2009). *Mikro-hidroelektrik ve rüzgar santralleri için düşük devirli eksenel akılı kalıcı mıknatıslı generatör tasarımı ve analizi*, M.Sc. Thesis, Gazi Üniversitesi Fen Bilimleri Enstitüsü, Ankara, 1-125.

280. Gürdal, O. (2015). *Elektrik makinalarının tasarımı*. Ankara: Nobel Akademik Yayıncılık, 1-535.

281. Krause, P. C., Wasynczuk, O., Sudhoff, S. D., and Pekarek, S. D. (2013). *Analysis of electric machinery and drive systems*. New York: John Wiley & Sons, 1-676.

282. Chapman, S. J. (2001). *Electric machinery and power system fundamentals*. New York: Mc Graw Hill, 1-713.

283. Petryshynets, I., Kovac, F., Petrov, B., Falat, L., and Puchy, V. (2019). Improving the magnetic properties of non-oriented electrical steels by secondary recrystallization using dynamic heating conditions. *Materials (Basel)*, 12(12), 1-15.

284. Zepf, V. (2013). *Rare earth elements: a new approach to the nexus of supply, demand and use: exemplified along the use of neodymium in permanent magnets*. New York: Springer, 1-161.

285. Gieras, J. F. and Shen, J. (2023). *Modern permanent magnet electric machines. theory and control*. New York: CRC Press, 1-307.

286. Material, M. A. M. (2007). *Permanent magnet selection and design handbook*. New York: National Imports LLC, 1-15.

287. Krishnan, K. M. (2016). *Fundamentals and applications of magnetic materials*. New York: Oxford University Press, 1-275.

288. Croat, J. J. and Ormerod, J. (2022). *Modern permanent magnets*. New York: Woodhead Publishing, 1-439.

289. Jiles, D. (2016). *Introduction to magnetism and magnetic materials*. New York: CRC Press, 1-255.

290. Roy, S. B. (2022). *Experimental techniques in magnetism and magnetic materials*. New York: Cambridge University Press, 1-360.

291. Chen, W. and Jiaying, J. (2022). *Frontiers in magnetic materials: from principles to material design and practical applications.* New York: CRC Press, 1-290.

292. Sintex Magnetic Technologies. (2020). IP magnet. *SINTEX*, Gujarat, 1-2.

293. Eisenhüttenleute, V. D. (1993). *Steel - a handbook for materials research and engineering*. New York: Springer, 1-737.

294. Jamali Fard, A. and Mirsalim, M. (2022). An adaptive method for calculation of iron losses in switched reluctance motors using a minimum number of magnetostatic finite element simulations. *COMPEL - The international Journal For Computation And Mathematics In Electrical And Electronic Engineering*, 41(5), 1566-1583.

295. Min, K., Kang, H., Park, M., Cho, H., and Choi, J. (2014). Eddy current loss analysis in radial flux type synchronous permanent magnet coupling using space harmonic methods. *The Transactions of The Korean Institute of Electrical Engineers*, 63(10), 1377-1383.

296. Kanazawa, S., Takahashi, N., and Kubo, T. (2006). Measurement and analysis of AC loss of NdFeB sintered magnet. *Electrical Engineering in Japan*, 154(4), 8-15.

297. Lovatt, H. C. and Walterson, P. A. (1999). Energy stored in permanent magnets. *IEEE Transactions on Magnetics*, 35(1), 505-507.

298. Magnetic Material Producers Association. (2017). Magnet guide and tutorial. *ALLIANCE LLC*, Chicago, 5-25.

299. Campbell, P. (2000). Comments on "Energy stored in permanent magnets". *IEEE Transactions on Magnetics*, 36(1), 401-403.

300. Zhang, Y., Leng, Y., Zhang, H., Su, X., Sun, S., Chen, X., and Xu, J. (2020). Comparative study on equivalent models calculating magnetic force between permanent magnets. *Journal of Intelligent Manufacturing and Special Equipment*, 1(1), 43-65.

301. Elies, P. and Lemarquand, G. (1998). Analytical optimization of the torque of a permanent-magnet coaxial synchronous coupling. *IEEE Transactions on Magnetics*, 34(4), 2267-2273.

302. Charpentier, J. F. and Lemarquand, G. (2001). Calculation of ironless permanent magnet couplings using semi-numerical magnetic pole theory method. *COMPEL - The International Journal for Computation and Mathematics in Electrical and Electronic Engineering*, 20(1), 72-89.

303. Akoun, G. and Yonnet, J.-P. (1984). 3D analytical calculation of the forces exerted between two cuboidal magnets. *IEEE Transactions on Magnetics*, 20, 1962-1964.

304. Ose-Zaļā, B. and Pugachov, V. (2012). The comparison of active and reactive magnetic couplers. *2012 Electric Power Quality and Supply Reliability*, 1-4.

305. Elia, S., Pasquali, M., Remigi, G., Sabene, M. V., and Santini, E. (2001). A modified Maxwell Stress Tensor method for the evaluation of electromagnetic torque. *WIT transactions on engineering sciences,* 31, 1-10.

306. Ravaud, R., Lemarquand, G., Lemarquand, V., and Depollier, C. (2009). Torque in permanent magnet couplings: Comparison of uniform and radial magnetization. *Journal of Applied Physics,* 105(5), 1-16.

307. Santra, T., Roy, D., and Yamada, S. (2016). Calculation of force between two ring magnets using adaptive Monte Carlo technique with experimental verification. *Progress In Electromagnetics Research M,* 49, 181-193.

308. Al-Timimy, A., Giangrande, P., Degano, M., Galea, M., and Gerada, C. (2017). *Comparative study of permanent magnet-synchronous and permanent magnet-flux switching machines for high torque to inertia applications.* 2017 IEEE Workshop on Electrical Machines Design, Control and Diagnosis (WEMDCD), Nottingham, 45-51.

309. Nagrial, M., Rizk, J., and Hellany, A. (2011). Design of synchronous torque couplers. *World Academy of Science, Engineering and Technology, International Journal of Mechanical, Aerospace, Industrial, Mechatronic and Manufacturing Engineering,* 5, 1319-1324.

310. Frank, N. W. (2011). *Analysis of the concentric planetary magnetic gear*, Ph.D. Thesis, Texas A&M University Electrical Engineering, College Station, 1-145.

311. Li, K. (2018). *An investigation into the torque capabilities of high gear ratio magnetic gearboxes*, Ph.D. Thesis, The University of North Carolina at Charlotte Electrical Engineering, North Carolina, 1-336.

312. Montague, R. G. (2011). *Control of drive trains incorporating magnetic gears*, Ph.D. Thesis, The University of Sheffield Department of Electronic and Electrical Engineering, Sheffield, 1-172.

313. Painter, D. (2016). *A comparative study of the performance capabilities of magnetic gears,* Bachelor Thesis, Portland State University Physics, Portland, 1-307.

314. Penzkofer, A. (2016). *Analytical modelling and analysis of magnetic gears and pseudo direct drives for large wind turbines*, Ph.D. Thesis, The University of Sheffield Department of Electronic and Electrical Engineering, Sheffield, 1-192.

315. Othman, N. (2012). *Design and evaluation of high power density brushless DC permanent magnet machines*, Ph.D. Thesis, University of Nottingham Department of Electrical and Electronic Engineering, Nottingham, 1-177.

316. Gieras, F. (2013). *Permanent Magnet Motor Technology: Design And Applications, Third Edition*. New York: CRC Press, 1-603.

317. Mansouri, M., Kaboli, S. H. A., J., A., and J., S. (2012). *A hybrid Neuro-Fuzzy — P.I. speed controller for B.L.D.C. enriched with an integral steady state error eliminator.* 2012 IEEE International Conference on Control System, Computing and Engineering, Beijing, 234-237.

318. Geest, M. (2015). *Design and modeling of high performance permanent magnet synchronous machines*. New York: Gildeprint, 1-236.

319. Filizadeh, S. (2013). *Electric Machines and Drives: Principles, Control, Modeling, and Simulation*. New York: CRC Press, 1-233.

320. Gieras, J. F. (2016). *Electrical Machines: Fundamentals of Electromechanical Energy Conversion*. New York: CRC Press, 1-451.

321. Wang, G., Xu, D., and Zhang, G. (2019). *Position sensorless control techniques for permanent magnet synchronous machine drives*. New York: Springer, 1-305.

322. Vaez-Zadeh, S. (2018). *Control of permanent magnet synchronous motors*. New York: Oxford, 1-358.

323. Masmoudi, A. (2018). *Control oriented modelling of ac electric machines*. New York: Springer, 1-87.

324. Kim, S.-H. (2017). *Electric Motor control DC, AC, and BLDC motors*. Amsterdam: Elsevier, 1-428.

325. Doncker, R. W. D., Pulle, D. W. J., and Veltman, A. (2010). *Advanced electrical drives: analysis, modeling, control*. New York: Springer, 1-475.

326. Krishnan, R. (2001). *Electric Motor drives: modeling, analysis, and control*. New York: Prentice Hall, 1-652.

327. Mohan, N. (2001). *Advanced electric drives: analysis, control and modeling using simulink*. New York: Wiley, 1-199.

328. Petruzella, F. D. (2009). *Electric motors and control systems*. New York: Mc Graw Hill, 1-298.

329. Pyrhöonen, J., Hrabovcová, V., and Semken, S. (2016). *Electrical machine drives control: an introduction*. New York: Wiley, 1-527.

330. Dursun, M. (2015). The analysis of different techniques for speed control of permanent magnet synchronous motor. *Tehnicki Vjesnik-Technical Gazette*, 22(4), 947-952.

331. Sain, C., Banerjee, A., and Biswas, P. K. (2022). *Control Strategies of Permanent Magnet Synchronous Motor Drive for Electric Vehicles*. New York: CRC Press, 1-179.

332. Zhu, Z., Wang, S., Shao, B., Yan, L., Xu, P., and Ren, Y. (2021). Advances in dual-three-phase permanent magnet synchronous machines and control techniques. *Energies*, 14(22), 1-46.

333. Bulgan, D. (2014). *A software for analysis of permanent magnet AC motors*, M.Sc. Thesis, Middle East Technical University Electrical and Electronics Engineering, Ankara, 1-175.

334. Hendershot, J. and Miller, T. J. E. (2010). *Design of brushless permanent-magnet machines*. New York: Motor Design Books LLC, 1-824.

335. Murthy, K. V. (2008). *Computer-aided design of electrical machines*. New York: BS Publications Hyderabad, 1-335.

336. Pyrhonen, J., Jokinen, T., and Hrabovcova, V. (2009). *Design of rotating electrical machines*. New York: Wiley, 1-614.

337. Lee, T., Kim, Y., and Jung, S. (2015). *Reduction of permanent magnet eddy current loss in interior permanent magnet synchronous motor according to rotor design optimization.* 2015 9th International Conference on Power Electronics and ECCE Asia (ICPE-ECCE Asia), South Korea, 1712-1717.

338. Gieras, J. F. (2002). *Permanent Magnet Motor Technology: Design and Applications, Second Edition*. New York: CRC Press, 1-602.

339. Matt Hein. (2020). Demystifying BLDC motor commutation: Trap, Sine, & FOC. *TEXAS INSTRUMENTS*, Dallas, 1-49.

340. Li, M., He, J., and Demerdash, N. (2014). *A flux-weakening control approach for interior permanent magnet synchronous motors based on Z-source inverters.* 2014 IEEE Transportation Electrification Conference and Expo (ITEC), Detroit, 1-6.

341. NXP Semiconductors. (2018). S12zvc256 basic training. *NXP*, Eindhoven, 4-6.

342. Fisher, P. (2014). *High performance brushless DC motor control*, Bachelor Thesis, CQ University Australia School of Engineering &Technology, Norman Gardens, 1-105.

343. Giri, F. (2013). *AC electric motors control: advanced design techniques and applications*. New York: Wiley, 1-574.

344. Krishnan, R. (2009). *Permanent Magnet Synchronous and Brushless DC Motor Drives*. New York: CRC Press, 1-588.

345. Bida, V. M., Samokhvalov, D. V., and Al-Mahturi, F. S. (2018). *PMSM vector control techniques - a survey*. Proceedings of the IEEE Conference of Russian Young Researchers in Electrical and Electronic Engineering (EICONRUS 2018), Moscow, 577-581.

346. Melexis Inspired Engineering. (2018). General information for Melexis Latch & Switch sensors. *MELEXIS*, Flandre Orientale, 1-26.

347. Glumineau, A. and Morales, J. D. L. (2015). *Sensorless AC electric motor control: robust advanced design techniques and applications*. New York: Springer, 1-258.

348. Shen, J. X., Zhu, Z. Q., and Howe, D. (2004). Sensorless flux-weakening control of permanent-magnet brushless machines using third harmonic back EMF. *IEEE Transactions on Industry Applications,* 40(6), 1629-1636.

349. Shen, J. X. and Iwasaki, S. (2006). Sensorless control of ultrahigh-speed PM brushless motor using PLL and third harmonic back EMF. *IEEE Transactions on Industrial Electronics*, 53(2), 421-428.

350. Gamazo-Real, J. C., Vazquez-Sanchez, E., and Gomez-Gil, J. (2010). Position and speed control of brushless DC motors using sensorless techniques and application trends. *Sensors (Basel)*, 10(7), 6901-47.

351. Kronberg, A. (2012). *Design and simulation of field oriented control and direct torque control for a permanent magnet synchronous motor with positive saliency*, Examensarbete, Uppsala University Department of Electricity, Uppsala, 1-66.

352. Microchip. (2018). AN2757: Sensored (encoder-based) field oriented control of three-phase permanent magnet synchronous motor (PMSM). *MICROCHIP*, Arizona, 1-27.

353. Morales, D. A. (2014). *Motor controller simulation and embedded implementation for a blood pump*, M.Sc. Thesis, Queensland University of Technology, Brisbane City, 1-120.

354. Saxena, S. (2020). *Impedance network based advanced boost converter with energy storage capability for light electric vehicle applications*, M.Sc. Thesis, University of Michigan-Dearborn Automotive Systems Engineering, Michigan, 1-45.

355. Peddapelli, S. K. (2014). *Recent advances in pulse width modulation techniques and multilevel inverters.* World Academy of Science, Engineering and Technology International Journal of Electrical and Computer Engineering, Indonesia, 1-9.

356. Gaikwad, V., Mutha, S., Mundhe, R., Sapar, O., and Chinchole, T. (2016). *Survey of PWM techniques for solar inverter.* 2016 International Conference on Global Trends in Signal Processing, Information Computing and Communication (ICGTSPICC), United States, 501-504.

357. Gajula, U. and Eragamreddy, G. (2020). Multicarrier PWM strategies for hybrid symmetrical multilevel inverter with reduced switch count. *International Journal of Advanced Technology and Engineering Exploration*, 9, 2249-8958.

358. Al-Dawoodi, H. H. T. (2023). *Field oriented control of induction motor by metaheuristic methods*, M.Sc. Thesis, Karabuk University Department of Electrical and Electronics Engineering, Karabuk, 1-76.

359. Şahin, İ. (2010). *Measurement of brushless dc motor characteristics and parameters and brushless dc motor design*, M.Sc. Thesis, Middle East Technical University Electrical and Electronics Engineering, Ankara, 1-219.

360. Hanselman, D. C. (2003). *Brushless permanent magnet motor design*. New York: The Writers' Collective, 1-411.

361. Jamali Fard, A. and Mirsalim, M. (2022). Proposing a sequential iterative method based on a per-unit model for rotor shape optimization in permanent magnet assisted synchronous reluctance motors. *COMPEL - The International Journal for Computation and Mathematics in Electrical and Electronic Engineering*, 41(5), 1826-1848.

362. Boldea, I. and Tutelea, L. (2009). *Electric Machines: Steady State, Transients, and Design with MATLAB*. New York: CRC Press, 1-800.

363. Ali Jamali Fard. (2022). Introductory course on design of BLDC motors. *COMPROGEXPERT*, Tahran, 1-86.

364. Bianchi, N. (2005). *Electrical machine analysis using finite elements*. New York: Taylor & Francis, 1-298.

365. Ali Jamali Fard. (2021). Introductory course on design of V Type IPM motors. *COMPROGEXPERT*, Tahran, 1-171.

366. Emetor Glossary. (2022). Winding factor. *EMETOR*, Vasteras, 1-2.

367. Gill, R. and Andrea, R. D. (2017). *Propeller thrust and drag in forward flight.* 2017 IEEE Conference on Control Technology and Applications (CCTA), Hawaii, 73-79.

368. Burgers, P. (2019). A thrust equation treats propellers and rotors as aerodynamic cycles and calculates their thrust without resorting to the blade element method. *International Journal of Aviation, Aeronautics, and Aerospace*, 1-22.

369. Ansys Electronics. (2020). Maxwell help: Optimizations. Release 20.1, *ANSYS*, Canonsburg, 2260-2400.

370. Siemens Simcenter. (2021). FLOEFD help. Release 2021.2, *SIEMENS*, Oregon, 70-230.

371. Niguchi, N. and Hirata, K. (2012). Cogging torque analysis of magnetic gear. *IEEE Transactions on Industrial Electronics*, 59(5), 2189-2197.

372. Zaytoon, H., Abdel-Khalik, A. S., Ahmed, S., and Massoud, A. (2015). *Cogging torque reduction of axial magnetic gearbox using pole pairing technique*. IEEE International Conference on Industrial Technology (ICIT 2015), Seville, 652-657.

373. Wang Yu, L., Liu Pin, K., Wu, J., and Ding, H. (2008). near-optimal design and 3-D finite element analysis of multiple sets of radial magnetic couplings. *IEEE Transactions on Magnetics*, 44(12), 4747-4753.

374. Jian, L., Xu, G., Song, J., Xue, H., Zhao, D., and Liang, J. (2011). Optimum design for improving modulating-effect of coaxial magnetic gear using response surface methodology and genetic algorithm. *Progress In Electromagnetics Research*, 116, 297-312.

375. Ansys Electronics. (2020). Maxwell help: Core loss coefficients. Release 20.1, *ANSYS*, Canonsburg, 906-908.

376. Egorov, D., Petrov, I., Pyrhonen, J. J., Link, J., Stern, R., Sergeant, P., and Sarlioglu, B. (2022). Hysteresis loss in NdFeB permanent magnets in a permanent magnet synchronous machine. *IEEE Transactions on Industrial Electronics*, 69(1), 121-129.

377. Ouamara, D. and Dubas, F. (2019). Permanent-magnet eddy-current losses: A global revision of calculation and analysis. *Mathematical and Computational Applications,* 24(3), 1-18.

378. Zhao, W., Wang, X., Gerada, C., Zhang, H., Liu, C., and Wang, Y. (2018). Multi-physics and multi-objective optimization of a high speed PMSM for high performance applications. *IEEE Transactions on Magnetics,* 54(11), 1-5.

379. Varaticeanu, B. D., Minciunescu, P., and Fodorean, D. (2014). Mechanical design and analysis of a permanent magnet rotors used in high-speed synchronous motor. *Electrotehnica, Electronica, Automatica,* 62(1), 1-9.

380. Zhang, F., Du, G., Wang, T., Liu, G., and Cao, W. (2015). Rotor retaining sleeve design for a 1.12-MW high-speed PM machine. *IEEE Transactions on Industry Applications,* 51(5), 3675-3685.

381. International Electrotechnical Commission, *Rotating Electrical Machines - Part 1: Rating and Performance*, *IEC 60034-1*, 2011.

382. Kim, T.-W. and Chang, J.-H. (2013). Effective step-skew method for cogging torque reduction in surface-mounted permanent magnet synchronous motor. *Journal of the Korean Physical Society*, 63(3), 288-292.

383. Cheng, Z. Y., Cao, Z., Hwang, J. T., and Mi, C. S. (2023). A novel single-turn permanent magnet synchronous machine for electric aircraft. *Energies,* 16(3), 1-15.

384. Wu, J., Wang, J., Gan, C., Sun, Q., and Kong, W. (2018). Efficiency optimization of PMSM drives using field-circuit coupled FEM for EV/HEV applications. *IEEE Access,* 6, 15192-15201.

385. Hsiao, C.-Y., Yeh, S.-N., and Hwang, J.-C. (2011). A novel cogging torque simulation method for permanent-magnet synchronous machines. *Energies,* 4(12), 2166-2179.

386. Zhao, W., Lipo, T. A., and Kwon, B.-I. (2015). Torque pulsation minimization in spoke-type interior permanent magnet motors with skewing and sinusoidal permanent magnet configurations. *IEEE Transactions on Magnetics,* 51(11), 1-4.

387. Ayari, E., Hadouaj, S. E., and Ghedira, K. (2012). *Serial and Parallel Robot Manipulators - Kinematics, Dynamics, Control and Optimization*. IntechOpen, 1-470.

388. Zhao, N., Zhu, Z. Q., and Liu, W. (2011). Rotor eddy current loss calculation and thermal analysis of permanent magnet motor and generator. *IEEE Transactions on Magnetics,* 47(10), 4199-4202.

389. Chin, Y.-K. R. (2004). *A permanent magnet synchronous motor for an electric vehicle - design analysis*, degree of Technical Licentiate, Royal Institute of Technology School of Computer Science, Electrical Engineering and Engineering Physics, Stockholm, 1-95.

390. Hall, S. (2015). *Dynamic testing of permanent magnet synchronous machines*, Licentiate Thesis, Lund University Department of Biomedical Engineering, Lund, 1-134.

391. Internet: UMS. (2023). Web: https://www.umskalite.com, Last Date Access: 22.06.2023.

392. Ramsden, E. (2006). *Hall-effect sensors: Theory and applications*. New York: Newnes, 1-265.

393. Armando, E., Rubino, S., Boglietti, A., Carpaneto, E., Musumeci, S., and Martinello, D. (2021). A test procedure to evaluate magnets thermal time constant of permanent magnet machines. *IEEE Transactions on Industry Applications,* 57(5), 4694-4706.

394. Cerovsky, Z. and Lev, M. (2017). Permanent magnet synchronous machine parameters identification for load characteristics calculation. *Automatika,* 56(2), 217-225.

395. Dambrauskas, K., Vanagas, J., Zimnickas, T., Kalvaitis, A., and Ažubalis, M. (2020). A method for efficiency determination of permanent magnet synchronous motor. *Energies,* 13(4), 1-15.

396. Karmaker, H. (2012). *Report on IEEE standard working group P1812 on guide for testing permanent magnet machines.* 2012 IEEE Energy Conversion Congress and Exposition (ECCE), North Carolina, 2326-2333.

397. Novak, M. and Novak, J. (2018). *Test setup with a permanent magnet synchronous machine for efficiency maps of an electric vehicle.* 2018 Xiii International Conference on Electrical Machines (Icem), Alexandroupoli, 1698-1703.

398. Swanke, J., Zeng, H., Bobba, D., Jahns, T. M., and Sarlioglu, B. (2021). *Design and testing of a modular high-speed permanent-magnet machine for aerospace propulsion.* IEEE International Electric Machines & Drives Conference (IEMDC 2021), Hartford, 1-8.

399. Dahham, R. Y., Wei, H. Q., and Pan, J. Y. (2022). Improving thermal efficiency of internal combustion engines: Recent progress and remaining challenges. *Energies,* 15(17), 1-60.

400. Micheli, D., Clemente, S., and Taccani, R. (2022). Chapter 2 - Energy Systems on Board Ships. In Baldi, Coraddu and Mondejar. *Sustainable Energy Systems on Ships*. Elsevier, s. 27-78.

401. Ali, K., Amna, R., and Ali, M. I. H. (2023). Numerical study to improve the combustion and thermal efficiencies of off-gas/synthesis gas-fueled HCCI-engine at different loads: Piston-shape and crevice design. *Case Studies in Thermal Engineering,* 45, 1-15.

APPENDIX

ANNEX-1. Winding scheme

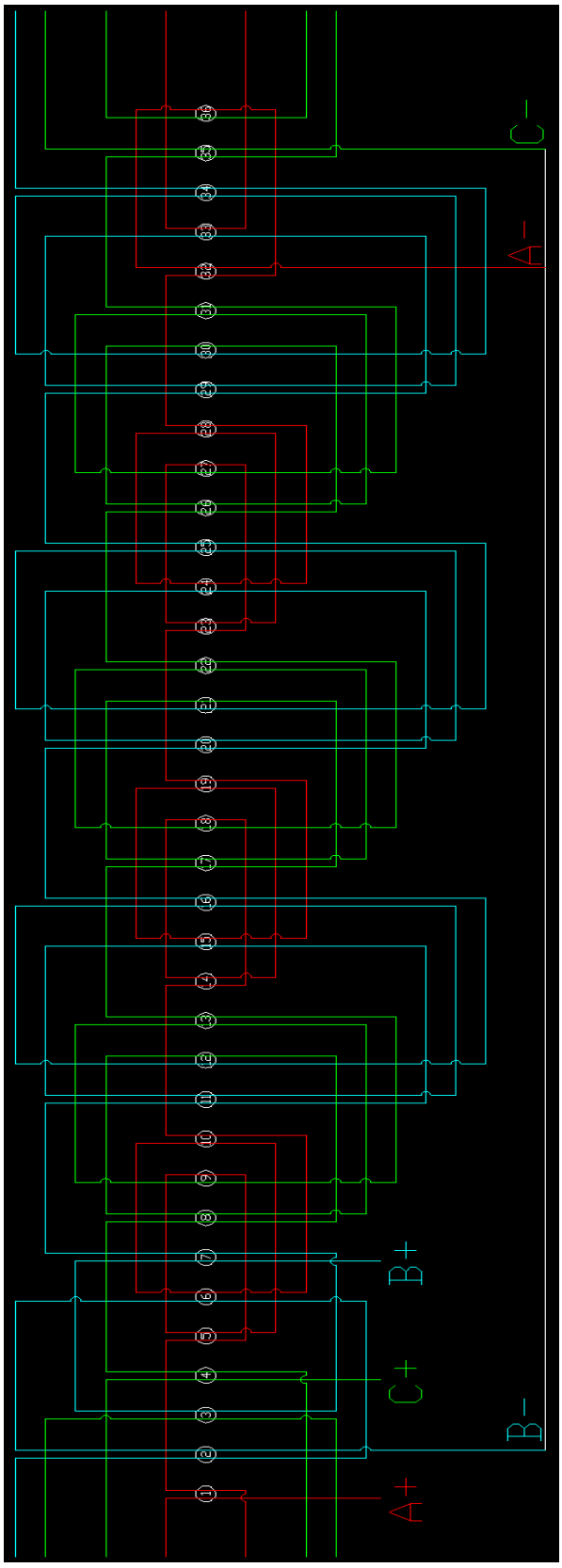


Figure 1.1. Winding scheme of the 36 slot/8 pole Starter/Generator stages of DCSG model

ANNEX-2. Industrial Starter/Generators



Figure 1.2. Review of the industrial Starter/Generators (a) DCSG model (b) DLE128HD hybrid (c) Power4Flight B29i (d) Skurka DC brushless (e) Honeywell DC brushed (f) Safran PMAC (g) Hartzell PMAC (h) Sullivan out-runner



Gazili olmak ayrıcalıktır